Ministry of Education and Science of Ukraine

Ternopil Ivan Puluj National Technical University (Ukraine)

National Academy of Sciences of Ukraine; Institute of Electrodynamics (Ukraine)

National Technical University «Kharkiv Polytechnic Insti-tute» (Ukraine)

Institute of Ionosphere of NAS and MES of Ukraine (Ukraine)

University of California, Irvine (USA)

University of Žilina (Slovakia)

Slovak University of Technology in Bratislava (Slovakia)

Technical University of Košice (Slovakia)

Lublin University of Technology (Poland)

West Pomeranian University of Technology in Szczecin (Poland)

O. M. Beketov National University of Urban Economy in Kharkiv (Ukraine)

V.E. Lashkaryov Institute of Semiconductor Physics NAS of Ukraine (Ukraine)

PROCEEDINGS of INTERNATIONAL CONFERENCE ADVANCED APPLIED ENERGY and INFORMATION TECHNOLOGIES 2021

Edited by: Keyue SMEDLEY, Alexander ABRAMOVITZ, Frantisek DUCHON

ICAAEIT 2021

December, 15-17, 2021,Ternopil, Ukraine

ADVANCED APPLIED ENERGY and INFORMATION TECHNOLOGIES 2021. Proceedings of the International Conference (Ternopil, 15-17 of December 2021.) / Ministry of Education and Science of Ukraine, Ternopil Ivan Puluj National Technical Universtiy [and other.]. – Ternopil : TNTU, Zhytomyr : «Publishing house "Book-Druk"» LLC, 2021. – 222 c.

Title: INTERNATIONAL CONFERENCE ADVANCED APPLIED ENERGY and INFORMATION TECHNOLOGIES 2021, ICAAEIT 2021

Subtitle: December 15– 17, 2021, Ternopil, Ukraine

ISBN: 978-617-8079-60-4

Organizing Committee:

Chairman:
YASKIV Volodymyr, Prof., Dr. (Ternopil Ivan Puluj National Technical University, Ukraine)
Co-Chairmen:
VADIM Koval, Ph.D , Assoc. Prof. (Ternopil Ivan Puluj National Technical University, Ukraine)
Secretary:
FILIUK Yaroslav, Ph.D ,. (Ternopil Ivan Puluj National Technical University, Ukraine)
Members:
BABIUK Serhii - Ph.D , Assoc. Prof. (Ternopil Ivan Puluj National Technical University, Ukraine);
BELYAKOVA Iryna - Ph.D , Assoc. Prof. (Ternopil Ivan Puluj National Technical University, Ukraine);
HETMANYUK Volodimir - leading engineer (Ternopil Ivan Puluj National Technical University, Ukraine);
KOSTYK Liubov - Ph.D , Assoc. Prof. (Ternopil Ivan Puluj National Technical University, Ukraine);
KOTYK Maria - Assistant Lecturer (Ternopil Ivan Puluj National Technical University, U
KUZEMKO Nataliia - Ph.D , Assoc. Prof. (Ternopil Ivan Puluj National Technical University, Ukraine);
NAKONECHYI Myroslav - Ph.D , Senior Lecturer (Ternopil Ivan Puluj National Technical University, Ukraine);
OROBCHUK Bogdan Ph.D , Assoc. Prof. (Ternopil Ivan Puluj National Technical University, Ukraine);
OSADTSA Yaroslav - Ph.D , Assoc. Prof. (Ternopil Ivan Puluj National Technical University, Ukraine);
POTALITCYN Sergiy - Ph.D , Senior Lecturer (Ternopil Ivan Puluj National Technical University, Ukraine);
ROMAN Kotsiurko - Assistant Lecturer (Ternopil Ivan Puluj National Technical University, Ukraine);
SYSAK Ivan - Ph.D , Assoc. Prof. (Ternopil Ivan Puluj National Technical University, Ukraine);
VAKULENKO Oleksandr - Ph.D , Senior Lecturer (Ternopil Ivan Puluj National Technical University, Ukraine);
VIKTOR Khomyshyn - Postgraduate Student (Ternopil Ivan Puluj National Technical University, Ukraine)

CONTENTS

Cross-sectional: ELECTRICAL ENGINEERING AND POWER ELECTRONICS

ELECTROMAGNETIC INTERFERENCES IN TRANSISTOR CONVERTERS AND METHODS OF INTERFERENCES MITIGATION

V.K. Gurin[1], V.O. Pavlovskyi[1], O.M. Yurchenko[1], V.I. Senko[2]

[1]Institute of Electrodynamics of National Academy of Science of Ukraine, Prosp. Peremogy, 56, Kyiv, 03057, Ukraine. E-mail: yuon@ied.org.ua
[2]Technical University of Ukraine "Igor Sikorsky Kyiv Polytechnic Institute" , Prosp. Peremohy, 37 Kyiv, 03056, Ukraine. E-mail: ecampus@kpi.ua

Abstract: This paper describes the main types of conductive electromagnetic interference that occur in modern high-frequency transistor converters and shows methods for these interferences' mitigation.

A network interference-suppression device which makes it impossible penetration of conductive electromagnetic interference (EMI) from a consumer to a mains and back is introduced. The device also provides the complete galvanic decoupling between the power mains and the consumer. This is achieved through the introduction of an intermediate link between the consumer and the network, the link being powered by a rechargeable battery, and time separation of electrical energy between consumption and transmission cycles due to the special algorithm of charging and discharging the batteries of the consumer. It provides mutual protection of the consumer and the network from all types of conductive EMI, as well as protection of the consumer from possible electric shock.

Keywords: *galvanic decoupling, conductive electromagnetic interference, rechargeable battery.*

1. Introduction

Any electrical device that is connected to the mains is known to generate electromagnetic interference (EMI) in the mains and in the environment [1]. Among such devices, the most common EMI generators are high-frequency transistor converters [2 - 6]. EMI levels generated by such converters may exceed the maximum allowable levels regulated by world standards for electromagnetic compatibility [7, 8]. This may cause to fail the converter itself or other devices connected to the mains.

The power network itself can act as a source of conductive EMI [9], such as differential mode (DM), common mode (CM), or power line disturbances, electrical fast transients that occur due to breaks or short circuits in power lines, lightning surges, human factor, etc. Such cases of power failures can cause great material damage, lead to breakdowns in the insulation of power wires and even to electric shocks.

2. Traditional tools and methods of EMI mitigation in modern transistor converters

The main ways and means of reducing conductive noise and EMI radiation in modern **transistor** converters (TC) include circuitry and design methods of these TC. Circuitry methods include circuit solutions that provide minimum levels of its conductive noise and EMI radiation. Schemes with the so-called "hard" or "soft" switching of TC power switches are a prime example.

In the first of these methods, the switching of the switch is carried out at a full voltage applied to the switch, or during the flow of maximum power current through the switch. In the second method, switching of the switch is performed in a period of time when the voltage on the switch or the current flowing through the switch is close to zero.

Design methods of reducing conductive noise and EMI radiation include rational installation of the TC circuit from the electromagnetic capability (EMC) point of view, correct organization of the path by which the power current is returned to the power supply, proper grounding of functional units and the TC itself.

For example, an effective design means of reducing conductive noise is the correct voltage supply to the power switch from the EMC) point of view, or, in other words, minimizing the inductance of the wires that supply voltage to the switch.

The fact is that, as it was mentioned above, the voltage U_L which occurs at the ends of the conductor when switching current, is equal to:

$$U_L = L \cdot \frac{di}{dt}. \quad (1)$$

At a given change rate of current (it is determined by the switch's speed and the nature of the load), U_L is proportional to the inductance of the conductor.

It is known that the inductance of a conductor is directly proportional to its length and depends on the shape of the conductor: the maximum inductance have round conductors, the minimum inductance - flat conductors when the width of the conductor significantly exceeds its thickness.

From these properties follows another method of reducing conductive interference – under designing the TC it is necessary to place the switches as close as possible to the input voltage terminals, and connect the switches to the voltage source by not round wires, but wide and flat busbars.

For modern types of field-effect transistors and IGBT, this method of applying voltage to the power switches of the TC is the most suitable.

Along with the above methods of reducing interference from TC, power line filters (they are also being called “noise filters” and “EMI filters”) have been widely used. The properties of these filters and their disadvantages are discussed in more detail below.

In practice, in order to increase electrical safety and attenuation introduced into the CM interference at low frequencies, a power transformer which provides galvanic isolation between the primary and secondary windings is being used between the mains and the consumer. The transformer with galvanic isolation between primary and secondary electrical circuits is also being used in modern transistor voltage converters. This technical solution increases the attenuation of CM noise at low frequencies, but is not a radical solution to the problem of isolation between the grid and the consumer at high frequencies due to the parasitic capacitance between primary and secondary windings of the transformer.

3. EMI filters and their disadvantages

To reduce the levels of conductive EMI generated by devices connected to the mains, EMI filters are widely used . Such filters have to meet to a number of specific and often contradictory requirements. The filter operates at a voltage of 220/380 V, the operating current up to hundreds of A, which is being consumed by the TC from the network, flows through the filter, and the voltage drop of industrial frequency (50 or 400 Hz) at the filter terminals should not exceed several volts. At the same time, such a filter must make a large and sufficiently uniform attenuation at frequencies where the noise of the TC can disrupt the normal operation of radio receivers, control and management circuits - from tens of kHz up to tens of MHz and above.

The capacitance of EMI capacitors which are included in the "phase-to-grounded case” circuit, is also subject to mutually opposite requirements. On the one hand, the larger the capacitance, the more attenuation the EMI filter inserts in the noise from the TC at the low-frequency end of the frequency range, which is to be protected. However, this increases EMI filter’s leakage current, i.e. the current that can flow in the circuit “ungrounded filter case - ground". This current is a danger to a human when the ungrounded filter case and grounded equipment are touched by a human at the same time. Therefore, the total capacitance of the EMI filter in a circle "phase-to case” is usually limited to 0.02 - 0.05 μF. It should be noted that the leakage current of the filter reduces the electrical safety of the device that is powered through the filter. It is caused by the fact, that according to an electrical safety standard, the maximum allowable current that can pass through the human body in normal (non-emergency) mode of operation of the electrical installation should not exceed 0.3 mA - for alternating current and 1 mA - for direct current [10].

The use of EMI filters may not always be acceptable in situations where it is necessary to ensure the minimum weight and size, or ultra-low levels of EMI [11-12].

Studies have shown that the attenuation introduced by the EMI filter is limited primarily by its own and mutual parasitic parameters [13], which, in turn, does not provide complete protection against conductive EMI.

The first of the mentioned parameters mainly includes parasitic inductances of filter capacitor’s terminals and the parasitic winding capacitance of its inductor (Fig. 1).

Mutual parasitic parameters include inductive and capacitive parasitic coupling between different elements of the same filter, which reduce the attenuation of the filter for noise voltage (Fig. 2).

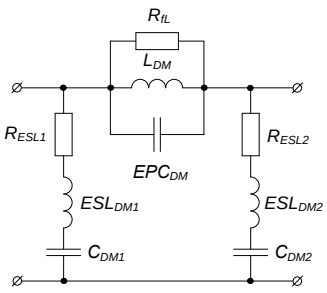

Fig. 1 Own parasitic parameters of EMI filter

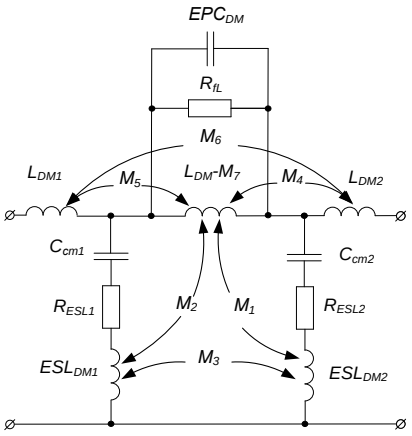

Fig. 2 Mutual parasitic parameters of EMI filter

In fig. 1 and 2: EPC_{DM} - parasitic winding capacitance of the choke; L_{DM} - choke’s inductance; $L_{DM1,2}$ – parasitic inductances of input and output conductors of the filter; R_{fL} - equivalent resistance of the choke at its resonant

frequency; R_{ESL} - equivalent resistance of the capacitor at its resonant frequency; ESL_{DM} - parasitic inductance of capacitor's terminals; M_1,M_2 - inductive couplings between parasitic inductances of capacitors terminals and choke's inductance; M_3 – inductive coupling between parasitic inductances of capacitors terminals; M_4 – inductive coupling between parasitic inductances of output conductor of the filter and choke's inductance; M_5 – inductive coupling between parasitic inductances of input conductor of the filter and choke's inductance; M_6 – inductive coupling between parasitic inductances of input and output conductors of the filter; M_7 – inductive coupling between ground plane and filter's choke.

In fig.3 it is showed curves of the transfer factor (in dB) of the filter for CM noise in the frequency range of 100 kHz… 30 MHz [14].

Line 1 shows the transfer factor of the filter with ideal capacitors and an inductor; line 2 - the result of modeling taking into account its own parasitic parameters in the inductor of the noise filter; line 3 - the result of measurements of the transfer factor of the real filter for CM noise.

Fig. 4 shows graphs of the filter transfer factor for DM noise.

In these graphs, line 1 shows the transfer factor of the filter with ideal capacitors and an inductor; line 2 - the result of modeling, taking into account its own parasitic parameters; line 3 - the results of measurements of the transfer coefficient of the filter for DM noise.

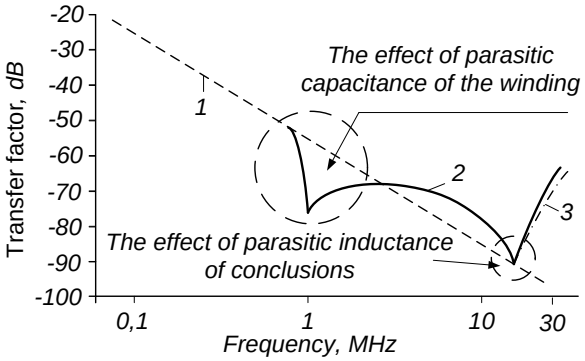

Fig. 3.Transmission ratio graphs CM noises

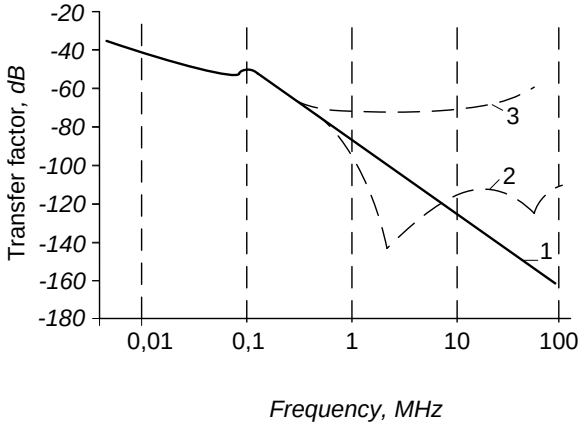

Fig. 4. Graphs of the filter transfer factor for DM noises

In practice, there were situations when the EMI filter itself turned into a source of EMI [15]; such a transformation created additional problems in the design of the filter and its functioning.

Ensuring the permissible level of EMI with the aid of RFI filters is being complicated by the fact that in the absence of RFI filters' grounding the filter can cause the tripping of differential relays [16], and in the relays absence - can cause electric shock or even death.

4. The role of parasitic parameters of transistor converters in generation and propagation of conductive EMI

Fig. 5 schematically shows a power transistor with a collector or drain isolated from the radiator housing (by means of a thermally conductive electrical insulating gasket); this design is found in almost every transistor converter. This technical solution provides cooling of the power transistor, but at the same time it forms a parasitic capacitance between the collector or drain of the transistor and ground. A design option is also possible (in high-frequency converters of low and medium power), when the power transistor is installed on a radiator that has no electrical connection with the housing.

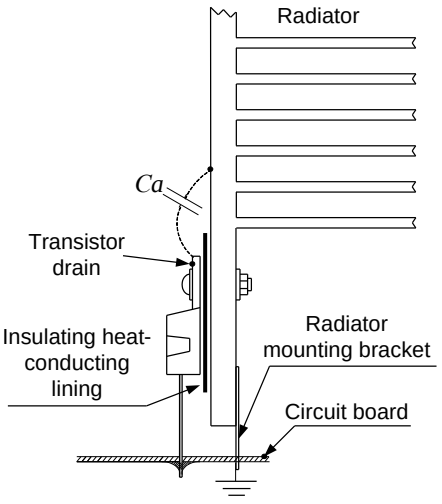

Fig. 5 Power transistor with grounded radiator

The parasitic capacitance C_a consists of two parts. The first part is the parasitic capacitance between the transistor drain and ground, and the second part is the capacitance between the PCB tracks and ground. C_b - includes: parasitic capacitance between the cathode of the diode D_b and ground, as well as parasitic capacitance between consumer and ground. C_c - includes the parasitic capacitance between the printed circuit board and the "ground", the parasitic capacitance between load and the grounded housing. Parasitic capacitance C_a, is one of the main reasons for the formation of a path for CM EMI current.

EMIs can penetrate into switch mode power supply (SMPS) through parasitic capacitances that are formed between the power

contacts of the SMPS and its grounded housing. A simplified diagram of one of these converters is shown in fig.6.

Conductive EMI is divided into two separate subtypes: DM EMI, which acts between the supply and return lines, and CM EMI, which acts between each supply's power line and ground.

The paths of DM EMI and CM EMI at the input of the power supply in a simplified form are shown in fig.7 which also shows the connecting of the LISN network with a spectrum analyzer as an EMI meter, and SMPS.

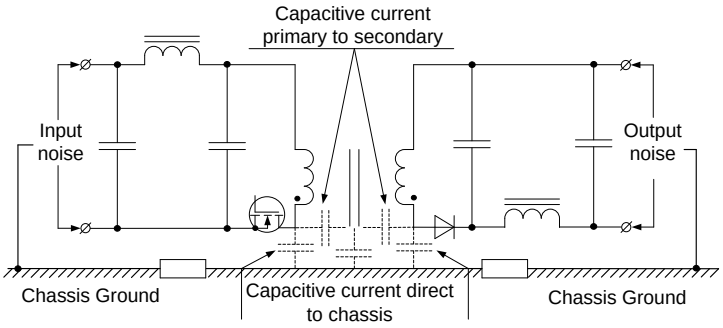

Fig. 6 (CM) the interference is caused by transients through the parasitic capacitor

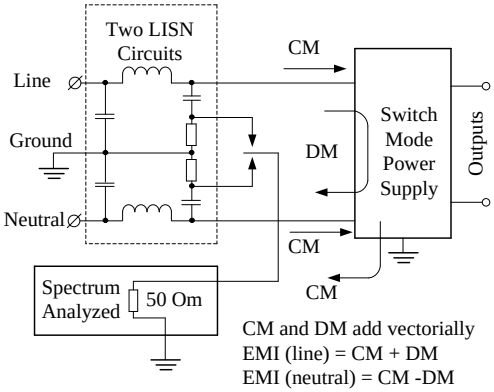

Fig. 7 (CM) and (DM) currents at the input of the power supply system

Modern transistor converters often use galvanic isolation from the network, but this solution does not provide protection against the mutual influence of EMI between the network and the consumer due to the structural interwinding capacitance in the transformer (fig. 6), which plays a major role in transmission high-frequency EMI from the consumer into the mains and vice versa.

Therefore, in practice, a special shielding winding is used to protect the EMI through the parasitic interwinding capacitance of the power transformer (fig. 6), but even such a technical solution does not provide full protection against mutual penetration of the EMI between the network and the consumer.

EMI filters also cannot provide galvanic isolation between the mains and the consumer, because functionally they are a low-pass filter in which the choke winding is connected between the mains and the consumer (fig. 1). In addition, due to parasitic parameters in the EMI filters elements they also cannot provide a complete EMI mitigation at high frequencies.

To radically solve this problem, more sophisticated methods are needed that allow almost complete elimination of EMI while providing a galvanic isolation between the grid and the consumer. One of this methods is described below.

5. An innovative method of providing a complete decoupling between the power mains and the consumer

The proposed technical solution was based on developing an anti-interference device with relay galvanic isolation from the mains, which eliminates direct electrical contact of the network with the consumer, which, in turn, will provide a high level of protection against all types of conductive EMI. The concept of relay galvanic isolation means the absence of conductive connection of the network with the consumer, which is provided by the rupture of the relay contact. This technical solution will protect the consumer from overvoltage and accidents in the grid that may be caused by natural or human factors.

Under the functioning of the device, the consumer which is connected to the mains must continuously receive electricity from the mains and at the same time be protected from the conductive EMI of all types that can be generated by this mains.

This functionality can be achieved due to the lack of conductive connection between the mains and the consumer, and this makes it possible to achieve a high level of protection against EMI and ensure a high level of electrical safety.

The problem is solved by the fact that to ensure a high and continuous level of protection against conductive EMI in the anti-interference device, a complete galvanic isolation is used fig.8.

The complete galvanic isolation is achieved with the aid of controlled switches, which interrupt the path for conductive EMI by the algorithm of the control circuit. To ensure the smooth operation of the consumer, electrical energy storage devices - rechargeable batteries are used.

Description of the anti-interference device components and principle of their operation.

The functional scheme of the proposed anti-interference device fig.8 includes: two-channel charger based on AC/DC converter, which is powered by a standard power supply V_1 - 220V 50Hz; switches K_1 - K_8, which are controlled by the control circuit, which generates control pulses to switch these switches according to the programmed algorithm.

Switch pairs (K_1K_2; K_3K_4; K_5K_6; K_7K_8) are switched synchronously.

The central part of fig. 8 shows the connection of two batteries (battery 1 and battery 2) which are connected to the AC/DC converter - charger, and to the DC/DC converter through the controlled switching switches K_1-K_8. Battery 1 and battery 2 allow to provide autonomous transfer of energy to the consumer.

The switch management scheme controls the charge-discharge cycles of the battery1 and battery2 in such a way as to provide galvanic isolation of the grid from the consumer at any time and at the same time maintains a stable transmission of energy from the grid to the consumer.

DC/ DC converter includes an external regulator R_1 which adjusts the output voltage level required by the consumer.

An output voltage stabilizer is connected to the DC/DC converter, the function of which is to set the output voltage level V_2. Diodes D_1 and D_2 protect against the interaction of battery 1 on battery 2 when they are connected in parallel to the consumer.

From the diagram shown in fig. 8 it can be seen that the anti-interference device is structurally similar to UPS (uninterruptible power supply). The main difference is that the control algorithm of switches provides the complete galvanic isolation between the network and the consumer due to physical ruption of the conductive path between them which is formed by opening the switches in a proper moment of time.

The operation of the anti-interference device fig.8 is to alternately reconnect the batteries between the mains and the consumer according to the algorithm issued by the control circuit (the switch management scheme). This control algorithm allows the charge and discharge cycles of the batteries to be separated in time [17], so that when charging one battery from the mains, the other battery is completely galvanically isolated from the first one, supplying accumulated energy to the consumer.

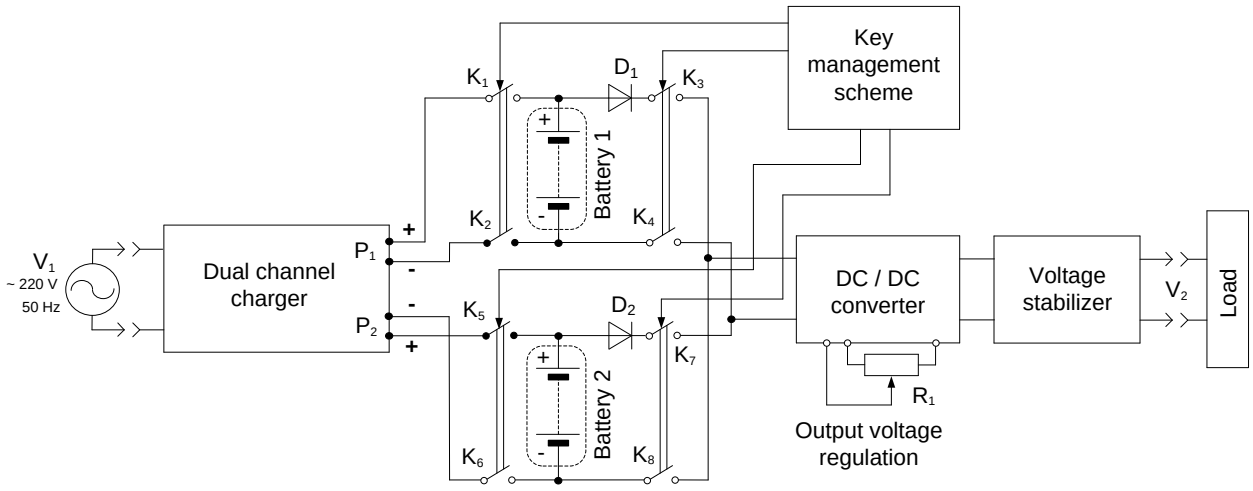

Fig.8 Anti-interference device with complete galvanic isolation

Rechargeable batteries (battery1, battery2) fig.8 are charged independently of each other, and the process of charging is controlled by the switch management scheme. Battery1 and battery2 alternately are being switched between the charger and the consumer by controlled switches K_1 - K_8 to provide galvanic isolation between the mains and the consumer at any time, providing a stable and continuous supplying the consumer with electrical energy while charging the battery which needs recharging.

Fig. 9 shows the switching modes of the eight switches K_1-K_8, which are controlled by the control circuit.

The duration of batteries' charge and discharge is recorded by charge-discharge sensors of battery 1 and 2, and transmitted to the switch control circuit. It depends on consumer's power and is being regulated by the algorithm of switches K_1 - K_8 switching. Charge-discharge of battery 1 and 2 occurs according to the algorithms presented below.

At the initial moment of time, when the anti-interference device is not connected to the mains, all switches K_1 - K_8 are in the open state, thus ensuring a minimum discharge of the battery 1 and 2 in the standby mode.

Fig. 9 (a) shows mode I at the first moment in time, when the anti-interference device is connected to the mains, the control circuit (switch management scheme) generates the control signal to close the switches K_1; K_2; K_5; K_6. In this mode, it is being provided the simultaneous charging of two parallel and independently connected batteries at least up to 95% of the full battery charge, the switches K_3; K_4; K_7; K_8 remaining open.

During the period of charging the battery 1 and 2 - (Battery charging mode) the consumer is disconnected from them and does not receive energy until one of the batteries is charged and ready to give out its energy.

There is an inter-commutation pause after the mode I. This is a short-term mode in which one of the batteries is disconnected from the charger before connecting the battery to the consumer. This mode provides the complete galvanic isolation of the consumer from the mains during the time of switching the battery between the consumer and the charger.

After the battery1 or 2 is charged to at least 95% of their capacity, the battery that has reached the 95% charge level faster is the first to be disconnected from the charger and connected to the consumer.

Figure 9 (b) shows mode II for the situation when the battery 1 is first charged. In this mode, the switches K_1 and K_2 are being opened, and after them the switches K_3 and K_4 are closed and the battery 1 begins to give the accumulated energy to the consumer.

The battery gives its energy until discharged to 5% of the battery capacity, then the batteries are reconnected (switches K_5; K_6 - open, and K_7; K_8 - close) and the consumer begins to receive energy from the battery 2. This mode allows continuous energy transfer to the consumer while providing the complete galvanic isolation from the mains at the time of switches switching.

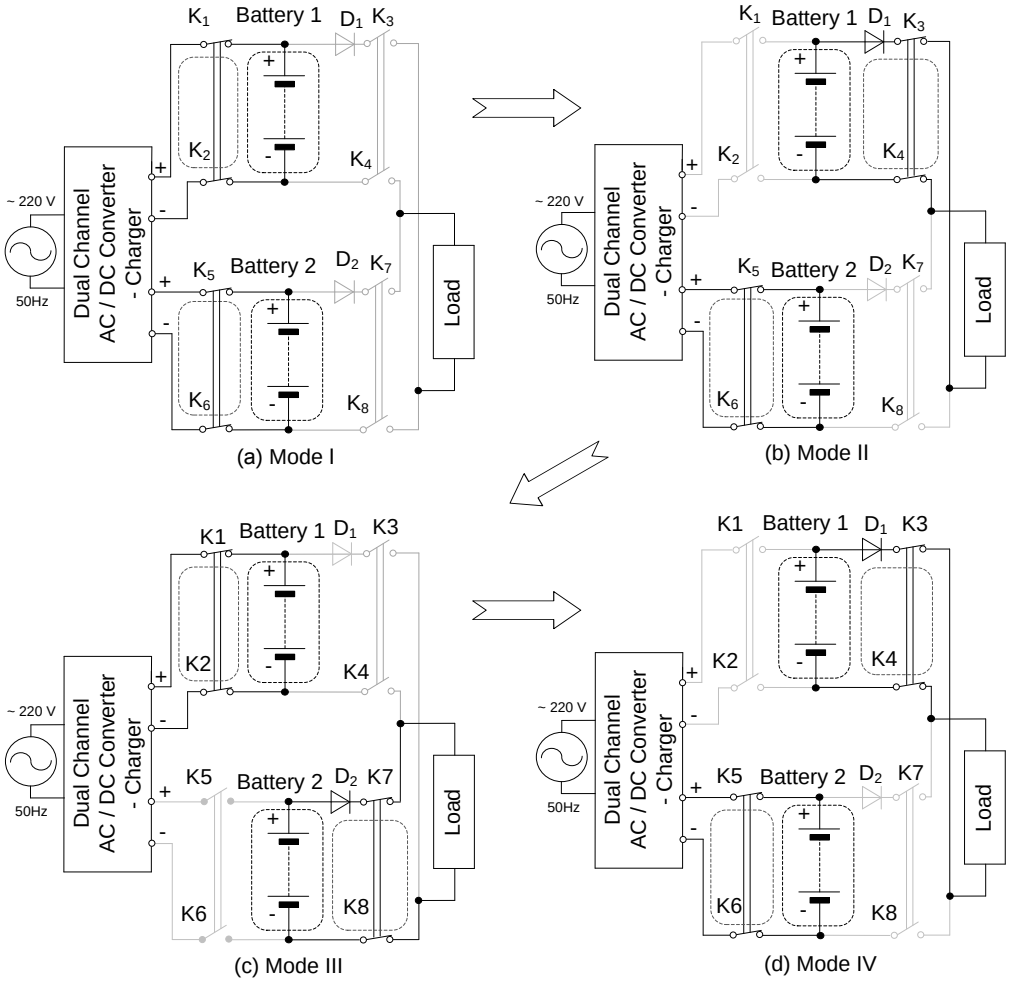

Fig.9 Description of algorithms for controlled switches.

Fig. 9 (c) describes mode III, during which the switches K_1; K_2; K_7; K_8 are closed, and switches K_3; K_4; K_5; K_6 - opened. In this mode, the battery1 is connected to the charger, and the battery2 gives the stored energy to the consumer until discharged to 5% of battery capacity.

After that another mode of inter- commutation pause begins, which is activated before connecting the battery 2 to the charger and the battery 1 to the consumer. In this mode the switches K_1; K_2; K_5; K_6; K_7; K_8 are open, and K_3; K_4; - closed. It allows to provide the complete galvanic isolation between the mains and the consumer at the time of switching the switches between the batteries.

The next mode IV (Fig. 9 (d)), in which the switches K_1; K_2; K_7; K_8 are opened and switches K_3; K_4; K_5; R_6 - closed. In this mode power is transferred again from the battery1 to the consumer, and the battery 2 is being charged from the AC/DC charger connected to the mains.

Thus, the full charge-discharge cycle of battery1 and battery 2 between the mains and the consumer is realized.

Conclusions

Due to use of the proposed anti-interference device, which provides the complete galvanic isolation between the mains and the consumer being connected to the mains, a new technical result is achieved compared to traditional methods of reducing conductive EMI – providing the complete protection against mutual penetration of all types of conductive interference between the main and the consumer, and ensuring a high level of electrical safety, which is

characterized by the absence of current leakage from the ungrounded housing of a device powered by the mains, to the ground.

References

1. Ott, H. W. (2009). *Electromagnetic Compatibility Engineering*. New Jersey: John Wiley & Sons, Inc.

2. Gurin, V.K. (2019). *Improving the effectiveness of noise reduction means in power supply systems with high-frequency transistor converters*. (Candidate's thesis). Institute of Electrodynamics of National Academy of Sciences of Ukraine. Kyiv: 150 p. (in Ukrainian) Available from: http://ied.org.ua/disertac/disert_Gurin.pdf

3. Xu, L., Wang, J., Illindala, M.S. (2013). *EMI Modeling and Characterization for Ultra-Fast Switching Power Circuit Based on SiC and GaN Devices.* (PhD thesis). Ohio State University. Available from: https://etd.ohiolink.edu/apexprod/rws_etd/send_file/send?accession=osu1385983252&disposition=inline

4. Lantsov, B., Eranosyan, C. (2006). Electromagnetic compatibility of switching power supplies: problems and solutions. Part I. *Power electronics*, 4-2006, 58-64. (in Russian). Available from: http://power-e.ru/pdf/2006_04_58.pdf

5. Zagorskiy, V. (2004). Electromagnetic compatibility of switching power supplies and its optimization. Part 1. *Components and technologies*. 2-2004, 30-35. (in Russian). doi:10.0000/cyberleninka.ru/article/n/elektromagnitnaya-sovmestimost-impulsnyh-istochnikov-pitaniya-i-ee-optimizatsiya-chast-1

6. Beloturov, V. (2005). Filtration and overvoltage protection modules from Vicor. *Power Electronics*. 2-2005, 104-107. (in Russian). Available from: http://powel.ru/files/library/VicorAC_DC.pdf

7. EN 55022:2014. Information technology equipment - Radio disturbance characteristics - Limits and methods of measurement.

8. IEC 61000-2-4-2002. Electromagnetic compatibility (EMC) - Part 2-4: Environment - Compatibility levels in industrial plants for low-frequency conducted disturbances.

9. Lundmark, M. (2006) *High-Frequency Noise in Power Grids, Neutral and Protective Earth*. Luleå University of Technology.

10. DSTU GOST 12.1.038:2008 "Occupational safety standards system. Electrical safety. Maximum permissible values of pickup voltages and currents".

11. Gurevich, V. (2005). Electromagnetic Terrorism: New Hazards. *Electrical Engineering and Electromechanics*. 4. 81-83.

12. Napp, A., Joosten, S., Stunder, D., Knackstedt, C., Zink, M., Bellmann, B., … Silny J. (2014) Electromagnetic interference with implantable cardioverter-defibrillators at power frequency. *Circulation*, 129, 441-450. doi: 10.1161/CIRCULATIONAHA.113.003081

13. Wang, S., Chen, R., Van Wyk, J.D. (2005). Developing Parasitic Cancellation Technologies to Improve EMI Filter Performance for Switching Mode Power Supplies. *IEEE Transactions on Electromagnetic Compatibility*, *47*(4), 921-929.

14. Gurin V.K.; Pavlovskyi V.O.; Yurchenko O.M. (2012). Self-parasitic and mutual parasitic parameters in power line filters for switching mode power supplies. *Tekhnichna Elektrodynamika*. *2012*(2), 119-120. (in Ukrainian) Available from: http://dspace.nbuv.gov.ua/bitstream/handle/123456789/62135/57-Gurvin.pdf?sequence=1

15. Pavlovskyi V.A. (1990) Power line filter as a source of noise. *Tekhnichna Elektrodynamika*, *1990*(5), 65-70. (in Russian) Available from: http://previous.techned.org.ua/index.php?option=com_content&view=article&id=907&Itemid=77

16. Li, C., Liang, J., Wang, S. (2018). Interlink Hybrid DC Circuit Breaker. *IEEE Transactions on industrial electronics*, *65*(11), 8677-8686. Available from: https://ieeexplore.ieee.org/stamp/stamp.jsp?arnumber=8304668

17. Basin, E.N. (1988). Network rectifier for secondary power supplies with increased conversion frequency. *Radiotehnika*, *1988*(4). 29-31. (in Russian)

MEASURING DEVICE FOR PHOTOVOLTAIC MODULES ELECTRICAL CHARACTERISTICS TESTING

Vadym Koval[1], Bogdan Orobchuk[2], Nataliia Kuzemko[3], Gao Lijin [4]

[1] Ternopil National Ivan Puluj Technical University, Rus'ka str. 56, 46001, Ternopil, Ukraine; koval_vp@ukr.net
[2] Ternopil National Ivan Puluj Technical University, Rus'ka str. 56, 46001, Ternopil, Ukraine; E-mail: kuna@ukr.net
[3] Ternopil National Ivan Puluj Technical University, Rus'ka str. 56, 46001, Ternopil, Ukraine;
[4]Jinan Caigao Intelligent Technology Co., Ltd., China

Abstract: There has been developed and produced a measuring device for measuring the electrical characteristics of photovoltaic modules. It has been experimentally tested. Its Volt-Ampere and Volt-Watt dependencies on its temperature and radiation spectrum have been collected. There have been made conclusions about device visible range spectrum radiation sensitivity and its effectiveness drop with temperature growth.

Keywords: Photovoltaic module, measuring device, radiation spectrum, temperature

1. Introduction

Problem description. Photovoltaic modules' high prices and low effectiveness are the main obstacles to their global implementation nowadays. The low effectiveness depends on many operational factors, the photovoltaic module's own temperature and the solar spectrum among them. The influence of the solar spectrum to the energy effectiveness of photovoltaic modules is especially noticeable in the morning and evening hours, as well as in cloudy weather conditions. High temperature effect is the most noticeable in the noon. That is why automated measuring devices development is important for production of new materials and protective glasses for photovoltaic devices. They are to correct photovoltaic devices' VA characteristic for their own temperature and the spectrum they are exposed to.

Recent researches of photovoltaic devices [1-4] are concentrated mainly on heating effect corrections [1,2,3], with their electrical characteristics being corrected manually. Still, sensitivity of photovoltaic modules to the different radiation spectrum has not been sufficiently studied, because the authors rely on their passports characteristics [4]. However, in this case the lighting characteristics of the protective coating or glazing are not taken into consideration.

The purpose of the present work is to design and produce more sensitive and accurate measuring device to measure electrical characteristics of photovoltaic module corrected for its temperature and the spectrum it is exposed to.

2. The description of measuring device

We have made a measuring device for automated measuring of the electrical characteristics of photovoltaic modules (Fig. 1) [5]. It is based on a personal computer with a built-in type SDI-ADC12-128H ADC board [6,7]. It digitizes data from current, voltage and temperature sensors. It features a PC-controlled variable active load, which reduces measurement time and enhances its accuracy. Lamp КГ 500 is the solar spectrum radiation and heating source for tested photovoltaic module. Light filters are used to change the radiation spectrum scope. After their replacement, the falling radiation energy is set at the level 1000 W /sqm, as required by the state standards.

A digital (typesetting) resistor is used as a controlled load. Its resistance can be varied widely with a small step according to a given digital signal. It uses high-precision non-induction resistors, which provide a purely active load without a reactive component [9]. The scheme of the variable resistor is shown on fig.2. Switching is done by a reed relay, which provides complete electrical insulation of the control (digital) part of the device.

The scheme operation is simple. It uses a set of series-connected resistors. The resistance value of each next one is twice as big as the previous one. It corresponds to the change of the binary control signal bits weight. Every resistor is shortened with a normally closed contact of a reed relay that is operated by a digital signal of a corresponding number. The initial resistance is zero. The lower digit control signal closes the contact of the first resistor. The number of bits and the lowest resistance in the set can be set according to the specific requirements. The relay is controlled by electronic keys (fig. 3). This version of the scheme can be used in combination with a binary forward/backward counter or with a microcontroller.

Current and voltage measuring converters. Current and voltage measuring converters were used to measure the time characteristics of physical values in electric circuits with photocells. The shunts of high accuracy non-inductive resistors were used as current measuring converters (their tolerance is within 0.1%). The resistors values were $0{,}05 \pm 0{,}0002\ \Omega$, $0{,}1 \pm 0{,}0003\ \Omega$,, $1 \pm 0{,}008\ \Omega$. Voltage drop was measured on them. These values were chosen due to the following reasons. The resistance should have the least effect on the current of the tested electrical circuit and its

voltage drop should be not more than 5 V (to meet the ADC channels input voltage requirements of Vin < < ± 5 V). These shunts were calibrated at the Ternopil Research and Production Standardization, Metrology and Certification Center, which is confirmed by calibration certificates № 60 and 61. Thus, the current measuring converters rates are 1:20, 1:10 and 1:1. Since the ADC can measure voltage within -5 V … +5 V, serial dividers realized via probes to the type HP-9258 and HP-9251 oscilloscope with division rates of 1: 100 and 1:10 respectively were used.

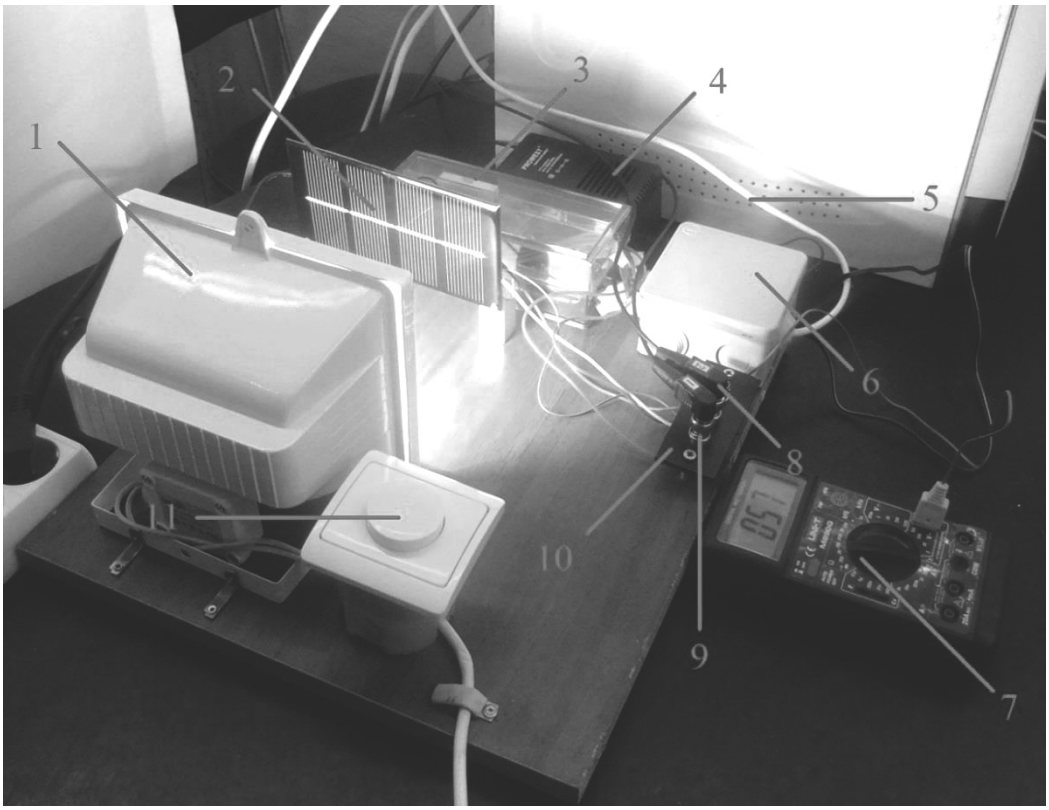

Fig.1 The device for photovoltaic modules electrical characteristics measurements

1 –lamp;
2 –photovoltaic module;
3 –variable active load unit;
4 –power supply;
5 –data bus;
6 –control unit;
7 –digital multimeter;
8 –voltage sensor output;
9 –current sensor output;
10 –temperature sensor output;
11 –light switch/dimmer

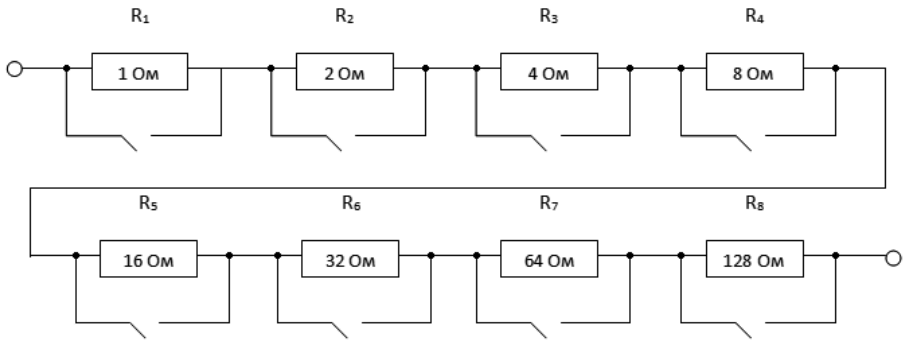

Fig.2 Variable controlled resistor

Software. The designed measuring device data were processed by the specialized and standard software. Specialized software sets the measurement algorithm, according to the method of testing, and processes the output data.

Specialized software was developed to measure and process the initial data. Microsoft Excel, MathCAD and Advanced Grapher software was used for data math processing and visual representation. The testing algorithm was realized on Delphi, because its set of commands allows addressing the PC ports directly. This fact is very important, because specialized software, in addition to the data processing, involves writing and reading data from parallel ports to which the ADC and switches are connected.

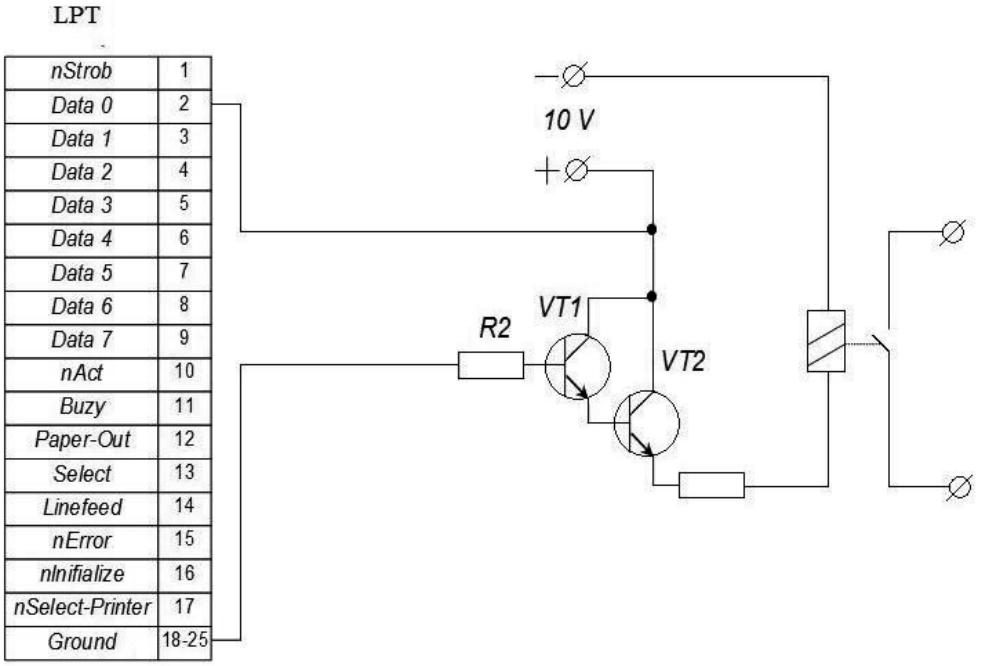

Fig. 3 Electronic switching device based on a reed switch schematic diagram

Measuring device software algorithm. The measuring device can work in two modes: manual and automatic (fig. 4). You can switch between them after power is turned on.

The temperature of the photovoltaic module (Tfm) and the max current (Imax) for the load of 0 Ω (R = 0) is measured in each mode. It is accepted by the software as a basic one, in relation to which the photovoltaic module generated current value is read out. The load resistance is increased by 1 Ω on every stage, that results in the drop of the current and the load (photovoltaic module) voltage increase that are accordingly measured at every stage. This process is carried out until the load current is less or equal to the 10% of max current (I> = 0.1 · Imax). This condition is met coming out of photovoltaic module VA characteristics. That is, the max power collected from the photovoltaic module is within Imax to 0.1 · Imax. This way, one VA dependency is collected.

In manual mode you can collect either single VA characteristic or any number of them. The latter can be done by selecting "Select next measurements?" choice box appropriate option.

In automatic mode, the photovoltaic module VA characteristics are measured as many times as necessary for the photovoltaic module transient heating to settle down. This function is performed by the operator "dTfm = <0.05 · Tfm". That means, when the temperature difference between the measurements is less or equal to 5% of the initial temperature, the measurements will stop.

The number of measurements can be adjusted by setting the time delay after the loop operator.

The measurement results are stored in the file for further processing in mathematical and tabular editors after measurement process is over.

The designed measuring device was used to test the single-crystal photovoltaic module, which is shown at fig. 1. The dependencies of the photovoltaic module generated current and power on the voltage at different temperatures (fig. 5, 6) and the radiation spectrum (fig. 7, 8) were collected. The radiation power on the surface of the photovoltaic module was controlled at the level of 1000 W / sqrm during the measurements. The radiation spectrum was changed by changing the filters. The temperature was registered by the thermocouple and monitored by the pyrometer.

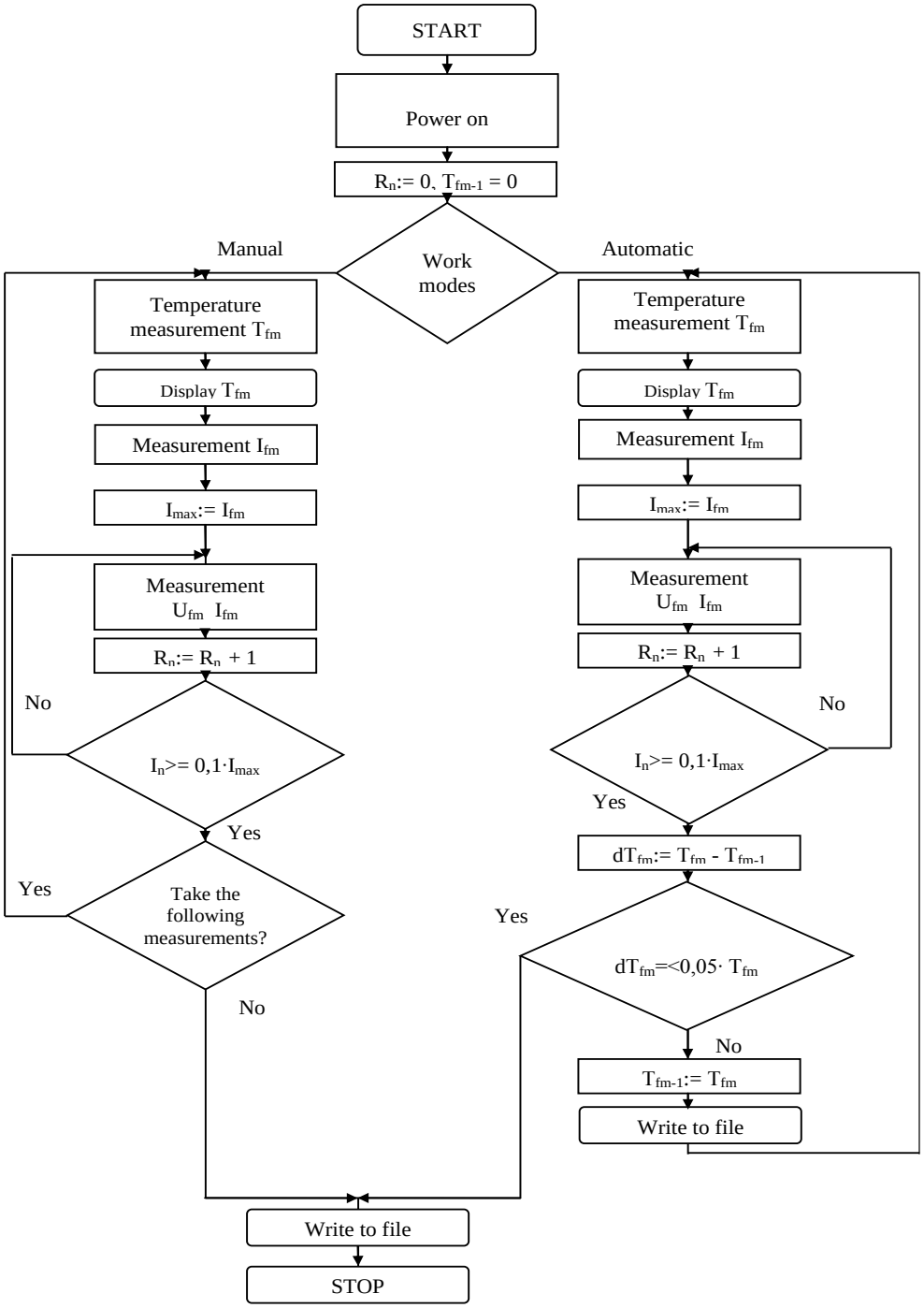

Fig. 4 Software algorithm

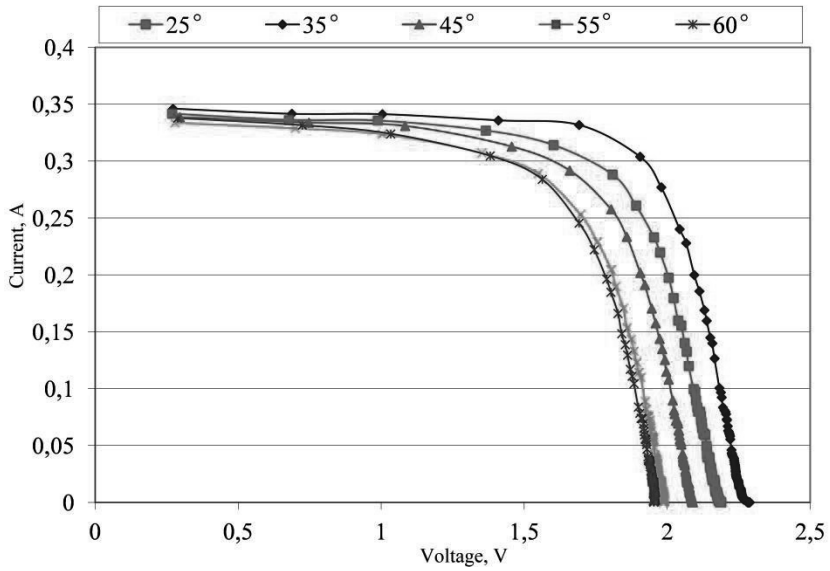

Fig. 5 The photovoltaic module generated current dependence on the voltage for different temperatures (25..60 °C)

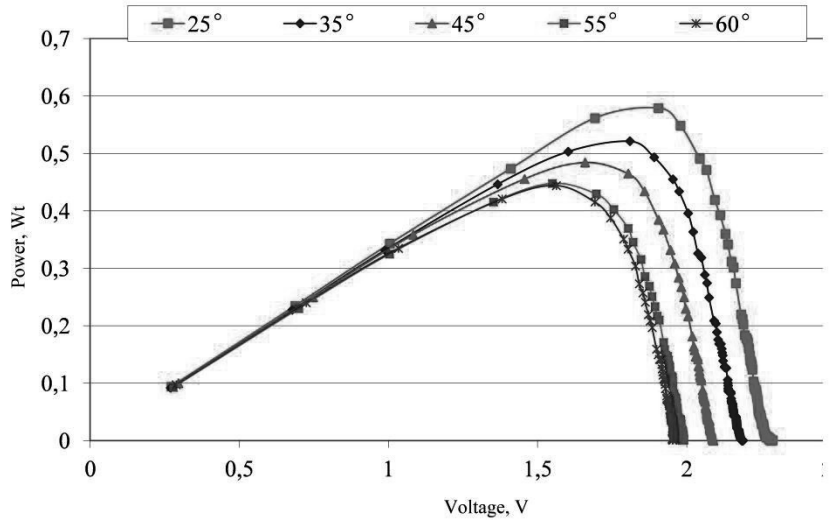

Fig. 6 The photovoltaic module generated power dependence on the voltage for different temperatures (25..60 °C)

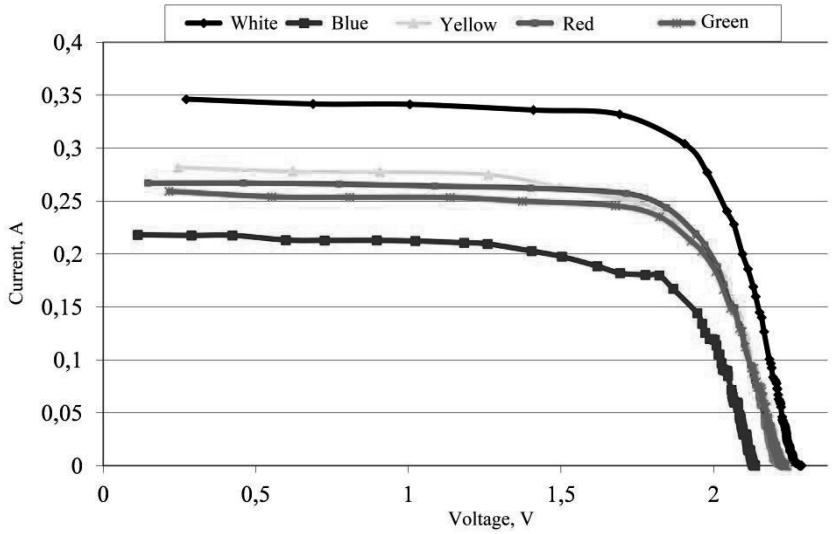

Fig. 7 The photovoltaic module generated current dependence on the voltage for different radiation spectrum

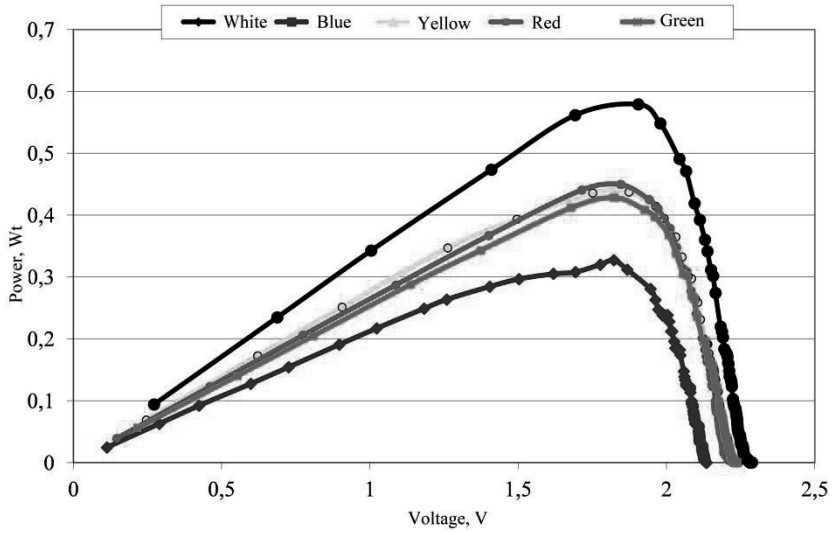

Fig. 8 The photovoltaic module generated power dependence on the voltage for different radiation spectrum

3. Conclusions

1. There has been developed and produced a measuring device for measuring the electrical characteristics of photovoltaic modules in both automatic and manual modes by use of a 16-bit ADC module personal computer.

2. Software was developed to control the operation of the measurement device and process the testing data. It allowed to automate the measurement process and has a flexible structure for the algorithm change according to the measurement techniques that allows to store and display large arrays of digital data graphically.

3. It can be stated from the obtained measurement results that when the temperature of the photovoltaic module increases from 25 to 60 ° C, the max power drops by 25%, and the green and blue lines of the spectrum are lesser absorbed than yellow and red ones.

References

1. Priyanka S. (2008). Temperature dependence of I–V characteristics and performance parameters of silicon solar cell. Solar Energy Materials and Solar Cells, 92, 1611–1616.

2 Cuce, E., Cuce, P.M. (2013). An experimental analysis of illumination intensity and temperature dependency of photovoltaic cell parameters. *Applied Energy*, 111, 374–382.

3. Libra, M., Poulek, V., Kouřím, P. (2017). Temperature changes of I-V characteristics of photovoltaic cells as a consequence of the Fermi energy level shift. *Research in agricultural engineering*, 63, 10–15.

4. Barukcic M., Hederic Z., Spoljaric Z. (2017). The estimation of I–V curves of PV panel using manufacturers' I–V. 63, 447–458.

5.Chen C.J. (2011). Physics of Solar Energy. – Willey, 352 p.

6. Tarasenko, M.H., Koval, V.P. (2006). Virtualnyi vymiriuvalnyi kompleks dlia doslidzhennia perekhidnykh protsesiv v elektrychnykh kolakh dovilnoi konfihuratsii. *Reiestratsiia, zberihannia i obrobka danykh*, 8(1), 84–91.

7. Koval V, Ivasechko R, Kozak K. (2015). Enerhetychna efektyvnist system pozytsionuvannia ploskykh soniachnykh panelei. Enerhozberezhennia. Enerhetyka. Enerhoaudyt. 2-10

8. Ime A., Koval V. (2020). Pidvyshchennia efektyvnosti soniachnykh panelei shliakhom vykorystannia vodianoho okholodzhennia. Actual problems of modern technologies: book of abstracts of the IX International scientific and technical conference of young researchers and students, 2, 80-81.

9. Andriychuk V, Filyuk F. (2017). Use of solar energy for the outdoor lighting of Ternopil. Visnyk Ternopilskoho natsionalnoho tekhnichnoho universytetu. 126-133.

10. Brownson Jeffrey R.S. (2014). Solar Energy Conversion Systems. 1st Edition. – Academic Press. Elsevier, 457 p.

ANALYSIS OF TWO-SECTION RESONANT VOLTAGE CONVERTER FOR MATRIX LED LIGHT SOURCE DRIVERS

Anatolii Lupenko[1], Ivan Sysak[2], Michal Frivaldsky [3], Taras Chomko [4]

[1]Ternopil Ivan Puluj National Technical University, Ruska str. 56, 46001, Ternopil, Ukraine; lupenkoan@gmail.com
[2]Ternopil Ivan Puluj National Technical University, Ruska str. 56, 46001, Ternopil, Ukraine; sisak.tntu@gmail.com
[3]University of Zilina, Slovakia; michal.frivaldsky@feit.uniza.sk
[4]Ternopil Ivan Puluj National Technical University, Ruska str. 56, 46001, Ternopil, Ukraine; tarasvarikap@gmail.com

Abstract: Analysis of two-section resonant DC-to-DC converter with phase power control, which is the basis of the matrix LED light source driver is carried out. Two-section converter is considered as a boundary case of the multi-section converter with one controlled section and other uncontrolled sections. Analysis is carried out by the fundamental harmonic approximation method. Analytical expressions for complex voltages and currents in the converter sections are determined, its control characteristic is obtained. It is shown that the converter power can be controlled within the range from the maximum value to zero. The problems of operation of section transistor switches in their zero-voltage switching mode is considered. The verification of the proposed analysis by means of converter simulation is carried out. The simulation results are in good agreement with the analysis results.

Keywords: *two-section resonant inverter, power, phase control, zero-voltage switching.*

1. Introduction

Matrix LED light sources are becoming widespread in modern lighting systems, due to their high light output, the ability to create powerful lighting systems, long service life, small size, ease of implementation of lighting devices for both indoor and outdoor lighting [1]. They make it possible to build high-quality dimming energy-efficient lighting devices. Matrix LED is powered by drivers - power electronics devices that form a comfortable electromagnetic environment for both matrix LED and electrical network. The main stage in the chain of power conversion in such drivers is a DC-DC converter with controlled output voltage (current) to operate the matrix LED. Therefore, the investigation of approaches to the design of such DC-DC converters is of great interest to the scientists.

2. Analysis of the available investigations

A considerable part of investigations of DC-DC converter for LED drivers is devoted to DC-DC converters with pulse width modulation (PWM) control. The driver with Buck-Boost converter which simultaneously performs the function of power factor correction of the driver is considered in paper [2]. In papers [3, 4], a Buck converters which operate in a wide range of input voltages are considered as a LED drivers. In paper [5] a Flyback converter and in paper [6] a modified SEPIC-converter are considered as well. The main disadvantage of PWM converters is relatively low efficiency due to switching losses in power switches. Since the switching losses are proportional to the switching frequency, the operating frequencies of such converters are relatively low, which restrain the improvement of their mass and volume parameters.

In papers [7, 8] drivers of LED light sources with resonant DC-DC converters are considered. Such converters have a high efficiency due to low switching losses in power switches ("soft" switching) and better electromagnetic compatibility. Thus, in paper [7] the driver is implemented on the basis of a half-bridge resonant inverter, but such driver does not provide light source dimming, which limits its use by individual lamps. In the driver [8], a full-bridge resonant inverter with wide range power control by means of changing the phase shift between the rectangular pulses of the inverter arms is used as DC-DC converters. This driver is well suited for controlling of matrix LED in high-quality lighting systems, but its maximum power may be limited by the power of transistor switches and magnetic components. In order to remove this limitation, we can apply the approach proposed in paper [9], which consists in the parallel operation of N (N - number of sections) individual half-bridge resonant inverter sections on a common load. The maximum power of such inverter is proportional to the number N of its sections. The power control in such inverter is carried out by changing the phase shifts between rectangular pulses in individual sections.

In this paper, two-section (N=2) resonant DC-DC converter with phase power control is analyzed as a boundary case of multi-section resonant inverter [9]. A similar two-section converter is considered in paper [10], but in its analysis it is assumed that phase shifts of the resonant sections are mutually opposite and identical in modulus, which complicates the application of such analysis for multi-section converters, where phase shifts in inverter sections can be arbitrary (non-identical) and independent of each other. In multi-section DC-DC converter, only one section can be taken as reference (unregulated), relatively to which the phase shifts of other (regulated) sections are controlled. Then, by switching off the "redundant" sections of multi-section converter, it is possible to realise a step-continuous phase power control which provides less ouput LED power with a smaller number of sections, making it possible to increase the efficiency of the multi-section converter at medium and low power [11].

In this paper, such approach is proposed in the analysis of two-section DC-DC converter as a boundary case of multi-section DC-DC converter with phase control, for its further development in the analysis of multi-section resonant converter with arbitrary number of sections.

The objective of the paper is to investigate the parameters and characteristics of two-section resonant DC-DC converter, made on the basis of two half-bridge resonant inverter sections, while ensuring constant operating frequency.

Statement of the problem. Two-section resonant converter is shown in Fig.1. Each of its sections consists of half-bridge inverter on transistors *VT1, VT2* (*VT3, VT4*), the which outputs are connected to parallel resonant capacitor *C* by means of coupling capacitors C_s and inductors *L* and the primary winding of transformer *T*. Half-bridge voltages at nodes A_1 and A_2 are periodic rectangular pulses (Fig. 2), shifted by controlled angle $\varphi=0\div\pi$ rad. The amplitude of these pulses is equal to the supply voltage *E*, and their duty-cycle is close to 0.5. Almost sinusoidal alternating voltage of the resonant capacitor *C* is applied to the rectifier through the transformer *T* with transformer turns ratio *n*. The rectifier output voltage is supplied to the load *R* (LED matrix) through the filter $L_\phi C_\phi$.

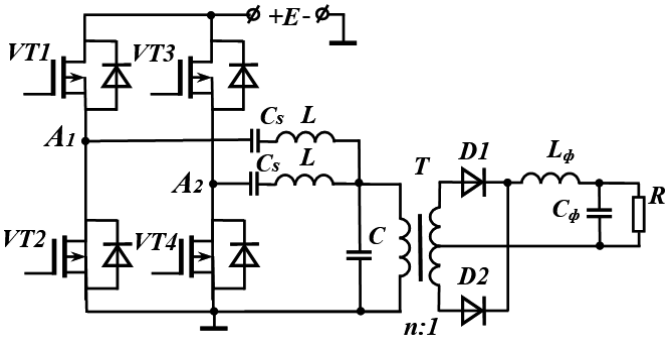

Fig. 1 Two-section resonant converter

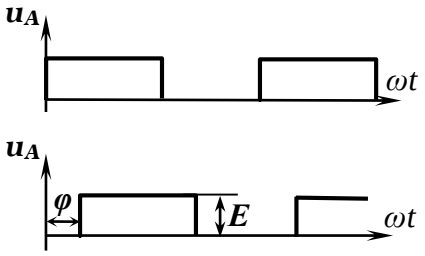

Fig. 2 Output voltages of half-bridge sections

Let us analyze the inverter by means of fundamental harmonic approximation, taking into account the filtering properties of the resonant circuits.

Statement of basic materials. The equivalent circuit of two-section inverter is shown in Fig. 3.

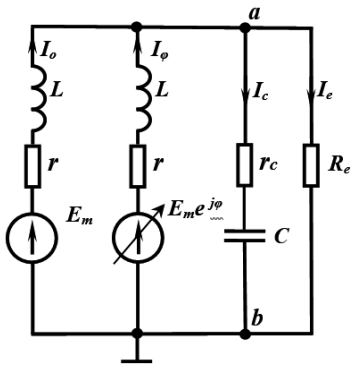

Fig. 3 Equivalent circuit of two-section inverter

In this circuit, the half-bridge square-wave sources are represented by fundamental harmonic voltage sources. The complex amplitudes of these voltage sources in reference and controlled sections are equal relatively to:

$$\underline{E}_m = \frac{2E}{\pi},\ \underline{E}_N = E_m e^{-j\varphi}. \tag{1}$$

The inverter effective load resistance R_e in Fig. 3 is the resistance of rectifier loaded by matrix LED reduced to the transformer primary winding. The effective resistance R_e of the center-tapped rectifier (Fig. 1) with ideal components is determined by the expression [12]:

$$R_e = \frac{\pi^2 n^2 R}{8}. \tag{2}$$

Switching and conductive losses in transistors and losses in inductors in each section may be taken into account by resistances *r*, and losses in the capacitor by resistance r_C (Fig. 3). These losses are considered to be significantly less than the power in the load, so these losses are neglected in order to simplify the analysis.

The parameters of the inverter and the relationship between them are shown in Table. 1: ω_0 is resonant frequency; ω is the inverter operating frequency; Z_0 is characteristic impedance of resonant tanks; Q is quality factor; Ω is relative operating frequency (the ratio of the inverter operating frequency ω to the resonant frequency ω_0).

Table 1

Inverter parameters and the relationship between them

$\omega_0 = \sqrt{\frac{2}{LC}}$	$Z_0 = \frac{2}{\omega_0 C}$
$R_e = \frac{QZ_0}{2}$	$Q = \frac{2R_e}{Z_0}$
$\omega C = \Omega \frac{2}{Z_0}$	$\omega L = \Omega Z_0$

The impedance at nodes *a*, *b* (Fig. 3) is equal to:

$$\underline{Z} = \frac{1}{j\omega C + \frac{1}{R_e}} = \frac{QZ_0}{2(1 + j\Omega Q)}. \tag{3}$$

The complex voltage amplitude at nodes *a, b* is represented by the following expression:

$$\underline{U}_{ab} = \frac{\sum_{i=1}^{2} \underline{E}_i \underline{g}_i}{\sum_{i=1}^{2} \underline{g}_i + \frac{1}{\underline{Z}}} = \frac{1}{2} \frac{E_m \frac{1}{j\Omega Z_0} + E_m e^{j\varphi} \frac{1}{j\Omega Z_0}}{\frac{1}{j\Omega Z_0} + \frac{1 + j\Omega Q}{QZ_0}} = \frac{E}{\pi} \frac{1 + \cos\varphi - j\sin\varphi}{\left(1 - \Omega^2\right) + j\frac{\Omega}{Q}}. \tag{4}$$

The maximum value of the inverter transfer function at the voltage of the first harmonic will be at the phase shift φ=*0*:

$$M_{1\max} = \frac{\left|U_{ab\max}\right|}{E_m} = \frac{1}{\sqrt{\left(1 - \Omega^2\right)^2 + \left(\frac{\Omega}{Q}\right)^2}}, \tag{5}$$

where $\left|U_{ab\max}\right|$ is the modulus of the maximum value of the complex voltage (4).

The quality factor of the resonant tank, which provides the maximum output voltage is equal to:

$$Q = \frac{M_{1\max}\Omega}{\sqrt{1 - M_{1\max}^2\left(1 - \Omega^2\right)^2}}. \tag{6}$$

The phasor of current $\underline{I}_0$ of the reference section is equal to:

$$\underline{I}_0 = \frac{E_m - \underline{U}_{ab}}{j\Omega Z_0} = \frac{2E}{\pi Z_0} \frac{\left[-\Omega + \frac{1}{2\Omega}(1 - \cos\varphi)\right] + j\left[\frac{1}{2\Omega}\sin\varphi + \frac{1}{Q}\right]}{j\left(1 - \Omega^2\right) - \frac{\Omega}{Q}}. \tag{7}$$

The phasor of current of the inverter controlled section is described by the following expression:

$$\underline{I}_{\varphi} = \frac{E_m e^{-j\varphi} - \underline{U}_{ab}}{j\Omega Z_0} = \frac{2E}{\pi Z_0} \frac{\left[\left(\frac{1}{2\Omega} - \Omega\right)\cos\varphi + \frac{1}{Q}\sin\varphi - \frac{1}{2\Omega}\right] + j\left[\left(\Omega - \frac{1}{2\Omega}\right)\sin\varphi + \frac{1}{Q}\cos\varphi\right]}{j\left(1-\Omega^2\right) - \frac{\Omega}{Q}}. \quad (8)$$

The phasor of current I_c of the resonant capacitor is represented by the expression:

$$\underline{I}_c = j\frac{2\Omega}{Z_0}\underline{U}_{ab} = \frac{2E}{\pi Z_0}\Omega \frac{\sin\varphi + j(1+\cos\varphi)}{j\left(1-\Omega^2\right) - \frac{\Omega}{Q}}. \quad (9)$$

The phasor of inverter output current (in effective resistance R_e) is equal to:

$$\underline{I}_e = \frac{\underline{U}_{ab}}{R_e} = \frac{2E}{\pi Q Z_0} \frac{1+\cos\varphi - j\sin\varphi}{j\left(1-\Omega^2\right) - \frac{\Omega}{Q}}. \quad (10)$$

Using expressions (7 ÷ 10) the dependences of normalized amplitudes of the currents I_c, I_0, I_φ, I_e (reduced to factor $2E/\pi Z_0$) as a function of a phase shift are calculated and shown in Fig. 4. The inverter parameters are Ω=1.08 and Q=2.7.

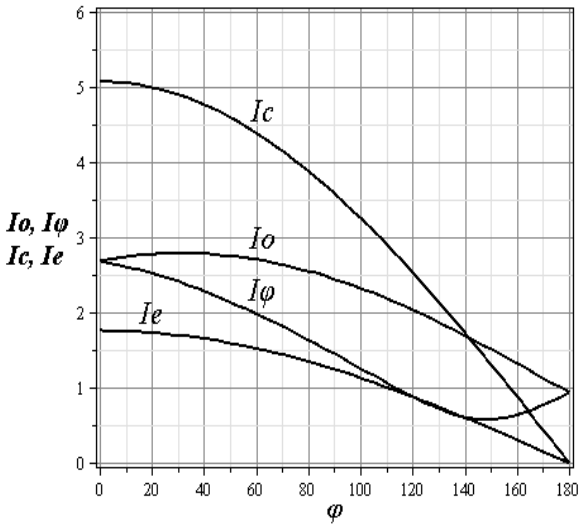

Fig. 4 Normalized amplitudes of the currents versus phase shift

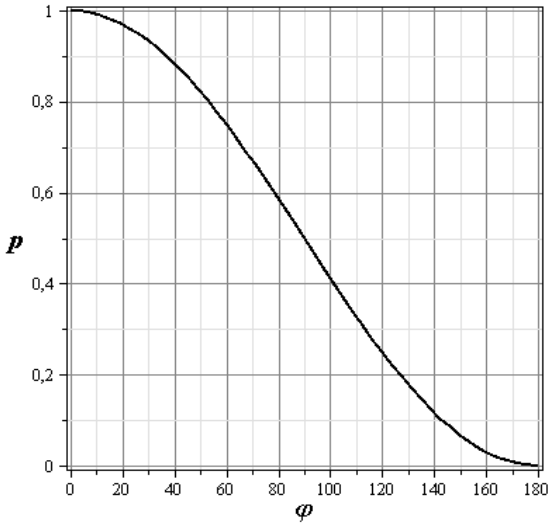

Fig. 5 Inverter normalized power versus phase shift

The inverter power is determined by the following expression:

$$P = \frac{\underline{U}_{ab}\underline{I}_e^*}{2} = \frac{2E^2}{\pi^2 Q Z_0} \frac{1+\cos\varphi}{\left(1-\Omega^2\right)^2 + \left(\frac{\Omega}{Q}\right)^2}. \quad (10)$$

Maximum power of the inverter (at φ=0) is as follows :

$$P_{\max} = \frac{2E^2}{\pi^2 Q Z_0} \frac{2}{\left(1-\Omega^2\right)^2 + \left(\frac{\Omega}{Q}\right)^2}. \quad (11)$$

The dependence of the inverter normalized power $p = P/P_{\max}$ on the phase shift is shown in Fig.5. The inverter power is regulated within the range from 100% to 0 when changing the phase shift whithin the range from 0 to 180º.

The complex power supplied by reference section is equal to:

$$\underline{S}_0 = \frac{1}{2} E_m \underline{I}_0^* = \frac{E^2}{\pi^2\ \Omega\ Z_0} \frac{\sin\varphi + 2\frac{\Omega}{Q} + j\left(1-\cos\varphi-2\Omega^2\right)}{\left(1-\Omega^2\pi\right) - j\frac{\Omega}{Q}}. \quad (12)$$

The phase shift between voltage and current in the reference section is equal to:

$$\varphi_0 = arctg\ \frac{\left(1-\Omega^2\right)\left(1-\cos\varphi-2\Omega^2\right)+\frac{\Omega}{Q}\left(\sin\varphi+2\frac{\Omega}{Q}\right)}{\left(1-\Omega^2\right)\left(\sin\varphi+2\frac{\Omega}{Q}\right)-\frac{\Omega}{Q}\left(1-\cos\varphi-2\Omega^2\right)}. \quad (13)$$

The complex power supplied by control section is equal to:

$$\underline{S}_\varphi = \frac{1}{2} E_m e^{j\varphi} \underline{I}_\varphi^* = \frac{E^2}{\pi^2\ \Omega\ Z_0} \frac{\left(1-\Omega^2\right)\left(\sin\varphi-2\frac{\Omega}{Q}\right)-j\frac{\Omega}{Q}\left(1-\cos\varphi-2\Omega^2\right)}{\left(1-\Omega^2\right)-j\frac{\Omega}{Q}}. \quad (14)$$

The phase shift φ_φ between voltage and current in the control section is equal to:

$$\varphi_\varphi = arctg\ \frac{\left(1-\Omega^2\right)\left(1-\cos\varphi-2\Omega^2\right)+\frac{\Omega}{Q}\left(2\frac{\Omega}{Q}-\sin\varphi\right)}{-\frac{\Omega}{Q}\left(1-\cos\varphi-2\Omega^2\right)+\left(1-\Omega^2\right)2\frac{\Omega}{Q}-\sin\varphi}. \quad (15)$$

According to expressions (13), (15) the dependences of the phase shift φ_0 and the phase shift φ_φ between voltages and currents relatively in the reference (Fig. 6) and controlled (Fig. 7) sections on the phase shift φ between the sections at quality values Q=1, Q=3, Q=5 are shown. These dependences correspond to the results obtained in paper [10]. As a result of the computational experiment, it is determined that at frequency values Ω<1.08, the phase shift φ_φ in the controlled section becomes negative at some interval of phase shift φ_φ. Therefore inverter turns into capacitive operating mode and transistor zero-voltage switching becomes lost. Thus, in the case of two-section converter, the switching frequency should not exceed this value.

The efficiency value η is determined by the following expression:

$$\eta_i = \frac{1}{1+\frac{r\left(I_o^2+I_\varphi^2\right)}{I_e^2 R_e}}. \quad (16)$$

where I_0, I_φ are the amplitude (or current) values of the inverter currents .

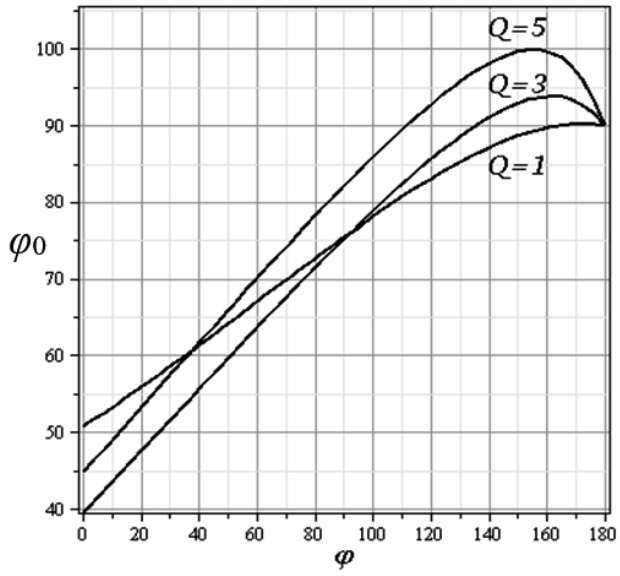

Fig. 6. Dependences of the phase shift φ_0 between voltage and current in the reference section on the phase shift φ between the sections for the quality factor values Q=1, Q=3, Q=5

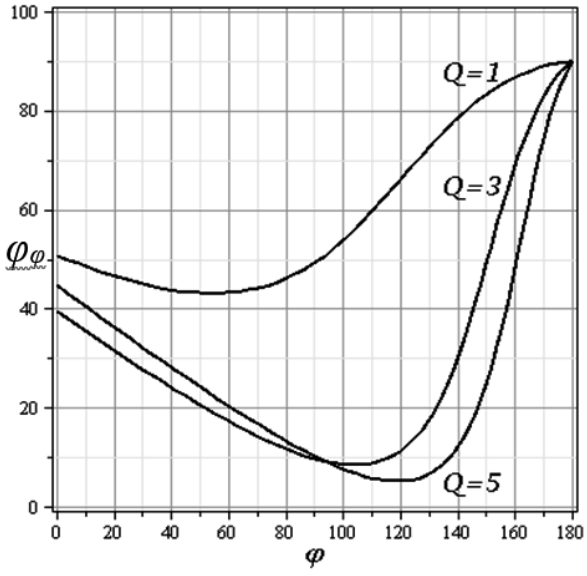

Fig. 7. Dependences of the phase shift φ_φ between voltage and current in the controlled section on the phase shift φ between the sections for quality values Q=1, Q=3, Q=5

Based on the carried out analysis, the parameters of the driver with two-section resonant voltage converter for power supply of EPSX-VF88 LED matrix are calculated. The matrix has nominal voltage 26 V and current 2.3 A. The converter is implemented on IRF730 transistors and MBR10100 diodes. The converter input voltage is E=110 V; the transformer turns ratio is n=4; operating frequency is f=110 kHz; inductance is L=239 μH; the capacity of the resonant capacitor is C=17.5 nF.

Simulation of the converter is carried out by means of the circuit simulator MicroCap-10. The simulation model is presented in Fig.8. In this model, the LED matrix EPSX-VF88 is replaced by resistor R=11.6 Ω. In order to take into account the losses in the inductors, 0.5 Ω resistors are connected with them in series.

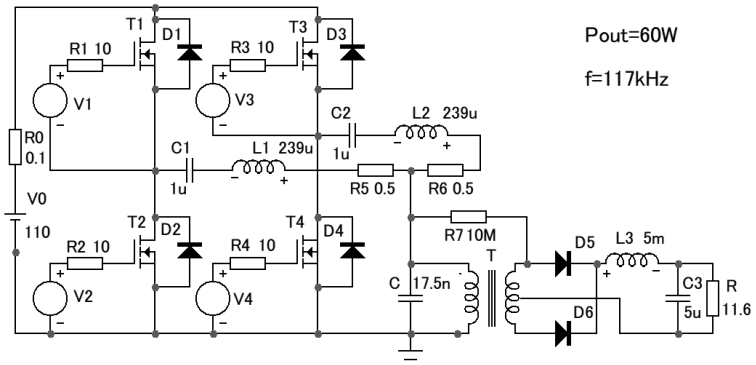

Fig. 8 The simulation model

The simulation results are presented in Fig. 9, that is: the upper oscillogram is voltage on the resonant capacitor (amplitude is 156 V); the middle oscillogram is voltage (26 V) on the LED matrix; the lower oscillogram is converter efficiency (0.96). The simulation results are in good agreement with the results of the analysis.

The carried out analysis can be extended to multi-section resonant inverters with continuous phase power control in one regulated section and step control by switching off the redundant sections when the inverter operates at medium and low power. Further research is required for the rational choice of the inverter operating frequency, at which the transistors zero-voltage switching is ensured in the entire converter power range.

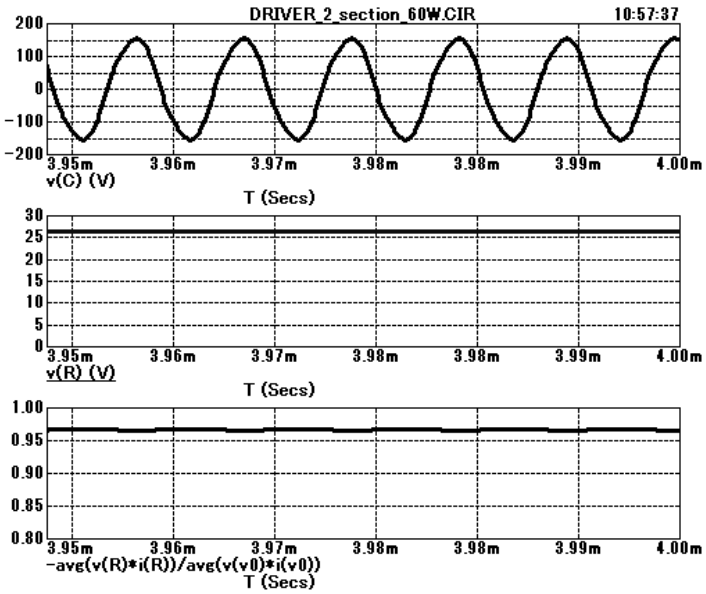

Fig. 9 Simulation results

3. Conclusions

The maximum inverter output power occurs during in-phase work of inverter sections. The inverter provides a wide range of power control in the load from the maximum value to zero when changing the phase shift between resonant sections from 0 to 180º. At the same time, the change of the phase shift between the sections causes the change of the phase shift between voltages and currents in its sections, which can turn the inverter into capacitive operating mode. Therefore, to ensure zero voltage switching of transistors in the whole power range, it is necessary while designing the inverter to select the inverter operating frequency in such a way that the phase shifts between voltages and currents are greater than zero by performing the computational experiment. The carried out analysis can be extended to multi-section resonant inverters with continuous phase power control with one controlled section and step control by switching off the redundant sections when the inverter operates at medium and low power.

References

1. Antypyn, S., Korolev, H. (2011). Svetodyodnuye matrytsu protyv odynochnukh svetodyodov. *Poluprovodnykovaia svetotekhnyka*, 5, 52-54.

2. Xu, R., Li, Y., Zhong, L., Liu, J. (2014). Research of an Efficient LED Lighting Driver Based on Boost-Buck Converter. *Circuits and Systems*, 5, 153-159.

3. Hamza, S., Mustafa, A. (2014). The use of Pulse Width Modulation "PWM" Technique in LED Lighting Systems. *International Journal of Science and Research*, *3*(11), 2316-2320.

4. Hu, Y., Huber, L., Jovanovic, M. (2012). Single-Stage, Universal-Input AC/DC LED Driver With Current-Controlled Variable PFC Boost Inductor. *IEEE Transactions on Power Electronics*, *27*(3), 1579-1588.

5. Lavanya, M., Tamilmani, S. (2017). Design and Analysis of Modified SEPIC Converter for LED Lamp Driver Applications. *International Journal of Advanced Research in Electrical, Electronics and Instrumentation Engineering*, *6*(3), 1627-1636.

6. Shrivastava, A., Singh, B. (2012). LLC Series Resonant Converter Based LED Lamp Driver with ZVS, *2012 IEEE Fifth Power India Conference*, Proceedings of International Conference, Murthal.

7. Jagadeesh, R. Vishwanathan, N. Porpandiselvi, S. (2018). An Efficient Parallel Resonant Converter for LED Lighting, *National Power Systems Conference*, Proceedings of the Conference, Tamilnadu.

8. Branas, C., Azcondo, F.J., Casanueva, R. (2008). A generalized study of multiphase parallel resonant inverters for high-power applications", *IEEE Transactions on Circuits and Systems I: Regular Papers, 55*(7), 2128-2138.

9. Kazimierczuk, M.K. (1993). Phase-controlled series-parallel resonant converter. *IEEE Transactions on Power Electronics*, *8*(3), 309 – 319.

10. Lupenko, A. (2020). Step-continuous phase power control of multi-section resonant inverter. *Computational problems of electrical engineering*, *10*(2), 7-12.

11. Kazimierczuk, M.K., Czarkowski, D. (2011). *Resonant power converters, 2nd Edition*. John Wiley & Sons.

FEATURES OF THE ENAMELED WIRES INSULATION DIAGNOSING BY VOLTAGE

Oleksandr Vakulenko[1], Ivan Sysak[2], Serhii Babiuk[3] Bunko Vasyl[4]

[1]Ternopil National Ivan Puluj Technical University, Rus'ka str. 56, 46001, Ternopil, Ukraine;
vakol1811@gmail.com
[2]Ternopil National Ivan Puluj Technical University, Rus'ka str. 56, 46001, Ternopil, Ukraine;
sisak.tntu@gmail.com
[3]Ternopil National Ivan Puluj Technical University, Rus'ka str. 56, 46001, Ternopil, Ukraine; sermuk@gmail.com
[4] Separated Subdivision of National University of Life and Environmental Sciences of Ukraine BEREZHANY AGROTECHNICAL INSTITUTE, Academichna st. 20, 47501, Berezhany, Ternopil region, Ukraine;
VBunko@gmail.com

Abstract: It is established that the standard methods of the enameled wires insulation tests by voltage have low informativeness.The advantage of statistical modeling in the study of the enamel wires insulation defects is proved. The mathematical model of technological process influence of the electrical device coil element winding on the electrical strength of enameled wire insulation is presented.

Keywords: *Enameled wire, voltage insulation tests, insulation defects, statistical methods*

1. Introduction

Insulation of enameled wire during the manufacture of electrical appliances coiled elements is subject to intense technological factors. As a result, the varnish layer of the enameled wire insulation decreases in thickness, there are places with weakened insulation, as well as obvious defects. It is obvious that when testing the insulation of such a wire for electrical strength, a significant variation will be obtained: from the minimum values at the locations of obvious defects to the nominal values which inherent in the insulation of this type enamel wire.

It should be noted that currently there is no single methodologically sound approach to the method of determining the electrical strength of winding enameled wires insulation, which would allow to assess the actual state of insulation at both the point micro and macro level of uniaxially oriented long object. Here, various types of loads, including voltage, are applied to the enameled wire as an object of research, and different sample lengths are set. However, after conducting such tests, the researcher often does not receive an answer about the real state of the enamel wire insulation, about its reserve of electrical strength.

The problem of uncertainty is that the recognized methods of insulation tests to determine its main indicator - breakdown voltage: two-wires "twisting" of a specially wound sample of enamel wire (the method is supported by Ukrainian and international standards: TU U 31.3-20006134-015, TU U 13970259.001, TU U 31.3–00214534.035, GOST 21428, GOST 26615, IEC 60317, DIN 46416, etc.), two-node wires system with mechanical tensile load (according to the Japanese standard JIS C 3003), two-turn wires model of the well-known electrotechnical firm "Vossloh Schwabe Urbach" (according to the instruction LS – QW – 03) are constructed in such a way that there is always an air gap in the discharge gap, and of different lengths (depending on the test method and mutual placement of insulation defects). This causes a significant variation in the values of insulation breakdown voltages and their overestimation, which does not allow to unambiguously assess the quality of the winding enamel wires insulation, as well as the degree of the technological factors influence on its deterioration.

In addition, quite often the statistical series of test results for breakdown voltages of enamel insulation, obtained, for example, on samples such as two-wire "twisting", contain individual results that "fall out" from the statistical pattern. These "emissions" also increase uncertainty in assessing the quality of their insulation. It should be noted that the extreme values of this series are recommended by the relevant regulations to be rejected as "problematic" measurement results and those that violate the normality of the variation series members. These recommendations are based on the methods of the well-known researcher of statistical series F. Grubbs (Grubbs Frank E.) [1]. The development of Grubbs's methods is the recommendations [2], which can be used to distinguish from the normal range of variation several abnormal minimum or maximum values in their various combinations. Greater constructiveness is inherent in other researchers who question the claims of the all-encompassing broad applicability of the normal distribution law at the study of statistical series [3].

Obviously, the researcher is most interested in these "emissions" in the variation series. Investigation of their origin and establishment of the occurrence reasons by means of other test methods would allow to estimate a real condition of an enamelled wire insulation.

The purpose of the research was to propose new approaches to determine the real state of enameled wires insulation defectness on the basis of performed analysis and features comparison of the existing voltage test methods.

Enameled wires for winding elements of electrical machines and devices of the following nominal diameters were subjected to research: 0.30; 0.40; 0.56; 0.67; 0.71; 1.0 and 1.18 *mm*. The breakdown voltages of air discharge gaps

and the distance between the weakened insulation points on the samples of the enamel wires "twisting" type were measured. The presence of weakened insulation points before the breakdown of the discharge gap was assessed by visual observation of the visible corona discharge development on the working part of the two-wire "twists".

2. The results of the enameled wires insulation research.

It is known that the duration of the discharge process in the intervals between weakened or defective places in the lacquer film of enameled wire, as in any discharge gap, is subject to statistical scatter and consists of the discharge formation duration and, depending from the rate of voltage rise on the discharge gap, time the onset of the voltage initial value at which the discharge process becomes possible [4]. In addition, during the voltage rise, the insulating lacquer film is in the zone of intensive discharge process, which for this system of the two segments wires "twist" type is a discharge in a sharply inhomogeneous electrical field - corona discharge, can heat up and break. Thus, at voltages which used to test the "twist" type of enamel wires samples, it is possible to pre-break the air gap and then burning of the lacquer insulation by spark, if there is enough time for this process.

Observations of the visible crown location on the working part of the "twisting" (see Fig. 1, 2) confirmed the assumption that at the location of the defect or weakening of the insulation is an increase in electrical field strength as a consequence of proportional reduction of the dielectric constant. which is accompanied by a characteristic glow in the purple region of the visible light spectrum. At sufficient voltage between the defects there is a streamer discharge, which very quickly turns into an arc (see Fig. 3).

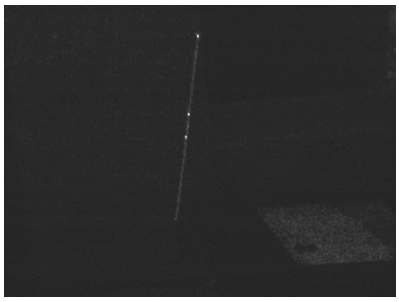

Fig. 1 Beginning of corona discharge visualization in places of insulation weakening (U_k = 3.8 *kV*)

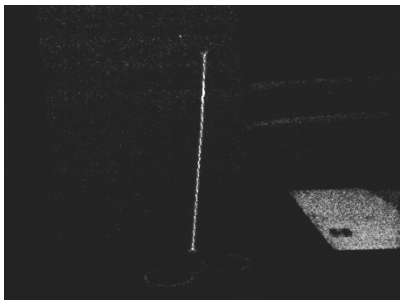

Fig. 2 Development of corona discharge along the sample and increase in the brightness of the defect (U_k = 6.4 *kV*)

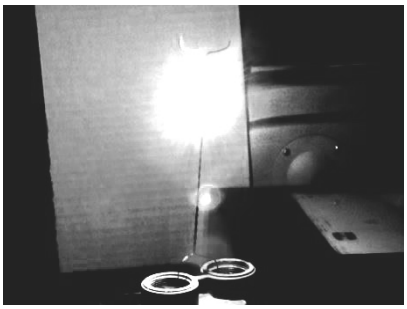

Fig. 3 Breakdown of the discharge gap in places of the insulation weakening (U_{br} = 10.2 *kV*)

The voltage of the visible corona discharge occurrence U_k (see (2)) practically coincided with the calculated value according to the empirical formula [4] for the electrical field intensity E_k of the corona discharge occurrence (see (1)). In fact, when the air density at the test plase changes within δ = 0.98 ... 1.03, the diameters of the investigated enamel wires with denomination d = (0.30; ...; 0.71) *mm* and the roughness coefficient m = 0.99 … 1.00 the electrical field strength E_k occurrence of corona discharge in the visible region of the light spectrum is equal to:

$$E_k = 30.3 \cdot m \cdot \delta \cdot \left(1 + \frac{0.301}{\sqrt{\frac{d}{2} \cdot \delta}} \right); \quad E_k = (78.6 \ldots 104.2)\, kV \cdot cm^{-1}. \tag{1}$$

The voltage U_k of the ionization process in the corona gap of a sharply inhomogeneous electrical field of the test wires "twisting" at a distance between their centers D = (0.328; ...; 0.786) *mm* is equal to:

$$U_k = E_k \cdot \frac{d}{2} \cdot \ln \frac{2D}{d}; \quad U_k = (0.98 \ldots 2.96)\, kV. \tag{2}$$

In the conditions of the conducted researches the appearance of the visible corona is fixed at voltages U_k = (1.6 ... 3.2) *kV* that, taking into account subjectivity of visual perception of the observer, is quite sufficient confirmation validity of application for calculations of the above expression (2). It is obvious that the fixed point places of the corona discharge on the "twisting" correspond to the local weakening of the enamel insulation.

To establish the electrical strength of these points, it is necessary to get rid of the air gap in the test method. Thus, the investigated section of the two-wire twisting insulation at a length of 125 *mm* was immersed in a conductive liquid to create a continuous contact between the individual sections of the insulation. The breakdown voltage U_{br} of the insulation was recorded when the leakage current value (5.0 ± 0.5) *mA* was reached. It is obvious that the voltage thus obtained was corresponded to the minimum value at the investigated segment of the enamel insulation sample.

As a result of the investigated enamel wires tests, the distributions of insulation breakdowns relative frequencies were obtained by the standard method on samples of two-wire "twists" (designation 1), detection of defects by visual method in corona discharge (designation 2) and by continuous contact in current-conductive liquid (designation 3). Analyzing the obtained results and making the appropriate proportions of the most probable voltages U_{50}, we obtained the following relations: U_{50} (1) : U_{50} (2) : U_{50} (3) = (7.2 ... 10.0) : (1.6 ... 6. 8) : (1.6 ... 3.4) = 3.4 : 1.7 : 1.

Thus, the excess of the actual insulation breakdown voltages at the location of defects due to the presence of an air discharge gap in the standard tests of the investigated enamel wires was ~ 3 times, which is unacceptable, and such test methods can be considered only evaluative or suitable for comparative tests. The general regularity of the inverse dependence for scattering voltage of visual fixation and breakdown on the quality of insulation is also revealed: the insulation of the wire in the initial state has, as a rule, one weakened place on the normalized length of the standard sample. The insulation breakdown at high voltages for a given thickness of insulation with a minimum excess from the detected visual level.

It is established that the discharge on a two-wire "twisting" is a complex process that requires a separate study of the actual process enamel insulation destruction at the place of weakening or insulation defect under a sharply inhomogeneous electrical field, and the development of the discharge process through the air gap to the nearest place.

To describe such a complex process, a combined method is used: experimental and mathematical modeling. Before making two-wire "twists" on the insulation of enamel samples, such as Grade 2-0.56 IEC 60 317-3, artificial through defects are applied so that after making "twists" the distances between them at the smallest distance were within (2 .. 20) *mm*. The obtained statistical scatter of breakdown voltages U_{br}, *kV*, of the two-wire "twisting" samples according to the standard method (see Fig. 4) and depending on the distance between the artificial defects L_d, *mm*, (see Fig. 5) was subjected to mathematical modeling according to three factors in planning factorial experiment type 2^3.

The corresponding statistical polynomial model of the discharge gap breakdown voltage on samples of the two-wire "twists" type contains the response function (*Y*) - the dependence function of the discharge gap breakdown voltage U_{br}, *kV*, from the factors:

- a distance L_d along the curve of the smallest length between the breakdown points of artificial insulation defects (factor *X*1), *mm*;
- the same, for the distance L_{ins} between the places of insulation breakdown according to the standard method (factor *X*2), *mm*;
- nominal diameter of the investigated enameled wire (factor *X*3), *mm*.

Optimal for such an enamel wire is a linear model of the form: $Y = 9.1 + 0.24 \cdot X1 + 2.74 \cdot X2 + 0.81 \cdot X3$. The statistical significance of the model coefficients corresponds to the standards [3]: $\frac{a_{i\max}}{a_{i\min}} = \frac{a_2}{a_1} \le 50$; $\frac{2.74}{0.24} = 11.4 = 50$. In this case, the adequacy of the model at the level of: $r_{\bar{y}} = 0.98$. Influence of the maximum factor *X*2 on the response function *Y*: $\delta Y_{+-}(X2) = \pm 30.1\%$. Influence of concomitant factor *X*1 on the response function *Y*: $\delta Y_{+-}(X1) = \pm 2.6\%$.

From the type of the breakdown voltages statistical series for the discharge process in air at intervals of length *L* for the factor *X*1 use the modeling method - approximation by a quadratic function of the form: $\varphi(x) = a_0 \cdot x^2 + a_1 \cdot x + a_2$. The coefficients of the function a_0, a_1, a_2 are calculated by the least squares method. Then for two-wire "twists" with pre-applied defects on the enameled wire type Grade 2–0.56 IEC 60 317-3 (see Fig. 6) the quadratic function for breakdown voltages will look like: $U_{mod}(L) = -0{,}034 \cdot L^2 + 0{,}89 \cdot L + 0{,}239$.

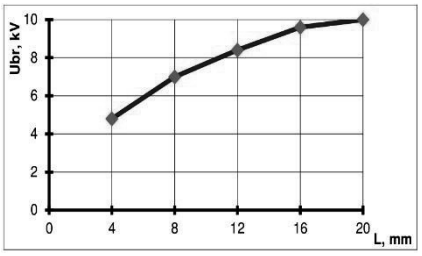

Fig. 4 The distribution of the enamel wire diam. 0.56 *mm* insulation breakdown voltage in the initial state according to the standard method

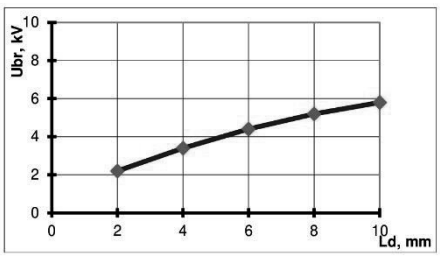

Fig. 5 The distribution of the enamel wire diam. 0.56 *mm* insulation breakdown voltage with artificially applied defects

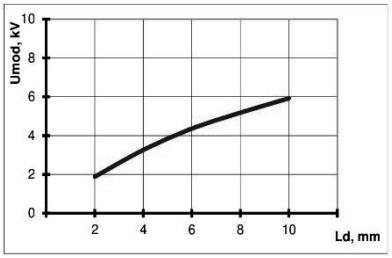

Fig. 6 The dependence model of the enamel wire diam. 0.56 *mm* insulation breakdown voltage from the distance between defects

The influence of factor *X*2 on the response function is estimated at (27 ... 30)%, and the reason is the statistical distribution of the insulation electrical strength, depending from its longitudinal inhomogeneity, and the length of the corresponding air discharge gaps. To establish the contribution of factor *X*2 to the insulation breakdown voltage, tests are performed to assess the longitudinal inhomogeneity of the enameled wire insulation by the method of so-called “continuous contact” in a current-conductive liquid on samples with a length of (1.0 ± 0.1) *m* [5]. As a result of tests, a

statistical series of discrete random values of the minimum insulation breakdown voltages, which are normalized to a unit of enamel length, is obtained.

After mathematical processing of this variation series, a probabilistic estimate of the favorable for the discharge process location of defects or places of insulation weakening is obtained, as well as the type of breakdown voltage distribution function at the locations of insulation defects or its weakening.

There are five options for the random values distribution of breakdown voltage *U*, which make it possible to estimate the degree of insulation defectness of the investigated enamel wire using numerical characteristics of the probability distribution laws of random variables: mathematical expectation *M(U)*, mode $\mathcal{M}$, median μ, asymmetry S_k, excess ε, statistical (integral) distribution function *F*(U)* and compare with the mathematically described laws of random variables distribution (Gram-Charlier, with uniform density, normal), applying the Kolmogorov's consistency criterion for the integral distribution function. Namely [5]:

– defect-free enamel wire (theoretically): $S_k = 0$, $\varepsilon = 0$, $M(U) = \mathcal{M}$;

initial nominal electrical insulation strength at the values of the distribution functions $F^*(U) = 0.1$ and $F^*(U) = 0.75$, respectively: $E_{init}(0.1) > 200$ *kV·mm*$^{-1}$, $E_{nom}(0.75) > 250$ *kV·mm*$^{-1}$;

– enamel wire with a low degree of defectnees: $S_k < 0$, $\varepsilon \geq 0$ or $\varepsilon < 0$, $\mathcal{M} > M(U)$;
$E_{init}(0.1) > 20$ *kV·mm*$^{-1}$, $E_{nom}(0.75) \geq 200$ *kV·mm*$^{-1}$;

– enamel wire with a medium degree of defectness: $S_k < 0$, $\varepsilon \geq 0$ or $\varepsilon < 0$, $\mathcal{M} > M(U)$, or $\mathcal{M} \approx M(U)$;
$E_{init}(0.1) > 20$ *kV·mm*$^{-1}$, $E_{nom}(0.75) \geq 150$ *kV·mm*$^{-1}$;

– enamel wire with a high degree of defectness: $S_k > 0$, $\varepsilon \geq 0$ or $\varepsilon < 0$, $\mathcal{M} < M(U)$;
$E_{init}(0.1) > 20$ *kV·mm*$^{-1}$, $E_{nom}(0.75) \geq 100$ *kV·mm*$^{-1}$;

– enamel wire with a raised degree of defectness: $S_k > 0$, $\varepsilon \geq 0$, $\mathcal{M} \approx M(U)$;
$E_{init}(0.1) < 20$ *kV·mm*$^{-1}$, $E_{nom}(0.75) < 100$ *kV·mm*$^{-1}$;
the extreme case is the normal distribution law ($S_k \approx 0$, $\varepsilon \approx 0$) with extremely small values of insulation breakdown voltages at the level (0… 0.2) *kV* and $E_{init}(0.1) \approx 0$, $E_{nom}(0.75) < 20$ *kV·mm*$^{-1}$.

It should be noted that the above term "electrical insulation strength" at the point of breakdown, i.e. at the point of weakening of the insulation or its defect corresponds to the measured breakdown voltage reduced to the nominal half diametrical thickness of the insulation.

The test results according to the method [5] confirm their accuracy and homogeneity of samples. In addition, depending on the intensity of the factors acting on the insulation, there is a clear abnormality of modal breakdown voltage groups: obvious defects are accompanied by accumulation of results with low voltage values, which have asymmetry towards smaller values, thus eliminating uncertainty about insulation defectness in standard tests "twisting" of enameled wires samples.

The most effective mathematical law for modeling the breakdown voltage distributions of enameled wires, which takes into account their existing asymmetry and excess, is the Gram-Charlier's convergent statistical series derived from the normal distribution law [6], which is described by the distribution density function equation (3):

$$f_s(x) = \varphi(x) - \frac{S_k}{6} \cdot \varphi^{III}(x) + \frac{\varepsilon}{24} \cdot \varphi^{IV}(x), \tag{3}$$

where $\varphi(x) = \frac{1}{\sqrt{2 \cdot \pi}} \cdot \exp\left(-\frac{y^2}{2}\right)$ - the density of the normal standard distribution; $\varphi^{III}(x) = -\left(y^3 - 3 \cdot y\right) \cdot \varphi(x)$; $\varphi^{IV}(x) = \left(y^4 - 6 \cdot y^2 + 3\right) \cdot \varphi(x)$ - derivatives of III-th and IV-th orders from the function $\varphi(x)$, respectively; $y = \frac{x - \mu_1}{\sqrt{\mu_2}}$ - centered and normalized function variable $\varphi(x)$; $S_k = \frac{\mu_3}{\left(\sqrt{\mu_2}\right)^3}$; $\varepsilon = \frac{\mu_4}{\mu_2^2} - 3$ - asymmetry and excess of the researched distribution, respectively; $\mu_1 = \frac{1}{n} \cdot \sum_{i=1}^{n} x_i$; $\mu_k = \frac{1}{n} \cdot \sum_{i=1}^{n} \left(x_i - \mu_1\right)^k$, where $k = 2, 3, 4$ - centering moments of a random variable *x*.

By the method of "continuous contact" in the current-conductive liquid according to [5] tests the above enameled wires according to the research program, which includes testing the electrical strength in the initial state and after the action of technological factors at the manufacture of electrical appliances winding elements.

The generalizing result is given below on an example of enamelled wire brand Grade 2–0.56 IEC 60 317-3, wound from a winding element of the investigated batch before impregnation with sealing compound, according to the method [7].

Variation series of insulation breakdown voltages, which contained the following values, in *kV*: 0.32; 0.56; 0.62; 0.68; 0.68; 0.70; 0.76; 0.78; 0.82; 0.86; 0.98; 1.00; 1.04; 1.12; 1.26; 1.40, distributed at intervals of 0.14 *kV* in accordance with the Sturges's rule. As a result of their statistical processing, the following characteristics of the insulation breakdown voltage distribution are obtained: mathematical expectation $M(U) = 0.86$ *kV*; mode $\mathcal{M} \approx 0.76$ *kV* < $M(U)$; standard deviation $\sigma(U) = 0.24$ *kV*; asymmetry $S_k = +0.60 \geq 0$; excess $\varepsilon = -0.50 \leq 0$, as well as interval values of

relative frequencies *w* (see Fig. 7).

Given the existing asymmetry, it is assumed that the breakdown voltage distribution of the insulation is mathematically described by Gram–Charlier's statistics (3) with the calculated coefficients S_k, as well as ε and the relative frequency w_s (4):

$$w_s = \frac{h}{\sigma(U)} \cdot \frac{1}{\sqrt{2 \cdot \pi}} \cdot \exp\left(-\frac{y^2}{2}\right)\left\{1 + \frac{S_k}{6} \cdot y \cdot \left(y^2 - 3\right) - \frac{\varepsilon}{24} \cdot \left[y^2 \cdot \left(y^2 - 6\right) + 3\right]\right\}. \quad (4)$$

Then the relative frequency of the enameled wire insulation breakdown distribution after winding according to the simulation results, taking into account (4) can be represented by expression (5), as well as the corresponding histogram (see Fig. 7):

$$w_{s_2} = \frac{0.14}{0.24} \cdot \frac{1}{\sqrt{2 \cdot \pi}} \cdot \exp\left(-\frac{y_2^2}{2}\right)\left\{1 + 0.1 \cdot y_2 \cdot \left(y_2^2 - 3\right) - 0.021 \cdot \left[y_2^2 \cdot \left(y_2^2 - 6\right) + 3\right]\right\}; \quad y_2 = \frac{U - 0.86}{0.24}. \quad (5)$$

To confirm the hypothesis about the Gram–Charlier's statistical series, the criterion of modeling accuracy - the parametric Kolmogorov's criterion (*D* - criterion) is used [6]. To do this, calculate the corresponding statistical distribution function *F*(x)* and the theoretical (integral) distribution function *F(x)*, which is used in this criterion to determine the parameter λ according to the equation: $\lambda = D \cdot \sqrt{N}$; $D = \max\left|F^*(U) - F(U)\right|$, where the maximum interval difference D = 0.040; λ = 0.27. Then, the numerical value of the probability $P(\lambda) = 1 - \sum_{j=-\infty}^{+\infty} (-1)^j \cdot \exp\left(-2 \cdot j^2 \cdot \lambda^2\right)$ (in this case $P(0.27) \approx 1.0$) indicates the validity of the accepted hypothesis (see Fig. 7).

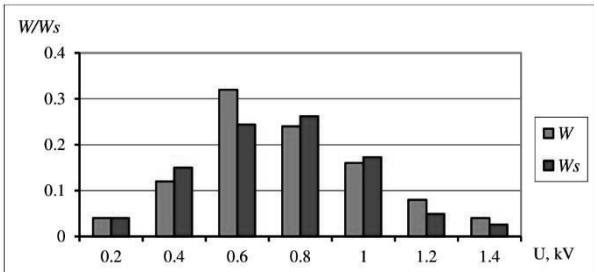

Fig. 7 Histograms of the enamel wire diam. 0.56 *mm* insulation breakdown voltage relative frequencies after winding:
- according to statistical data (*w*);
- according to the applied model (w_s)

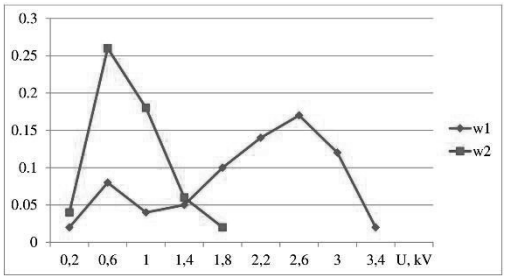

Fig. 8 Diagrams of the enamel wire diam. 0.56 mm insulation breakdown voltage relative frequencies:
- in the initial state (*w*1);
- after winding (*w*2)

Since the initial and nominal electrical insulation strengths of enamelled wire type Grade 2–0.56 IEC 60 317-3 with a diametrical insulation thickness (0.052 ... 0.060) *mm* after winding are, respectively:

$$E_{2\,init}(0.1) = \frac{2 \cdot (0.46 \ldots 0.52)}{0.052 \ldots 0.060} = (16 \ldots 20)\ kV \cdot mm^{-1} \le 20\ kV \cdot mm^{-1}$$

and

$$E_{2\,nom}(0.75) = \frac{2 \cdot (0.88 \ldots 0.92)}{0.052 \ldots 0.060} = (32 \ldots 36)\ kV \cdot mm^{-1} \le 100\ kV \cdot mm^{-1},$$

then, according to [5], the investigated enameled wire should be referred to the classification group: insulation with a raised degree of defectness.

The same statistical calculations are applied to the variation series of the insulation breakdown voltages enameled wire type Grade 2–0.56 IEC 60 317-3 in the initial state, in *kV*: 0.36; 0.48; 0.64; 0.78; 0.86; 1.12; 1.24; 1.32; 1.46; 1.62; 1.84; 1.92; 2.12; 2.36; 2.48; 2.64; 2.86; 3.02; 3.16; 3.34; 3.48, which is distributed at intervals of 0.45 *kV* according to the Sturges's rule. As a result of their statistical processing, the following characteristics of the insulation breakdown voltage distribution are obtained: mathematical expectation *M(U)* = 2.28 *kV*; mode $\mathcal{M} \approx 2.06\ kV < M(U)$; standard deviation $\sigma(U)$ = 1.01 *kV*; asymmetry $S_k = +0.24 \ge 0$; excess $\varepsilon = -0.60 \le 0$, as well as interval values of relative frequencies *w*1 (see Fig. 8).

According to (4), the relative frequency of the enameled wire insulation breakdown voltage in the initial state according to the simulation results taking into account (4) can be represented by expression (6):

$$w_{s_1} = \frac{0.45}{1.01} \cdot \frac{1}{\sqrt{2 \cdot \pi}} \cdot \exp\left(-\frac{y_1^2}{2} \right) \left\{ 1 + 0.039 \cdot y_1 \cdot \left(y_1^2 - 3 \right) - 0.025 \cdot \left[y_1^2 \cdot \left(y_1^2 - 6 \right) + 3 \right] \right\}; \quad y_1 = \frac{U - 2.28}{1.01}. \tag{6}$$

Since the electrical insulation strength of the enamel wire in the initial state is:

$$E_{1\,init}(0.1) = (78 \ldots 92)\ kV \cdot mm^{-1} \geq 20\ kV \cdot mm^{-1} \quad \text{and} \quad E_{1\,nom}(0.75) = (152 \ldots 164)\ kV \cdot mm^{-1} \geq 150\ kV \cdot mm^{-1},$$

then, according to [5], the investigated enamel wire should be referred to the classification group: insulation with a medium degree of defectness.

The increase in the defectness degree of the enamel wire insulation as a result of technological action is shown in Fig. 8 by shifting the relative frequencies of the insulation test results towards lower voltage values. The same figure shows that the breakdown voltage distribution is bimodal in nature with some concentration in the low voltage range. Such distributions are typical for enamel wires either due to the presence of areas with weakened insulation in the initial state, or acquired damage under the action of technological loads, or during operation.

In the mathematical description of such statistical series there is a problem of taking into account the so-called. "emissions" of individual modalities, i. e. random results that clearly fall out from the statistical regularity. Then it is effective to use the credibility function $L\left[M(U); \sigma(U); S_k; \varepsilon \right]$ according to the method of "maximum credibility" in combination with the robust method of grouping a data set in a sample with equal probability intervals, as a result of which the estimation of the individual modalities distribution parameters becomes most resistant to deviations. At the same time the new characteristics of the each modalities law distribution with the corresponding relative frequencies corrected by such procedure are receive [8].

Therefore, researches using the method [5], which eliminated the air gap from the discharge gap and, thus, increased the accuracy of the tests, found that in the manufacture of the electrical appliances coiled elements from enameled wire, its insulation due to the action of intensive technological factors [7] acquires significant damage, which, however, are manifested in tests using standard methods only implicit "emissions" of the statistical distribution law.

3. Conclusions.

The conducted researches have established that the informativeness increase of the enameled wires insulation tests methods for the purpose of revealing their weakened or defective places should occur in the direction of defects immediate research. One of such directions is the application of the "continuous contact" method in a current conductive liquid with a simultaneous mathematical description of the insulation defects distribution density along the unit length of the enamel wire.

As a result of elimination from the discharge gap uncontrolled air component it is possible to build a mathematical model of the insulation breakdown voltage distribution density in its most defective places, which is quite consistent with the statistical model obtained during the insulation tests of the enameled wire both in the initial state and after the action of technological factors at the manufacture of coiled elements.

The proposed methodology is a more accurate tool at the research of the enameled wires insulation, which allows to increase the informativeness of the existing standard methodology, especially at the presence in statistical samples of the breakdown voltage minimum values.

The application of the developed methodology significantly increases the efficiency of diagnosis and reliability of the enamelled wires test results, as a result of which it becomes possible to adjust the technological units for defect-free production of the electrical machines and devices coiled elements.

References

1. Grubbs, F.E., Beck, G. (1972). Extension of sample sizes and percentage points for significance tests of outlying observations. *Technometrics, 14*(4), 847–854.

2. Lemeshko, B.Yu. (2005). Rasshyreniie oblasti primienieniia kritieriiev tipa Grabbsa, ispolzuiemykh pri otbrakovkie anomalnykh izmierienii. *Izmieritielnaia tiekhnika*, 6, 13–19 (in Rus.).

3. Orlov, A. I. (2004). *Prikladnaia statistika*. Moskva: Ekzamien (in Rus.).

4. Brzhezyts′kyy, V., Isakova, A., Rudakov, V. (2005). *Tekhnika i elektrofizyka vysokykh napruh*. Kharkiv: Tornado (in Ukr.).

5. Patent Ukrainy 54560 UA. 2003. Sposib otsinky stupenia defektnosti izoliatsii emalprovodiv. Vakulenko O., № 2000042307, Biuleten №3/2003 (in Ukr.).

6. Kobzar, A. I. (2006). *Prikladnaia matiematichieskaia statistika. Dlia inzhenierov i nauchnykh rabotnikov*. Moskva: Fizmatlit.

7. Yevtukh, P., Vakulenko, O. (2010). Modeliuvannia defektnosti izoliatsii emalprovodiv pid chas vyhotovlennia obmotkovykh elementiv elektrychnykh aparativ. *Visnyk NU "Lvivska politekhnika", 677*, 138–147 (in Ukr.).

8. Rudenko, V. M. (2012). *Matematychna statystyka. Navchalnyi posibn*. Kyiv: Tsentr uchbovoi lit. (in Ukr.).

KINETICS OF LEDS WHITE LIGHTING UNDER PULSE POWER SUPPLY

Volodimir Andriichuk [1], Myroslav Nakonechyi [1], Yaroslav Filiuk [1], Yaroslav Osadtsa [1], Gao Xinzhong [2].

[1] Ternopil Ivan Puliui National Technical University, 46 Mykulynetska Street, Ternopil, Ukraine,filuk.slavik.91@gmail.com
[2] HangZhou Sinodod Electronic Technology Co. Ltd., China

Abstract: The paper presents the results of the study of energy and dynamic characteristics of white glow LEDs FYL-3014 and ARPL-1W when powered by U-shaped pulses. Based on the obtained oscillograms, it is established that the increase and decrease of the luminous flux is described by an exponential dependence, from which the constants of the relaxation time are determined. As the frequency of the pulsed power supply increases, the time constant of increase and decrease of the luminous flux decreases. Based on the analysis of the parameters of the light flux LEDs kinetics and its behavior with a change in the frequency of the pulse supply and the amplitude of the pulses, it is shown that one-component phosphor YAG:Ce is used. The most energetically favorable frequency range of pulsed power supply FYL-3014 and ARPL-1W of white glow is from 1 to 100 kHz.

Keywords: *LED, pulse-width modulation, energy efficiency, attenuation coefficient.*

1.Introduction.

Pulse power supply of LED light sources (LED) with pulse-width modulation has become the most common in lighting systems. It allows to use modern determination of the optimal pulse frequency is based on the analysis of the LEDs glow kinetics. Unfortunately, this problem is studied insufficiently, so the task was to conduct such studies for white glow LEDs.

This work is devoted to experimental studies of the kinetics of white glow LEDs based on InGaN-GaN structures (with a color temperature of 3000 °K and 6000 °K), which is a continuation of the study of transients in an electric circuit with commercially available LEDs FYL-3014 and ARPL-1W of 1 W and 3 W when powered by U-shaped pulses with latitude modulation [1-3].

2.Experimental installation

Measurements of spectral and dynamic LED characteristics were performed on an experimental installation, the block diagram of which is shown in Fig.1.

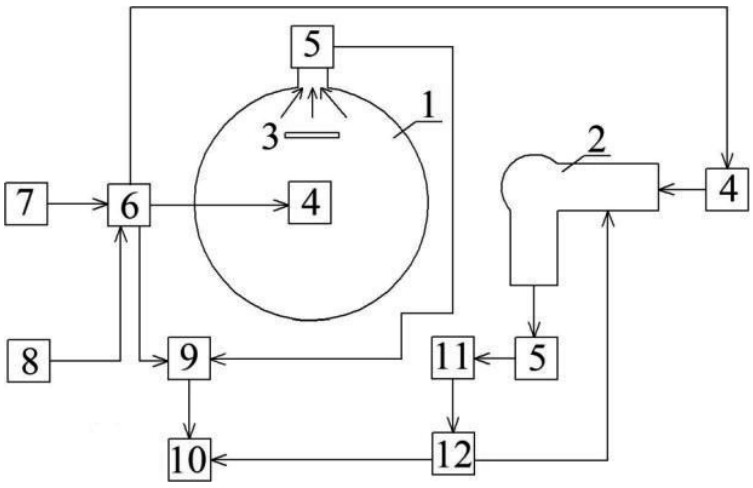

Fig.1. Block diagram of the research installation: 1 - integrated photometer; 2 - monochromator UM-2; 3 - screen; 4 - research light source; 5 - photodetector; 6 - switching device; 7 - adjustable voltage source SW3010D; 8 - SIGLENT SDG 1050 generator; 9 - SEA C8-22M / 1 oscilloscope; 10 - personal computer; 11- converter current - voltage; 12 - unit for processing of input signals and controlling the operation of the monochromator UM-2.

To study the energy characteristics, the light source (4) was placed in an integrated photometer (1). The electrical signal from the photodetector (5) was transmitted to the digital oscilloscope SEA C8-22M / 1 (9). An adjustable voltage source SW3010D (7), an SDG signal generator 1050 (8) and an electronic switch (6), which allowed switching current up to 10 A and voltage up to 100 V, were used to provide switching power of the LEDs. It allowed to supply light sources both with direct current and in pulse mode with a pulse frequency of up to 1 MHz with different fill factors. The

current and the voltage, the amplitude and the pulse duration were monitored using a SEA C8-22M / 1 digital oscilloscope. Processing and storage of measurement results were performed using a personal computer.

UM-2 monochromator was used to study the spectral distribution of LEDs and to isolate the individual parts of the spectrum. The light pulse was measured by a photodetector (5), FEU-85 photoelectron multiplier (PhEM). The signal from the PhEM was fed to the operational amplifier (11), which was operated in the mode of the converter current - voltage. The operation of the monochromator was performed using ARDUINO NANO (12).

3.Research results and their discussion

Before proceeding to the study of lighting LED characteristics, measurements of its electrical parameters during switching power supply were carried out. Measurements were performed for two types of white light LEDs FYL-3014 and ARPL-1W. 1W LEDs were powered by the SIGLENT SDG 1050 generator, and an electronic key was additionally used to power the 3W LEDs [1].

Figure 2 shows the oscillograms of current and voltage pulses on the rising and falling edges, in an electric circuit with the studied LEDs. The oscillating nature of the transient process indicates the presence of reactive elements, contained in the structure of the LED, in the electrical circuit. The time constant of increase and decrease voltage, which is applied to the LED, is close to the constant pulse time at the output of the generator and the switch. The time constant of the current increase, which is the current of LED emission, is much bigger than the time constant of its decrease. On the oscillograms of the rising edge of the voltage pulse oscillations are observed. Their amplitude exceeds the established data. The reverse voltage appears on the falling edge.

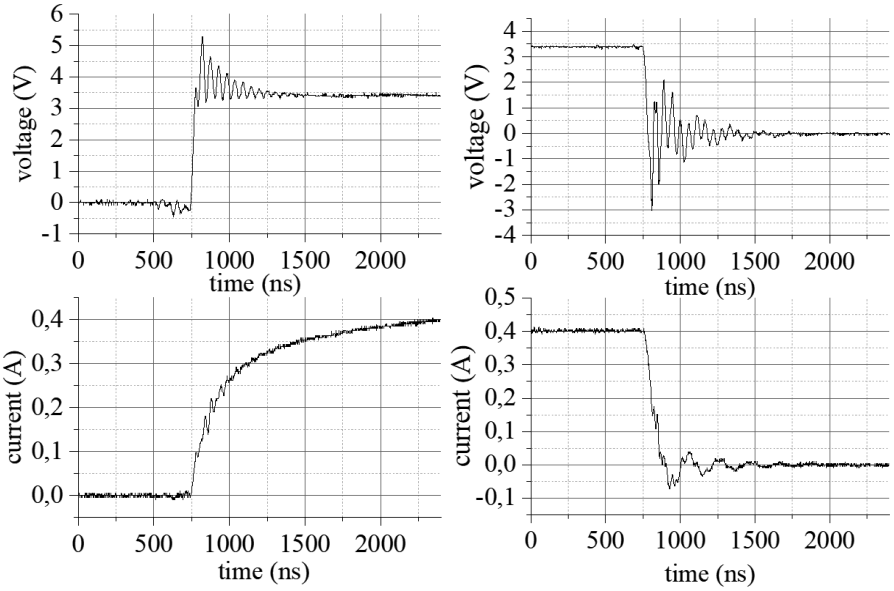

Fig.2. Oscillograms of current and voltage pulses on the rising and falling edges in an electric circuit with LED capacity

Based on the analysis of transients in an electric circuit with different types of LEDs, its equivalent wiring diagram was proposed [1]. Here, the LED is represented by a parallel link consisting of a resistance R_d, which is determined by the resistance of the LED active area, and a capacitor C_d, the capacitance of which is equal to the diffuse capacitance of the heterojunction. The resistance R_s is connected serially, it includes the resistance of the LED passive areas, as well as the resistance of the conductive elements of the electrical circuit [4].

Investigation of the kinetics of increasing and decreasing luminous flux is performed for LEDs, in which radiation of InGaN-AlGaN heterostructure (450 nm) and photoluminophore with high quantum efficiency and wide spectrum in yellow-and-orange area (500-710 nm) were used for obtaining the white glow. The chemical composition and the kinetic parameters of LED phosphors are not indicated by manufacturers, though most of them use yttrium-aluminum garnet doped with cerium as a phosphor. The maximum of its radiation is at 550-560 nm. By modifying it with gadolinium or gallium additives, the shift of its luminescence spectrum to the long-wavelength or short-wavelength side is achieved, in accordance [5,6]. The blue glow of the heterojunction, which excites the phosphor glow, in the sum with it gives cold-white or warm-white radiation.

Two-color and three-color photoluminophores are also used to achieve a high color rendering index, but their energy efficiency is lost [7 – 9].

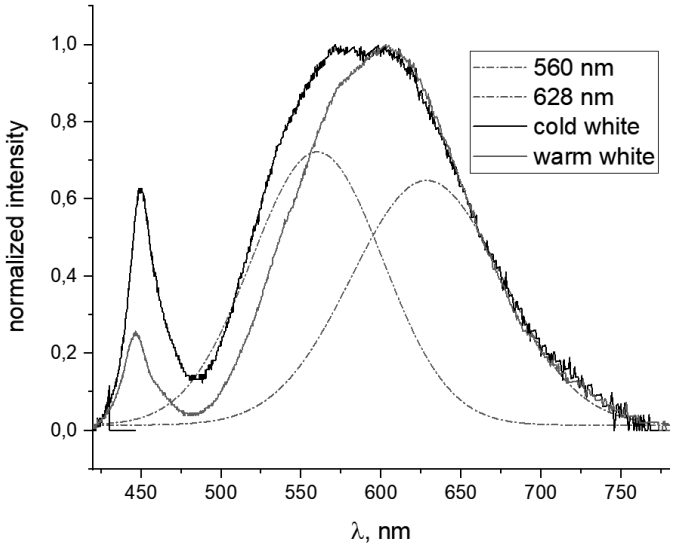

Fig.3. Glow spectra: 1) cold-white; and 2) warm-white.

Analyzing the electroluminescence spectrum of the studied LEDs, a wide band in the yellow-and-orange region was divided into two elementary bands with maxima of 560 nm and 628 nm (Fig. 4). That is, the manufacturer could use a two-color phosphor: yellow YAG:Ce and unknown red in the LEDs data. To test this hypothesis, studies of the glow kinetics in each of the individual bands, which were isolated using a monochromator were conducted. Figure 4 and Figure 5 show the oscillograms of the increase and decrease of light flux in the selected spectral areas. The graphs ln (1-I / I0) = f (t) and ln (I / I0) = f (t) are also given here [10]. They show that the kinetics of luminous flux are described by the exponential dependence, and on the attenuation curve two components - fast and slow - can be distinguished. Table 1 shows the constant growth and attenuation in each of the selected bands at a pulse frequency of 50 kHz and an amplitude of 3.4 V.

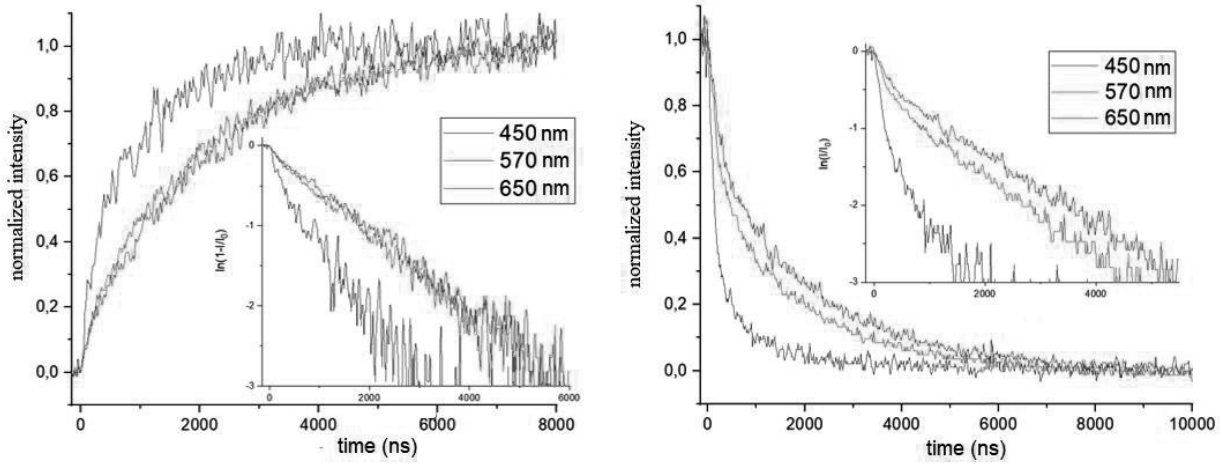

а) б)

Fig.4 The rising (a) and falling (b) edge of the light flux pulse for separate spectral areas of the warm-white ARPL-1W LED.

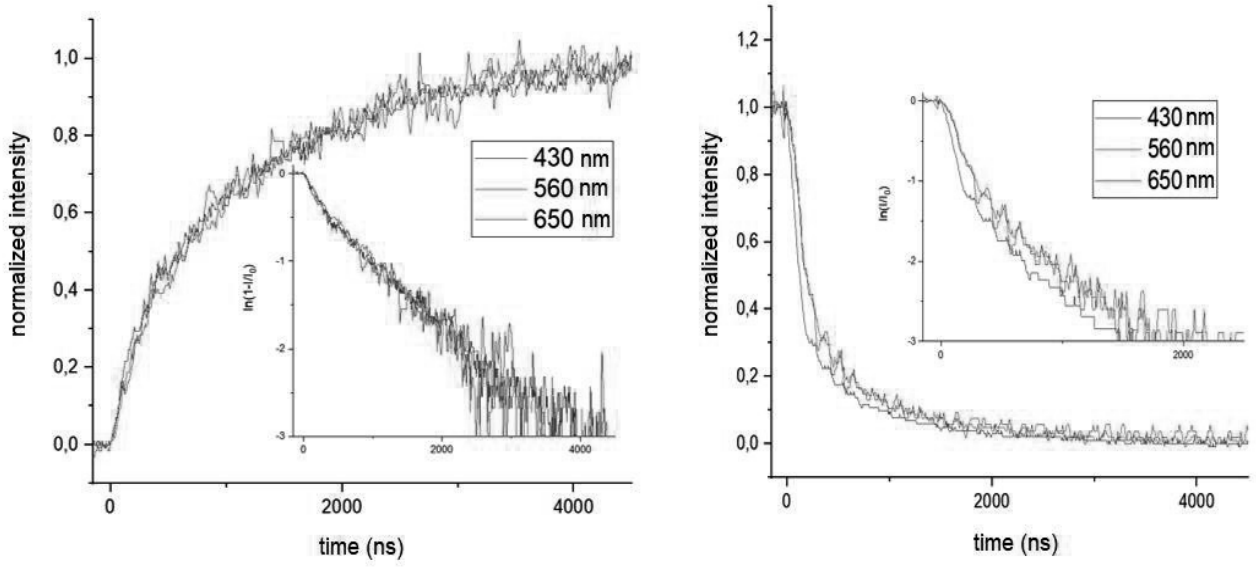

а) б)

Fig.5 The rising (a) and falling (b) edge of the light flux pulse for the separate spectral areas of the cold-white ARPL-1W LED.

Table 1 Average values of constant increase and decrease

Type	Wave length (nm)	decrease		increase	
		τ_1,(*ns*)	τ_2,(*ns*)	τ_1,(*ns*)	τ_2,(*ns*)
Warm-white 1W	452	180	800	1250	
	560	500	1900	2200	
	628	500	1950	2250	
Cold-white 1W	460	170	850	1200	
	560	300	900	1200	
	628	300	950	1230	

The kinetics of light flux growth for both blue and yellow-and-orange bands of both LED types has one component. The time constants of the increase in luminous flux in the blue band for both LED types coincide and vary in the range of 1200-1250 ns. The fast and slow components in their attenuation are very close and their time constant is in the range of 170-180 ns and 800-850 ns, in accordance.

Investigations of the luminous flux kinetics in the yellow-and-orange part of the 500-700 nm spectrum, which is connected with a one- or two-component phosphor, were performed in two spectral areas of 560 ± 5 and 630 ± 10 nm, which were isolated using a monochromator. The constant increases and attenuations in these bands for both LED types are significantly different. For warm-white LED, the constant increases of luminous flux for both bands coincide and are changed in the range of 2200-2250 ns, and for cold-white LED they also coincide and are changed in the range of 1200-1250 ns (Fig. 4, a and 5, a).

For both LED types, the decrease of luminous flux in both bands has two components: fast and slow. For warm-white LED, the time constants of the fast component for both bands are very close and they are in the range of 500-550 ns (Fig. 5, b). The same is observed for cold-white LED, their time constant is in the range of 300-350 ns (Fig. 6, b). The slow components of both bands for warm-white and cold-white LED differ significantly, from 2200-2250 and 1200-1250 ns, in accordance, although for each in particular they coincide (Fig. 4, b and 5, b).

It was found that the kinetics of the studied LED glow depends on the frequency of the pulse power supply. To do this, measurements of the increase and decrease of the luminous flux in all selected spectral areas when changing the pulse frequency from 1 to 500 kHz were performed.

Figure 6 shows the frequency dependences of the time constant of the luminous flux increase for warm-white (a) and cold-white (b) LED ARPL-1W. As the frequency τ increases for both bands in the yellow-and-orange area of the spectrum, it decreases from 2250 ns at 10 kHz to 480 ns at 400 kHz for warm-white LED, and from 1300 to 400 ns for cold-white LED. In the blue area for both LEDs the frequency τ decreases from 1250 to 450 ns.

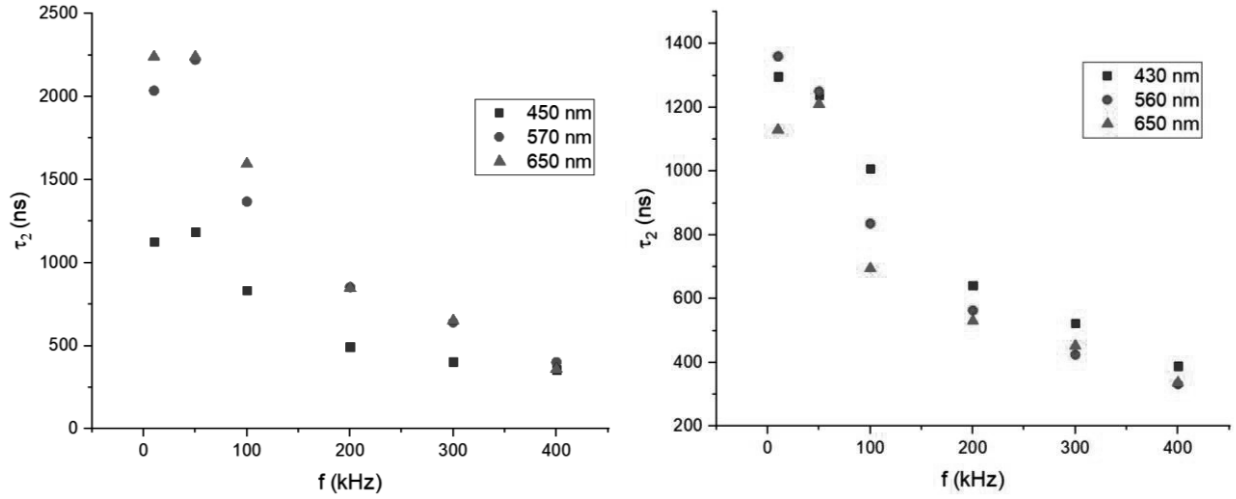

а) б)

Fig. 6. Frequency dependences of the time constant in light flux increase of warm-white (a) and cold-white (b) LED ARPL-1W.

The frequency dependences of the luminous flux decrease for both LED types are shown in Fig. 7 and Fig. 8. The decrease time constant of the slow component for both selected bands, at increased frequency from 10 to 400 kHz, decreases from 2050 to 450 ns for warm-white LED and from 1050 to 400 ns for cold-white LED. The fast component constant also decreases with increasing frequency from 550-600 to 200-230 ns for warm-white LED, and from 300-320 to 180-200 ns for cold-white LED. In the blue area the slow component constant decreases with a frequency of 850 to 500 ns for warm-white LED, and from 1050 to 400 ns for cold-white LED. The change of the fast component constant for both LED types is very close and occurs in the range from 180 to 120 ns.

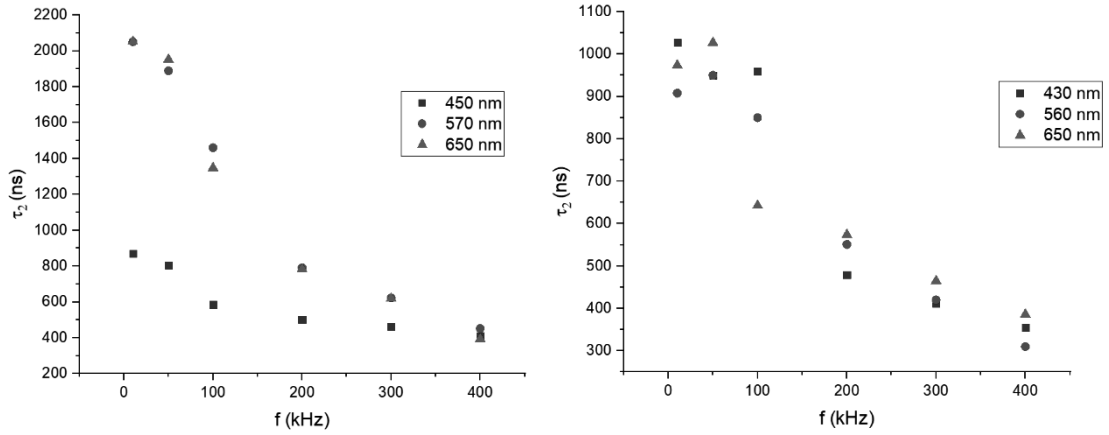

а) б)

Fig. 7. Frequency dependences in the time constant of slow component decrease of the light flux in warm-white (a) and cold-white (b) LED ARPL-1W.

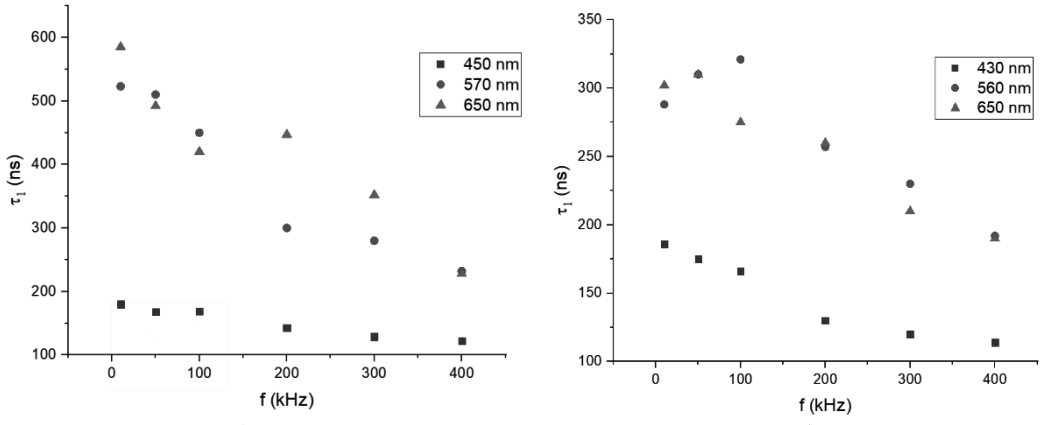

а) б)

Fig. 8. Frequency dependences in the time constant of fast component decrease of the light flux in warm-white (a) and cold-white (b) LED ARPL-1W.

Experimental studies on the effect of current pulse amplitude and voltage on the glow kinetics of the studied LEDs were performed. Fig. 9 and fig. 10 show the dependences of the time constant of increase and decrease of the LED luminous flux on the amplitude of voltage and current pulses. In the yellow-and-orange area for warm-white LED the time constant of increase in luminous flux in selected spectral areas varies within 2200 ± 100 ns with increasing amplitude of voltage and current pulses, and for the band in the blue area it is 1150 ± 50 ns (Fig. 9, a). For cold-white LED with increasing amplitude of pulses, the time constant of increase in luminous flux is almost unchanged, although the relative scatter of experimental data is greater than 1220 80 ns (Fig. 9, b).

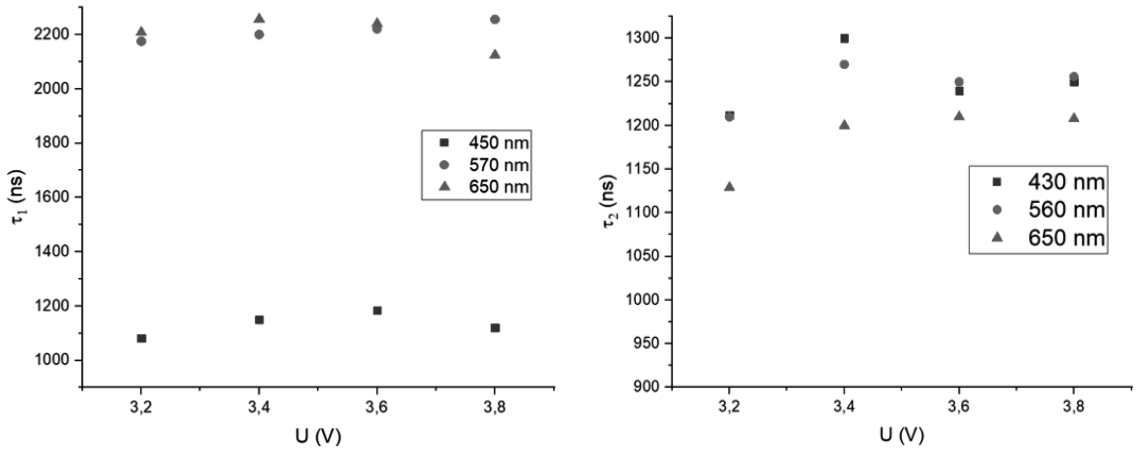

а) б)

Fig. 9. Dependence of the time constant of light flux increase on the amplitude of voltage and current pulses of warm-white (a) and cold-white (b) LED.

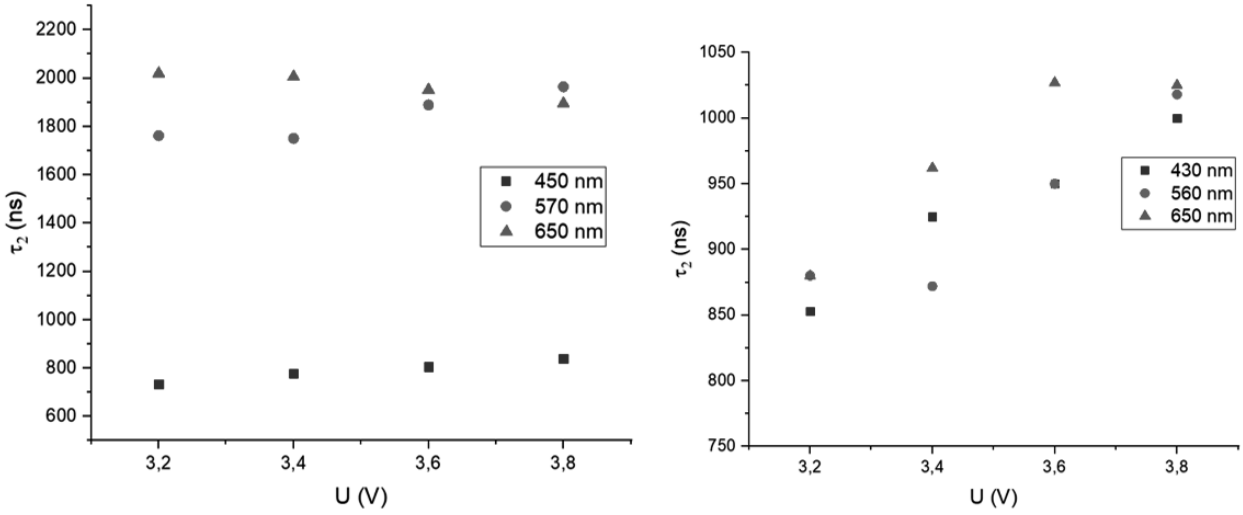

а) б)

Fig. 10. Dependence of the time constant of light flux decrease on the amplitude of voltage and current pulses of warm-white (a) and cold-white (b) LED.

The time constant of the slow component of the decrease in luminous flux in the yellow-and-orange area for warm-white LED varies within 1900 ± 100 ns, and in the blue area it varies within 800 ± 50ns. For cold-white LED in both blue and yellow-and-orange parts of the spectrum, it increases from 850 ± 50 to 1020 ± 50 ns (Fig. 10).

From the analysis of the luminous flux kinetics in two selected spectral bands of 560 and 628 nm, obtained by decomposing the yellow-and-orange band of warm-white and cold-white LED and its behavior with the changing frequency of the pulse power supply and pulse amplitude, it can be stated that in white LED such as FYL-3014 and ARPL-1W the manufacturer used one-component phosphor YAG:Ce. The shift of its luminescence maximum into the short-wavelength area of the spectrum, which takes place for cold-white LED, was achieved by introducing Ga and choosing x in $Y_3Al_{5-X}Ga_XO_{12}$:Ce.

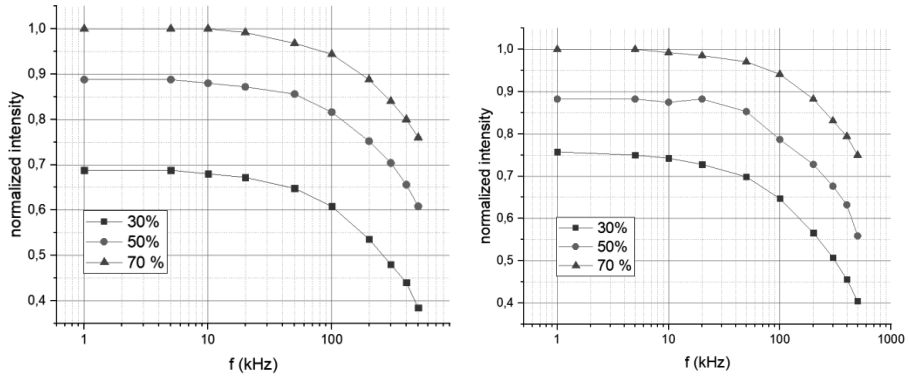

а) б)

Fig. 11. Dependence of light flux of a) warm-white and b) cold-white LED on the frequency and degree of pulses filling.

In addition to studies of the light flux kinetics of selected LEDs, a study of the luminous flux magnitude from the pulse frequency and the degree of their filling was performed. From 1 kHz to 10 kHz the luminous flux hasn't been changed. It correlates well with the time constant of the increase. It changes less at 70% filling than at 50% and 30%. When the pulse frequency increases to 100 kHz and fills 70%, it decreases by 5%, while at 50% and 30% it decreases by 10%.Thus, based on the analysis of the glow kinetics of white LEDs such as FYL-3014 and ARPL-1W and the frequency dependence of their luminous flux, it follows that the most energetically favorable frequency range of their pulse power is from 1 to 100 kHz. This will let approximate the operating time of the elements in the PWM power supply circuits to the operating time of the main circuit element - the LED.

4.Conclusions

The time constant of increase and decrease in the luminous flux in the yellow-and-orange photoluminescence band of warm-white LED is twice as much as the time constant for cold-white LED. As the frequency of the pulsed power supply increases, the time constant of the increase and decrease in the luminous flux in this band for both LED types decreases to 350-400 ns at 400 kHz.

The kinetic parameters of the luminous flux in the blue band remain the same for both types of LEDs. As the pulse frequency increases, the time constant of increase and decrease decreases equally for both types of LEDs.

Based on the analysis of light flux kinetics in the yellow-and-orange luminescence band of white LEDs FYL-3014 and ARPL-1W and its behavior with changes in the frequency of the pulse power supply and the amplitude of the pulses, it is shown that one-component phosphor YAG:Ce is used.

The most energetically favorable frequency range of LED pulsed power supply FYL-3014 and ARPL-1W is warm-white and cold-white glow from 1 to 100 kHz.

References

1. Andriichuk, V., Nakonechnyi, M. , Osadtsa, Ya. i Filiuk, Ya. (2021). Doslidzhennia svitlodiodnykh dzherel svitla u vypadku impulsnoho zhyvlennia. *Tekhnichna elektrodynamika*. 1, 68-72. doi: 10.15407/techned2021.01.068.

2. Moshhnye svetodiody linzy i platy. (2010) [Elektronnij resurs] // http://arlight-group.com. – 2010. Rezhim dostupu do resursu: http://arlight-group.com/upload/iblock/d0a/arlight_led_power_2010.pdf

3. Savkova, T. N. (2015). Issledovanie jenergeticheskih i opticheskih harakteristik moshhnyh svetodiodov pri impul'snom vozbuzhdenii. *Vestnik GGTU imeni P. O. Suhogo: nauchno - prakticheskij zhurnal*. 3, 78-85.

4. Ford, D. (2009). The secret world of oscilloscope probes. *SiliconChip, 253*. 16-23.

5. Schubert F.E.(2008). LEDs, 2nd ed M .*: Fizmatlit*, 500 p.

6. Soshchin, NP, Galchina, NA, Kogan, LM, Shirokov, SS, & Junovich, AE (2009). Warm white LEDs based on p− n heterostructures of the InGaN / AlGaN / GaN type covered with yttrium-gadolinium garnet phosphors. *Semiconductor Physics and Engineering*, 43 (5), 700.

7. Shukajlo, V. P., Obolenskij, S. V., Basargina, N. V. (2012). Issledovanie spektrov jelektroljuminescencii svetodiodov na osnove GaN-struktur pri nejtronnom obluchenii. *Vestnik Nizhegorodskogo universiteta im. N.I. Lobachevskogo, 6*(1), 51-55.

8. Meng, X., Wang, L., Hao, Z., Luo, Y., Sun, C., Han, Y., ... & Li, H. (2016). Study on efficiency droop in InGaN/GaN light-emitting diodes based on differential carrier lifetime analysis. *Applied Physics Letters, 108*(1). doi: 10.1063/1.4939593.

9. Morozov AS, Kovalenko AV, Ushakov Yu. V., Prokofiev TA (2008). Methods of decomposition of photoluminescence spectra of Zns: Mn crystals into individual components. *Bulletin of Dnepropetrovsk University, series "Physics. Radioelectronics ".* 15, 147-152.

10. Lisitsyn V.M., Korepanov V.I (2008). Spectral measurements with temporary resolution: a textbook. *Tomsk: Tomsk Polytechnic University Press*,

LIGHT PULSED IRRADIATION IN GROWING SEEDLINGS

Mariia Kotyk[1], Volodymyr Andriychuk[1], Pavol Spanik [2], Liubov Kostyk[1], Sergiy Potalitcyn[1]

[1] Ternopil Ivan Puluj National Technical University, Ruska str. 56, 46001, Ternopil, Ukraine; mariakotyk1510@gmail.com
[2]University of Zilina, Slovakia; pavol.spanik@fel.uniz.sk

Abstract: This work presents the research results of dynamic characteristics of ARPL-1W LEDs with a narrow-spectrum composition of luminescence (red, green, blue) using switching power supply of U-shaped pulses. Based on the results of increase and decrease of light flux and analysis of the kinetics of photosynthetic processes, from light absorption to absorption of CO_2 from the atmosphere and the formation of carbohydrates, the LED irradiation installation is designed and approbated for growing seedlings. According to the results of experimental studies it is shown that pulsed irradiation stimulates faster plant growth without losing their morphometric parameters.

Keywords: *pulse irradiation, plants lightculture*

1. Introduction

The efficiency of plant growing systems in a controlled environment largely depends on energy consumption, most of which is for lighting. The spectral composition, intensity and period of irradiation play a leading role in the regulation of photosynthesis processes and, accordingly, determine the morphogenesis and productivity of plants.

Changing the intensity and spectral composition of the light affects the formation of structural and functional organization of the photosynthetic apparatus, prevention of metabolic reactions and morphogenesis of plants. Energy metabolism requires a large number of pigments that absorb a significant portion of solar radiation in the photosynthetically active part of the spectrum. In contrast to energy metabolism, photoregulation reactions can be carried out with a very small amount of pigment that absorbs a small part of the incident light. In this case, the energy of Therefore, it is important to comprehensively assess the effect of radiation of both individual and various combinations of spectral ranges on the photosynthetic activity of cenoses throughout the growing season using light irradiation with those spectral and energy characteristics that are really suitable for full crop conditions.

Radiation intensity and its spectral composition are one of the many factors that determine not only the yield but also the quality of crop products. When growing plants under artificial irradiation, its level is usually lower than in natural conditions. Therefore, the formation of pigments depends largely on the spectral composition of radiation. In turn, the content of pigments in the leaves determines their absorption of energy flow and the intensity of photosynthesis. The photosynthetic apparatus of plants responds to different light regimes, adapts and is characterized by its activity. The degree of plants resistance to light of different spectral composition is determined by the pigment composition.

Recently, alternating and light-pulsed irradiation is used in the lightculture of indoor plants. The system of utilization of light energy and the dynamics of its transformation in plants attract special attention. It opens up the possibility to find the most effective radiation sources and optimal radiation regimes.

In this work, based on the analysis of the photosynthetic processes dynamics and the kinetics of LED light sources luminescence, an irradiation unit with narrow-spectrum LEDs was made and its experimental tests of growing pepper seedlings in greenhouse conditions were performed.

Kinetics of photosynthetic processes. Photoenergetic processes in plants begin with the absorption of light quanta by pigment molecules and the transfer of absorbed energy to the reaction centers. The main pigment in plants is chlorophyll a and b. Its absorption spectrum is shown in Fig.1. Its energy scheme, which corresponds to this spectrum, is shown in Fig.2 [1-3].

There are two levels of excitation in the chlorophyll molecule as there are two absorption bands in the blue-violet and red regions of the spectrum. In the unexcited state, the chlorophyll molecule is at the basic singlet level S_0, when all electrons are arranged in pairs, and their total spin is equal to zero. During absorption in the blue-violet region, the molecule moves to the highest energy level S_2, at which the total spin moment of the electrons remains unchanged. The lifetime of the chlorophyll molecule in this state is 10^{-12} s. During light absorption in the red part of the spectrum, the molecule moves to a lower singlet level S_1 with a lifetime of $10^{-9} – 10^{-8}$ s. This transition also occurs without changing the spin moment of the electron. The maximum lifetime of the chlorophyll molecule in the triplet state is T_1 - $10^{-4} – 10^{-2}$ s. This transition runs with a change in the spin of the electron. In addition to chlorophyll, the light-harvesting complex also includes carotenoids and phycobilins. They absorb light in those spectral regions where the absorption of chlorophyll is weak and thus increase the photosynthetic efficiency of light [4].

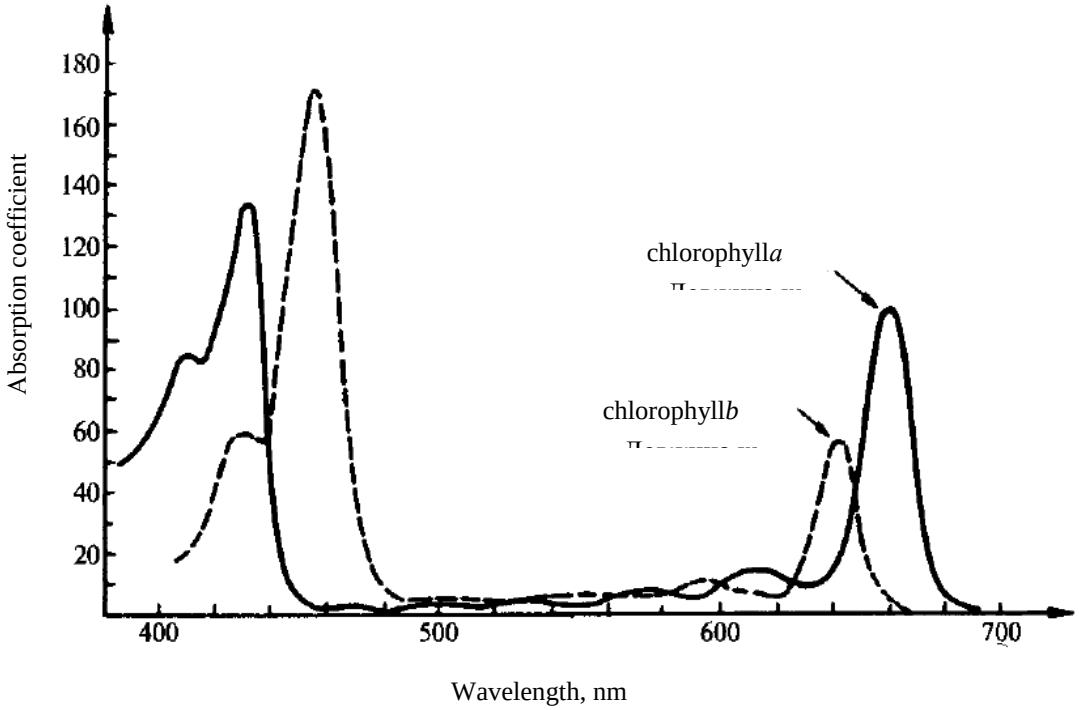

Fig.1 Absorption spectra of chlorophyll.

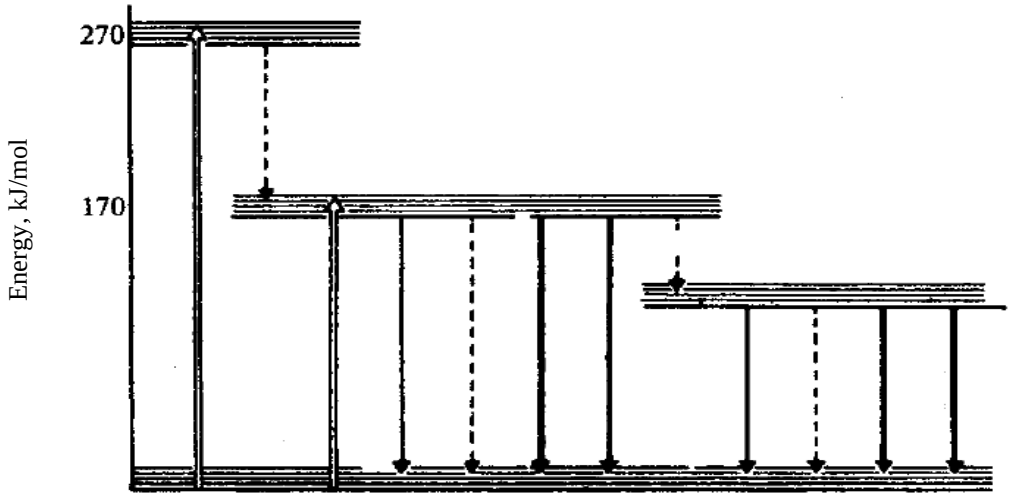

Fig.2. Energy levels of chlorophyll molecules.

The following photovoltaic process is the transfer of absorbed energy to the reaction centres. Energy is transferred to the reaction centre through a chain of pigments. The energy transfer between the pigment molecules occurs mainly by resonance way without charges separation with high speed. The energy transfer time from one chlorophyll molecule to another is 10^{-12} s. It is less than the lifetime of the chlorophyll molecule in the excited state S_1. While transferring, energy is partially lost, so the final energy state of the chlorophyll molecule to which energy flows is the S_1-state. Thus, the duration of the initial photophysical stage of absorption and transmission of light energy, which ends with the transfer of energy to the reaction centre, does not exceed 10^{-6} - 10^{-5} s [5].

The next stage of light energy conversion in plants, which runs in reaction centres, is photochemical. It like the absorption and transfer of energy, is part of the light phase of photosynthesis. Photochemical stage proceeds using light energy to reduce CO_2 to carbohydrates and oxidize H_2O to O_2. The general equation of photosynthesis is the following:

$$6CO_2 + 12H_2O + h\nu \rightarrow C_6H_{12}O_6 + 6O_2 + 6H_2O.$$

Here the water in the right part of the equation is produced from CO_2.

The time of photochemical processes is short and does not exceed 10^{-5} s.

The next stage of the conversion of absorbed energy is enzymatic. It proceeds without quanta of light and is called the dark stage of photosynthesis. At this stage, CO_2 is absorbed from the atmosphere and carbohydrates are formed. The enzymatic stage proceeds with a number of complex biochemical reactions. The time of dark photosynthesis reactions is more long-lasting than light and is about 10^{-2} s.

2. Research results and their discussion

This analysis of the kinetics of photoenergetic processes is the important information for planning experiments using alternating and light-pulse irradiation of plants. Experiments with pulsed light showed that the maximum intensity of photosynthesis is observed not in continuous, but in pulsed lighting, especially in cases where the duration of dark intervals was 0.04-0.06 sec, and the flash time is about 10 sec. The high efficiency of pulsed light proves the presence of dark reactions in photosynthesis, because dark processes are slower than photochemical ones[1].

Creating a pulsed irradiator, it was assumed that LED light sources are the most effective at this stage. They allow to form an irradiating installation with a given spectral distribution and the necessary lighting characteristics, switching power supplies with wide modulation. The information about the glow kinetics of LEDs is important for designing a pulsed irradiation system. The processes of increasing and decreasing luminous flux of narrow-spectrum LEDs of red, green and blue glow were studied.

To study the kinetics of the increase and decrease of the LEDs luminous flux, the photocurrent pulses of the photodetectors were used both at the output of the monochromator and the integrated photometer. Fig. 3 shows the front (a) and rear (b) fronts of photocurrent of the photoelectronic multiplier (PhEM) pulse for single-color ARPL-1W LEDs. They are also presented in a semi-logarithmic scale, which indicates the exponential nature of the increase and decrease of luminous flux. Time constants τ were determined from these graphs.

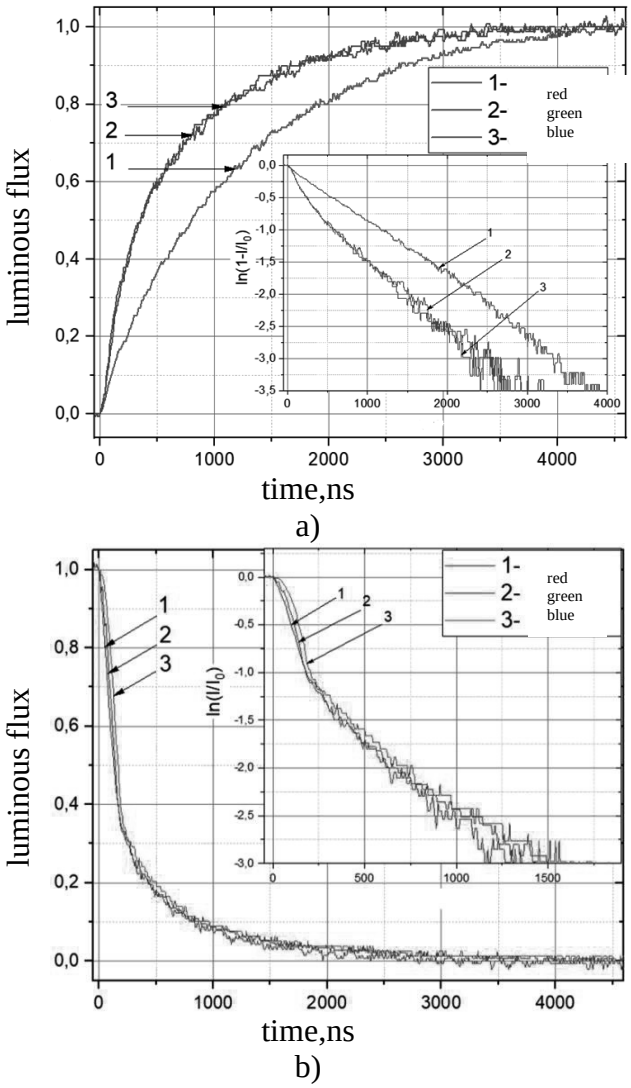

Fig.3 Front (a) and rear (b) fronts of PhEM photocurrent pulse of the single-color LED ARPL-1W.

Two components - fast and slow – are observed on the curves of increase and decrease of light flux. The values of their time constants at a pulse frequency of 50 kHz are given in table 1.

On the increase curves, the proportion (area) of the fast component is very small, which is 0.05-0.1 of light pulse amplitude, and for some of the studied samples (red glow LEDs) it is absent.

Table 1

Time constant of decrease and increase of luminous flux at a pulse frequency of 50 kHz.

Glow	LED type	decrease		increase	
		τ_1,(*ns*)	τ_2,(*ns*)	τ_1,(*ns*)	τ_2,(*ns*)
Red	1W	90	420	1200	
	3W	282	564	1497	
Blue	1W	100	495	1100…1200	
	3W	268	790	382	1212
Green	1W	250	500	1000	
	3W	245	581	500	1131

Determining the maximum pulse frequency f and the amount of filling D, it is necessary to take into account τ of increase and decrease of luminous flux.If it is assumed that the transient process in a LEDs electric circuit ends within 5τ, then fmax = 5τ / D. For the studied narrow-spectrum LEDs, f_{max} does not exceed the pulse frequency of 75 - 100].

Based on previous studies, where a Magnum LNF 150 luminaire and a pulse power device were used as a pulsed irradiator, light pulses in the dark are ineffective, so an experiment in which pulsed light acted as an additional light on the background of constant light irradiation of compact fluorescent lamps was set up.

S e e d l i n g s o f p e p p e r t . l e ( ] a i c i (w e r e u s e d

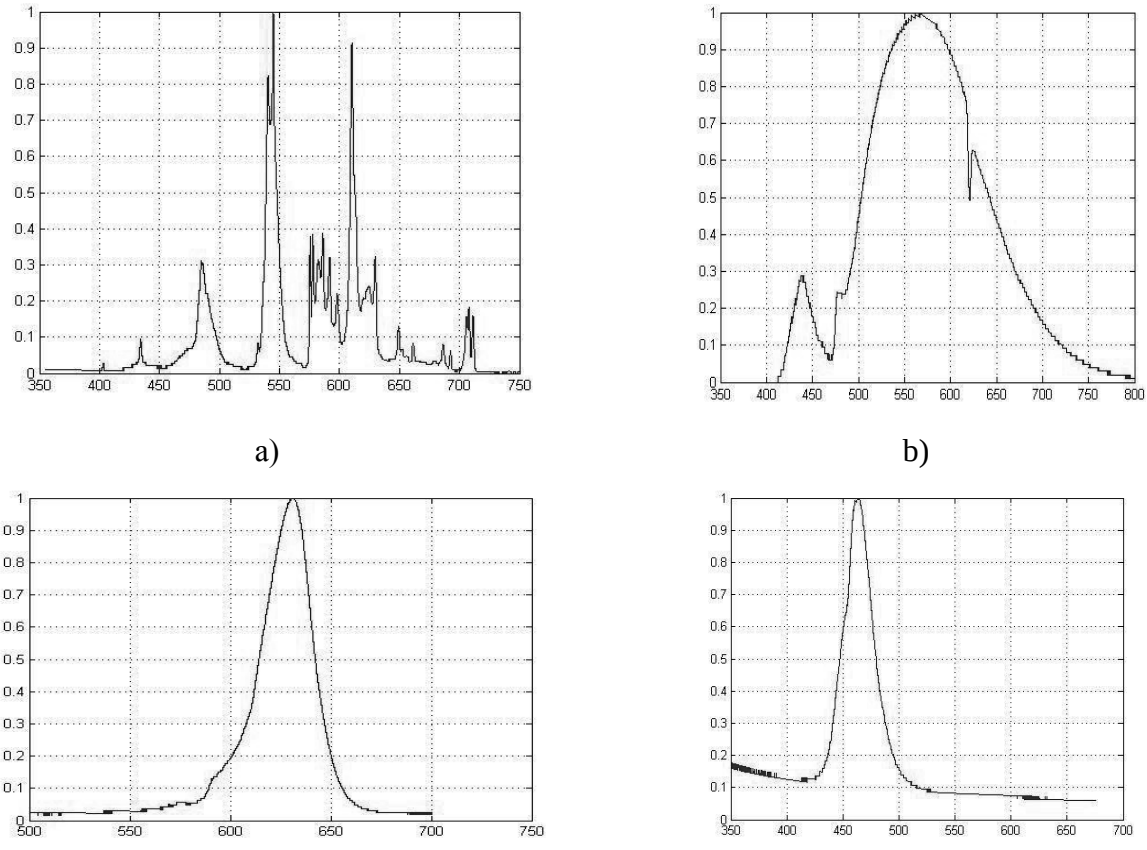

Fig.4 The emission spectrum: a) CFL; b) white LEDs; c) red LEDs; d) blue LEDs.

To assess the effectiveness of pulsed irradiation, the fluorescence intensity of the plant leaf was measured. Fluorescence parameters are the indicators of the state and efficiency of photosynthesis processes, because the decrease

of the efficiency of light energy in photosynthesis leads to the increase of fluorescence intensity. Usually during fluorescence there is a shift of luminescence radiation relative to the absorption towards greater wavelengths.

To excite the fluorescence of chlorophyll [10], in the range spectrum of 660-800 nm, used radiation with a wavelength of 480 nm or 532 nm. Under favourable conditions, no more than 3% of the energy of electronic excitation of chlorophyll is converted into the energy of fluorescence light in the form of so-called background fluorescence. If its value is small, it indicates the active use of energy of absorbed light by cells. This level of fluorescence corresponds to the conditions when all the reaction centres of the photosystem are in the so-called "open" operating state, in which they are unsaturated. Then the absorbed light energy is no longer used for photosynthesis, and the fluorescence of chlorophyll increases, reaching a maximum value. Saturation of the reaction centres can occur with increasing light intensity. Therefore, the intensity of chlorophyll fluorescence spectral lines is influenced not only by the current conditions of the plant but also by the intensity and duration of the light flux of excitation.

In the general case, the fluorescence intensity is proportional to the concentration of the fluorescent substance. However, this statement is valid only for relatively small concentrations. With the increasing concentration of the fluorescent substance, there are a number of effects. Due to these effects, the dependence of fluorescence intensity on concentration experiences significant deviations from linearity. Calibration graphs based on fluorimetry of the reference solutions are used in analytical fluorimetry and photometry procedures.

The results of the pulsed irradiation effect on the photosynthesis efficiency are presented in [5]. Based on chlorophyll fluorescence measurements, it was found that additional pulsed irradiation on the background of constant irradiation with compact fluorescent lamps led to the changes in the functional state of the photosynthetic apparatus and subsequently had a positive effect on plant productivity.

2 CFL of Osram Duluxstar 18W/840 type operating in continuous mode and providing 3000 lx radiation level were used for lighting in the first greenhouse.

The second greenhouse also used Constant irradiation produced by LED irradiation facility, consisting of red and blue LEDs with total capacity of 13.5 W was also used in the second greenhouse (2) and was installed above plants.

2 CFL of OsramDuluxstar 18W/840 type were used as permanent exposure in the third greenhouse. LED matrix of white luminescence with 1ms impulse duration and interval between pulses of 10s was used for pulsed irradiation. Its power consumption is 17.3 W.

Also measured morphometric parameters of plants (leaf area, cheese and dry weight of the leaf, growth parameters). To determine the morphometric and growth parameters of plants, 15 samples were cut and used to get the average measurement results. Received results are in table 2.

During the experiment, a constant temperature of the environment and the operating mode (16 hours of irradiation) was observed.

Table 2 shows that the raw and dry weight of leaves and the weight of the plant as a whole, which are important indicators for seedlings, as well as chlorophylls a and b, the area and % of dry matter with additional pulsed irradiation are higher, compared to those that were not accompanied by light pulses.

Table 2

Morphometric parameters at different irradiation modes

Morphometric parameters	Constant irradiation (CFL)	CFL + LED Red + Blue matrix (pulse)	CFL + LED White matrix (pulse)
raw mass of plant, g	0.73	0.75	0.78
raw mass of leaves, g	0.54	0.56	0.61
raw mass of the taken leaves, g	0.48	0.47	0.53
dry mass of leaves, g	0.08	0.09	0.1
% of dry matter	17.6	18.8	18.6
chlorophyll*a*	7	5.9	8.1
chlorophyll*b*	12.8	10.1	13.6
area, cm^2	23	25	30

3. Conclusions

From the analysis of the kinetics of photosynthetic processes, the duration of absorption and transmission of light energy to the reaction center does not exceed 10^{-6} - 10^{-5}sec. The time of photochemical processes does not exceed 10^{-5} sec. The time of dark reactions of photosynthesis is about 10^{-2}sec.

Based on the results of studies of the LEDs glow kinetics in pulsed power supply, a LED irradiation unit was designed, which was tested in the cultivation of pepper seedlings.

According to the results of experimental studies, it has been shown that pulsed irradiation stimulates faster plant growth without losing their morphometric parameters.

References

1. Andriychuk, V., Kostyk, L., Kotyk, M. (2019). Kinetyka fotoenerhetychnykh protsesiv u roslynakh, *Aktual'ni problemy svitlotekhniky*, Abstracts of VIIInternational conference. Ternopil.

2. Markov V.M. Ovoshchevodstvo. – M.: Vysshaya shkola, 1974. – 256 s.

3.Chervins′kyy L.S, Storozhuk L.O. «Svitlokul′tura roslyn – istoriya vynyknennya i stanovlennya» URL: http://inb.dnsgb.com.ua/2006-1/06clsivs.html

4. Yakushkyna, N.Y. (1980). *Fiziolohiya rastenyy*. Moscow: Prosveshchenye.

5. Biofizyka [onlayn tsyt .: 2021-08-22]. Retrieved from URL: http://biophys.msu.ru/general_courses/laboratory_classes/material/mprac/8new002.pdf

6. Andriychuk, V., Nakonechnyy, M., Osadtsa, Ya., Filyuk, Ya. (2021). Doslidzhennya svitlodiodnykh dzherel svitu u vypadku impul′snoho zhyvlennya. *Tekhnichna elektrodynamika*. *68*(1). doi: https: //doi.org/10.15407/techned 2021.01.068.

7. Herts, A., Kotyk, M., Andriychuk, V. (2018). Lighting instalations for plants lightculture with additional impulsive radiation. *Visnyk TNTU*, 92(4), 91-97.

8. Andriychuk, V.A., Hnatovych, M.I., Herts, A.I. (2014). Enerhooshchadni dzherela svitla dlya osvitlennya roslyn. *Svitlotekhnika ta elektroenerhetyka*, 41-48.

9. Kotyk, M.I., Andriychuk, V.A., Kostyk, L.N., Gerts, N.V., Gerts, A.I. (2019) Pulse light stimulation of pepper sprouts cultivation. *Light&Engineering, 27*, 84-91.

10. Tarnovs′kyy, M., Yankovs′kyy, Ya. (2012). Optychni metody analizu fiziolohichnoho stanu roslyn dlya zavdan′ sil′s′koho hospodarstva ta ekolohichnoho monitorynhu. 127-130.

Cross-sectional: AUTOMATION AND COMPUTER INTEGRATED TECHNOLOGIES

SUBSTANTIATION OF DESIGN PARAMETERS OF BERNOULLI GRIPPERS WITH AUTOMATED CONTROL OF THE SIZES OF OBJECTS OF MANIPULATION

Volodymyr Savkiv[1], Roman Mykhailyshyn[2], Frantisek Duchon[3], Michal Kelemen[4]

1 Ternopil National Ivan Puluj Technical University, Rus'ka str. 56, 46001, Ternopil, Ukraine; E-mail: s_v@tntu.edu.ua
2Ternopil National Ivan Puluj Technical University, Rus'ka str. 56, 46001, Ternopil, Ukraine; E-mail: mykhailyshyn@tntu.edu.ua
3Slovak University of Technology in Bratislava, Ilkovičova 3, SK-812 19, Bratislava; Slovak Republic, E-mail: frantisek.duchon@stuba.sk
4Technical University of Kosice, Letna 9, 04200, Kosice, Slovak Republic, E-mail: michal.kelemen@tuke.sk

Abstract: The advantages of using jet gripping devices with integrated function of size control of objects of manipulation in robotic systems are substantiated. Rational designs of gripping devices are proposed, which allow to measure the diameter of the object held by them, their design parameters are substantiated. The interaction of air flows flowing from the annular nozzle and measuring ejector nozzles in the gap between the outer surface of the jet gripper and the inner surface of the object of manipulation is carried out. Reynolds-averaged Navier-Stokes equations of viscous gas dynamics, SST-model of turbulence and γ-model of laminar-turbulent transition were used for this purpose. As a result of numerical simulation in the Ansys-CFX software environment, the influence of the spatial location of the measuring nozzles on the load capacity of the jet gripper, the range and accuracy of measuring the diameters of manipulation objects was determined.

Keywords: *Bernoulli gripping device, object manipulation, air gaging, nozzle, industrial robot, RANS, SST-model of turbulence.*

1. Introduction

One of the main requirements for technological equipment of flexible automated production systems is a combination of high productivity with precision operations. Effective provision of these requirements is achieved by the maximum concentration of technological operations in a unit of technological equipment using an automatic control system [1-2]. One of the promising ways to increase the productivity of automated production systems is the integration of transport and loading operations with operations to control the parameters of transportation facilities [3-4].

In addition, in modern machining there is a need to organize the modes of optimal and adaptive processes, which are implemented using methods of active control of the parameters of the objects of manipulation (OM). The obtained information about the parameters of the OM is used for further calculations of the most efficient processing modes.

Robotization of transport and loading operations using Bernoulli grippers creates additional opportunities for automation of a number of ancillary operations. The advantage of these grippers is that they carry out contactless capture and retention of OM, the air flow has the ability to clean the surface of the object from various contaminants, can work with objects heated to high temperatures, and create opportunities for pneumatic control and orientation. objects. Design and operational features of jet grippers provide the following advantages over classical methods of measurement by pneumatic means: accurate centering of OM relative to the axis of the gripper in the measuring position, control of axisymmetry and taper OM, increased measurement accuracy, increasing the range of measured dimensions and others. [5-12].

Determination of manipulation object's mass during the robot's handling operations creates a number of additional opportunities for automation of the following processes: sorting of objects of production according to weight or control of a deviation of weight from necessary; definition of the inertial force operating on OM connected with acceleration (braking) of links of the manipulator that allows regulations of power characteristics of a gripping device and to carry out its reorientation for the purpose of decrease in energy consumption [13-20].

The pneumatic method of measurement was widely used for control of the linear sizes [21-23]. This method of measurement provides high accuracy, allows to exercise remote control in hard-to-reach spots. The pneumatic method of measurement allows to control without contact easy to break and fragile details and also details with coverings which can be damaged by mechanical contact. It is easy to automate and operate air measuring devices, they have high reliability and durability of work.

However the typical pneumatic method of measurement has considerable inertance that reduces measurement speed. For speeding up and the accuracy of a pneumatic method of measurement it is necessary to minimize volumes of flowing cameras, to use an ejector nozzle and modern high-precision and low-inertia pressure sensors.

2. Methodology

Fig. 1 shows a BGD circuit that combines the functions of capturing, centering relative to its own axis and conducting active non-contact control of the inner diameter of the OM with the inner blind hole. The jet gripper is structurally simple and provides high operational indicators on reliability and durability of work at preservation for all time of its service of constantly high accuracy of measurement.

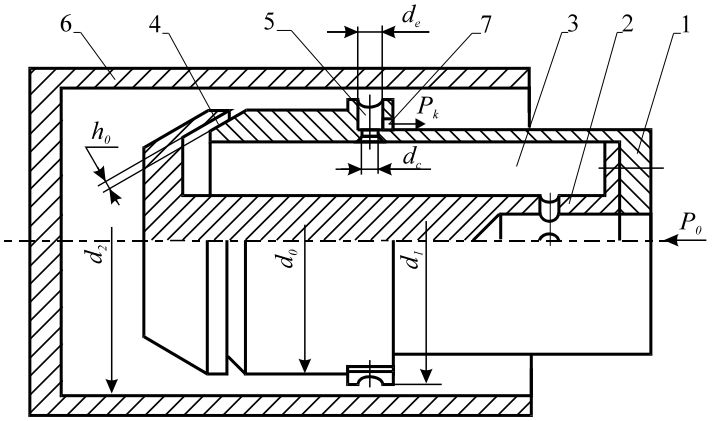

Fig.1 Structural diagram of the jet device for capturing and controlling the inner diameter of the object of manipulation

The device consists of a housing 1, in which the insert 2 is fixed, forming with it a closed chamber 3 for the supply of compressed air. Between the outer chamfer of the housing 1 and the inner chamfer of the insert 2, an adjustable annular conical slit 4 is formed for the release of compressed air from the chamber 3 into the atmosphere. In the body of the housing 1 in the direction of air flow from the annular conical slit 4, perpendicular to its axis is made an even number of symmetrical ejector nozzles 5. To ensure high measurement accuracy and load-carrying capacity of the jet gripper, it is necessary that the active surfaces of the ejector nozzles 5 protrude relative to the side surface of the housing 1 at a distance $\delta=(d_1-d_0)/2$. Their 2-row arrangement for measuring the conicity of the OM surface and 2-pair placement of symmetrical nozzles in a row when measuring axisymmetry in mutually perpendicular diameters are allowed. In the nozzles 5 perpendicular to their own axis made holes 7, which are mounted sensors for converting pressure into voltage (not shown). Piezoceramic transducers, which best meet the requirements of sensitivity and small size, are the most suitable for conversion.

The device in gripping mode works on the following principle. Compressed air from the main, which flows through the slit 4 into the atmosphere, is supplied to the chamber 3. When gripping OM 6, the air in the annular gap between the side surface of the housing 1 and the inner surface of OM forms a continuous annular flow causing due to ejection lowering the absolute pressure p_1 at the end of the insert 2 to less than atmospheric. Under the action of aerodynamic force, the workpiece is attracted to the end of the insert 2 and in the process of movement is centered by an annular flow of air relative to the axis of the gripping device. In this case, the inner cylindrical surface of the OM overlaps the ejector nozzles 5, causing them to increase the absolute pressure to the level of p_k.

The value of the pressure p_k depends on the design parameters of the nozzle, the main pressure p_0 and the interval h_2 formed by the end of the nozzle and the inner surface of the OM and equal to $h_2=(d_2-d_1)/2$. By measuring the value of the pressure p_k in the ejector nozzle and taking into account the dependence $p_k(h_2)$, the inner diameter d_2 OM 6 is determined. The pressure value p_k is directly measured in a transducer of the converter type, the output signal of which is the voltage $U_D=f[p_k(h_2)]$, which is converted by an analog-to-digital converter into a digital code. It is further processed by the processor and transferred to the local control system of technological equipment.

In order to select the optimal design parameters of the BGD that would provide the greatest load capacity and measurement accuracy, it is necessary to simulate air flows in the intervals between the interacting surfaces of the gripper and OM. The solution of this problem is based on the approaches of computational hydrodynamics and information technology for simulation of numerical modeling by the finite element method (FEM). FEM allows to determine with high accuracy the distributions of pressure, velocities, to obtain flow lines and other flow parameters. Modeling of various design options for BGD measuring nozzles was performed using the Ansys CFX CFD package, which is designed to model the flow of liquids and gases.

The mathematical model of course of air in radial interval between the interacting surfaces of BGD and OM is based on Navier-Stokes's (Reynolds averaged Navier-Stokes equations) equations (RANS) average according to Reynolds [24, 25]. Neglecting mass forces the system of the equations will have the following appearance:

$$\frac{\partial \rho}{\partial t}+\frac{\partial(\rho \cdot V_j)}{\partial x_j}=0, \qquad (1)$$

equation of continuity of stream:

$$\rho \frac{\partial V_i}{\partial t} + \rho \cdot V_j \cdot \frac{\partial V_i}{\partial x_j} = \frac{\partial P_{ji}}{\partial x_j}, \tag{2}$$

energy equation:

$$\rho \frac{\partial E}{\partial t} + \rho \cdot V_j \cdot \frac{\partial E}{\partial x_j} = -\frac{\partial q_j}{\partial x_j} + \frac{\partial}{\partial x_j}\left(P_{ji} \cdot V_i\right); \tag{3}$$

ideal gas law equation:

$$\rho = \frac{p_a + p}{R \cdot T}; \tag{4}$$

where *i*, *j* - indexes, accept values 1, 2, 3; ρ - firmness of air; *t* - time; *x* - coordinate; *V* - vector of speed of the movement of air; *p* - excessive pressure of air; **P** - tensor of tension; *E* - total energy of air; *q* - the vector of firmness of heat flux considering transfer of heat due to heat conductivity and diffusion; *R* - gas constant; *T* - absolute air temperature.

Turbulence modeling is one of the most important aspects of CFD modeling, and choosing the right turbulence model is key to receive reliable results. Since our working gaps are quite small, namely between the measuring nozzle and the surface of the manipulation object, we chose the SST model of turbulence [26-28] and the γ-model of the laminar-turbulent transition [29], as they better describe near-wall flows.

The γ-model of a laminar-turbulent transition is described by one differential equation for the coefficient of interference γ:

$$\frac{\partial(\rho\gamma)}{\partial t} + \frac{\partial(\rho V_j \gamma)}{\partial x_j} = P_\gamma - E_\gamma + \frac{\partial}{\partial x_j}\left[\left(\mu + \frac{\mu_t}{\sigma_\gamma}\right)\frac{\partial \gamma}{\partial x_j}\right] \tag{5}$$

where ρ - air density; *t* – time; *x* – coordinate; *V* – vector of air velocity; P_γ, E_γ - respectively generative and dissipation members of managing directors of laminar and turbulent transition; μ - molecular dynamic viscosity of gas; μ_t - turbulent dynamic viscosity of gas; $\sigma_\gamma = 1.0$ - model constant.

In the γ-model of the transition, the modified SST model equations are used:

$$\frac{\partial}{\partial t}(\rho k) + \frac{\partial}{\partial x_j}(\rho V_j k) = \tilde{P}_k + P_k^{\lim} - \tilde{D}_k + \frac{\partial}{\partial x_j}\left((\mu + \sigma_k \mu_t)\frac{\partial k}{\partial x_j}\right) \tag{6}$$

$$\frac{\partial}{\partial t}(\rho \omega) + \frac{\partial}{\partial x_j}(\rho V_j \omega) = \alpha \frac{P_k}{\nu_t} - D_\omega + Cd_\omega + \frac{\partial}{\partial x_j}\left((\mu + \sigma_\omega \mu_t)\frac{\partial \omega}{\partial x_j}\right) \tag{7}$$

where k - kinetic turbulent energy; ω - the specific speed of dissipation of kinetic energy of turbulence; P_k, D_k - original generation and dissipation of the SST model; $P_k^{\lim}$ - the additional part, which provides the correct gain of turbulent viscosity in transitional area at very low level of turbulent viscosity of the running stream; ν_t - turbulent kinematic viscosity of gas; σ_k, α, a_1 - empirical constants of model.

3. Results of the investigation

The jet gripper, depending on the design and location of the measuring nozzles, has different operating characteristics (holding force OM, range of measured diameters, measurement accuracy). In order to improve the operational characteristics of the SZP with an integrated control function of the diameter of the OM, a number of structural schemes of grippers (Fig. 2) with different arrangement of measuring nozzles are considered. In particular, the use of measuring nozzles inclined relative to the axis of symmetry of the BGD at an angle of 30… 45 ° (Fig. 2b, c) allows to increase the load capacity of the gripper. The displacement of the active peripheral surface of the measuring nozzle relative to the basic active cylindrical surface of the BGD provides it with a more efficient mode of operation, as it achieves higher measurement accuracy and load capacity.

To compare the presented design variants, we analyze the influence of the interval $h_2=(d_2-d_1)/2$, which characterizes the change in the diameter of OM, on the load capacity of these grippers and on the measuring characteristic $p_k(h_2)$. The following design parameters of BGD are accepted: h_0=0,1 mm, d_0=32,62 mm, δ=0,25 mm, d_c=0,5 mm, d_e=0.79 mm. The load capacity of the BGD is directly proportional to the vacuum of p_{e1} created by it in the cavity of the gripped OM

$$F = p_{e1}\pi d_2^2/4, \tag{8}$$

therefore, we will analyze how the change in the annular interval h_2 will affect this rarefaction.

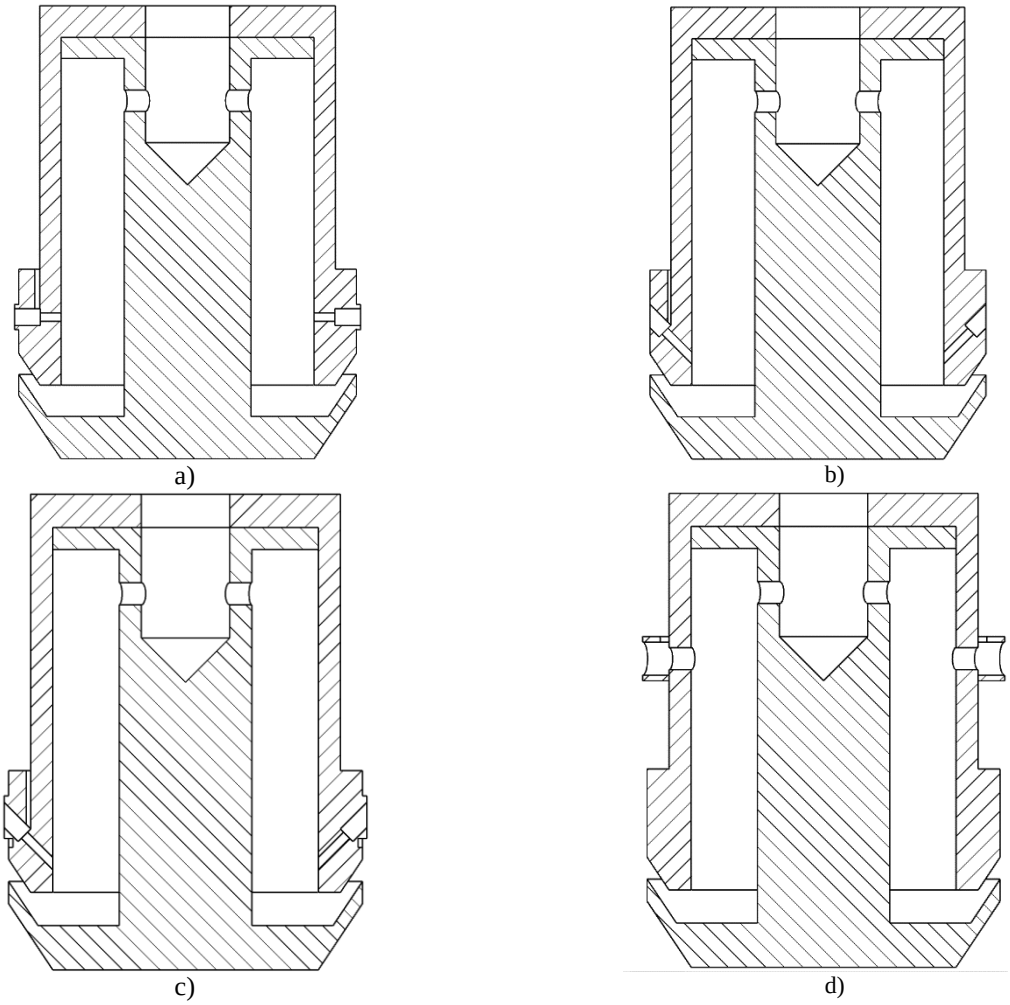

Fig. 2 Variants of Bernoulli gripper designs with the function of controlling the diameter of the object to be manipulated

Construction of characteristics $p_{в1}(h_2)$ and $p_k(h_2)$ for each circuit presented in Fig. 2, was performed on the basis of the mathematical model presented above and the accepted assumptions using the Ansys CFX package, which is designed to model the flow of liquids and gases.

An example of a geometric model of air flows with a scheme of finite element partition of the calculation area is shown in Fig. 3, and the calculation scheme of the model after setting the boundary conditions in Fig. 4. These models correspond to the structural scheme presented in Fig. 2d. Similar models were built for other structural schemes, and the value of the interval h_2 varied within 0.1…0.7 mm. Grids were built either in the CFX-Mesh package application or in the universal ANSYS ICEM CFD network package.

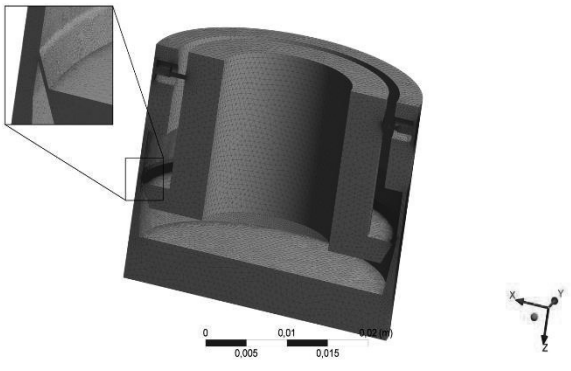

Fig. 3 Geometric model of air flows and the scheme of finite-element partition of the calculation area

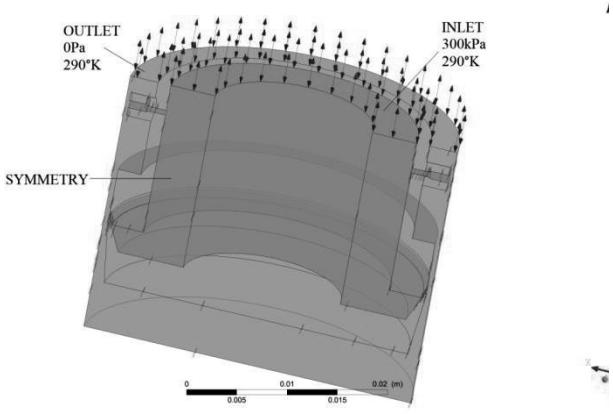

Fig. 4 Calculation scheme of the model after setting the boundary conditions

As a result of modeling the air dynamics in the intervals between the interacting surfaces of the BGD and OM, the values of pressure and velocities for all elements of the flow were obtained. As an example in fig. 5 and 6 present the simulation results in the form of pressure contours and flow lines with color notation of specific values. This graphical representation of the simulation results allowed for a deeper understanding of the interaction of flows and to develop approaches to the rational spatial arrangement of the nozzles and profiling of the active surfaces of the BGD.

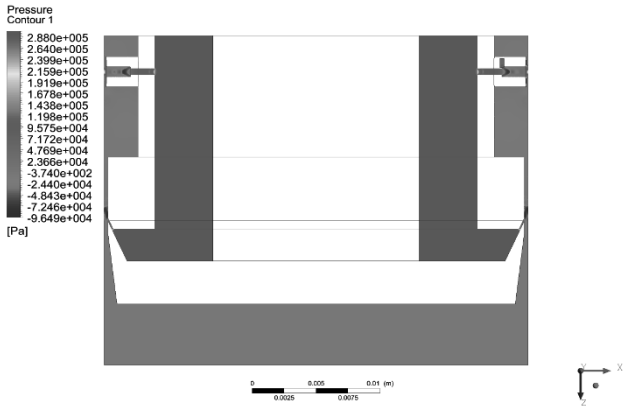

Fig. 5 The results of modeling the pressure circuits

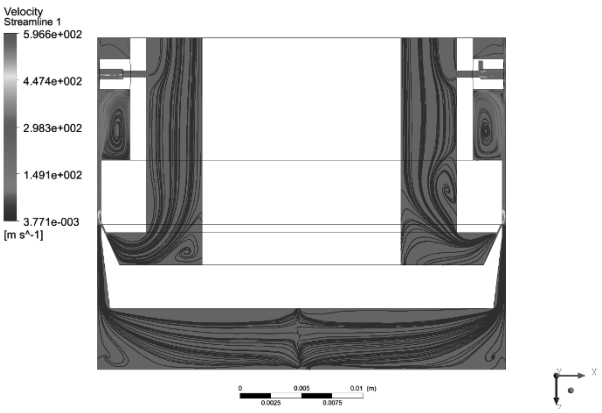

Fig. 6 Results of modeling of flow lines and velocity distribution (Fig.5)

The results of modeling the operational characteristics of BGD (Fig. 2) are presented in Fig. 7.

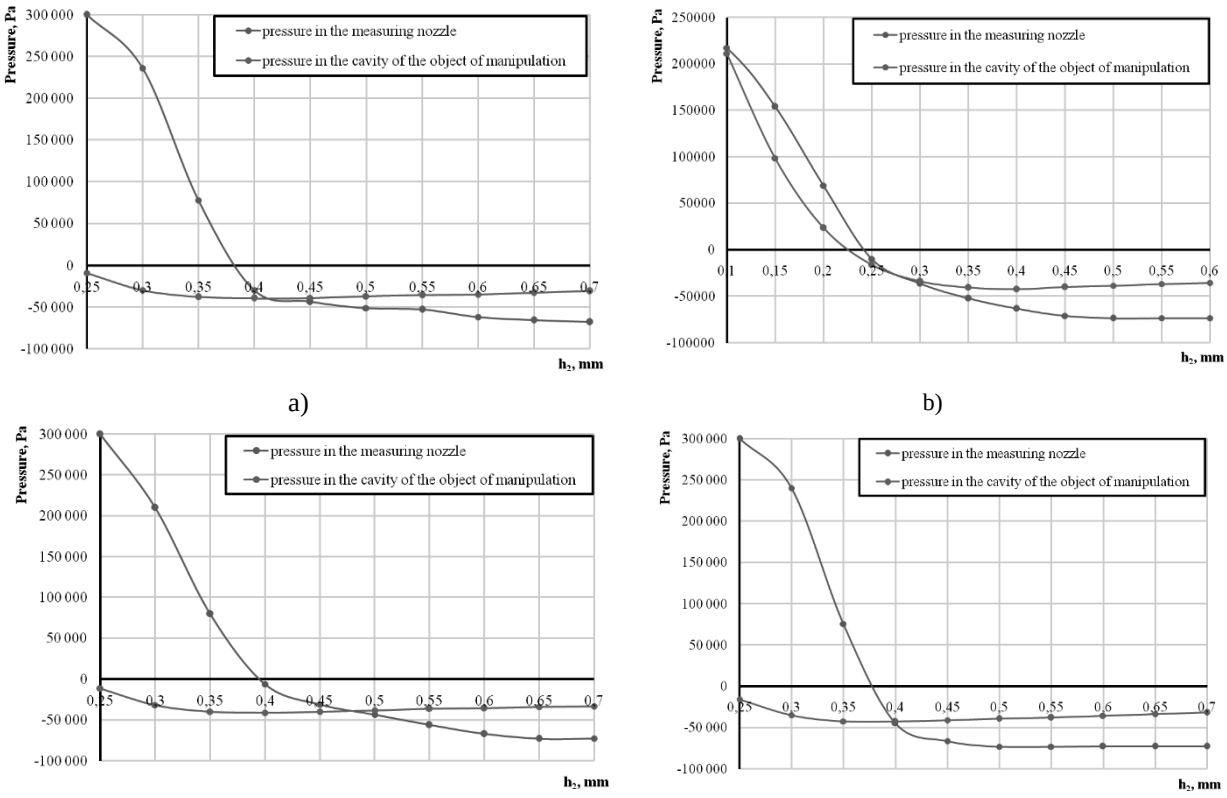

Fig. 7 The results of modeling the performance of Bernoulli grippers with the function of controlling the diameter of the manipulation object (graphs in Fig. a correspond to the design of Fig. 2a, etc.)

As can be seen from the presented graphs, design options (Fig. 2b, c) with inclined relative to the axis of symmetry of the BGD measuring nozzles can increase its load capacity by 5…12%. The displacement of the active surfaces of the measuring nozzles relative to the base cylindrical surface of the BGD by the value of δ=0.2…0.25 mm

allows more efficient operation of this device, as in this case the range of maximum load capacity corresponds to the linear part of the measuring characteristic diameters.

To select rational structures of BGD it is necessary to determine their load capacity according to formula (8) and the sensitivity of their measuring characteristics. Sensitivity is defined as the tangent of the angle of inclination of the linear part of the measuring characteristic

$$s = \frac{|p_{k\max} - p_{k\min}|}{h_{2\max} - h_{2\min}}, \tag{9}$$

where $p_{k\max}$ and $p_{k\min}$ are the maximum and minimum values of the pressure on the linear part of the measuring characteristic, corresponding to the maximum and minimum values of the annular gap $h_{2\max}$ and $h_{2\min}$.

In the presented graphs, the central point of the linear part of the measuring characteristic corresponds $h_2 \approx 0.35$ mm. At this point, the load capacity of the presented structures of the BGD is also almost maximum. Accordingly $h_{2\min} \approx 0.3$ mm and $h_{2\max} \approx 0.4$ mm. For these points, the load capacity and sensitivity of the measuring characteristics were determined. The results are summarized in the table.

Table 1

The results of load capacity and sensitivity of different structures

Type of construction	Lifting capacity, [N]	*s*, [kPa/mm]
Fig. 2a	36,2	2650
Fig. 2b	41	1350
Fig. 2c	37,7	2150
Fig. 2d	37,7	2840

As can be seen from the table, the set of characteristics is best to use structures with measuring nozzles located perpendicular to the axis of the BGD.

4. Conclusions

It is proved that the use of Bernoulli grippers of industrial robots with an integrated function of controlling the size of manipulation objects increases the productivity of technological processes.

Based on numerical simulations in the Ansys-CFX software environment, it was found that the designs of Bernoulli grippers that use measuring nozzles inclined relative to their axis of symmetry have a 5…12% higher load capacity.

The displacement of the active surfaces of the measuring nozzles relative to the base cylindrical surface of the Bernoulli gripper by 0.2…0.25 mm allows operating this device more efficiently, as in this case the range of maximum load capacity corresponds to the linear part of the measuring characteristic. .

It is established that the jet gripping devices have best aggregate operational characteristics in which the measuring nozzles are located perpendicular to their axis.

References

1. Benhabib, B. (2003). *Manufacturing: design, production, automation, and integration*. CRC Press.

2. Wang, Yi., Martinsen, K., Yu, T., Wang, K. (2021). *Advanced Manufacturing and Automation X*. Springer Nature.

3. Savkiv, V., Mykhailyshyn, R., Duchon, F., Prentkovskis, O., Maruschak, P., Diahovchenko, I. (2019). Analysis of operational characteristics of pneumatic device of industrial robot for gripping and control of parameters of objects of manipulation. *Transportation Science and Technology*, Proceedings of the International Conference *TRANSBALTICA*. doi:10.1007/978-3-030-38666-5_53.

4. Savkiv, V., Mykhailyshyn, R., Maruschak, P., Kyrylovych, V., Duchon, F., Chovanec, Ľ. (2021). Gripping devices of industrial robots for manipulating offset dish antenna billets and controlling their shape. *Transport*, *36*(1), 63-74. doi:10.3846/transport.2021.14622.

5. Stühm, K., Tornow, A., Schmitt, J., Grunau, L., Dietrich, F., Dröder, K. (2014). A novel gripper for battery electrodes based on the Bernoulli-principle with integrated exhaust air compensation. *Procedia CIRP*, *23*, 161-164. doi:10.1016/j.procir.2014.10.065.

6. Li, X., Kagawa, T. (2013). Development of a new noncontact gripper using swirl vanes. *Robotics and Computer-Integrated Manufacturing*, *29*(1), 63-70. doi:10.1016/j.rcim.2012.07.002.

7. Savkiv, V., Mykhailyshyn, R., Duchon, F., Fendo, O. (2017). Justification of design and parameters of Bernoulli–vacuum gripping device. *International Journal of Advanced Robotic Systems*, *14*(6). doi:10.1177/1729881417741740.

8. Savkiv, V., Mykhailyshyn, R., Duchon, F. (2019). Gasdynamic analysis of the Bernoulli grippers interaction with the surface of flat objects with displacement of the center of mass. *Vacuum*, *159*, 524-533. doi:10.1016/j.vacuum.2018.11.005.

9. Mykhailyshyn, R., Savkiv, V., Boyko, I., Prada, E., Virgala, I. (2021). Substantiation of Parameters of Friction Elements of Bernoulli Grippers With a Cylindrical Nozzle. *International Journal of Manufacturing, Materials, and Mechanical Engineering (IJMMME)*, *11*(2), 17-39. doi:10.4018/IJMMME.2021040102.

10. Mykhailyshyn, R., Savkiv, V., Duchon, F., Chovanec, L. (2020). Experimental Investigations of the Dynamics of Contactless Transportation by Bernoulli Grippers. *Methods and Systems of Navigation and Motion Control (MSNMC)*, Proceedings of the 6th International Conference. doi: 10.1109/MSNMC50359.2020.9255521.

11. Savkiv, V., Mykhailyshyn, R., Duchon, F., Maruschak, P. (2019). Justification of influence of the form of nozzle and active surface of Bernoulli gripping devices on its operational characteristics. *Transportation Science and Technology*. Proceedings of the International Conference TRANSBALTICA. doi: 10.1007/978-3-030-38666-5_53.

12. Savkiv, V., Mykhailyshyn, R., Maruschak, P., Chovanec, L., Prada, E., Virgala, I., Prentkovskis, O. (2019). Optimization of design parameters of Bernoulli gripper with an annular nozzle. *Transport Means 2019: Sustainability: Research and Solutions.*Proceedings of the 23rd International Scientific Conference.

13. Savkiv, V., Mykhailyshyn, R., Fendo, O., & Mykhailyshyn, M. 2017. Orientation modeling of Bernoulli gripper device with off-centered masses of the manipulating object. *Procedia Engineering*, 187, 264-271.

14. Savkiv, V., Mykhailyshyn, R., Duchon, F., Mikhalishin, M. (2018). Modeling of Bernoulli gripping device orientation when manipulating objects along the arc. *International Journal of Advanced Robotic Systems*, *15*(2). doi:10.1177/1729881418762670.

15. Mykhailyshyn, R., Savkiv, V., Mikhalishin, M., Duchon, F. (2017). Experimental research of the manipulatiom process by the objects using bernoulli gripping devices. *International Young Scientists Forum on Applied Physics and Engineering*. Proceedings of International Forum. https://doi.org/10.1109/YSF.2017.8126583.

16. Savkiv, V., Mykhailyshyn, R., Duchon, F., Mikhalishin, M. (2017). Energy efficiency analysis of the manipulation process by the industrial objects with the use of Bernoulli gripping devices. *Journal of Electrical Engineering*, *68*(6). doi:10.1515/jee-2017-0087.

17. Mykhailyshyn, R., Savkiv, V., Duchon, F., Trembach, R., Diahovchenko, I.M. (2019). Research of energy efficiency of manipulation of dimensional objects with the use of pneumatic gripping devices. *2nd Ukraine Conference on Electrical and Computer Engineering* (UKRCON). Proceedings of Conference. doi:10.1109/UKRCON.2019.8879957.

18. Savkiv, V., Mykhailyshyn, R., Duchon, F., Maruschak, P., Prentkovskis, O. (2018). Substantiation of Bernoulli grippers parameters at non-contact transportation of objects with a displaced center of mass. *Transport Means.* Proceedings of the 22nd International Scientific Conference. Klaipeda.

19. Mykhailyshyn, R., Savkiv, V., Duchon, F., Koloskov, V., Diahovchenko, I.M. (2018). Investigation of the energy consumption on performance of handling operations taking into account parameters of the grasping system. *Intelligent Energy and Power Systems.* Proceedings of the 3rd International Conference. doi: 10.1109/ieps.2018.8559586.

20. Mykhailyshyn, R., Savkiv, V., Duchon, F., Koloskov, V., Diahovchenko, I.M. (2018). Analysis of frontal resistance force influence during manipulation of dimensional objects. *Intelligent Energy and Power Systems*, Proceedings of the *3rd International Conference*, doi: 10.1109/ieps.2018.8559527.

21. Jermak, C.J., Jakubowicz, M., Dereżyński, J., Rucki, M. (2016). Air gauge characteristics linearity improvement. *Journal of Control Science and Engineering*. doi:10.1155/2016/8701238.

22. Jermak, C.J., Rucki, M. (2016). Static characteristics of air gauges applied in the roundness assessment. *Metrology and Measurement Systems*, *23*(1), 85-96. doi:10.1515/mms-2016-0009.

23. Jakubowicz, M., Derezynski, J. (2017). The measuring position designed to determine the metrological properties of air gauges. *Advances in Science and Technology*, *11*(4), 198-205. doi:10.12913/22998624/79830.

24. Snegiryov, A.Y. (2009). *High-performance computing in technical physics. Numerical Simulation of Turbulent Flows*. S. Petersburg: Polytechnic University Publ.

25. Garbaruk, A.V. (2016). *Modern approaches to modeling turbulence*. S. Petersburg: Polytechnic University Publ.

26. Menter, F.R. (1994). Two-equation eddy-viscosity turbulence models for engineering applications. *AIAA journal*, *32*(8), 1598-1605. doi:10.2514/3.12149.

27. Menter, F.R., Esch, T., Kubacki, S. (2002). Transition modelling based on local variables. *Engineering Turbulence Modelling and Experiments*, *5*, 555-564. doi:10.1016/B978-008044114-6/50053-3.

28. Menter, F.R., Langtry, R., Völker, S. (2006). Transition modelling for general purpose CFD codes. *Flow, turbulence and combustion*, *77*(1-4), 277-303. doi:10.1007/s10494-006-9047-1.

29. Menter, F.R., Smirnov, P.E., Liu, T., Avancha, R. (2015). A one-equation local correlation-based transition model. *Flow, Turbulence and Combustion*, *95*(4), 583-619. doi:10.1007/s10494-015-9622-4.

THE INCREASING OF PHOTOVOLTAIC POWER SUPPLY SYSTEM EFFICIENCY FOR THE MOBILE UNIT OF POLYMER WASTE PROCESSING INTO AN ALTERNATIVE TYPE OF FUEL

Valeriy Martynyuk[1], Mykola Fedula[2], Denys Makaryshkin[3], Tomasz Kałaczyński[4]

[1]Khmelnytskyi National University, Khmelnytsky, Ukraine, 11 Institutska street
+380673477457, martynyuk.valeriy@gmail.com
[2]Khmelnytskyi National University, Khmelnytsky, Ukraine, 11 Institutska street
+380988592335, mailfm2000@gmail.com
[3]Khmelnytskyi National University, Khmelnytsky, Ukraine, 11 Institutska street
+380973113300, makaryshkin@ukr.net
[4]UTP University of Science and Technology, Bydgoszcz, Poland, Al. Prof. S.Kaliskiego 7
+48606230909, kalaczynskit@utp.edu.pl

Keywords: Photovoltaic power supply system, Mobile polymer waste processing unit, Alternative type of fuel, Rechargeable batteries, Supercapacitor batteries

2. Introduction

A very important task is to prevent plastic waste from entering natural ecosystems, as well as their recycling for reuse [1]. The production of fuel from plastic waste will not only help clean the planet of plastic waste, but will also save the planet's energy resources and reduce the negative impact on the environment from the process of oil production and refining [2].

The polymer waste processing mobile unit (PWPMU) of Obolon Oil (Ukraine) [3, 4] requires an autonomous power supply using photovoltaic technologies and a storage system for use directly at waste disposal sites, and sorting stations. This eliminates the need to transport the waste to recycling points and reduces recycling costs and the induced transportation air pollution.

Today, autonomous energy supply systems, which use renewable energy sources, are intensively studied, both theoretically and experimentally, and applied in different geographical parts of the world [5, 6]. The publications analyze the performance of autonomous power supply systems, taking into account the average hourly insolation of sunlight, ambient temperature and load power profile [7]. The mathematical models are developed to estimate the size, control and evaluate the efficiency of the autonomous power supply systems, which contain solar photovoltaic modules (PM), a diesel generator and rechargeable accumulator batteries [7-9]. In publications on autonomous power supply systems, there are no studies of the processes and methods to increase the efficiency of energy extraction from solar module, compensation of the peak (starting) load currents, balancing electrochemical capacitor cells, operating temperature control and multi-stage battery charge for longevity. All these scientific problems require in-depth research.

We propose the structure of the highly efficient autonomous power supply system for the PWPMU. It includes solar photovoltaic modules, rechargeable accumulator batteries, and electrochemical capacitor batteries, with smart model-based control technology. We developed and investigated the dynamic solar tracking system (DSTS) with optimized control of the PM in fog, clouds, heavy rainfall, and strong winds. The overall robust and optimal performance is achieved by using the improved control methods for DSTS. It will increase the PM productivity by up to 30% and reduce the land occupied by the PM.

1. Improving the efficiency of energy extraction from photovoltaic modules by tracking the sun position

The maximum energy can be received by the photovoltaic module from the sun when the panel of photocells is located perpendicular to the direction of solar radiation. Even small deviations (5 to 15 degrees) from the perpendicular orientation can reduce the generated power by 25 percent or more [10-12].

Thus, to obtain high efficiency of energy extraction from the photovoltaic module, it is necessary to implement a device for tracking the sun position, which can provide constant support of the angle between the solar module surface and the direction of solar radiation as close as possible to 90 degrees. Fig. 1 shows the process of tracking the sun position with the angle of 90 degrees [10, 11].

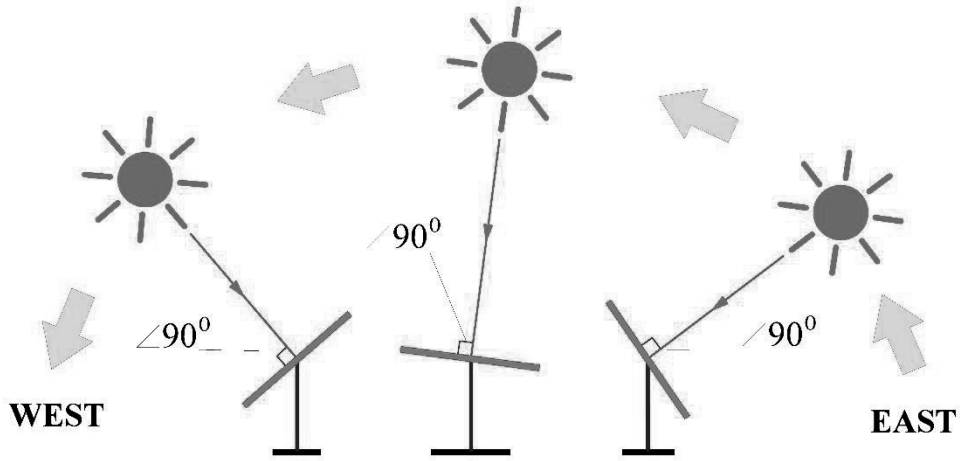

Fig. 1 shows the three optimal positions of the photovoltaic module for different times of the day. The arrows show the direction of the solar radiation.

The generalized block diagram of the device for tracking the sun position is shown in Fig. 2.

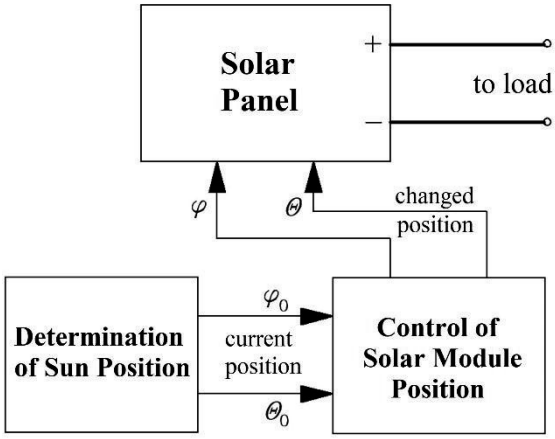

Fig. 2. Structure of sun tracking device

The device for tracking the sun position includes a unit for determining the sun position, which transmits to the control device the required values of the angles of azimuth φ_0 and zenith θ_0 of solar module. Then, the solar module position control device rotates to the appropriate angles φ (azimuth) and θ (zenith).

Characteristics such as tracking accuracy, the energy consumed by the sun tracking device, and the reliability of mechanical devices and structures are important in the development of a solar position tracking device. According to these characteristics, the basic conditions for the development of a sun position tracking device can be formulated as

$$\begin{cases} 90° - \alpha \to \min, \\ 90° - \beta \to \min, \\ W_T << W_{SM}, \end{cases} \tag{1}$$

where W_T - the energy consumed by the sun tracking device;

W_{SM} - energy produced by the solar module;

α - the angle of deviation from the perpendicular in azimuth;

β - the angle of deviation from the perpendicular to the zenith.

In addition, important characteristics are the weight and strength of the mechanical structure of the tracker. Increasing the mass of the structure leads to an increase in energy consumption for its rotation. At the same time, increasing the strength of the structure requires increasing its mass.

Among the electric elements of the tracker, electric motors consume the most energy. Therefore, to ensure high efficiency of energy extraction from solar modules, the calculation of electric motors requires special attention.

2. Development of new types of electric drives for turning the solar panel

In most electromagnetic stepper motors of linear and rotating types, the tangential component of traction force in the air gap is used according to the principle of operation [13]. This component is an order of magnitude lower than the normal component of the traction force of the lifting electromagnet.

In this work, the design of a linear stepper electric motor is proposed. Accordingly to the principle of operation, the motor uses the electromagnetic force of gravity between the inductor and the armature, and has a large length of movement.

The disadvantage of the known designs of electric motors is that the friction force of the brake pads must exceed the traction force of the traction electromagnets, which requires a large area of the brake pads. In addition, when operating in the positioning modes of the winding of the brake electromagnets are energized, which in terms of power loss is inefficient.

In the course of research, the design of the linear stepper electric motor which does not have the above-stated shortcomings and can be applied for turning of solar panels, is developed. The design is made in a cylindrical version.

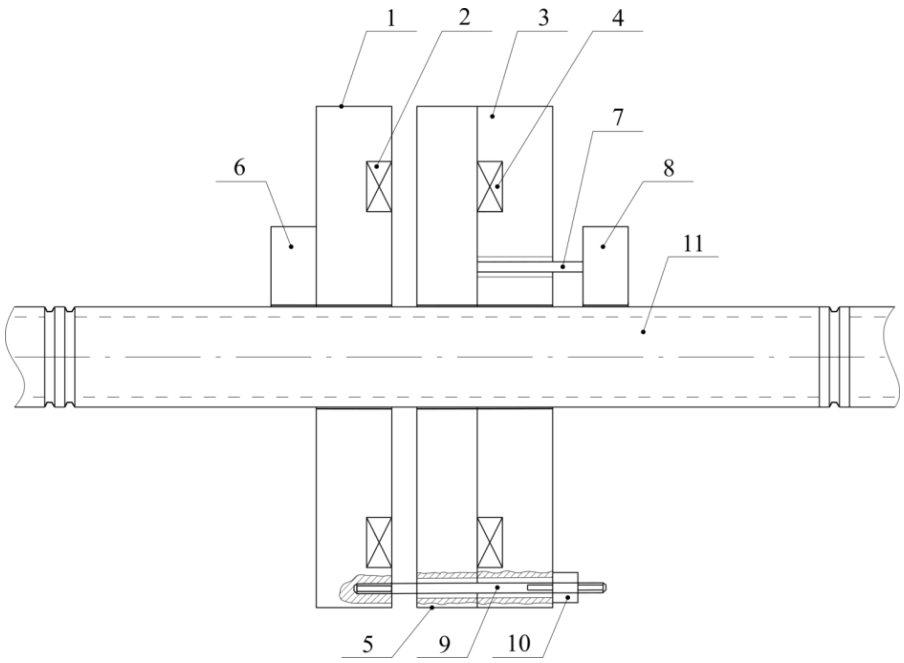

Fig. 3. The design of a linear step electromagnetic motor.

In the design (Fig. 3) the active part of the motor contains a traction electromagnet 1 with a winding 2, a traction electromagnet 3 with a winding 4, an anchor 5 and electromagnets-clamps 6 and 8.

The latch 6 is rigidly connected to the electromagnet 1, and the latch 8 by the rod 7 is connected to the armature 5. Each latch includes its own magnetic circuit, excitation winding, spring, which acts on the movable stopper.

The electromagnets 1 and 3 are connected by a pin 9. The pin 9 is screwed into the body of the electromagnet 1. The electromagnet 3 has the ability to move on the pin 9 to adjust the total air gap between the traction electromagnets and the armature 5. Adjustment is nut, which is rigidly connected to the electromagnet 3 and on which the limb is applied to establish the required size of the gap (movement step).

The moving part is a non-ferromagnetic guide - a rod (for example, stainless steel, bronze, etc.). In the simplest case, when the working gap (movement step) is not adjustable, the rod 11 has transverse grooves with a distance between them equal to the movement step, and the width corresponds to the size of the stopper clamps 6 and 8.

To be able to adjust the movement step on the guide rod, several longitudinal rows of non-through holes are made with each for its series of center-to-center distance between the holes (movement step). Then, to change the movement step, a corresponding step (gap) is set between the electromagnets 1, 3. The armature 5, and the guide 11 are attached to the drive mechanism so that in front of the stoppers 6, 8 there was a corresponding number of holes.

The engine works as follows. Let the rod guide move to the left relative to the fixed traction electromagnets. In this case, the electromagnet of the latch 8 is de-energized and its stopper engages with the rod 11, and power is supplied to the electromagnet 1 and the electromagnet-latch 6 (the stopper of the latch is disengaged from the rod 11). Then the armature 5 is attracted to the electromagnet 1 and moves the rod 11 by the amount of air gap between the electromagnet and the armature.

The electromagnetic force of gravity is determined by the formula:

$$Q = \frac{B_0^2}{2\mu_0} S \tag{2}$$

where B_0 is the magnetic induction in the air gap; μ_0 is the magnetic constant; S is the total area of the pole pieces of the cylindrical electromagnet.

Next, the electromagnet latch 6 is turned off and its stopper engages with the rod 11, and the electromagnet latch 6 is connected to the power supply with a time delay and its stopper is disengaged with the rod 11. Then power is supplied to the electromagnet 3 and the armature 5 is attracted to it. Now the latch 8 is de-energized and the system is ready for a new step.

7) The anchor movement time is described by the next expression:

$$t_n = \sqrt{\frac{2m(\delta_0 + \delta_f)}{Q_H}}, \tag{3}$$

where m is the mass of the moving part; δ_0 - the initial value of the air gap; δ_f - the final value of the air gap (technological gap).

Then the total time of the electromagnet operation

$$t_{cnp} = \tau \ln \frac{1}{1 - \frac{I_p}{U/R}} + \sqrt{\frac{2m(\delta_0 + \delta_f)}{Q_H}}. \tag{4}$$

8) If at a certain resistance R and current I_p the supply voltage exceeds the allowable range, you must choose a larger wire diameter d_w, calculate the number of turns, winding resistance, current I_p and check $U = I_p \cdot R$.

For example, if you increase d_w twice, the number of turns will decrease 4 times (the length of the winding wire will also decrease 4 times), and the area of the wire will increase 4 times. Therefore, the resistance of the winding will decrease 16 times, and the current Ip will increase 4 times. Then the required voltage will decrease 4 times.

The energy for one working cycle (for one step):

1) The energy for time t_p:

$$\begin{aligned} W_p &= \int_0^{t_p} i^2 R dt = R \int_0^{t_p} \left[\frac{U}{R} (1 - e^{-t/\tau}) \right]^2 dt = \frac{U^2}{R} \int_0^{t_p} (1 - 2e^{-t/\tau} + e^{-\frac{2t}{\tau}}) dt = \\ &= \frac{U^2}{R} (t_p - 2(-\tau)(e^{-\frac{t_p}{\tau}} - 1) + (-\frac{\tau}{2})(e^{-\frac{2t_p}{\tau}} - 1) = \\ &= \frac{U^2}{R} \left[t_p + 2\tau e^{-\frac{t_p}{\tau}} - 2\tau - \frac{\tau}{2} e^{-\frac{2t_p}{\tau}} + \frac{\tau}{2} \right] = \frac{U^2}{R} \left[t_p - 1{,}5\tau + 2\tau e^{-\frac{t_p}{\tau}} - 0{,}5\tau e^{-\frac{2t_p}{\tau}} \right] \end{aligned} \tag{5}$$

2) The energy during the time t_p provided that $I = I_p = const$ (considering $t_F < t_p$):

$$W_F = I_p^2 R t_F. \tag{6}$$

3) The energy in one step:

$$W_{st} = W_p + W_F. \tag{7}$$

3. Power supply system based on solar photovoltaic modules with sun position tracking

Based on the results of the research, a structural diagram of the power supply system based on photovoltaic modules with tracking the sun position is built with the possibility of electrical energy accumulation by supercapacitors and batteries [14].

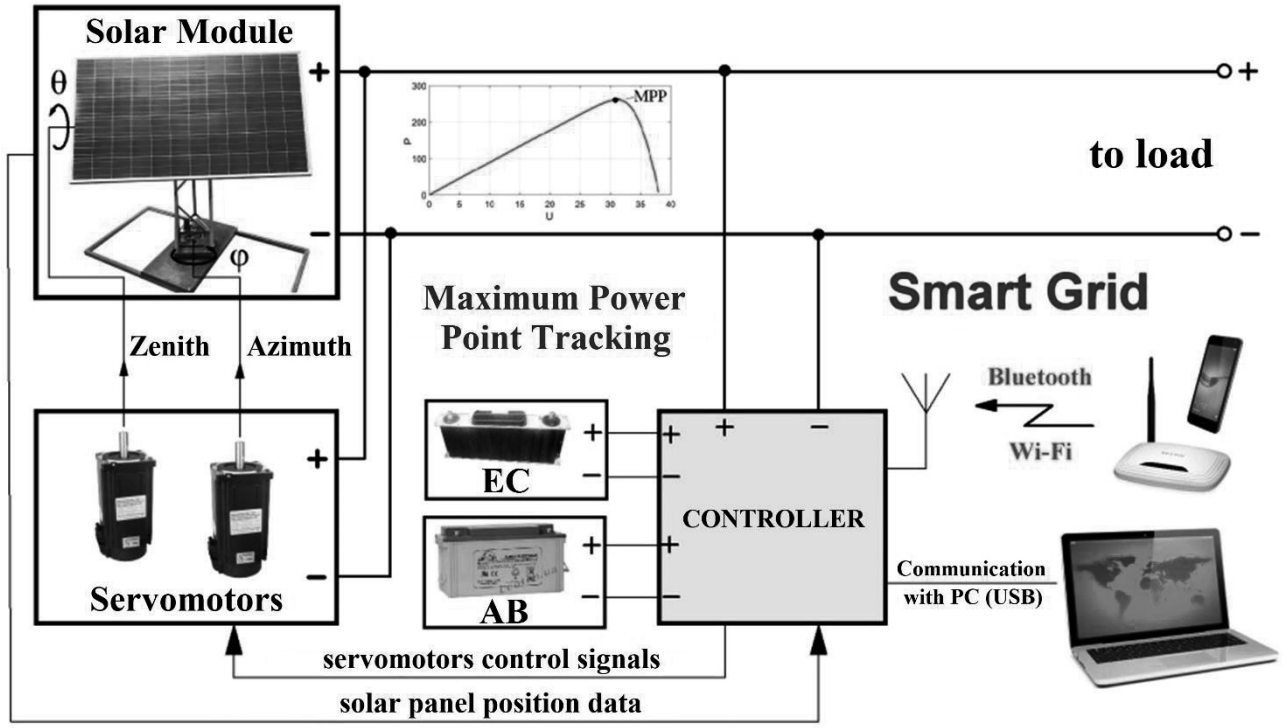

Fig. 4. Block diagram of the power supply system based on photovoltaic modules with sun position tracking

The developed system can be connected to the Internet using wired and wireless technologies. It is possible to integrate the system with a PC via a USB port for additional settings and measurements.

The connection of additional energy storage devices based on batteries and supercapacitors is provided. It can significantly increase the efficiency of tracking the maximum power point of the solar module in conditions of long-term high-power loads.

Fig. 5. The research of the developed solar power supply system

The proposed power supply system (Fig. 5) can be used in mobile waste recycling units. The use of solar energy can significantly reduce the negative impact of the unitss on the environment by reducing emissions of carbon compounds and greenhouse gases. Solar trackers can be deployed on the roof of a mobile unit or near it. The power supply system allows remote control and adjustment of parameters according to the operating conditions of the mobile waste recycling unit.

4. Conclusions

As a result of research, the new methods are developed for tracking the maximum power point using electrochemical capacitors, battery and solar tracker control, which provide maximum light flux and operation of the solar module at the point of maximum power in different weather conditions. To implement the development, new methods of the theory of fractional calculus and nonlinear dynamics are used, which make it possible to increase the

accuracy and adequacy of the used models. In the course of researches of converter circuits, the analysis of current source energy harvesting methods with nonlinear parasitic elements is performed.

An experimental study of the maximum power point for the solar module was performed. The mode of the maximum power point is supported by the inverting converter with the filling factor which is defined from the proposed model. The experiments show that the proposed model provides the values of the fill factor of the inverter converter, which practically correspond to the values obtained experimentally in the mode of the point of maximum power.

In the process of research, the main scientific results were obtained as follows:

1. The method of two-coordinate tracking of the sun trajectory with dynamic positioning of the solar module working surface perpendicular to solar radiation and appropriate control of the tracker in difficult weather conditions (fog, clouds, heavy precipitation, strong wind);

2. The method of electrical energy harvesting from the solar module using electrochemical capacitors, which in comparison with analogues works effectively even in rapidly changing weather conditions as well as unlike works with sufficient accuracy, can determine the point of maximum power without power fluctuations.

3. The design of a linear step electromagnetic motor is proposed. The electromagnetic motor energy losses are reduced due to the improvement of the stopping mechanism.

An additional advantage of using electrochemical capacitors (over existing analogues) in the device of tracking maximum power point is the ability to obtain a large instantaneous output power (power gain effect) due to the low internal resistance and high discharge currents.

Due to the scientific and applied solutions based on tracking the maximum solar radiation and the maximum power point of the photovoltaic module, the developed power supply system allows to obtain a significant increase in the efficiency of energy extraction from photovoltaic modules and provides a significant reduction of harmful effects on the environment from plastic waste processing units.

References

1. Hahladakis, J.N. (2020). Delineating and preventing plastic waste leakage in the marine and terrestrial environment. *Environ Sci Pollut Res*, *27*(11), doi:10.1007/s11356-020-08139-y

2. Thahir, R., Altway, A., Juliastuti, S.R., Susianto, (2019). Production of liquid fuel from plastic waste using integrated pyrolysis method with refinery distillation bubble cap plate column. *Energy Reports*, *5*, 70-77. doi:10.1016/j.egyr.2018.11.004

3. https://innovoucher.com.ua/portfolio-items/obolon-oil-and-its-poly-euro-diesel-made-of-waste/?lang=en

4. Martynyuk, V., Radelchuk, G., Kashtalyan, A., Verjbyckyi, Y. (2020). System analysis and simulation of electric power processes of automated mobile plastic bottle processing plant in diesel fuel. *Measuring and computing devices in technological processes*, *1*, 111-115.

5. Berbaoui, B. (2019). Performance investigation of a hybrid PV- diesel power system for remote areas. *International Journal of Energy Research*, *43*(2), 1019-1031.

6. Akbar, M.A. (2018). Modeling and optimum design of an off-grid PV/WT/FC/diesel hybrid system considering different fuel prices. *Low-Carbon Technologies*, *13*(2), 140–147.

7. Nayak, A., Kasturi, K., Nayak, M.R. (2018). Cycle-charging dispatch strategy based performance analysis for standalone PV system with DG & BESS, *Technologies for Smart-City Energy Security and Power (ICSESP)*, Proceedings of the Conference. Bhubaneswar, India.

8. Tsai, C.T., Shen, T.W., Chen, Y.P., Hsu, P.H. (2018). Control Strategy of PV/Diesel/Battery Hybrid System for Island-based Microgrid, *International Symposium on Computer, Consumer and Control (IS3C)*, Proceedings of the International Symposium. Taichung, Taiwan.

9. Tripathi, P., Momtaj A.M., Khan M.J., Yadav, S. (2018). Modelling of Energy Efficient PV-Diesel-Battery Hybrid system, *Computational and Characterization Techniques in Engineering & Sciences (CCTES)*, Proceedings of the International Conference, Lucknow, India.

10. Tiwari, G.N. (2016). *Handbook of solar energy. Theory, analysis and applications*. Springer.

11. Subudhi, B. (2013). A comparative study on maximum power point tracking techniques for photovoltaic power systems. *IEEE transactions on sustainable energy*, *4*, 89–98.

12. Roy, C.P., Naick, B. K., Shankar, G. (2014). Comparative study of photovoltaic mppt algorithms. *Recent trends in engineering and technology*, *11*, 191–201.

13. Ramu, G., Nagesh Kumar, G. V., Dharma Raj, C. H. (2016). Performance analysis of boost fed DC drive under load uncertainties. *Indian Journal of Science and Technology*, *9*(45), 1–11. doi:10.17485/ijst/2016/v9i45/103878

14. Martynyuk, V., Ortigueira, M., Fedula, M., Savenko, O. (2018). Methodology of electrochemical capacitor quality control with fractional order model. *AEU - International journal of electronics and communications*.

THE MATHEMATICAL MODELING OF COORDINATE DETERMINATION OF ACOUSTIC SIGNALS WITH PRIORITY PLACEMENT OF MICROPHONES

Bohdan Trembach[1], Rostyslav Trembach [2], Mykhailo Mykhailyshyn[3], Volodymyr Savkiv[4], Roman Mykhailyshyn[5]

[1] *Lviv Polytechnic National University, Bandery str 28 a., Lviv, Ukraine; trembach.bogdan@gmail.com*
[2] *Ternopil National Ivan Puluj Technical University, Rus'ka str. 56, 46001, Ternopil, Ukraine; trb@tntu.edu.ua*
[3] *Ternopil National Ivan Puluj Technical University, Rus'ka str. 56, 46001, Ternopil, Ukraine; mms@ukr.net*
[4] *Ternopil National Ivan Puluj Technical University, Rus'ka str. 56, 46001, Ternopil, Ukraine; v.b.savkiv@gmail.com*
5 Ternopil National Ivan Puluj Technical University, Rus'ka str. 56, 46001, Ternopil, Ukraine; mykhailyshyn@tntu.edu.ua

Abstract: The structural model of the spatial identification of sources of acoustic signals in Cartesian coordinates of a two-dimensional Hemming space with the priority placement of microphones as receivers of acoustic signals is proposed. [2] Examples of analytical calculations of the system characteristics of the hardware and time complexity of the correlation system based on a certain number of microphones and the corresponding number of interrelations are presented. The structural solutions of the hardware special processor implementation of such a class of multichannel devices for recognition and identification of types and the spatial location of sources of acoustic signals are developed. It is shown the possibility of using such a class of devices in the field of special military equipment.

Keywords: acoustic signals, correlators, special processors, Hemming space.

1 Introduction

The works [1], set forth the principles and theoretical base of the method of location finding, identification of the spatial angle and angular-position measurement of acoustic signal sources (ASS) based on two acoustic signal receivers (ASR). The method is characterized by finding the angle β between the perpendicular drawn from middle point of the acoustic base, and the line traced between middle point of the acoustic base and the source point (Figure 1) [1], [2]:

$$\sin\beta = \sin(NDO) = \frac{(t_2 - t_1)\times C}{L} = \frac{\Delta t \times C}{L}, \quad (1)$$

where: c - the speed of sound in the atmosphere;
t_1 and t_2 - periods of time at which the acoustic waves cover the distance from the source to the first and second acoustic signal receivers respectively;
Δt - time difference in audio signal registration by first and second sound receivers
L - length of acoustic base.

Multichannel digital correlator (MDC) [2] structure can be improved by means of a special arrangement of ASR beyond the demarcation line when one of ASR is preferentially placed closer to the demarcation line than other ASR, as shown in Figure 2.

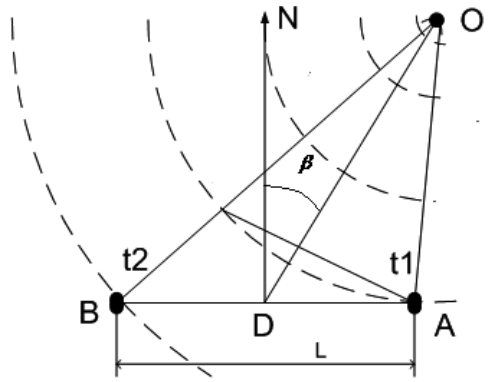

Fig. 1 Acoustic base elements arrangement: A, B - microphones; O - sound source

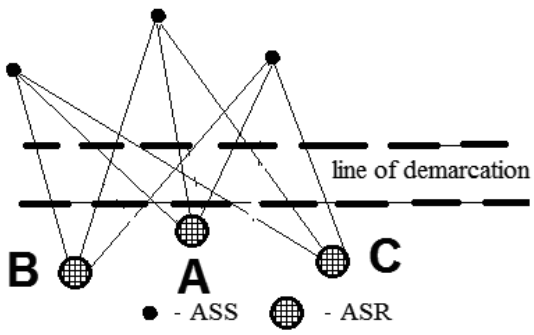

Fig. 2 Examples of priority arrangement of one the ASR beyond the ASR and ASS demarcation line

Figure 2 shows that the length of AS distribution from ASS in this case, is the lowest for ASR A, which makes it possible to reduce the number of necessary correlators in the MDC structure to two. Moreover only priority ASR A

correlator will include one block of delay register (BDR), and the number of accumulating memory items is reduced to two. The structure of the optimized MDC is shown in Fig. 7.

As shown in Fig. 3, compared with the principles of the correlation processing of ASS signal at random spatial arrangement of ASR in optimized MDC structure due to given priority spatial positioning of one of ASR, the hardware complexity of microelectronic components can be reduced, which results in:

1) the number of BDR is reduced from three to one;

2) the number of integrators (I) is reduced from the three stages to two, plus one;

3) such MDC structure has a high regularity and many similar utilities that significantly simplifies its design and implementation on PLIC chip .

When processing software and hardware implementation of analytical expression of definition integrated assessment of correlation by expression it has been found that this method is cumbersome and not effective, as multiplicative correlation algorithm requires alignment of signals $x_i(t)$ and $x_j(t)$ as well as performing their multiplication and accumulation taking into account ± signs.

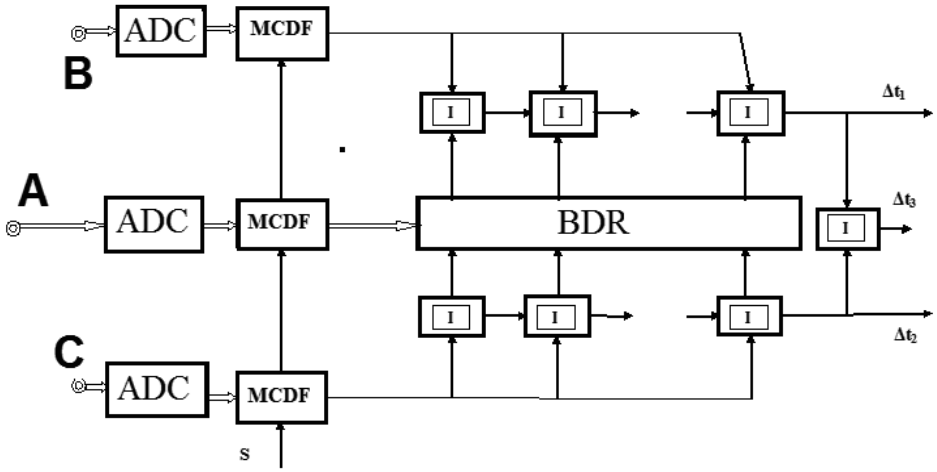

Fig. 3 The structure of the optimized MDC

Multiplicative correction of digitized AS values is characterized by low information content as with the existence of zero values in centered codes x_i and x_j out of *n* – bit sample more than 30 – 40% products are zero, which significantly reduces the information value of multiplicative correlator with respect to, for example, structural and modular ones according to expressions (2) and (3) [3].

$$C_{xx}(j) = \frac{1}{n}\sum_{i=1}^{n}(x_i - x_{i+j})^2 \; ; \tag{2}$$

$$G_{xx}(j) = \frac{1}{n}\sum_{i=1}^{n}| x_i - x_{i+j} | . \tag{3}$$

Analysis of analytical expressions of structural (2) and modular (3) correlation functions shows that the latter is characterized by much simpler algorithm with respect to the expression (3), which determines the feasibility and effectiveness of the module correlation for MDC implementation.

Fig. 4 shows an example of the correlation interaction of two AC timebase deflections according to the module correlation function $C_{xx}(j)$.

Fig. 5 [3] shows the characteristics of the $C_{xx}(j)$ function at discrepancy and concurrence of signal-wave envelopes x_i and x_{i-j} at a certain time, i.e. cross-correlation modular function verges towards "0" when signal-wave envelopes x_i and x_{i-j}, concur at τ moment of time.

The application of module correlation function in the system of ASS monitoring and spatial parameters identification in the event of priority placement of ASR beyond demarcation line requires an additional introduction into MDC structure certain differentiating units (D) between ASR and ADC inputs, as shown in Fig. 6.

The stated analysis of existing systems of recognition and identification of ASS and ASR spatial distribution allows us to ascertain that the use of multiplicative correlation and chaotic spatial distribution of ASS and ASR is not effective enough in the design of PLIC-based software and hardware special processors [3].

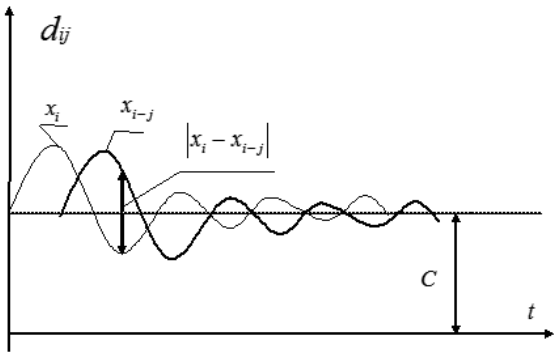

Fig. 4 x_i and x_{i-j} signals timing interaction at calculation of module correlation $C_{xx}(j)$:
C - constant of amplitude signal shift

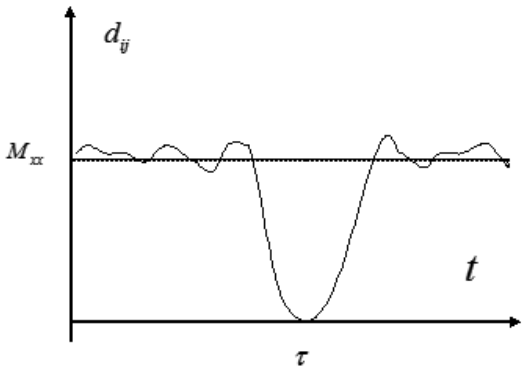

Fig. 5 Timing performance of module function of correlationv

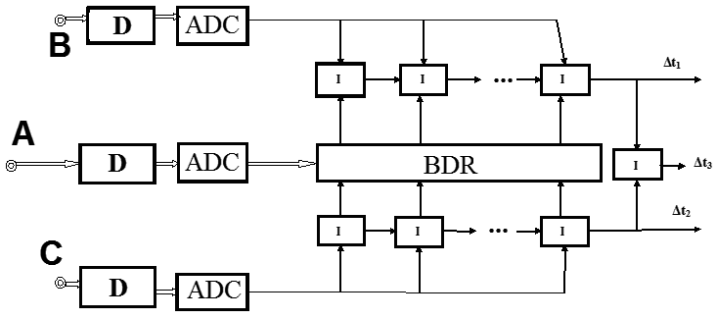

Fig. 6 MDC structure based on integrated calculation of module correlation function *I* and differentiator *D*

The proposed optimized structure of multichannel digital correlator with priority spatial placement of one of ASR microphones beyond the line of demarcation with ASS and application of module correlation function for acoustic signal processing can significantly simplify the calculation algorithm, reduce hardware complexity of correlator and enhance its performance, thus justifying feasibility and effectiveness of these solutions at establishing ASS monitoring system and implementation of PLIC-based special microelectronic processors.

2 Main part

The problem of identifying the spatial location of the DAS belongs to the class of problems in the theory of pattern recognition in the Hamming space.

Pattern recognition information technology in the Hamming space is based on the processing and transformation of signals presented in a discrete form, which include: algebraic, correlational, structural, spectral, geometric, fuzzy sets, statistical, spatially related processes, etc.[5]

The analytics of known methods of pattern recognition are formalized by the following functionals:

$d_{i\,j}$ – estimation of the Euclidean distance between the i and j objects;

$x_{i\,\kappa}$ – a discrete value of the κ sign of *i* object;

$x_{j\,\kappa}$ – a discrete value of the κ sign of *j* object;

υ – the number of features that describe the objects.

According to the provisions of cluster analysis, it is determined that the estimate of the Euclidean distance between objects in the Hamming space for the whole set of features describing classified objects is some value $d_{i\,j}$, which is determined by the expression:

$$d_{ij} = \sum_{k=1}^{k} | x_{ik} - x_{jk} | \qquad (4)$$

and satisfies the following axioms:

1) $d_{i\,j} > 0$ (the positivity of the Hamming distance);
2) $d_{i\,j} = d_{ji}$ (symmetry);
3) $d_{i\,j} + d_{ji} > d_{\kappa}$ (triangle inequality);
4) $d_{i\,j} \neq 0$ то $i \neq j$ (non-identical objects);
5) $d_{i\,j} = 0$ то $i = j$ (inseparability of identical objects).

In addition to the linear estimation of the Euclidean distance (4), a quadratic estimate of the species is used:

$$d_{ij} = \sum_{k=1}^{k} (x_{ik} - x_{jk})^2 . \quad (5)$$

This estimate gives a quadratic increase in information and accuracy of object class boundary recognition. That is equivalent to a estimated value of the Euclidean distance according to the expression

$$d_{ij} = \sum_{k=1}^{k} v_k \left| x_{ik} - x_{jk} \right|,$$

where v_k - estimated function.

An example of a estimated value of the Euclidean distance is Minkowski's step distances, in which some numbers "p" are used

$$d_{ij} = (\sum_{k=1}^{k} v_k \left| x_{ik} - x_{jk} \right|)^{\frac{1}{p}} . \quad (6)$$

The marginal estimate of such Euclidean distance is the estimate of the "Manhattan distance" when $p \to \infty$, also called dominance or sup-metric and is calculated by the expression

$$d_{ij} = (\sum_{k=1}^{k} v_k \left| x_{ik} - x_{jk} \right|)^{\frac{1}{\infty}} .$$

Fundamentally different from the given Euclidean distance metrics in the Hamming space is the Mahalanobis metric, which is determined by the expression

$$d_{ij} = (X_i - X_j)^T \times S^{-i} (X_i - X_j),$$

where X_i and X_j – the corresponding vectors of the columns of the variable attributes of the i-th and j-th objects; the symbol T defines the vector transposition operation, and the symbol S defines the group variance-covariance matrix.

Thus, when the correlations between the variables i - th and j - th objects are equal to zero, the Mahalanobis distance is equivalent to the Euclidean distance.[5]

The analysis of theoretical foundations of pattern recognition based on Euclidean distance estimates in Hemming space allows us to state the following:

1) known methods are highly specialized and problem-oriented and are not characterized by versatility;

2) the most general Hamming distance estimates are based on the calculation of the covariance and statistical characteristics of the features of the i-th and j-th objects;

3) known applications of pattern recognition methods in the Hemming space apply binary values of the vectors of the signs of the i-th and j-th objects of type "0" and "1", which implies the use of correlation analysis on the basis of sign-correlation function:

$$H_{ij} = \frac{1}{n} \sum_{i=1}^{n} sign(\overset{o}{x}_i) \times sign(\overset{o}{x}_j),$$

where $sign(x_i) = \begin{cases} +1, at\ \overset{o}{x}_i \geq 0; \\ -1, at\ \overset{o}{x}_i \langle 0 \end{cases}$; $sign(x_j) = \begin{cases} +1, at\ \overset{o}{x}_j \geq 0; \\ -1, at\ \overset{o}{x}_j \langle 0 \end{cases}$;

$\overset{o}{x}_i = x_i - M_x$; $\overset{o}{x}_j = x_j - M_j$; $M_i = \frac{1}{n} \sum_{i=1}^{n} x_i$; $M_j = \frac{1}{n} \sum_{i=1}^{n} x_j$.

Significant expansion and enhancement of the pattern recognition efficiency in the Hamming space can be achieved by applying different discrete estimates of the character correlation x_i and y_i binary multi-bit Rademacher bases.

A two-dimensional Hamming space given by a lattice with two-dimensional nodes can be represented in Cartesian (Fig. 7) and polar coordinates (Fig. 8).

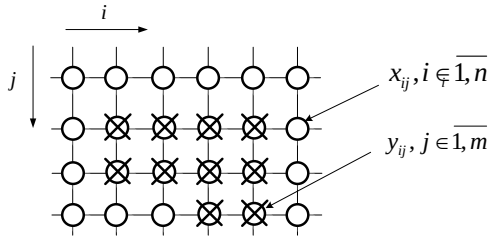

Fig. 7 Information nodes of two-dimensional Hemming space

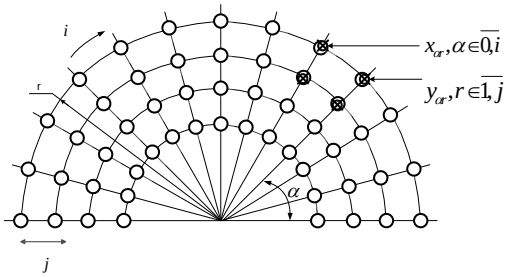

Fig. 8 Two-dimensional Hamming space in polar coordinates

The solution of the problem of pattern recognition in two-dimensional Cartesian Hamming space (see Fig. 7) is performed according to the Euclidean distance estimate

$$d_{ij} = \frac{1}{n \cdot m} \sum_{i=1}^{n} \sum_{j=1}^{m} \left| x_{ij} - y_{ij} \right|,$$

where n, m - the corresponding number of knots of the Hemming space horizontally and vertically.

The solution of the problem of pattern recognition in two-dimensional polar Hamming space is performed according to the expression [5]

$$d_{ij} = \frac{1}{\alpha \cdot r} \sum_{i=0}^{\alpha} \sum_{j=0}^{r} \left| x_{ij} - y_{ij} \right| \cdot$$

These algorithms differ in the wau that in Cartesian coordinates the accuracy of calculations and discretes between nodes of the Hemming space are the same, and in polar coordinates the accuracy of calculations decreases as the radius characteristic () increases.

In pattern recognition, the Hamming distance between the characteristics of the objects according to the Euclidean metric in the linear space according to expression (7) was applied effectively.

$$d_{ij} = \frac{1}{n} \sum_{i=1}^{n} | x_i - y_i |, \tag{7}$$

where x_i, y_i - digital object feature codes.

The application of such a metric can be performed in code systems of various theoretical and numerical bases, in particular in Unitary, Rademacher and Krestenson, which give rise to code systems of unitary, binary and modular residuals.

The most widely used in our time is the Rademacher basis, which is based on the presented characteristics (in the case under study) of binary acoustic signals *n* – bit codes x_i and y_i, which are formed at a sampling interval over time Δt at the outputs of two ADC.

Formalization of the algorithm for determining the integral is differential result of processing of acoustic signals is realized according to the following sequence of operations on binary codes x_i and y_j:

1) record digital codes x_i and y_i in according *n* – bit memory registers on D–triggers, and direct outputs are formed by direct binary codes x_i and y_i, and inverse outputs are formed on the inverted outputs of the D - triggers of the memory registers $\overline{x_i}$ and $\overline{y_i}$:

$$P_{11} := x_i,\ P_{12} := \overline{x_i},\ P_{21} := y_i;\ P_{22} := \overline{y_i};$$

2) parallel operations of adding the formed lines are performed x_i, y_i and inverse $\overline{x_i}$, $\overline{y_i}$ codes in *n+1* – bit binary adders according to expressions:

$$S_{i1} = x_i + (\overline{y_i} + 1);\ S_{i2} = y_i + (\overline{x_i} + 1),$$

where addition of "1" is performed to ensure the addition operations in adders and S_{i2} above the direct and complementary codes;

3) analysis of transfers on the outputs of adders S_{i1}, S_{i2}, moreover, if there is a transfer of a unit in one of the adders, it indicates the fact of subtracting a smaller number from a larger one:

$$x_i \rangle y_i;\ (x_i + \overline{y_i}) = Z_i;$$
$$x_i \langle y_i;\ (\overline{x_i} + y_i) = \overline{Z}_i,$$

where Z_i – the result of determining the difference $|x_i - y_i|$ in direct code, $\overline{Z}_i$ – respectively in the complementary binary code;

4) Z_i value obtained from the output of the multiplexer, which performs the following operation:

$$\left.\begin{matrix} S_1 = 1 \\ S_2 = 0 \end{matrix}\right\} S_1 \vee S_2;\ \sum := \sum + Z_i;$$

where S_1, S_2 – the bits of hyphenation in the higher digits of difference adders, at the outputs of which codes are formed Z_i and $\overline{Z}_i$, $\sum$ – integrating $n + \log_2 k$ – bit binary adder, *k* – the number of accumulations of the sum of difference codes Z_i;

5) integrative accumulation of the sum of modular differences according to the expression

$$d_{ij} = \sum_{i=1}^{n} Z_i \cdot$$

Implementation of the described algorithm for determining the integral - difference estimation of the Hamming distance between digital values of acoustic signals x_i and y_i in the Rademacher basis is illustrated by the following structural graph, which is shown in Fig. 9.[5]

$$
\begin{array}{l}
\begin{array}{cccc}
 & 1 & 0 & x_i + \bar{y}_i \to S_1 \\
 & 0 & 1 & 1+0+0 \\
 & \dots & \dots & 0+0+0 \\
x_i \Rightarrow & 1 & 0 & \dots+\dots+\dots \Rightarrow \\
 & 0 & 1 & 1+0+0 \\
 & 1 & 0 & 0+1+0 \\
 & & & 1+0+1
\end{array} \\
\begin{array}{cccc}
 & 1 & 0 & y_i + \bar{x}_i \to S_2 \\
 & 1 & 0 & 1+0+0 \\
 & \dots & \dots & 1+1+0 \\
y_i \Rightarrow & 1 & 0 & \dots+\dots+\dots \Rightarrow \\
 & 0 & 1 & 1+0+0 \\
 & 1 & 0 & 0+1+0 \\
 & & & 1+0+1
\end{array}
\end{array}
\Rightarrow Z_i \Rightarrow \sum_{i=1}^{n} Z_i = d_{ij}
$$

Fig. 9 Structural graph of the algorithm for determining the integral - difference code of the Hamming distance Euclid linear metric

When implementing such an algorithm (Fig. 9), the minimum result is obtained d_{ij} (approaching to zero) indicates a high level of AS similarity and a corresponding close to +1 correlation level.

Accordingly, the increase in valuation d_{ij} indicates a low similarity of acoustic signals and close to "0" coefficient of correlation.

3 Results of the investigation

The application of multiple autonomous systems of parallel direction finding of acoustic signal sources with respectively small number of nodes in the Hamming space allows to significantly reduce the accuracy requirements of the digital representation of values $\Delta t_1, \Delta t_2$ and Δt_3 [6].

The required memory for tactical representation of coordinates of the acoustic signal source at $i \in \overline{1,256}$ and $j \in \overline{1,256}$ equals 256 Kbytes.

Generalized chart of acoustic signal processor operation in the Hamming distance based on the modular correlation function is shown on Figure 10.[6]

The input to the simulation is the coordinates of the triangle locations of the sound receivers *A, B, C, v* is the speed of sound constant. Denote $A(X_A, Y_A)$, $B(X_B, Y_B)$, $C(X_C, Y_C)$. There is an acoustic signal source that we will mark $O(X, Y)$. Coordinates $O(X, Y)$ remain unknown and need to be found (Fig. 11).

Let the source of the acoustic signal produce sound that is captured at the observation points. The thing is to capture this sound at the point of observation, which is closest to the signal source. The time at which the sound overcame O to A is unknown. Let's mark it t_A. The next sound-recording observation point will be, for example, point B (or C). Observers can only record the time difference between sound arrival to point A and point B lets mark this difference Δt_{BA}. Therefore, the time for the sound to pass from point O to point B will be $t_A + \Delta t_{BA}$. Similarly, there is a time difference between C and, for example, A – Δt_{CA}. Then the sound will come to point C in time $t_A + \Delta t_{CA}$. Values Δt_{BA} i Δt_{CA} – know, t_A – unknown. We know that the path that will pass the sound in time t equal $v_s \cdot t$.

$$\text{So } |OA| = v_s t_A; \quad |OB| = v_s(t_A + \Delta t_{BA}); \quad |OC| = v_s(t_A + \Delta t_{CA}).$$

Finding the distance between two points:

$$(x - x_A)^2 + (y - y_A)^2 = v_s^2 t_A^2;$$
$$(x - x_B)^2 + (y - y_B)^2 = v_s^2(t_A + \Delta t_{BA})^2 = v_s^2(t_A^2 + 2t_A \Delta t_{BA} + \Delta t_{BA}^2);$$
$$(x - x_C)^2 + (y - y_C)^2 = v_s^2(t_A + \Delta t_{CA})^2 = v_s^2(t_A^2 + 2t_A \Delta t_{CA} + \Delta t_{CA}^2).$$

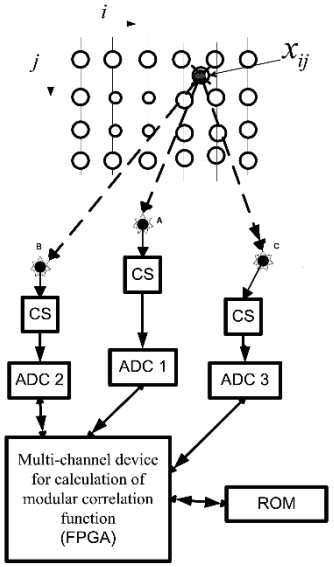

Fig. 10 Basic structure of digital special processor for correlation processing of acoustic signals in the Hamming distancev

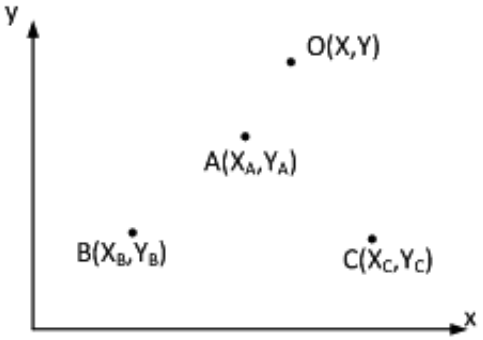

Fig. 11 Coordinates of acoustic signal sources (A, B, C) and acoustic signal receivers O

Denote $X_{AB} = x_A^2 - x_B^2 + y_A^2 - y_B^2 + v_s^2 \cdot \Delta t_{BA}(2t_A + \Delta t_{BA})$,
$X_{AC} = x_A^2 - x_C^2 + y_A^2 - y_C^2 + v_s^2 \cdot \Delta t_{CA}(2t_A + \Delta t_{CA})$,

$\tilde{X}_{AB} = x_A^2 - x_B^2 + y_A^2 - y_B^2 + v_s^2 \cdot \Delta t_{BA}$ $\tilde{X}_{AC} = x_A^2 - x_C^2 + y_A^2 - y_C^2 + v_s^2 \cdot \Delta t_{CA}$.

Then

$X_{AB} = \tilde{X}_{AB} + 2v_s^2 \cdot \Delta t_{BA} \cdot t_A$, $X_{AC} = \tilde{X}_{AC} + 2v_s^2 \cdot \Delta t_{CA} \cdot t_A$.

Denote $Z_N = 2\left[(x_A - x_B)(y_A - y_C) - (x_A - x_C)(y_A - y_B)\right]$.

Then

$$x = \frac{\tilde{X}_{AB}(y_A - y_C) - \tilde{X}_{AC}(y_A - y_B)}{Z_N} + \frac{2v_s^2 \cdot t_A}{Z_N}\left[\Delta t_{BA}(y_A - y_C) - \Delta t_{CA}(y_A - y_B)\right],$$

$$y = \frac{\tilde{X}_{AC}(x_A - x_B) - \tilde{X}_{AB}(x_A - x_C)}{Z_N} + \frac{2v_s^2 \cdot t_A}{Z_N}\left[\Delta t_{CA}(x_A - x_B) - \Delta t_{BA}(x_A - x_C)\right].$$

We introduce the notation:

$$a = \frac{\tilde{X}_{AB}(y_A - y_C) - \tilde{X}_{AC}(y_A - y_B)}{Z_N}; \quad b = \frac{2v_s^2}{Z_N}\left[\Delta t_{BA}(y_A - y_C) - \Delta t_{CA}(y_A - y_B)\right];$$

$$c = \frac{\tilde{X}_{AC}(x_A - x_B) - \tilde{X}_{AB}(x_A - x_C)}{Z_N}; \quad d = \frac{2v_s^2}{Z_N}\left[\Delta t_{CA}(x_A - x_B) - \Delta t_{BA}(x_A - x_C)\right].$$

Then $x = a + b \cdot t_A$; $y = c + d \cdot t_A$.

Substitute this solution into the first equation and obtain the equation for finding t_A

$$t_A = \frac{-\left[b(a - x_A) + d(c - y_A)\right]}{b^2 + d^2 - v_s^2} \pm$$

$$\pm \frac{\sqrt{v_s^2\left[(a - x_A)^2 + (c - y_A)^2\right] - \left[b(c - y_A) - d(a - x_A)\right]^2}}{b^2 + d^2 - v_s^2}.$$

To simulate the algorithm for calculating the coordinates of the sound source, we use MathCAD 15:

ORIGIN:= 0

Coordinates of points (x,y)

$A := (0 \ 250)$, $B := (-500 \ 0)$, $C := (500 \ 0)$

The difference in the timing of signals

$\Delta t BA_i := i \cdot 2$, $\Delta t CA_j := j \cdot 2$,

$i := 0..33$, $j := 0..33$.

Speed of sound

$V := 333$.

$$XAB_i := X_A^2 - X_B^2 + Y_A^2 - Y_B^2 + V^2 \cdot (\Delta t BA_i)^2 .$$

$$XAC_j := X_A^2 - X_C^2 + Y_A^2 - Y_C^2 + V^2 \cdot (\Delta t CA_j)^2$$

$$ZH := 2 \cdot [(X_A - X_B) \cdot (Y_A - Y_C) - (X_A - X_C) \cdot (Y_A - Y_B)] .$$

$$a_{i,j} := \frac{XAB_i \cdot (Y_A - Y_C) - XAC_j \cdot (Y_A - Y_B)}{ZH} .$$

$$b_{i,j} := \frac{2 V^2}{ZH} \cdot [\Delta t BA_i \cdot (Y_A - Y_C) - \Delta t CA_j \cdot (Y_A - Y_B)] .$$

$$c_{i,j} := \frac{XAC_j \cdot (X_A - X_B) - XAB_i \cdot (X_A - X_C)}{ZH} .$$

$$d_{i,j} := \frac{2 \cdot V^2}{ZH} \cdot [\Delta t CA_j \cdot (X_A - X_B) - \Delta t BA_i \cdot (X_A - X_C)] .$$

$$t01_{i,j} := \frac{-[b_{i,j} \cdot (a_{i,j} - X_A) + d_{i,j} \cdot (c_{i,j} - Y_A)]}{(b_{i,j})^2 + (d_{i,j})^2 - V^2} ;$$

$$t02_{i,j} := \frac{\sqrt{V^2 \cdot [(a_{i,j} - X_A)^2 + (c_{i,j} - Y_A)^2] - [b_{i,j} \cdot (c_{i,j} - Y_A) - d_{i,j} \cdot (a_{i,j} - X_A)]^2}}{(b_{i,j})^2 + (d_{i,j})^2 - V^2}$$

$$t0_{i,j} := t01_{i,j} + t02_{i,j} , \quad X0_{i,j} := a_{i,j} + b_{i,j} \cdot t0_{i,j} , \quad Y0_{i,j} := c_{i,j} + d_{i,j} \cdot t0_{i,j} .$$

$$x0 := (X_A \ X_B \ X_C)^T , \quad Y0 := (Y_A \ Y_B \ Y_C)^T .$$

The simulation results are presented in Figure 12.

4 Conclusions

The characteristics of the algorithms for determining the Hamming distance according to existing metrics according to non- estimated and estimated of the quadratic Euclidean distance of the Manhattan dominance, Sup - and Mahalanabis metrics are systematized and investigated.

This method of representing and encoding image characteristics greatly simplifies computational complexity and increases the processing speed of data. The simplest Hamming distance estimation algorithm is implemented according to the linear Euclidean distance by representing the characteristic x_i and y_i in Rademacher bases.

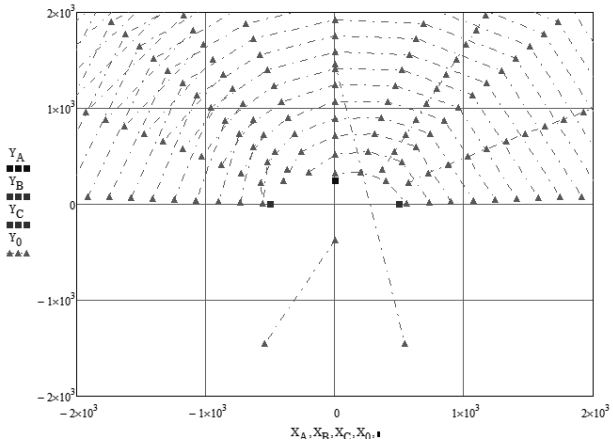

Fig. 12. The simulation results

Formalized structures and arrays of information nodes of one-dimensional and two-dimensional Hamming spaces given in Cartesian and polar coordinates.

The mathematical foundations for the calculation of the coordinate of the acoustic signal source have been developed, which allow to clarify the spatial determination of the location of the acoustic signal source relative to the Cartesian Hemming space node.

References

1. Kochan, R.V., Trembach, B.R. (2016). Approach of distributive automatic sound ranging system based on cellular communication. *Modern information technologies in the sphere of security and defense*, *1*(25), 59 – 63.

2. Trembach, B., Kochan, R., Trembach, R. (2016). Multiplex digital correlator with high priority deployment of one of the acoustic signal receivers, *Scientific Journal of TNTU*, *4*(84), 99-104. Retrieved from http://visnyk.tntu.edu.ua/pdf/84/339.pdf

3. Trembach B., Kochan R., Trembach, R. (2017). Methods of structural design optimization of software hardware problem identification of the spatial parameters of acoustic signals sources, *Scientific Journal of KNU*, *1*(245), 136-139. Retrieved from http://lib.khnu.km.ua/pdf/visnyk_tup/2017/(245)2017-1-t.pdf

4. Trembach, B., Kochan, R., Trembach, R. (2017). The method of correlation investigation of acoustic signals with priority placement of microphones, *Experience of Designing and Application of CAD Systems in Microelectronics*, Proceedings of the 14th International Conference. Polyana, Ukraine.

5. Trembach, B. (2017). Method of spatial identification of acoustic signals source in the two-dimensional Hemming space. *Visnyk Natsionalnoho universytetu "Lvivska politekhnika". Serie: Kompiuterni systemy ta merezhi*. *881*. 166-177. doi: org/10.23939/csn2017.881.166

6. Trembach, B., Kochan, R., Trembach. R. (2018). The method of correlation investigation of acoustic signals with priority placement of microphones. *Advances in Science, Technology and Engineering Systems Journal*, 3(1), 412-417. Retrieved from https://astesj.com/v03/i01/.

CONSTRUCTION AND RESEARCH OF REVERSE FREQUENCY DIVIDERS

Serhii Tsyrulnyk, Volodymyr Tromsyuk, Yaroslav Borodai, Artem Metelitsa, Vasyl Tkachuk

Vinnytsia Technical College, Khmelnytske highway, 91/2, 21021, Vinnytsya, Ukraine; E-mail: tech.college@vtc.vn.ua

Abstract: In the work, the reversible schemes of frequency dividers are constructed based on JK triggers are offered. It is proved that reversible frequency dividers work with insignificant differences in forward and reverse inclusions. When studying the frequency divider with direct inclusion, it was found that its real frequency differs from the calculated by 1.87%. And at return inclusion frequency dividers from are calculated on 2,17%. In general, such a relative error cannot be caused by the inaccuracy of the marker placement in the Multisim virtual oscilloscope. Such reversible frequency dividers can be used in unidirectional automated systems to build neural networks. **Keywords:** frequency divider, chichby module, division factor, trigger, counter.

1. Introduction

Appropriate electronic components must be used to receive, synchronize, decode and recognize high-speed data streams in real time [1]. The solution of these problems largely depends on the availability of high-quality synchronization signal generation systems produced by frequency dividers. Whether you need one (less) than the frequency of the master oscillator or a "grid" of interconnected frequencies, division by integer or fractional number, the basis of frequency dividers are always counters or registers with appropriate links between bits. In neural networks, this question becomes even more relevant because most of the problems that arise in information systems are poorly formalized and difficult to predict based on traditional mathematical methods. Each component of the information system can have its own reliability factor, which leads to a large amount of input information and a cumbersome solution [1-4].

The main parameters of the dividers are the division factor, speed, and complexity. When using frequency dividers to build neural networks, there is a need for their reversible use. They must work the same, both at the entrance and at the exit, depending on the mode of operation. Since these parameters are influenced directly by the organization of the circuitry of the device, the choice, and adoption of effective and original circuit solutions is an urgent task. The urgency of the problem has also increased because today for the creation of digital systems widely used chips programmable logic arrays (FPGA). If you do not specify a specific circuit solution, the means of the design package implements the node efficiently and optimally, but trivially, regardless of the method or language of description. This implementation will yield the original solution. With the neural network paradigm applying, it is possible to create parallel and distributed structures with high computing speed and greater efficiency to implement control tasks and ensure the reliability of information systems [1-3].

The obvious trend in the development of frequency dividers is to increase the range of their operating frequencies, performance, and usability in neural networks. Modern radio frequency applications, such as wireless personal and short-range LANs and car radars, make extensive use of millimetre-wave ranges. In addition, promising communication standards are being developed to service new applications, such as cellular communications and wireless data transmission in several new bands, including 28, 36, 45, 73, and 79 GHz.

To organize the divider (counter) with an arbitrary coefficient of division (conversion) using different methods [4]:

- exclusion of unnecessary states;
- use of feedback; - use of multiple modules;
- compulsory accrual (compulsory installation in 1 separate digit);
- reversible connection of digits.

This paper uses the feedback method, which gives less frequency division error.

Important components in radio equipment are frequency synthesizers with a wide range of tuning, high resolution, low cost, and low power consumption, so their technical implementation is of great interest to professionals.

2. Features of construction of reversible frequency dividers

A frequency divider is a counter with an arbitrary module M_0, which is covered by feedback with two triggers. The first trigger doubles the module, and the latter adds one, so in General, the module of such a counter is $D = 2 * M_0 + 1$. In this work, the frequency divider is built according to the scheme shown in Figure 1, *a*. To obtain the division of the frequency by an even number, you need to apply the input clock signal only to the first trigger, which multiplies the result by 2 (Fig. 1, *b*) [5-7].

Reversibility in the operation of frequency dividers allows you equivalently process the signal through these devices in the direction from input to output and in the opposite direction, i.e. the inputs and outputs of reversible

devices are inverted. The study of the operation of frequency dividers in the reverse mode is to build a switching circuit that allows the signal to flow, both in the forward and reverse directions. To do this, you need to provide a large input resistance at the input of the frequency divider: more than 50 kO and a load resistance of the order of several hundred kilohms. The output resistance, to avoid a decrease in the level of the output signal, must correspond to the ratio [8-11]:

$$R_{in} \geq 2R_{out} \tag{1}$$

where Rin and Rout – input and output pair of reversible frequency divider.

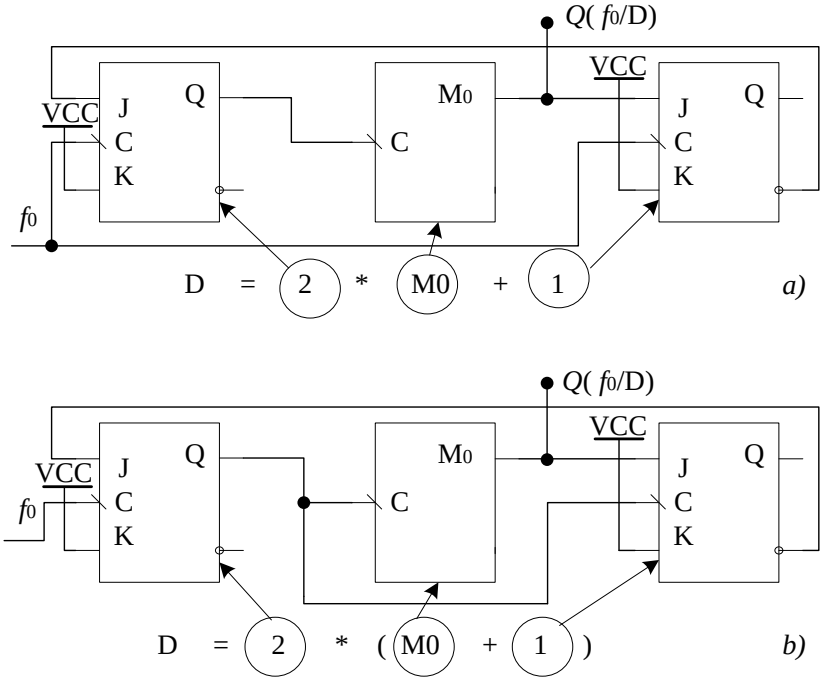

Fig. 1 Typical scheme of the frequency divider: *a*) for an odd number; *b*) on an even number

To ensure minimal amplitude-frequency distortion of the output signals, the circuit of the frequency dividers must be symmetrical, both in input and in output. At such inclusion, frequency dividers will work equally both indirect inclusion and in return (Fig. 2). When a signal source (IN) is connected to terminal ***b***, the load to terminal ***a*** of the logic element will operate in direct connection (input on the left and output on the right). When a signal source (IN) is connected to pin ***a***, the load on pin ***b*** of the logic element will operate in reverse (input on the right and output on the left).

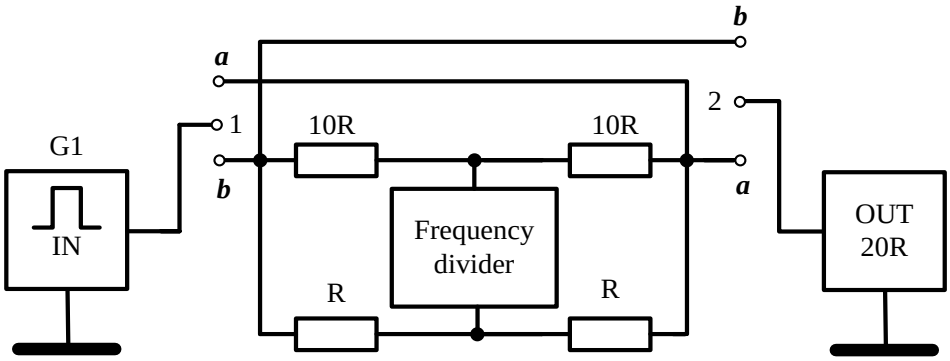

Fig. 2 Frequency divider switching scheme

Based on the general scheme shown in Fig. 2, we construct the scheme of the simple frequency divider with by 2 (Fig. 3). This version of the scheme allows using one trigger in reverse mode to divide the frequency by 2.

A resistive divider (R-10R) and the ratio of the input resistance of the signal source and the output load resistance, according to formula 1, provide the reversibility of the circuit (Fig. 3).

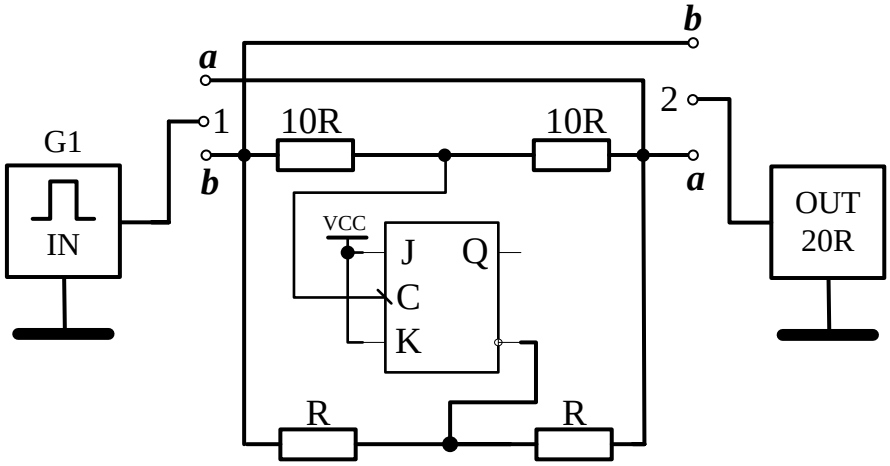

Fig. 3 Scheme of a simple frequency divider based on a JK-flip-flop

Devices are often needed that can divide the frequency by any number, not just 2, so the construction and simulation of the frequency divider circuit by 45 will be carried out further.

3. Simulation of the frequency divider in Multisim

Figure 4 shows a diagram of the study of the frequency divider by 45 in reverse mode. The circuit consists of: a rectangular signal generator G1 with a frequency of 45 kHz and a voltage of 5V; resistors R1 and R3 to provide high input resistance [11]; resistors R2 and R4 to provide output decoupling (matching output resistances); load resistance R5 (signal receiver); switches SA1 and SA2, which act as controllers, determining the input and output of the reversible frequency divider, in this case, the divider by 45.

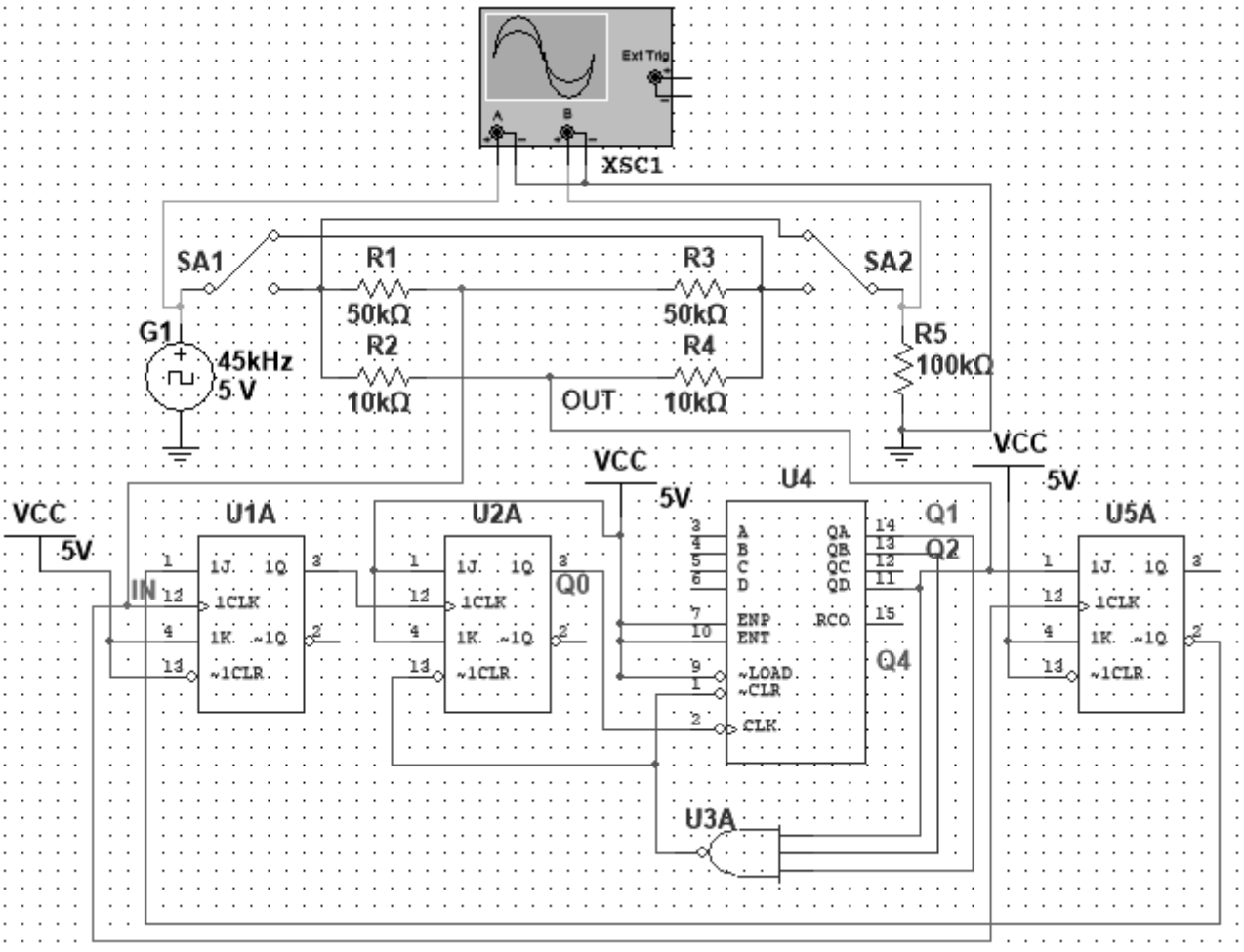

Fig. 4 Scheme of a frequency divider by 45 based on three JK-flip-flops, 4-digit counter and logical element NAND-3

The frequency divider based on: the counter (chips 74107N (U2A) and 74AS161N (U4)); trigger that multiplies the result of the counter by 2 (chip 74107N (U1A)); trigger, which adds to the result 1 (chip 74107N (U5A)) and the feedback element (chip 7410N (U3A)).

Figure 5 shows the timing diagrams of the buffer indirect inclusion, which show that such a frequency divider by 45 repeats the input signal without significant distortion.

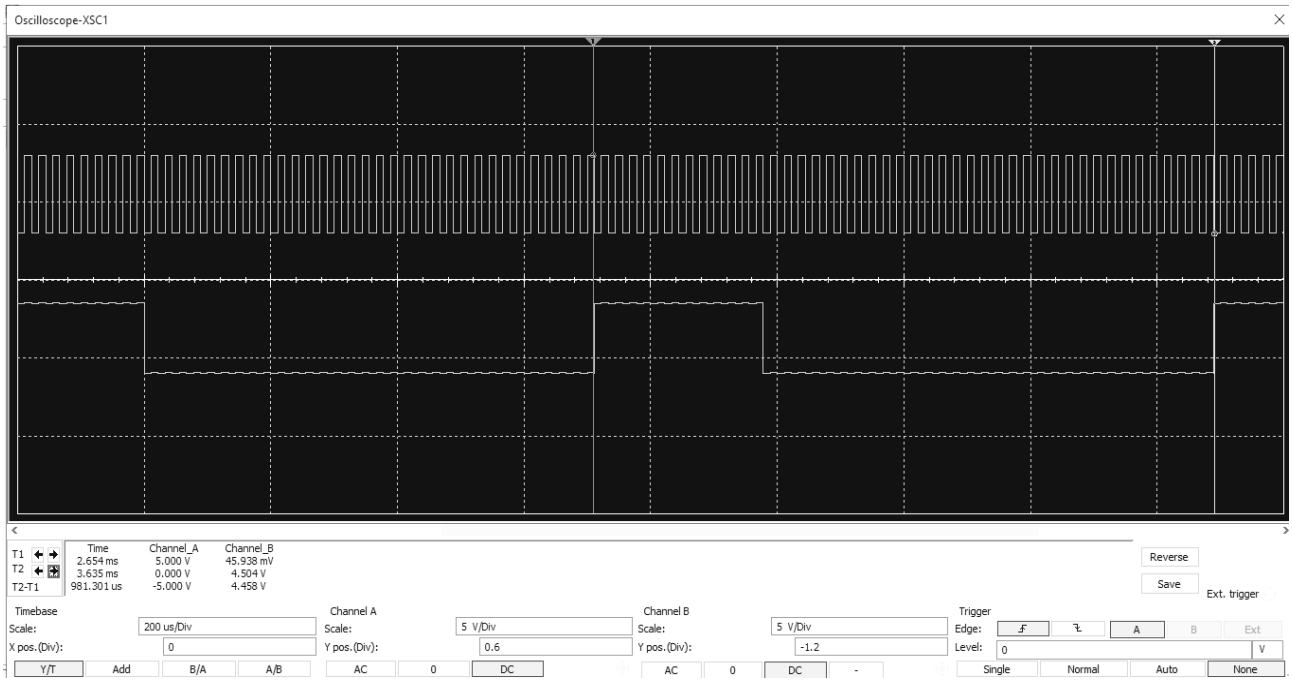

Fig. 5 The Oscillograms of the frequency divider by 45 in the direct-on mode

To conduct a study of the frequency divider in the reverse inclusion, you need to turn the switches SA1 and SA2 in the opposite position, as shown in Fig. 6. With this inclusion, the input became the output, and the output became the input.

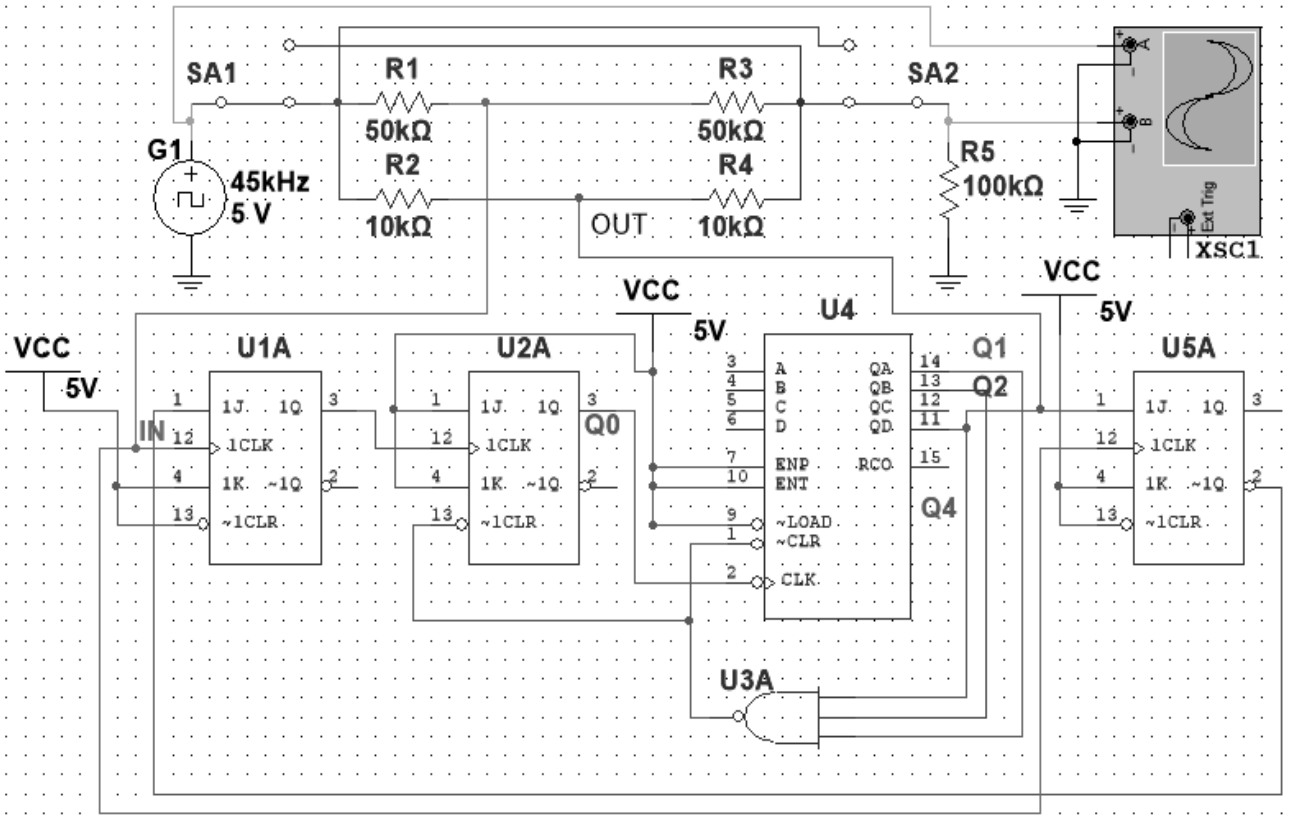

Fig. 6 Scheme of a frequency divider by 45 in reverse inclusion

By the simulation (Fig. 5) and the obtained oscillograms of the output signal, when directly connected, we calculate the frequency f_{out1} of the output signal and determine its relative error $\varepsilon_{out(1)}$. The measured period is equal to T_1 = 981.301 *us*.

$$f_{out1} = \frac{1}{T_1} = \frac{1}{981.301 \cdot 10^{-6}} = 1019,05 Hz;$$

$$\varepsilon_{out(1)} = \frac{|f_{out} - f_{out1}|}{f_{out1}} \cdot 100\% = \frac{1000 - 1019,05}{1019,05} \cdot 100\% = 1.87\%,$$

where f_{out} = 45000/45 = 1000 *Hz* – theoretical value of the output frequency of the divider, f_{out1} – the measured value of the frequency at the output of the divider in the direct-on mode.

The results of the study of the frequency divider in the inverse mode are shown in Figure 7. The measured period is equal to T_2 = 978.310 *us*.

By the simulation and the obtained oscillograms of the output signal, when directly connected, we calculate the frequency f_{out2} of the output signal and determine its relative error $\varepsilon_{out(2)}$.

$$f_{out1} = \frac{1}{T_2} = \frac{1}{978.310 \cdot 10^{-6}} = 1022,17 Hz;$$

$$_{out(2)} = \frac{|f_{out} - f_{out2}|}{f_{out2}} \cdot 100\% = \frac{1000 - 1022,17}{1022,17} \cdot 100\% = 2.17\%,$$

where f_{out2} – the measured value of the frequency at the output of the divider in reverse inclusion.

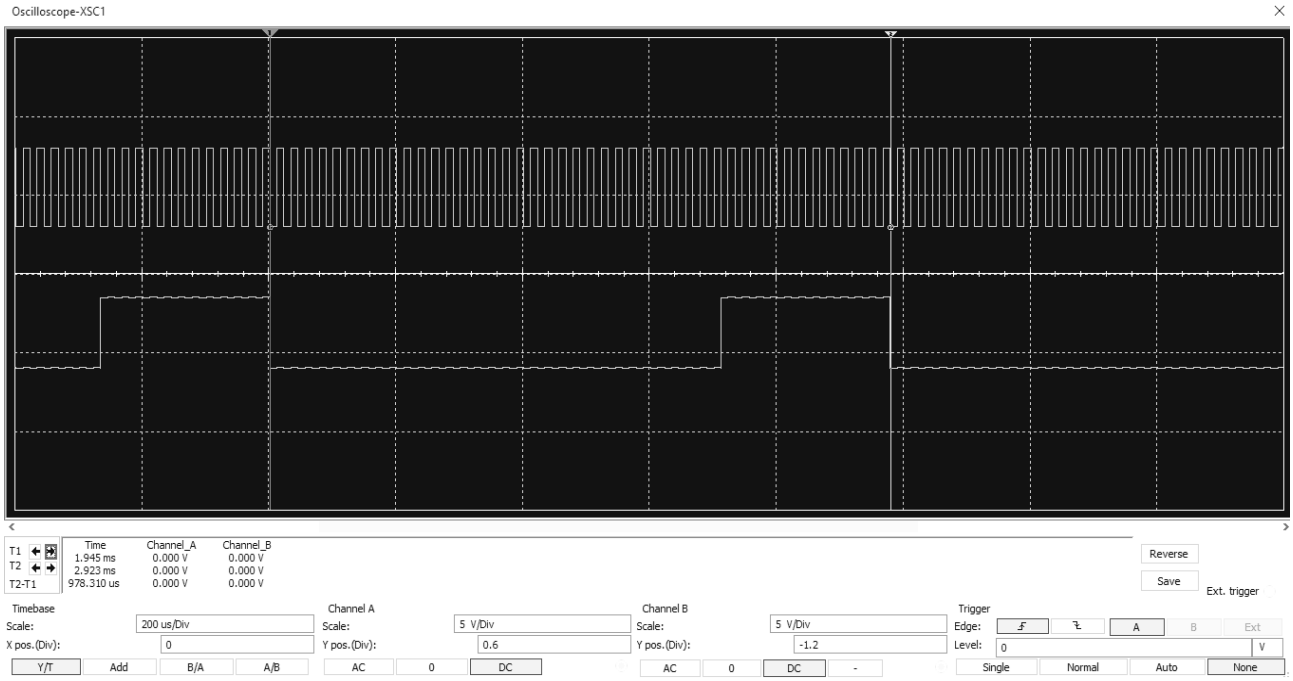

Fig. 7 The Oscillograms of the frequency divider by 45 in reverse inclusion

Modeling of the frequency divider with a division factor of 45 in the direct and reverse inclusion showed that the frequency deviation from the theoretical differs in the direct inclusion by 1.87%, and in the reverse by 2.17%.

The circuit of the reversible frequency divider is limited to a maximum frequency of 180 MHz. The frequency deviation will decrease as the division factor decreases and will increase as the division factor increases. This dependence was determined experimentally in the Multisim simulator.

The power supply of frequency dividers operating in reverse mode can be carried out both in the usual way, from DC power supplies 5V, and one or more external pulse signal generators, by summing them, for example, adder and subsequent filtration filter [10-11]. Such a load will not affect the shape and amplitude of the signals of the digital

generators. Note that the diode-resistive circuit protection of the inputs and outputs of CMOS chips allows their operation in low-current modes without the use of its power supply when applying signals to the input(s) of the chip.

4. Conclusions

A study of the reversible operation of frequency dividers has shown that they can work equally in both direct and reverse inclusion. Thus indirect inclusion of the output signal is closer to the theoretical value. Although such values may be the result of the inaccurate setting of markers in the virtual oscilloscope. But in general, such a deviation will not greatly affect the result of frequency division and the possibility of using such dividers in neural networks to build artificial intelligence systems.

For such frequency dividers, there is no difference between input and output, the main thing is to ensure the ratio of resistance between the signal source and the load.

The main task of this work was to show in principle the possibility of using ordinary frequency dividers in reverse mode. Because of the simulation, it was proved that the frequency dividers could work in reverse mode, using a special circuit of frequency synthesizers.

References

1. Ali, U., Bober, M., Thiede, A., Wagner S. (2015). 100-166 GHz wide band high speed digital dynamic frequency divider design in 0.13 μm SiGe BiCMOS technology, *Microwave Integrated Circuits Conference*, Proceedings of 10th European Conference.

2. Centurelli, F., Scotti, A., Palumbo, G. (2021). A very low voltage frequency divider in folded MOS current mode logic with complementary n- and p-Type Flip-Flops. *IEEE Transactions on Very Large Scale Integration Systems*, 998–1008. doi:10.1109/TVLSI.2021.3058730

3. Хайкин, С. (2006). Нейронные сети: полный курс. Москва: Издательский дом Вильямс.

4. Паралюх, І.П. (2014). Швидкодіючий подільник частоти із змінним коефіцієнтом ділення. *Вісник Національного університету «Львівська політехніка»*, *806*, 221-225.

5. Кофанов, В.Л., Осадчук, О.В., Гаврілов, Д.В. (2007). Лабораторний практикум з цифрових пристроїв на основі САПР Quartus II. Вінниця, Україна: Універсум.

6. Cetin, K.K. (2009). *Cryptographic Engineering*. Springer.

7. Кофанов, В.Л., Осадчук О.В., Гаврілов Д.В. (2006). Лабораторний практикум з дослідження цифрових пристроїв на основі САПР MAX+PLUS II. Вінниця, Україна: Універсум.

8. Shustov, M.A., Shustov, A.M. (2017). *Electronic Circuits for All*. London: Elektor International Media BV.

9. Tsyrulnyk, S.M., Roptanov, V.I., Zymoglyad, A.S. (2013) Practical approaches to the application of MIMS - Effect. *Optoelectronic information and energy technologies*, *1*(25). 39-46.

10. Shustov, M.A. (2019). Reversible operation of logical elements. *Electronic magazine Radio Pilot*, *8*, 44-46.

11. Tsyrulnyk, S., Tromsyuk, V., Vernygora, V., Borodai, Y. (2021). Simulation of logic elements in reverse mode for building neural networks. *Computational Linguistics and Intelligent Systems*, *Proceedins of the 5th International Conference*. Lviv, Ukraine.

USE OF COMPUTER-INTEGRATED TECHNOLOGIES IN TRAINING OF ENGINEERING SPECIALISTS

Vasyl Vasylkiv, Myhajlo Pylypets, Larysa Danylchenko, Dmytro Radyk

Ternopil National Ivan Puluj Technical University, Rus'ka str. 56, 46001, Ternopil, Ukraine; snt.tu.edu@gmail.com

Abstract: The article considers the peculiarities of the use of computer-integrated technologies (CIT) for the training of specialists in engineering and technical specialties, analyzes the latest research and scientific publications on the introduction of information technologies in the educational process of higher technical educational institutions. Based on the theoretical analysis of scientific sources on the essence of CIT, the specifics of training future engineers and the study of practical experience, the scientific and pedagogical conditions for the use of computer-integrated technologies in the educational process were determined. The role, tasks and possibilities of CIT introduction for mastering engineering and technical disciplines are determined. Approaches to understanding the readiness of future engineers to use CIT during training are generalized. The peculiarities of the introduction of computer-integrated technologies in the educational process of training specialists of higher educational institutions in the specialty 131 "Applied Mechanics" are considered, the structuring of educational programs in this specialty is carried out. Ways to increase the efficiency of training of engineering skills in the specialty 131 "Applied Mechanics" given the widespread use of software products for mastering engineering disciplines.

Keywords: *educational process, computer-integrated technology, application software*

1. Introduction.

Fierce competition in the labor market of Ukraine and the economic conditions in which the state finds itself have exacerbated the problem of training graduates of higher education institutions. The main problem is the discrepancy between the socially necessary and the actual levels of training. At the present stage of the development of society, the volume and complexity of information flow is quite large and increase every year. Today, the use of modern CIT in education is one of the most important and sustainable trends in the world educational process, which is considered an expectable development of the informatization of all spheres of human activity. The process of informatization of education has acquired a purposeful character of national importance, due to modern requirements for training of future engineers, defined by the Laws of Ukraine "On Higher Education", "On Basic Principles of Information Society Development in Ukraine", the National Doctrine of Education Development of Ukraine in the XXI Century, the National Informatization Program, the State Program "Information and Communication Technologies in Education and Science".

The modern development of post-industrial states is characterized by the continuous increase of new knowledge, the strengthening of the intellectualization of labor, and the expansion of high technologies. This necessitates an acute problem for qualified engineering personnel for all industries. Higher education faces the task of training future engineers acquainted with the concept of CIT, able to form a strategy for automation of production, ensuring their competitiveness and professional mobility in today's market economy.

An essential aspect of studying the comprehensive problem of training future engineers is research related to finding optimal ways and means to improve the educational process, allowing at a high professional level to solve important problems related to the strategic direction of scientific and technological progress - computerization and operation of machines and equipment.

Solving such problems has led to the emergence of a large number of computer programs, which are increasingly used in the study of most subjects in higher education. Scientific and technical progress in social production and the introduction of information technologies in various spheres of life necessitates the training of specialists in engineering and technical specialties with established professional competencies. Therefore, the traditional system of training future engineers needs to be improved on the basis of modern advances in science and technology, optimization of forms, methods and tools of training using information technologies and CIT [8].

Analysis of recent researches and publications has shown that issues related to information technology in education have paid attention to V. Ivanov, A. Kalensky, I. Zakharova and others. Problems of computerization of education were studied by Y. Doroshenko, Y. Zhuk, Y. Mashbyts, O. Torubara, O. Yatsyuk and others. The use of modern computer hardware and software and improving the quality of education is shown in the works of F. Medvedev, K. Grebennikov, G. Kruchin, V. Sydorenko, N. Tverezovskaya and others. Issues of application of multimedia technologies in the educational process were studied by V. Bykov, Y. Zhukov, R. Gurevich, Y. Loboda and others. Almost all authors note that the use of information technology can increase the intensity and efficiency of the learning process; creates conditions for self-education and distance education, thus allowing the transition to continuing education; in combination with telecommunication technologies solves the problem of access to new sources of various information. However, the use of modern computer information programs and multimedia technologies in the training of future engineers is insufficiently represented in scientific materials.

Based on the generalization of the results of analysis of scientific sources, the study of practical experience of training engineers using CIT revealed the contradictions that objectively exist in the training process, namely [3]:

– between the level of training of future engineers and employer requirements in modern conditions market economy;

– between the number of national and foreign software products most suitable for solving engineering problems and the content, focus, technical level of higher education, which provides training for future engineers to apply these software products in practice.

In this regard, the article aims to analyze the features of the use in the educational process of future specialists in engineering specialties of information computer-integrated technologies, to provide recommendations for the use of software products and application packages in the study of engineering disciplines.

2. The use of computer-integrated technologies in the educational process for students of engineering specialties

Improving the professional training of future engineers is impossible without the use of new computer programs. They open up advanced opportunities for the development of computer (information) literacy, which affects the quality of competence of specialists in the use of modern information technology in educational and professional activities, knowledge of modern techniques and methods of using CIT in conducting various types of training sessions that are implemented in educational and extracurricular activities [4, p. 290].

Computer literacy is a component of professional competence, a necessary condition for the effectiveness of professional and pedagogical activities of lectures and future professionals in modern conditions. The future engineer must be able to use electronic resources to ensure the formation of basic skills in their engineering and technical activities in editorial and publishing systems, as well as to maintain a proper professional level [1, p. 23].

Information technology can be used as a powerful tool that encourages lectures to seek new non-traditional forms and methods of training and education of future professionals, developing his abilities. CIT are one of the forms of working with modern information technologies. They are based on the use of complex software systems and subsystems, are the basic critical technologies, i.e. technologies that underlie the creation of a wide range of knowledge-intensive products. The main principles of their development are complex automation, computer-integration, system integration, intellectualization, individualization, specialization, reengineering, technology transfer, and features: uniqueness of each implementation, multiplicity, diversity of systems and subsystems that are part of them, randomness and uncertainty processes (factors) operating in them, the vagueness of tasks, the unpredictability of consequences, etc.

The future professional character of the activity requires a combination of classical engineering education with in-depth mastery of computer technologies and special software. Note that over the past ten years, the principles of building technological systems have undergone significant changes. Traditional technological processes have been replaced by modern automated lines with microprocessor control devices and computer-integrated technologies. Therefore, the higher technical educational institution must provide training of highly qualified personnel who are familiar with the concept of computer-integrated industries and can implement it in industrial enterprises of Ukraine and the world. Given the features and specifics of computer-integrated technologies, we note that CIT in the process of training future engineers is a new generation of technologies that combine advanced information and industrial technologies, describe physical and mathematical models, study processes, and allow to manage the creation of the model, the process of calculation, processing and analysis of the obtained results.

CIT has an active influence on the process of teaching and educating students, as they change the scheme of knowledge transfer and teaching methods. At the same time, the introduction of CIT in the education system not only affects educational technologies but also introduces new ones into the educational process. They are associated with the use of computers and telecommunications, special equipment, software and hardware, information processing systems. They are also associated with the creation of new tools for learning and preserving knowledge, which includes electronic textbooks and multimedia; electronic libraries and archives, global and local educational networks; information retrieval and information reference systems [9].

The use of CIT tools should not become an end in itself, but should only be a tool for solving certain problems of learning, expanding and forming the thinking of future professionals to solve professional and educational problems.

In our opinion, creating a special environment, focused on the formation of professional competencies of the future engineer - one of the most advanced approaches to the introduction of modern CIT in the educational process.

Analysis of the situation in higher education institutions for the training of future engineers shows that the use of information technology and CIT significantly changes the role and functions of teachers and students, significantly affects all components of the educational process. The introduction of CIT into the educational process inevitably causes significant changes in the structure of the educational system of the higher technical institution.

The final goal of education of the future engineer is the inclusion of the individual in professional engineering activities. Therefore, according to the curriculum, the process of training future engineers begins with mastering the skills of working with modern computer technologies and the basic packages of applications.

The result is the acquisition of future engineers of certain skills in a graphic activity, namely in:

– rational and correct use of the capabilities of computer technology, in particular, in the use of graphics editors;

– fulfillment of algorithmic geometric constructions and creation of design documents;

– work with personal computers in geometric modeling of objects and processes, execution of various technical drawings.

Thus, disciplines from the cycle of natural science (basics of computer science and computer engineering, engineering and computer graphics) create conditions for in-depth mastery of fundamental engineering disciplines, but this course is not enough for the development of engineering thinking and professional competencies of future professionals. In the process of training specialists, there is a process of creating a theoretical foundation, accumulation of practical experience and professional methods of work. The use of the possibilities of new CIT tools in the educational process makes it possible to improve the process of forming the professional competencies of a specialist.

Drawing up the optimal structure of the educational process of future engineers is based on the integration of various scientific fields, interdisciplinary links and the principles of continuity in education. Ultimately, it is a combination of disciplines of the cycle of general training and the cycle of professional and practical training of future engineers, using information computer technology - COMPAS 3D, based on CAD (Computer-Aided Design) systems; because they are endowed with a high degree of clarity, form a spatial imagination and lead to an intuitive understanding of the essence of geometric transformations.

Computer-aided design means the development of a design project based on three-dimensional geometric modeling of parts, followed by the automated formation of a set of drawings and design documentation.

The thinking of a designer who uses 3D modeling is different from the thinking of a designer who only works with drawings. These differences are as follows:

1. The use of 3D modeling develops spatial thinking and facilitates faster decision-making.
2. Freedom in creating complex geometric shapes and understanding that these shapes can be easily implemented using integrated technologies, stimulate creativity, increase interest in work.
3. Organizing information about completed developments, leads to greater systematization of thinking.
4. The number of errors in the project decreases; the designer sees the result of his work in the design process.

The use of this program is accompanied by an increase in the individual work of students, which requires the constant support of the educational process by teachers. The important role of didactic goals: they are preserved as independent forms of organization of the educational process and at the same time are the elements of other forms of educational activities (lectures, practices, seminars, laboratory workshops).

Multimedia technologies allow using a computer to integrate processes and reproduce different types of signals, different environments, tools and methods of information exchange [2, p. 298]. It should be noted that scientists emphasize the ability of multimedia technologies not only to facilitate and make interesting the process of knowledge transfer but also to stimulate creative activity and independent human activity [5]. For the learning process to be effective during the creation of multimedia presentations, we adhere to the didactic principles of learning [6]:

- the principle of scientificity (presented information must meet modern requirements of science, be reliable);
- the principle of clarity (the design of a multimedia presentation should be aesthetically complete and descriptive);
- the principle of accessibility (the content of the presentation should correspond to the opportunities for students to learn);
- the principle of systematicity and consistency (presentation should be presented as an element of systematic learning following the curriculum of the discipline);
- the principle of connection with life (visual illustrations used in the creation of multimedia presentations must be modern and relevant);
- the principle of educational training (the content of presentations should solve not only the task of training but also education, for example, aesthetic).

The readiness of future engineers to use CIT can be defined as a state of mobilization, characterized by the presence in their minds of a holistic structure of the use of CIT in future professional activities and the motivation to implement it. The generalization of different approaches to understanding readiness allowed us to identify three interrelated components in its structure [4]:

- motivational and value (a set of motives, interests, needs and value orientations, the desire to independently set and achieve goals in professional activities, a set of ideas about themselves as a professional, the ability to think unconventionally and in different areas, integrating technological, mathematical and scientific knowledge to solve practical tasks);
- semantic (system of theoretical knowledge in the field of computer-integrated technologies, awareness of the importance of using these technologies in the preparation and further professional activity);
- operational (system of skills in the field of computer-integrated technologies, the ability to absorb the necessary information using various learning tools, the ability to independently organize their cognitive activities, the formation of which reflects the practical readiness of the future engineer to use computer programs).

Based on the theoretical analysis of scientific sources on the essence of computer-integrated technologies, the specifics of training future engineers and the study of practical experience, the scientific and pedagogical conditions for the use of CIT in the training of future engineers were determined. The most significant are:

- providing scientific and methodological support in the process of forming the readiness of future engineers to use computer-integrated technologies;
- awareness of future engineers of the importance of using e-learning tools as a resource of computer-integrated technologies;
- updating the independence of future engineers to create modern computer programs.

Scientific and methodological support should take into account the maximum use of the scientific potential of the university, i.e. the use of real opportunities that the university has for research and use of their results in the training process, as well as the support of each subject of the educational process to prepare future engineers for use computer-integrated technologies.

Regarding the awareness of future engineers of the importance of using e-learning tools as a resource of computer-integrated technologies, in our opinion, the use of e-learning tools can increase the level of training of future engineers through the formation of guidelines, interest, strong motivation, increased activity of students to use CIT in their professional activities. We interpret e-learning tools as software products that are created and worked with the use of computer and telecommunications equipment and provide creative and active acquisition by future engineers of knowledge, skills and abilities necessary for future professional activities [3].

Actualization of the independence of future engineers to create modern computer programs will be presented in the process of creating computer programs to perform cognitive and practical tasks. The presence of this quality determines the specific character of participation in professional activities. The future engineer, performing design and engineering production functions, must design applications and software interfaces for communication with engineering programs using object-oriented programming. Actualization of independence is provided by the ability to determine the purpose, the ability to systematize, plan, regulate, act consciously and proactively not only in acquainted circumstances but also in new conditions that require non-standard solutions.

We have proposed a method of forming the readiness of future engineers to use computer-integrated technologies; criteria, indicators and levels of readiness of future engineers for the use of CIT are defined; the results of the ascertaining and formative stages of the research are analyzed.

Three criteria for the readiness of future engineers to use CIT were identified:

– professional orientation with indicators (motivation of professional activity, satisfaction with the choice of profession; the need to achieve professional knowledge, skills and abilities; persistence in achieving their goals, the desire to succeed),

– cognitive with indicators (completeness of acquired professional knowledge; awareness of the use of computer-integrated technologies; the degree of skills to implement the acquired professional knowledge);

– technological with indicators (ability to use basic software packages and database management systems to solve problems of professional activity; ability to develop modern computer programs for communication with engineering programs using object-oriented programming; ability to design and structure computer networks, choose software, network topology and network hardware).

According to the criteria, four levels of readiness of future engineers to use CIT were determined: critical, basic, user and design [4].

The critical level of readiness of future engineers to use CIT is characterized by absence of motivation for professional activity; satisfaction with the choice of profession; low need to achieve professional knowledge, skills and abilities; absence of professional orientation; persistence in achieving their goals; absence of knowledge of the basics of computer science; principles of algorithmization, methods of numerical analysis, user skills, awareness of the use of computer-integrated technologies; absence of skills to apply basic software packages and database management systems; develop computer programs using object-oriented programming, design and structure computer networks.

The basic level of readiness of future engineers to use CIT is characterized by the presence of motivation for professional activity, the need to achieve professional knowledge, skills and abilities; insufficient professional orientation, persistence in achieving their goals; completeness of acquired professional knowledge; possession of skills for the implementation of professional knowledge; the desire to use CIT in future professional activities. Future engineers can apply basic software packages and database management systems, develop modern computer programs using object-oriented programming, perform numerical calculations, design and structure computer networks, choose software and hardware.

The user-level of readiness of future engineers to use CIT is characterized by a conscious motivation for professional activity, the need to achieve professional knowledge, skills and abilities; available professional orientation, persistence in achieving their goals; sufficient amount of acquired professional knowledge, the desire to use computer-integrated technologies. Future engineers have a strong ability to use basic application packages and database management systems to solve professional problems; develop modern computer programs for communication with engineering programs using object-oriented programming; set and solve optimization problems; design and structure computer networks, choose software and hardware, network topology and network hardware.

The design level of readiness of future engineers to use CIT is characterized by a strong motivation for professional activity; a conscious need to achieve professional knowledge, skills and abilities; expressed positive professional orientation, persistence in achieving their goals; the full amount of acquired professional knowledge; well-developed skills for the implementation of acquired knowledge; awareness of the use of computer-integrated technologies. Future engineers both in an acquainted field of activity and in unforeseen situations have the skills of a system design of engineering objects, methods of numerical analysis, understand the principles, structure and organization of automated integrated production, and can perform work in integrated software systems.

Based on the results of the research, a method of forming the readiness of future engineers to use CIT was developed. The stages of implementation of the proposed methodology were identified: initial-elementary, administrative-system and service-applied.

The initial-elementary stage was aimed at forming students' user skills (basic computer skills, peripherals, operating system, text editor, spreadsheet); knowledge of the basics of computer science (principles of algorithmization, fundamentals of formalization of logical processes and construction of programming languages, methods of numerical analysis, their program implementation).

The purpose of the administrative-system stage was the formation of skills to perform numerical calculations, to solve optimization problems; work with professional databases; know the architecture of computer systems, systems engineering integration and circuit technologies of computer systems.

At the service-applied stage, the students acquired theoretical knowledge, skills and abilities to work with appropriate software systems, have the principles of a system design of engineering objects, methods of numerical analysis in the professional field, understand the principles, structure and organization of automated integrated production, be able to perform work in integrated software systems.

Skills for developing training sessions in a new learning environment with the help of CIT play a key role in the successful professional activity of a future engineer. So, in our opinion, the introduction of CIT in the educational process of training specialists in engineering and technical specialties furtherer to:

- preparing students for the use of modern software in educational, research, professional activities;
- better mastering of educational material and its fuller comprehension;
- development of students' abstract thinking.

In addition, it allows you to use rationally learning time in the process of studying new material and allows to combine traditional and computer learning with the widespread use of computer-integrated technologies.

3. Features of the introduction of computer-integrated technologies in the educational process of training specialists in higher education in the specialty 131 "Applied Mechanics"

As noted, in modern society there are trends of constant growth of requirements for the professional level training of specialists in higher educational institutions of Ukraine following the modern needs of the world labor market. The engineering specialty "Applied Mechanics" is no exception.

Approval of the standard of higher education in the specialty 131 "Applied Mechanics" for different levels of higher education with details of general and professional competencies is an important factor in unifying the educational process in the global educational space and continuous improvement of national education.

However, a wide range of profiles of national and foreign machinery manufacturing enterprises and the rapid pace of creation of new generation industries, based on digital technologies in the sixth technological mode of design and production (global trend of implementation of programs "Industry 4.0" by Siemens and Chinese State Program "Chinese Production 2025"); as well as the limited terms of academic training in combination with new threats to human life through COVID complicates the possibility of in-depth study of certain professional practices according to the wishes of employers and students [7]. In addition, there is a need to use special hardware and software. For example, the introduction of additive technologies, which require special skills, is growing every year. Therefore, the structure of human resources needs to change, displacing the knowledge of computer engineering technologies.

Thus, we see the relevance of increasing the introduction of CIT in the educational process. In the market of educational services in Ukraine in this specialty, this approach is partially implemented in the following educational programs: "High-tech computer engineering", "Computer engineering in mechanics"; "Computer-aided design and machine design", "Mechatronic systems engineering", "Mechanical engineering technologies: computer-aided design systems", "Computer-aided design and development of mechanical engineering technologies", "Computer-aided design systems", "Industrial engineering" [5]. Such groups of educational programs are aimed at implementing the concept of mechanical engineering technologies using computer-integrated technologies.

All other educational programs can be structured into the following groups:

1. Mechanical engineering technologies in general ("Mechanical engineering and equipment programming technology", "Engineering mechanics", "Applied mechanics", "Innovative technologies", "Mechanical engineering technologies").

2. Technologies for the production of special products ("Aircraft production technologies"; "Tool production: computer-forming technologies and tool design").

3. Welding technologies and related special processes ("Technologies and engineering in welding"; "Technological systems of engineering of joints and surfaces", "Welding", "Engineering of welding and related processes", "Technologies and equipment of welding", "Laser equipment and computerized processes of physical and technical processing of materials"; "Applied Mechanics", "Welding").

4. Design and engineering of machine-building products ("Dynamics and strength of machines"; "Tool systems of engineering design"; "Technologies of computer design of machines", "Engineering of packaging and packaging equipment", "Hydraulic machines, hydraulic drives and hydropneumatic"; "Dynamics, the strength of machines and vehicles", "Metal-cutting machines and systems: computer design").

5. Technologies of service of machinery manufacturing products ("Rehabilitation and increase of wear resistance of parts and structures", "Technical service", "Resource and energy-saving systems, devices and apparatus").

6. Technologies that implement certain methods of manufacturing machine parts ("Equipment and technology of foundry production") and processing of materials by pressure ("Applied mechanics of ductility of materials"; "Equipment and technology of plastic forming of mechanical structures").

7. Automated technologies in mechanical engineering (“Automated and robotic mechanical systems”; “Mechatronics and industrial robot machines”, “Computerized technologies and mechatronic systems in mechanical engineering”, “Computerized complexes of printing and packaging industries”).

Therefore, based on the analysis of national and foreign experience, we have identified the following ways to increase the efficiency of training of engineers in this specialty.

1. Limiting the time of teaching certain fundamental disciplines due to the widespread use of application software. In particular, in the discipline of "Higher Mathematics" no need to spend time studying the methods of solving integrals, differential equations, finding derivatives, etc. It is advisable to introduce an additional discipline "Computer Mathematics", which will cover high-performance methods of these calculations in the environment of software products of symbolic mathematics such as Wolfram Mathematica, Derive, Maple, MathCAD, etc.

2. We consider it expedient in the curricula of training specialists in the specialty 131 "Applied Mechanics" to provide for the study of such disciplines.

In the discipline "Engineering surfaces of machinery products", it is necessary to reveal the features of ensuring the quality of product surfaces at all stages of their life cycle (design of structures and technological processes of their manufacture, implementation of technical solutions in production, operation, rehabilitation and disposal). It is advisable to detail the study of technological methods of corrosion protection (methods of obtaining organic and inorganic coatings) and increase wear resistance during the long service life of products.

The discipline "Application Software Development Technologies" may include methods of creating application programs based on the use of programming languages (C ++, C #) and environments of specialized software products (software interface Solidworks API, LabVIEW, MATLAB, Wolfram Mathematica).

In the subject "Control systems of technological equipment», it would make sense to reveal the most widespread CNC systems, PLC systems, controllers of tracking drives, etc. It is obligatory to study CNC-systems Mach3, EMC2 (LinuxCNC), HeeksCNC.

The content of the disciplines "Theory of Mechanisms and Machines", "Resistance of Materials", "Details of Machines" should be combined into one discipline "Applied Mechanics". The presentation of the material should be based exclusively on the use of modern CAD/CAE-systems (SolidWorks Motion, OnShape, CATIA, NX-Unigraphics) [10].

Fundamentals of work and geometric modeling in CAD systems (Autodesk Inventor, SolidWorks, COMPAS, AutoCAD, ProENGINEER, Delcam, Solid Edge Free 2D Drafting CAD, Heeks CAD/CAM), the theory of projection and technical drawing should be taught in the subject "Geometric modeling”.

The teaching of the discipline “Recycling Technologies” is relevant due to the threatening trends of increasing environmental annoyances and the technological need to use secondary raw materials due to limited material resources.

Questions of technologies and equipment of machine-building productions, features of designing of workpieces and necessary attachments can be allocated in the whole list of separate disciplines: "Technologies of molding of metals and alloys", "Technologies of forming from polymeric materials of ceramics, glass and rubber", "Technologies of powder metallurgy", “Assembly technologies”, “Additive technologies”, “Welding technologies”, “Pressure processing technologies ”, “Material cutting technologies”.

Moreover, their volume may be characterized by a variable number of credits depending on the wishes of employers and students in each case. Thus, the strategy of flexible credit volume of disciplines at their fixed total volume is realized. Laboratory-practical session in the mentioned disciplines is recommended to be carried out with the use of modern technologies of virtual modeling in CAM-systems. For example, teaching the subject "Technology of casting metals and alloys" can be carried out using software products ProCAST, Magma, WinCast, CastCAE, LVMFlow, NX-Unigraphics and Polygon for modeling foundry technology. Similarly, in the discipline "Technology of manufacturing parts by pressure" a large number of technological operations can be modeled by software products DEFORM, QFORM, ANSYS/LS-DYNA, AutoForm, MSC.SUPERFORM, PAMSTAMP and others. Welded joints are conveniently designed in NX/Weld Assistant as part of the study of the discipline "Welding Technology". In addition, the software packages MPI/Flow, Moldflow Plastics Insight should be studied in the discipline "Technologies of forming from polymeric materials of ceramics, glass and rubber".

It is desirable to pay much attention to the study of specialized software products and individual modules of CAD/CAM/CAE-systems that implement automated calculations of machining allowances; cutting modes (CAD TP VERTICAL, EdgeCAM, SecoCut, Timeline, Techcard, T-FLEX Technology, Sprut TP, CARUS, SWR-technology, Impulse, Technologist-Gepard, Temp and KONCUT); technological rate making and design of technological documentation and selection of technological equipment (Timeline, Technologist-Gepard, NATTA, TEMP, T-FLEX Technology, AUTOMAT, ARBAT, CARUS, ADEM SARR, Metalink, Technomatix, Solumina, Notixia, Metamatrix and Proplanner), optimization of sheet metal cutting (Astra S-Nesting and T- Flex nesting), calculation of dimensional chains (GRACON 7 in the environment AutoCAD, Pro/ENGINEER (specialized module - CE/TOL SixSigina (CE/TOL)); SolidWorks with the TASys Works module; Autodesk Inventor, TECHCARD with the module CADMECH, Tolerance Stackup Validation in NX environment, eM-TolMate module in CATIA environment, etc.).

Computer product optimization (generative design in Solid Edge, Ansys environments), the study of principles and conservation and packaging technologies should be covered in the discipline of "Engineering Design".

It is important to conduct an environmental expert study of technical solutions using modern software products. An example is SOLIDWORKS, which allows you to perform the environmental examinations in real-time as

part of the process of designing a new product. This product uses life cycle assessment criteria according to industry standards, allows you to quickly assess the environmental impact of a part, reduce material and energy consumption, and adhere to the development of environmentally harmful products.

Social, economic and scientific-technical effects should be determined using modern software products and online services in the presentation of the discipline "Efficiency of engineering solutions". A modern engineer needs knowledge, which is covered in the discipline "Bibliography and its use in modern search engines".

Students should be able to get acquainted with the structure and features of practical use of automation systems of engineering (design) data (PDM), planning and management of enterprise (ERP) and production (MES) when studying the discipline "PDM/ERP/MES - systems in machinery production".

Problematic questions of acquisition licensed software products can be solved by the wider activity of universities with the conclusion of agreements with international companies, the use of student and trial versions with limited functionality or period of use. This requires a clear structuring of the schedule and the order of presentation of the material. Each discipline can be characterized by a list of software products that can be used in the educational process. Since the universities train foreign students from around the world, the variability of these software products should be wide. However, the choice of specific software should be based on the results of monitoring its use in machinery enterprises in certain regions and countries of the world, as well as taking into account the wishes of foreign students. Therefore, during all types of internships (introductory, design and technological, etc.), the provision of information on the use of computer programs in enterprises of possible employment of foreign students should be an obligatory element of their reporting.

The creation of training courses in these disciplines and the implementation of these recommendations will lead to the in-depth study of educational material by saving time, structuring and increasing the productivity of students' learning material using computer-integrated technologies.

Conclusions

Thus, modern higher education is tightly coupled to the development of computer technology, information technologies and information systems in production. It is proved that the use of CIT in the training process of engineers is an objective process of forming the professional competencies of future specialists. The method of determination and ways to increase the readiness of future engineers to use CIT are proposed. Recommendations for the introduction of professional disciplines in the curriculum of future specialists in the specialty 131 "Applied Mechanics" with the use of CIT are given. The conducted researches do not exhaust all completeness of their coverage and do not claim to comprehensive disclosure of the specified problem. We see the prospect of further research in a deeper study of factors, consistent patterns, and features of the use of CIT in the training of specialists in engineering and technical specialties.

Further research should be aimed at creating educational and methodological complexes focused on the formation and development of the creative potential of students, the formation of skills to acquire knowledge, to carry out design, experimental researches and independent activities using computer-integrated technologies.

References

1. Bochar, I. (2011). Methodical aspects of preparation of engineering specialists for the use of ADOBE PHOTOSHOP CS5 in editorial and publishing systems. *Computer-integrated technologies: education, science, production, Proceedings of the Conference*. Lutsk, Ukraine.

2. Bykov, V. (2009). *Models of organizational systems of open education.* Kiev: Atika.

3. Danylchenko, L., Sipravska, M. (2020). Features of the educational process for foreign students with the purpose of effective using the components of the studing system. *Teaching and Learning of International Students in Ukraine. Challenges and Perspectives.* Preceeding of the Vth International Scientific Conference. Ternopil, Ukraine.

4. Gurevich, R., Cademija, M. (2005). *Information and telecommunication technologies in the educational process and scientific researches.* Vinnitsa: Planer.

5. Radyk, D. (2020). Peculiarities of planning the educational process of higher education from foreign citizens on autumn and spring admission to study. *Teaching and Learning of International Students in Ukraine. Challenges and Perspectives*, Preceeding of the Vth International Scientific Conference. Ternopil, Ukraine.

6. Stavyts'ka, I. (2015). Information and communication technologies in education. *Modern Trends in Teaching a Foreign Language for Professional Purposes in Higher Education*, Preceeding of the XIst International Scientific and Practical Conference. Kiev, Ukraine.

7. Vasylkiv, V., Dyachun, A. (2020). Improving the efficiency of training engineering personnel in the specialty "Applied Mechanics". *Teaching and Learning of International Students in Ukraine. Challenges and Perspectives,* Preceeding of the Vth International Scientific Conference. Ternopil, Ukraine.

8. Zaharova, I. (2003). *Information technologies in education*. Kiev: Academy Publishing Center.

9. http://www.nbuv.gov.ua/e-journals/ITZN/em4/cjntent/07popeso

10. Abdullah, Z. (2020). Conventional milling into CNC machine tool remanufacturing: Sustainability modeling. *Economics, Management and Sustainability, 5*(2), 39-65. doi:10.14254/jems.2020.5-2.3

COMPUTER MODELING OF THE STRESS-STRAIN STATE OF THIN-WALLED TUBULAR STRUCTURAL ELEMENTS FOR PREDICTING THE LIMITING STATE

Halyna Kozbur[1], Oleh Shkodzinsky[2], Ihor Kozbur[3], Gashchyn Nadiia[4]

[1]Ternopil National Ivan Puluj Technical University, Rus'ka str. 56, 46001, Ternopil, Ukraine, kozbur.galina@gmail.com

[2]Ternopil National Ivan Puluj Technical University, Rus'ka str. 56, 46001, Ternopil, Ukraine, shkod@tntu.edu.ua

[3]Ternopil National Ivan Puluj Technical University, Rus'ka str. 56, 46001, Ternopil, Ukraine, kozbur.igor@tntu.edu.ua

[4]Ternopil National Ivan Puluj Technical University, Rus'ka str. 56, 46001, Ternopil, Ukraine, gashchyn_n@tntu.edu.ua

Abstract: If a thin-walled pipe loaded with internal pressure and axial tension allows the appearance of plastic strains, then the uniform plastic stability loss with the emergence of a local plastic deformation zone is considered the limit state, the corresponding stresses are considered as the limit ones. Correct prediction of the stress-strain state at the moment of strain localization requires taking into account the actual size of the loaded pipe and the calculation of true stresses. The paper proposes the implementation of the methodology of predicting the limit values of true stresses in the pipe at different ratios of internal pressure and axial tension values through the development of an algorithm for its computer modelling. Unlike existing, the methodology takes into account the physical and mechanical properties of the material, the type of stress state and the change in the actual dimensions of the loaded pipe. The algorithm is based on analytical dependences, established by the authors.

For two grades of steels (carbon steel 45 and alloy steel 10MnH2MoV), an increase in the calculated strength threshold is shown with an insignificant additional load of a pipe loaded with pressure and axial tension. Analysis of the numerical results showed that it is possible to establish a balance between the actual geometry of the element and the load, which will solve the problem of finding the optimal ratio of «weight-strength», important for practical applications in aircraft, rocket and mechanical engineering. The developed computing modelling algorithm for finding the limit values of actual stresses makes it possible to calculate a realistic safety factor and make improved engineering solutions at the design and operation stages of structural elements; to increase the efficiency and safety of using pipeline and shell-type saving systems.

Keywords: *computer modelling, large plastic strains, true stresses, the uniform plastic stability loss, complex stress state, localization of strains*

1. Introduction

The accurate prediction of maximum load (burst pressure, fracture pressure) is critical for the engineering design, assessment of integrity and on-line control of oil- and gas pipeline and other vessels under internal pressure [1]. Thus, computer modelling of strain-stress behavior of tubes and containers under combined load conditions is quite important.

As it is shown in [2 – 6], the influence of axial tension on loading capacity of main pipelines is quite essential. In papers [7, 8] some experimental research and theoretical models to determine the stress state impact on the pipes loading capacity has been proposed. Based on the Mises criterion, Updike and Kalnins [9] developed a general mathematical model for stress strain and internal pressure limit values forecasting for axially symmetric thin wall vessels. It was found that calculated fracture pressure causing the local plastic strains has resulted in higher values compared to the experimental ones.

A great number of analytical and empirical equations are known to be used for pipelines and vessels limit pressure predicting. Nevertheless, it is very difficult to calculate the exact value of fracture pressure and to estimate the accurateness of these equations. The problem of determining the real ultimate stress and ultimate strength factors values hasn't been studied properly. Most studies haven't taken into account the material strengthening and the change in actual dimensions of structural elements under load. Nominal stress is assumed lower the liquidity limit at design of heavy loaded shell-type structures like reactors bodies, collector bodies, steam generators and their elements. Though, some plastic deformation is quite allowable for the elements operating under intense short-term single load conditions. At a certain ultimate level of stress the structural element either loses its plastic resistance or undergoes plastic deformation localization. In both cases the structural element loses its further functionality dealing with shape and size change. Thus, one should be able to calculate real stress taking into account these changes to predict stress-strain state of the element at the moment of the uniform plastic stability loss as accurate as possible. In case when plastic deformation is allowed to be occurred the correct assessment of limit stress is especially important preceding the moment of the uniform plastic stability loss resulting in local deformation area appearance and further ductile fracture of the structural element. The analytical review of literary sources has shown that the problem of predicting the real stress values in loaded structural elements at the moment of plastic strains localization hasn't been studied properly. The conventional existing models and methods do not take into account the material properties, a type of stress state and a

change of actual size of loaded structural elements in the complex restricting the areas of their use. At the same time, the continuous increase of cost-efficiency, structure efficiency and performance safety requirements has made the task of improvement of analytical-calculation approach to ultimate states of metal materials forecasting under complex stress state very important and quite urgent.

The paper purpose is to introduce a new methodology and computer modelling algorithm for predicting the ultimate states for thin-walled pipes loaded with internal pressure in order to analyze the influence of physical-mechanical properties of the material, pipe geometry and a type of stress condition on the values of actual stress and real force factors at the moment of local plastic strains formation.

2. Problem setting

If a structural element under loading allows some plastic strains occurred then the correct estimation of ultimate stresses at the moment of the uniform plastic stability loss resulting in local strain area appearance and further ductile fracture of the structural element will be necessary. When it comes to the area of large plastic strains, the change of the element size will be important. That is why it will be worth saying about the real strength limit which prediction requires taking into account the actual size of loaded element and true stress-strain curve building. The calculation of ultimate values of true stresses at the moment of strains localization under uniaxial strain conditions is based on the use of Swift-Marceniak criterion and analytical dependence $\sigma = d\sigma / d\varepsilon$ between true stresses and tangent modulus in true stresses use. In the papers [10, 11] the criterion of the uniform plastic stability loss was offered to use for ultimate pressure prediction in thin-walled pipes. Analytically the moment of the uniform plastic stability loss in this case is described by the formula $\sigma = \frac{1}{2} d\sigma / d\varepsilon$ containing a correcting multiplier ½ at the tangent modulus $d\sigma / d\varepsilon$. The authors explained the appearance of a correcting multiplier by the loaded element geometry impact.

The algorithm implementation to find the ultimate values of true stresses occurring at the moment of the uniform plastic stability loss in the pipe loaded simultaneously by internal pressure q and strain N has been proposed in the study under discussion. The main analytical dependencies of the method under discussion have been obtained in [12]. The following equation was obtained due to the development of summarized methods of true stresses prediction in the pipe at the beginning of localization of uniform plastic strains [13]:

$$\sigma = \mu \cdot d\sigma / d\varepsilon \tag{1}$$

where μ is a correcting multiplier (factor) taking into account the physical-mechanical properties of the material, stress state type and element geometry as a whole set. The limit values of equivalent strains and real equivalent stresses in the pipe walls at the moment of strain localization are found as coordinates of the point of real deformation curve $\sigma(\varepsilon)$ and the curve of the right–hand side of the formula (1) intersection.

3. The model of plastic deformation of thin-walled tubular elements

For computer modeling of the true ultimate strength of the metal of thin-walled cylindrical pipes, two structural materials were considered:

- structure carbon-based high-quality steel 45 [14];
- heat resistant alloy steel 10MnH2MoV [15].

The load was considered simple, so $\sigma_z = k\sigma_\theta$ for different values k.

The technique which allows predicting the true stresses at the moment when local plastic strains appeared has been described in [16]. The technique has been used for thin-walled pipe of wall thickness h=2,5 mm and external diameter d=65 mm made of steel 45. The results of the experiment under discussion have been given as hoop and axial stresses and strains – $(\varepsilon_\theta)_i$, $(\sigma_\theta)_i$ $(\varepsilon_z)_i$, $(\sigma_z)_i$ respectively, for k=0; 0,5; 1; 2. The points have been chosen for which the condition was satisfied $\min\left((\varepsilon_z)_i, (\varepsilon_\theta)_i\right) \geq 1\%$ ($i = \overline{1, n}$, where n = 30 is a number of observations).

From the set of values $(\varepsilon_\theta)_i$, $(\sigma_\theta)_i$, $(\varepsilon_z)_i$, $(\sigma_z)_i$ equivalent stresses and strains were found by formulas:

$$(\sigma_{eq})_i = \frac{p}{2}\left[\frac{\left|(\sigma_z)_i - (\sigma_\theta)_i\right|^p + \left|(\sigma_\theta)_i\right|^p + \left|(\sigma_z)_i\right|^p}{2}\right]^{\frac{1}{p}}, \tag{2}$$

$$(\varepsilon_{eq})_i = \frac{p}{2(p+1)}\left[\frac{\left|(\varepsilon_z)_i - (\varepsilon_\theta)_i\right|^p + \left|(\varepsilon_\theta)_i - (\varepsilon_r)_i\right|^p + \left|(\varepsilon_z)_i - (\varepsilon_r)_i\right|^p}{0,5}\right]^{\frac{1}{p}}. \tag{3}$$

Radial stresses were neglected taking into account the assumptions of the theory of thin-walled shells, i.e. $(\sigma_r)_i = 0$. Under simple loading the following relation between hoop and axial strains is valid: $\varepsilon_z = n\varepsilon_\theta$. Radial strains $(\varepsilon_r)_i$ were linked with hoop and axial ones by using of material incompressibility:

$$(\varepsilon_r)_i = 1 - \frac{1}{\left(1+(\varepsilon_z)_i\right)\left(1+(\varepsilon_\theta)_i\right)}. \quad (4)$$

The discrete values of parameter *p* were chosen from the interval (1; 2) with a step 0,01. For the given set of points the Pearson correlation coefficient *r* and variation coefficient have been calculated. The Pearson correlation coefficient maximums were correlated with variation coefficient minimums. As optimum of *p* the value was chosen for which $r_{\max}$ was reached. For steel 45 99% the interval of confidence for $r = r_{\max}$ equals to 0,969±0,038, optimum *p=1,30*, and for steel 10MnH2MoV the interval of confidence 0,927±0,026, optimum *p*=1,59.

Thus summarized stress-strain curve was constructed by the points $\left((\varepsilon_{eq})_i, (\sigma_{eq})_i\right)$, which were obtained for the optimum parameter *p*. The segment of strengthening was approximated by the power model $\sigma_{eq} = A\varepsilon_{eq}^{\ B}$. So we get:

$$\sigma_{eq} = 721,42 \cdot \varepsilon_{eq}^{\ 0,23} \quad \text{(for steel 45)}, \quad (5)$$

$$\sigma_{eq} = 687,32 \cdot \varepsilon_{eq}^{\ 0,11} \quad \text{(for steel 10MnH2MoV)}. \quad (6)$$

Having calculated the values of true hoop and axial stresses by formulae $(\sigma_z)_i = (\sigma_z)_i\left(1+(\varepsilon_z)_i\right)$, $(\sigma_\theta)_i = (\sigma_\theta)_i\left(1+(\varepsilon_\theta)_i\right)^2$, true equivalent stresses were obtained by using the formula $(\sigma_{eq})_i = \frac{p}{2}\left[\frac{\left|(\sigma_z)_i - (\sigma_\theta)_i\right|^p + \left|(\sigma_\theta)_i\right|^p + \left|(\sigma_z)_i\right|^p}{2}\right]^{\frac{1}{p}}$. The computer program was developed to obtain the true stress-strain dependence $\sigma_{eq}(\varepsilon_{eq})$ [16]. True stress-state curves and experimental points, equations of power regression and determination coefficient R^2 are given on fig. 1.

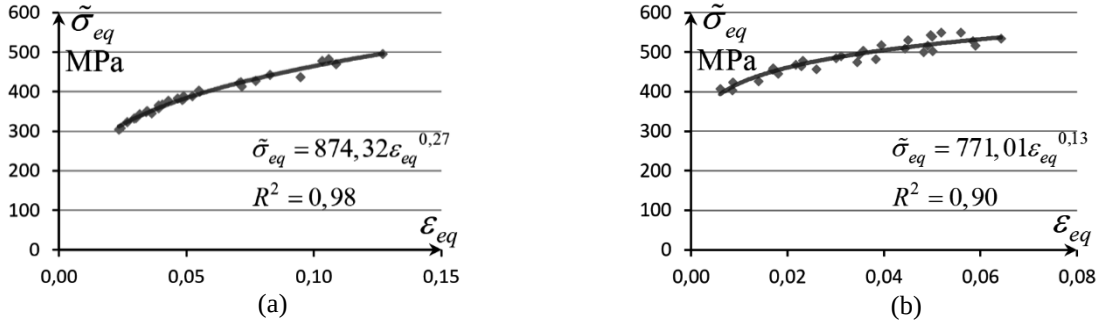

Fig. 1. Approximation of the true stress-strain curve by a power model and coefficients of determination for: a) steel 45; b) steel 10MnH2MoV.

To solve the equation (1) and to find the true ultimate stresses in the system of coordinates $(\varepsilon_{eq};\ \sigma_{eq})$ the graphs of both sides of the equations have been constructed. At *k*>>2 the pipe stress-and-strain state is close to the uniaxial one, so on the figures the calculations results are given for the interval which is important in practical engineering, $k \in (0,5;\ 2)$.

As a power model was chosen for the analytical description of the stress-strain curve, then the derivative $d\sigma_{eq} / d\varepsilon_{eq}$ was defined by the formula $d\sigma_{eq} / d\varepsilon_{eq} = A \cdot B \cdot \varepsilon_{eq}^{\ B-1}$. From (5) and (6) the expression was obtained which made it possible to find tangent modulus:

$$\frac{d\tilde{\sigma}_{eq}}{d\varepsilon_{eq}} = 240,0 \cdot \varepsilon_{eq}^{-0,7255} \text{ (for steel 45),} \quad (7)$$

$$\frac{d\tilde{\sigma}_{eq}}{d\varepsilon_{eq}} = 101,4 \cdot \varepsilon_{eq}^{-0,8685} \text{ (for steel 10MnH2MoV).} \quad (8)$$

Graphical solution of equation (1) for h/R=0,08, where R=(d–h)/2 – radius of the pipe middle surface is given on fig. 2. The value μ has been calculated by the formula obtained in [17] by the known values p, k, h, R. Solid curves show the true generalized stress-strain curves constructed at optimal values of the parameter p for each of the materials. True stress-strain curve is a graph representation of the equation left-hand side (1). Curves of the equation (1) right-hand side are given as dotted graphs – the product of tangent modulus and correcting factor μ taking into account the geometry of a pipe at the moment when local plastic strains appeared. Fig. 2 shows that the type of stressed state k makes a great impact on the pipe strength.

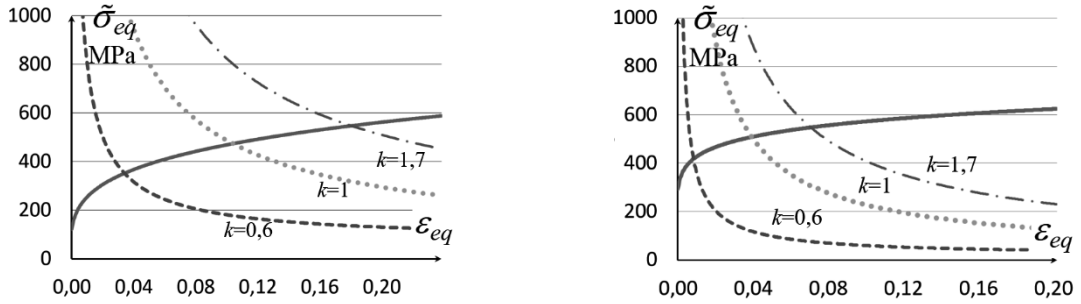

Fig. 2. Graphical solution of equation (1) for thin-walled pipes made of: a) steel 45; b) steel 10MnH2MoV. A solid line is a true stress-strain curve

The dependences of limiting true equivalent stresses $\tilde{\sigma}_{eq}$ on k for several values of h/R are shown on fig. 3.

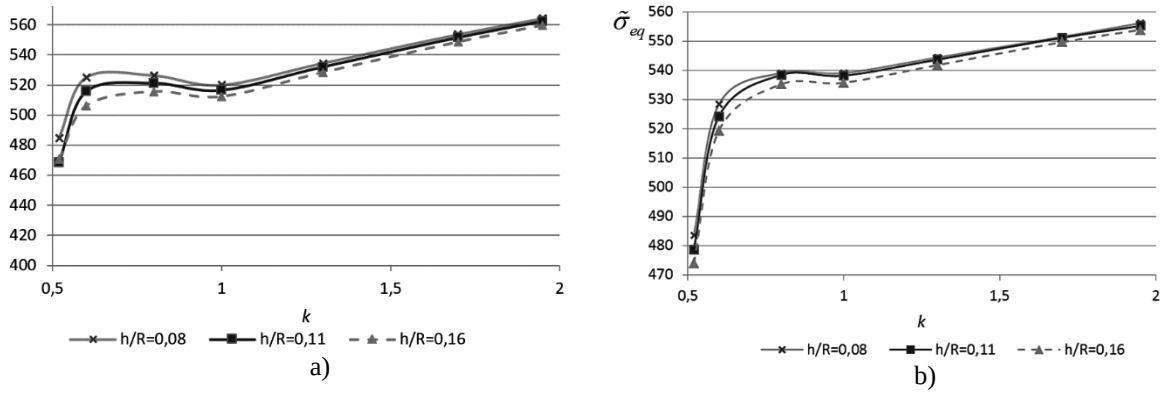

Fig. 3. Dependence of limiting stresses $\tilde{\sigma}_{eq}$ on k for certain h/R for: a) steel 45; b) steel 10MnH2MoV

Fig. 3 shows that the smallest calculated durability occurs when pipe is loaded only by internal pressure (k=0,5). Under stress state with a coefficient k=0,5..1 the uniform plastic stability loss occurs at higher values of true equivalent stresses for all patterns, the pipe durability is getting higher. The increase of h/R from 0,08 to 0,11 for k=0,6..0,7 makes the calculated ultimate values of true equivalent stresses 10 MPa (or ≈2%) lower on average. In pipes of smaller parameter h/R the higher level of calculated true equivalent stresses has been found at the moment of deformation localization. At k = 1 the increase of correlation h/R from 0,08 to 0,11 results in average 5 MPa (or ≈1%) decrease of calculated true ultimate equivalent stresses for steel 45. For steel 10MnH2MoV the level of limit equivalent stresses at the correlations h/R=0,08 and h/R=0,11 is the same. Under further increase conditions of correlation h/R from 0,11 to 0,16 the limit calculated equivalent stresses are 1-1,5% smaller for both materials.

Dependence $\tilde{\sigma}_{eq}$ on the type of stressed state at $k = 1..2$ is close to the linear one for all chosen values h/R.

The dependencies of calculated ultimate values of true hoop and axial stresses under combined loading conditions of the pipe by internal pressure and tension for both steel grades are shown on fig. 4. The graphs allow to understand the behavior of dependence of limit true hoop and axial stresses on k in the interval (0,5; 2) taking into account its real geometry of element. In case of pipe loading only with internal pressure the calculated ultimate true

axial stress coincides with the referencing one. It can be explained by zero axial strains. The engineering ultimate values of stresses are much lower than true calculated ones. For k=1 the calculated true stresses are 1,2-1,3 higher than referencing ones, and for k = 2 – 1,1-1,2 higher. The two times increase of thin wall index (from 0,08 to 0,16) results in 4-5 % decrease of the level of maximum calculated ultimate hoop stresses (for k=0,6). The dependence for steel 10MnH2MoV is close to the previous one. The two times increase of thin wall index (from 0,08 to 0,16) results in 2-3% decrease of the level of maximum calculated ultimate hoop stresses (for k=0,6). Separate symbols denote the points corresponding the engineering ultimate values of stresses for steel 45 at three types of stressed state (for k=0,5; 1; 2).

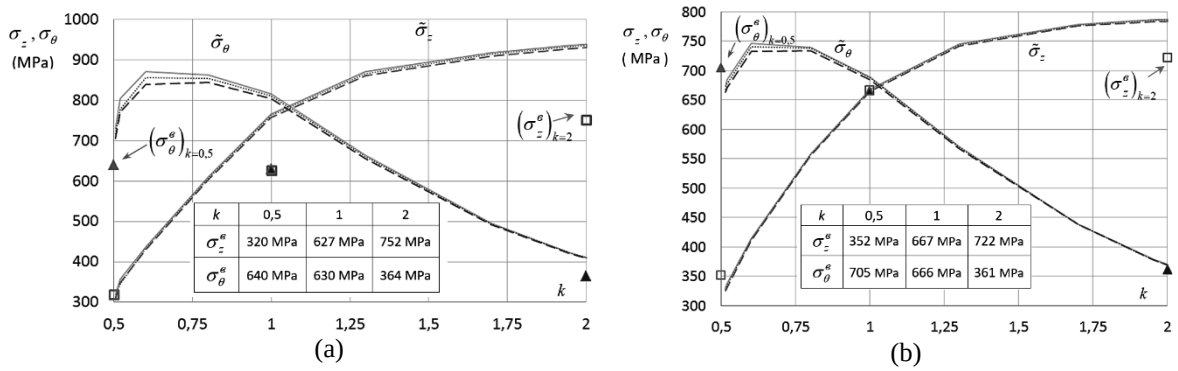

Fig. 4. Dependence of limit values of calculated stresses on k for certain h/R.
Denoted: ——— – h/R=0,08; ..... – h/R=0,11; — — . – h/R=0,16.
Separate points show the engineering strength limits for k=0,5; 1; 2

Fig. 4 proves that the calculated true ultimate hoop stresses are on average 1,01..1,3 times higher than engineering ones for k = 1, the true ultimate axial stresses are on average 1,1..1,2 times higher than engineering ones. The two times increase of h/R (from 0,08 to 0,16) makes the level of calculated ultimate stresses 1-3% lower. It shows the importance of improvement of strength properties of structural elements not only due to their mass increase.

The whole algorithm of computer modelling the ultimate strength of thin-walled cylindrical pipe with cupped ends loaded by internal pressure q and axial strain N, and determination of limit values of strength factors is formed from the task sequence (fig. 5):

1) finding the constant p by the initial stress-strains curves built for several values $k = \sigma_z / \sigma_\theta$ and building of generalized stress-state curve;
2) obtaining the dependence between true stresses and strains in equivalent coordinates;
3) determination of the true ultimate stresses in equivalent coordinates;
4) calculating the limit values of internal pressure q and tension N.

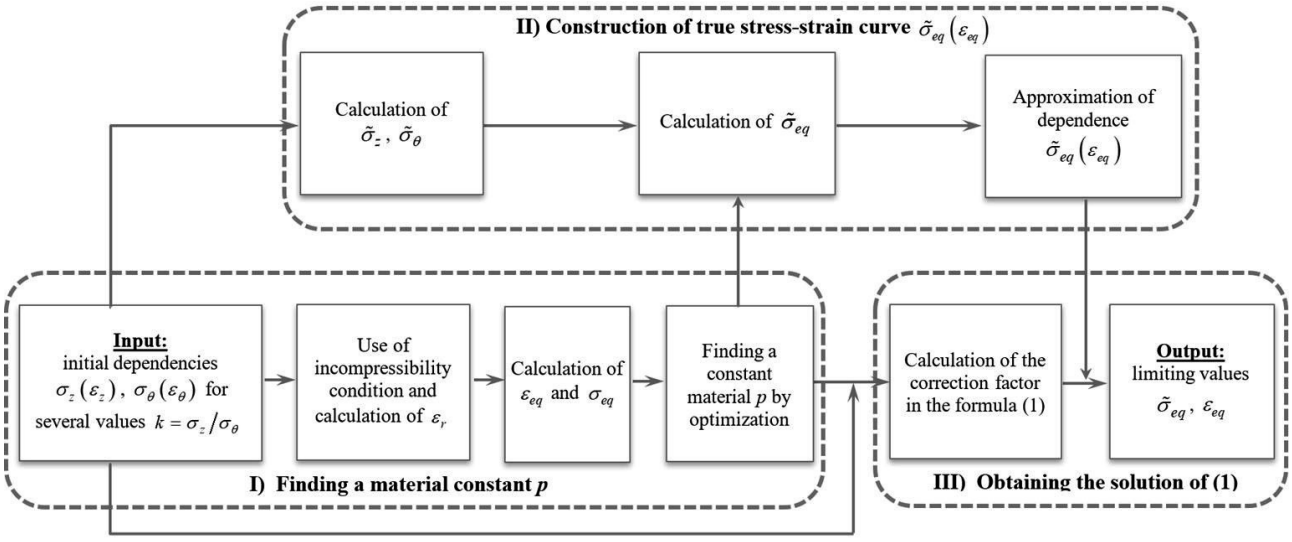

Fig. 5. Algorithm for computer modeling of the stress-strain state of thin-walled cylindrical pipe loaded by internal pressure q and axial tension N

4. Conclusions

The algorithm for computer modeling of the influence of stress state type and thin-walled cylinder geometry on the ultimate values of true stresses at the moment of the uniform plastic stability loss has been developed. The results of

the calculations showed that the ratio *h*/*R* increasing to some extent allows the ultimate values of axial strain and internal pressure be increased for both materials. Though the further increase of ratio *h*/*R* increases the allowable value of internal pressure but makes the maximum allowable values of strains lower. These facts prove the existence of optimal balance between the pipe geometry and its strength. The above-mentioned results can be used for calculation of loaded thin-walled pipes aimed at their material consumption saving, safety level increase under performance conditions and choose real safety factor.

Calculating of the limiting values of actual stresses makes it possible to predict the strength of thin-walled pressure vessels (pipelines, collectors of steam generators, reservoirs, etc., in mechanical engineering, aircraft construction, chemical, food, energy and other industries); choose a realistic safety factor and make optimal engineering solutions at the design and operation stages of structural elements; to increase the efficiency and safety of using pipeline and shell-type saving systems.

References

1. Luchko, J., Ivanyk, E. (2017). Diagnostics of the main gas pipelines and assessment of their residual life under the conditions of long-term operation. *Scientific Journal of TNTU*, *87*(3), 48-63. https://doi.org/10.33108/visnyk_tntu2017.03.048

2. Bony, M., Alamilla, J. L., Vai, R., Flores, E. (2010). Failure pressure in corroded pipelines based on equivalent solutions for undamaged pipe. *ASME. J. Pressure Vessel Technol*., *132*(5). doi:10.1115/1.4001801

3. Hillier, M.J. (1965). Tensile plastic instability of thin tubes–I. *International Journal of Mechanical Sciences*, *7*(8), 531–538, doi: 10.1016/0020-7403(65)90010-X

4. Tomita, Y., Shindo, A., Nagai, M. (1984). Axisymmetric deformation of hoop elastic-plastic tubes under axial tension and internal pressure. *International Journal of Mechanical Sciences*, *26*(6–8), 437–444. doi:10.1016/0020-7403(84)90033-X

5. Dilman, V.L., Ostsemin, A.A. (2000). O vliyanii dvuhosnosti nagrujeniya na nesuschuyu sposobnost trub magistralnyih gazonefteprovodov. *Izv. RAN. Mehanika tverdogo tela*, *5*, 179–185 [in Russian]

6. Dilman, V.L., Ostsemin, A.A. (2000). O potere plasticheskoy ustoychivosti tonkostennyih tsilindricheskih obolochek. *Problemyi mashinostroeniya i nadejnosti mashin*, *5*, 50–57 [in Russian]

7. Degtyarev, V.P. (1987). *Deformatsii i razrushenie v vyisokonapryajennyih konstruktsiyah*. Moskva: Mashinostroenie [in Russian]

8. Kollinz, Dj. (1984). *Povrejdenie materialov v konstruktsiyah. Analiz, predskazanie, predotvraschenie*. Moskva: Mir [in Russian]

9. Updike, D.P., Kalnins, A. (1998). Tensile plastic instability of axisymmetric pressure vessels. *ASME. J. Pressure Vessel Technol*, *120*(1), 6–11. doi: 10.1115/1.2841888.

10. Zhu, X.-K., Leis, B., (2011). Evaluation of burst pressure prediction models for line pipes. *International Journal of Pressure Vessels and Piping*. doi:10.1016/j.ijpvp.2011.09.007

11. Law, M. (2005). Use of the cylindrical instability stress for blunt metal loss defects in linepipe. *International Journal of Pressure Vessels and Piping*, *82*(12), 925–928. doi:10.1016/j.ijpvp.2005.04.002

12. Kozbur, H. (2020). Prediction technique for thin-walled cylindrical tubes boundary state. *Scientific Journal of TNTU*, *94*(2), 145–155. doi: 10.33108/visnyk_tntu2019.02.145

13. Kozbur, H. (2020). Method of predicting necking true stress in a thin-walled tube under a complex stress state. *Strojnícky časopis - Journal of Mechanical Engineering*, *70*(2), 101-116. doi:10.2478/scjme-2020-0024

14. Kaminskiy, A.A., Bastun, V.N. (1985). *Deformatsionnoe uprochnenie i razrushenie metallov pri peremennyih protsessah nagrujeniya*. Kyiv: Naukova dumka [in Russian].

15. Lebedev, A.A. (Ed.), Kovalchuk, B.I., Giginyak, F.F., Lamashevskiy, V.P. (2003). *Mehanicheskie svoystva konstruktsionnyih materialov pri slojnom napryajennom sostoyanii*. Kiev: Izdatelskiy dom “In Yure” [in Russian]

16. Copyright for the work "Computer modeling" The modeling of stress-state-independent deformation curve". Ministry of Economic Development, Trade and Agriculture of Ukraine, copyright registration certificate т 96585 dated 10.03.2020. (authors – Kozbur H., Gladio O.)

17. Kozbur, H. (2020). Method of predicting necking true stress in a thin-walled tube under a complex stress state. *Strojnícky časopis – Journal of Mechanical Engineering*, *70*(2), 101-116. doi:10.2478/scjme-2020-0024.

USING A BROADBAND SIGNAL BASED ON M-SEQUENCE FOR AUTOMATIC PREVENTING OF ACOUSTIC RESONANCE IN HIGH PRESSURE DISCHARGE LAMPS

Volodymyr Medvid[1], Iryna Beliakova[2], Vadim Piscio[1]

[1] Department of Automation Technological Processes and Production, Faculty of Applied Information Technologies and Electrical Engineering, Ternopil Ivan Puluj National Technical University, Ukraine
[2] Department of Electrical Engineering, Faculty of Applied Information Technologies and Electrical Engineering, Ternopil Ivan Puluj National Technical University, Ukraine.

Abstract: In the article, a method for preventing acoustic resonance of high-pressure lamps has been proposed. The main idea of which is the filing on the lamp of a modulated pseudo-random signal. For the set of a "discharge lamp - prototype of the device" an analysis of the spectral characteristics of the voltage on the lamp are made. The mathematical modeling of the set of a "discharge lamp - prototype of the device" is implemented. The results of simulation, which confirms the results of theoretical research, are presented.

Keywords: *preventing of acoustic resonance; high-pressure discharge lamp; pseudo-random signal.*

1 Introduction

In order to increase the efficiency of a gas-discharge low-pressure lamp, for a long time uses electronic ballasts that operate at high frequencies [1], [2]. Their advantages are:

- ◊ high coefficient of efficiency that significantly exceeds the similar parameter of electromagnetic ballast;
- ◊ the possibility of adjusting the current of the lamp in the specified limits;
- ◊ increase of light output;
- ◊ eliminating the possibility of lamp operation emergencies.

At the use of high-frequency electronic ballasts for work with high-intensity discharge lamps (mercury and sodium vapor, metal halide, etc.), there is a problem of the occurrence of acoustic resonance in the arc tubes of these lamps [1], [2]. Acoustic resonance has been studied in many scientific papers. Acoustic resonance frequencies range from 3 kHz to 150 kHz. The reason for this phenomenon is that when the direction of current flow changes due to the redistribution of charge carriers, acoustic waves arise which cause the forced mechanical vibrations of the gas medium of the arc tube, its walls, and even the fittings of its suspension. The spectrum of the resonant frequencies of mechanical oscillations depends on the geometric dimensions of the lamp arc tube, the speed of sound in it (which, in turn, depends on the pressure), the features of the designs of the arc tube and many other parameters [3], [4], [5]. At the some frequency, the frequency of acoustic waves in an arc may coincide with the resonant frequency of mechanical oscillations in the system.

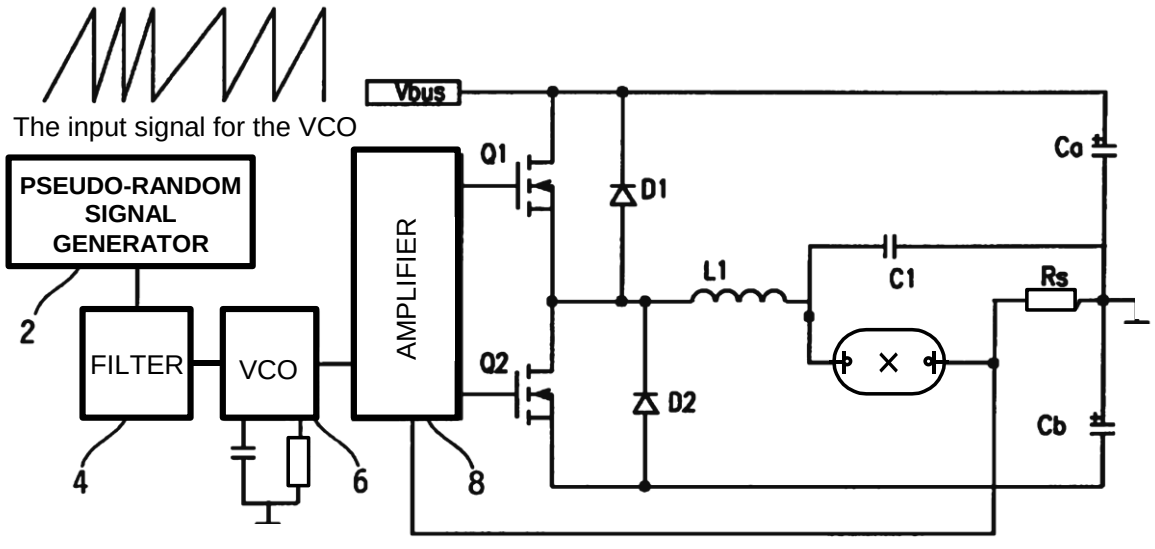

Fig. 1. Scheme of electronic ballast [6] for gas-discharge lamp:
VCO (voltage controlled oscillator)

Each of lamps, including the same type and the same power, can have different frequencies of the major resonance due to different electrical and structural parameters, which change in the direction of decrease or increase with the increase of the lamp's life time. In addition to the major resonance, there are resonances on other frequency harmonics, which negatively affects the lamp gas discharge state. The consequences of acoustic resonance are the instability of the lamp burning, the arc extinction and, at worst, the physical destruction of the arc tube [4].

Therefore, as a voltage supply of a high-pressure lamp, in most cases, alternating voltage is used, the frequency of which does not exceed 200 Hz, thus excluding the possibility of an acoustic resonance. These operating frequencies lie in the audio range and therefore the process of lamp discharges is accompanied by significant interfering noises. In addition, the size of the reactive elements used in the lamp's switching scheme remains significant compared to the ballasts at 50/60 Hz. Therefore, the search for ways of supplying high-pressure gas discharge lamps is still relevant.
The one of the effective methods for controlling acoustic resonance is the use of modulation of the main frequency of the supply voltage of the lamp by another signal. One of these schemes (US Patent No 6,144,172) [6] (Fig. 1) contains a white noise generator, which is based on a linear feedback shift register, the output signal of which flows through a filter to a voltage-controlled variable frequency generator (VCO). The signal from the generator's output enters to the output amplifier and is fed to the circuit of the inductive ballast, which are constructed in the usual way. The frequency range of the frequency of the VCO generator is usually chosen small. As a result, the output frequency of the signal coming to the lamp is changed by some pseudorandom behavior. The frequency of the change of the output signal of the pseudorandom signal generator is chosen much less than the average frequency of the VCO.
When working on the circuit, the frequency of the signal on the lamp is constantly changing and the resonance of the arc tube has no time to develop due to the inertia of the processes in the lamp.
The analysis of the described scheme allows us to conclude that in the case when a broadband signal is presented to a lamp, the energy distributed in a dangerous frequency interval will be small and the acoustic resonance phenomena will not occur or will have little effect.
The signal must also meet these requirements:

- ◊ the average value of the signal must be zero; otherwise, the phenomenon of migration of ions to the one of the electrodes of a lamp may occur;
- ◊ the duration of the constant state at the lamp inlet does not exceed the set value T, which is connected with the current limitation by means of reactive elements.

2 The offered device

The block diagram of the offered device is shown in Fig. 2. It consists of a clock generator (Gen), which generates at its output a meander at frequency of 10-40 kHz. This meander is fed to the input of the modulator sequence shaper (Mod Seq) and to the frequency divider on K (Div K). The divider generates a synchronization signal of the pseudo-random sequence generator based on the linear feedback shift register (LFSR) and simultaneously outputs to the inputs of the modulator sequence generator the clock number from the moment of switching the LFSR register.

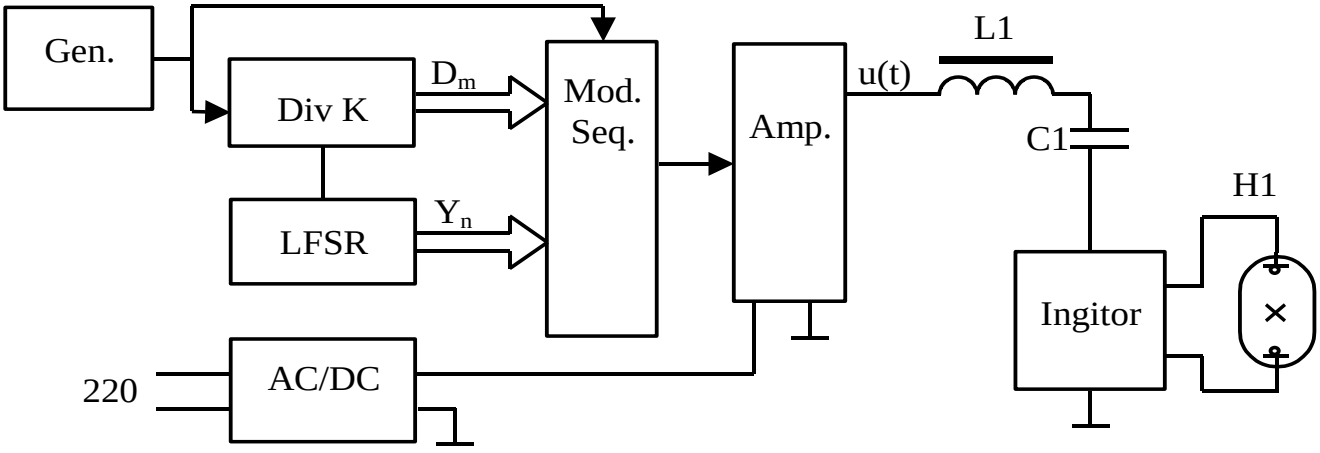

Fig. 2. Block diagram of the offered device

The modulator sequence generator (Mod Seq) also receives a signal from the LFSR register, which shows the current and previous state of the register LFSR. The modulator sequence generator based on the above signals generates an output signal to the Amp amplifier. The modulated signal at the output of the last circuit will be determined by both the current state of the LFSR register and the previous state of the register. The amplifier (Amp) operates in switch mode, the output signal of which is fed through the ballast circuit (L1 C1), and, if necessary, the ignition device (Ingitor), and the lamp H1.

Structure of random signal generator with linear feedback and signal properties

An LFSR generator (Fig. 3) consists of, the shift register 1, synchronized with pulses received from divider, and the feedback circuit 2, which calculates the value of the next bit, which enters the information inputs (A and B) of the sixteen bit register DD1/DD2. The register consists of two eight-bit registers that have a common CLK clock signal.
The number of flip-flop circuits, which are covered by feedback circuit, considered as register length and denoted as N. The bits of the cells will be numbered *i=0, 1,..., N-1*, the contents of the cell with the number and denoted as Qi. The new bit value Q_0 is determined by the shift of the bits in the register by the feedback circuit. The feedback circuit function is a linear Boolean function from the values of some case bits of register. The function executes the multiplication of the register bits by the coefficients and the "Exclusive-OR" operation above the multiplication results:

$$A = \overline{\bigoplus_{i=0}^{N-1} c_i \vee Q_i} \,. \tag{1}$$

The number of coefficients coincides with the number of bits in the register, the coefficients c_i take the value $\{0,1\}$, with the coefficient $c_{N-1} = 1$, and the remaining coefficients are selected in a special way to obtain a given sequence length.

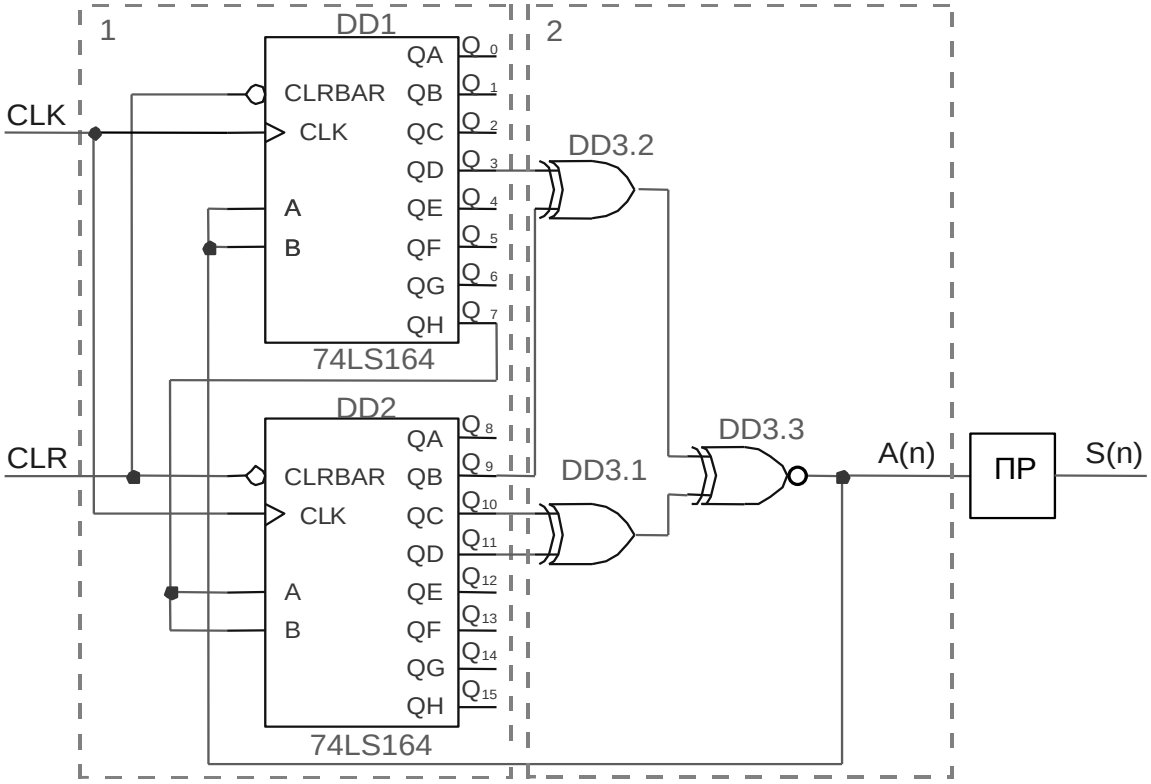

Fig. 3. Generator based on a linear feedback shift register LFSR (N = 12)

During each step, the linear feedback shift register performs the following operations:

- ◊ reads the bit placed in the $N-1$-th flip-flop. This bit is the next bit of the output sequence;
- ◊ the feedback circuit function calculates a new value for a zero flip-flop circuit using the values of other bits by the corresponding formula;
- ◊ the content of each flip-flop moves to the next cell;
- ◊ the value of the bit calculated earlier is written to into zero trigger.

Obviously, the state of "all units" at register output can generate only a single value output feedback circuit, resulting in a sequence, which consists only of the units, so getting to this state should be deleted. A shifting register has 2^N initial states, which are given by the same combination of bits in the register. Consequently, the number of permissible states is $2^N - 1$, and the maximum sequence has a period not exceeding $M = 2^N - 1$.
Consider a signal $S(k)$ that is built based on signal $A(k)$ (signal $S(k)$ takes values -1 or +1, and the signal $A(k)$ is 0 or 1, respectively):

$$S(k) = 2A(k) - 1 \,. \tag{2}$$

The sequence $S(k)$ with a maximum length $M = 2^N - 1$ at the output of the circuit is called the M-sequence [7]. For signal $S(n)$ S (n) discrete autocorrelation function:

$$K_S(d) = \lim_{L\to\infty} \frac{1}{2L} \sum_{n=-L}^{L} S(n)\overline{S(n-d)} = \begin{cases} 1 & for\ d = kM; \\ -1/M & for\ d \neq kM; \end{cases} \quad (3)$$

where k - integer number, M -sequence period. Note that the discrete autocorrelation function can be written as:

$$K_S(d) = \frac{1}{M} \sum_{n=0}^{M-1} S(n)\overline{S(n-d)}. \quad (4)$$

3 Modulator sequence generator and output signal representation

As denoted above, the signal at the output of the modulating sequence generator determined by the current state and N-1 previous states of the output of the LSFR register, and state of divider. Then the signal at the output of the modulating sequence generator is defined as:

$$u(t) = \sum_{i=0}^{P-1} S(n(t)-i)\, q\left(\frac{t}{\Delta T} - i\right), \quad (5)$$

where $n(t)$ - the LSFR register state number at the time t. $q\left(\frac{t}{\Delta T}\right)$ - some filling signal, which is equal to 0 outside the range from 0 to $\Delta T\ N$.

The filling signal must have the following properties:

1) the signal becomes -1, 0 or 1;

2) must be: $q(\lambda)q(\lambda+n) \equiv 0,$ for all λ, if integer $n \neq 0$;

3) for all $\lambda \notin [0,N]$ ($N \leq M$), $q(\lambda) = 0$.

Introduce the function $\psi(\eta)$ equal to 1 at the interval $t \in [0,1/P)$. Then the signal can be represented in the form:

$$q(t/\Delta T) = \sum_{n=0}^{P-1} A_n\, \psi\left(\frac{t}{\Delta T} - \frac{n}{P} - B_n\right), \quad (6)$$

where A_n takes values -1, 0 and 1, B_n -changes from 0 to $N-1$. Then the condition of non-overlapping of the function with its copies shifted by $\Delta T\ k$ is satisfied automatically, and condition 3 is satisfied at $N \leq M$. The signal can also be recorded as a convolution:

$$u(t) = U_0 \int_{-\infty}^{\infty} q(\tau/\Delta T)s(t-\tau)d\tau, \quad (7)$$

where $s(t,L) = \lim_{L\to\infty} \sum_{n=-L}^{L-1} S(n)\delta(t-\Delta Tn)$ - representation of the impulse sequence through a set of Dirac delta functions. Indeed, substituting the impulse sequence into the equation and considering that $q(\lambda) = 0$ if $\lambda \notin [0,N]$, $|q(\lambda)| \leq 1$ and using the filtering property of delta functions, we can rewrite signal as:

$$u(t) = U_0 \sum_{n=-\infty}^{\infty} S(n)q(t/\Delta T - n) = \sum_{i=0}^{P-1} S(n(t)-i)\, q\left(\frac{t}{\Delta T} - i\right). \quad (8)$$

This expression can be written by selecting the terms of each period separately, due to the periodicity of the sequence, the expression can be written as:

$$u(t) = U_0 \sum_{n=0}^{M-1} S(n)\left(\sum_{l=-\infty}^{\infty} q(t/\Delta T - n + M\ l)\right). \quad (9)$$

Representation of the signal u (t) as a Fourier series

Since the sequence $S(n)$ is periodic with the period M, and the interval of nonzero values $q(t/\Delta T)$ is limited, it is easy to prove that the signal $u(t)$ is also periodic with the period $T_u = M\Delta T$, and can be decomposed into a Fourier series by frequencies $\omega_k = \frac{2\pi k}{\Delta T M}$. Using representations $u(t)$ through (9) we obtain:

$$U(\omega_k) = \frac{U_0}{T_u}\sum_{n=0}^{M-1} S(n)\int_0^{T_u}\sum_{l=-\infty}^{\infty} q(t/\Delta T - n + M\,l)\exp(-j\omega_k t)dt\,. \tag{10}$$

The internal sum and $\exp(-j\omega_k t)$ has a period equal $M\ \Delta T$, therefore, the value of the integral will not change while the integration boundaries shifted:

$$U(\omega_k) = \frac{U_0}{T_u}\sum_{n=0}^{M-1} S(n)\int_{n\,\Delta T}^{T_u+n\,\Delta T}\sum_{l=-\infty}^{\infty} q(t/\Delta T - n + M\,l)\exp(-j\omega_k t)dt\,. \tag{11}$$

Now change the order of integration and introduce the replacement of variables $t/\Delta T - n + Ml = \eta$:

$$U(\omega_k) = \frac{U_0\Delta T}{T_u}\sum_{n=0}^{M-1} S(n)\sum_{l=-\infty}^{\infty}\int_{M\,l}^{T_u/\Delta T+M\,l} q(\eta)\exp(-j\omega_k\Delta T(\eta+n-Ml))d\eta\,. \tag{12}$$

Again, taking into account the frequency of the expression $\exp(-j\omega_k\Delta T(\eta+n)$ in the variable n with a period M and the value of $T_u = M\ \Delta T$, we get:

$$U(\omega_k) = \frac{U_0}{M}\sum_{n=0}^{M-1} S(n)\sum_{l=-\infty}^{\infty}\int_{M\,l}^{M(l+1)} q(\eta)\exp(-j\omega_k\Delta T(\eta+n))d\eta\,. \tag{13}$$

From the definition of the $q(\eta)$ it follows that under the sign of the internal sum there will be only one non-zero term, which corresponds to $l = 0$:

$$U(\omega_k) = \frac{U_0}{M}\sum_{n=0}^{M-1} S(n)\int_0^{M} q(\eta)\exp(-j\omega_k\Delta T(\eta+n))d\eta\,, \tag{14}$$

grouping the factors we get:

$$U(\omega_k) = \frac{U_0 Q(\omega_k)}{M}\sum_{n=0}^{M-1} S(n)\exp(-j\omega_k\Delta T n)\,, \tag{15}$$

where:

$$Q(\omega_k) = \int_0^{M} q(\eta)\exp(-j\omega_k\Delta T\eta)d\eta = \int_{-\infty}^{\infty} q(\eta)\exp(-j\omega_k\Delta T\,\eta)d\eta\,, \tag{16}$$

it was taken into account that the function $q(\eta)$ is equal to zero outside the interval $[0..M]$.

Fourier series representation of the signal autocorrelation function

Proceed to consider the continuous autocorrelation function of the signal, which we write for the periodic continuous signal in the following form.

$$K_u(\tau) = \frac{1}{T_u}\int_0^{T_u} u(t)\overline{u(t-\tau)}dt\,. \tag{17}$$

The signal $u(t)$ are limited, so the $K_u(\tau)$ value are also limited. Due to the periodicity $u(t)$, the autocorrelation function is also periodic with period T_u, and can be decomposed into a complex Fourier series at frequencies $\omega_k = \frac{2\pi k}{T_u} = \frac{2\pi k}{M\Delta T}$ with coefficients:

$$K_u(\omega_k) = \frac{1}{T_u}\int_0^{T_u} K_u(\tau)\exp(-j\omega_k\tau)d\tau = \frac{1}{T_u^{\,2}}\int_0^{T_u}\int_0^{T_u} u(t)\overline{u(t-\tau)}\exp(-j\omega_k\tau)d\tau dt\,. \tag{18}$$

Introduce the substitution of variables $\tau = t - \eta$ and take into account the periodicity on η:

$$K_u(\omega_k) = \frac{1}{T_u^2}\int_0^{T_u}\int_0^{T_u} u(t)\overline{u(\eta)}exp(-j\omega_k(t-\eta))d\eta dt\,. \tag{19}$$

Where does follow:

$$K_u(\omega_k) = U(\omega_k)\overline{U(\omega_k)},\ \text{and}\ |U(\omega_k)| = \sqrt{K_u(\omega_k)}\,, \tag{20}$$

therefore

$$K_u(\omega_k) = \frac{U_0^{\,2}Q(\omega_k)\overline{Q(\omega_k)}}{M^2}\sum_{n=0}^{M-1}\sum_{m=0}^{M-1} S(n)\overline{S(m)}exp(-j\omega_k\Delta T(n-m))\,. \tag{21}$$

Let $m = n - p$, since the sequence $S(n-p)$ and function $exp(-j\omega_k\Delta T)$ are periodic with index p with the period M, the summation limits can be rearranged:

$$K_u(\omega_k) = \frac{U_0^{\,2}Q(\omega_k)\overline{Q(\omega_k)}}{M^2}\sum_{p=0}^{M-1}\sum_{n=0}^{M-1} S(n)\overline{S(n-p)}exp(-j\omega_k\Delta T p)\,. \tag{22}$$

Using the value of the discrete autocorrelation function of the signal $S(n)$, we have:

$$K_u(\omega_k) = \frac{U_0^{\,2}Q(\omega_k)\overline{Q(\omega_k)}}{M}\left(1 - \frac{1}{M}\sum_{p=1}^{M-1} exp\left(-j\omega_k\Delta T\ p\right)\right). \tag{23}$$

If $exp\left(-j\omega_k\Delta T\right) \neq 1$, then the internal sum can be calculated as sum of the geometric progression:

$$\sum_{p=1}^{M-1} exp\left(-j\omega_k\Delta T\ p\right) = \frac{exp\left(-j\omega_k\Delta T\right)\left(1 - exp\left(-j\omega_k\Delta T(M-1)\right)\right)}{1 - exp\left(-j\omega_k\Delta T\right)} = -1\,. \tag{24}$$

If $exp\left(-j\omega_k\Delta T\right) = 1$, then the internal sum equal to M. Thus:

$$|U(\omega_k)| = \frac{U_0|Q(\omega_k)|}{M}\times\begin{cases}\sqrt{M+1} & if\ k \neq zM\\ 1 & if\ k = zM\end{cases} = \frac{U_0|Q(\omega_k)|}{(2^N-1)}\times\begin{cases}2^{N/2} & if\ k \neq z\,M;\\ 1 & if\ k = z\,M.\end{cases} \tag{25}$$

It can be concluded that with an increase in the size *N* of the shift register by one bit, the amplitude of the harmonics of the modulated signal decreases by about $\sqrt{2}$ times.

Determination of frequency characteristics of current through the lamp and voltage on the lamp

For simplicity a pseudo-linear model of a discharge lamp are used. In this model ohm resistance of the lamp $R_л$ "almost do not change" for the period T_u, and depend only on the RMS value of the current of the period T_u. Suppose that a circuit with a transfer function $W(\omega)$ is connected between the amplifier output and the lamp. In this case, the harmonics of current $I_л(\omega_k)$ and voltage $U_л(\omega_k)$ of the lamp are determined by the harmonics of the signal $u(t)$:

$$I_л(\omega_k) = \frac{W(\omega_k)U(\omega_k)}{R_л},\ U_л(\omega_k) = W(\omega_k)U(\omega_k)\,. \tag{26}$$

In this case, the amplitudes of the harmonics are defined as:

$$|I(\omega_k)| = \frac{U_0\,|W(\omega_k)||Q(\omega_k)|}{R_л\,M}\times\begin{cases}\sqrt{M+1} & if\ k \neq zM,\\ 1 & if\ k = zM,\end{cases}, |U_л(\omega_k)| = \frac{U_0\,|W(\omega_k)||Q(\omega_k)|}{M}\times\begin{cases}\sqrt{M+1} & if\ k \neq zM\\ 1 & if\ k = zM\end{cases}. \tag{27}$$

Therefore, the signal on the lamp behaves similarly to the signal at the output of the amplifier and with increasing bit rate of the LFSR register by 2 bits, the amplitude of the voltage harmonics decreases by about 2 times.

Determination of power harmonics on a lamp

Since at least the instantaneous value of the power is limited, and the current and voltage after the transients are periodic functions with a period T_u then the power will be periodic, so it can also be formally decomposed into a Fourier series

by frequencies. $\omega_k = \frac{2\pi\, k}{\Delta T\, M}$. Formally, we can write the Fourier series coefficients of lamp power $P(t) = u_л(t)\, i_л(t)$ at $[0, T_u]$.

$$P(\omega_k) = \frac{1}{T_u}\int_0^{T_u} u_л(t)\, i_л(t) \exp(-j\omega_k t)dt\,. \tag{28}$$

Substituting the voltage and current representations in the form of a Fourier series and changing the order of integration/summation, we obtain:

$$P(\omega_k) = \sum_{n=-\infty}^{\infty}\sum_{m=-\infty}^{\infty} U_л(\omega_n)\,\overline{I_л(\omega_m)}\frac{1}{T_u}\int_0^{T_u} \exp\left(jt(\omega_n - \omega_m - \omega_k)\right)dt\,, \tag{29}$$

if $\omega_n - \omega_m - \omega_k = 0$, the internal integral is equal to T_u, otherwise it is 0. So, we can write:

$$P(\omega_k) = \sum_{n=-\infty}^{\infty} U_л(\omega_n)\,\overline{I_л(\omega_n - \omega_k)}\,. \tag{30}$$

Substitute the representation of the voltage and current of the lamp, and changing the order of summation, obtain

$$P(\omega_k) = \frac{U_0^{\,2}}{R_л\, M^2}\sum_{n=-\infty}^{\infty} W(\omega_n)\,\overline{W(\omega_n - \omega_k)}\,Q(\omega_n)\,\overline{Q(\omega_n - \omega_k)}\sum_{m=0}^{M-1}\sum_{l=0}^{M-1} S(m)\,\overline{S(l)}\exp\left(\frac{2\pi j}{M}\left(-nm + nl - kl\right)\right). \tag{31}$$

Let $l = m - p$, and $n = q + k$. Due to the periodicity of the function $\overline{S(m-p)}\exp\left(\frac{2\pi j}{M}(k\, m - q\, p)\right)$ in the variable p with the period M, the summation can be performed in the range from 0 to $M-1$.

$$P(\omega_k) = \frac{U_0^{\,2}}{R_л\, M^2}\sum_{q=-\infty}^{\infty} W(\omega_{q+k})\overline{W(\omega_q)}Q(\omega_{q+k})\overline{Q(\omega_q)}\times\sum_{m=0}^{M-1}\sum_{p=0}^{M-1} S(m)\,\overline{S(m-p)}\exp\left(\frac{2\pi j}{M}(k\, m - q\, p)\right). \tag{32}$$

An attempt to sum the internal sum showed that the values obtained for the same M depend not only on k and p, but also on the initial value in the shift register and on the type of characteristic polynomial, so the search for a "general formula" that would give harmonic values power in a simple closed form is doomed to failure.

The power harmonics estimation

Let us estimate the power components that correspond to the value of k, which is either equal to 0 or a multiple of M (i.e. $k = iM$). In this case: $\exp\left(\frac{2\pi j}{M}(k\, m\, M)\right) = 1$, therefore, the sum (32) will be significantly simplified:

$$P(\omega_{iM}) = U_0^{\,2}\sum_{q=-\infty}^{\infty}\frac{W(\omega_{q+iM})\overline{W(\omega_q)}Q(\omega_{q+iM})\overline{Q(\omega_q)}}{R_л\, M^2}\times\sum_{p=0}^{M-1}\left(\sum_{m=0}^{M-1} S(m)\,\overline{S(m-p)}\right)\exp\left(\frac{2\pi j}{M}(-q\, p)\right). \tag{33}$$

Given the value of the discrete autocorrelation function of the signal $S(m)$, we have:

$$P(\omega_{iM}) = U_0^{\,2}\sum_{q=-\infty}^{\infty}\frac{W(\omega_{q+iM})\overline{W(\omega_q)}Q(\omega_{q+iM})\overline{Q(\omega_q)}}{R_л\, M}\times\sum_{p=0}^{M-1}\exp\left(\frac{2\pi j}{M}(-q\, p)\right)\times\begin{cases} 1 & if\ \ p = zM; \\ -\dfrac{1}{M} & if\ \ p \neq zM; \end{cases} \tag{34}$$

where *z* is an integer, that can be written as

$$P(\omega_{iM}) = U_0^{\,2}\sum_{q=-\infty}^{\infty}\frac{W(\omega_{q+iM})\overline{W(\omega_q)}Q(\omega_{q+iM})\overline{Q(\omega_q)}}{R_л\, M}\times\left(1 - \frac{1}{M}\sum_{p=1}^{M-1}\exp\left(\frac{2\pi j}{M}(-q\, p)\right)\right). \tag{35}$$

We can find the interior sum as the sum of geometric progression and obtained

$$P(\omega_{iM}) = \frac{U_0^{\,2}}{R_л\, M^2}\sum_{q=-\infty}^{\infty} W(\omega_{q+iM})\overline{W(\omega_q)}Q(\omega_{q+iM})\overline{Q(\omega_q)}\times\begin{cases} 1 & if\ \ q = z\,M; \\ M+1 & if\ \ q \neq zM. \end{cases} \tag{36}$$

As can be seen from the formula, as the length of the sequence increases, the value obtained under the sign of the sum increases almost proportionally M, so the power will not go to 0 when increases the length of the shift register. However, unwanted power harmonics can be reduced by selecting a modulating sequence.

With the parameter $i = 0$, the zero harmonic of the power will be determined, which are corresponding to the average power on the lamp:

$$P(0) = \frac{U_0^2 (M+1)}{R_л M^2} \sum_{q=-\infty}^{\infty} W(\omega_q)\overline{W(\omega_q)}Q(\omega_q)\overline{Q(\omega_q)} - \frac{U_0^2}{R_л M} \sum_{r=-\infty}^{\infty} W(\omega_{rM})\overline{W(\omega_{rM})}Q(\omega_{rM})\overline{Q(\omega_{rM})}. \quad (37)$$

Simulation result

The schematic diagram that corresponds to the above structural scheme and generates the signal described, was modeled in the MicroCAP environment (Fig. 5). The clock source X1 generates a signal with a period of 60 μs and a frequency of 16.6 kHz, which is used for general synchronization of the circuit.

The functional generator U1 generates a reset signal that enters the corresponding inputs of the shift registers. The counter D2 (74HC393) divides the frequency received from V1 by 8. The shift registers DD3, DD4, (74HC164) together with the logical elements DD5_1, form a linear feedback shift register. The logic elements DD1_3 and DD1_4 together with the multiplexer DD6 (74HC251) create a sequence modulation generator and form a modulated pseudorandom signal that enters the output amplifier U2. To the output of the amplifier is connected sequentially LC ballast and discharge lamp HL1 (which is modeled by a resistor HL).

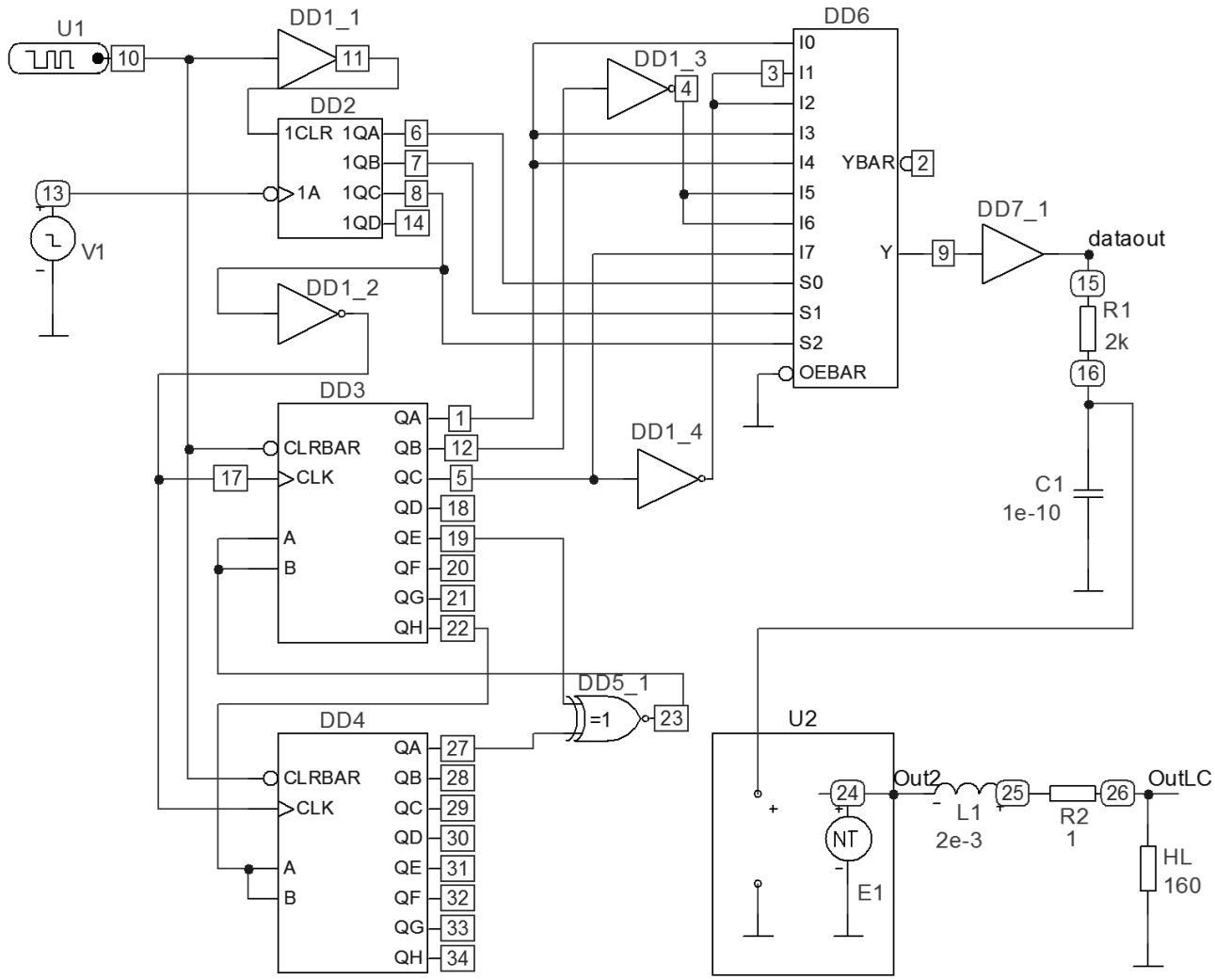

Fig. 5. Model of the offered scheme in MicroCAP environment

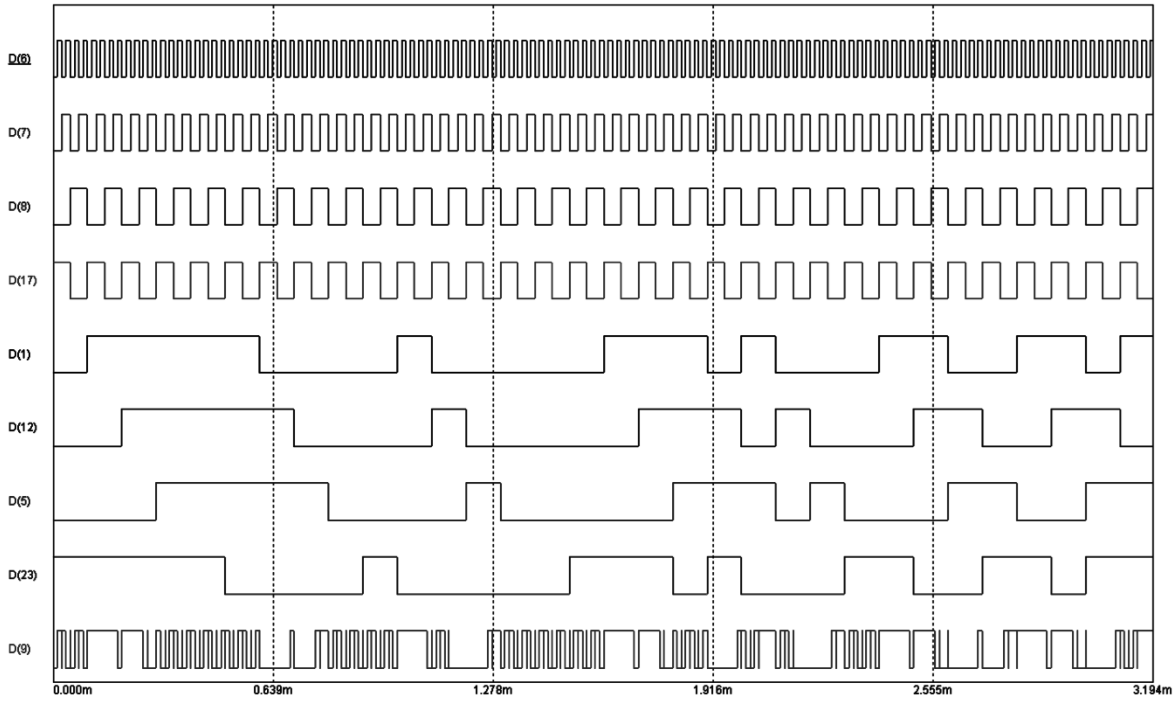

Fig. 6. Timing diagram of the main binary signals in the proposed circuit

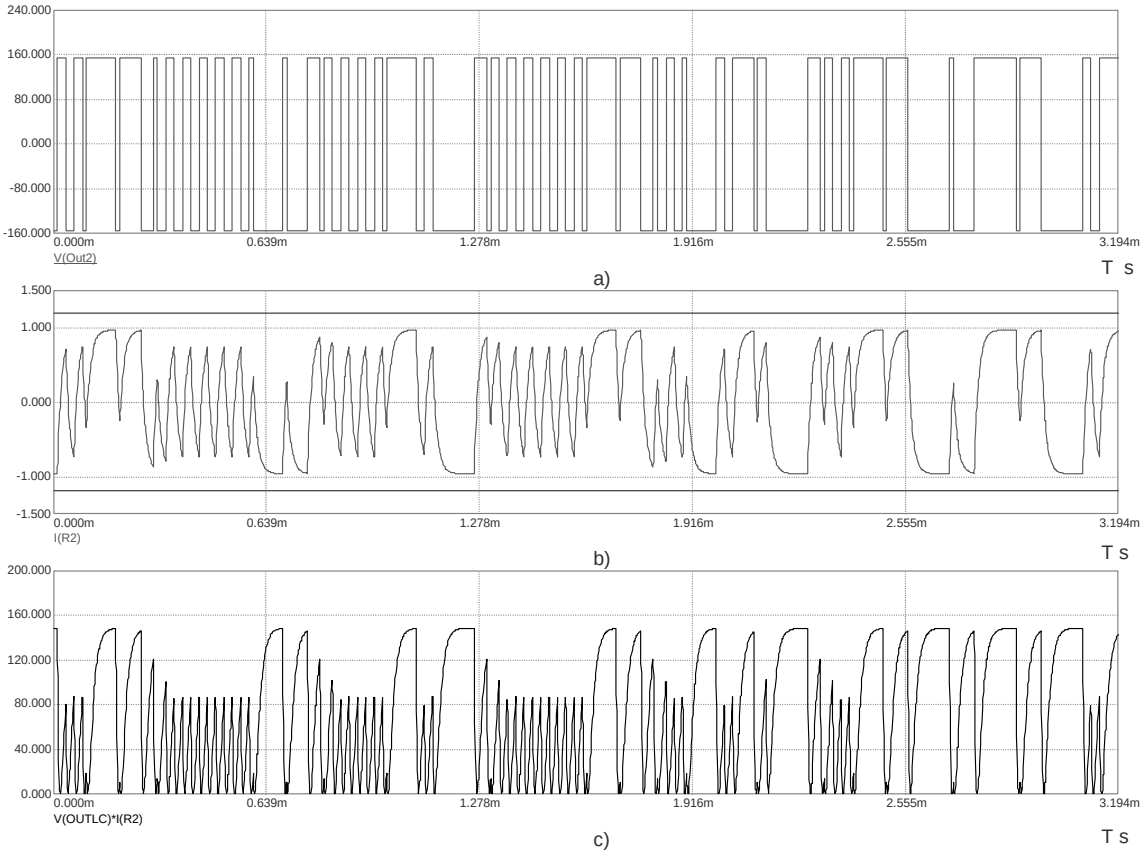

Fig 7. Fragment of the output signal: a) output voltage b) the lamp current c) instant power on the lamp

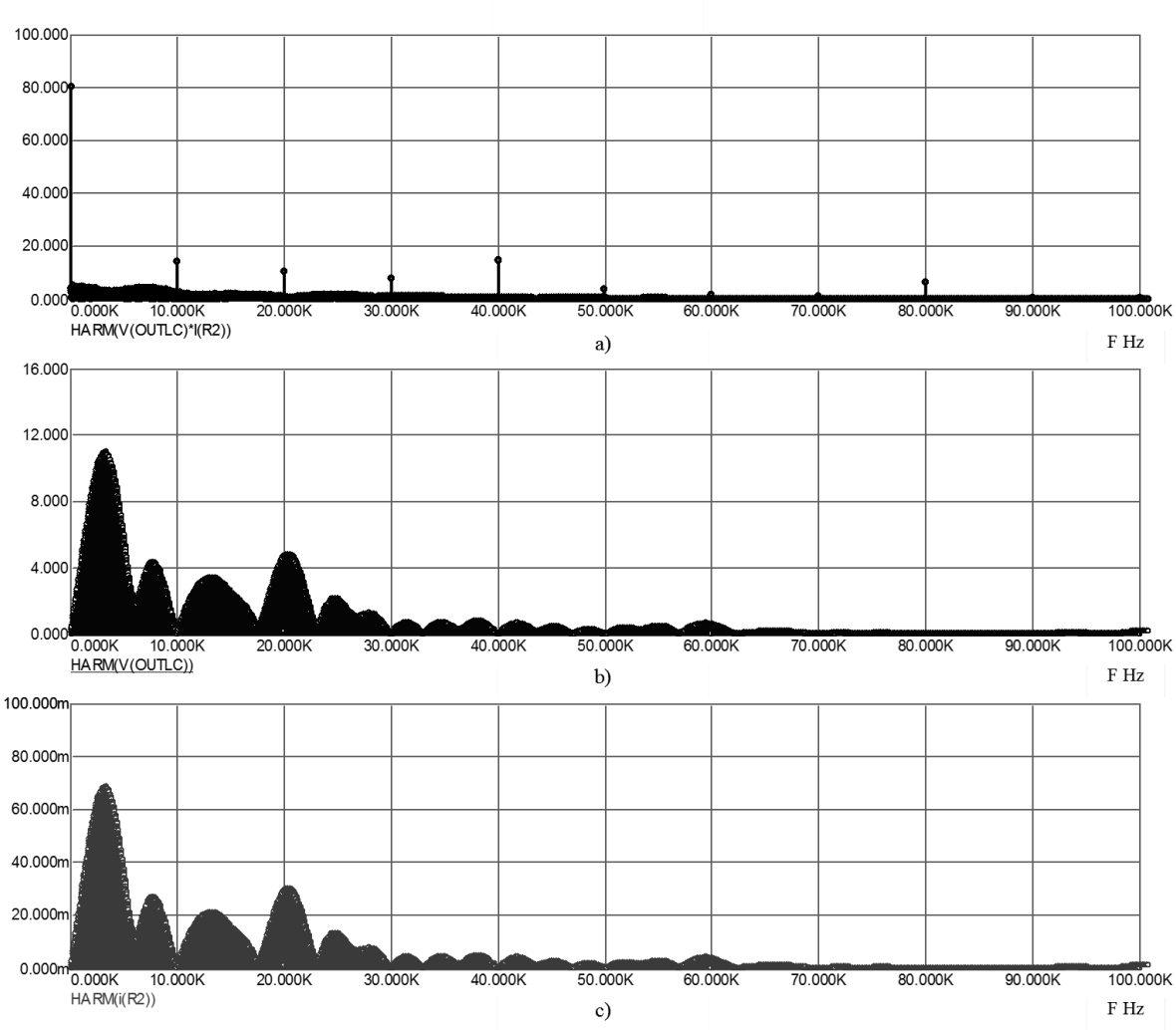

Fig. 8. Amplitude of harmonics of instant power of lamp (a), lamp voltage (b) and lamp current (c)

Results of simulation of the digital part of the scheme are shown in Fig. 6. Its shown the main digital signals of the proposed device: the counter DD2 output signals (D (6), D (7), D (8)), the synchronization signal of the LFSR register D (17), the LFSR register output signal D(1) and the output signal of the digital part of the circuit (D(9)). As follows from the figure, the output signal (D (9)), as it were, consists of low frequency and high frequency components alternating with each other in a pseudo-random order. The low frequency component gives the main switching of the current, while the high frequency component fills in the pauses of the low-frequency signal. The output signal of the analog part of the proposed device is shown in Figure 7.

The harmonics of the voltage across the lamp and the harmonics of the lamp power taken over the cycle of the shift register are shown in Figure 8. As can be seen from Figure 8, although the amplitude of the voltage across the lamp approaches hundreds of volts in the nominal operating mode, and the amplitude of the current to 0.8 A, the amplitude of each voltage harmonic does not exceed 12 V, and the amplitude of the current harmonic does not exceed 70 mA. In addition, while the average power - the power corresponding to the zero frequency is 80 W, each power harmonic does not exceed 17 VA.

Conclusions

The proposed principle of controlling high-pressure discharge lamps allows avoiding the phenomenon of acoustic resonance or reducing its effect. The main point of the scheme is to distribute energy over the largest possible frequency spectrum, which is being successfully implemented. As can be seen from Fig. 8, each harmonic of the output signal does not exceed the amplitude of 12 V in the frequency range from 0 to 100 kHz.

The circuit also reduces power harmonics at hazardous frequencies. Thus, the conditions for the occurrence of acoustic resonance are not created. Therefore, the use of a broadband signal based on the M-sequence automatically prevents acoustic resonance in high pressure discharge lamps.

The circuit implementation of the principle is quite simple and does not require the presence of a microcontroller. But, of course, the scheme for generating the necessary pseudo-random signal can be transformed into an algorithm and executed by some microcontroller.

Since the circuit is in no way tied to the properties of a particular type of lamp, there are no fundamental problems with the applicability of the proposed principle of power supply to discharge lamps of other types, for example, sodium.

References

1. Medvid, V., Beliakova, I., Piscio, V. (2019). Acoustic resonance prevention in high-pressure discharge lamps with a pseudo-random power signal, *Theoretical and applied aspects in radio engineereing, instrument making and computer technogies*, Proceedings of the International Conference. Ternopil, Ukraine. Retrieved from: http://www.chipnews.ru/html.cgi/arhiv_i/99_02/stat-15.htm.

2. Medvid, V., Beliakova, I., Piscio, V. (2018). Analysis of methods and schemes for preventing occurrence of the acoustic resonance phenomenon in high-pressure gas discharge lamps, *Fundamental and applied problems of modern technologies*, Proceedings of the international scientific and technical conference. Ternopil, Ukraine. Retrieved from: http://elartu.tntu.edu.ua/handle/lib/25419.

3. Medvid, V., Beliakova, I., Piscio, V., Savkiv, V., Duchon, F. (2020). Preventing method of acoustic resonance in the high-pressure discharge lamps. *Journal of Electrical Engineering*, *71*(2), 69-77.

4. Epron, S., Aubes, M., Damelincourt J., Cojocaru, A. (1999). Acoustic resonance phenomena in high-pressure discharge lampю. *High Temperature Material Processes, 3*(2-3), 141-155, Retrieved from: 10.1615/hightempmatproc.v3.i2-3.10.

5. Chhun L., Maussion, P., Bhosle, S., Zissis, G. (2011). Characterization of Acoustic Resonance in a High-Pressure Sodium Lamp, *IEEE Transactions on Industry Applications*, *47*(2), 1071-1076, Retrieved from: 10.1109/tia.2010.2102993.

6. Sun Yiyoung Panasonic Electric Works Co Ltd, "Method and driving circuit for HID lamp electronic ballast", USA pat. US6144172A, 2000.

7. Varakin, L. (1985). *Communication systems with noise-like signals*. Moskow: Radio and Communication.

CLASSIFICATION OF ROLLED METAL DEFECTS USING RESIDUAL NEURAL NETWORKS

Ihor Konovalenko[1], Pavlo Maruschak[1], Lyubomyr Mosiy[1], Frantisek Duchon[2], Michal Kelemen[3]

[1] Department of Industrial Automation, Ternopil National Ivan Puluj Technical University, Rus'ka str. 56, 46001 Ternopil, Ukraine; icxxan@gmail.com (I.K.); maruschak.tu.edu@gmail.com (P.M.)
[2] Slovak University of Technology in Bratislava, Ilkovičova 3, SK-812 19, Bratislava; Slovak Republic, E-mail: frantisek.duchon@stuba.sk
[3] Technical University of Kosice, Letna 9, 04200, Kosice, Slovak Republic, E-mail: michal.kelemen@tuke.sk

Abstract: The authors investigated deep residual neural networks, which are used to detect and classify defects found on the rolled metal surface. Based on the neural network with ResNet152 architecture, a classifier for recognizing defects of three classes was built. The proposed technique allows recognizing and classifying surface damage with high accuracy in real-time based on its image. The average binary accuracy of the classification made based on the test data is 97.3%. Neuron activation fields were studied in the convolutional layers of the model. The results obtained show that areas, which correspond to those with damage in the image, are activated. False-positive and false-negative cases of classifier application are investigated. Errors were found to occur most frequently in ambiguous situations when surface artefacts of different types are similar.

Keywords: metallurgy; steel sheet; surface defects; visual inspection technology; classification; neural network.

1. Introduction

The condition of its surface layer, to a large extent, evaluates rolled metal quality. Tasks related to eliminating damage on the surface layer are most relevant for improving the quality of finished products in metallurgy (Luo, 2016; Zhou, 201; Dhua, 2019). At the same time, automated control systems are most promising, as they ensure maximum sensitivity and resolution, high performance, accuracy and ease of realisation. Neural network technologies are used to develop modern algorithms for high accuracy defects (Chen, 2020; Lee, 2019; Fang, 2020). During training, they make it possible to automatically generate datasets that describe defects of different classes and then detect them in new images effectively.

To date, regulations that provide for an unambiguous classification of rolled metal surface defects (GOST 21014-88) are limited in number. Approaches to evaluating rolled metal based on such standardized features allow for an averaged analysis of defects only. Therefore, as evidenced by Tao (2018) and Kostenetskiy (2019), finding new approaches to the analysis of surface defects is relevant.

Our research aims to develop a neural network classifier, which can detect defects of different types with high accuracy in near real-time and classify them according to a given set of defect types.

2. Training datasets and their peculiarities

The sample for training the neural network classifier was formed using photo images of rolled metal steel surfaces with various defects. Most images were taken from a dataset provided in 2019 by Severstal, a Russian public company that participated in the international Kaggle competition. In total, we selected 14830 images of steel surfaces, both undamaged and with defects of three types. All images were reviewed and marked by experts using a specially developed application – Image Labeling Tool. The dataset formed this way was divided into three parts: the training part, which contained 10482 images, the validation part (2790 images), and the test part (1558 images). Images for all three parts were selected so that the ratio of classes was the same. Training and validation parts were used during training, and the test part was used during testing the model on unknown images.

The images below show the defects of the three classes. Each of them primarily differs in occurrence (Konovalenko, 2020), which causes morphological and, consequently, visual differences. Examples of images of surface fragments with defects of different classes are shown in Fig. 1, and their description is presented in Table 1.

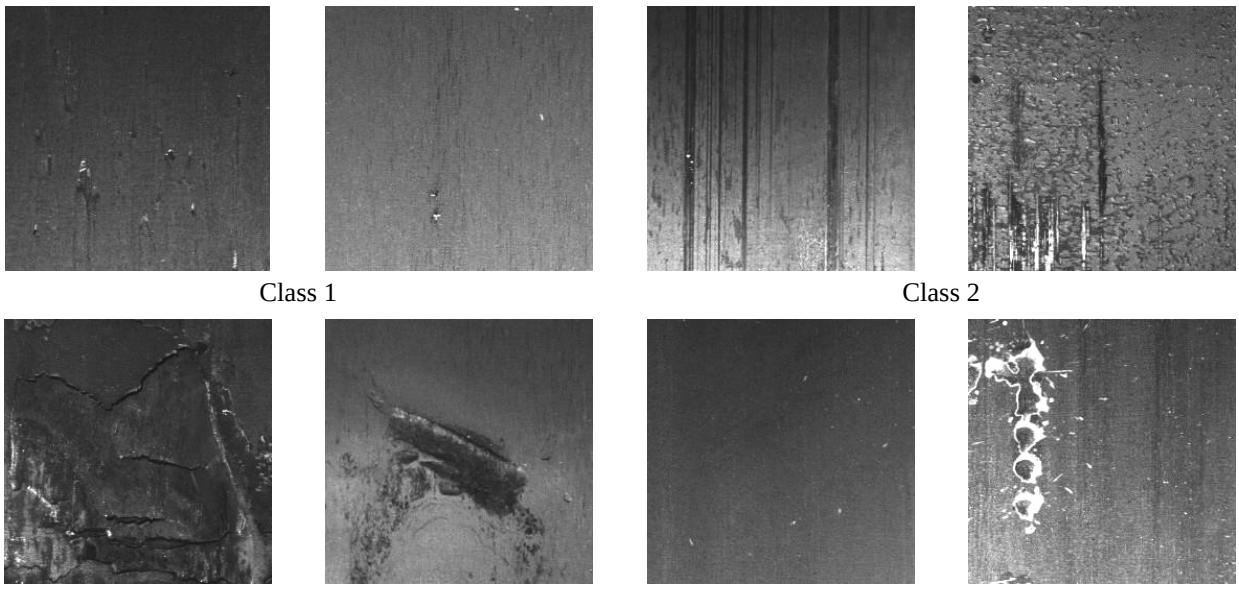

Fig. 1. Classes of surface defects

Table 1. Classes of defects found on rolled metal

Defect class	Description
I	Small round defects, in particular, rolled-in scales. Other damage of this type can be formed by pressing a solid body into the surface. Most often, such defects have no pronounced orientation. Sometimes they appear in groups. Areas of damage of the first class are usually the smallest ones compared to defects of other classes.
II	Lines, scratches and abrasions. They can be both single and multiple. Scratches are usually oriented in the direction of rolling. Defects of this type are usually caused by friction of the metallurgical equipment against the sheet surface. Defects of this class are most numerous, have different shapes, directions and staining. Scratches of the second class can be very small lines (which sometimes make them look like defects of the first class) and large ones passing through the entire surface of the image.
III	Rolling films, which have the form of surface "tears-out" with uneven edges. They usually have no orientation, can be of any shape and occupy a significant area on the surface.

It is noteworthy that undamaged surfaces are also characterized by high inhomogeneity. They are distinguished by a significant variability of morphological and visual features. Such surfaces are often texturally homogeneous but may contain glare; sometimes, they are strongly illuminated or darkened in places. Undamaged areas often contain rough formations with different structures or various coloured artefacts of different shapes. Industrial images may contain the specimen edge and background behind them, which is not informative in defectometry. Some undamaged surfaces contain corrugations.

The topology, types and shape of defects of different classes are very diverse, which causes difficulty in classifying them even at the expert level. The similarity between small defects of the first and second classes is most common. Small defects contain fewer morphological features; therefore, it is more difficult to form sets of characteristics that can be reliably distinguished. They often occur in adjacent parts of the image or even form a single structure of the defect. The elements of specific surface images of defect-free surfaces are similar to damage of a particular class, further complicating the situation. In addition, the damage is often located on a structurally inhomogeneous surface, which also makes it challenging to identify it. Furthermore, the second- and third-class defects can end up in a smooth gradient, which complicates their identification in border areas. To bring the working conditions of the classifier closer to the industrial ones, all such cases are sufficiently presented in the training sample.

The frequency of defects of different classes is different in the production environment; therefore, various defects are presented unevenly in the training dataset. In total, 1919 images with first-class defects, 6667 images with second class defects, and 6238 images with third-class defects were used for training. However, many images contain defects of several classes at a time. Most images contain defect-free surfaces.

3. Methodology for training neural network classifier

Based on the previously obtained results (Konovalenko, 2020), the neural network model ResNet152 presented in 2015 by He *et al.* was chosen as the basis for the classifier. Since 2015, networks based on ResNet architecture have shown excellent results in various areas related to image processing. The main feature of ResNet models is shortcut connections that transmit the input directly to the end of the residual block. This makes it possible to significantly reduce the vanishing gradient problem in deeper layers of the network and increase the model depth.

The input layer of the classifier receives an image of 256 × 256 pixels. Blocks of ResNet model layers follow this. However, the last ResNet model layer was replaced by a fully connected layer of 3 neurons. Each of the neurons is responsible for a defect of its class. Sigmoid activation function was used for output neurons. A defect of a specific class present on the input image causes the appearance of 1 on the corresponding output neuron (or 0 – in the opposite case). The model used is a multilabel classifier, which makes it possible to identify defects of several classes on the same image.

The augmentation technique was used to diversify the training sample. This allowed us to increase the training sample significantly and thus contribute to developing the best generalizing properties of the model (Luo, 2016). Previous research aimed at solving our problem also showed that augmentation allows attaining better performance of the model. Therefore, in addition to standard augmentation methods (horizontal and vertical flip, rotation at an angle multiple of 90º). In this case, sections measuring 256 × 256 pixels were selected randomly on the input images during training (according to input layer shape). From these sections, the tensor was formed, which was fed to the neural network input. This made it possible to significantly diversify training data (especially insufficient ones) and provide conditions under which training batches will never be repeated in practice.

Another feature of training data is a significant imbalance of images, especially "defect – defectless" ones. This is primarily due to the varying frequency of defects of different types in the production environment. Firstly, most images do not damage (this corresponds to an actual situation when production shortages are not very common). Secondly, many defects occupy a small area of the image, so frames can also get into undamaged areas when using the random crop technique. In addition, more significant defects are more likely to fall into random frames.

While training, the majority class (class 2 in our case) quickly becomes well-classified since we have much more data. Therefore, the focal loss function proposed by Lin *et al.* in 2017 was used to solve unbalanced classes. Thus, to ensure that we also achieve high accuracy for minority classes, we use the focal loss function to give these minority classes examples of more relative weight during training. Focal loss applies a modulating term to the cross-entropy loss to focus training on hard detective examples. It down-weights the well-classified examples and puts more training emphasis on the data that is hard to classify.

ResNet classifiers were realised in Python 3.8 language using the Keras and TensorFlow libraries. We used a workstation based on Intel Core and 7-2600 CPU for training and testing and two NVIDIA GeForce GTX 1060 GPUs with 6 GiB of video memory.

4. Best models result

About 30 neural network models based on ResNet36, ResNet50 and ResNet152 architectures were developed and trained. The training was performed at different hyperparameters of the model. Each of the trained models was investigated on test data. A model with ResNet152 architecture achieved the best result. It has a greater depth, which allows forming a complete set of features for the defects of each class.

The graph, which illustrates the model's training process, is shown in Fig. 2, a, b. Over several epochs, the model attains its maximum level of generalization, and validation loss begins increasing gradually, while training loss keeps decreasing. During the training of both models, validation binary accuracy varied from approximately 0.95 to 0.98.

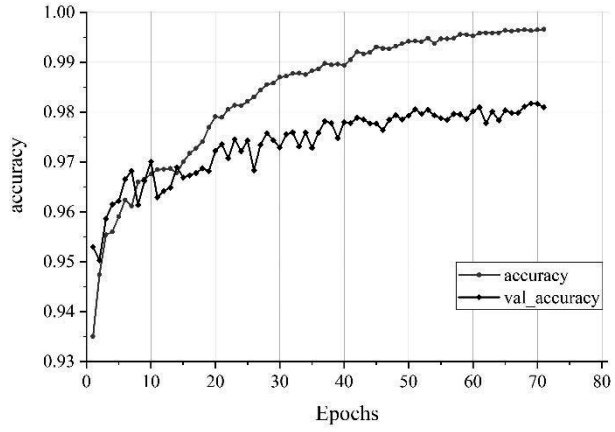

a

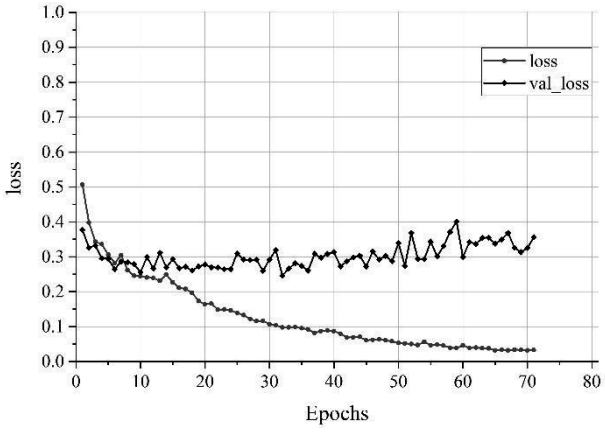

b

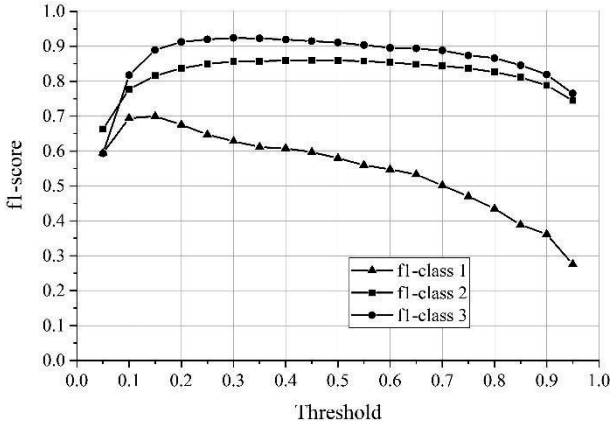

c

Fig. 2. Variation of binary accuracy metric (a) and focal loss function (b) during training; graph *f1-score* (c) versus threshold value on the source layer for different classes of defects

However, the accuracy metric does not fully reflect the quality of the model. Since the distribution of images by class is unbalanced, and defect-free images dominate the training sample, the accuracy metric primarily shows the success of detecting defect-free images. Therefore, other metrics were considered to study the model quality, including the recall, precision, and f1-score metrics.

The recall metric ($Recall = TP/(TP + FN)$) shows the proportion of images with defects of a specific class, which the model recognizes as defects of this class. The highest recall value was attained for defects of third class - 0.908. This means that the model detects almost 91% of the damage of this class. Defects of the second class are recognized a little worse (the recall value is 0.824). Minor defects of the first class are the most difficult to classify - the recall value is equal to 0.627. Experiments have shown that defect-free specimens are the easiest to recognize - more than 97% are detected correctly.

The precision metric ($Precision = TP/(TP + FP)$) shows what proportion of images recognised as defects of a specific class contain such defects. The highest values of this metric were obtained for defects of the third class. High values were also obtained for defects of the second class. The worst accuracy of detection was observed in the case of defects of the first class.

The sigmoid activation function is used in the initial layer of classifiers. Therefore, at the output of each neuron, the value is in the range of $[0\ldots 1]$. Whether a specific pixel of an image belongs to a specific class of damage is made if the value of the corresponding output neuron exceeds a certain threshold. The value of this threshold affects the model quality metrics for this class of defects. To select the optimal threshold value for each class, the f1-score metric was calculated.

The integral f1-score metric ($f1 = 2 \cdot (Precision \cdot Recall)/(Precision + Recall)$) is a harmonic mean of the precision and recall metrics and generally characterizes the model's ability to recognize defects of a specific class. Graphs showing f1-score for three classes of defects are presented in Fig. 2,c. Small defects of the first class are assumed to be the most difficult to identify: in addition to being located below other classes, the maximum of the f1 curve is the fastest to decrease after the maximum. This is consistent with the above-mentioned morphological features of defects of the first class: they are small and may resemble either defects of other classes or the surface formations of defect-free zones, which leads to difficulties in identifying them. Most stable is identifying defects of the second class: a significant area of the corresponding curves is almost horizontal. This indicates that the model is "confident" when recognizing defects of the second-class in a wide range of thresholds. The curve of the f1 metric attains the highest maximum for defects of the third class. Therefore, the set of features of this class must be the easiest to be detected by the model and most different from the features of other classes.

Based on the data obtained, the optimal threshold values were selected for each class.

The model quality metrics determined based on the test data are given in Tables 2 and 3. Table 2 contains the values of binary accuracy (acc), precision (prc), recall (rcl) and f1-score for defects of the classes considered. Table 3 contains the same metrics for defect-free images.

Table 2. Quality metrics of classifiers determined based on test data for defects of various kinds

Class 1				Class 2				Class 3			
acc	prc	rcl	f1	acc	prc	rcl	f1	acc	prc	rcl	f1
0.976	0.792	0.627	0.700	0.945	0.897	0.824	0.859	0.993	0.939	0.908	0.923

Table 3. Quality metrics of classifiers determined based on test data for defect-free images

Defectless			
acc	prc	rcl	f1
0.938	0.944	0.973	0.958

5. Model feature maps

To better understand the operation of the model, we investigated feature maps formed by convolutional layers of the developed classifier. As François Chollet (2017) showed, the activation pattern of intermediate neurons reflects how successfully the neural network converts the input signal. It also shows how the input image is decomposed by intermediate filters of different layers formed during training. The initial layers of the model contain the whole image but with an emphasis on specific areas. At this stage, the model retains most of the information from the input image but already focuses on its most interesting features in terms of classification. The deeper we move through the convoluted layers of the model, the more abstract the picture of neuronal activation becomes. Moreover, it acquires more and more image elements inherent in a particular class of defects.

Most interesting and illustrative are feature maps from the last convolutional layer. From it, the data are fed to the last generalizing full-connected layer, which in the long run forms the decision about the presence of a particular type of damage and activates the corresponding output neuron.

This study showed that defects of different topologies are quite fully represented on the feature maps. This indicates that the model attains good generalizing properties and makes it possible to build tools for semantic segmentation, which allow locating damage and calculating its geometric characteristics (size, area, shape, etc.) in addition to assigning a class label to the image.

6. Problems of defect detection

From the perspective of the practical application of the model, it is crucial to understand what difficulties arise in its application and how it can give the wrong result. To investigate this, a test data set was prepared based on the test images. From each test image, ten random plots measuring 256 × 256 pixels (according to the input layer size of the model) were selected at random. To ensure an unambiguous identification of the results of the model operation, only those specimens were selected from the prepared test data set, which contain defects of only one class (such specimens make up the majority). The developed classifier was applied to the prepared array of image areas, and a confusion matrix was formed based on the results obtained (Fig. 3).

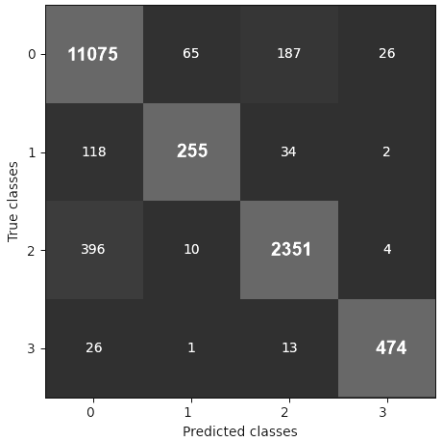

Fig. 3. Confusion matrix for images with defects of different classes

The results show that most misclassification problems arise in case of defects of the first class: a significant part of them (~29% of their total number) is recognized as a defect-free surface. Examples of such images are given in Fig. 4a. Most cases involve very small surface artefacts that merge with the surrounding background and are visible only when the image is magnified or similar to a defect-free surface's textural features. Some (~8%) defects of the first class are recognized as the second class, and very few - as the third class. This is because defects of the first and third classes differ primarily in area. Figure 4b presents examples of the first-class recognized as the second class. The vast majority of such cases involve defects similar to small scratches or abrasions of the second-class surface.

Thus, we can conclude that a relatively low classification result for defects of the first class is mainly due to their similarity with the morphological formations of defect-free surfaces and minor defects of the second class. Particularly noteworthy is that differences between these groups of surface formations are classified ambiguously even at the expert level.

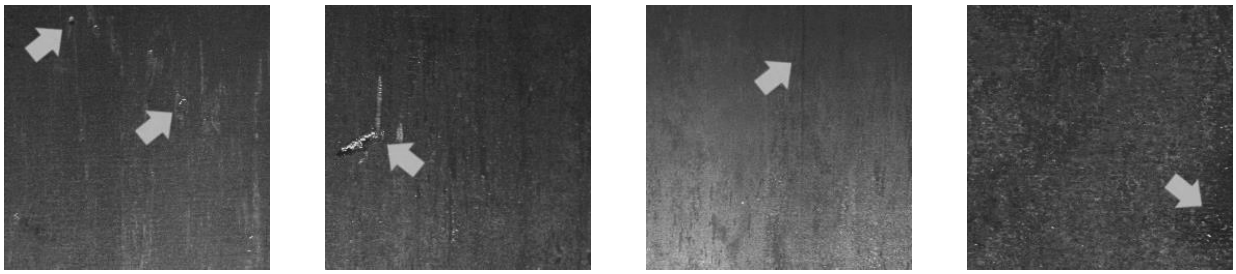

a b c d

Fig. 4. Examples of incorrect recognition of defects

The model perceives a particular part of defects of the second class (~14%) as a defect-free surface. At the same time, a minimal number (less than half a per cent) of these defects are mistakenly recognized as defects of other classes. Figure 4c shows examples of images with defects of the second class recognized as defect-free surfaces. Most of such cases involve mild defects that merge with light glare or are shaded. In some cases, we deal with marginal fragments, where damage is weakly expressed. Cases where damage is clearly visible, but its morphology is atypical for defects of the second class, are the smallest in number.

The classifier is the best at identifying defects of the third class. Of these, ~5% are perceived as defect-free surfaces by the model, and ~3% - as defects of another (primarily second) class. Figure 4d shows examples of defects of the third class recognized as defect-free surfaces. A vast majority of such cases involve marginal fragments of defects, where their morphological and visual features are weakly expressed. It is much less common in cases where a defect is well pronounced, but its area is so large that it resembles the background.

Defect-free surfaces are recognized correctly in approximately 98% of cases. Most often, the model perceives artefacts of such surfaces as defects of the second class (~1.6% of cases). As evidenced by the analysis of results, in such cases, the image contains artefacts that resemble the second class's defects. Experts classify such morphological formations on the image ambiguously (without investigating an actual surface).

Conclusions

A classifier for recognizing defects of various classes that occur on rolled metal surfaces has been developed and studied on a test dataset. The classifier is based on a deep convolutional neural network with ResNet152 architecture. The proposed technique allows classifying images with high accuracy in near real-time while recognizing three classes of defects. The average binary accuracy of the classification made based on test data is 97.3% for all images (including those containing defect-free surfaces). The model was found to be the best at detecting defects of the third class and undamaged surfaces.

The study of false negative and false positive classification cases showed that errors most often occur in the case of significant visual similarity of surface artefacts of different types or very small defects. However, even the expert assessment of images is ambiguous in such cases, and different experts may come to different conclusions. Such shortcomings can be eliminated by training the model on images with higher resolution.

The study of neuron activation fields in the convolutional layers of the model has revealed that feature maps reflect the location, size and shape of the objects of interest very well. This makes it possible to develop a model for semantic segmentation of defective images based on the architecture proposed. In addition to detecting and classifying defects, this model can localize them in the image, thus allowing the calculation of their area and other spatial characteristics.

References

1. Chen, H., Hu, Q., Zhai, B. et al. (2020). A robust weakly supervised learning of deep Conv-Nets for surface defect inspection. *Neural Comput & Applic, 32*, 11229–11244. doi:10.1007/s00521-020-04819-5

2. Dhua, S.K. (2019). Metallurgical analyses of surface defects in cold-rolled steel sheets. *J Fail. Anal. and Preven, 19*, 1023–1033. doi:10.1007/s11668-019-00690-2

3. Fang, X., Luo, Q., Zhou, B., Li, C., Tian, L. (2020). Research progress of automated visual surface defect detection for industrial metal planar materials. *Sensors , 20*, 5136, doi:10.3390/s20185136

4. François Chollet. (2017). *Deep Learning with Python*. Manning Publications.

5. GOST 21014-88. (1989). Rolled Products of Ferrous Metals. Surface Defects. Terms and Definitions; Izd. Stand.: Moscow, USSR; p. 61. (In Russian)

6. He, K., Zhang, X., Ren, S., Sun, J. (2015). Deep Residual Learning for Image Recognition. arXiv, arXiv:1512.03385v1.

7. Kaggle Severstal: Steel Defect Detection. Can You Detect and Classify Defects in Steel? (2019). *Kaggle*. Retrieved from https://www.kaggle.com/c/severstal-steel-defect-detection.

8. Konovalenko, I., Maruschak, P., Brezinová, J., Viňáš, J., Brezina, J. (2020). Steel Surface Defect Classification Using Deep Residual Neural Network. *Metals*, *10*, 846.

9. Kostenetskiy, P., Alkapov, R., Vetoshkin, N., Chulkevich, R., Napolskikh, I., Poponin, O. (2019). Real-time system for automatic cold strip surface defect detection. *FME Trans. 47*, 765–774. doi:10.5937/fmet1904765K.

10. Lee, S.Y., Tama, B.A., Moon, S.J., Lee, S. (2019). Steel Surface Defect Diagnostics Using Deep Convolutional Neural Network and Class Activation Map. *Appl. Sci. 9*, 5449, doi:10.3390/app9245449.

11. Lin, T.-Y., Goyal, P., Girshick, R., He, K., Dollár, P. (2017). Focal Loss for Dense Object Detection. arXiv, arXiv:1708.02002v2.

12. Luo, Q., He, Y. (2016). A cost-effective and automatic surface defect inspection system for hot-rolled flat steel, *Robotics and Computer-Integrated Manufacturing*, *38*, 16-30.

13. Takahashi, R., Matsubara, T., Uehara, K. (2018). RICAP: Random Image Cropping and Patching Data Augmentation for Deep CNNs. *Conference on Machine Learning*, Proceedings of The 10th Asian Conference.

14. Tao, X., Zhang, D., Ma, W., Liu, X., Xu, D. (2018). Automatic metallic surface defect detection and recognition with convolutional neural networks. *Appl. Sci. 8*, 1575, doi:10.3390/app8091575.

15. Zhou, S., Chen, Y., Zhang, D., Xie, J., Zhou, Y. (2017). Classification of surface defects on steel sheet using convolutional neural networks. *Mater Technology*, *51*(1):123.

COMPARATIVE ANALYSIS OF COMPUTER SYSTEMS FOR CASTING PROCESSES SIMULATION

Larysa Danylchenko

Ternopil National Ivan Puluj Technical University, Rus'ka str. 56, 46001, Ternopil, Ukraine; snt.tu.edu@gmail.com

Abstract: Casting processes simulation is one of the advanced research tendencies of foundry production. This article analyzes the current state and prospects for the development of innovative computer technologies in the national and world foundry. The main directions of the strategy for the further development of the foundry are formulated. An overview of the most well-known systems for computer modeling of foundry processes is presented, which allow simulating and controlling the quality of castings to maximize productivity and minimize defects. However, the choice of software for casting processes simulation is of decisive importance, which requires reliable information about the capabilities of computer programs and the principles of their operation. The purpose of the study is to carry out a comparative analysis of the most well-known systems for casting processes simulation and the possibility of their use for various casting methods. The software tools were compared by purpose, functionality, the number of simulated technological processes, the numerical method used for solving the problems of differential equations in the shaping of the casting, as well as the degree of completeness of the factors taken into account in the simulation. The research results can serve as recommended guidelines for specialists and managers of foundries on the choice of the necessary software, taking into account their requirements and the special aspects of the casting processes.

Keywords: *casting process, computer modeling, casting simulation, software*

1. Introduction.

Foundry is the main base of the mechanical engineering and metallurgical complex, and its development depends on the pace of development of these industries as a whole. However, manufacturing cast parts with improved physical-chemical characteristics is a very important production task, which scientists and industrialists are aiming to solve.

Metallurgy and foundry are science-intensive, complex and interconnected industries. Metallurgists and foundry workers, in addition to the tasks of direct control of technological processes, in their activities are often faced with the need to perform rather complex technological and engineering-economical evaluations.

From the analysis of the current circumstance and prospects for the development of innovative technologies, it follows that to modernize the foundry, first of all, it is necessary to significantly increase the volume of investments in science: researches and development; design of new machines, equipment and technologies; development efforts, the acquisition of patents or licenses, software products; education and training [9]. A whole range of technological solutions is needed to most effectively implement the priority areas.

Information technologies are such innovative technologies that can make the greatest contribution to accelerating economic growth and increasing the competitiveness of products. They are realized through computer design, an electronic archive, which contains all the information and from where it goes to the technologists, designers, and from them - to the design objects. At the same time, a large number of shortcomings in the organization of national production are revealed and there is an opportunity for their elimination [8].

At present, one of the main ideas for the development of industry should be neo-industrialization, which is a process of large-scale modernization based on waste-free technologies of automated, computerized, and robotic production [1].

The listed factors make it possible to define the main reference direction of the strategy for the further development of the foundry. These areas covered almost the entire range of problems of modern industrial production, namely:

- the maintenance and development directions of the world and national foundry production;
- modern technologies, materials, and equipment;
- diagnostics, certification and quality management of castings;
- computer technologies in the foundry.

As seen from the above, one of the main strategic tendencies of the foundry at the present stage is the development of simulation and computer technologies.

Mathematical simulation of casting processes is the most effective, reliable, and widespread method of manufacturing casting technology development in the world, which allows reducing the costs of both process engineering and production of castings.

Computer analysis at the stage of virtual design of the casting technology (before the manufacture of castings) allows: to minimize possible miscalculations and errors that inevitably arise in the development process; to reduce financial and time costs; to increase efficiency, competitiveness, quality, and reliability of products being developed. There is a saving of materials, energy carriers, operating time, equipment is saved, and in return, a lot of unique

information about the technological process is obtained. Only computer simulation of the technology allows to look inside the product and see the nature of the processes taking place in it, and understand the causes of defects.

The introduction of computer technologies also makes it possible to increase the efficiency of operations for creating and processing information - there is a real transition from paper to electronic document flow. At the same time, costs, the labor intensity of designing and mastering the production of new complex products are reduced. For example, the costs of preparing technical documentation are reduced by 30...40% and the lead time of the release of new complex products is reduced by more than 35% [1].

The development of simulation and computer technologies in foundry production involves:

- automated design of foundry technology;
- modeling the cast molding - a synthesis system for all elements of the process;
- design of foundry technology and tooling in a CAD system with its subsequent manufacture on CNC machines;
- development of a rapid prototyping system;
- computer control of technological equipment.

Computer programs for simulation the casting processes are designed to solve the following tasks:

- development of complex or essential casting technologies;
- determination of the parameters that are most important in influencing the quality and yield of suitable products;
- finding the causes of defects in already used technologies;
- determining the technology's resistance to changes in external parameters;
- searching for new technological solutions for obtaining complex castings.

The ability to correctly solve these problems acquires an important, and often decisive, competitive advantage. One of the reasons for this is that the use of computer modeling involves a high culture of design, modeling, and manufacturing.

Currently, dozens of different software products are used in the foundry production aimed at solving the problems facing the casting technologists. They differ in their characteristics, use various computational methods, mathematical algorithms and physical models, which, to varying degrees, satisfy the needs of a particular consumer. Only a comparison of the results of computer simulation with the results of industrial and experimental researches allows assessing the objectivity and adequacy of the software product used.

2. Review of the most well-known systems for computer simulation of foundry processes

Today in the world there are a large number of programs for computer simulation of foundry processes. In world practice, the programs presented in Table 1 have received the main distribution.

Currently, in the USA, England, and Europe, the most common are two modeling systems: ProCast and MagmaSoft. In addition, a certain market segment in Europe is occupied by WinCast, SolidCast, and Nova-Solid/Flow systems. In Eastern Europe and the countries of the former CIS, the most popular software systems are Polygon and LVMFlow.

Modern programs for casting processes simulation are based on physical theories of thermal, diffusion, hydrodynamic, and deformation phenomena. They can adequately simulate many processes occurring during the filling of a mold with liquid metal, crystallization of a multi-component alloy, and further cooling of the casting. Possibilities of the programs include hydrodynamic calculation of filling molds, analysis of temperature fields during crystallization and formation of shrinkage defects, calculation of stresses and residual deformations in castings, optimization of gating systems.

Table 1 - Casting simulation software [5]

Country-Vendor	Casting Simulation Software	Country-Vendor	Casting Simulation Software
Australia	CastFlow Castherm	Japan	JSCAST
		Korea	AnyCasting
China	InteCast	Russia	Polygon LVMFlow FlowVision
Finland	CastCAE		
France	ProCast QuikCast PAM-Cast CalcoSo	Spain	Vulcan
		Sweden	Nova-Solid/Flow
Germany	MagmaSoft WinCast	USA	PowerCast SolidCast CAPCast Flow3DCast RAPIDCast
Great Britain	MavisFlow		
India	AutoCast		

All programs mainly differ in purpose (Table 2), functionality, the number of simulated technological operations, the degree of completeness of the factors taken into account in the simulation, the equipment used. The main problems when choosing a specific program for modeling casting technological processes are the lack of reliable information about the capabilities of the program itself, the principles of working with it, as well as the absence of highly qualified specialists. A significant factor for national enterprises when choosing a program for modeling foundry processes is its cost.

Table 2 – Casting processes simulated by selected software

Casting process	AutoCast	CAPCast	CastCAE	Flow3D Cast	Magma Soft	Nova-Solid/Flow	ProCast	SolidCast	Polygon
Sand casting	+	+	+	—	+	+	+	+	+
High pressure die casting	—	+	+	+	+	+	+	—	+
Low pressure die casting	—	+	+	—	+	+	+	+	+
Continuous casting	—	—	—	+	—	—	+	—	—
Gravity die casting	+	—	+	+	+	+	+	+	+
Investment casting	+	+	+	—	+	+	+	+	+
Lost foam casting	—	—	—	+	+	+	+	—	—
Centrifugal casting	—	—	—	+	+	+	+	—	+
Tilt pouring	—	—	—	+	+	+	+	—	+
Squeeze casting	—	+	—	+	—	—	+	—	—

The main distinguishing feature of software products is the used numerical method for solving problems of differential equations in simulation the cast molding (Table 3).

Table 3 – Numerical methods in selected casting simulation software

Solution method	AutoCast	CAPCast	CastCAE	Flow3D Cast	Magma Soft	Nova-Solid/Flow	ProCast	SolidCast	Polygon
Finite Element Method	—	—	—	—	—	—	+	—	+
Finite Difference Method	—	—	—	+	+	—	—	+	—
Finite Volume Method	—	—	+	+	—	—	—	—	—
Vector Finite Element Method	+	—	—	—	—	—	—	—	—

Finite Difference Method (FDM), used in programs such as Magmasoft, SolidCast, CastCAE, JSCAST, AnyCasting and others, allows you to quickly obtain the stress pattern of shrinkage defects in the designed casting and correct the casting technology in time [7]. It is based on differential equations, in which the differential operators are replaced by finite-difference relations of varying degrees of accuracy [6]. As a rule, they are built on orthogonal meshes, which makes it possible to factorize operators and reduce the solution of a multidimensional problem to a sequence of one-dimensional problems, which means much simplify and speed up the solution of the general system of equations. The disadvantages include the poor boundary approximation of complex areas, which is not too fundamental for the heat-conduction equations, but rather essential for the hydrodynamic equations.

To eliminate internal shrinkage in critical castings, such a method is not suitable, since the applied mathematical tool does not work well enough in the case of rangy castings when the wall thickness becomes

comparable to the mesh spacing. This is because the splitting of the original geometric model occurs by imposing a rectangular mesh with a constant step, which leads to a sharp increase in the number of computational cells in the case of obtaining rangy castings of large overall dimensions [4].

The Finite Element Method (FEM) used in programs such as Polygon, WinCast, CAPCast, and others, allows maximum consideration of the casting geometry and reveals even minor defects. It is based on heat and mass transfer integral equations [6]. The solution region in which the equations are solved is divided into finite elements (most often - tetrahedrons), within which approximants of functions are constructed based on the system of basis functions defined on the element [7]. By projecting the integral equations onto these bases, we obtain a system of finite-difference equations. This system is much more complicated than the one adopted in FDM; its solution requires large memory resources and considerable time.

The advantage of FEM is a proper boundary approximation, the disadvantages include the need for a high-quality generator of finite elements; the complexity of equations, and impossibility of factorization [6]. The built-in generators of the mesh model give large errors in the programs. The problem is solved by using an external finite element mesh generator, which leads to an increase in the cost of purchased software, operating time, and also requires highly qualified personnel.

At first glance, FDM and FEM differ in the representation of geometry, in the FDM the geometry is represented by bricks (parallelepipeds), and the FEM uses a fairly smooth mesh of finite elements (tetrahedra) of arbitrary sizes and configuration. This difference is not always clearly visible, because the visualization does not necessarily show a distorted brick geometry on the computer screen. It is possible to visualize the different solution on smooth surface meshes of the original geometric models so that the bricks were not visible. However, it is not a question of the modeled casting configuration, but a significant difference in the basic postulates of these methods and, as a consequence, in the different reliability of the solution.

FEM has a fundamentally more complex and adequate mathematical apparatus and more accurately describes the processes occurring in the considered geometric model. When simulating foundry processes FDM and FEM can have significant differences in the adequacy of the solution. It should be noted that currently almost all universal modeling packages, such as ANSYS, Nastran, Patran, etc. have long ago waived the deprecated FDM and use only FEM. More advanced foundry packages, such as ProCast, WinCast, Polygon, have followed the same path. The fact is that FDM is not suitable for complex geometries in problems with a significant influence of boundary flows [2]. For casting conditions, this means that finite-difference methods can be adequately used for casting in disposable molds with low thermal conductivity when there is no jump in the simulated function (eg temperature) at the casting mold boundary.

For pressure die casting, especially for complex shaped geometries, FDM will always give a fundamental systematic inaccuracy that is absent in FEM [3]. In addition, FEM is a less resource-intensive and faster method. For the same geometries, both methods give the same solution, but the FEM, when requiring equal adequacy with FDM, always requires about an order of magnitude less computational resources and the calculation time will be several times less.

The use of FDM in the foundry processes simulation is now justified only for solving hydrodynamic problems during pouring, since the magnitudes and directions of the velocity vectors change with greater discreteness than can be described by a finite-element mesh without losing the advantages of FEM in terms of calculation speed.

In software packages such as ProCast, Flow3D Cast, and Polygon, all major foundry problems are solved base on FEM, and especially for hydrodynamic problems, either FDM or intermediate methods are used. Often, the visualization of the conditional-difference solution in such basic-element packages is performed on a finite-element mesh, which is faster and more convenient.

The disadvantage is that most FEM-based programs have a very complex user interface, which in combination with the lack of experience with software products of foundry technologists reduces the benefits of using any simulation program to zero.

The Finite Volume Method (FVM) used in Nova-Solid/Flow and CastCAE programs is an integrated circuit. In a sense, it is a development of FDM, although sometimes it is considered as some intermediate stage between FDM and FEM. This is probably not entirely true, although FVM takes into account arbitrarily oriented boundaries within the difference cell, but assumes orthogonal difference subdivision (sampling) into rectangular parallelepipeds and has several other features inherent in FDM. FVM is a convenient method for using integral formulations when considering boundary conditions, it allows to control of mesh elements at the casting-mold boundary and simulate the processes of pouring and solidification of casting. FVM successfully solves filling problems, where the use of FEM is difficult, and FDM does not give the necessary conformity in the geometry of the filled cavity.

The software products Flow3DCast and LVMFlow also use FVM, which combines the simplicity and factorization of FDM, as well as a good approximation of the boundaries between different materials and phases It allows simulations to be carried out as quickly as possible without losing the accuracy of the calculations and provides reliable results even with coarse meshes. In any case, FVM has not yet become widespread for modeling casting processes, this is probably due precisely to the intermediate nature of the method. In those cases when arbitrarily oriented boundaries are required, it is better to use FEM itself, and when it is permissible to represent the geometry by a set of parallelepipeds, it is easier to solve the problem with classical FDM.

The Vector Element Method (VEM) used in the AutoCast program is based on determining the greatest thermal gradient at any point inside the casting, which is set by the vector sum of the flux vectors in all directions from

this point [5]. The volume of the casting is divided into numerous pyramidal sectors from the considered point. Heat content and the surface area or cooling are calculated for each sector to determine the flux vector. The calculation is carried out in the direction of the resulting vector until the resulting one becomes zero. The feed line path is considered the curve along which the repetitions are done. It is possible to identify different hot spots in casting if the calculation starts with a plurality of starting points located in different areas of the casting.

VEM is relatively simple when compared to other numerical techniques but provides reliable and robust results [10]. Unlike FEM or FDM methods, VEM rectifies small errors while computing flux vectors at any point by automatically correcting them in subsequent repetitions. Moreover, VEM requires less memory and is also faster.

The boundary element method (BEM) is the most "strong" method since in its basic formulation it assumes within the boundary element the approximation of the distribution of the desired excosecant (for example, the temperature excosecant) directly according to the original differential equation, which describes the simulated process. In addition, when using BEM, spatial ordering occurs, which theoretically speeds up the solution and reduces the requirements for computing resources. However, for modeling casting processes, BEM is practically not used, because, despite of its advantages, it requires uniformity of physical properties in the areas of large boundary elements. This does not correspond to the physics of most casting processes associated with a significant change in the process parameters in local arbitrary areas, for example, in the area of heat output during solidification.

Practice shows that the optimal approach is not to choose a single numerical method to simulate casting processes but to use a combination of different methods, which makes it possible to increase the speed, accuracy, and adequacy of the results obtained to experimental data.

3. Research results of the advanced features and disadvantages of computer systems for casting processes simulation

In the course of the research, the possibilities, advantages, and disadvantages of the most common computer programs for casting processes simulation were investigated. The comparative analysis results of the compatibility options of computer programs for casting processes simulation are presented in Table 4.

MagmaSoft – is a multifunctional specialized program that allows you to simulate a variety of casting processes. This is one of the first commercial foundry packages, actually demonstrating for the first time that complex casting processes can be broadly simulated at a sufficiently high level. Thermal, hydrodynamic, and deformation processes are solved by numerical methods in MagmaSoft. The problem of predicting macroporosity and cavities is also numerically solved, although the models used in this case are simplified and do not fully take into account the complex and dynamic nature of the structuring of alloys during solidification. Forecast of microporosity, structural, mechanical, and other characteristics of casting is carried out at the level of criterion analysis.

The advantage of MagmaSoft is the presence of a sufficiently large number of empirical criteria, which at the level of criteria analysis allow predicting various properties, including the structure and mechanical characteristics of castings. In addition, the program implicitly integrates into the system various superimposed coefficients for a variety of casting methods, alloys, and materials, which to some extent compensates for the simplification of models and algorithms.

MagmaSoft has a convenient generator of difference meshes. If the initial geometry of the castings is relatively simple or the task of exact adherence the ratios of different wall thicknesses and a sufficient number of finite-difference elements along the wall thickness is not posed, then the generation of the calculated difference geometric model does not present any particular difficulties.

The disadvantage of this system is that the criteria used are hidden and it is impossible to edit, customize and supplement them, which significantly reduces the possibility of their adequate application. The above is also true of the choice of initial conditions, which are closed to the user and are determined by the casting method. This approach is acceptable for typical, widely used technologies. However, the lack of information on the choice of production parameters laid down in the system leads to the fact that the calculation results are often conditional.

In general, MagmaSoft is a system focused on solving typical casting tasks, except for special casting methods and technologies for producing castings of complex geometry. The program has good accuracy of the results obtained and a rich set of parameters for the simulation. MagmaSoft's long experience with foundries around the world has earned it a reputation for being a simple, reliable, and accurate package.

ProCast computer system, unlike MagmaSoft, is an extensive set of complex and physically universal models for solving serious production problems in the foundry industry, which significantly increases the adequacy of calculations. This system simulates thermal, hydrodynamic, and deformation processes, as well as processes of structurization and crystallization.

The program is able to forecast the occurrence of deformations and residual stresses in the casting and can be used to analyze such processes as core making, centrifugal casting, cavityless casting, and continuous casting. An accurate description of the geometry, due to the applied FEM, allows the ProCast system to simulate the filling of a mold with supernatant liquid and obtain reliable information about the erosion of a sand mold, air pockets, oxides, and turbulent flow, material age, non-spillages, and cold junctions, flow length and, overflows over-pours.

ProCast provides a complete solution for the simulation of the continuous and semi-continuous casting of billets. The program can simulate the steady-state mode, the initial and final stages of the process. The inverse

calculation module automatically calculates the parameters of a material or process based on temperatures measured at targeted points or at the predetermined times. Primary and secondary cooling can be determined by inverse calculation.

This computer system has its own finite element mesh generator, which can be successfully used for geometries of medium complexity. For complex geometry models, specialized external generators are commonly used, which are currently available on the market.

A large database of materials for foundry models comes with ProCast. Its content is constantly updated with reliable data, verified in the conditions of existing foundry production. It includes the unique thermodynamic database that allows the user (by entering the chemical composition of the alloy) to automatically obtain the temperature curves of the properties necessary for an accurate calculation of the casting process.

The main advantages of this package include the ability to take into account complex thermal boundary conditions and direction of solidification, complex rheology in deformation calculations, the ability to simulate complex processes and numerically calculate the structure in castings. To carry out numerical calculations of the structure in ProCast, it is necessary to select the correct crystallization model and its parameters.

The disadvantage of the program is a too low level of solving the shrinkage problem, as well as the high cost, but it is justified by the capabilities of the program.

Thus, ProCast can be recommended as a basic system for castings and technologies of any complexity, excluding those cases where it is required to simulate the formation of shrinkage defects, taking into account the real dynamic nature of the structuring of the two-phase zone and the pressure drop due to filtration flow in the two-phase zone during shrinkage. This package is effective when technologists need to solve deformation problems with complex rheology and structure in the casting.

WinCast is a software package for casting processes simulation capable of calculating metal pouring (hydrodynamic and thermal analysis), metal crystallization (location of heat units and shrinkage defects),the tension of a casting (forecasts technological and operational stresses), structure-forming processes, heat treatment, and welding. The basis of the modular system is made up of basic and additional modules for sequential or parallel passage of various stages of modeling, and the solution of problems can be carried out jointly, taking into account their cross-impact.

Compared to Procast, WinCast has a more convenient process for building a mesh models, not inferior in the accuracy of calculations. The advantages of this model are the following: more accurate approximation of complex surfaces; more accurate representation of thin walls and complex sections with fewer elements; the ability to carry out thermal, hydrodynamic, and strength analysis on one mesh; fewer heat units reduce the calculation time.

The accuracy of thermal calculations is ensured by the correct approximation of surfaces by finite elements and by taking into account the temperature dependence of the properties of alloys and auxiliary materials. The reliability of hydrodynamic and strength analyzes is guaranteed by the compatible calculation of temperature fields on the same finite element pentahedral mesh with a high level of regularity. Generation of an accurate finite element mesh for 3D geometry of any complexity, built in an external CAD system or using the program's tools, provides accurate engineering forecasts in a short time.

The advantage of WinCast is that the database, organized in text format, is easy to edit and supplement. It contains the properties of alloys and materials in the form of tabular function of temperature. Thanks to a flexible preprocessor, the program provides accurate geometry display and the availability of automatic mesh generation.

Among the disadvantages, it should be noted is an inconvenient interface, as well as the use of simplified models when solving the heat problem (solidification) and the shrinkage-filtration problem (the formation of micro-and macroporosity). The inability to automatically generate the computational grid requires additional spadework to create it. However, in WinCast, deformation processes are simulated at a sufficiently high level as a result of casting cooling.

SolidCast is an entry-level computer system that is designed to solve current production and technological problems, as well as to optimize the technology for each casting based on the geometry optimization of the gating-feeding system and the technological parameters of the casting process.

The computational capabilities of the package allow the user to trace the dynamics of filling the mold with metal and the crystallization process of the casting in the mold; to obtain information about the time of crystallization, the rate of cooling, shrinkage defects; to determine the possible areas of defect occurrences in the casting. The built-in hydrodynamic module allows you to simulate the flow of the melt in the mold, as a result of which it is possible to identify and forecast such defects as mold erosion, cast seams, surface contaminations, and misruns in the casting.

As a result of the calculation, the technologist receives information about the allocation of temperature fields in the casting and the mold, the values of the melt flow rate, and the pressure of the melt on the mold walls at any point.

SolidCast has a built-in mesh generator in two versions and an automatic generator of graphs and diagrams in the postprocessor, which allows comparing the simulation results of several variants of manufacturing technologies for the same casting. The availability in the SolidCast computer system of the possibility of automatic generation of the computational mesh permits optimizing the casting mold depending on scrap yield and the size of the flask. In addition, this software product allows to creation of a unique database on the used technological processes for casting production. The built-in database of molding materials and alloys is open to the user, it is constantly changing and supplemented.

The disadvantages of SolidCast are as follows: inconvenient interface, inability to take into account preliminary mold filling; inconvenient display of calculation results for visual analysis; excessive duration of computer calculations. Extensive functionality and unique pricing policy of developers make SolidCast the best in terms of price-functionalities-productivity since one acquired licensed program can be used at five workplaces within one enterprise.

Table 4 – Comparative analysis of the compatibility options of computer programs for casting processes simulation

Functionalities		MagmaSoft	ProCast	WinCast	SolidCast	Nova-Solid/Flow	Polygon
1	2	3	4	5	6	7	8
Problem definition	databases of additional technological elements	+	—	+	+	+	+
	addition and editing of databases	+	+	+	+	+	+
	applying filters	+	—	—	—	+	—
	modeling of gating bowls and separately filled gating systems	+	—	—	—	—	—
	boundary conditions correction	+	+ (except for the internal casting elements)	+	+	+	+
	simulation of filling the stopper and teapot ladles	+	+	—	—	—	—
	calculation of the sector of 1/p part of an axisymmetric casting	+	+	+		—	+
Mold filling calculation	basic hydrodynamic equation	Navier–Stokes	Navier–Stokes	Bernoulli		Navier–Stokes	3DFlow
	analysis of temperature fields during filling	+	+	—	+	+	—
	mold erosion analysis	+	—	—	—	—	—
	filling analysis (tracers of particulate movement in time, speed, and distance)	+	—	—	—	—	—
	accountancy of the effect of mold gastightness	+	—	—	—	—	—
	accountancy of the influence of the gas-generating abilities of mold and cores with binders	+	—	—	—	—	—
Calculation of solidification	used mathematical apparatus	Fourier	Fourier	Fourier	Fourier	Fourier	Fourier
	temperature field analysis	+	+	+	+	+	+
	calculation of solidification tracers	+	—	—	—	—	—
	calculation of thermal convection vectors	+	—	—	—	—	—
	alloy segregation calculation	+	+	—	—	—	—
	oriented crystallization analysis	+	+	—	+	+	—
	orientation analysis of direct-grown crystals	+	—	—-	—	—	—
Calculation of stresses	stress analysis	+	+	+	+	—	—
	analysis of casting and mold deformations	+	+	+	+	—	—
	analysis of stress-forming rate in the casting during solidification	+	—	—-	—	—	—
	calculation of hot and cold crackings during crystallization	+	+	—-	—	—	—
	calculation of hot and cold crackings after completion of the crystallization process	+	+	+	+	—	—
Heat treatment	calculation of the heat treatment process of the casting	+	—	—	—	—	—
	calculation of the heat treatment process of the casting after premachining	+	—	—	—	—	—

End of Table 4

1	2	3	4	5	6	7	8
Integration feasibility	admissibility to web deploy of custom applications and macros	+	—	—	—	—	—
	admissibility to export calculated data for sequent analysis in other CAE systems	+	+	—	—	—	—
Automatic calculation	optimization of casting technology parameters	+	+	—	—	—	—
Defects analyzed	micro flaws	+	+	+	+	—	—
	macro flaws	+	+	+	+	+	+
	gas unsoundness of casting	+	+	—	+	—	—
	erosion of mold and surface contaminations of casting	+	—	—	—	—	—
	cold and hot crackings in the solidificating process	+	+	—	—	—	—
	cold and hot crackings after solidification	+	+	+	+	+	+
	non-fills	+	+	—	+	+	—
	veining	+	—	—		—	—
Alloy casting analysis	steel	+	+	+*	+*	+*	+*
	cast iron	+	+	+*	+*	+*	+*
	aluminum alloys	+	+	+*	+*	+*	+*
	magnesium alloys	+	—	—	—	—	—
	zinc alloys	+	+	+	+	+	+
	titanium alloys	+	+	—	+	—	+
	copper alloys (bronze, brass)	+	+	+	+	+	+
	alloys with non-Newton' flow rheology	+	—	—	—	—	—
Analysis of casting methods	sand casting	+	+	+		+	+
	oblique casting	+	—	—	—	—	—
	permanent-mold casting	+	+	+	+	+	+
	investment casting	+	+	+	+	+	+
	cavityless casting	+	—	—	—	—	—
	high pressure die casting	+	+	+	+	+	+
	injection molding	+	+	—	—	—	—
	low pressure die casting	+	+	+	+	+	+
	centrifugal casting	+	+	—	+	—	—
	over-pressure casting	+	+	+	+	+	+

*without calculating the microstructure

The Polygon computer system is designed to simulate hydrodynamic, thermal, and shrinkage-filtration processes during casting. In addition, the problem of reticulation of electric potentials during solidification of casting in the electric fields is solved by numerical methods. Criteria analysis methods allow predicting strength, hardness, structural parameters, and erosion of forms.

When using the Polygon software, simulation is carried out based on the finite element method, which allows using the most adequate physical and geometric models. All models and functions are implemented for 3D geometric models. Solvers can use not only direct but also iterative calculation methods. This makes it possible to significantly reduce the calculation time and the required random access memory, which in combination with the finite element method, calculaties castings of any complexity available on a personal computer.

Based on the criterion analysis, the Polygon system package contains a special module that allows using not only the criteria proposed by the developers for predicting mechanical properties, but also to form a base of own complex criteria, taking into account the chemical composition and the logic of transition from one formula to another.

This enables the user to adequately forecast various technological and operational properties of the casting.

The possibility of taking into account complex boundary conditions for castings of complex geometry when using special casting methods makes it possible to use the Polygon computer program in complex foundries, in particular, by methods of directional solidification. One of the most important properties of Polygon is adequate and modern physical models of the shrinking process. It carries out a combined calculation of the formation of shrinkage micro and macro defects by two completely different mechanisms with the calculation of the filtration flow, pressure fields in the casting, and complex dynamic changes in the structuredness of the alloy in the solidification interval. The problem of shrinking the defects in numerical solutions in other casting packages is not solved.

When choosing the properties of alloys, materials, boundary, and other conditions, the user has full access to all parameters, also can change and supplement the initial databases by properties in any way.

The disadvantages of the package include the absence of a full-scale deformation task taking into account complex rheology and the excessive complexity of models when solving hydrodynamic problems, namely: an extremely inconvenient interface; the complexity of preparing mesh model, the complexity of data entry, an insufficient database of materials and alloys, as well as the need for purchasing additional software for generating the mesh model.

Thus, Polygon is a modeling system designed to solve the problems of casting technology simulation for any casting method with unlimited complexity of the casting geometry, taking into account the maximum number of operating factors. The advantages of the package, in addition to the use of finite elements, include complex and adequate physical models of thermal processes, the ability to take into account complex boundary conditions, and displacement of objects (for directional casting solidification, as well as a comprehensive problem solving of shrinking. Practice shows that for essential castings, the Polygon program can be used in combination with other packages for foundry processes simulation as testing tools for developing the optimal technology for producing castings.

Conclusions

This study presents a comparative analysis of the most well-known computer systems for casting simulation in terms of their functionalities for modeling hydrodynamic, deformation, filtration, crystallization, and other processes, following metallurgical and foundry technologies.

The analysis shows that at present it is impossible to offer a computer system that can satisfy both plant technologists and research engineers. When choosing a specific computer system or package, the user should proceed from his financial capabilities related to its cost, as well as from the volume of those tasks that need to be solved using modern simulating tools. Experience shows that the results of such studies are in great demand both by research scientists and by foundry specialists and managers.

References

1. Danylchenko, L., Radyk, D. (2021). Features of introduction the additive technologies in workpieces' manufacturing processes. *Problems of design theory and manufacture of transport and technological machines*, Preceeding of the International Scientific and Technical Conference dedicated to the memory of Prof. Hevko B. Ternopil, Ukraine.

2. Cleary, P., Ha, J., Alguine, V., Nguyen, T. (2002). Flow modelling in casting processes. *Applied Mathematical Modelling, 26*(2), 171-190, doi: 10.1016/S0307.

3. Fu, M.W., Yong, M. S. (2009). Simulation-enabled casting product defect prediction in die casting process. *International Journal of Production Research, 47*(18), 5203-5216, doi: 10.1080/00207540801935616.

4. Jolly, M. (2003). Castings (C'h. 1.18), Milne, 1., Ritchie, R., Karihaloo, B. L. (Eds.). *Comprehensive Structural Integrity*, Vol. 1, Elsevier, Pergamon, Amsterdam, pp. 377-466.

5. Khan, M.A.A., Sheikh, A.K. (2016). Simulation tools in enhancing metal casting productivity and quality. *Proceeding of the Institution of Mechanical Engineers, part B; Journal of Engineering Manufacture*, 230(10), 1799-1817, doi: 10.1177/0954405416640183.

6. Koptev, A. (2016). The Navier–Stokes equations. From theory forward to solution of practical problems. *International Research Journal, 49*(7-4), 86–89.

7. Lewis, R. W., Ravindran, K. (2000). Finite element simulation of metal casting. *International Journal for Numerical Methods in Engineering, 47*(1-3), 29-59, doi: 10.1002/(SIC1) 1097-0207(20000110/30)47.

8. Pylypets, M., Danylchenko, L. (2019). Simulation modeling in designing applications for sheet metal forming. *XXI-th scientific conference of Ternopil Ivan Pul'uj National Technical University,* Preceeding of the International conference. Ternopil, Ukraine.

9. Shirokikh, E., Perfilova, V. (2015). Improving pouring gate systems in casting process computer modeling. *Bulletin of the Moscow Region State University, 20*(4), 65–69.

10. Sutaria, M., Ravi, B. (2014). Computation of casting solidication feed-paths using gradient vector method with various boundary conditions. *The International Journal of Advanced Manufacturing Technology, 75*(1-4), 209-223, doi: 10. 1007/s00170-014-6049-3.

Cross-sectional: MECHATRONICS, RADARS, CONTROL SYSTEMS;

SOME ASPECTS OF DEVELOPING A MULTIPURPOSE RADIO SYSTEM FOR MONITORING THE GEOSPACE

Oleksandr Bogomaz, Volodymyr Barabash, Dmytro Iskra

Institute of Ionosphere, Kharkiv, Ukraine, 16 Kyrpychova, 61001; o.v.bogomaz1985@gmail.com

Abstract:
Hardware and software principles of building a multipurpose radio system for monitoring the geospace are considered. It is shown that Ettus Research USRP is the most suitable platform for such system. A structure of a multipurpose radio system for monitoring the geospace and developed software for VISCR2 ionosonde (based on USRP N200) as a part of this system are presented. The first results of testing new sowtware are shown.

Keywords: *radar, software defined radio, ionogram, ionosonde, ionosphere, geospace*

1. Introduction

Monitoring the geospace using ground-based radars allows to obtain unique information during various natural phenomena in the near-Earth environment (like magnetic storms, meteoroids entering the atmosphere) and on the Earth (for example, earthquakes), as well as anthropogenic events (rockets launches, powerful explosions, and nuclear tests).

The Institute of Ionosphere conducts studies of processes in geospace using mainly such ground-based remote sensing instruments as very high frequency (VHF) incoherent scatter (IS) radar and coherent high frequency (HF) radar for vertical sounding of the ionosphere (ionosonde). These radio systems are installed in the Ionospheric Observatory located near the town of Zmiiv, Kharkiv region. The first experimental IS radar and ionosonde data were obtained in 1972, and since then, the hardware and software components of these radio systems are continuously being modernized. The updated components include radio transmitting and receiving devices, analog-to-digital converters (ADC), computer data processing systems, and programs are running on them (Emelyanov and Zhivolup, 2013).

In 2012, a new data acquitting and processing system for IS radar was developed. It is based on two four-channel ADC E20-10 modules and which allowed not only to duplicate existing IS radar data processing systems ("Kentavr" and multi-channel PC based correlator), but also to expand radar capabilities in general (Bogomaz et al., 2017a; Bogomaz et al., 2017b). The improvements are as follows:

1. The maximal sampling rate has increased significantly, up to 10 MHz. This allowed to obtain the correlation functions of the IS signal with a step of 5.1 μs (previous processing systems used a step of 30.6 μs), which is necessary to increase the accuracy of determining the density of hydrogen and helium ions in the upper ionosphere.
2. The system includes a high-performance modern PC that is capable of processing a large amount of data coming from the E20-10 module via a high-speed USB 2.0 bus (in previous processing systems, data ware transmitted via the parallel LPT port to low-performance personal computers, in which part of the information was intentionally ignored to support real-time operating mode), as well as visualize data and processing results on high-resolution displays (computers in previous processing systems worked in graphics mode 640 by 480 pixels with a palette of 16 colors).
3. The developed E20-10-based data processing system can be quickly adapted for specific experiments on the Kharkiv IS radar. For example, work in the such modes was implemented:

- Probing the ionosphere with paired pulses for the study of the middle and lower ionosphere (Bogomaz et al., 2018).
- Using two radar antennas (zenith-directed NDA-100 with a diameter of 100 m in active mode and full-steerable PPA-25 with a diameter of 25 m in active mode) simultaneously for studying processes in the lower ionosphere (Emelyanov et al., 2018).
- Using two radar antennas (NDA-100 in active mode and PPA-25 in passive mode) simultaneously for studying processes in the lower ionosphere (Emelyanov et al., 2020).

Although the developed data acquitting and processing system based on E20-10 ADC module has allowed obtaining much more information about the processes in geospace, it needs further improvement in order to reduce energy consumption and optimize data processing methods. But analysis of publications on radars developed recently has shown that it is more appropriate to develop a new, multi-purpose radio system that will determine the parameters of the geospace and objects in it to conduct sounding at HF and UHF radio bands used in vertical sounding and incoherent scatter techniques, with generating, receiving and signal processing using computer software and hardware systems.

2. Prototypes

All monitoring radio systems being developed today belong to the class of software defined radio (SDR).

Low-cost HF software defined radar called the Penn State Ionospheric Radar Imager (PIRI) for use in ionospheric research is described in (Bostan et al., 2019). It is composed of commercial-off-the-shelf components and utilizing open-source software (GnuRadar) to perform pulse generation, pulse coding, downconversion, data acquisition, and signal processing. This system has better time resolution than ionosondes, is highly customizable, and it can be used to resolve the fine details of ionospheric features, as well as providing long-term ionospheric measurements at fixed frequencies.

A prototype IS radar system of Nanchang University, including system components and data processing, was introduced in (Li et al., 2020). This radar operates at frequencies from 490 to 510 MHz (i.e. in UHF range) and transmits just 100 kW peak power pulses, accounting for only 10% of the existing IS radars. However, this is enough to obtain reliable data up to an altitude of about 300 km.

SDR-based ionosondes designed recently are described in (Barona Mendoza et al., 2017; Zalizovski et al., 2018; Kalita et al., 2019). They operate in an active mode in contrast to a radio system presented in (Rejfek, 2019) working in a passive mode.

The above systems can monitor geospace as a media and obtain its characteristics and information about processes taking place there. Another objective is monitoring objects in the near-Earth space. An example of system for such purpose is described in (Holdsworth, 2020).

It is important to note that significant portion of systems listed above are built on USRP (Universal Software Radio Peripheral) developed by Ettus Research (National Instruments Corp., USA). This platform is a low-cost SDR that is commonly used for rapid prototyping and complex system design.

Table 1 summarizes the results of the review.

Table 1

Comparison of systems for monitoring the geospace

System (paper)	Range (HF, VHF, UHF)	Mode (active/passive)	Target (media/objects)	Ettus Research USRP is used (yes/no)
(Bostan et al., 2019)	HF	active	media	yes
(Li et al., 2020)	UHF	active	media	no
(Barona Mendoza et al., 2017)	HF	active	media	yes
(Zalizovski et al., 2018)	HF	active	media	yes
(Kalita et al., 2019)	HF	active	media	no
(Rejfek, 2019)	HF	passive	media	yes
(Holdsworth, 2020)	VHF	active	objects	no

As it can be seen, using of USRP platform is advisable for developing a new multipurpose radio system for monitoring the geospace.

3. Hardware

Analysis of existing systems for monitoring the geospace has given an opportunity to build a diagram which can be used for developing a multipurpose system based on multiple USRPs (Figure 1). The most suitable are USRP N2xx series (N200 and N210) which are recommended for Multiple-In-Multiple-Out (MIMO) applications. Two USRPs can be synchronized using a MIMO cable and if there is a need to synchronize more devices, the Ettus Research OctoClock can be used. To synchronize all the parts of the system, using the GPS-disciplined oven controlled crystal oscillator (OCXO) is strongly recommended. Ettus Research distributes an upgraded version of the OctoClock CDA-2990, which includes an internal GPS-disciplined OCXO (OctoClock-G CDA-2990).

Analog frontends include attenuators, filters, low-noise amplifiers for receiving signals, as well as filters, antenna switchers, power amplifiers, and various measurers for transmitting signals. The frontends work with receiving and transmitting HF and VHF antennas and interact with USRPs through radio frequency (RF) and digital interfaces. Digital interfaces are used for controlling antenna switcher, attenuators and obtaining information about power transmitted and consumed, standing wave ratio (SWR), and heatsink temperature.

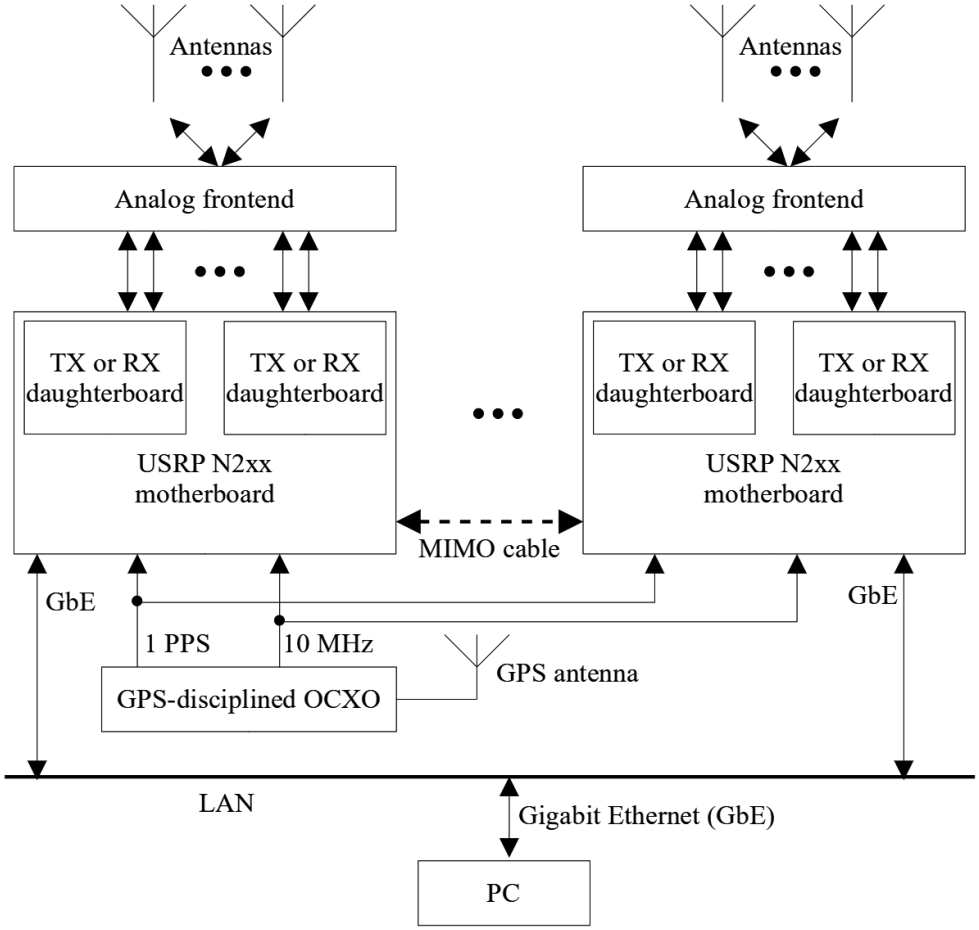

Figure 1. A structure of a multipurpose radio system for monitoring the geospace.

Depending on the range and operating mode, USRP can contain up to two daughterboards. It is supposed that the multipurpose radio system for monitoring the geospace is being developed will use boards listed in Table 2.

Table 2

USRP daughterboard can be used in the system for monitoring the geospace

Daughterboard	Frequency range	Mode
LFTX	DC–30 MHz	transmitting
LFRX	DC–30 MHz	receiving
BasicTX	1–250 MHz	transmitting
BasicRX	1–250 MHz	receiving

The USRPs are controlled by high-performance desktop personal computer through gigabit Ethernet local area network (LAN). Specification of a computer which is used currently for developing and testing is shown in Table 3.

Table 3

Specification of the computer used for developing and testing a multipurpose radio system for monitoring the geospace

Parameter	Value
CPU	Intel Core i5-8500
CPU frequency	3.0 GHz
CPU cores/threads number	6/6
RAM	16 GB, DDR4, 2666 MHz
SSD	256 GB
HDD	1 TB

4. Software

USRP Hardware Driver (UHD) is available on Linux, Windows, and Mac OS. Linux Mint 19 was chosen for the system development. UHD version 003.007.003 together with Boost C++ library version 1.55.0 are used. This combination showed a good stability in work. C++ programming language was chosen for software development.

A program for an active multipurpose radio system for monitoring the geospace should form arrays describing signal is being transmitted, synchronize receiving and transmitting, and store data containing received signal to files on disk. Data processing is performed using software written in Python programming language.

An example of a radio system for monitoring the geospace is ionosonde. It is a HF radar that sounds the ionosphere by numerous of frequencies and produces dependency of virtual height of the reflection from ionosphere layers on frequency. Virtual height *h*' corresponds to time from the radar to the ionosphere and back if velocity of signal propagation equals to speed of light (the speed of a radio wave propagation in ionosphere is less than speed of light, depends on electron density in the media, and it is unknown in this task). A typical vertical ionogram obtained on October 9, 2019 by VISRC2 ionosonde is shown on Figure 2.

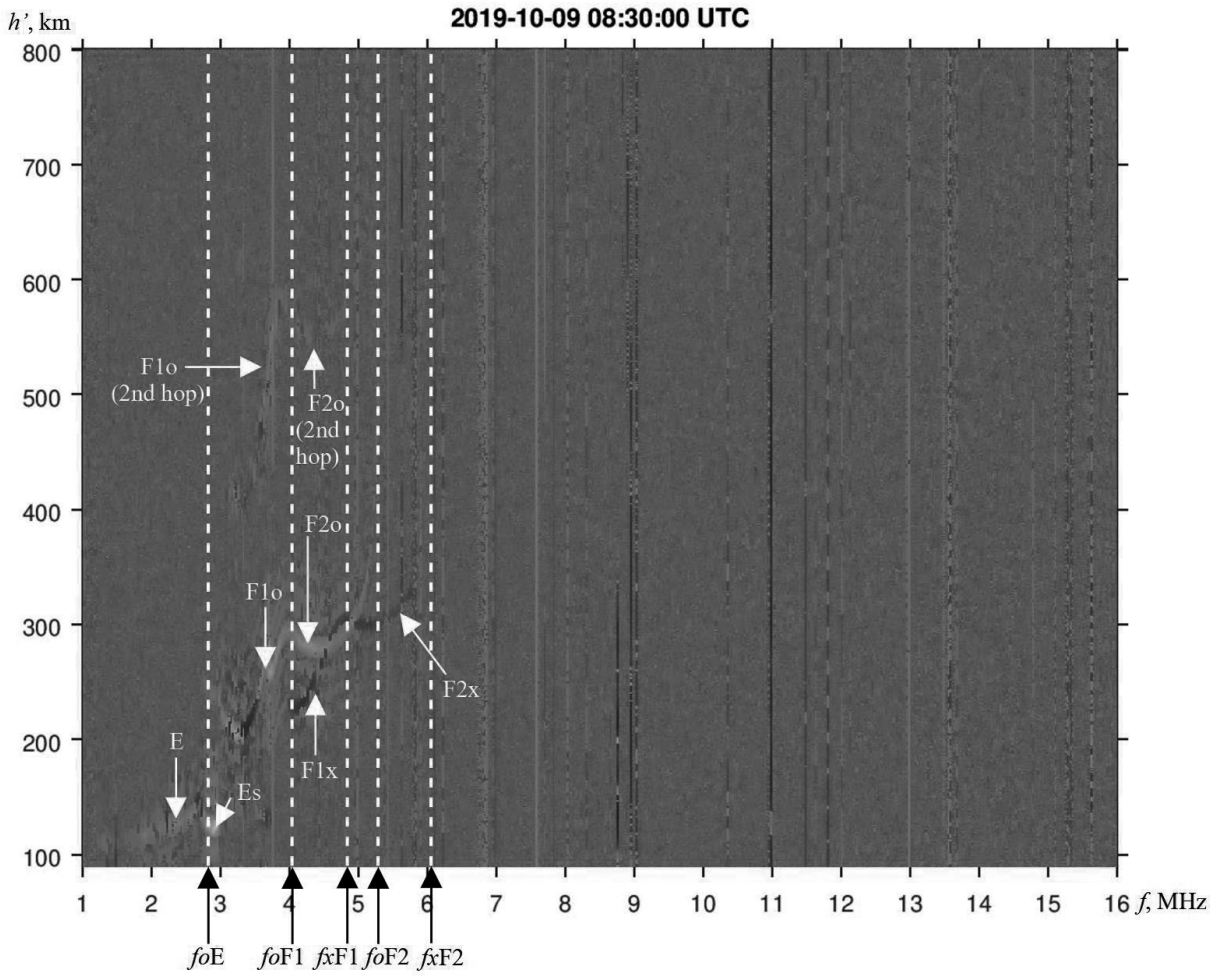

Figure 2. A typical vertical ionogram obtained on October 9, 2019 by VISRC2 ionosonde installed in the Observatory of the Institute of Ionosphere

VISRC2 ionosonde is developed and built at the Space Research Center in Warsaw, Poland, and installed in the Observatory of the Institute of Ionosphere (49.676° N, 36.292° E). It uses USRP N200 for generating and receiving signals. Software of the ionosonde is written on C++ and GNU Octave and is running in Linux operating system. On the ionogram shown on Figure 2, traces of E, Es, F1, and F2 ionosphere layers are clearly seen. Ionosonde is able to separate ordinary and extraordinary ("o" and "x" indices respectively on Figure 2). Using critical frequencies foE, foF1, fxF1, foF2, and fxF2, it is possible to calculate electron densities in maxima of ionosphere layers E, F1, and F2. A limitation of the ionosonde was its low flexibility. VISRC2 software initially was able to produce phase-shift keying pulses with constant code and element width (7-bit Barker code, 70 μs per element) and process signals obtained in the result of sounding the ionosphere by these pulses. Therefore a new program that manipulates VISRC2 ionosonde was developed. This program is a software base of the multipurpose radio system for monitoring the geospace is being developed in the Institute of Ionosphere.

5. The first results

Testing the new program was carried out on August 11, 2021.
Sounding using 7-bit Barker (+1, +1, +1, −1, −1, +1, −1) code has given an ionogram shown on Figure 3.

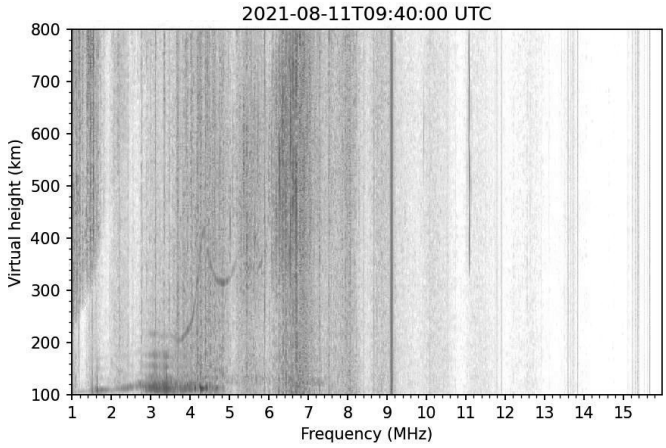

Figure 3. An ionogram obtained by VISRC2 ionosonde with a new program developed for using in the multipurpose radio system for monitoring the geospace

It can be seen that there are good visible traces of E, Es, F1, and F2 ionosphere layers (ordinary components) and extraordinary component of Es layer trace.

Ionograms obtained by sounding using 13-bit Barker code (+1, +1, +1, +1, +1, −1, −1, +1, +1, −1, +1, −1, +1) and different element width are shown on Figure 4.

Using a long sounding pulse (i.e. when element width is 70 μs and pulse width is 13 × 70 = 910 μs) leads to possible loss of information from lower altitudes (up to 136.5 km). Using sounding pulses of 40 μs and 30 μs width gives minimal altitudes of 78 km and 58 km respectively.

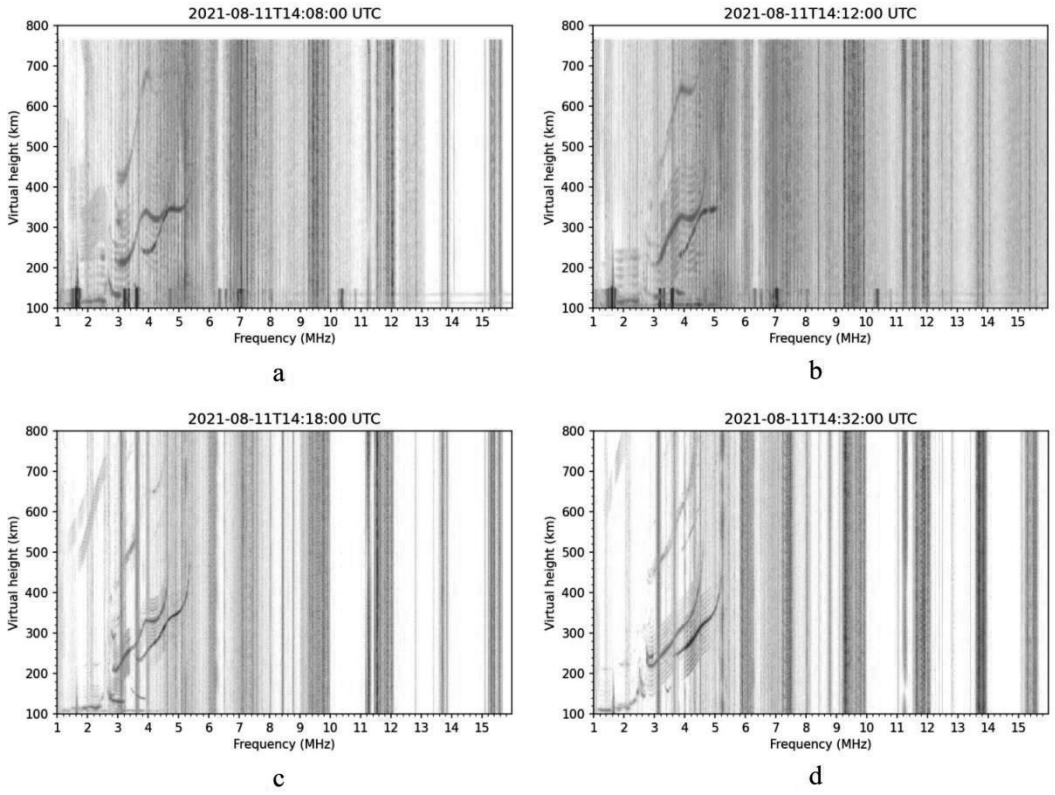

Figure 4. Ionograms obtained by VISRC2 ionosonde with a new program developed for using in the multipurpose radio system for monitoring the geospace. 13-bit Barker code is used. Width of each element is 70 μs (a, b), 30 μs (c), and 40 μs (d). Number of sounding pulses on every frequency is 8 (a, c, d) and 16 (b).

6. Conclusions

Developing a multipurpose radio system for monitoring the geospace has good perspectives due to its flexibility and mobility at the same time. It will allow decreasing energy consumption by radio monitoring hardware and improving quality of information about the near-Earth space and objects there.

A structure of the multipurpose radio system for monitoring the geospace being developed in the Institute of Ionosphere is shown. New software that is a part of this system was developed and successfully tested. Next steps in improvement the developed program are using decoding algorithm that produces zero sidelobes suggested by Lehtinen et al. (2004), noise reduction, and removal of radio frequency interference.

References

1. Mendoza, J.J.B., Ruiz, C.F.Q., Jaramillo, C.R.P. (2017). Implementation of an Electronic Ionosonde to Monitor the Earth's Ionosphere via a Projected Column through USRP. *Sensors*, *17*(5), 946. DOI:10.3390/s17050946.

2. Bogomaz, O., Miroshnikov, A., Domnin, I. (2017). Peculiarities of database for Kharkiv incoherent scatter radar. *Information and Telecommunication Technologies and Radio Electronics (UkrMiCo)*, Proceedings of the International Conference. doi:10.1109/UkrMiCo.2017.8095424.

3. Bogomaz, O., Kotov, D., Panasenko, S., Emelyanov, L. (2017). Advances in software for analysis of Kharkiv incoherent scatter radar data. *Information and Telecommunication Technologies and Radio Electronics (UkrMiCo)*, Proceedings of the International Conference. doi:10.1109/UkrMiCo.2017.8095425.

4. Bogomaz, A.V., Kotov D.V., and Iskra, D.A. (2018). Results of testing a new software and hardware system for processing incoherent scatter radar data in the mode of studying the middle ionosphere. *Bulletin of the National Technical University "KhPI"*, *43*(1319), 24-32.

5. Bostan, S.M., Urbina, J.V., Mathews, J.D., Bilén, S.G., Breakall, J.K. (2019). An HF software- defined radar to study the ionosphere. *Radio Science*, 54(9), 839–849. doi: 10.1029/2018RS006773.

6. Emelyanov, L.Y., Zhivolup, T. G. (2013). History of the development of IS radars and founding of the Institute of Ionosphere in Ukraine. *History of Geo-and Space Sciences*, *4*(1), 7–17. doi:10.5194/hgss-4-7-2013.

7. Emelyanov, L., Chepurnyy, Y., and Bogomaz, O. (2018). Simultaneous sounding of the ionosphere in the vertical and oblique directions using incoherent scatter radar. *Electronics and Nanotechnology (ELNANO)*. Proceedings of the 38th International Conference (pp. 458–463). doi:10.1109/ELNANO.2018.8477456.

8. Emelyanov, L., Chepurnyy, Y., Domnin, I., Panasenko, S. (2020). Two-Antenna Method for Characterizing Lower Ionosphere Processes Using Incoherent Scatter Technique. *Ukrainian Microwave Week (UkrMW). Proceedings of the.* doi:10.1109/UkrMW49653.2020.9252642.

9. Holdsworth, D.A., Spargo, A.J., Reid, I.M., Adami, C. (2020). Low Earth Orbit object observations using the Buckland Park VHF radar. *Radio Science*, *55*(2), 1–19. doi:10.1029/2019RS006873.

10. Kalita, B.R., Nath, S.J., Bhuyan, P.K., Khandare, A., Kulkarni, A. (2019). SAMEERDU–digital ionosonde: Brief system description and initial results from a low-latitude location Dibrugarh. *Radio Science*, *54*(11), 1142–1155. doi:10.1029/2019RS006813.

11. Lehtinen, M.S., Damtie, B., amd Nygrén, T. (2004). Optimal binary phase codes and sidelobe-free decoding filters with application to incoherent scatter radar. *Annales geophysicae*, *22*(5), 1623–1632. DOI:10.5194/angeo-22-1623-2004.

12. Li, Y., Yuan, K., Yao, M., Deng, X. (2020). The Prototype Incoherent Scatter Radar System of Nanchang University. In *IEEE Geoscience and Remote Sensing Letters*. (pp. 1184–1188). IEEE. doi:10.1109/LGRS.2020.2994082.

13. Zalizovski, A.V., Kashcheiev, A.S., Kashcheiev, S.B., Koloskov, A.V., Lisachenko, V.N., Paznukhov, V.V., Yampolski, Yu.M. (2018). A prototype of a portable coherent ionosonde. *Space Sci. & Technol.*, *24*(3), 10–22. doi:10.15407/knit2018.03.010.

METHODS TO IMPROVE THE ACCURACY OF GUIDANCE OF TERRESTRIAL ANTENNA STATION

Mykhaylo Palamar[1], MyroslavaYavorska[1], Vladislavs Bezrukovs[2], Anatolii Poikhalo [3] Volodymyr Kruglov[1], Yuriy Apostol[1], Vitaliy Batuk[1]

[1] Instrumentation Department, Ternopil Ivan Pul'uj National Technical University, UKRAINE, Ternopil, Ruska st.56, prilady@tntu.edu.ua, https://tntu.edu.ua
[2]Engineering Research Institute Ventspils International Radio Astronomy Centre (ERI VIRAC) of Ventspils University of Applied Sciences (VUAS), Ventspils, Latvia; vladislavsb@venta.lv
[3] National Center Of Space Facilities Control And Test, Ukraine, Kyiv, Moskovska str. 8, poikhalo@nkau.gov.ua

Abstract: The analysis of factors influencing accuracy of guidance of terrestrial antenna complexes and ways of improvement of a signal reception quality are considered. The above considerations are the result of authors many years practical experience in the AS ground stations setting and monitoring.

Keywords: *AS guidance, instalaton accuracy, surface control, control system*

1.Introduction

The design of high-precision control systems for massive objects in order to guide them to the specified coordinates, tracking on specified trajectories or tracking moving objects is relevant for the a terrestrial stations for the reception of information coming from a spacecraft.The technical problems, arising in providing an accuracy AS tracking are largely due to the precision of installation of work nodes and the antenna in overall [1]-[7]. The accuracy estimations of antenna tracking based on data on the precise geostationary orbit of the satellite are proposed in [8]. Antenna correct orientation with the given accuracy is also of great significance, taking into account the reflector's large weight and the requirements for dynamic characteristics of tracking process. In some AS constructions a correction in the separate regions of elevation angle setting are calculated by a special formula, taking into account the slope angle of the vertical axis [9]. However, the following study will be useful to make general recommendations to improve the quality of signal' reception.. Further the results of authors's practical experience in AS setting and monitoring, allowable deviations of installation parameters, their influence on the signal reception quality are presented.

2.Sources of Errors and Methods to minimize them

A. General classification of errors sources

The total error in the orientation of the antenna system is formed under the influence of many factors due to both design features and the influence of the external environment, systematic and random. Among the reasons of their occurrence it is possible to allocate methodical - due to astronomical coordinates determination inaccuracy – and instrumental, caused by angles measurement, influences of mechanisms angle sensors fastening, Support-Rotary-Device constructions influences, influence of the reflector construction. Behavior of them is unchangeable during a large period of time or changes according to the certain law. The most significant sources of errors in control system are: varyation of the inertia moments of modules with the angles of the reflector and with the ratio of positions of the antenna modules for different axes, change in stiffness of mechanical gear, changes in friction resistance, backlash, instability characteristics of electric drives. Systematic errors are caused by factors that are presented during a AS operating by a constant value or are changed with a time according to some law. Their influence on the AS control can be predicted due to mathematical modeling and neutralized to some extent in a constructive way.

.Random errors are due to the effect on the system of random processes. In a broad sense, all errors in the AS guidance are random with different correlation intervals.

The average value of the errors during the communication session are accepted as the systematic error of this cycle, the average value for a number of cycles - the systematic error of steering. The error random component is characterized by the value of standard deviation from the mean value.

Specific estimates of some the most influential errors arising in the AS setup and operation are given below, also an allowable deviations of installation parameters, their influence on the signal reception quality are presented.

B. Control of a AS installation accuracy

An inaccurate direction of initial AS platform setting cause to decreasing of antenna pattern effective area S:

$$S \sim S_{max} \exp(-(1.7 \frac{\theta}{\delta_{0.5}})),$$

where $\theta -$ the deviation angle of the maximum of the directional chart from the direction to the signal source;

$\delta_{0.5} -$ the diagram width at half power level.

The antenna axis will deviate on the angle from the position adopted as correct at the given azimuth and the elevation angles when the platform inclination on abscissa axis angle φ and ordinate axis σ take place. And

$$\delta = \cos^{-1}(\cos\varphi \cos\sigma).$$

The dependence of antenna pattern axis angle inclination on the abscissa axis angle φ and ordinate axis σ of platform inclination is shown in Fig.2 as the region in the values φ, σ (minutes), corresponding to the permitted values of platform angles inclination, in which the antenna axis deviation does not exceed an admitted level, in the problem under consideration $\delta_{max} = 6'$.

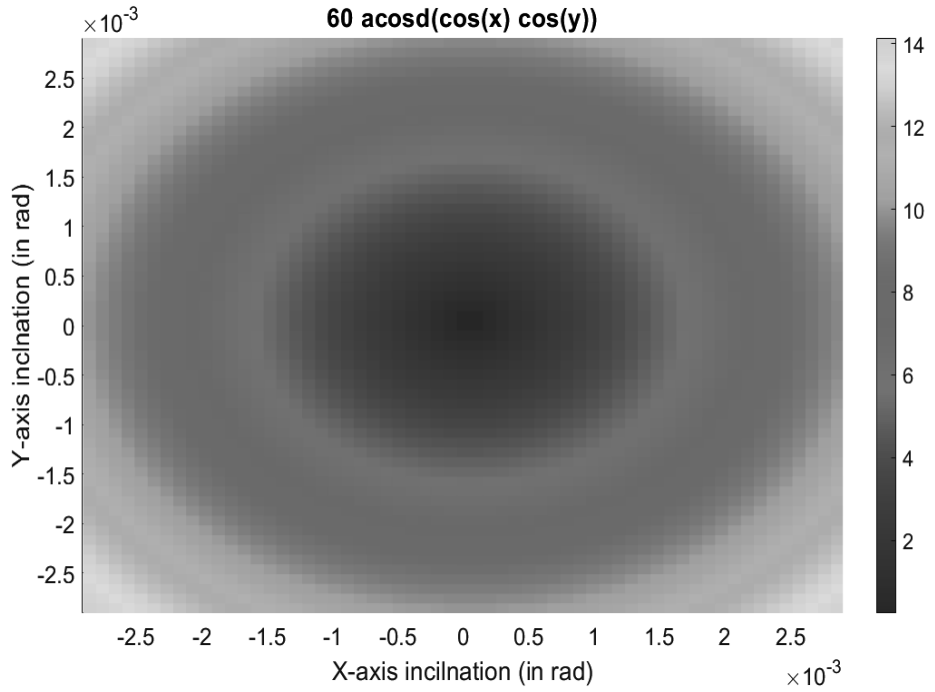

Figure 1. The antenna axis drift (in min), coursed by platform X-axis and Y-axis inclination on angles φ and σ

The method considered and the software developed have been used to simulate the influence of the platform deviation on the antenna setting, and thus, to improve the process of antennas installation and their maintenance.

C. AS properties as a dynamic object and their influence on control system accuracy

Construction of high-precision control systems for mass objects, , tracking of specified trajectories is actual for the synthesis of a control system for antenna systems in which the supporting structure of a turntable with large reflectors weighs from one to tens of tons. The main factors provided the accuracy of ground-based station are determined by:
a) the accuracy and rigidity of OPP design and guidance mechanisms as a whole and their individual parts, including the mirror system;
b) the accuracy of software control signals (targets) for guidance of the AS by means of the drives in accordance with the requirements of spacecraft support;

c) the accuracy with which the angular position of the executive axes can be determined at any time, ie the accuracy of the feedback sensors;
d) the dynamic accuracy provided by the power tracking drive in the conditions of perturbations and various kinds of noise acting on the system in the process of observing the spacecraft.
The increased accuracy of ground antenna stations (AS) with reflectors of large diameters (3-12 m) up to angular minutes units is desirable. To improve the quality of signal reception the following recommendations should be taken into account. A high dynamic accuracy of the antenna rays in the unit of angular minute at large angular velocities at several coordinates (up to 10 bps / sec) should be provided:

a) to ensure the required satellites pointing and tracking accuracy, to increase the reliability and to reduce the cost of AS control system the usage of asynchronous motors in conjunction with frequency speed regulation electronic devices are expedient.

b) the results of simulation and experimental researches show that the control system of AS with frequency-controlled asynchronous electric drive allowed to achieve the needed control accuracy on harmonic trajectories. Shortcomings of regulation during acceleration testing on a special test trajectory with more abrupt speeds change were found

c) the vector control method for asynchronous motors provides the smaller dynamic errors and better quality regulation. However, current consumption significant increasing at the low angular speeds during long-term operation may cause to motor overheat.

d) a frequency AM regulation based on the law U/f = const using RsIs - correction for torque support low turn based on the right parameters choice also can be used for pointing and tracking of AS on a lower dynamic ranges.

e) The frequency regulation can be also used for pointing and tracking of geostationary satellites or in AS with

In details the AS properties modelling as a dynamic management object allowed to synthesize the control system and to investigate the functionality and influence of regulation parameters quality of the AS control without using complex object was studied in [11,12].

The results of the experimental adjustment of the proportional and differential coefficient of feedback are shown in Fig. 2.

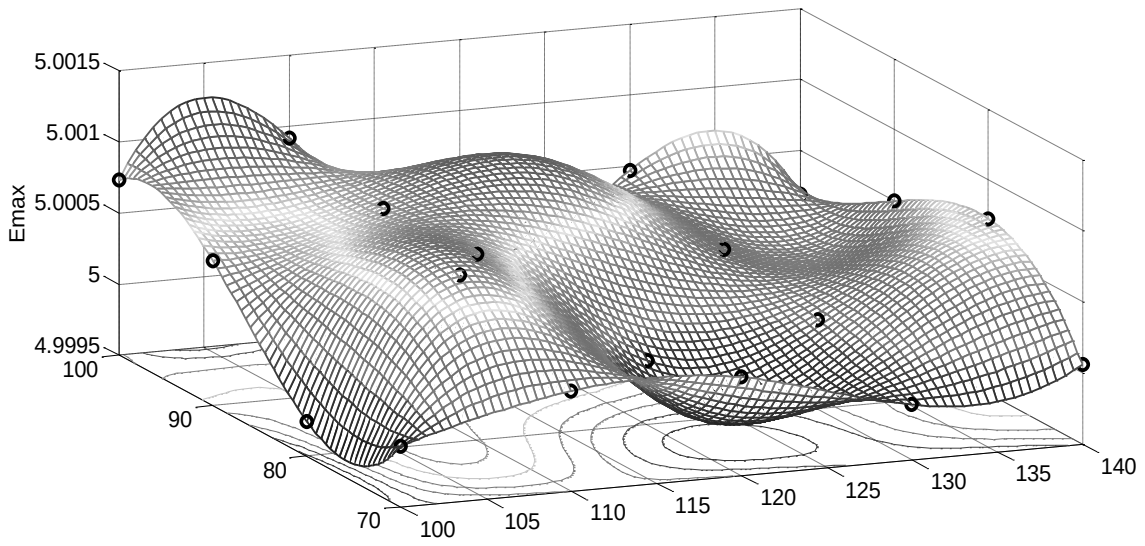

Figure 2. Spline approximation of control errors in the space of feedback coefficients kp=(70:10:100); and kd=(100:10:140);

By the spline approximation of control errors values in the space of feedback coefficients the map for optimal selection of feedback mode was constructed as is shown in Fig. 3.

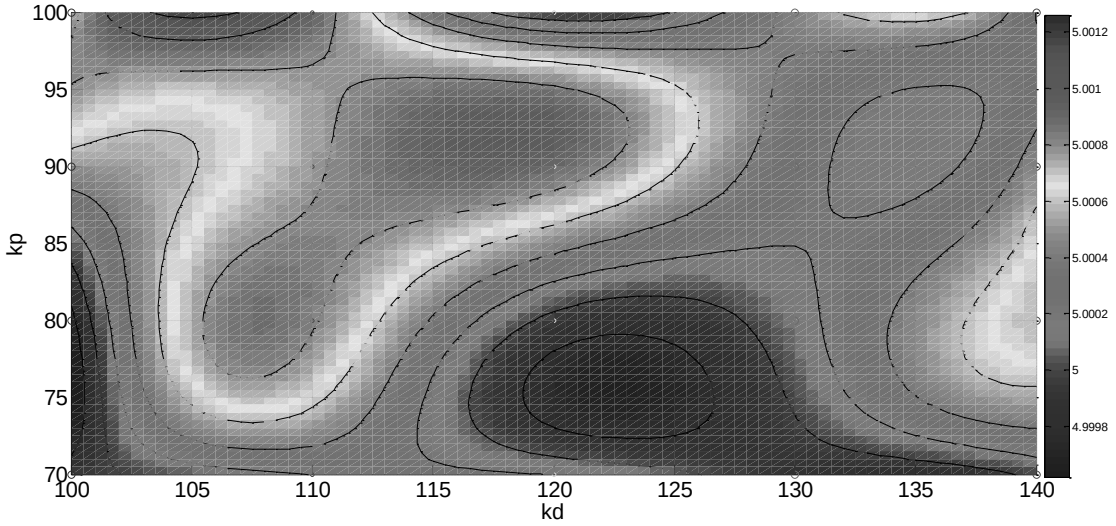

Figure 3. Errors map in the space of kp and kd for the feedback setting

D. Profile errors estimations

Manufacturing defects, inaccuracies in the assembly of the reflector surface elements, its weight and wind deformations cause a phase distortions of the antenna wave front and as a result the deterioration of electrical characteristics of the antenna, such as radiation pattern, directional coefficient, etc., influencing the guidance accuracy. If the mirror antenna operates in the range of centimeter wavelengths, it is necessary to control the deviation of the reflector surface with an accuracy of not less then ±0.9 mm for operating wave $\lambda = 3$ cm, or not less then ±0.3 mm for a wave of 1 cm. the case of less stringent requirements for the quality of the antenna, phase changes in $\Delta\varphi<\pi/2$ are allowed. The corresponding permissible deviation of the surface from the parabolic will be less then $\lambda/16$.

To control the reflector deviation from the theoretical one due to the influence of meteorological and operating conditions, it is important to optimize the reflector surface measuring procedure. These requirements are met by information systems for specialized measuring equipments or remote measurement of spatial coordinates, which in addition to the measuring device are outfited with means for automatic processing of measured data and visualization of the results for prompt decision-making, based on the total estimation of standard deviation of reflector surface displacements from theoretical profile. The map of reflector surface deviations from a test pattern on indications of the sensors placed in the specified positions is shown in Fig. 4.

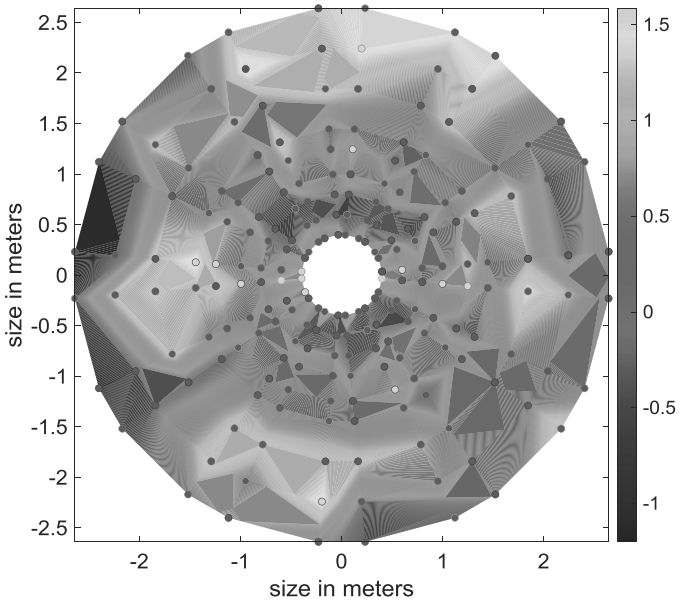

Figure 4. Reflector profile study due to a specialized equipment (in the places pointed)

When scanning the large sizes objects, the measuring device is placed from the object studied at the distances of several orders of magnitude greater than the profile deviation values, it is complicate to use the previous method. The peculiarity of research proposed in [13-17] is the application of a methodology that will allow to estimate the work surface profile displacement against reference sample due to its remote scanning, as shown in Fig.5.

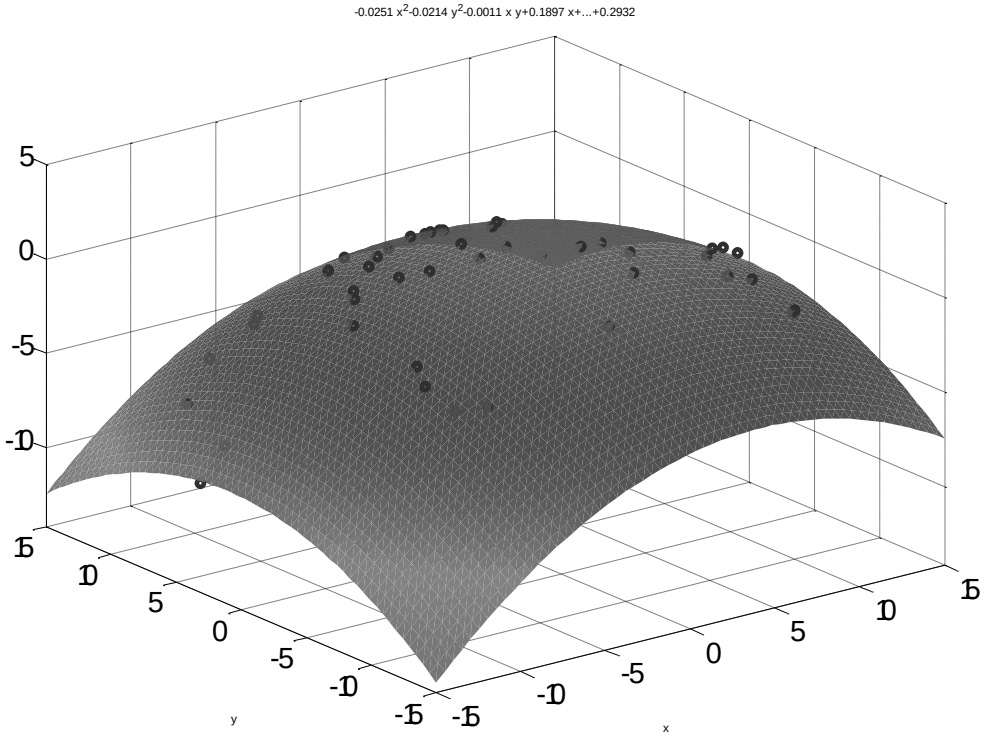

Figure 5. The reflector surface approximation by the least squares method according to remote measurement in separate points (distances in meters)

At first the surface studied measured coordinates are transformed into coordinates of pattern canonical system than real surface is approximated by least square method to pattern. The standard deviation of measured data errors is taken as a criterion for compliance the surface investigated with the design requirements. A similar approach ss proposed in [18].

E. The impact of meteorological factors on the guidance accuracy

As shown in [19,20], as a result of static wind load caused by wind flow with speed *V* AS is under the action of the moment

$$M = a\frac{\rho V^2}{2}S$$

where *p* -wind flow density; *V*- average wind velocity; *S* - the area of the reflecting surface of AS; *a*- aerodynamic coefficient, depending on *S.*

The aerodynamic coefficient wind load separate values, was obtained from the experimentally study in [21] in the process of purging the AS model with a mirror diameter of 32 m in the wind tunnel. Due to obtained data spline approximation in the space of elevation and azimuth and their visualization, as shown in Fig. 4, a wind moment map was reconstructed.

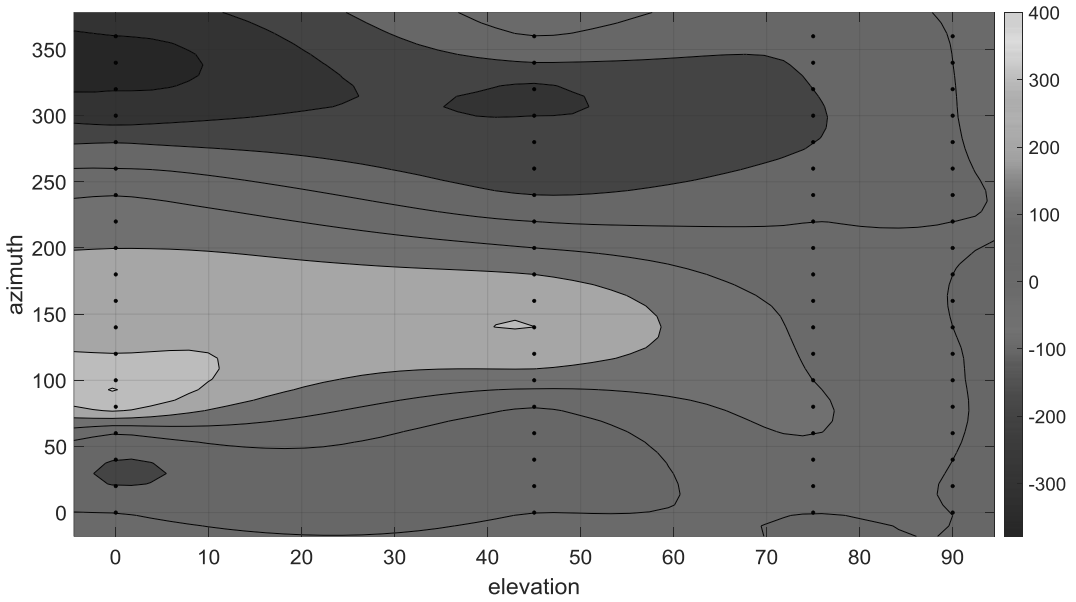

Figure 4 Distribution of aerodynamic coefficient of wind load for the antenna mirror with diameter of 32 m depending on its spatial orientation (in the coordinates of the angle of place and azimuth)

In the general case the nature of the terrain (open, with separate topographic fluctuations, built-up area or rough terrain), as well as the speed profile (location of the AS above ground level) should be taken into account

3.Conclusions

The error reducing methods based of constructive ways often are complicate mechanical parts of SRD and lead to increase costs for their projecting, adjustment and maintenance. To prevent additional correction of AS settings during its operation it is necessary to carry out a preliminary assessment of the limits of possible errors at the goal guidance process

The antenna axis drift when mounting causes the errors in installation of azimuth and of elevation angles. It may cause the communication session weakening. According to the estimates given, it is established deviations of the carrier platform at which the deviation of antenna pattern axis is within acceptable limits.

The vector control method for asynchronous motors provides the smaller dynamic errors and better quality regulation. However, current consumption significantly increase of AM in the low angular speeds during long-term operation may cause to motor overheat. A frequency AM regulation based on the law U/f = const using R_sI_s - correction for torque support low turn based on the right parameters choice also can be used for pointing and tracking of AS on a smaller dynamic ranges.

It is also important to correctly set the coefficients of the PID controller in the feedback line of the control system. Spline approximation of error values in the space of discrete tested values kp and kd allows us to select settings with minimal error for a particular system.

The reception quality is also affected by the possible deviation of the antenna profile from the theoretically calculated one. The profile control in the operating mode can be carried out periodically by means of remote measuring devises completed with the corresponding software for deviations calculation of the measured surface from the profile stated.

4. Acknowledgement:

Work is partially supported by: Latvian Science Council project Nr: lzp-2020/2-0121 "Joint Latvian-Ukrainian study of peculiar radio galaxy “Perseus A” in radio and optical bands”.

5.References

1. ITU-R SM.2424-0 (06/2018) *“Measurement techniques and new technologies for satellite monitoring”* https://www.itu.int/dms_pub/itu-r/opb/rep/R-REP-SM.2424-2018-PDF-E.pdf

2. Kiselev, A., Medvedev, A., Menshikov, V. (2003). *Astronautics. Summary and Prospects*. Springer-Verlag Wien.

3. Smida, B., Efthymoglou, G.P., Ghassemzadeh, S.S., Tarokh, V. (2011). On Effects of antenna pointing accuracy for on-the-move satellite networks. *Transactions on vehicular Technology*, *60*(4).

5. Liang, W., Jia, Z., Kang, l., Hong, J., Lei, B., Zhang, Q., Chen, Q. (2018). An accurate measurement method for azimuth pointing of spaceborne synthetic aperture radar antenna beams based on ground receiver. *Sensors (Basel), 18*(8).

6. Wang, Y. J., Zheng, A. V., Fu, Y. Q., Liu, Y. Q. (2011). Measurement of tracking accuracy of antenna using precise geostationary satellite orbit. *Applied Mechanics and Materials, 128-129*, 616–619.

7. Smida, B., Efthymoglou, G. P., Ghassemzadeh, S. S., Tarokh, V. (2011). On Effects of antenna pointing accuracy for on-the-move satellite networks. *Transactions on vehicular Technology*, *60*(4).

8. Palamar, M., Chaikovskyi, A., Pasternak, Y., Palamar, Y. (2015). Improvement of metrological characteristics of the antenna system using smart angle sensor. *Intelligent Data Acquisition and Advanced Computer systems. Proceedings of the 8th IEEE International Conference*.

9. Stutzman, W. L., Thiele, G. A. (1981). *Antenna theory and designe*. New York: John wiley and sons.

10. Palamar, M., Chaikovskyi, A., Pasternak, V., Shevchuk, V., Yavorska, M. (2020). The Influence of Antenna Installation Accuracy on Quality of Signal Reception, *International Symposium on Smart and Wireless Systems within the Conferences on Intelligent Data Acquisition and Advanced Computing Systems, Proceedings of International Conference*. Dortmund, German.

11. Palamar, M. (2012). Smart Station for Data Reception of the Earth Remote Sensing. In *Remote Sensing - Advanced Techniques and Platforms* (pp. 341-371). Rijeka: InTechBook.

12. AC Induction Motor Control Using Constant V/Hz Principle and Space Vector PWM Technique with TMS320C240. – Application Report: SPRA284A, Texas Instruments, 1998.

13. Palamar, M.I, Zelinskyj, I.M., Yavorska, M.I. (2017). The device for remote measurements of geometric dimensions and positions. Intelligent Data Acquisition and Advanced Computing Systems: Technology and Applications (IDAACS). Proceedings of the 9th IEEE International Conference. Bucharest, Romania.

14. Zelinskyj, I.M., Palamar, M.I, Yavorska, M.I. (2018). The optical device for coordinate measurement. *Coordinate Measuring Technique*, Proceedings of the XIII International Scientific Conference. Bielsko-Biala, Poland.

15. Zelinskyj, I.M., Palamar, M.I, Yavorska, M.I. (2019). Optical system for control of antenna mirror shape. *Scientific Journal of TNTU, 93*(1), 92–101.

16. Palamar, M., Yavorska, M., Zelinskyy, I., Strembitskyi, M. (2021). Computational intelligence application to reproduce a map of surface deviations based on the results of remote measurements, *Intelligent Data Acquisition and Advanced Computing Systems: Technology and Applications*, Proceedings of the International Conference. Cracow, Poland.

17. Zelinskyy, I., Palamar, M., Yavorska, M. (2021). Application of a Laser Total Station to Control the Shape of the Mirror Antenna Reflector. *Intelligent Data Acquisition and Advanced Computing Systems: Technology and Applications*, Proceedings of the International Conference. Cracow, Poland.

18. Власенко, В.П., Мамарєв, В.М., Ожінський, В.В. (2021). Методика побудови первинної матриці похибок радіотелескопа РТ-32 в автоматизованому режимі. *Космічна наука і технологія*, *27*(3), 66–75. - Режим доступу: http://knit.mao.kiev.ua/uk/archive/2021/3. doi: 10.15407/knit2021.03.066.

19. Cohen, E., Velossi, Sun, S. (1966). Calculaton of wind forces and preasures on antennas. *Design and Construction of Large Steerable Aerials*, Proceedings of the Brtish IEE Conference. London, UK.

20. Blaulock, R.B., Dayman, B., Fox, N.I. (1964). Wind tunnel testingof antennas models. Large Radio Antennas, Proceedings of the Conference New York Academy Sciensies. New York, USA.

21. Belyansky, P.V., Sergeev, B.G. (1980). *Control of Terrestrial Antennas and Radio Telescopes*, Moscow: Soviet Radio.

MECHATRONIC APPROACH TO THE DESIGN OF A TRIAXIAL ANTENNA WITH BACKLASH MINIMIZATION BY THE CONTROL SYSTEM

Mykhaylo Palamar[1], Vladislavs Bezrukovs[2], Yuriy Nakonechny[3], Andriy Palamar[4], Mykhailo Strembicky[5], Yuriy Pasternak[6]

[1]Ternopil National Ivan Puluj Technical University, Ruska str., 56, Ternopil, Ukraine; palamar.m.i@gmail.com
[2]Engineering Research Institute Ventspils International Radio Astronomy Centre (ERI VIRAC) of Ventspils University of Applied Sciences (VUAS), Ventspils, Latvia; vladislavsb@venta.lv
[3]Ternopil National Ivan Puluj Technical University, Ruska str., 56, Ternopil, Ukraine; vmestoram@gmail.com
[4]Ternopil National Ivan Puluj Technical University, Ruska str., 56, Ternopil, Ukraine; palamar.andrij@gmail.com
[5]Ternopil National Ivan Puluj Technical University, Ruska str., 56, Ternopil, Ukraine; m.strembitskyy@gmail.com
[6]Ternopil National Ivan Puluj Technical University, Ruska str., 56, Ternopil, Ukraine; yuriy.pasternak@gmail.com

Abstract: The features and advantages of the support-rotating platforms design for the antenna systems with three axes are analyzed in the paper. The expediency of using such systems for the satellite tracking without signal losses in the zenith area relative to the coordinate of the antenna system is reasoned. It is necessary in order to expand the antenna system functionality, improve the performance of the antenna device, and increase the control system efficiency and the information reliability from the spacecraft as a whole. The developed design of the 3-axial support-rotating platform is described. The platform is built on a modular principle using of modern autonomous rotary actuators, which are combined by a special design. This approach is proposed in order to ensure backlash sampling using special software algorithms of the support-rotating device control system.

Keywords: *antenna system, 3-axial rotary platform, control system, satellite tracking trajectories, "dead zones", rotary mechanism.*

1. Introduction

The so-called "dead zones" of space object tracking are available for classic azimuth-angular support-rotating devices of antenna systems. In order to increase the reliability of information reception by antenna systems it is important to minimize the dead zones area. To achieve this goal it is necessary to upgrade the design of the antenna system support-rotating devices. The design of a 3-axial antenna, which solves this problem is proposed in the paper.

2. Support-rotating device of the antenna system with three pointing axes

Antenna support devices (platforms) are designed to ensure the reliable exchange of digital information between ground stations and spacecraft (satellites). 2-axial rotary platforms have become predominant in practice. Their advantages are simplicity of a design, rather simple control systems and reasonable cost. They all consist of two electric drives. Guidance of the antenna axis in a given direction is provided by rotating of the antenna mirror relative to the azimuth and angular axis.

Although such 2-axis platforms have different kinematic schemes, but they all have a disadvantage. It is manifested when the trajectory of the accompanying spacecraft intersects the direction of the stationary (first) axis of rotation. Near this point, the speed of rotation relative to the fixed axis increases sharply. At the point of intersection, it reaches infinite value. Since the acceleration and rotation speed of the antenna drives are limited, and so called "dead zones" are formed in these areas. As a result, there are interruptions and loss of information. In addition, the speeds of tracking on one of the axes increase for trajectory tracks that are located near the special points. This leads to an increase in the dynamic guidance errors [1] and requires increased requirements for the dynamic characteristics of the antenna electric drive.

To avoid "dead zones" of satellite support in the areas of the zenith and horizon, it is necessary to use more complex 3-axial rotary platforms and appropriate control systems [2]. This is especially important for antenna systems of satellite tracking. In such systems, loss of communication or untimely issuance of a satellite command can cause significant economic and other losses.

The presence of the third axis is the essence of the 3-axial rotary platform. With this axis, the main vertical axis of the antenna column is inclined at a small angle (about 15^0). This design has three degrees of freedom and allows you to follow the trajectories of satellites through the zenith without "dead zones" [3]. The design of such a 3-axis antenna was developed at the Instruments and Control-measurement Systems Department of the Ternopil National Ivan Puluj Technical University by order of the Kharkiv Research Institute of Radio Engineering Measurements. It is designed to work as part of a ground station for the receiving and transmitting of information to a satellite. The development was carried out in accordance with the participation in the international Egyptian-Ukrainian project on the creation in

Ukraine. This project includes the launch of the satellite "EgyptSat-1" and the creation of ground-based infrastructure for its management.

A certain disadvantage of this 3-base antenna was its higher cost, complexity of design and high requirements for the accuracy of electromechanical drives. Figure 1 shows the developed design of the support-rotating platform of the antenna, in which these shortcomings are absent or minimized. The main technical characteristics of the platform are given in table 1.

The antenna has two azimuth axes E1 and E3. The E1 axis is inclined to the vertical azimuth axis E3 at an angle of 15 degrees. A modular electromechanical drive is used to rotate the antenna mirror relative to the E3 axis. It consists of a cylindrical welded housing on which a sealed rotary mechanism 1 of the company "IMO" (Germany) is fixed.

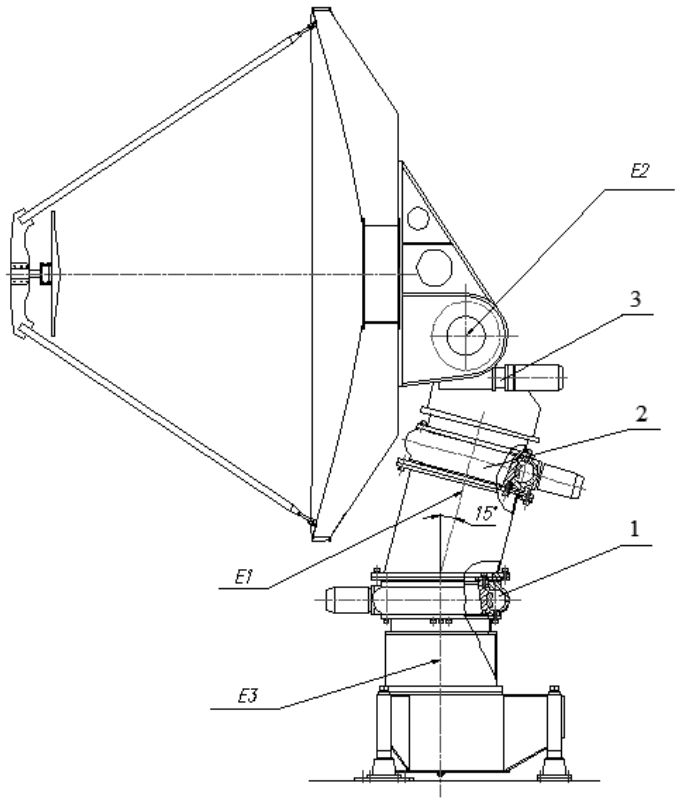

Fig. 1 Design of 3-axis antenna with sealed rotary electromechanical modules

This rotary mechanism is a double worm drive WD-H 0490/3 together with two high-precision planetary-gear reducers of the company "SUMITOMO". This mechanism also includes two asynchronous electric motors with frequency control [4], with electromagnetic brakes, electromagnetic shaft, incremental shaft and stand-alone cooling fans.

Table 1

The main technical characteristics of the antenna rotary platform

Parameter	Nominal value
Antenna mirror diameter, m	3…5
Number of control coordinates, pcs.	3
Limit angles of rotation, deg. on the axis E1 on the axis E2 on the axis E3	 ±170 120 ±170
Maximum speed, deg/s on the axis E1 on the axis E2 on the axis E3	 8 4 8
Maximum antenna acceleration, deg/s^2 on the axis E1 on the axis E2 on the axis E3	 1 0.3 1
Drive power on each axis, kW	1.1

"IMO" rotary mechanisms are delivered as a ready-to-install sealed module in order to replace a number of individual elements and components of the structure. This feature simplifies the construction and reduces the time for installation and dismantling of the device [5,6]. According to this design, it is possible significantly reduce the cost of the drive compared to the individual manufacture of such components.

Such universal modules have a fairly wide range of torques on the output shaft. This allows them to be successfully used in various components and mechanisms, including in the drives of antenna systems [7,8]. With the use of electric motors of the different power, the same rotary device can be used for drives with small and very large torques. For example, the torque on the azimuth axis E3 of the developed antenna, required for its guidance on this axis with the specified parameters (speed, acceleration), is equal to the moment of resistance of all opposing forces of the drive. It can be calculated by the formula:

$$T_{E3} = T_{dyn} + T_G + T_{wind} \tag{1}$$

where T_{dyn} – dynamic moment; T_G weight moment (from weight loads); T_{wind} – aerodynamic moment (from wind loads).

Dynamic load moment T_{dyn} is manifested by the rotation of the antenna with acceleration ε_{E3}. As this moment is reduced to the E3 axis, so it is calculated by the formula:

$$T_{E3} = T_{dyn} + T_G + T_{wind} \tag{2}$$

where I_Σ – the total moment of inertia of all moving masses relative to the axis E3.

The calculation is performed for the antenna diameter $D = 5\,m$ and weight of the antenna mirror $G_{mir} = 9700\,N$ Assume in the first approximation that the mass of the mirror is concentrated at one point in the distance $L_1 = 1.44\,m$ from the azimuth axis of rotation E3 (fig. 2).

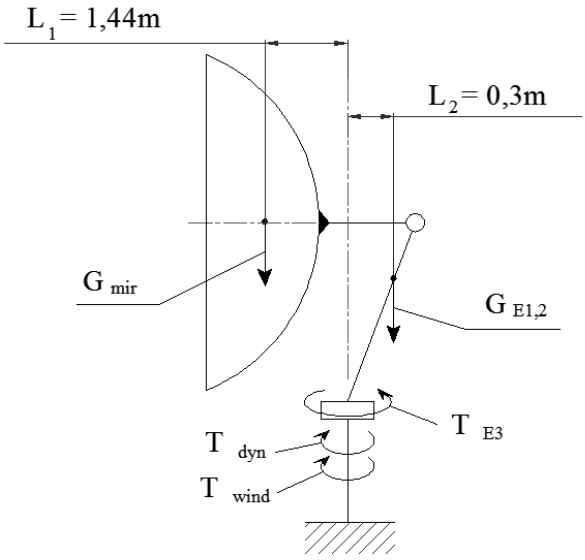

Fig. 2 Calculation scheme for determining of the torque on the azimuth axis E3

Then the moment of inertia of the antenna mirror

$$I_{mir} = \frac{G_{mir}}{g} \cdot (L_1)^2 = \frac{9700}{10} \cdot 1,44^2 = 2011\,kg \cdot m^2 \tag{3}$$

To simplify the calculations, we also assume that the weight of all parts and rotary actuators on the E1 axis and the angular axis of the E2 is equal to $G_{E1,2} = 17000\,N$. This weight is concentrated at one point in the distance $L_2 = 0.3\,m$ from axis E3. Then the moment of inertia of these moving masses of the antenna is

$$I_{E1,2} = \frac{G_{E1,2}}{g} \cdot (L_2)^2 = \frac{17000}{10} \cdot 0,3^2 = 153\,kg \cdot m^2 \tag{4}$$

Total moment of inertia is

$$I_{\Sigma} = I_{mir} + I_{E1,2} = 2011 + 153 = 2164\ kg \cdot m^2 \tag{5}$$

Dynamic moment on the E3 axis during its rotation with acceleration $\varepsilon_{E3} = 1\text{deg}/s^2 = 0.017 s^{-2}$ will be equal to

$$T_{dyn} = I_{\Sigma} \cdot \varepsilon_{E3} = 2164 \cdot 0,017 = 36,8\ Nm \tag{6}$$

Weight moments T_G depend on the weight of individual antenna components and can reach fairly large values in large systems. However, during azimuth mounting, the weight loads are directed parallel to the azimuth axis. For this calculation, this is the E3 axis. In this case, the weight moment is $T_G = 0$

The wind load on the working surface of the antenna mirror from the wind flow is calculated by the formula:

$$F_{wind} = \alpha \frac{\rho \cdot V^2}{2} S \tag{7}$$

where α – coefficient of the aerodynamic resistance; ρ – wind flow density; V – wind speed; S – antenna mirror area. For mirror diameter $D = 5\ m$ at maximum wind speed $V = 25\ m/s$ the wind load is $F_{wind} = 11000\ N$.

It is known that the maximum moment from the wind load relative to the azimuth axis E3 will act when the tilt of the focal axis to the air flow at an angle of 60^0. The lateral wind load in this position is equal to half of the full wind load F_{wind}, and the point of application is the central point of the half of the mirror. Then the aerodynamic moment from the wind loads is

$$T_{wind} = \frac{F_{wind}}{2} \cdot \frac{D}{4} = \frac{11000 \cdot 5}{8} = 6875\ Nm \tag{8}$$

Total torque on the azimuth axis E3 is

$$T_{E3} = T_{dyn} + T_G + T_{wind} = 36,8 + 0 + 6875 = 6912\ Nm \tag{9}$$

To implement such torque on the E3 axis, a rotary mechanism WD-H 0490/3 from "IMO" company is used. The torque on the output shaft of this mechanism can reach 49.5 *kNm*. When we use a double drive with two electric motors, the torque is doubled. Gear ratio of the mechanism is $i_{WD} = 40$.

The choice of this standard size with the increased torque is explained by convenience of its installation on a bearing column of a basic and rotary platform. The diameter of the cylindrical column is 630 mm, which coincides with the diameter of the centres of the mounting holes of the drive. This allows you to simplify its installation on the column without additional components and devices.

To ensure a given speed of rotation along the axis E3, it is necessary to perform a kinematic calculation of the drive shown in fig. 3.

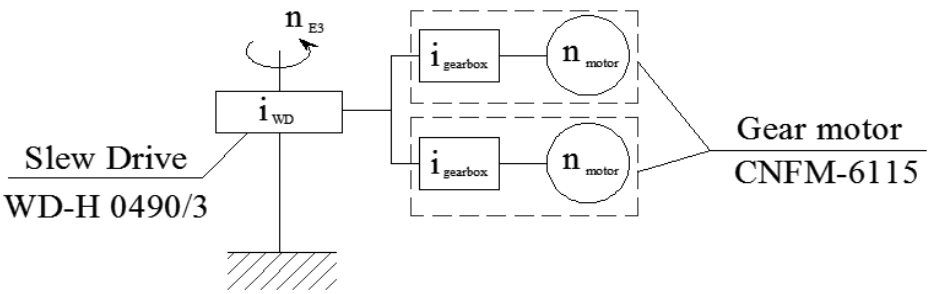

Fig. 3 Rotary drive with two motors

The calculation is based on the average speed $n_{E3} = 5\frac{\deg}{s} = 0.83\,rpm$. Maximum speed $n_{E3\,max} = 8\frac{\deg}{s} = 1.33\,rpm$ will be provided with frequency control of the rotational speed of the selected induction motor. As such motor we accept the 4-pole asynchronous electric motor with speed of rotation $n_{motor} = 1400\,rpm$. Such electric motors are well usable to frequency control of speed. Then the required gear ratio of the intermediate gearbox is equal to

$$i_{gearbox} = \frac{n_{motor}}{i_{WD} \cdot n_{E3}} = \frac{1400}{40 \cdot 0,83} = 42,2 \tag{10}$$

The minimum power of the electric motor is calculated by the formula:

$$N_{monor\ \min} = \frac{T_{E3} \cdot \omega_{E3}}{\eta_{WD} \cdot \eta_{gearbox}} = \frac{6912 \cdot 0,83 \cdot 2 \cdot \pi}{60 \cdot 0,6 \cdot 0,8} = 2085\,W \tag{11}$$

Since the used rotary mechanism WD-H 0490/3 is double (it has two motors), and we accept two 4-pole asynchronous motors with a capacity of 1.1 kW. For such scheme the motor-reducer CNFM-6115 of the «SUMITOMO» company with a power of 1.1 kW, with the planetary reducer of the increased accuracy and with a gear ratio is optimally suitable $i_{gearbox} = 32.8$. The maximum torque on the output shaft is $T_{gearbox} = 304\,Nm$.

Maximum speed on the axis $n_{E3max} = 1.33\,rpm$ E3 is achieved by increasing the speed of the motor

$$n_{motor\ \max} = n_{E3\,\max} \cdot i_{WD} \cdot i_{gearbox} = 1,33 \cdot 40 \cdot 32,8 = 1745\,rpm \tag{12}$$

For this speed, the motor is accelerated by increasing of the current frequency to 62.3 Hz using a frequency control device.

It should be noted that the used rotary devices, among other things, also perform the function of the backlash mechanism [9-11] . In these devices, one worm wheel 1 is driven by two worms 2 and 3. So these worms are driven by two motors 4 and 5 (with gearboxes 6 and 7), as it is shown in fig. 4.

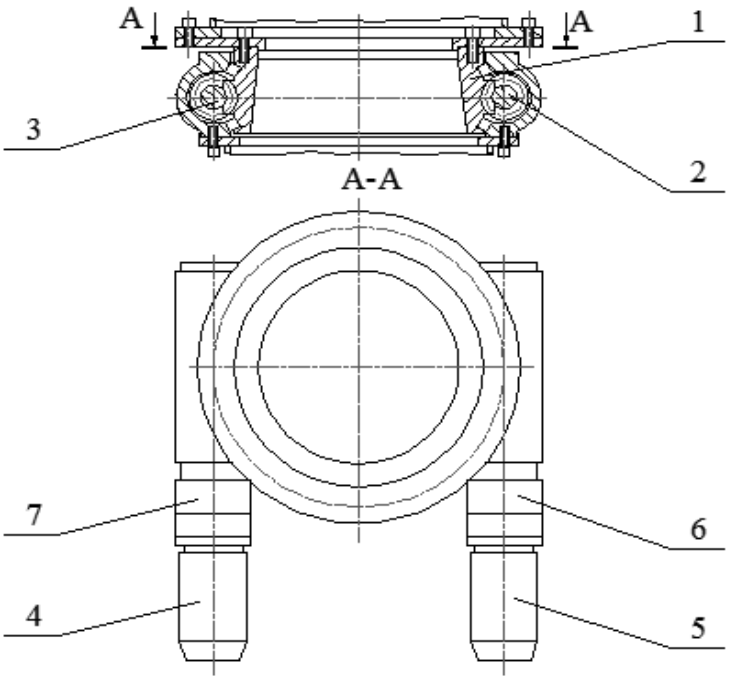

Fig. 4 Modular sealed rotary mechanism with double drive

They are identical and can work in parallel and synchronously. However, as we know, there are no absolutely identical mechanisms. As practice shows, the torques and friction losses (efficiency) of both drives, although slightly,

will be different. Then, due to the difference in torques on the drive worms of both drives, the lateral clearances (dead travel) in the engagement between the turns of the worm wheel 1 and two worms 2 will be selected. These clearances are directly transmitted to the antenna axis. Therefore, their elimination significantly increases the accuracy of working of the aiming angles along this axis.

To modulate the antenna mirror relative to the other two axes E1 and E2, the similar modular rotary actuators 2 and 3 of the company "IMO" are used (fig. 1).

3. Conclusions

The presence of the third axis in the support-rotating platform of the antenna system makes it possible to follow the trajectory of the satellite, which passes through the zenith, relative to the coordinates of the antenna without "dead zones". At the same time communication with the satellite for any directions of its movement is not lost.

The use of modern sealed modular rotary mechanisms, which is ready for installation, in the construction of the support-rotating platform allows to simplify the design of the platform. There is no need to install a number of elements and mechanisms that are already present in these drive mechanisms, such as angle sensors, manual drive, and backlash sampling. As a result, the cost of the structure was reduced. The installation and repair process was simplified.

Acknowledgement:

Work is partially supported by: Latvian Science Council project Nr: lzp-2020/2-0121 "Joint Latvian-Ukrainian study of peculiar radio galaxy “Perseus A” in radio and optical bands”.

References

1. Palamar, M., Nakonetchnyi, Y., Apostol, Y., Strembicky, M., Mashtalyar, S. (2018). Design source errors analysis in the angle measure devices to the precision antennas. *Scientific Journal of TNTU*, *92*(4), 98-103. doi:10.33108/visnyk_tntu 2018.04.098.

2. Palamar, M., Pasternak, Y., Palamar, A., Poikhalo, A. (2017). Precision tracking of the trajectory LEO satellite by antenna with induction motors in the control system, *Intelligent Data Acquisition and Advanced Computing Systems: Technology and Applications (IDAACS)*, Proceedings of the 9th IEEE International Conference. Bucharest, Romania.

3. Stone, M. L., Banner, G. P. (2000). Radars for the detection and tracking of ballistic missiles satellites and planets. *Lincoln Laboratory Journal*, *12*(2), 217-244.

4. Krishna, C., Meerimatha, G., Kumar, U. (2013). Indirect vector control of induction motor using Pi speed controller and neural networks. *International Journal of Modern Engineering Research (IJMER)*, *3*(4), 1980-1987.

5. Varlamov, I.D., Zuiko, V.V., Kozub, A.M., Pashkov, D.P. (2015). Space Systems of Earth Remote Sensing for Duplically Application. *A TextBook, National University of Defense of Ukraine*.

6. Palamar, M. (2005). Neurocontroller to Tracking Antenna Control of Information Reception from Earth Remote Sensing Satellites. *Intelligent Data Acquisition and Advanced Computing Systems: Technology and Applications, Proceedings of the IEEE Workshop* . Sofia, Bulgaria.

7. Kilsuregawa, T. (1990). *Advanced technology catellite communication antennas. Electrical mechanical design*. Artech House, Boston-London.

8. Palamar, M. (2012). Smart Station for Data Reception of the Earth Remote Sensing. *Remote Sensing - Advanced Techniques and Platforms. Rijeka: InTechBook*.

9. Zhang, Y., Pan, S., Deng, J. (2016). Methods for measuring and compensating ball screw error on multi-mode industrial CT scanning platform. *Measurement, Instrumentation and Automation (ICMIA)*, Proceedings of the 5th International Conference.

10. Chang, S.H., Herrin, G.D. (1991). Surface profile error evaluation 91-10 procedures using a coordinate measuring machine. *Technical report 91-10*. The University of Michigan.

11. Bolli, P., Mazzarella, G., Montisci, G., Serra, G. (2008). An Alternative Solution for the Reflector Surface Retrieval Problem. *Progress In Electromagnetics Research*, PIER 82, 167-188.

ELABORATION OF THE POLARIZER'S CONSTRUCTION FOR WORK IN Ka-BAND

Serhij Duda[1], Hryhorij Khymych[2]

Ternopil National Ivan Puluj Technical University, Rus'ka str. 56, 46001, Ternopil, Ukraine, sciencepark.t@gmail.com

Abstract: The problems of the polarizer`s construction over the basis of the circular waveguide for work in Ka-band are highlighted in the article. The purpose of the article is to establish the possibility of using the proposed design for the construction of high-tech Ka-band polarizers and to prove the correctness of analytical expressions for determining the structural dimensions by experimentally obtained characteristics. The analysis of the current decisions from the point of view of construction and technology is held. On the conclusion had been drawn more technological polarizer`s construction with the calculation of the main constructive sizes is proposed.

Theoretical principles of construction and calculation of structural dimensions of the C and Ku ranges polarizers' phase-shifting sections are covered in detail in the works of modern researchers and tested on real devices. However, while constructing AFT elements designed to operate in higher frequency operating bands, such as the Ka-band (20/30 GHz), there are certain difficulties, the solution of which continues.

In order to check the proposed decision, an experimental model of the polarizer was made and an investigation of the main characteristics corroborating the right theoretical assumption was held. For a practical study of the proposed design, a mock-up of a polarizer based on a round waveguide with an inner diameter of 11 millimeters was made. In the prototype, the rod structure was implemented in the form of five pairs of adjusting screws with a diameter of one millimeter. The final length of the polarizing plate, taking into account the smooth transitions designed to align the plate with the waveguide, was defined as the sum of the lengths of its regular part and one smooth transition multiplied by 0.9.

The experimentally obtained characteristics confirm the possibility of using the proposed design for the construction of high-tech Ka-band polarizers, and the correctness of analytical expressions for determining the structural dimensions. Further development of the proposed solution may be the analysis and finding the necessary analytical relationships between the structural dimensions of the rod and dielectric structures in order to expand the operating range of the polarizer.

Keywords: Polarizer, frequency, metal-rod type, Ka-band (20/30 GHz), design.

Problem Statement.

Increasing requirements for the information resource of modern satellite communication channels determines the need to create radiant systems of mirror antennas operating at higher frequencies and in wider frequency bands for both reception and transmission. To increase the bandwidth of communication channels on modern satellites, there is also a requirement to use signals with orthogonal polarization for both reception and transmission. In addition to the fact that modern irradiation systems must operate in a wide frequency band with signals of different polarization, it is also necessary that the irradiator has a small mass and size.

Analysis of recent research and publications.

Modern irradiation systems consist of three main components, namely: irradiator, polarizer, and orthomode selector. The components of frequency polarization signal processing include a polarizer and an orthomode selector. A polarizer is a device that provides primary polarization processing of received signals. In the case of circular polarization signals, the latter are converted into signals with linear polarization, and in the case of signals with linear polarization, it is possible to change the orientation of their dimensions.

An orthomode selector is a device that provides further frequency and polarization selection of signals into individual channels [1]. In fact, the orthomode selector is a passive waveguide splitter [2; 3], the function of which is the frequency and polarization selection of signals received by the antenna. [4; 5]. Given the tendency to polarize the communication channels, the task of achieving high values of the cross-polarization decoupling is a significant problem. Successful examples of technical solutions of such problems are in the C- and Ku- frequency bands, and in solving similar problems in the Ka-band there are some difficulties in achieving the required values of the cross-polarization decoupling.

Highlighting previously unsolved parts of the overall problem.

Theoretical principles of construction and calculation of structural dimensions of phase-shifting sections of polarizers of the C- and Ku- ranges are covered in detail in the works of modern researchers [1-4] and tested on real devices that have found application. However, when designing AFT elements designed to operate in higher frequency

operating bands, such as the Ka-band (20/30 GHz), when designing such devices, there are certain difficulties, the finding the solution of which continues.

The purpose of the article.

To establish the possibility of using the proposed design for the construction of high-tech Ka-band polarizers, and the correctness of analytical expressions for determining the structural dimensions by experimentally obtained characteristics.

Presenting main material.

In antenna-feeder paths of antenna systems (AS), for polarization signal processing, polarizers based on circular waveguides are widely used. As is known, such devices are structurally a segment of a circular waveguide where there are certain longitudinal inhomogeneities at the angle of 45 degrees to the polarization dimension of the incident wave, which create a phase shift between the components of the electric field, respectively parallel and perpendicular to the inhomogeneity plane. In the general, the value of the phase shift in the polarizers is determined as follows

$$\Theta = (\beta_1 - \beta_2)l \qquad (1),$$

where $\beta_{1,2}$ - phase constants of the vector E components;

l - the length of the phase shift section.

Depending on the AS type and purpose, the phase shift between the components should be 90 degrees (circular polarization) or 180 degrees (linear polarization). The main task posed in the development of such devices is to compensate for the variance of the phase shift in a given band of operating frequencies, resulting from the specified values of the ellipticity factor, or cross-polarization solution of the AS.

At the moment, in the antenna-feeder paths (AFP), the most widely used designs of polarizers, e.g. metal-rod, dielectric and metal-dielectric types, schematic images of which are shown in Fig.1 (a,b,c)

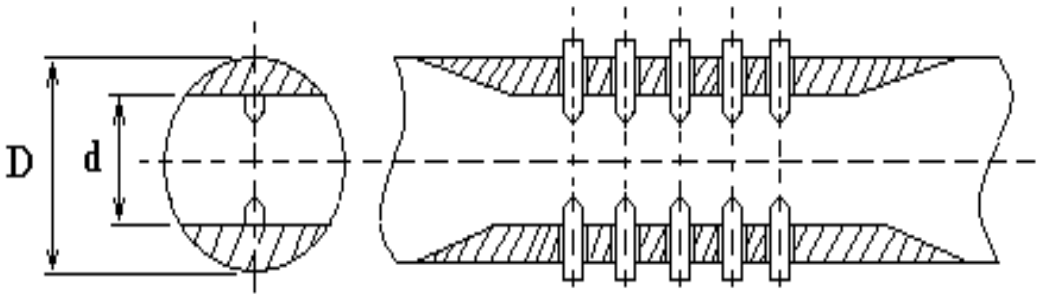

Fig.1a. Polarizer metal-rod type

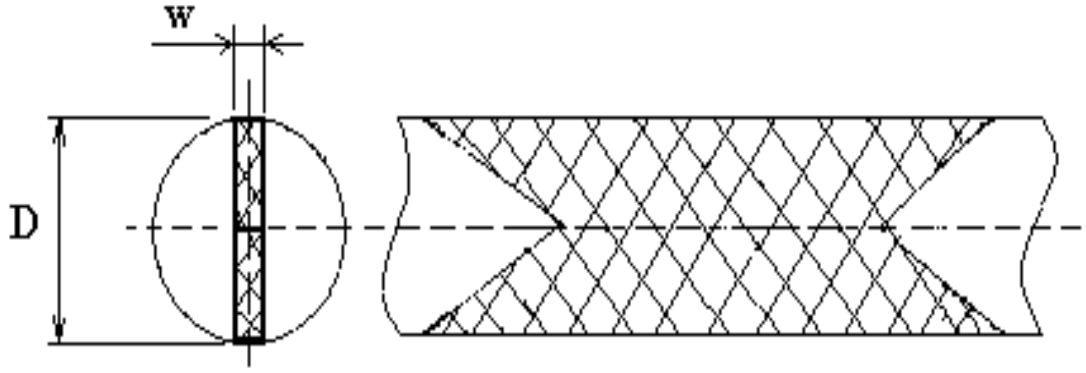

Fig.1b. Polarizer dielectric type.

The principles of construction and calculation of the design dimensions of phase-shifting sections of these types of polarizers, elaborated in sufficient detail theoretically [1, 2, 3, 4], and tested on real devices that are used in different operating ranges at frequencies from 4 to 14 GHz. However, the development of AFP elements designed to operate in higher frequency operating bands, such as Ka-band (20/30 GHz), faces some difficulties associated with the following factors: significant increase in the requirements for the required accuracy of manufacturing elements; decrease in the geometric dimensions of the elements themselves; grow of the influence of heterogeneity of physical and geometrical characteristics of materials on radio technical characteristics of devices.

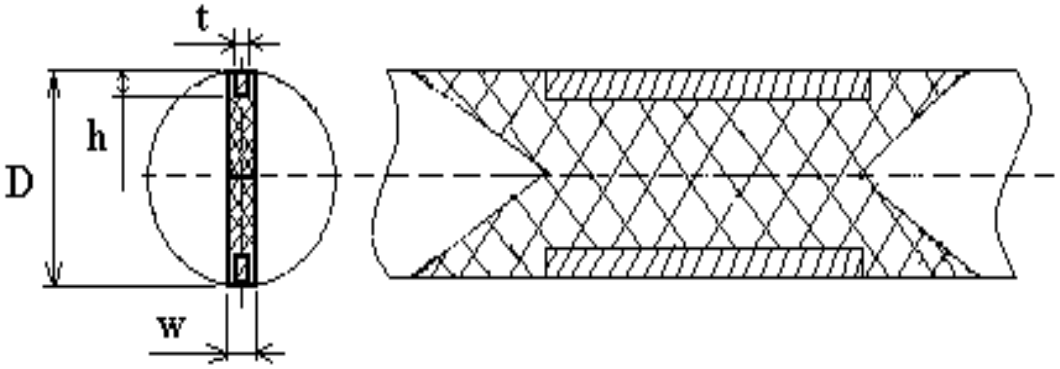

Fig.1c. Polarizer metal-dielectric type.

Taking into account these factors, we will analyze the features of structural-technological implementation of the designs of polarizers shown in Fig. 1 in the frequency band of 20/30 GHz. Preliminary calculation of the main structural dimensions of phase-shifting sections gives the following results:

- based on the operating conditions on the main type of wave for a round waveguide, the inner diameter of the waveguides 11 mm is chosen;

- the optimal ratio between the phase shift created by the narrowed part of the waveguide Fig.1a and the rod structure is defined as

$$(\frac{D-d}{2})/R\times 0{,}095 \qquad (2),$$

where R is the radius of the waveguide, determines the size d equal to approximately 8 mm. Accordingly, the thickness of the narrowing plate should not exceed one millimeter;

- the thickness of the dielectric plate of Fig.1b, is chosen under the condition of performing a ratio $w = 2R$ that determines the approach to zero of the coefficients of interconnection between the closest to the main types of waves H_{mn}, E_{mn}. According to the selected waveguide diameter, the thickness of the dielectric plate should not exceed two millimeters;

- the conditions for determining the thickness of the dielectric plate are correct for the design of the polarizer shown in Fig.1c. it is obvious that when $w \le 2i\ i$ the thickness of the metal plate should not exceed one millimeter.

The analysis of the obtained results shows that the application of the designs of polarizers of metal-rod and metal-dielectric types, in a given frequency range, is quite problematic. The latter is due to the fact that technologically, longitudinal metal inhomogeneities must be soldered into the main waveguide, and given the obtained design dimensions, compliance with the required values of tolerances for dimension parallelism, coaxiality, etc., is if impossible, then quite complex technological task.

In this context, the design of a dielectric polarizer looks the most suitable for the application. The main technological problem in the implementation of such a structure is the mechanical fixation of the plate inside the waveguide. In order to minimize active losses, the dielectric plate is made of fluoroplastic. However, the determined thickness of the plate and the physical properties of the material itself do not allow to ensure a reliable mechanical fit of the plate in the waveguide, which determines the need for the technological process of gluing the plate. To ensure the latter, it is necessary to carry out a complex physical and chemical treatment of the fluoroplastic plate, which, given the harmfulness of technological processes, is possible only at a few enterprises in Ukraine. From a radio technical perspective, the disadvantages of the design of dielectric type polarizers include the relative narrowband of the latter, as a consequence of the absence in the design of the polarizer of additional elements to compensate for phase shift dispersion created by the dielectric plate in the operating frequency range.

In order to solve the above technological difficulties and improve the radio technical characteristics, we propose to modify the dielectric polarizer. Conventionally, the proposed design can be classified as a polarizer of dielectric-rod type. A schematic view of the proposed design is shown in Fig.2.

Obviously, from a technological point of view, the proposed design allows for reliable mechanical fixation of the plate in the waveguide and does not require significant technological training in the manufacture. From a radio engineering point of view, the principle of construction of the phase-shifting section in the proposed structure is to combine the phase shift generated by the dielectric plate and a series of rods in the form of adjusting screws.

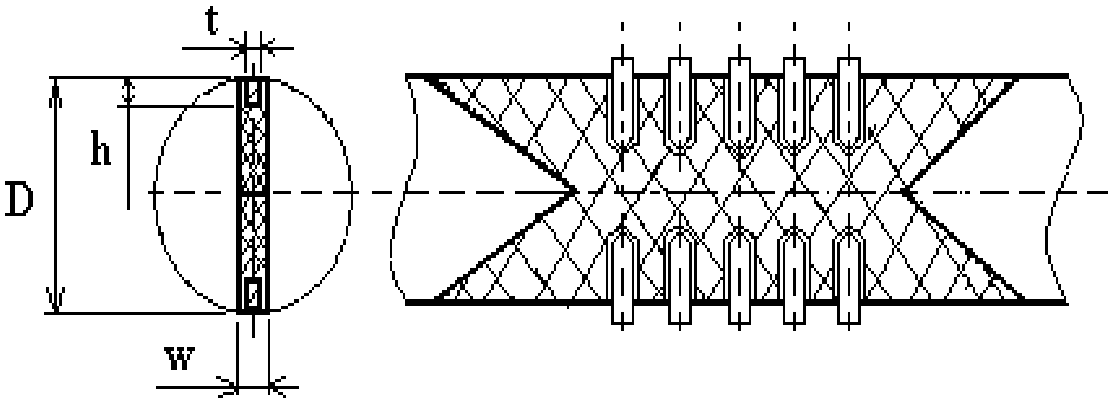

Fig.2. Polarizer dielectric - rod type.

Despite the need for adjustment work and the corresponding increase in complexity, the design solution allows for rapid adjustment of the characteristics of the ellipticity coefficient over the range, as well as to compensate for possible differences in physical and geometric properties of fluoroplastic plates from different batches. Given the presence of adjusting screws, the calculation of the linear size of the dielectric plate, determined by expression (1), must be performed for the value of the phase shift slightly less than that required for this type of polarizer. For example, for a 90-degree polarizer, the value of the phase shift generated by the dielectric plate should be around 80 degrees.

In this case, in the case of partial filling of the waveguide with a dielectric, the phase constants of the respective components of the electric field vector E can be determined as follows.

In this respect, in the case of partial filling of the waveguide with a dielectric, the phase constants of vector E of the electric field can be determined as follows:

$$\beta_0 = \sqrt{(k_{1,2}^2 - \chi^2)} \tag{3}$$

where $\kappa_{1,2} = \dfrac{2\pi\sqrt{\varepsilon_{1,2}^{ефект.}}}{\lambda_0}$ - wave numbers of the vector E components

$\chi = \dfrac{2\pi}{\lambda_{хвил.}}$ - critical wave number of the main type wave H_{11}

$\varepsilon_{1,2}^{ефект.}$ - effective equivalent relative dielectric constants parallel and perpendicular to the plane of the plate of the vector E components

λ_0 - working wavelength

The values of relative dielectric constants are based on the method of wave equations [5]. In this case, the system of wave equations for several types of waves $Í_{m,n}, E_{m,n}$ in the waveguide is solved, taking into account the mutual connection between them, which is a consequence of the presence of a dielectric plate. For relatively thin plates, the system of equations can be solved in the diagonal or zero approximation. Since this condition is met when choosing the thickness of the polarizer plate, the values of the effective dielectric constants of the respective components of the vector E can be determined by the following expressions [3]:

$$\varepsilon_{1,2}^{ефект.} = 1 + (\varepsilon_m - 1)S_\varepsilon / S + [(\varepsilon_m - 1)/\pi]\sin(\pi S_\varepsilon / S) \tag{4}$$

$$\varepsilon_1^{ефект.} = 1 + (\varepsilon_m - 1)S_\varepsilon / S \quad (5),$$

where ε_m - the value of the dielectric constant of the plate material (for fluoroplastic ε_m=2,25)

S_ε / S - the cross-sectional plane of the dielectric plate and the waveguide, respectively

Using the above analytical expressions, the length of the fluoroplastic plate with a thickness of two millimeters, required to obtain a phase shift between the orthogonal components of the vector E, which would be equal

to 80 degrees at a frequency of 20 GHz, was determined. Given that the adjusting screws of the rod structure are located in a waveguide structure partially filled with dielectric, the distance between the latter was determined $\lambda_p / 4$

where λ_0 the wavelength for the vector E_{01} components.

The results of experimental studies.

Based on the obtained results, for the practical study of the proposed design, a mock-up of a polarizer based on a round waveguide with an inner diameter of 11 millimeters was made (Fig. 3).

Fig.3. Polarizer prototype.

In the prototype, the rod structure was implemented in the form of five pairs of adjusting screws with a diameter of one millimeter. The final length of the polarizing plate, taking into account the smooth transitions designed to align the plate with the waveguide, was defined as the sum of the lengths of its regular part and one smooth transition multiplied by 0.9. Figure 4a shows the results of measuring the ellipticity coefficient, and Figure 4b shows the results of standing wave ratio measurement, performed by a prototype of the polarizer.

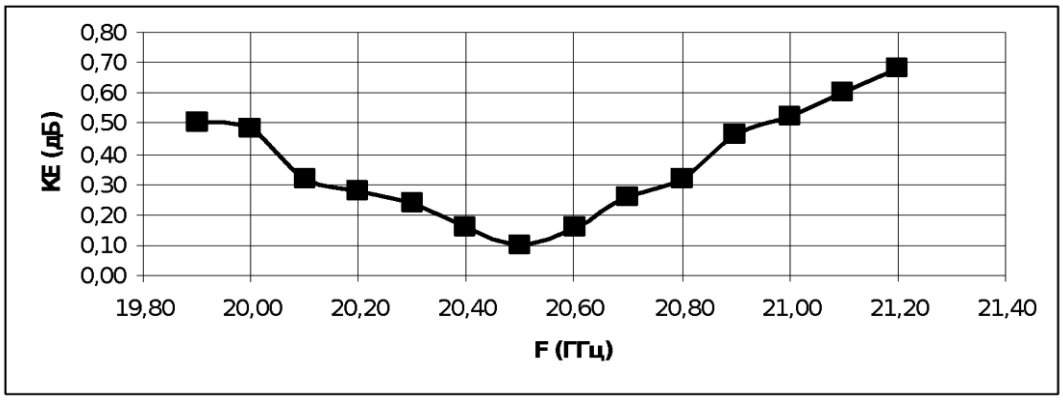

Fig.4a Results the ellipticity of the polarizer measurement

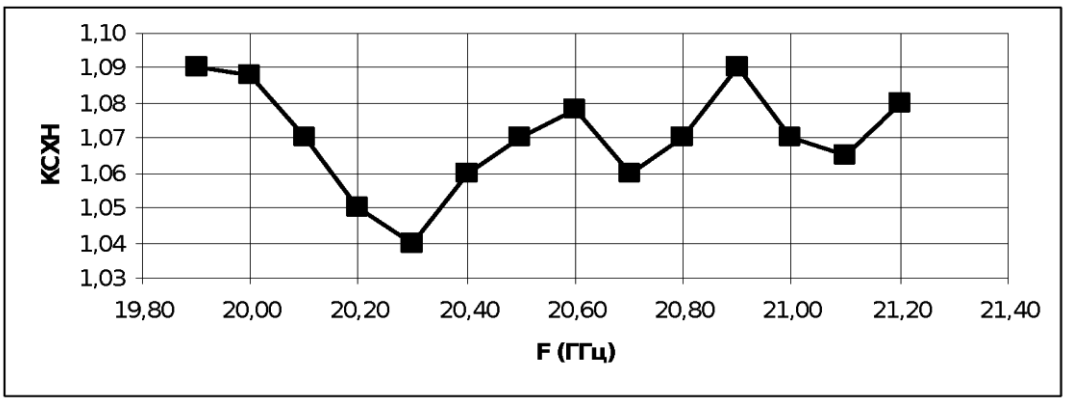

Fig.4b Results of the polarizer standing wave ratio measurement

Conclusions.

The experimentally obtained characteristics confirm the possibility of using the proposed design for the construction of high-tech Ka-band polarizers, and the correctness of analytical expressions to determine the structural dimensions.

Further development of the proposed solution may be the analysis and finding the necessary analytical relationships between the structural dimensions of the rod and dielectric structures in order to expand the operating range of the polarizer.

References:

1. Adamenko, Ye.O. (2019). Poliaryzator iz pozdovzhnoiu perehorodkoiu [Polarizer with a longitudinal partition]. *Radio elektronika v XXI stolitti*, Proceedings of conference. Kyiv, Ukraine.

2. Dëmin, D.A., Chubinskiy N.P. (2014). Obluchatel' s dvumya ortogonal'nymi kru govymi polyarizatsiyami [An irradiator with two orthogonal circular polarizations]. *Zhurnal radioelektroniki*, *6*, 11–23.

3. Sazonov, D.M.(1988). *Antenny i ustroystva SVCH* [Antennas and MWF devices]. Moscow: Vyssh. shk. (in Russian).

4. Kantor, L.YA. (ed.). (1997) *Sputnikovaya svyaz' i veshchaniye: spravochnik* [Satellite communication and broadcasting: a handbook], Moskva: Radio i svyaz'(in Russian).

5. Tuzbekov, A.R., Gol'berg, B. Kh.(2013). Shirokopolosnyy volnovodnyy polyarizatsionnyy selektor dlya diapazona S s malym poperechnym razmerom [Broadband waveguide polarizing selector for S band with small transverse dimension]. *Radiolokatsiya i radiosvyaz'*, Proceedings of the conference. Moscow, Russia.

Cross-sectional: BIOMEDICAL ENGINEERING

THE CORONAVIRUS DISEASE COVID-19 SPREADING PREDICTION IN UKRAINE BY MEANS OF MICROSOFT EXCEL

Yuri Palaniza[1], Halyna Shadrina[2], Mykola Khvostivskyy[3]

[1]*Ternopil National Ivan Puluj Technical University, Rus'ka str. 56, 46001, Ternopil, Ukraine; palaniza@ukr.net*
[2]*Ternopil National Ivan Puluj Technical University, Rus'ka str. 56, 46001, Ternopil, Ukraine; shadrinagal@gmail.com*
[3]*Ternopil National Ivan Puluj Technical University, Rus'ka str. 56, 46001, Ternopil, Ukraine; hvostivskyy@tntu.edu.ua*

Abstract: COVID-19 has completely eclipsed the morbidity, mortality, and economic impact of any other seasonal flu or communicable disease in the past century, and it is vitally important to have means that make it possible to predict its spreading. Analysis of the situation regarding the course of COVID-19 as well as diagrams of the future pandemic emphasizes their ability to change the configuration and behavior, which requires a rapid response to these changes. In view of this, an important factor is the efficiency and the need to develop a simple model, suitable for understanding even by non-specialists and with the possibility of use in the "field". Based on the Excel-project of the North-Western University, a system of automatic identification of the SIR-model (Susceptible, Infectious, Recovered) of COVID-19 was developed.

Keywords: *SARS-CoV-2, COVID-19, Microsoft Excel, Software, SIR Model, GRG Nonlinear solving method*

1. Introduction

In the context of a global pandemic, the question of the value of human life arises as never before. At the same time it is necessary to provide, if not comfortable, then at least proper conditions for the patient's stay in the hospital and provide him with medical care at the minimum allowable level in accordance with state-approved treatment protocols.

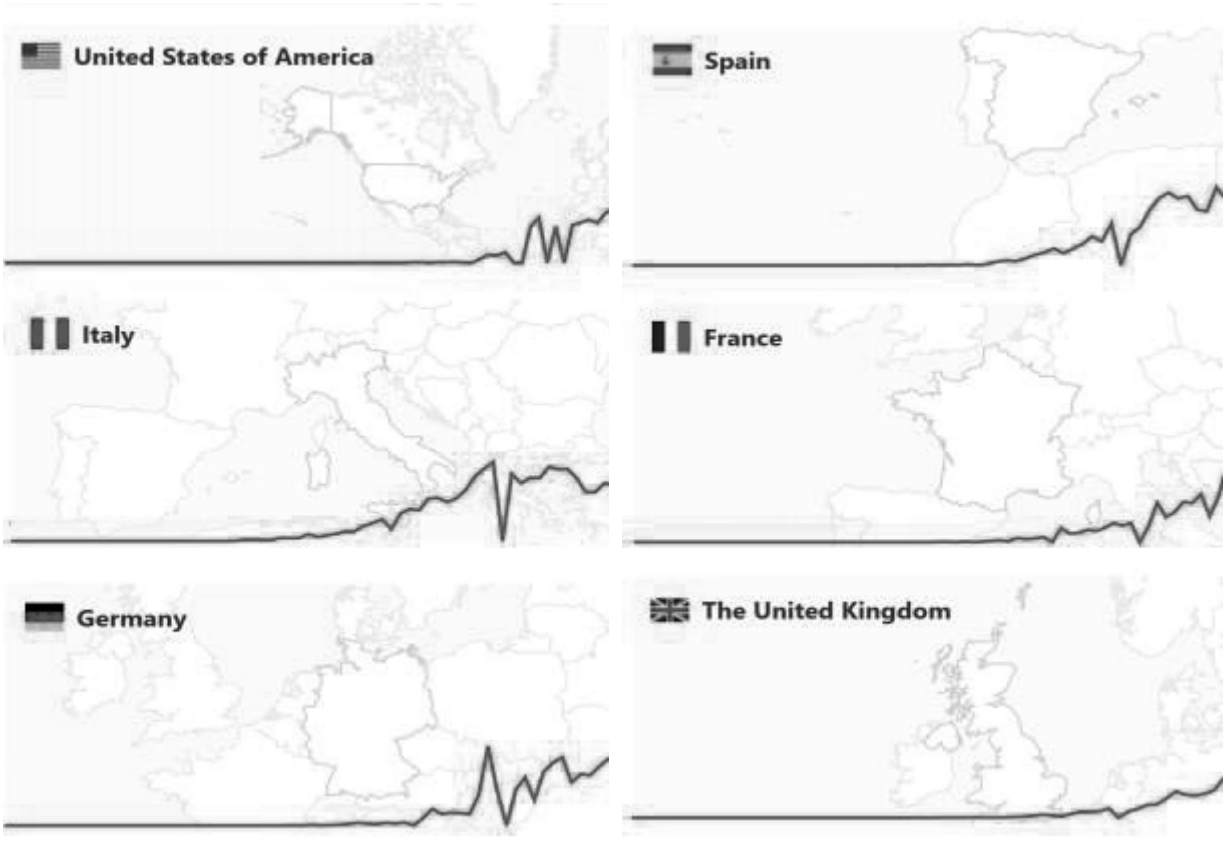

(Single space 5pt)

Fig.1 Dynamics of COVID-19 distribution in endemic countries (O. Kryvorot′ko).

At the end of the winter of 2021, Ukraine was on the rise of the second wave of SARS-CoV-2 coronavirus infection, which causes a corresponding syndrome / disease called COVID-19. Taking into account the macro- and microeconomic situation, social irresponsibility of citizens for their own safety in the environment and a number of other negative aspects, the state is extremely difficult to respond quickly and adequately to new challenges. Every effort should be made to prevent such a situation, in case of permanent development of which, medical staff will have to choose who to include in the so-called "red" category of hopeless patients, and in a total lack of resources to focus on providing priority care to other categories. patients at random. Therefore, it is critical to use all available means to smooth the peak incidence below the capacity of medical facilities. It is mathematical modeling to predict the dynamics of the epidemic can provide such tools.

2. Basic approaches to pandemic processes modeling

The development of an adequate mathematical apparatus to describe the course of pandemic processes was a primordial problem of mankind, according to the analysis conducted by O. Kryvorotko, the review of such mathematical models has the form:

D. Bernoulli (1760) - Mathematical methods for evaluating the effectiveness of smallpox vaccination methods;

J. Brownlee (1906) – Statistical approach to immune protection: the theory of epidemics (Pearson's distribution);

W.O. Kermack, A.G. McKendrick (1927) – For the first time, the "law of active masses" was applied, according to which the number of newly infected in the population is directly proportional to the product of the current number of susceptible and infected individuals. Development of deterministic SIR-model (Susceptible - Infected - Recovered):

$$\begin{cases} \dfrac{dS}{dt} = -\dfrac{\beta IS}{N}, \\ \dfrac{dI}{dt} = -\dfrac{\beta IS}{N} - \gamma I, \\ \dfrac{dR}{dt} = \gamma I. \end{cases} \tag{1}$$

here S - is the stock of susceptible population; I - is the stock of infected; R - is the stock of removed population (both processes of death or recovery); N - is population (is considered stable).

L. Reed, U.H. Frost (1931)) - Using a number of binomial distributions to describe the number of infected individuals in each time period;

W.H. Frost (1937) - Mathematical model of the tuberculosis epidemic;

D.G. Kendall (1957) - One of the first spatial models of epidemics based on equations in partial derivatives;

H.T. Waaler (1962) - A holistic linear mathematical model (which includes 5 equations) of the spread of the tuberculosis epidemic (which includes a description of the processes of infection, the development of latent (asymptomatic) infection and disease and the subsequent spread of infection);

C.S. ReVelle (1967) - The first mathematical model of epidemic tuberculosis based on five nonlinear ordinary differential equations. The task of the economically optimal strategy of tuberculosis control was formulated;

Noble (1974), Bailey (1975), Murray, Staley & Brown (1986) – Spatial SIR model (reaction-diffusion model):

$$\begin{cases} \partial_t S = -\beta(I + \alpha\nabla^2 I)S + d_s\nabla^2 S, \\ \partial_t I = (I + \alpha\nabla^2 I)S - \gamma I + d_I\nabla^2 I, . \\ \partial_t R = \gamma I + d_R\nabla^2 R. \end{cases} \tag{2}$$

O.O. Romanyukha (2004) Development of mathematical models of tuberculosis spread, published in the territory of the former USSR - 6 equations;

J. Zhang (2005) Severe Acute Respiratory Syndrome (SARS) model in China in 2003 - 7 equations;

M. Tahir (2010) Model of the Middle East Respiratory Syndrome (MERS) epidemic in Saudi Arabia and South Korea;

T. Chen (01.2020) Mathematical model of the spread of coronavirus COVID-19 from a source of infection (bats) to humans in Wuhan Province - 14 equations;

J. Cheng (02.2020) Inverse problem for a system of 4 integro-differential equations with a delay with information about the number of infected and cured individuals in 2 weeks;

OI Krivorotko, SI Kabanikhin (02.2020) Inverse problem for a system of 6 differential equations. forecasting and identification;

R. Sameni (03.2020) Mathematical model of COVID-19 propagation with real data - 5 equations.

Existing mathematical models for the spread of COVID-19 coronavirus have a number of limitations.

• Natural births and deaths, and some other parameters that lead to changes in population.
• Differences between men and women are not taken into account (but statistics suggest that men were more vulnerable to the virus than women).
• Age ranges (but older people are known to be more vulnerable to the virus).
• Possibility of vaccination.
• Indicator of infected visitors.
• Freight and road flows.
• Indicator of social distance.
• Duration of stay in the group of infected (intensive care).
• Individual countermeasures against the spread of the virus.

3. Pandemic processes prediction

The basic approach to modeling epidemiological processes is the use of regression models. They are one of the most popular methods of predicting viral diseases. The main task of regression is to find a functional relationship between morbidity and factors that affect it, for which unknown parameters are set.

The main types of regression models in the study of viral infections are adaptive and non-adaptive. They can be used in the study of different types of diseases, to determine the information that can be used only for a particular type of model.

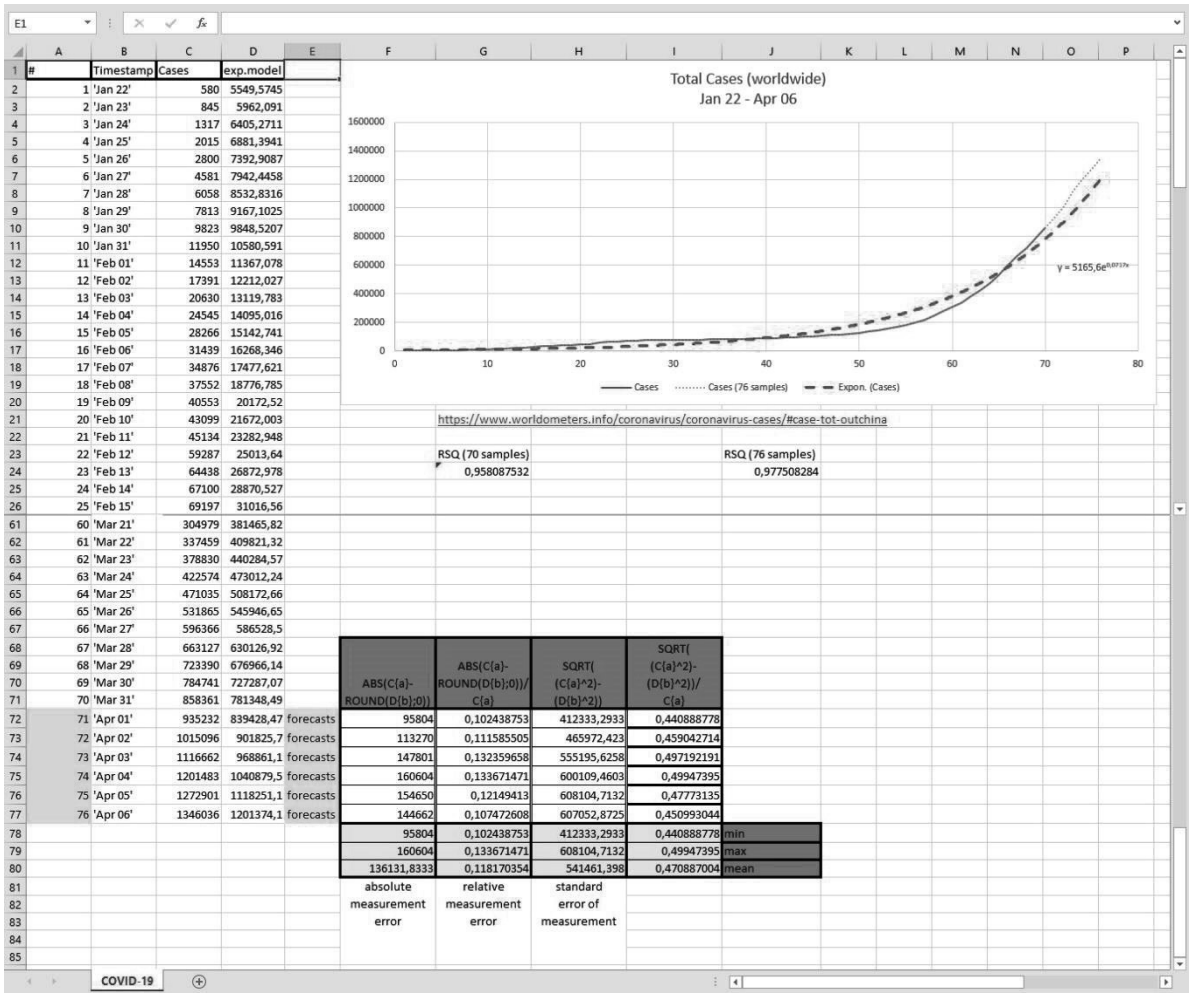

Fig.2 Prediction of the spread of the incidence of coronavirus COVID-19 in the world by means of MS Excel (as of 07.04.2020).

Adaptive regression models are mostly used during the course of the disease, to analyze and predict its future behavior. Adaptive models use the so-called concept of window width, which reflects the number of cases of manifestation of the pathogen over a period of time and are used to form an estimate of the prognosis. Depending on the width of the window, the accuracy and complexity of the model changes: as the width of the window increases, the accuracy decreases, this is due to the fact that the complexity of the function required to process a larger data stream

increases. The effectiveness of this type of model is the ability to detect all local fluctuations in epidemiological indicators.

A feature of non-adaptive models is the ability to take into account previous cases of disease. Such models use all the accumulated data to construct a prognosis, as well as data from indicators of similar viruses. This type of prediction is mostly effective in using to predict seasonal virus types. A striking example of such a model is the Surfling model for detecting and predicting new outbreaks of epidemics with pronounced seasonal manifestations.

Another approach is Bayesian networks using. This type of modeling of epidemiological processes is based on the display of the model in the form of an oriented graph, on the vertices of which are variable models, and the edges correspond to the probabilistic relationships between these indicators.

The capabilities of MS Office / Excel, installed on the vast majority of personal computers running the Windows operating system, may be used for prediction the course of epidemiological processes. In this case, people without relevant skills, including epidemiologists, will be able to use the developed software..

The data of the electronic resource Worldometer [1] for the period from 22.01.2020 to 06.04.2020 were used for analysis, the last 5 of them were used for verification.

It was assumed that in the interval of explosive growth in the number of infected system can be described by the equation of the form:

$$Cases(n) = a * e^{kn}, \tag{3}$$

where: $Cases$ – the number of cases on the n - th count, k – - speed of virus spread,, a – a constant component.

The built-in exponential regression technique was used here. Metric values R^2 throughout the interval becomes ≈ 0.98, and the relative error in the prognosis interval is smaller than 12%.

Therefore, we can conclude that the application of the technique of exponential regression, which is part of the interactive user-friendly graph data analysis interface in a spreadsheet processor environment MS Office/Excel and the corresponding mathematical model is adequate to the problem of predicting the spread of coronavirus COVID-19 in the world. This model is suitable for use by individuals without special skills in IT or Digital signal processing / System identification / regression and data fitting and without the use of specialized software on any personal computer running Microsoft Windows.

Exponential regression is a very simplified approach and is suitable for predicting the dynamics of infection spread only for a short period of time.

Derivative SIR-models operate with a large number of variables, some of which have to be set a priori, based on subjective expert assessment of epidemiological processes, which leads to low repeatability of results. Otherwise, there is a need to solve a multifactor optimization problem: the potential existence of local minima leads to "stuck" optimization process on a certain intermediate iteration and to the inadequate reality of the values of individual parameters. At the same time application of linear methods (such as Simplex algorithm) becomes impossible and it is necessary to use nonlinear (for example the Generalized Reduced Gradient algorithm). These models give acceptable results only for predicting the next wave of morbidity, while others due to sporadic processes give results that differ significantly from the true data.

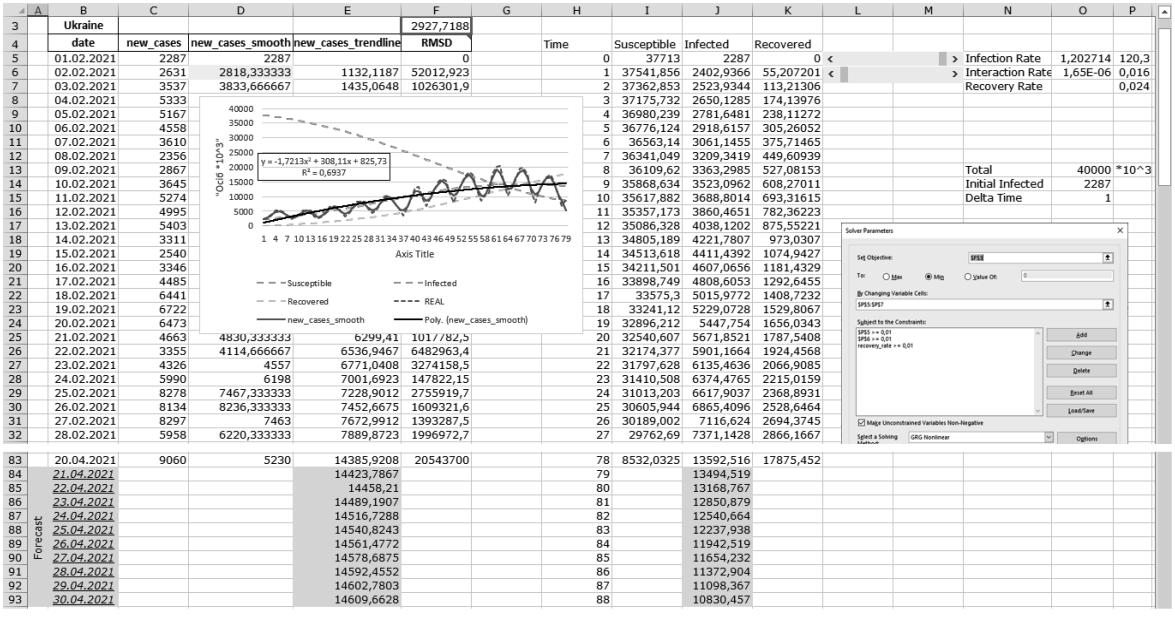

Fig.3 Prediction of the spread of the incidence of coronavirus COVID-19 in Ukraine by means of MS Excel (as of 21/04/2021).

In view of this, an important essential factor is the efficiency and the need to develop a simple model, suitable for understanding even by non-specialists and with the possibility of use in the "field". Often available tools, including Matlab, Python, R Language, are purely professional for non-medical professionals, in particular STATISTICA, Statistical Neural Network, are too difficult to master, they are paid to use, and the use of various solutions, including mobile applications, are specific. In contrast, the tabular interface is familiar to most users [2].

Based on the Excel project of Northwestern University, a system of automatic identification of the SIR (Susceptible, Infectious, Recovered) model has been developed in the interval [3] 01.02… 20.04.2021 adapted for COVID-19 in Ukraine (Fig. 3) with accuracy $RMSD \approx 2927{,}7$ persons (Root-mean-square deviation) over the entire interval compared to real data. The automatic selection of the optimal values of the coefficients is performed by solving the optimization problem - minimization of the root mean square error between the actual and calculated values of the number of infected persons.

Figure 4 shows the algorithm for calculating the indicators [4] of infected S, currently infected I and rehabilitated R.

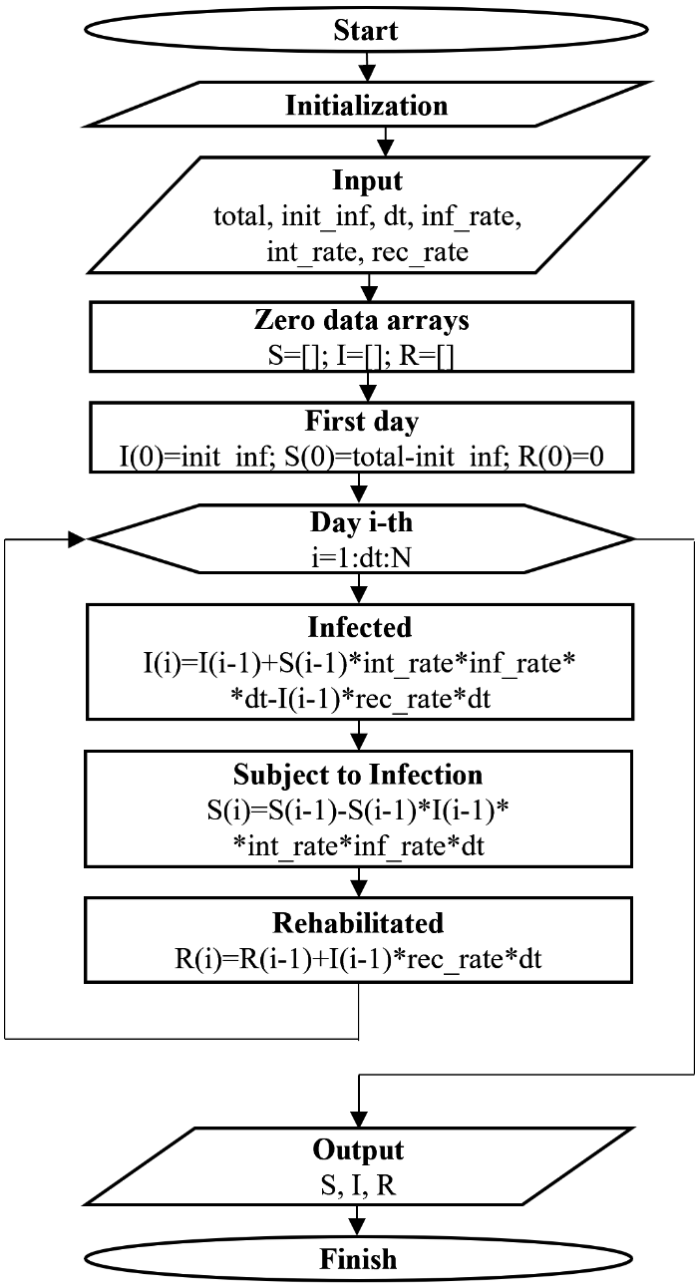

Fig.4 An algorithm for indicators calculating

In Fig.4 marked: **total** – total population; **dt** – step; **N** – number of observation days; init_inf – number of patients; **inf_rate** – infection rate; **int_rate** – intensity of individuals interaction; **rec_rate** – rehabilitation speed.

The analytical expression for the variable S (the stock of susceptible population) has the form:

$$S_i = S_{i-1} - S_{i-1} * I_{i-1} * interaction\_rate * infection\_rate * delta\_time, \quad i = \overline{0, N}, \tag{4}$$

here N - general number of days.

The analytical expression for the variable I (the stock of infected population) has the form:

$$I_i = I_{i-1} + S_{i-1} * Ii - 1 * interaction\_rate * infection\_rate * delta\_time - I_{i-1} * recovery\_rate * delta\_time, \quad i = \overline{0, N} \tag{5}$$

the analytical expression for the variable R (is the stock of removed population) has the form:

$$R_i = R_{i-1} + I_{i-1} * recovery\_rate * delta\_time, \quad i = \overline{0, N} \tag{6}$$

4. Conclusions

A system of automatic identification of the SIR model has been developed in the interval 01.02… 20.04.2021 with accuracy $RMSD \approx 2927,7$ persons over the entire interval compared to real data, adapted for COVID-19 in Ukraine.

Advantages of the model.

Simplicity.

The application of the smoothing technique the curve on three adjacent samples manually makes it possible to neutralize the impact of local emissions on the shape of the curve;

Using the built-in option of generating a trend line and regression equation allows both manual detranding of the signal and extrapolation / forecast of data to any number of steps forward.

Optimization of the SIR-model coefficients, as adequate to the objects of reality, by the help of automatically built-in means, allows to forecast a specific epidemic situation for any number of steps forward.

The main advantage of the approach is the convenience of an interactive user-friendly interface for data analysis in a spreadsheet environment MS Office Excel / Google Spreadsheets.

Appropriate mathematical model, adequate to the problem of predicting the spread of coronavirus COVID-19 in Ukraine, suitable for repetition without the use of specialized software by persons without special skills in the field of processing, identification of complex systems, regression analysis.

Disadvantages of the model.

A very simplified approach which allows predicting the dynamics of the infection spreading only for a short time period.

References

1. Coronavirus Cases. Total Cases (worldwide) [online cit.: 2020-04-07]. Retrieved from: https://www.worldometers.info/coronavirus/coronavirus-cases/#case-tot-outchina

2. Tatskov, O.O., Palaniza, Yu.B. (2020). The problem of predicting the spread of coronavirus COVID-19 in the world by people without special skills and without the use of specialized software on a personal computer with the operating system MICROSOFT WINDOWS. *Natural Sciences and Humanities. Topical issues*, Proceedings of the III International Student Scientific and Technical Conference. Ternopil, Ukraine.

3. Coronavirus Cases. Total Cases (Ukraine) [online cit.: 2021-04-21]. Retrieved from: https://www.worldometers.info/coronavirus/country/ukraine/

4. Suba, M. Current Mathematical Models and Numerical Simulation of SIR Model for Coronavirus Disease-2019 (COVID-19). European Journal of Molecular & Clinical Medicine 7.05 (2020): 41-54.

ANALYSIS OF THE COMPLEXITY OF ALGORITHMS FOR FINDING THE COEFFICIENTS OF THE MATHEMATICAL MODEL OF LOW-INTENSITY ELECTRORETINOSIGNAL

Pavlo Tymkiv

Ternopil National Ivan Puluj Technical University, Rus'ka str. 56, 46001, Ternopil, Ukraine; t_pavlo_o@ukr.net

Abstract: The complexity of methods of parametric identification is analyzed and their comparison is carried out at definition of coefficients of mathematical model of response of a retina of an eye at decrease in intensity of test light irritation. The algorithm of parametric identification of the mathematical model of retinal response based on direct complete search has a significant time complexity, which prevents rapid readjustment of the expert system in the case of remote, automated processing of low-intensity retinal response to diagnose the functional state of the body. Therefore, it is necessary to study the complexity of search algorithms and apply other approaches to solving problem of optimization or parameter identification. In this case, the criterion *K* of the optimality of the selection of coefficients will be the proximity of the simulated retinal response to the reference, pre-developed response.

Keywords: *electroretinosignal, parametric identification, complexity, optimization, low intensity.*

1. Introduction

With the development of scientific and technological progress, the negative man-made impact on the human body increases. There is a need for research to identify and early diagnosis of the risks of toxicity. A study of the Environmental Health Criteria 223 medical standard showed that the detection of risks (type of toxins, dose, duration of exposure, etc.) and early diagnosis of toxicity of the body is possible by assessing small characteristic changes in retinal response to light stimuli (electroretinosignals (ERS)). At the same time, the use of electroretinography helps to increase the level of objectivity of medical research, reduce the time of examination and the possibility of autonomous, remote use.

The obtained low-intensity retinal response is significantly distorted by noise due to the decrease in the ratio of signal energy to noise energy. At the same time, the complexity of processing is further increased due to the unknown or hidden nature of the toxin and its effect on the human body, which is reflected in changes in the amplitude-time parameters of waves or the emergence of new wave elements in ERS. For processing low-intensity ERS use optimal (morphological parameters of the signal) filtering, which in the case of autonomous and/or remote application, requires rapid reconfiguration, requires optimization and reduction of pre-processing time of the obtained low-intensity ERS.

2. Investigation of the complexity of methods for finding the coefficients of the mathematical model of low-intensity ERS

In computational complexity theory, the term "computational process complexity" is defined as the result of estimating the resources (usually time) required to perform an algorithm [1]. The limiting behavior of such complexity with increasing size of the problem will be called asymptotic time complexity.

Let *A* be the method of finding the coefficients of the mathematical model in the adaptive-recursive filter, and *N* be the dimension of the computational array of coefficients from the whole set of selection. Denote - a function that gives the upper limit of the maximum number of basic operations (addition, multiplication), which must perform method *A*, solving a problem of dimension *N*.

All methods are divided into polynomial and exponential, and some method *A* can be considered polynomial if it increases no faster than some polynomial from *N*. Otherwise, method A can be considered exponential. Typically, exponential problem-solving methods involve a complete direct search of all possible options, and due to the practical impracticability of solving such a problem, other approaches are developed for them. However, if there is a certain exponential algorithm for finding the optimal solution of such a problem, then another, more efficient (in the sense of less complexity) polynomial algorithm is used for practical implementation. In this case, there are not necessarily optimal solutions, but only acceptable for this type of problem or area of application of the solution (close to optimal). Such polynomial algorithms can differ significantly depending on the degree of the polynomial that approximates.

Consider one of the components of the concept of "complexity of the method" - time complexity [2,3]. By time complexity we mean the time spent by the algorithm of the method to obtain the final results. To record the time complexity, use the expression:

$$f_A(N) = O(g(N)) \tag{1}$$

where, $f_A(N)$ grows as $g(N)$ for N .

If there is a positive constant $C_{const} > 0$, such that

$$\frac{\lim\limits_{N\to\infty} f_A(N)}{g(N)} = C_{const} \tag{2}$$

The estimate *O(g(N))* will be called the time asymptotic complexity of such an algorithm. In this case, the estimate *O(g(N))* for the function $f_A(N)$ can be used when the exact value $f_A(N)$ is unknown, and only the order of increasing time is known, which is spent when solving a problem with dimension *N* using this method *A*. Such exact values $f_A(N)$ will be depend on this implementation, while *O(g(N))* will be a characteristic of the method itself. In the case when the asymptotic time complexity of this method is equal $O(N^2)$ (then this algorithm will be called quadratic), with increasing *N*, the time to solve the problem increases by N^2. The exponential time complexity of a method in terms of complexity theory is written as $f_A(N) = O(k^N)$, where k – is an integer that is greater than one.

According to the classification given by D. Knut, there are both upper and lower estimates of complexity. In this case, the upper estimate of complexity will be determined from the expression:

$$O(f(N)) \quad - \quad \{g(N) | \exists \quad C > 0 \quad i \quad N_0 > 0 : | g(N) | g(N) \quad \leq \quad Cf(N), \forall N \geq N_0\} \tag{3}$$

Thus, the lower estimate of complexity will be determined by the expression:

$$\Omega(f(N)) \quad - \quad \{q(N) | \exists C > 0 \quad i \quad N_0 > 0 : | g(N) \quad \geq \quad Cf(N), \forall N \geq N_0\} \tag{4}$$

The following effective complexity estimates are defined as follows:

$$\theta(f(N)) \quad - \quad \{g(N) | \exists C_1, C_2, \quad N_0 \quad > \quad 0 : C_2 f(N) \quad \leq \quad g(N) \quad \leq \quad C_2 f(N), \forall \quad N \geq N_0\} \tag{5}$$

In this case, *O(f(N))* will be used to indicate the upper estimate of the growth rate of such functions or to indicate the totality of all functions that grow no faster than the function *f(N)*. If the method is executed for the specified time *O(f(N))*, it means that the time for its implementation can be limited at the top by the value of the function *O(f(N))* for all inputs of dimension n. Execution time in the worst situation is also limited by the function O (f (N)), in this situation it is called the execution time of the algorithm.

Estimation $\Omega(f(N))$ is used to indicate lower estimates of the growth rate of functions or to indicate the set of all functions that grow slightly slower than the function *f(N)*.

The estimate *q(f(N))* is used to indicate functions of the same order as the function *f(N)*. This method is necessary to describe the "optimal" methods. If a certain method of solving the problem processes inputs with data of size *n* for such time cn^2, where *c* – is a certain constant, and the time complexity of such an algorithm is $O(n^2)$, for the whole number *n*, except for a finite (i.e. empty) set, non-negative values. Such a record $O(n^2) \cap \Omega(n)$ will denote a class of functions that have a velocity of not less than *n*, but not more than n^2.

Spatial and temporal complexity, i.e. functions in relation to the size of the problem, are two fundamental estimates of efficiency in the analysis of methods. We will consider the complexity of computational methods as an estimate of the resources (often time) required for the operation of the algorithm of this method.

The complexity of the algorithms of the methods will be measured by the required resources, i.e. the duration of calculations or the required amount of memory. The time complexity measured in this way is independent of implementation. Estimation of numerical computational complexity qualitatively demonstrates the influence of the amount of input data on time and the amount of memory [4,5].

The mathematical model of the reference low-intensity ERG in each cycle n = 0,1,2,… can be represented by summing:

$$a_2 s_{n-2} + a_1 s_{n-1} + s_n = \xi_n \tag{6}$$

where, s_{n-1}, s_{n-2} – initial conditions [6,7].

In the prototype method, sequential direct selection of coefficients (parameters) a_1, a_2, and initial (baseline) conditions s_{n-1}, s_{n-2} evaluated the proximity of the simulated $\hat{s}_n$ ERS to the previously known S_n retina ERS response (for example, in a database displaying known response types) by the value of the criterion:

$$\kappa = \sqrt{\frac{1}{N-1}\sum_{n=1}^{N}\left(s_n - \hat{s}_n\right)^2} \tag{7}$$

where N – is the number of values S_n and $\hat{S}_n$. And the difference between the value of the reference and simulated low-intensity electroretinogram (ERG) is defined as the root mean square error (RMS) of the simulation,

which will serve as a measure of the choice between the prototype method and the improved method when using binary classification. The block diagram of the prototype method is shown in Fig.1.

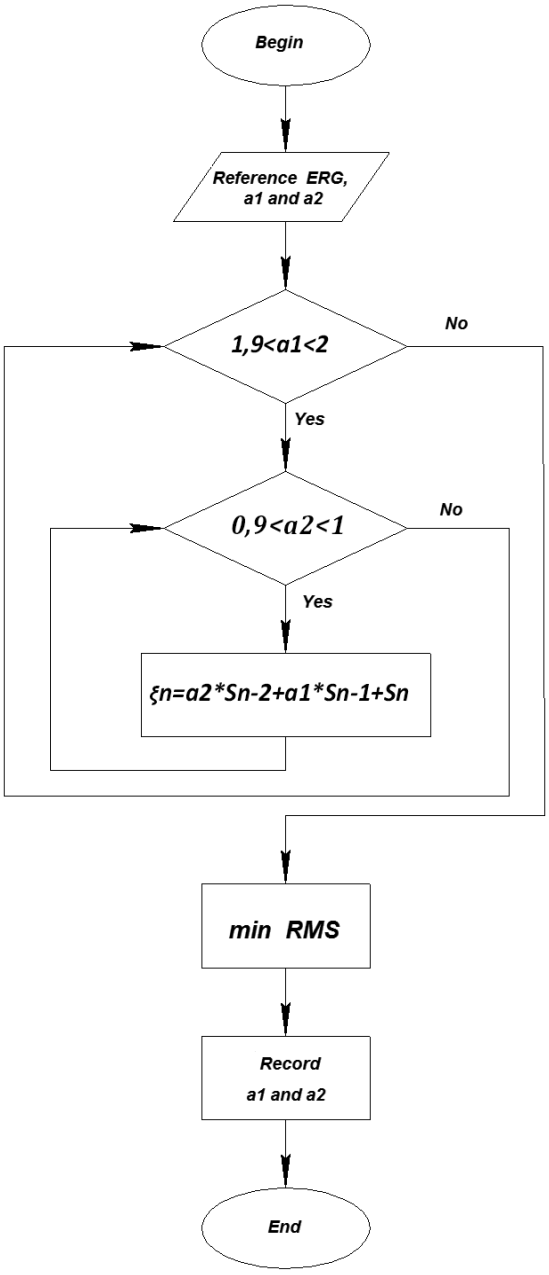

Fig. 1. Algorithm for finding coefficients by direct directed search

In this case, the complexity of this method of estimating the parameters of the model will be determined by:

$$C = n_{a_1} \cdot n_{a_2} \cdot n_{S_{n-1}} \cdot n_{S_{n-2}} \cdot n_{\tau} \tag{8}$$

where, n • – the number of values, coefficients a_1, a_2, the number of initial conditions s_{n-1}, s_{n-2}, the number of ERS samples. The value of all numbers n • depends on the value of the predetermined criterion (K) and can be determined, for example, by the number of smaller digits m • in the binary code of the corresponding coefficients, or the initial conditions and the number of retinal response samples. Hence, the complexity of the method is exponential, type *O(2M)* [8], where:

$$M = m_{a1} + m_{a2} + m_{Sn-1} + m_{Sn-2} + m_{\tau} \tag{9}$$

which necessitates the improvement of the method. In [9] developed an improved method for finding the coefficients of the computational mathematical model of low-intensity ERS, the block diagram of which is shown in Fig. 2.

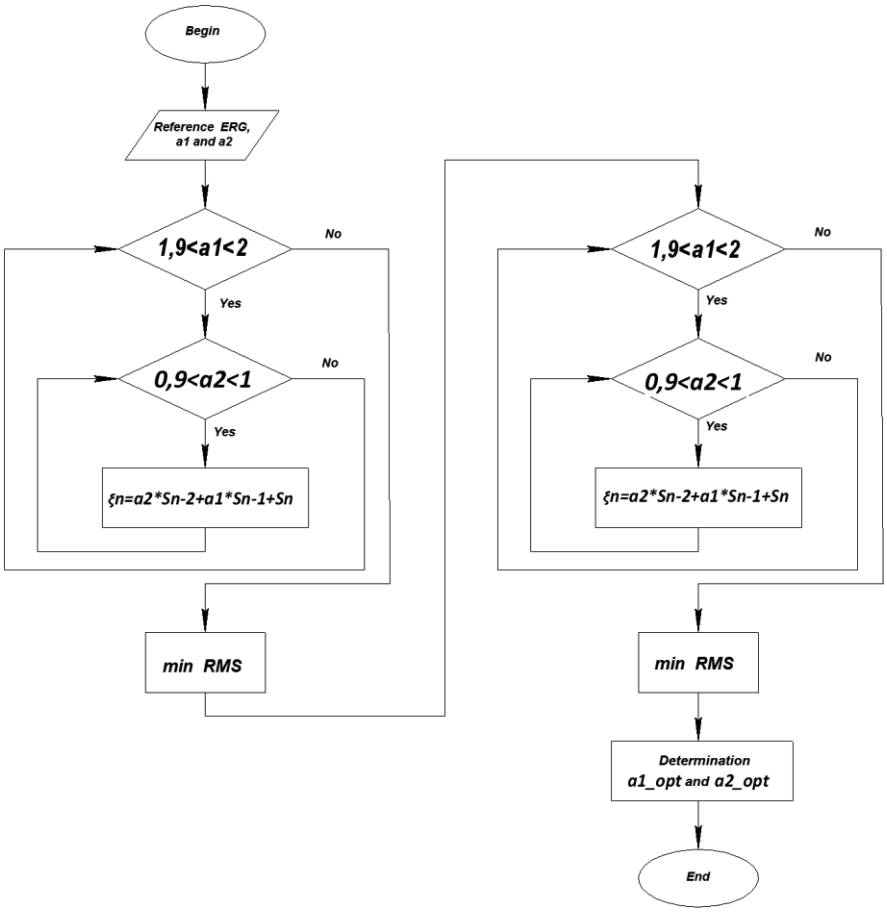

Fig. 2. Optimized method for determining the coefficients of the Hooke-Jeeves search strategy.

To compare and evaluate the prototype method and the improved method, we determine the time of selection of coefficients by the prototype method and the improved method at different numbers of search points (table 1).

Table 1

Comparison of calculation time of algorithm of direct full directed search and search on the basis of Hooke-Jeeves search strategy

Number of points, *N*	**Processing time with direct directional search algorithm, *s***	**Processing time with the algorithm according to Hook-Jeeves strategy, s**
100	0,6698	0,7666
200	1,6306	1,3215
300	3,7987	1,7511
400	6,7140	2,0514
500	10,5308	2,7493
600	15,7425	3,1958
700	22,2913	3,6477
800	29,5568	4,4972
900	37,9793	5,0008
1000	48,1306	5,8352
2000	245,9232	10,4593
3000	658,2834	16,9708
4000	1365,1457	23,1177
5000	3702,8461	30,1974

Graphically, the results of the comparison are shown in Fig. 3

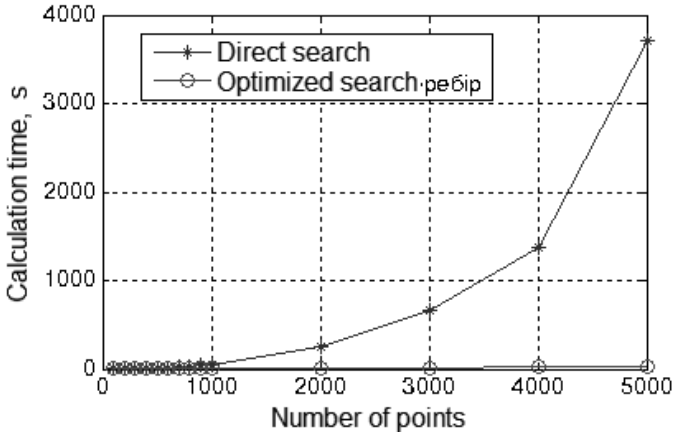

a)

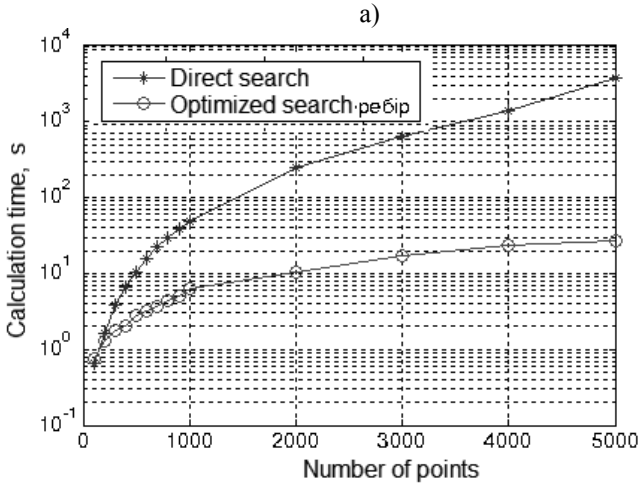

b)

Fig. 3. The dependence of the search time of the coefficients by the prototype method and the improved method on the number of points (a - linear scale, b - semi-logarithmic scale)

However, the time advantage of the improved method of finding coefficients requires research and comparison of their accuracy. In this case, the measure of accuracy will be the RMS modelling of low-intensity ERS according to pre-determined coefficients by two methods.

As can be seen from Fig. 3, direct search has polynomial complexity. And the optimized search on the basis of Hooke-Jeeves search strategy, allowed to reduce time of definition of algorithm. However, its implementation is somewhat limited due to shortcomings: The algorithm is based on cyclic motion in coordinates, which can lead to the degeneration of the algorithm into an infinite sequence of searches through research without searching for a sample. When using the method, it is assumed that the objective function under study is unimodal, i.e. has only one optimum in the study interval. This means that the solution may be a local minimum, not a global one, if there are several minima in the study area.

Therefore, the application of genetic algorithms for solving the optimization problem is promising in terms of finding the optimal values of the coefficients of the mathematical model of low-intensity ERS.

Genetic algorithm is a method that reflects the natural evolution of problem-solving methods, and especially optimization problems. Genetic algorithms are search procedures based on the mechanisms of natural selection and inheritance. They use the evolutionary principle of survival of the most adapted individuals. They differ from traditional optimization methods by several basic elements. In particular, genetic algorithms:

a) process not values of parameters of the task, and their coded form;

b) carry out search of the decision proceeding not from a single point, and from their some population;

c) use only the objective function, not its derivatives or other additional information;

d) apply probabilistic rather than deterministic selection rules.

These four properties, which can also be formulated as parameter coding, population operations, the use of minimum task information, and randomization of operations, result in the stability of genetic algorithms and their superiority over other widely used technologies.

3. Conclusions

It was found that the processing of the retinal response to test light stimulation with reduced intensity, methods regulated by the ISCEV standard (bandpass filter) was ineffective due to the reduction of the ratio of retinal response energy to noise energy in the selected ERS. And the use of coordinated filtration (in the value of the Norse filter) or optimal filtration in the Kolmogorov-Winner value (with the criterion of optimum minimum deviation) to process such a response is further complicated by an unknown change in retinal response or the appearance of new segments when exposed to toxins.

The study of the method of parametric identification of the model of low-intensity retinal response on the basis of direct directed search, requires a significant amount of time, i.e. great time complexity. Therefore, there are works in which the possibilities of using the method of parametric identification based on the Hooke-Jeeves algorithm are investigated.

The application of the optimization method based on the Hooke-Jeeves algorithm has disadvantages, which in some cases limits its application in expert systems for processing low-intensity ERS. Therefore, the use of genetic algorithms is promising. However, will require additional research and comparisons of complexity, statistical research and determination of the reliability of the decision on the choice of method for determining the coefficients of the mathematical model of low-intensity retinal response ERS

References

1. Papadimitriou, C. H. (1994). *Computational complexity*. Addison-Wesley.

2. Cobham, A. (1965). The intrinsic computational difficulty of functions. *Logic, methodology and philosophy of science*, Proceedings of the 1964 International Congress. Amsterdam, The Netherlands.

3. Tymkiv, P.O., Yavorskyi, B.I. (2011). Parametrychna identyfikatsiia matematychnoi modeli elektroretynosyhnalu. *XV naukova konferentsiia*.. Ternopil, Ukraine.

4. Tymkiv, P.O., Zabytivskyi, V.P., Yavorskyi, B.I. (2016). Syntez filtru Kalmana dlia opratsiuvannia nyzko intensyvnoho elektroretynosyhnalu. *Vymiriuvalna ta obchysliuvalna tekhnika v tekhnolohichnykh protsesakh*, *1*. 168-176.

5. Tymkiv, P.O. (2018). Veryfikatsiia udoskonalenoho metodu vyznachennia koefitsiientiv filtru Kalmana u nyzko intensyvnii elektroretynohrafii. *FUNDAMENTALNI TA PRYKLADNI PROBLEMY SUChASNYKh TEKhNOLOHII, Proceeings of the International Conference*. Ternopli, Ukraine.

6. Tkachuk, R., Yavorskyi, B. (2009). Metod pobudovy biotekhnichnoi systemy dlia otsiniuvannia elektroretynohram z pidvyshchenymy virohidnistiu ta efektyvnistiu. *Visnyk TDTU, 14*(3), 102-110.

7. Tkachuk, R. A. (2009). Optymalna obrobka elektroretynosyhnalu dlia vyznachennia formy elektroretynohramy. *Vymiriuvalna tekhnika ta metrolohiia*, *70*, 9-13.

8. Bakulev, P.A. (2004). *Radyolokatsyonnye systemy: uchebnyk dlia vuzov*. Moskva: Radyotekhnyka.

9. Tymkiv, P.O., Demchuk, L.B. (2020). Application of Hooke-Jeeves algorithm for electroretinosignal processing, *Innovatsii partnerskoi vzaiemodii osvity, ekonomiky ta sotsialnoho zakhystu v umovakh inkliuzii ta prahmatychnoi reabilitatsii sotsiumu, Proceedings of the International Conference*. Kamianets-Podilskyi, Ukraine.

THE METHODS OF BIOSIGNALS PROCESSING AND THEIR IMPLEMENTATION IN THE STRUCTURE OF THE SYSTEM OF IMPAIRED HUMAN COMMUNICATIVE FUNCTION COMPENSATION

Oksana Dozorska,[1] Vasil Dozorskyi,[1] Evhenia Yavorska,[1] Yuriy Kapatsila,[1] Iryna Pankiv,[1] Andriy Kubashok[1]

[1]Ternopil Ivan Puluj National Technical University, Rus'ka str. 56, 46001, Ternopil, Ukraine; vasildozorskij1985@gmail.com

Abstract: The methods of biosignals processing and structure of the system of impaired human communicative function compensation are proposed. The methods of biosignals processing are based on the application of spectral-correlation analysis methods using the sliding window method and include preparatory and main stages. The sequence of steps of biosignals processing at the preparatory and main stages is substantiated. Also technical parameters and features of practical realization of constituent elements of the system of impaired human communicative function compensation are offered. The principle of operation of the system is based on the parallel selection and processing of electroencephalographic and electromyographic signals. At the same time the features of electrode constructions for selection of electroencephalographic signals, which are widespread today, as well as possible artifacts that will arise in the process of selection of these signals are analyzed. The design of electrodes for registration of electroencephalographic and electromyographic signals is proposed, the selection and processing of which is the basis of the method of indirect compensation of the impaired communicative function, which is realized by this system. A variant of realization of the functional diagram of the block of biosignals selection is proposed. The proposed design of the system of impaired human communicative function compensation can be manufactured using 3D printing technology, which will reduce its cost.

Keywords: *human communicative function, compensation system, processing methods, spectral-correlation analysis, electrodes, block of biosignals selection*

1. Introduction

The communicative function is the most important means of exchanging information between people.Given the significant increase in the number of people with disabilities or complete loss of ability to speak (exchange information) due to various injuries or diseases of organs that realize the human communicative function, it is important for medicine to develop technical means to compensate for violations of this function. Such a system can be implemented through the use of indirect methods of compensation, which will make it possible to obtain sufficient information to recognize what the person was trying to say.

Promising in this case is the use of a method based on the selection and processing of biosignals that control the work of organs and systems that directly implement the communicative function in the state of medical norm. These signals occur in certain areas of the cerebral cortex in the form of nerve impulses, which move along the nerve fibers innervate the organs of the articulatory apparatus, vocal folds, organs of the respiratory system. At the same time it becomes possible to recognize speech - to identify in the structure of these biosignals informative features of individual elements of speech when patients try to say something. Analysis of known studies shows that different types of biosignals and methods of their selection and next processing are used for speech recognition, in particular electroencephalographic (EEG) signals [1-4]; electromyographic (EMG) signals of facial muscles [5-9]; EMG signals selected from the surface of the patient's neck [10]. In this case, the methods of statistical and spectral-correlation analysis are used for processing when presenting such biosignals in the form of a stationary random process. However, in the case of processing EMG signals of facial muscles, it is possible to obtain information only about the processes of innervation of the articulatory apparatus, in the case of processing of EMG signals from the neck - only about the processes of innervation of the vocal folds. EEG signal processing involves the elimination of all artifacts associated with the work of other parts of the brain, taking into account the methods of coding and transmission of speech information in the flow of nerve impulses in the neural structures of speech centers of the brain and the reflection of these processes on the patient's head. The use of a stationary model and appropriate processing methods is possible only for short implementations of these signals lasting 0.2-10 sec, while to compensate the impaired human communicative function it is necessary to process much longer implementations of biosignals.

For indirect compensation of impaired communicative function is particularly promising to use a method based on the parallel selection and processing of a group of biosignals, in particular EEG signals recorded from the surface of the head near speech centers, and EMG signals recorded from the neck of patients near vocal folds [11]. On the basis of methods of processing of such biosignals algorithms of functioning of biotechnical system of compensation of the impaired human communicative function can be realized.

Actually, the method of compensation of the impaired communicative function involves the formation of a sequence of time intervals that correspond to vowel, consonant vocalized and non-vocalized sounds (based on the results of EEG and EMG signals processing). In this case, the method of selection of the obtained intervals can be matched to a particular word that the patient tried to pronounce, and which best fits the resulting combination of sounds. Then, to compensate the impaired communicative function, it will suffice to obtain such a sequence of time intervals.

The division into individual sounds is proposed to be performed according to the presence of signs of the main tone (MT) in the structure of EMG signals (for vowel sounds) and changing the value of MT (for vocalized consonant sounds). However, if a mentally spoken word begins with one or more unvoiced consonant sounds, the probability of error in recognizing this word only by EMG signals increases.

It is proposed to form a conditional time interval of the beginning and end of a mentally spoken word based on the results of EEG signal processing, followed by segmentation of this interval into sections corresponding to vowel, consonant vocalized and unvocalized sounds, based on the results of EMG signal processing.

The use of this method will allow the selection of biosignals, the structure of which will contain sufficient information for subsequent identification of individual structural elements of speech in patients with impaired communicative function, and implement a biotechnical system of indirect compensation of this function.

2. The methods of biosignals processing

To implement the algorithms of functioning of the system of impaired communicative function compensation, the methods of EMG and EEG signals processing have been developed [11]. EMG signal processing is performed to detect time intervals for the presence of signs of MT and includes two stages, namely: preparatory and main. The purpose of the preparatory stage is to estimate the approximate value and interval of the MT frequency existance by analyzing the test EMG signal. Such a signal must be pre-recorded from the patient trying to pronounce test sounds and phrases at strictly defined intervals. In this case, the EMG signal areas where the signs of MT should be present become known and it becomes possible to isolate these signs and, accordingly, to estimate the approximate value of the MT frequency and the interval of its existence.

The purpose of the main stage is to actually find time intervals of the presence of signs of MT in the structure of EMG signals, which are recorded in real time from the same patient who tries to pronounce arbitrary sounds and phrases at arbitrary moments of time.

For processing of EMG signals it is expedient to use methods of spectral-correlation analysis of stationary random processes, and processing of signals to be carried out on time intervals of a certain duration - within the sliding window.

The preparatory stage includes the following substages: 1) the formation of a sliding window of a given width, which is moving in time on the test part of the registered EMG signal; 2) within each translation of the sliding window, the distribution of the spectral power density of the EMG signal is estimated; 3) estimation of the presence of the maximum in the distribution of the spectral power density in the range of 80-450 Hz (the range of the MT frequency). The frequency of placement of the first maximum in the estimates of the distribution of the spectral power density corresponds to the frequency of MT (formant analysis); 4) estimation of the approximate value of the MT frequency; 5) estimation of the interval of existence of the MT frequency.

The main stage includes the following substages: 1) the formation of a sliding window with a specified width, which is translating in time on the main register of the EMG signal; 2) within each translation of the sliding window, the distribution of the spectral power density of the EMG signal is estimated (similarly as for the preparatory stage); 3) averaging estimates of the distribution of the spectral power density of the EMG signal in the range of the MT frequency; 4) the formation of the criterion for deciding on the presence of signs of MT in the structure of EMG signals.

Substantiation of the choice of sliding window parameters as well as estimation of the approximate value and interval of the existence of the MT frequency was carried out in works [11, 12].

The method of EEG signals processing to detect the time moments of the beginning and the end of the speech process by detecting signs of changes in brain activity when trying to implement the communicative function has also been developed. The method includes the following steps: 1) the formation of a sliding window of a given width, which is moving in time on the registered EEG signal; 2) within each sliding window, the distribution of the power spectral density of the EEG signal is estimated in the same way as for the processing of the EMG signal; 3) averaging of estimates of the distribution of power spectral density; 4) on the basis of the received average estimations of distribution of power spectral density formation of criterion of decision-making on existence of signs of communicative function realization is carried out. As a criterion, it is proposed to use the variation of the average estimates of the power spectral density distribution with the assumption that the values of variation of these estimates for the state of rest will differ significantly for the state of attempt to implement the communicative function and will not overlap.

The method is based on the calculation of estimates of the power spectral density distribution of EEG signals registered in leads in the immediate vicinity of the speech centers of the brain. The calculation is performed within a sliding window, the width of which is selected in the same way as for the case of processing EMG signals. Next, the averaging of the obtained estimates of the power spectral density distribution within each translation of the sliding window.

The proposed method also includes two stages: preparatory and main. The purpose of the preparatory stage is the selection of EEG signals, when the patient tries to mentally pronounce certain test sounds and words at certain intervals. Through a set of test statistics and its subsequent analysis, ranges of numerical values of averaged estimates of the distribution of power spectral density for EEG areas during the mental pronunciation of test sounds and words and areas for rest are formed.

During the main stage, the EEG signals are constantly selected and the average estimates of the power spectral density distribution within the sliding window translations are calculated. The numerical values of these estimates are used to calculate the time intervals of the presence or absence of signs of the speech process (attempts to mentally pronounce arbitrary sounds or words or silence) based on the results of these values in the appropriate ranges of numerical values of these estimates.

Using the two described methods of EEG and EMG signals processing, it becomes possible to implement the proposed method of compensation for impaired human communicative function and to develop the structure of a biotechnical system that will implement this method.

3. The structure of the system of impaired human communicative function compensation

To implement the described method of indirect compensation of impaired communicative function, it is possible to use an electroencephalograph and electromyograph. However, the use of an electroencephalograph to solve this problem in practice will be difficult for physicians and inconvenient for patients, because in the process of experimental selection of EEG signals found imperfections in the design of the cap for fixing electrodes and imperfections in the design electrodes, which significantly affects the quality of selected statisticals material and the final result. According to the first type of imperfections, most modern electroencephalographic complexes use caps made of silicone or rubber tubes to which electrodes are attached. However, in the selection process it is especially difficult to ensure reliable fixation of the electrodes to the cap in the necessary places (according to the system of imposition "10-20%") and reliable contact with the surface of the patient's head. The use of 16 leads (or more) requires control of fixation and contact of each of the electrodes. Also, the registration method is sensitive to involuntary movements of the head, eye movements of the patient, etc., which leads to the appearance in the structure of selected EEG signals of movement artifacts, which during further processing can be mistaken as signs of trying to implement the patient's communicative function.

After analyzing the design of EEG electrodes, it was noticed that most modern complexes for EEG research are equipped with cup electrodes, which work on the principle of creating a capacitive system between the conductive surface of the electrode and the skin surface. The electrodes are placed on the surface of the scalp through the hair. This degrades the quality of contact of the electrodes with the scalp and causes a noise component in the structure of the selected signals, the appearance of movement artifacts and more. When using the wetting method or special conductive gel, the last is squeezed out from under the electrode and spreading on the hair or scalp and as a result the contact area is increasing . The use of the gel is uncomfortable for the patient when it comes to long-term selection of EEG signals. Features of the design of cup electrodes are shown in Fig. 1 and Fig. 2.

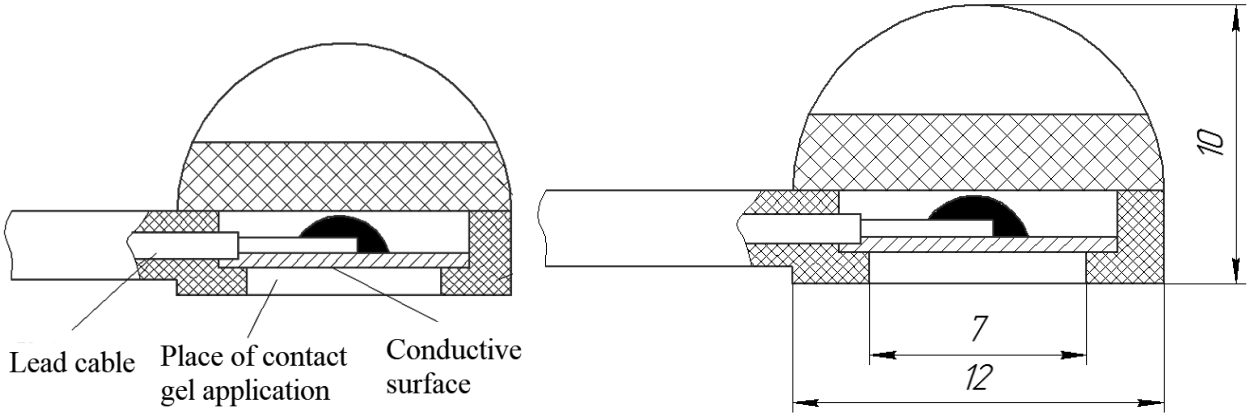

Fig.1 Design of cup electrodes of the encephalograph

It is proposed to use a design that will be a block of biosignals selection and amplification, which will be located on the back of the neck. From the upper frequency of the block will go two long plates (with bends according to the shape of the head) to the left and right temple.

At the ends of these plates will be placed three electrodes (because the speech centers in different people can be located on the right and left side of the brain and the electrodes are proposed to be placed on both sides). Two short plates will protrude from the lower part of the block and will completely wrap around the neck. Electrodes for selection of EMG signals in the area of vocal folds will be placed on them. Both the upper and lower plates will be able to adjust their length and bending to ensure maximum fit to the head (head sizes may vary from person to person) and reduce patient discomfort. Inside the plates will be conductors that connect the electrodes to the corresponding inputs of the block of biosignals selection. The view of the proposed design is shown in Fig. 3.

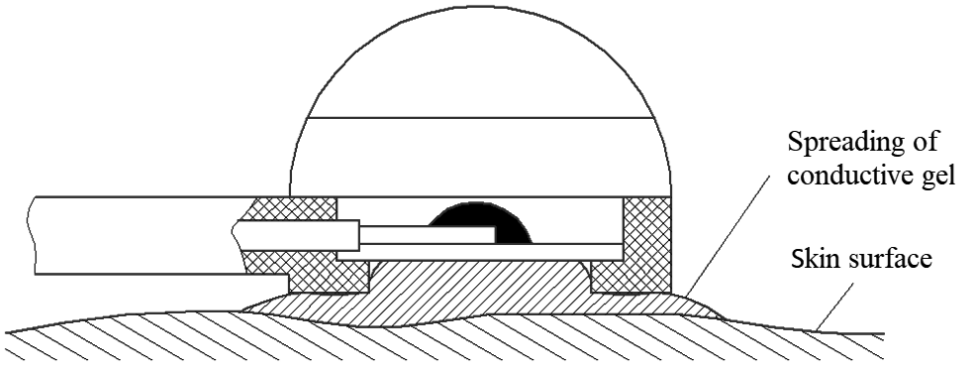

Fig. 2 Spreading of conductive gel on the skin surface

It is proposed to make electrodes with an uneven shape of the sensitive surface, in particular in the form of small needles with rounded tips, which will freely penetrate through the hair to the surface of the patient's scalp. This eliminates the need for conductive gel, which will be more comfortable for patients.

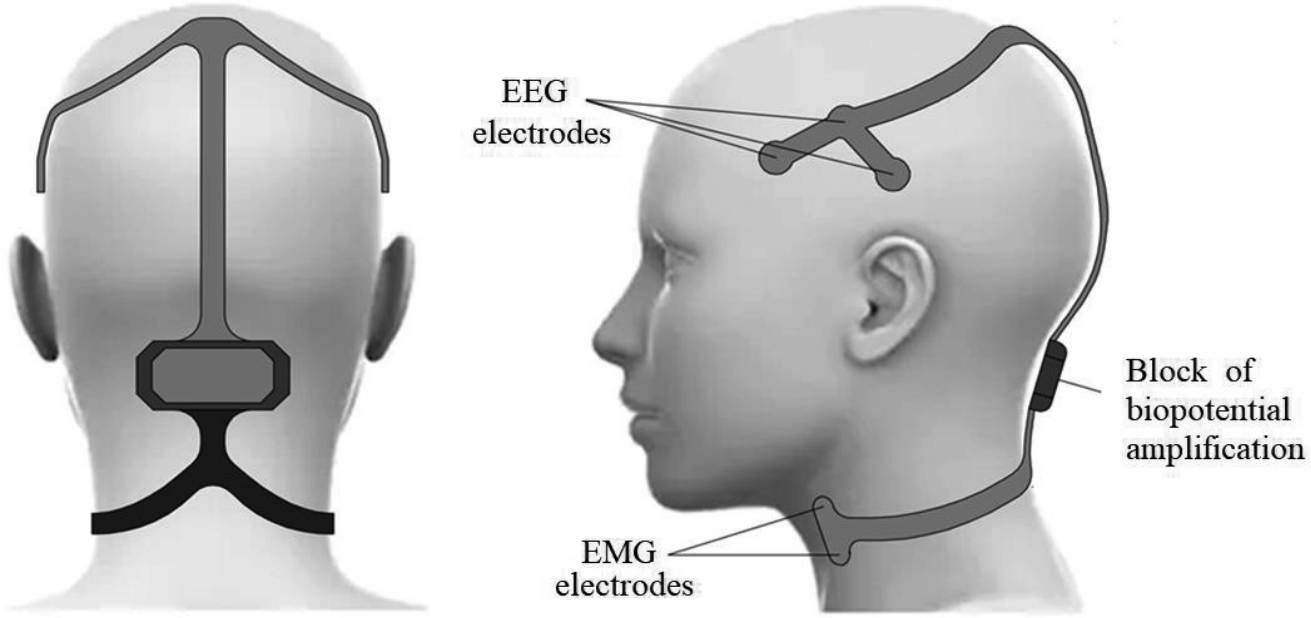

Fig. 3 The design of the system of impaired communicative function compensation

An example of the proposed design of such dry electrodes is shown in Fig. 4. The same electrodes are proposed to be used for the selection of EMG signals. Since the use of such electrodes will significantly reduce the area of contact of the sensitive surface of the electrode with the skin surface, the resistance of the lead will increase significantly (up to tens of megohms). Therefore, it is proposed to install in the design of the electrodes operational amplifiers with high input resistance, which are included in the circuit of the voltage repeater. This will increase the input resistance of the sampling unit and match it with the resistance of the signal source. As such operational amplifiers can be used amplifiers from Texas Instruments TLC272CP, the input resistance of which is 10^{12} Ohms, or similar. In the design of the electrode shown in Fig. 4, provides for the installation inside such an amplifier in SMD version.

In fact, the block of biosignals selection will include two identical selection modules, each of which will contain 4 gain channels - three of which are designed to select EEG signals in monopolar mode (relative to the signal common output SGND) and one channel to select EMG signals. Each amplification channel is constructed by analogy with the amplification channels of the electroencephalograph "Neurocom". Amplified EEG and EMG signals are fed to the inputs of an analog multiplexer, which alternately switches them to the output (TDM - Time Division Multiplexing technology).

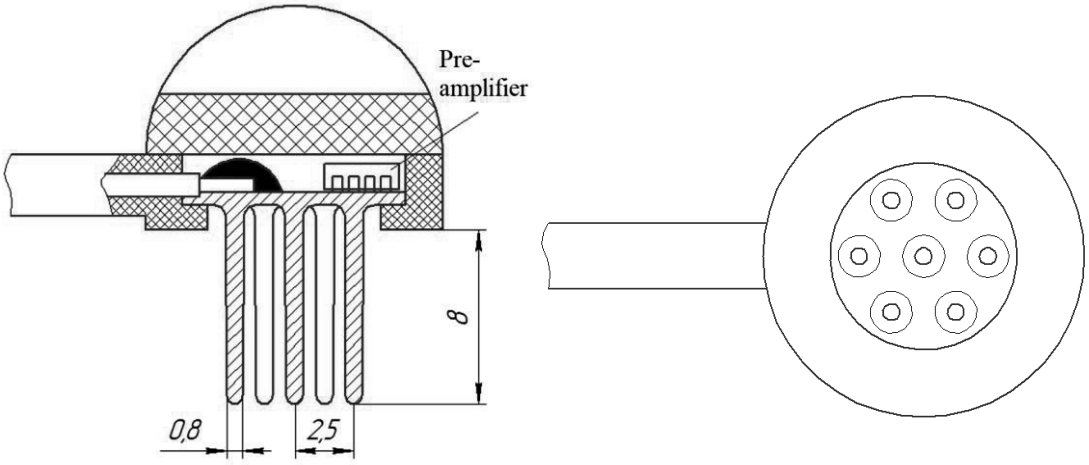

Fig. 4 The proposed design of the dry electrode

The received signal is digitized and fed to the computer through the interface module. For autonomous operation, a small battery and a power supply unit are included in the block of biosignals selection, which generates the required values of supply voltages of the component units of the block. The functional diagram of the proposed block is shown in Fig. 5. Between the amplifiers in each channel there are RC links, which are HPF tuned to a cutoff frequency of 0.7 Hz to prevent the passage of a constant component, that can appear in the structure of EEG and EMG signals. The gain of surgical amplifiers will also be different for EEG and EMG signals and will require individual selection due to the individual characteristics of patients (skin conductivity, the magnitude of the potential applied to the skin surface, etc.). The use of two modules is provided for the selection of EEG and EMG signals from both the left and right surfaces of the neck and head.

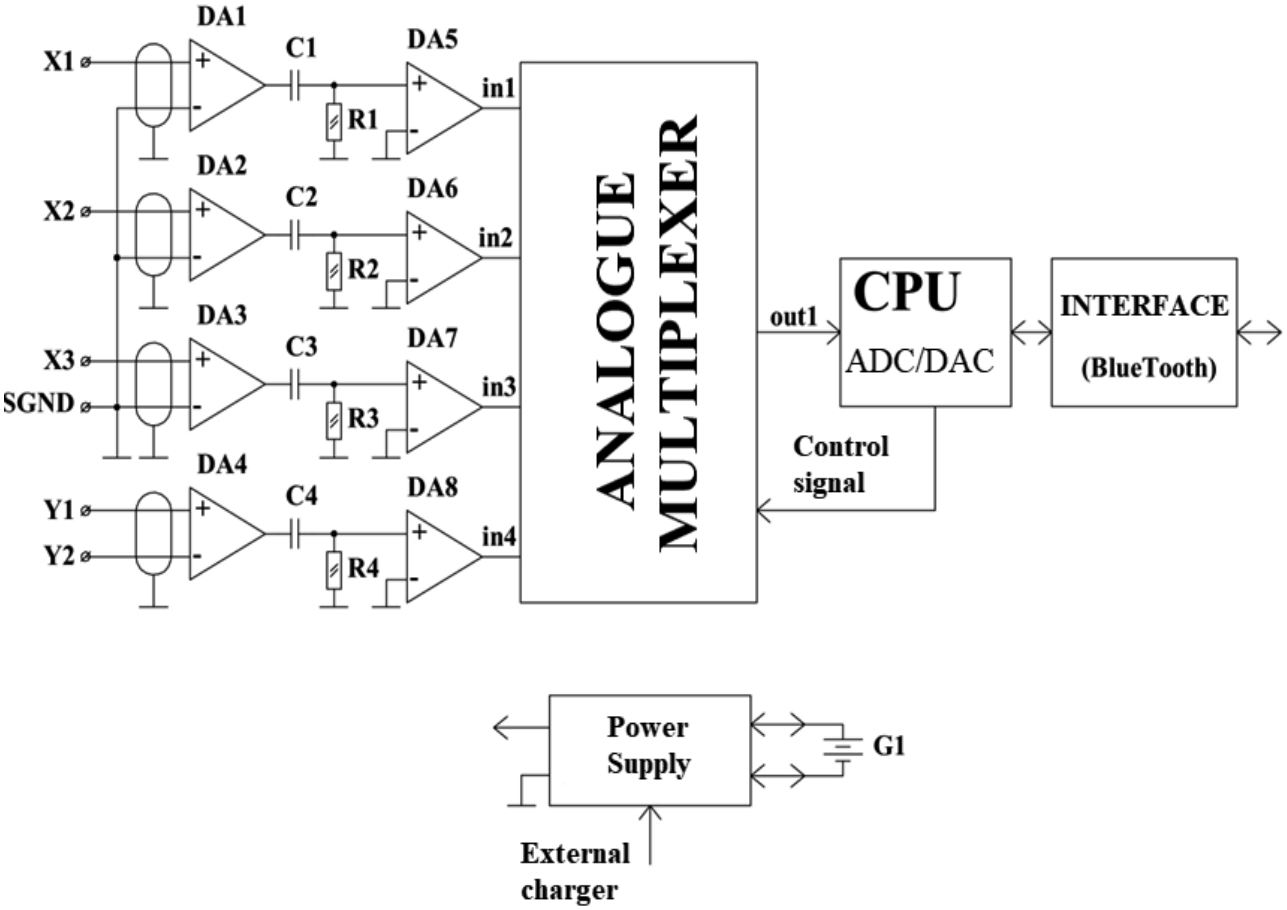

Fig.5 Functional diagram of the proposed block of biosignals selection

Using the interface module (BlueTooth) and a stand-alone power supply will eliminate the need to use any wires to connect the system to the computer, other than charging the internal battery. A personal computer or smartphone can be used as a computing tool, on which software will be installed, which will process the selected signals by the developed methods. The results of the processing (according to the third stage of the proposed method of compensation for impaired human communicative function) will be displayed on the screen of a smartphone or personal computer in the form of text that the patient tried to say, or on speakers placed on short plates of the proposed system.

As a power source can be used a battery from a smartphone with a working voltage of 3.7 V, followed by the use of a booster converter, which will charge the battery via a USB port of a computer or portable charger, and get voltages greater than 3.7 V, including a voltage of 5V to power all the chips of the sampling unit.

The structural elements of the system of impaired communicative function compensation and the electrodes themselves are proposed to be made using 3-D printing technologies from special biologically stable antistatic materials, such as ABS Antistatic or nylon. The sensitive surface of the electrodes must be coated with a sparingly soluble conductive material, such as silver chloride.

4. Conclusion

The paper describes methods of processing biosignals, in particular electroencephalographic and electromyographic, which can be used to develop a biotechnical system for compensation of impaired human communicative function. They include the preparatory and the main stage. The purpose of the preparatory stage is to obtain data on the features of the manifestations of the signs of the speech process by analyzing the test statistics of such signals. These data are necessary for the correct processing of electroencephalographic and electromyographic signals at the main stage, when the mental recognition of sounds or words spoken by patients and their translation into text or spoken language. A method of implementing these methods into the structure of the system of compensation of impaired communicative function is also proposed. The design of dry electrodes is proposed, which is better in comparison with the common designs of electroencephalographic electrodes and allows to reduce the number of artifacts in the structure of such biosignals.

Thus, the proposed method of indirect compensation of impaired human communicative function, methods of processing biosignals, including electroencephalographic and electromyographic, as well as the option of technical implementation of the biotechnical system for such compensation will allow creating an effective rehabilitation system to compensate the impaired communicative function. and the use of the proposed design of electrodes and 3-D printing technologies will reduce the cost of the system and increase its accessibility to the public.

References

1. Brigham, K., Vijaya Kumar B.V.K. (2010). Imagined Speech Classification with EEG Signals for Silent Communication: A Preliminary Investigation into Synthetic Telepathy. *Bioinformatics and Biomedical Engineering*, Proceedings of the 4th International Conference. Chengdu, China.

2. Porbadnigk, A., Wester, M., Schultz, T. (2009). EEG-Based Speech Recognition: Impact of Temporal Effects. *Bio-inspired Systems and Signal*, Processing, Proceedings of the 2nd International Conference. Porto. Portugal.

3. Meltzner, G.S., Heaton, J.T., Deng, Y., De Luca, G., Roy, S.H., Joshua, C. Kline. (2017). Silent Speech Recognition as an Alternative Communication Device for Persons with Laryngectomy. *IEEE/ACM Trans Audio Speech Lang Process*, Proceedings of the Conference.

4. Herff, C., Schultz, T. (2016). Automatic speech recognition from neural signals: A focused review. *Frontiers in Neuroscience*, *10*, 1-7.

5. Wand, M., Schmidhuber, J. (2016). Deep Neural Network Frontend for Continuous EMG-based Speech Recognition. *International Speech Communication Association (Interspeech)*, Proceedings of the 17th Annual Conference. San Francisco, USA.

6. Jorgensen, C., Lee, D.D., Agabon, S. (2003). Sub Auditory Speech Recognition Based on EMG/EPG Signals. *Neural Networks*, Proceedings of the International Joint Conference.

7. Khan, M., Jahan, M. (2016). Sub-vocal speech pattern recognition of Hindi alphabet with surface electromyography signal. *Perspectives in Science*, *8*, 558-560.

8. Gonzalez, J.A., Cheah, L.A., Gilbert, J.M., Bai, J., Ell, S.R., Green, P.D., Moore, R.K. (2016). A silent speech system based on permanent magnet articulography and direct synthesis. *Computer Speech & Language*, 67–87.

9. Xueqian, J., Li, J., Du, Y. (2008). Unvoiced Speech Recognition Based on One-Channel Facial Myoelectric Signal. *Intelligent Control and Automation*, Proceedings of the Sixth World Congress. Dalian, China.

10. Sannykov, V. (2008). Syloj mysli. *Populiarnaia mekhanika*, *6*(68), 72-75. (in Russian).

11. Dozorska, O. (2018). The mathematical model of electroencephalographic and electromyographic signals for the task of human communicative function restoration. *Scientific jornal of the Ternopil National Technical University*, *92*(4), 126–132.

12. Nykytyuk, V., Dozorskyi, V., Dozorska, O. (2018). Detection of biomedical signals disruption using a sliding window. *Scientific jornal of the Ternopil National Technical University*, *91*(3), 125–133.

ENSURING HIGH-PRECISION TESTING OF IMPLANTS IN THE REGULATION OF INTRA-EYE PRESSURE

Roman Tkachuk[1], Andriy Tkachuk[1], Diana Stadnik[1], Oleksiy Yanenko[1]

[1]Ternopil Ivan Puluj National Technical University, Rus'ka str. 56, 46001, Ternopil, Ukraine;
romantkachuk48@gmail.com
[2]Igor Sikorsky Kyiv Polytechnic Institute

Abstract: Among the diseases that lead to partial or complete loss of visual function is glaucoma, which is characterized by increased intraocular pressure (IOP) due to changes in the structures of the eye and the human body, which inevitably leads to blindness. According to the WHO in 2020. more than 5 million people suffer from vision loss in glaucoma, which accounts for 13.5% of all cases of blindness in the world. Today this figure in Ukraine reaches more than 200 thousand patients. Visual problems significantly reduce the level of information perception and cause a pathological condition with progressive death of ganglion cell axons, which causes a decrease and complete loss of the visual field. Known methods of glaucoma treatment use drug therapy, laser therapy and surgical implantation of drainage devices. It was found that the main cause of the disease is a decrease in the speed of movement and outflow of intraocular fluid through the trabecular system of the eye, due to a significant increase in pressure. The optimal rate of fluid formation is normally 2-2.5 μl / min., Ie during the day through this natural system of the patient should be released in a controlled manner and about 3 ml. It is obvious that the implantation of drainage devices in glaucoma is performed after previous unsuccessful treatment procedures and is the last chance to preserve the patient's vision, provided that the rate of fluid leakage is successfully regulated. Therefore, there is often a need for preoperative individual selection of implants with the necessary parameters.

Keywords: glaucoma, intraocular fluid, intraocular pressure measurement, implant, automation of blood pressure control process, working range of intraocular pressure (IOP).

1. Introduction

Among the known surgical methods of glaucoma treatment is the implantation of drainage devices of various designs and types. Currently, the Ahmed valve system is widely used in Ukraine [1-3], which provides for the removal of intraocular fluid from the anterior chamber of the eye in glaucoma and the creation of sufficient fluid reserve in the eye chamber space for gradual resorption and evacuation through existing ducts. Known such devices and methods of verification of preoperative testing of drainage valves are described and presented in the form of separate patents and protocols [3,4]. The valve drainage system, which is simplified, is a silicone membrane, which opens at the outlet of the device with increasing pressure, and then closes. The main disadvantages of such a system were identified, namely - the lack of individual selection of parameters and regulation of fluid excretion, which as a result after some time of use took place and there were complications for the patient after surgery. The aim of the work was to create a prototype of the implant testing system for individual selection and regulation of the parameters of intraocular fluid excretion at the predicted rate for a patient with glaucoma.

2. Synthesis and construction of a prototype system for individual selection of implants

To achieve this goal, the authors analyzed the existing methods and identified shortcomings and proposed on the basis of elements of microsystem technology to create a functional diagram and prototype of an automated system for measuring and controlling the required parameters of implants. This approach provides: simplification of the technical solution of the scheme with the possibility of automating the process of preoperative examination of implants of known systems Ahmed, Krupin and other structures; to increase the sensitivity and accuracy of measurement and objectivity in determining the individual parameters of implants; determine their individual suitability for use in medical and surgical practice on the parameters of fluid removal, namely the minimum pressure of the valve opening, closing and reproducibility characteristics with the probable re-inclusion, which will increase the efficiency of operations; will reduce the time of inspection of the implant with the ability to save information about its parameters, their deviation. Therefore, the synthesis of the required scheme with a reasonable range of parameters was performed. Figure 2 shows the developed functional diagram of the prototype of the automated testing system of Ahmed implants to verify their individual characteristics, taking into account the compatibility and adaptation of the patient for optimal regulation of intraocular pressure within the required limits [4].

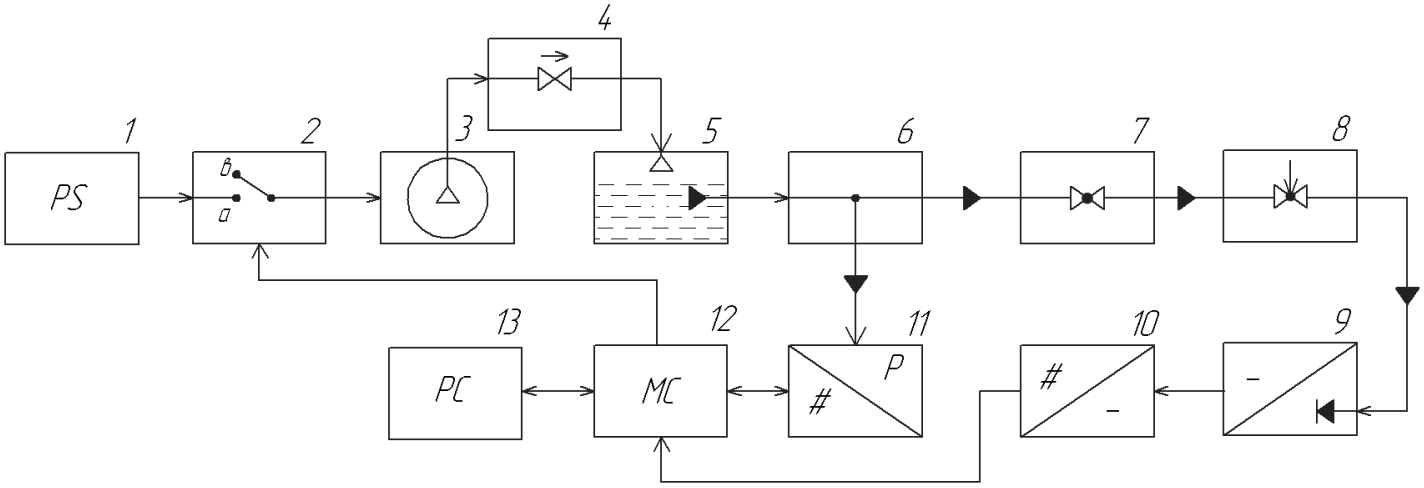

Fig. 2 Functional scheme of the implant testing system for the regulation of intraocular pressure.

The proposed testing system includes: power supply 1, electronic key 2, miniature compressor 3, connected through a check valve 4 to a tank filled with saline 5, inlet manifold 6, with electromechanical pressure gauges 11 connected to it, final data transfer with the implant 8. To the output of the implant is connected a liquid detector 9 and an ADC 10, which is connected to the input of the microcontroller 12. The first output, which is connected to the input of the computer 13, and the other from the input of the electronic control key 2.

The presented system of testing implants works as follows. First, the implant was connected to the cannula, which was connected to the multiple overlap of the supply of saline 7. In computers 13 includes the mode of checking the implant, the microcontroller 12 through the electronic key 2, the compressor 3 to increase the pressure in the tank 5 by means of the pre-valve 4 air does not go to the compressor from the tank. The pressure in the system gradually increases and is continuously monitored by its value by microelectromechanical pressure gauges 11, the pressure level continues to be read by the microcontroller and recorded in the computer memory taking into account the graphical pressure. The pressure in the system is close from zero to the value of the implant being tested. During the time of simplification of the implant for its upbringing meets the fluid that flows to the fluid detector 9, then the pressure level of the opening of the implant is fixed. The signal of the detector 9 through the ADC 10 is transmitted in digital form and fed to the microcontroller 11, which by means of an electronic key 2 stops the compressor 3 to turn off the supply voltage. The value of the pressure, its dynamics changes and opens and closes the microcontroller 11 is fixed and remembers the parameters of the computer 3. Due to the open valve the pressure in the system gradually decreases, the dynamics changes throughout the time controlled by microelectromechanical measuring pressures 11 and is introduced into the computer. 'ютер. When the valve is closed, the pressure is set at constant levels, which means the closing of the electromechanical pressure gauge 6, which is transmitted to the microcontroller 11 and entered into the computer. Using the software, the computer plots the pressure of this implant and determines the operating pressure range in which it can operate. The pressure in the system is monitored until the initial discharge of the fluid in which the fluid sensor is registered is implanted. At the time of passage of fluid through the implant system, the pressure level is determined, when it begins to enter the fluid during the test mode, after the detector of the fluid system registers the parameters of implant opening, and after achieving results or need to stop its supply. Opening the valves gradually reduces the pressure level in the system until they are completely closed. Thus, the sensitivity of the systems to the establishment of the necessary parameters, including the rate of fluid introduction, increases. All results are recorded in the computer's memory in graphical form or figures of all achieved pressure parameters, which is then used for documentation.

To ensure the modes of operation of the prototype systems, a product database was selected. The microcontroller uses the ATmega8L-8PU chip, which controls the SPS-15RF-172KP stepper motor using the Texas Instruments DRV8825 motor driver. The redundancy function uses a dispenser. Important elements of the system are the pressure gauge, which requires the required accuracy - microelectromechanical pressure gauge ST Microelecronics LPS33HW and microcontroller ST Microelecronics STM32F103RET6 uses its function. The microcontroller uses meters to access the SPI interface and communicates with the computer. The pressure measurement when using the basic elementary base is 0.075 mm Hg. Art. or 0.25% at the maximum determination of the pressure in the tanks. As a liquid detector used a resistive liquid detector WAVGAT MH RD with the size of the sensor part of 4 cm x 5 cm, with an ADC based on the comparator LM393, where the supply voltage is 5 V, the response speed of the comparator is 1.3 μs. The conversion characteristic for the analog output of such a sensor is a discrete function of the presence of liquid on the sensor plastic detector with a view:

$$\begin{cases} y = 0, \; npu - w = 0 \\ y = 1, \; npu - w \neq 0 \end{cases}$$

0 or 1 is generated at the digital output, in the absence or presence of fluid in the system, and the sensitivity is adjusted by changing the operating modes during debugging.

3. The methods of processing

For testing it was necessary to create an algorithm of the system, the block diagram of which is presented in Figure 3. Algorithm of the testing system which shows the sequential steps starting from the start and subsequent actions in the system of implant testing [4].

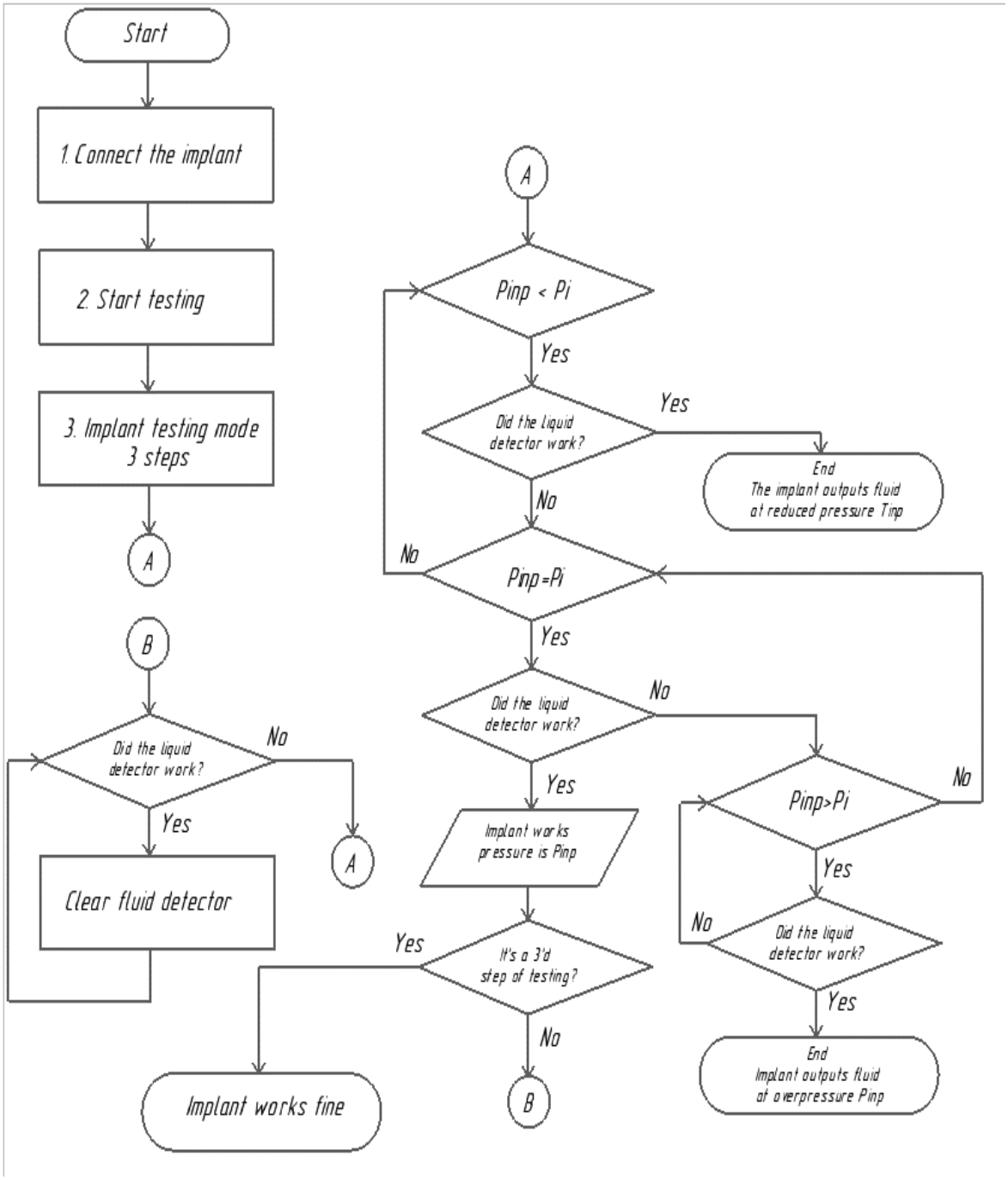

Fig. 3 Algorithm of the implant testing system for the regulation of intraocular pressure.

The quality of the implant testing system is ensured depending on the quality and rigidity achieved by the manufacturer, which affects different removal rates, when the pressure in the system changes before the removal of fluid by the implant, it is registered by the fluid sensor. As fluid passes through the implant, the system determines the pressure level at which the implant begins to drain fluid. After the fluid detector is activated, the system registers the implant opening pressure and stops fluid delivery at certain points.

In the process of testing, the parameters and conditions are checked, which are very important for further quality assurance of implants and three possible variants of the obtained result. Figure 4 shows the graphs of the pressure parameters for several instances of implants of different hardness, denoted by the symbols a, b and c.

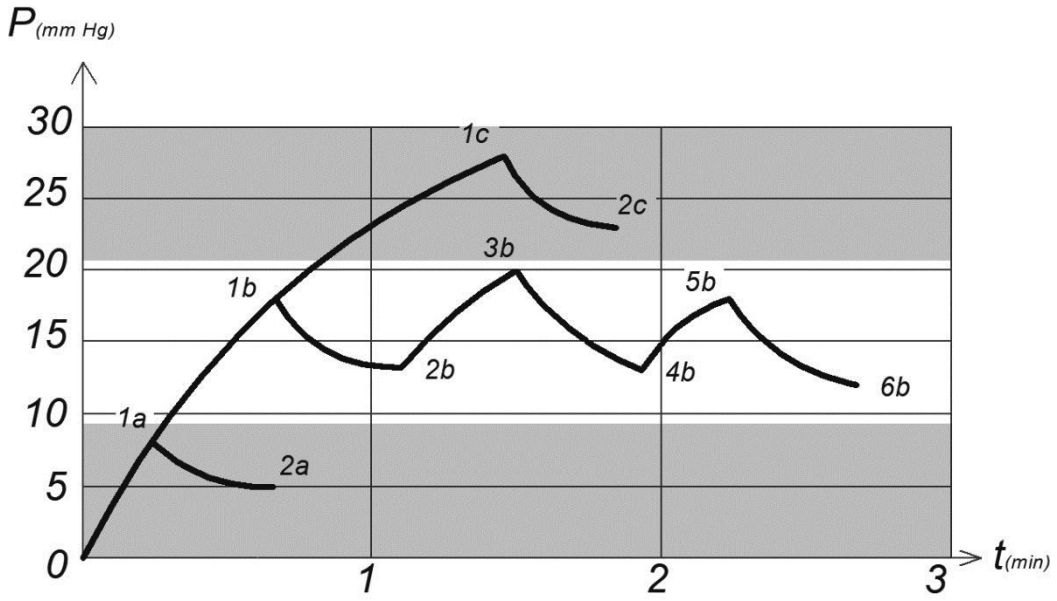

Fig.4. Graph of pressure change during tests of implants of different modification: a, c - conditionally defective, b - serviceable implant

The first implant a (pictured) has a reduced degree of hardness and is characterized by a pressure change of 8 mm Hg. Art. (valve opening point 1a) up to 5 mm Hg. Art. (closing point 2a). The test cycle of such an implant can last up to 1-2 minutes. Activation of the fluid detector at this stage is a sign of implant failure with the risk of hypotension after surgery, so such drainage is not suitable for use.

The second implant, denoted by the symbol b has a higher hardness, and therefore for its opening occurs at a higher pressure level also increases the test time. The change in the pressure parameters of the second implant points 1b and 2b are within the norm of 18–13 mm Hg. Art. Activation of the fluid sensor indicates that the implant operates within the normalized intraocular pressure range of 9–21 mm Hg. Art. After determining the implant that meets the regulatory requirements, the reproducibility of the parameters is checked by repeatedly increasing the pressure. To do this, the operator removes the fluid from the indicator plate of the detector and turns on the system again, until the operation of the fluid detector, which again fixes the moment of reopening of the implant at point 3b. The signal from the detector stops the compressor, after which the pressure of the open valve decreases and stabilizes at point 4b. This step is then repeated (points 5b and 6b). In the case of reproducibility of the characteristic due to three tests, the drainage is recognized as high quality and can be used for its intended purpose.

The third implant c is characterized by high rigidity and a change in operating pressure in the range of 28–23 mm Hg. Art. at points 1c and 2c, which exceeds the set range of intraocular pressure. Activation of the liquid detector due to a certain pressure indicates a malfunction of the implant.

The proposed version of the prototype system allowed for a short time (several minutes) to conduct a preoperative examination of Ahmed Glaucoma Vision implants to determine individual compatibility and controlled removal of intraocular fluid for a particular patient. It has the feature of ensuring the success of the operation and preserves the vision of patients with glaucoma for a long time due to the individual selection of implants with the necessary parameters of intraocular fluid excretion.

4. Conclusion

In this publication, the authors propose a method and tools that improve the known technical solutions for the construction of schemes with the possibility of automating the process for preoperative examination of implants of different types. A functional diagram of a prototype of the automated system for testing Ahmed implants has been developed to verify their individual characteristics, taking into account compatibility and adaptation of the patient for optimal regulation of intraocular pressure. An algorithm of the testing system was created and a prototype was built on which the software was tested and the automated testing system was tested, which allows to increase the sensitivity, measurement accuracy and objectivity of determining the parameters of implants; determination of their individual suitability for the patient with use in medical surgical practice on parameters of removal of liquid, namely pressure of opening, closing and reproducibility of the characteristic at repeated operation that will promote increase of efficiency of the carried out operations; reduction of time of check and selection of an implant. It is possible to save information about the fixed parameters and the final results of the inspection of implants of different types.

References

1. Brigham, K., Vijaya Kumar B.V.K. (2010). Imagined Speech Classification with EEG Signals for Silent Communication: A Preliminary Investigation into Synthetic Telepathy. *International Conference on Bioinformatics and Biomedical Engineering*, Proceedings of the 4th International Conference. Chengdu, China.

2. [electronic resource] http://www.who.int

3. Choudhari, N.S., Badakere, S.V., Richhariya, A., Harsha S.N.S., Senthil, S., Garudadri, C.S. (2018). Is Ahmed glaucoma valve consistent in performance. *Translational Vision Science and Technology*, *7* (3):19, 1-8.

4. Tkachuk, R., Tkachuk, A., Yanenko, O. (2020). Automated system of preoperative control of implant parameters for glaucoma treatment, *INSTRUMENTATION: State and Prospects*, Proceedings of the 1X International Scientific and Technical Conference. Kyiv, Ukraine.

5. Tkachuk, R., Tkachuk, A., Yanenko, O. Implant testing device for regulation of intraocular pressure: Pat. 143236 UA, IPC A 61B 1/00. No. 2019 09764; 12. 09. 2019; bulging 27.07. 2020, Byul.No 14. 4 ths.

Cross-sectional: MATHEMATICAL MODELING IN POWER ENGINEERING AND INFORMATION TECHNOLOGIES

MODELING OF THERMAL PROCESS PARAMETERS IN THE IONOSPHERE DURING THE DECLINE PHASE OF SOLAR ACTIVITY CYCLE

Vyacheslav Kolodyazhnyi, Mykhaylo Lyashenko

Institute of Ionosphere of the National Academy of Sciences of Ukraine and the Ministry of Education and Science of Ukraine, Kyrpychova str. 16, 61001, Kharkiv, Ukraine; e-mail: Vyacheslav.Kolodyazhnyi@infiz.khpi.edu.ua, M.Lyashenko@nas.gov.ua

Abstract: Simulation of spatial-temporal variations of parameters of thermal processes in ionospheric plasma during the decline phase of solar activity cycle according to the Kharkiv incoherent scatter (IS) radar of is performed. For typical geophysical periods, the diurnal and altitude dependences of the energy supplied to the electron gas and the heat flux density transferred by electrons from the plasmasphere to the ionosphere are constructed. The analysis of spatial and temporal variations of parameters of thermal processes in the ionosphere is given. The obtained calculation results are used for further development of the CERIM IION regional model of ionosphere.

Keywords: *ionosphere, modeling, incoherent scattering, parameters of thermal processes.*

1. Introduction

As is known, at the altitudes of the F2 region of the ionosphere and above, the processes of plasma and energy transfer become more significant than the photochemical processes of formation and disappearance of charged particles. Dynamic and thermal processes play an important role in the formation of the altitude profile of the electron concentration in general, in particular in the F2 region of the ionosphere. Thus, observation, analysis and modeling of variations in the parameters of physical processes in geospace plasma are currently important and relevant tasks of modern geophysics, as they expand our knowledge of the behavior of the parameters of the Earth's atmosphere, ionosphere and magnetosphere.

A large number of publications have been devoted to the study of variations in ionospheric plasma parameters in different heliogeophysical conditions [see, for example, 1–4]. Particular attention is paid to the study of the effects of rare and unique events in the geospace – the strongest geomagnetic storms, solar eclipses and others. However, the study and analysis of the behavior of ionospheric plasma in quiet conditions is no less relevant, because all perturbations unfold against this background.

At present time the Kharkiv IS radar is the only reliable and most informative data source of the geospace plasma parameters in the mid-latitude of Central Europe [5]. The parameters of dynamic and thermal processes in the ionosphere can be calculated with the involvement of experimental IS radar data. The obtained results of calculations are useful for further development of the regional model of the ionosphere CERIM IION [6, 7], which was created at the Institute of the Ionosphere.

The aim of the work is to simulate the spatial-temporal variations of the parameters of thermal processes in the ionospheric plasma during the equinoxes and solstices in 2017–2019 using experimental data of the IS radar in Kharkiv. An empirical model of the atmosphere NRLMSISE-00 was used to calculate the parameters of the neutral atmosphere [8].

2. Observation means

Kharkiv incoherent scatter radar. To study the effects in the ionosphere, the radar of the Institute of Ionosphere of the NAS and MES of Ukraine was used. It is located 50 km from Kharkiv and is the only, most informative source of information on parameters and processes characterizing the behavior of geospace plasma in the European middle latitudes [9]. Radar coordinates: 49.6° N, 36.3° E; geomagnetic: $\Phi = 45.7°$, $\Lambda = 117.8°$; the inclination of the geomagnetic field is 66.4°, the McIlvain parameter $L \approx 1.9$.

The radar is equipped with an zenith two-mirror parabolic antenna with a diameter of 100 m. The operating frequency of the radar is 158 MHz. The effective area of the antenna is about 3700 m^2, the gain of the antenna is about 104, and the width of the main petal of the pattern is about 1°. The pulse power of the radio signal is 2–4 MW. The frequency of transmission of radio pulses is 24.4 Hz. The noise temperature of the radio-receiving device is 120 K, and the bandwidth of the path, which is determined by the low-pass filters, is 5.5–9.5 kHz. The effective noise temperature of the system is 470–980 K.

Digital ionosonde. The digital ionosonde is used for general control of the ionosphere and calibration of the normalized altitude profile of the electron concentration at its maximum (determined by the IS method). The main parameters of the ionosonde: pulse power – 15 kW, duration of radio pulses – 100 μs, frequency range in the mode of vertical sounding 1–20 MHz, receiver sensitivity – 15 μV. Receiving and transmitting antennas – rhombic with vertical

radiation, arranged orthogonally. The error in determining the critical frequency of the layer F2 is not more than 0.05 MHz.

3. Space weather condition

Experimental studies of ionospheric plasma parameters were performed for four characteristic geophysical periods – summer and winter solstice, as well as vernal and autumn equinoxes in quiet geomagnetic conditions in the phase of decline/minimum of the 24th cycle of solar activity. Table 1 presents the dates selected for a detailed analysis of variations in ionosphere parameters and provides information on the state of space weather. In table 1, the indices indicate: $F_{10.7}$ – flux of solar radio radiation at a wavelength of 10.7 cm; A_p – is the total planetary index of geomagnetic activity; K_p – is the value of the planetary index of the magnetic field.

Table 1

Parameters of the space weather condition for the selected dates

Date	$F_{10.7}$	A_p	K_p
Vernal equinox			
23.03.2017	72	11	4 4 2 2 1 2 1 1
29.03.2018	69	4	0 0 1 2 1 2 1 1
21.03.2019	80	2	0 1 1 1 1 0 0 0
Summer solstice			
22.06.2017	74	6	3 2 1 1 1 1 3 2
21.06.2018	82	3	1 1 1 1 1 0 1 0
20.06.2019	68	7	1 2 3 2 1 1 2 2
Autumn equinox			
06.09.2017	133	11	2 2 2 3 3 2 0 4
19.09.2018	68	4	1 3 2 1 0 1 0 0
19.09.2019	67	4	1 1 1 1 1 1 1 1
Winter solstice			
25.12.2017	76	10	3 1 2 3 1 2 3 2
19.12.2018	70	6	1 1 1 2 1 2 1 2
17.12.2019	71	2	0 0 1 1 0 0 0 0

Table 1 shows that almost all periods considered were characterized by quiet geomagnetic conditions and low solar activity. The values of the index $F_{10.7}$ varied in the range from 67 to 82 units. However, on September 6, 2017, there was a slight disturbance of the space weather condition (the value of the index $F_{10.7}$ was 133 units). This is due to the increase in the total area of sunspots and the number of flashes in the active areas.

4. Initial theoretical relations

In this paper, we simulate the parameters of thermal processes in the ionosphere – the energy supplied to the electrons Q/N and the heat flux density Π_T, which is transferred by electrons from the plasmasphere to the ionosphere.

Energy supply to electronic gas. The thermal energy source of charged particles are photons of solar ionizing radiation. The nature of the heating of thermal electrons by photoelectrons differs significantly in the lower ($z \leq$ 250 km) and upper (z>250 km) ionosphere. In regions D and E of the ionosphere, photoelectrons are thermalized mainly at the site of their formation due to the relatively short free path length. This heating of the electron gas is called local. In the upper ionosphere, the frequency of electron collisions with neutrals becomes lower than with ions, and the main mechanisms of electron gas cooling are heat loss during electron collisions with ions, excitation of the fine structure of oxygen atoms, and thermal conductivity of the electron gas. In this case, the transfer of photoelectrons can be neglected, and the associated heating of the electron gas is called non-local.

Consider the altitude range of 210–450 km. At altitudes $z \leq 350$ km, the thermal conductivity of the electron gas can be neglected and the equation of energy balance of electrons in the stationary case has the form [10]

$$\begin{aligned} Q &= L_{ei} + L_e, \\ L_{ei} &= 8\cdot 10^{-32} N^2 (T_e - T_i) T_e^{-3/2}, \\ L_e &= 6.4\cdot 10^{-37} NN(\mathrm{O})(T_e - T_i) T_n^{-1}, \end{aligned} \tag{1}$$

where Q – is the energy transferred to thermal electrons in Coulomb collisions with photoelectrons; L_{ei} – energy loss in electron-ion collisions; L_e – energy loss on the excitation of the fine structure of oxygen atoms; N – the concentration of electrons in the ionosphere; $N(\mathrm{O})$ – concentration of oxygen atoms; T_e – the temperature of electrons; T_i – the temperature of ions; T_n – the temperature of the neutrals.

The electron concentration N, the electron temperature T_e and the ion temperature T_i were obtained experimentally using the IS radar in Kharkiv.

The temperature of the neutrals T_n and the concentration of N(O) are calculated according to the model NRLMSISE-00 [8].

The flux of heat transferred by electrons. The flux of heat from the plasmasphere to the ionosphere plays an important role in the heat balance of the electron gas. The accumulation of heat in the plasmasphere occurs due to the heating of thermal electrons fluxing from the place of its formation into the outer ionosphere. Some electrons lose their energy during Coulomb collisions with thermal electrons and ions. The rest of the electrons enter the magnetic field tube and are heated in it by repeated reflections from the ends of the magnetic tube. Thus, heat accumulates in the plasmasphere, which is then transferred to the ionosphere due to the high thermal conductivity of the electron gas.

The heat flux can be determined from the kinetic equation taking into account the transfer of thermal electrons. The vertical component of the heat flux coming from the plasmasphere is calculated by expression [10]

$$\Pi_T = -\kappa_e \sin^2 I \frac{\partial T_e}{\partial z} \tag{2}$$

where $\kappa_e = 2.08 \cdot k^2 N T_e / m\nu_{ei}$ – the longitudinal component of the thermal conductivity tensor of the electron gas; k – the Boltzmann constant; m – the mass of the electron; I – inclination of the geomagnetic field; z – height.

The frequency of collisions of electrons with O^+ ions to calculate the longitudinal component of the thermal conductivity tensor can be found using the expression

$$\nu_{ei} \approx 5.5 \cdot 10^{-6} N T_e \ln (2.2 \cdot 10^4 T_e N^{-1/3}). \tag{3}$$

5. The results of thermal process parameter modeling under quiet conditions

To calculate the parameters of thermal processes in the geospace plasma, we used experimental data (electron concentration in the ionosphere N, electron temperature T_e, ion temperature T_i), which were obtained on the Kharkiv IS radar during the equinoxes and solstices in 2017–2019. Consider in more detail the spatial-temporal dependences of the thermal process parameters.

The amount of energy supplied to the electrons. The main characteristic of diurnal variations of Q/N is that at night, energy is not supplied to the electrons, and the values of Q/N at this time are close to zero. The increase in the value of Q/N begins at sunrise, and decreases to the background night values – after sunrise. Maximum daily values of Q/N occur in the altitude range of 210–250 km, then with increasing altitude, the value of Q/N decreases.

Vernal and autumn equinoxes. In Fig. 1*a* and Fig. 1*b* presents the diurnal variations in the amount of energy supplied to the electrons for the periods of the vernal and autumn equinoxes in 2017–2019, respectively. For the period of the vernal equinox, these Q/N variations are similar. Maximum Q/N values are observed at an altitude of 210 km and are approximately $27 \cdot 10^{-22}$ J s^{-1} at noon. At an altitude of 350 km $Q/N \approx 1.7 \cdot 10^{-22}$ J s^{-1}. For the period of the autumn equinox we have similar values, however, there is a difference – the values of Q/N for 2017 are many times higher than in 2018 and 2019. One of the reasons for this behavior of Q/N is the disturbed state of the ionosphere.

Summer and winter solstices. In Fig. 1*c* and Fig. 1*d* presents the diurnal variations in the amount of energy supplied to the electrons for the periods of summer and winter solstice in 2017–2019, respectively.

As can be seen from Fig. 1*c*, Q/N values in summer are slightly lower compared to Q/N values during the equinoxes at altitudes of 210–250 km. Thus, the daily values of Q/N at an altitude of 210 km did not exceed $20 \cdot 10^{-22}$ J s^{-1}, and at altitude of 250 km – $Q/N \approx 9 \cdot 10^{-22}$ J s^{-1}. In the altitude range of 300–350 km, Q/N values ranged from $3.7 \cdot 10^{-22}$ J s^{-1} to $2 \cdot 10^{-22}$ J s^{-1}. For the period of the winter solstice Fig. 1*d*, a narrower form of diurnal variations of Q/N was observed in comparison with the forms of diurnal variations in the periods of the equinox and summer solstice, but the maximum value of Q/N in winter was not inferior to the summer values and in the periods of the equinoxes. At altitudes of 210, 250, 300 and 350 km, the value of $Q/N \approx 25 \cdot 10^{-22}$, $7.5 \cdot 10^{-22}$, $3.5 \cdot 10^{-22}$ and $1.25 \cdot 10^{-22}$ J s^{-1}, respectively.

Altitude profiles Q/N are presented in Fig. 2. At night, the value of Q/N is close to zero over the entire range of altitudes. During the day, the maximum values of Q/N occur in the altitude range of 200–300 km, and then with increasing altitude, the value of Q/N decreases to almost zero.

The results obtained in this study are in good agreement with the results obtained earlier in [1–4]. In general, it can be concluded that the extremal values of Q/N strongly depend on the phase of the solar activity cycle, the season, and the space weather state.

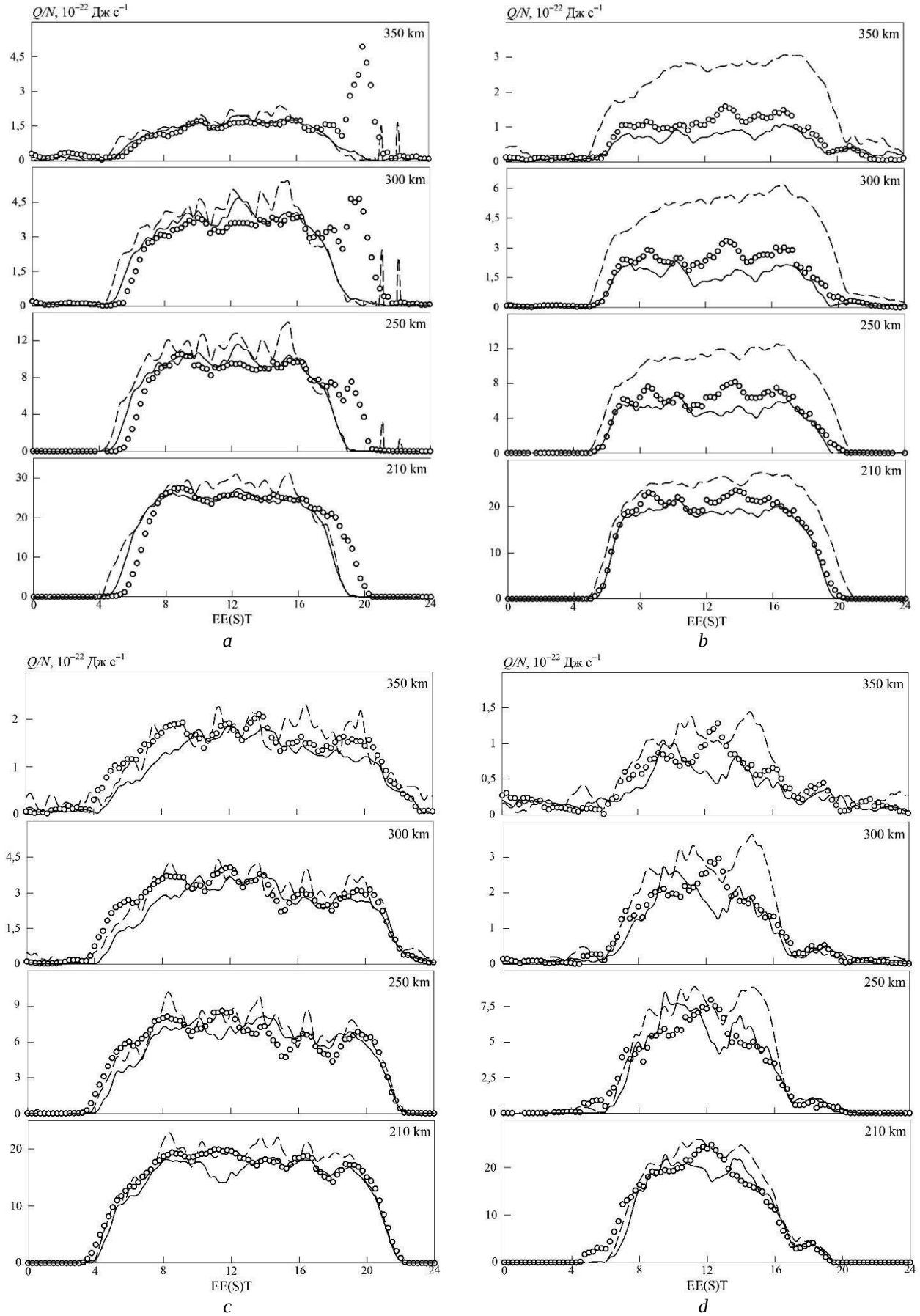

Fig. 1. Diurnal variations in the amount of energy supplied to the electrons *Q/N* in the periods: vernal (*a*) and autumn (*b*) equinoxes; summer (*c*) and winter (*d*) solstice during 2017–2019. Here and further, on the graphs the periods are indicated: dotted line – 2017, circles – 2018, solid line – 2019.

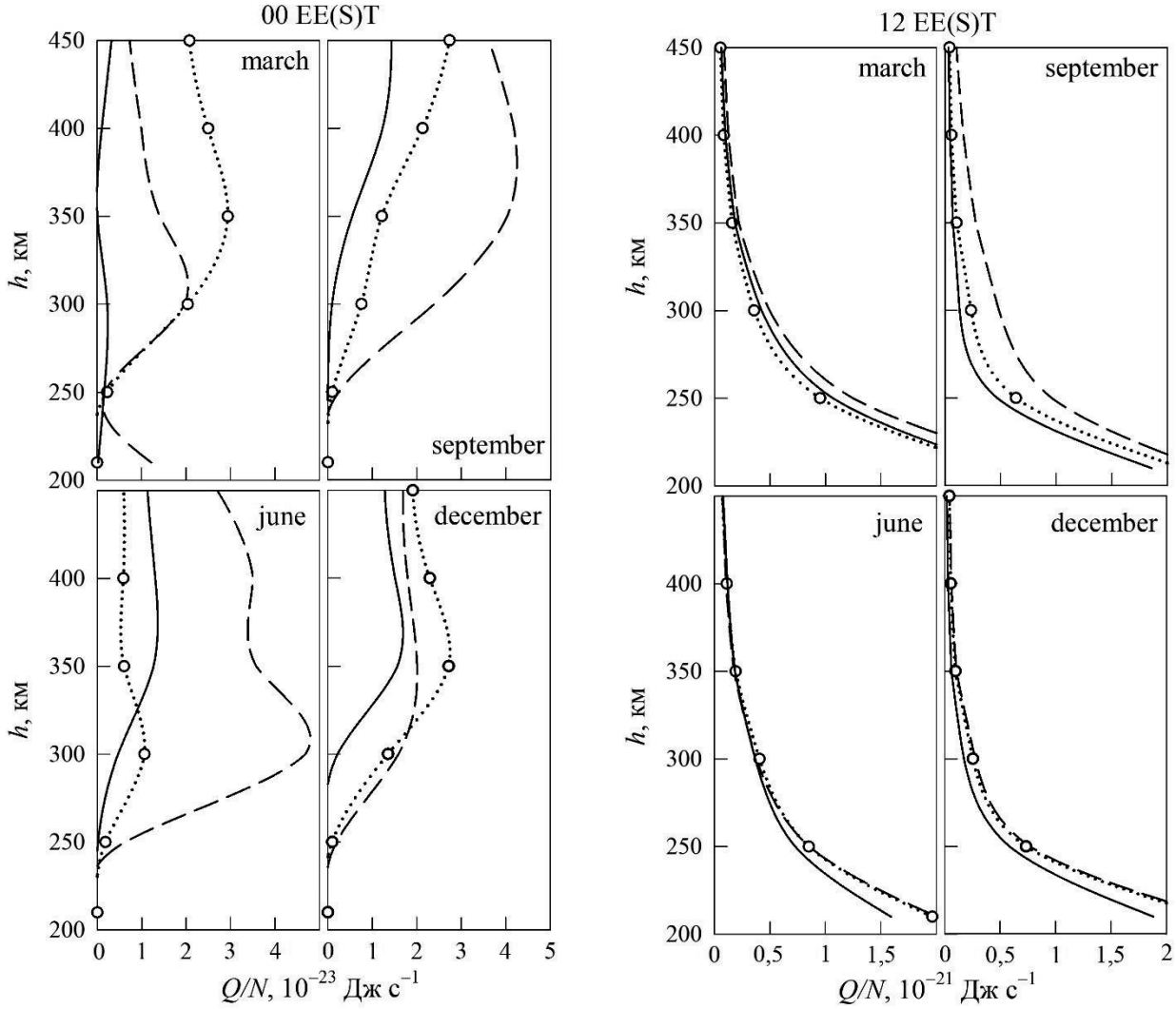

Fig. 2. Altitude profiles of the amount of energy supplied to the electrons *Q/N* in the typical geophysical periods during 2017–2019 for 00 (left panel) and 12 EE(S)T (right panel)

Heat flux density. The main features of the diurnal variations of Π_T are the practical absence of flux at night and the maximum values (by modulus) in the morning and evening.

Vernal and autumn equinoxes. In Fig. 3*a* and Fig. 3*b* shows the diurnal variations in the heat flux transferred by electrons from the plasmasphere to the ionosphere during the vernal and autumn equinoxes in 2017–2019. As can be seen from the Figures, the diurnal variations in Π_T are quantitatively and qualitatively similar. The behavior of Π_T in the vernal and autumn of 2017 is influenced by the state of space weather. In the considered periods of March 23, 2017 and September 6, 2017, the effects of moderate magnetic storms were noticeable in the variations of Π_T (maximum values of K_p index were equal to 4). The main effect of disturbed conditions is an increase in the value of Π_T and an increase in the downward flux of heat into the Earth's ionosphere.

Winter and summer solstice. In Fig. 3*c* and Fig. 3*d* shows the diurnal variations of Π_T in the periods of summer and winter solstice in 2017–2019 at fixed altitudes. The form of diurnal variations during the solstice periods is similar to the forms of time dependences obtained during the vernal and autumn equinoxes. The value of Π_T in summer is about 2 times less than in winter.

As well as for *Q/N*, the magnitude of the heat flux density depends on the level of solar activity and the state of space weather. As can be seen from the figures, even a small perturbation can lead to significant quantitative and qualitative changes in the diurnal variations in Π_T.

In Fig. 4, presents model height profiles of Π_T for noon and midnight. As can be seen from the Figure, at night in the entire altitude range there are quite small values of Π_T compared to daytime. At noon, in the range of altitudes of 300–400 km, the maximum values of the heat flux density, which is transferred by electrons from the plasmasphere to the ionosphere, are observed.

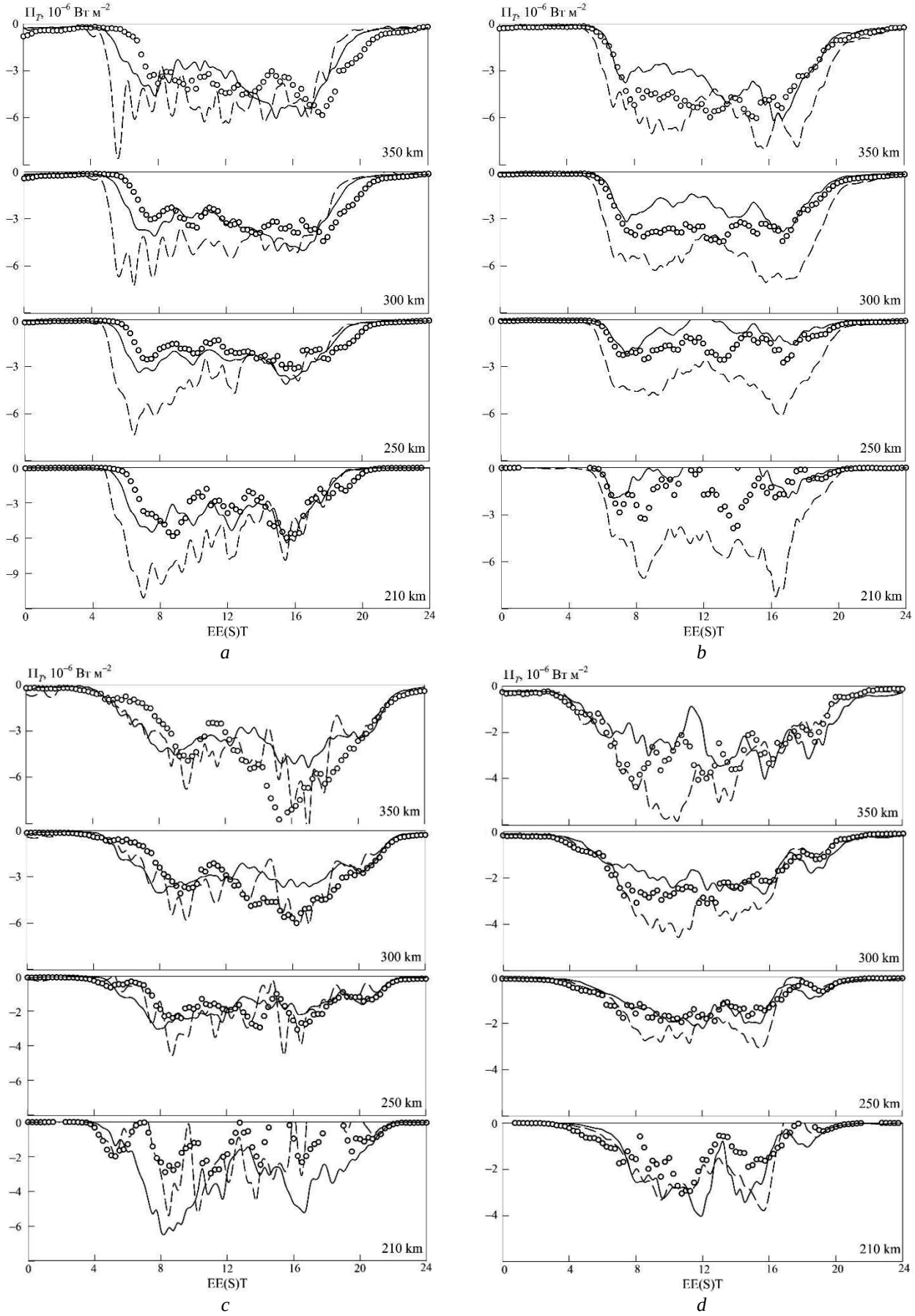

Fig. 3. Diurnal variations in the heat flux density of Π_T, which is transferred by electrons from the plasmasphere to the ionosphere in the periods: vernal (*a*) and autumn (*b*) equinoxes; summer (*c*) and winter (*d*) solstice during 2017–2019

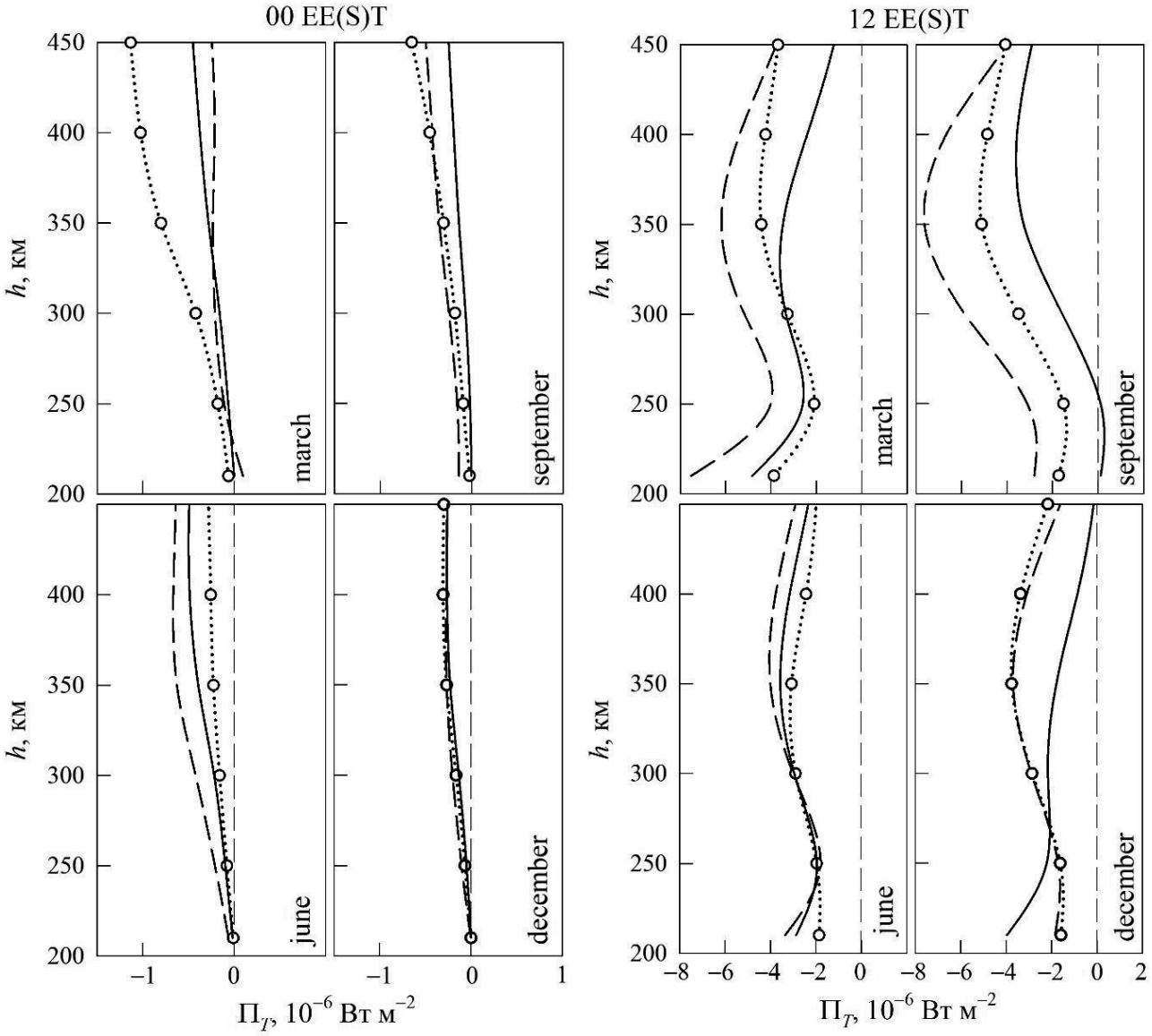

Fig. 4. Altitude profiles of the heat flux density transferred by electrons to the ionosphere from the plasmasphere in the typical geophysical periods during 2017–2019 for 00 (left panel) and 12 EE(S)T (right panel)

6. Conclusions

In this paper, we simulate variations in the parameters of thermal processes in the ionospheric plasma for periods close to the periods of summer and winter solstices, vernal and autumn equinoxes in 2017–2019.

The analysis of spatial-temporal and seasonal variations of parameters of thermal processes in the ionosphere on the phase of decline/minimum of the 24th cycle of solar activity is presented. The values of the energy supplied to the electron gas and the heat flux density transferred by electrons from the plasmasphere to the ionosphere are calculated. The obtained quantitative characteristics of the parameters, the shape of their height profiles and diurnal variations are typical for the considered seasons.

The obtained simulation results can be used in basic research of solar-terrestrial relations and geospace, for further development of the CERIM IION regional ionosphere model, as well as for solving applied problems related to the possibility of space weather predicting.

References

1. Lyashenko, M.V., Sklyarov, I.B., Chernogor, L.F. (2006). Diurnal and seasonal variations of ionospheric plasma parameters during the period of solar activity decline. *Space Science and Technology, 12*(2/3), 45–58.

2. Lyashenko, M.V., Chernogor, L.F., Chernyak, Yu.V. (2006). Diurnal and seasonal variations in the parameters of the ionospheric plasma during the maximum solar activity. *Space Science and Technology, 12*(4), 56–70.

3. Lyashenko, M.V., Pulyaev, V.A., Chernogor, L.F. (2006). Diurnal and seasonal variations in the parameters of the ionospheric plasma during the growth of solar activity. *Space science and technology*, *12*,(5/6), 58–68.

4. Dzyubanov, D.A., Lyashenko, M.V., Chernogor, L.F. (2008). Research and modeling of variations in ionospheric plasma parameters during the minimum period of the 23rd solar activity cycle. *Space Science and Technology*, *14*(1), 44–56.

5. Domnin, I.F., Chepurnyy, Ya.M., Emelyanov, L.Ya., Chernyaev, S.V., Kononenko, A.F., Kotov, D.V., … Iskra, D.A. (2014). Kharkiv incoherent scatter facility. *Bulletin of NTU "KhPI". Series: Radiophysics and ionosphere*, *47*(1089), 28–42.

6. Chernogor, L., Domnin, I., Lyashenko, M. (2010). Development of Central Europe Regional Ionospheric Model (CERIM IION) for Space Weather Forecasting. *EGU General Assembly 2010*. Proceedings of the Conference. Vienna, Austria.

7. Iskra, D.A., Kolodyazhnyi, V.V., Lyashenko, M.V. (2019). Development of the CERIM IION regional ionosphere model as part of the creation of the space weather forecast service. *Theoretical and applied aspects of radio engineering, instrument making and computer technologies*, Proceedings of the IV International Scientific and Technical Conference. Ternopil, Ukraine.

8. Picone, J.M., Hedin, A.E., Drob, D.P. (2002). NRLMSISE-00 empirical model of the atmosphere: Statistical comparisons and scientific issues. *Journal of Geophysical Research*, *107*(A12), 1–16.

9. Yemelyanov, L.Ya. (2017). Development of principles and instrumentation for generation of test and control signals of the incoherent scatter radar. *Telecommunications and Radio Engineering*, *76*(14), 1259–1271. doi: 10.1615/TelecomRadEng.v76.i14.50.

10. Schunk, R.W., Nagy A.F. (2009). *Ionospheres: Physics, Plasma Physics, and Chemistry*. Cambridge University Press.

THEORETICAL AND EXPERIMENTAL ASPECTS OF OPTIMAL DESIGNING OF DYNAMIC VIBRATION ABSORBERS – ROTATING MACHINES SYSTEM

Hennadiy Cherchyk,[1] Bohdan Diveyev,[2] Roman Yuzefovych[1,2]

[1]Karpenko Physico-mechanical Institute NAS Ukraine, Lviv, 5, Naukova Str., 79060, Lviv, Ukraine, e-mail: hcherchyk@gmail.com, roman.yuzefovych@gmail.com
[2]Lviv Polytechnic National University, 12 Bandera Str., 79000, Lviv, Ukraine, e-mail: divboglviv@yahoo.com

Abstract: Significant issue in the development of modern machines is the reduction of vibration. Dynamic vibration absorbers are widely used to reduce vibration and noise levels in vehicle cabs, to reduce vibration of rotating machines, to reduce vibration amplitudes of various towers and structures and the like. Along with dynamic vibration absorbers tuned to the resonant frequency of the main design, DVAs used to reduce vibration in a given narrow frequency range are widely applied. These are, for example, turbo-generators, gas compressor units, pumps and other rotating machines with a standard speed over a period of exploitation time. Vibration in such machines is narrow-frequency and is caused by imbalances of rotating elements.

Keywords: *dynamic vibration absorbers, rotating machines, frequency range*

1. Introduction

The design of the DVA was probably first proposed in [1] in 1911 by Fram. Tanks to reduce ship oscillations are named after him. However, the first mentioning of the use of DVA to reduce ship oscillations is found in [2]. The theory of DVA was first proposed in [3] (Ormondroyd & den Hartog (1928)). In [4] (Den Hartog (1985)) optimal values for frequency and damping in DVA were determined. The most well-known DVA equations are in [4] (den Hartog) and [5] (Timoshenko). A large amount of DVAs research is described in [6]. Here the optimal values for variable amplitude are found. The calculation of DVAs in pulsed and random perturbation is considered. Some constructive forms of DVAs are considered.

In addition to dynamic vibration dampers, various devices for absorbing energy of oscillations and shocks are widely used in the construction of devices and machines. The book [7] shows various devices for energy dissipation in structures under seismic loading. These are various types of dampers: dampers with viscous, dry friction, liquid-type dampers. DVAs of such different types are considered, too. Damping is considered on the basis of both a linear viscous model and hysteresis for nonlinear oscillations. Damping is not a simple process. Some basics can be found in [8–11].

Optimization of a DVA for a non-damped single-mass basic system under influence of harmonic excitation belongs to standard problems. A detailed review of the methods for calculating DVA was performed in papers [1–3]. Considerable attention was paid to the calculation and optimization of DVAs when interacting with the rotor [12–16]. Such studies are conducted in "time space" as opposed to studies in the "frequency domain". Most practical applications of DVAs are based on insufficiently complete mathematical models of complex structures and inefficient designing of DVAs. It does not take into account elastic properties of the structure itself, elastic properties of the node joining DVA to the main structure, and characteristics of the attached elements.

Also significant is the study of DVAs efficacy beyond the main system's own resonances. After all, the design of the DVA is often required to be effective for some fundamental external disturbance frequency, such as in pumps, turbines, motors etc. The shock mass model was used to correct both the DVAs masses and damping in their joints. Rigidity of the elastic plate elements was corrected based on both the refined determination of the elastic and damping properties of the plate and the refined calculation of the elastic plate clamping parameters. An alternative way to determine the model parameters is to experiment [16–18].

2. Rotating machines with DVA on the example of a pump. Identification

For accurate calculation of the design, it is necessary to develop a detailed theoretical model of the oscillating pump – DVA system and to determine factual parameters of this model. This requires a series of specific experimental studies that allow identification of the required number of parameters and determine their factual values. In this case, a number of model parameters are specified a priori (masses, geometric dimensions), but such parameters as elastic characteristics and damping require additional study.

To determine optimal parameters of a DVA it is necessary to determine its dynamic characteristics depending on the design parameters as well as investigate appropriate characteristics of the pump housing at the points of connection of the DVA. According to the simplified calculation scheme developed in the section, it is necessary to determine a number of model parameters that reflect both properties of the DVA and properties of the pump on the foundation: stiffness coefficients, damping coefficients, parameters of nonlinear stiffness and nonlinear friction of granular mass in the containers.

Let us consider the scheme of a DVA inertial masses of which are made in the form of containers filled with lead balls. Fig. 1 shows ~~a~~ general view of an adjustable wide-frequency dynamic vibration absorber of a rotor machine developed in the course of scientific research.

The following designations are used in Fig. 1: 1 and 2 are vibration absorbing elements (containers filled with damping material); 3 is an elastic plate element; 4 and 5 are connecting devices of the DVA vibration absorbing elements; 6 is a rotary machine; 7 is a support platform; 8 is a foundation; 9 are lead balls freely inserted into containers 1 and 2.

The principle of operation of the dynamic vibration absorber of the rotary machine is as follows: vibration from the rotary machine 6 (see Fig. 1) is transmitted to the vibration absorbing elements 1, 2. Each of them begins absorbing vibrational energy of the system independently in a certain frequency range. By adjusting the distance of the vibration absorbing elements 1, 2 with respect to the axis of the rotary machine 6 by means of the couplings 4, 5 we adjust each of the vibration absorbing elements 1, 2 to the main resonant frequency of the rotary machine.

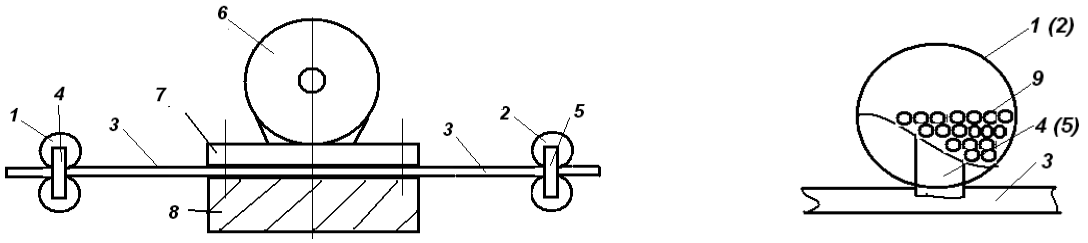

(a) (b)

Fig. 1 Adjustable wide-frequency DVA of a rotary machine: (a) front view, (b) element of DVA with particles

Changing the number and weight of lead balls 9 freely mounted in the hollow containers of the vibration absorbing elements 1, 2, they provide the corresponding values of damping in the vicinity of a given operating frequency. In this way, operational properties of the integral elastic-damping system are changed and the tuning parameters of the DVA vibration absorption are precisely adjusted, which allows you to solve two main tasks: 1) to provide highly efficient absorption of energy of mechanical vibrations of the system; 2) to prevent occurrence of resonant oscillations in the area of the calculated frequencies which are selected in the vicinity of the frequency of the most intense oscillations of the rotor machine.

The DVA described above has several advantages lying in that the DVA provides adjustable wide-frequency vibration absorption, does not create parasitic resonance perturbations around the operating frequency, and is characterized by improved performance.

The DVA having been developed was adopted as the basic model in the process of analytical and experimental studies of the working processes of fire pumps equipped with DVA.

The calculation model was described by the following system of differential equations:

$$m_1\ddot{x}_0+\left(k_1D_K+k_AD_A+k_{A2}D_{A2}\right)\dot{x}_0+\left(k_1+k_A+k_{A2}\right)\omega_o-k_AD_A\omega_A-k_A\dot{x}_a-k_{A2}\omega_{A2}=F;$$

$$m_A\ddot{x}_A+k_AD_A\dot{x}_A+k_A\omega_A-k_AD_A\dot{x}_0-k_A\omega_0=0; \quad (1)$$

$$m_{A2}\ddot{x}_{A2}+k_{A2}D_{A2}\dot{x}_{A2}+k_{A2}\omega_{A2}-k_{A2}D_{A2}\dot{x}_0-k_{A2}\omega_0=0.$$

where, m_1, m_A, and m_{A2} are masses, respectively, of the basic structure, the first and second DVA; k_1, k_{A1}, and k_{A2} are appropriate stiffness values; D_K, D_A, and D_{A2} are viscosity coefficients; ω_0, ω_A, and ω_{A2} are displacements; F is harmonic perturbation.

To simulate the motion of particles (crumbs or lead balls) of the filling of the containers, a shock mass model was used [12, 16], see Fig. 2).

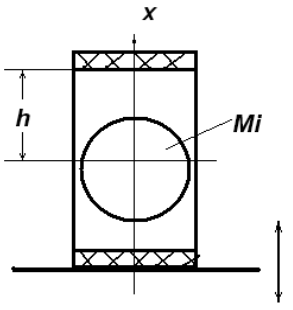

Fig. 2 DVA with shock mass *Mi*

The dynamic equilibrium equations for the mass *Mi* are as follows:

$$m_i\ddot{x}_i + m_i g + k_G(x)(\omega_i - \omega_0) + C_G(x)(\dot{x}_i - \dot{x}_0) = 0,\ |\omega_i - \omega_0| > |h - R|,$$

$$m_i\ddot{x}_i + m_i g = 0,\ |\omega_i - \omega_0| \le |h - R|, \quad (2)$$

where m_i is mass of the filler; k_G is stiffness of elastic gaskets; C_G are coefficients of viscous damping of gaskets; ω_i are displacements of equivalent mass; ω_0 is displacement of the container base, R is radius of mass m_i.

Analysis having been conducted confirmed that the experimentally derived characteristics of the processes of oscillation damping were similar to the results derived theoretically.

3. Multi-criteria identification of the main design – DVA system parameters

To determine appropriate parameters and characteristics of the DVA design scheme of which is shown in Fig. 3 it is necessary to perform parametric analysis of its properties.

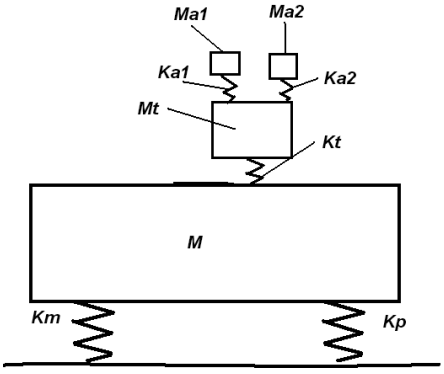

Fig. 3 Design scheme of the DVA under investigation

According to Fig. 3 we select the following for the DVA parameters:

1) Mass of the first DVA – M_{A1};

2) Mass of the second DVA – M_{A2};

3) Distance from the clamping point (shoulder) of the first DVA – L_{A1};

4) Distance from the clamping point (shoulder) of the second DVA – L_{A2};

5) Damping in the first DVA – D_{A1};

6) Damping in the second DVA – D_{A2}.

Stiffness magnitudes of the elastic elements of the DVA will be (without taking into account the compression force) as follows [5]:

$$K_{A1} = \frac{3EI}{L_{A1}^3},\ K_{A2} = \frac{3EI}{L_{A2}^3}. \quad (3)$$

We also take into account inertial properties of the elastic element. We use the method given in [5]. We consider that the first form of oscillation of a beam with mass is approximated fairly accurately by the line of deflection of this beam. We obtain a modification of the formula given in [5]:

$$M_{D1} = M_{A1} + M_B \frac{33}{140}, \quad (4)$$

where M_B is mass of the beam; M_D is the equivalent mass centered at the end of the beam.

In our case, we obtain equivalent masses concentrated at the locations of the masses of DVA:

$$M_{D1} = M_{A1} + M_B \frac{33\chi_1}{140}\left[1 + 3\left(\frac{1}{\chi_1} - 1 + \left(1 - \frac{1}{\chi_1}\right)^2\right)\right], \quad (5)$$

$$M_{D2} = M_{A2} + M_B \frac{33\chi_2}{140}\left[1 + 3\left(\frac{1}{\chi_2} - 1 + \left(1 - \frac{1}{\chi_2}\right)^2\right)\right], \quad (6)$$

where $\chi_1 = \frac{L_{A1}}{L}$, $\chi_2 = \frac{L_{A2}}{L}$, L is the length of DVA beam.

Instead of the masses of the DVA we consider reduced masses concentrated at the same points. This allows you not to consider additional equations of dynamic equilibrium of massive elastic elements (beams).

Fig. 4 shows a block diagram of a measuring and recording hardware complex, which shows the following designations: 1 is a mounting unit of a DVA; 2 is a DVA; 3 are lead balls; 4 is a container; 5 is an electric motor; 6 are screws; 7 is a vibrating platform.

In further studies we will use the first method of determining of damping based on the calculation of the monotonic decrease in the amplitude of oscillations at some initial perturbation of two types: kinematic and shock. Let us consider first kinematic perturbation which was carried out according to the layout shown in Fig. 5 and used to determine the elastically-damping properties of the plate DVA (Fig. 5).

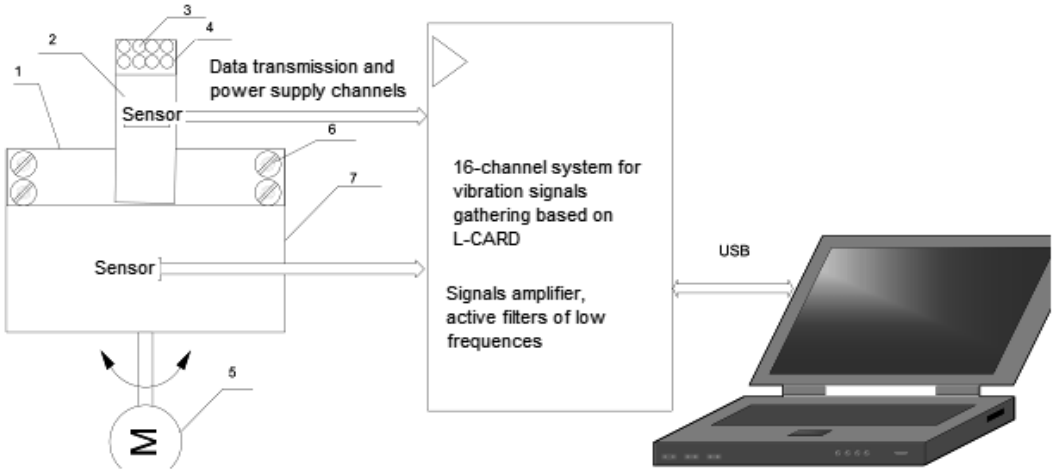

Fig. 4 Layout of measuring and recording hardware complex

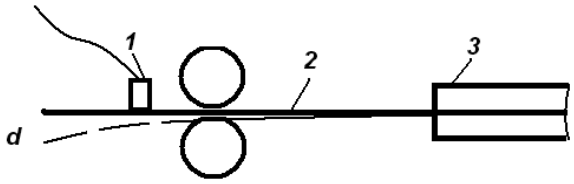

Fig. 5 Setup of the experimental bench used for the studying of kinematic perturbation of DVAs

In Fig. 5 the following designations are accepted: 1 is a vibration sensor, 2 is a DVA; 3 is a clamping; d is the set initial kinematic deviation of the elastic plate 2 of the DVA.

In Fig. 6 shows view of the plate DVA under investigation (equipped with vibration sensor).

Fig. 6 Appearance of the plate DVA under study

In the first stage of the oscillation process the amplitude of oscillations sharply decreases. This is caused by considerable dissipation of energy due to interaction of the lead balls moving the container with its walls. Further, as the amplitude of oscillations of the bulk decreases, when the acceleration of the container becomes less than gravitational, the balls fall to the bottom of the container and function only as additional mass without creating effect of internal intergranular friction.

Fig. 7 shows the oscillogram of oscillations (experimental and theoretical) of the platform in the presence of filling (lead balls) in containers of the DVA.

The total weight of lead balls was 0.1 kg and the diameter of each ball was 3 mm. Even with such a small (1/15) ratio of the masses of the DVA and the filler, a significant decrease in the amplitude of the DVA oscillations was achieved initially (as long as the DVA acceleration exceeded the gravity acceleration and the balls were movable and provided internal friction). Fig. 7b shows results of the analytical calculations.

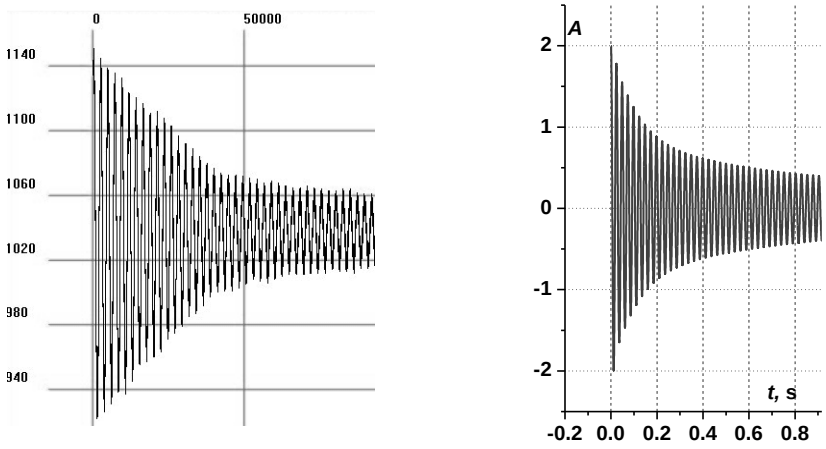

(a) (b)

Fig. 7 Experimental (a) and theoretical (b) oscillograms of the DVA oscillations with filling

In the course of the experiment, such parameters as C_i, k_G, C_G were set in the shock mass equation to maximize the coincidence of theoretical and experimental results. However, it is quite difficult to study the complete system (1), especially in the wide frequency spectrum. Therefore, only system (2) with modified parameters was considered. The damping coefficients based on the experimental results were set as follows: $D_{A2} = 0.0001$ for the filled container; $D_{A2} = 0.00033$ for the empty container.

4. Determination of the dynamic characteristics of the pump housing

The layout of the experiment is shown in Fig. 8. Impact excitation was used to investigate dynamic characteristics of an oscillating engine – pump system. Fig. 9 shows experimental and theoretical vibrorecords.

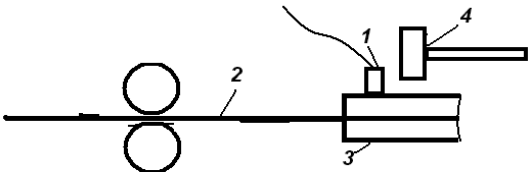

Fig. 8 Layout of the experiment for determining parameters of the oscillatory system in shock perturbation: 1 is a vibration sensor; 2 is a DVA; 3 is a clamping; 4 is an impact device

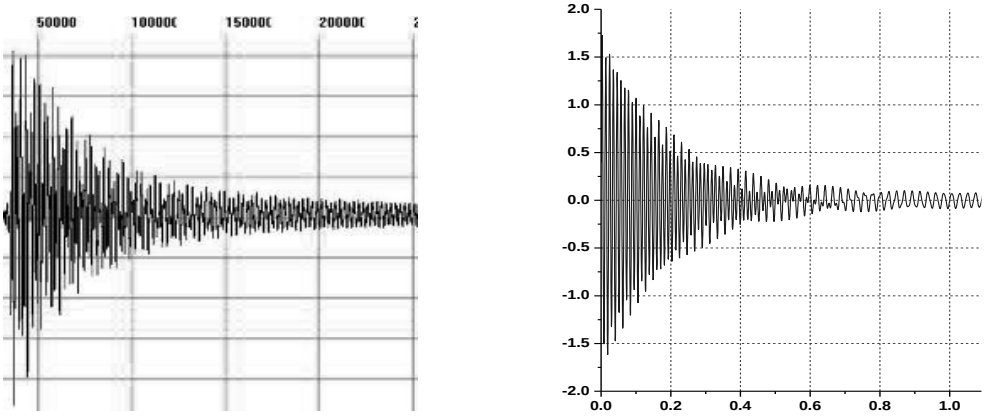

(a) (b)

Fig. 9 Experimental oscillogram of oscillations being dampened at pulse perturbation of the pump base (a), theoretical waveform oscillogram of oscillations being dampened at pulse perturbation of the pump base (b)

For further research, it is advisable to consider only the initial stage, since oscillations of the operating DVAs with high frequency and damping of oscillations of the pump housing are observed after that. Comparing the oscillograms the natural oscillation frequency of the pump housing can be estimated as (70/36) × 50 = 90 Hz. The damping is quite high and equals to $D_M = 0.0002$.

Identification of pump parameters based on design schemes. For more precise determination of the model parameters, a number of additional experiments were carried out (concerning determination of the parameters of m_1 and k_1 i.e. mass and stiffness of the main system). At the same time, parameters of DVA, in particular m_A and k_A should have been determined. Although they could be calculated more accurately than the parameters of the main system, it still required considerable effort both to determine elastic properties of the DVA itself and elastic properties of the clamping of the DVA plate. Although a detailed theoretical analysis can be made here [19], however, on the basis of a series of simple experiments it is possible to quite accurately define these parameters as complex quantities included in the system of equations (1) and (2). First, let's find out correctness of these schemes. Fig. 10 shows charts of frequency deviation from the centered values depending on changing of m_{1i} and k_{1i} parameters:

$$R = \left| f(m_{10}, k_{10}) - f(m_{1i}, k_{1i}) \right|,$$
$$m_{1i} = m_{10}(i - N/2), i = 1,...N, \quad k_{1i} = k_{10}(i - N/2), i = 1,...N \ . \tag{7}$$

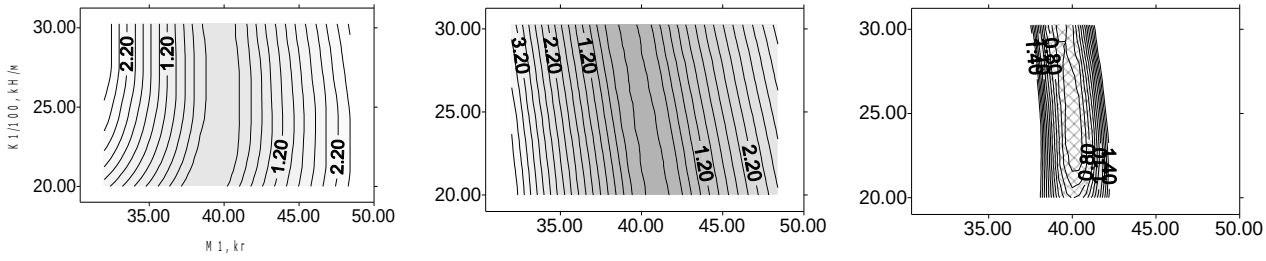

(a) (b) (c)

Fig. 10 Charts of deviations of frequency of oscillations of the DVA from the centered values depending on changing of appropriate parameters, for the following mass of the DVA: $m_A = 1.5$ kg (a) and $m_A = 3.0$ kg (b), and intersection of these charts (c)

Fig. 10 shows that each chart in particular does not define these parameters uniquely, but if we take the sum of these charts $R_\Sigma = R_1 + R_2$ (Fig. 10), this point will be determined unequivocally.

Table 1

Natural oscillation frequencies of a DVA for its different masses

M, kg	0	0.669	1.100	1.521	3.115
f, Hz	69	48	36	32.3	24.4

To determine all the parameters of k_1, m_1, m_A, and k_A we apply the method of genetic minimization for the objective function $F_{c=}\sum_i \left| f_T\left(M_i\right) - f_e\left(M_i\right) \right|$, where $f_T\left(M_i\right) = f_T\left(M_i, k_1, m_A, k_A\right)$ are theoretically obtained values of natural frequency, and $f_e\left(M_i\right)$ are experimental values.

Influence of mass is difficult to track due to the complexity of the pump design, but oscillation frequency can be observed on vibrorecords on fig. 7 in case of shock perturbation. We see that it is in the region of 65 Hz (as theoretically determined). That is, the principal construction's natural frequency is higher than the operating frequency of 50 Hz. This gives information in which neighborhood of DVAs natural frequencies to look for the optimum vibration absorption at the operating frequency.

5. Optimization of DVA at actual parameters of the oscillatory system

Based on the theoretical and experimental analysis the parameters of the basic design were determined: m_1 = 35 kg, f_1 = 65.5 Hz. Let's optimize a DVA at these parameters. Fig. 11 shows ~~the~~ results of optimization at different frequency ranges: *47 Hz < f < 50.5 Hz* is optimization for a wide range of frequencies; *48.5 Hz < f < 50.5 Hz* is optimization in a narrower range.

As shown above, the main parameter of the DVA optimization is its own oscillation frequency within the structure.

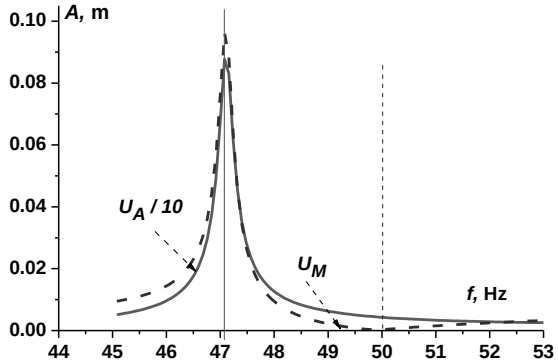

Fig. 11 Frequency response of the main design at different frequency ranges

Experimental verification of the optimality of the DVA system. Based on the the theoretical and theoretical-experimental studies having been conducted, optimal parameters of the DVA system were determined. ~~In~~ Fig. 8.12 shows the vibration diagrams of the basic design at operating frequency $f_R \approx 50$ Hz. Measured deviations from the operating frequency were in the range of 0.1 to 0.15 %. The following algorithm was applied: the mass of the DVA was moved along the plate with some fixed step (1 cm). Based on the kinematic perturbation scheme, the natural frequency of DVA was measured. Then measurements were made on the basis of the pump.

Weight of the DVA was 1.881 kg.

As we can see , at a frequency close to the theoretically determined optimum (47Hz, Fig. 12), the oscillation amplitude of the basic structure decreases by an order of magnitude.

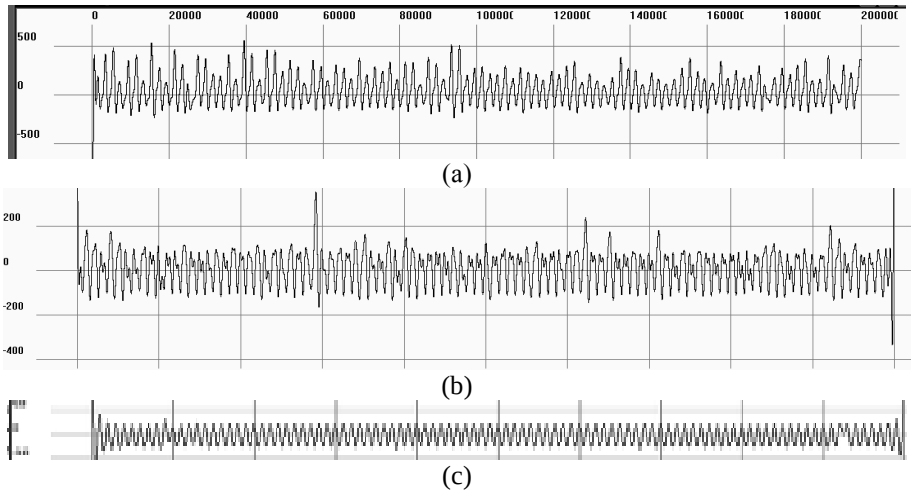

Fig. 12 Vibrorecords of the basic design at different natural frequencies of DVA:
(a) – $f_A = 46Hz$; (b) – $f_A = 46.5Hz$; (c) – $f_A = 47Hz$

Thus, taking into account appropriate characteristics of a rotating machine and ~~a~~ sufficiently large numerical experiment it is possible to select optimal characteristics of a DVA. For the majority of low-power pumps of fire-fighting systems the dominant factor is vibration absorption in the operating frequency range. Frequency response of the optimum DVA in this case will deviate significantly to the left (item 2), too, from the operating frequency of the main structure (oscillating system of motor – pump) which is 50 Hz.

6. DVA strength

Important criteria for DVA designing are its durability and compactness. Strength of the vast majority of structures is determined by strength of their joints. In addition, connections often serve as stress concentrators. In the case of DVA in the form of mass on a console maximum stresses should be expected in the clamping beam-plate which is an elastic element of a DVA.

The influence of different parameters of DVA on its effectiveness was studied above. If the stiffness parameters influence very significantly, but the damping parameters are much less influential. At the same time, one should expect ~~a~~ significant effect of the damping properties of DVAs on the maximum amplitude of their oscillations, and thus on their strength. The maximum strength in the elastic element of the DVA, which is the plate element, will be as follows:

$$\sigma_{MAX} = \frac{M}{W} = \frac{\omega^2 A M_A L_A z_{MAX}}{EI}. \tag{8}$$

Here M is the moment, W is the moment of section resistance, ω is the circle frequency $\left(\omega = 2\pi \times 50\right)$, A is the oscillation amplitude, M_A is the mass of DVA, L_A is the distance of mass from clamping, z_{MAX} is maximum deviation of section of plate from midline (in our case half thickness of plate), EI is the moment of bending resistance of the cross section. If we substitute in (8) $z_{MAX} = \frac{h}{2}$ and $I = \frac{bh^3}{12}$, then we obtain

$$\sigma_{MAX} = \frac{\omega^2 A M_A L_A}{6bh^2 E}. \tag{9}$$

This value shall be less than the allowable multi-cycle allowable strength

$$\sigma_{MAX} < [\sigma]^{-1}, \tag{10}$$

which for the 65G spring steel is approximately equal to 240 MPa. All geometrical parameters of a DVA spring are regulated both by its frequency characteristics and by design requirements. The only independent adjustable parameter is the oscillation amplitude *A* of the DVA mass. Fig. 13a shows frequency response of the basic structure with low (optimized) damping and some larger damping. Fig. 13b shows corresponding frequency response of a DVA (one DVA is considered).

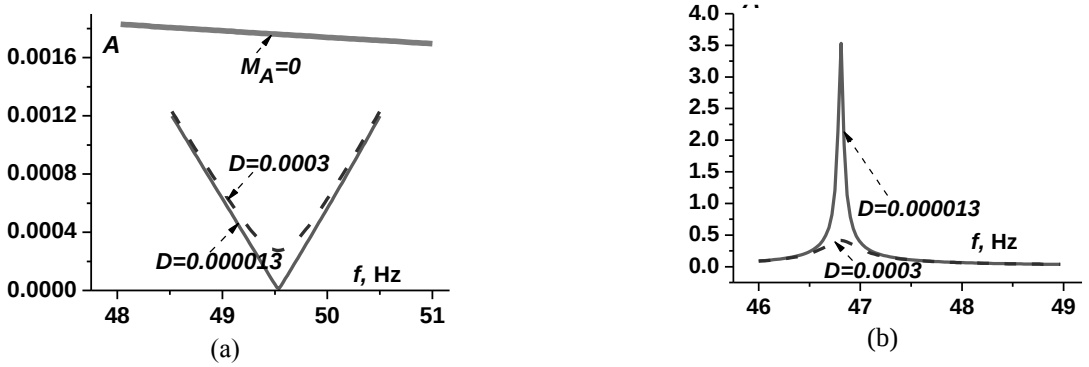

(a) (b)

Fig. 13 Frequency response of the basic structure (a) at low (optimized) damping and some greater damping and frequency response of DVA (b)

It can be not~~ice~~ed that with a slight deterioration of the vibration-absorbing properties of a DVA (only in some narrow frequency range, which will not necessarily correspond exactly to the operating frequency) the amplitude of the DVA vibration is reduced by an order of magnitude. That is, the risk of DVA destruction is significantly reduced. In our DVA design this was achieved by using containers filled with lead balls instead of solid masses of DVA. Large damping in this type of DVA design does not lead to the destruction of the elastic element in critical cases, when the operating frequency approaches the natural frequency of the DVA or when the transient process of the pump acceleration is slow enough and the DVA manages to gain large oscillation amplitudes in the pre-working zone.

7. Conclusions

A theoretical and experimental complex for determining characteristics of both DVA and the basic structure are shown. Two dynamic methods were used to determine dynamic characteristics experimentally: some initial kinematic

deviation for the DVA and some initial shock excitation for the basic structure were specified. A sufficiently large damping was shown in the construction of DVA with containers filled with lead beads. There is also a large enough damping of the pump body itself on the foundation. Based on the comparison of experimental data with the theoretical ones specific parameters of the mathematical model were determined.

A method of determining dynamic characteristics of the basic structure at the point of attachment of the DVA was developed. Here, the same DVAs, but with different mass parameters, were used as a test models. This allowed us to determine uniquely dynamic characteristics of the basic structure. It should be noted that in our system the natural frequency of the structure was higher than the frequency of perturbation. This result was obtained in two ways: by direct analysis of vibrorecords during shock perturbation and Based on the multi-mass method developed. Thus, this section determines dynamic parameters of the DVA and the pump housing which enables optimal designing.

Based on the preliminary theoretical and experimental analysis (clause 2.3) theoretical and experimental methods were developed to reduce vibration of the pump due to optimally designed DVA. The following optimization algorithm was proposed:

1) Theoretical and experimental determination of the parameters of both the basic design and DVA.

2) Vibrorecords of the basic structure were derived by changing the DVA frequency in some predetermined theoretically determined frequency range.

3) Optimum ones shall be received from the vibrorecords, be selected.

It was shown that the optimum values of DVA frequencies are not necessarily the same or even close to the operating frequency. The optimal value of the DVA frequency is close to the frequency of f_A = 47 Hz; the optimized DVA reduced the oscillation amplitude of the pump at an operating frequency of 50 Hz.

References

1. Frahm, H. (1911). Device for damping vibration of bodies,U.S. Patent. No. 989958

2. Watts, P. (1883). On a method of reducing the rolling of ships at sea. *Transactions of Institution of Naval Architects, 24*, 165.

3. Ormondroyd, J., den Hartog, J.P. (1928). The theory of the dynamic vibration absorber. *Transactions of the American Society of Mechanical Engineers, 50*, A9-A22.

4. Den Hartog, J.P. (1985). *Mechanical Vibrations*. New York: Dover Publications.

5. Timoshenko, S.P. (1954). *Vibration Problems in Engineering*. New York: Van Nostrand.

6. Korenev, B.G., Reznikov L.M. (1993). *Dynamic vibration absorber*. Wiley.

7. Constantinou, M.C., Soong, T.T., Dargush, G.F. (1998). *Passive energy dissipation systems for Structural design and retrofit*. New York, Multidisciplinary Center for Earthquake Engineering Research.

8. Truesdell, C., Noll, W. (2004). *The Non-Linear Field Theories of Mechanics. Third Edition*. Berlin-Heidelberg-New York: Springer-Verlag.

9. Ashley, S. (1984). On the passive damping mechanisms in large space structures. *Journal of Spacecraft and Rockets, 21*(5), 448–455.

10. Nashif, A.D., Jones D., Henderson, J.P. (1985), *Vibration Damping*. John Wiley & Sons.

11. Ungar, E.E., Kerwin, E.M. (1962). Loss factors of viscoelastic systems in terms of energy concepts. *The Journal of the Acoustical Society of America*, *34*(7), 954–957.

12. Diveyev, B. (2017). Impact and particle buffered vibration absorbers optimization and design. *Ukrainian Journal of Mechanical Engineering and Material Science*, *1*(2), 35–50.

13. Diveyev, B., Vikovych, I., Martyn V., Dorosh I. (2015). Optimization of the impact and particle vibration absorbers. *Sound and Vibration*, Proceedings of the XXII International Congress. Florence, Italy.

14. Diveiev, B. (2003). Rotating machine dynamics with application of variation-analytical methods for rotors calculation. *Implementation and Education Problems*, Proceedings of the XI Polish – Ukrainian Conference on CAD in Machinery Design. Warsaw, Poland.

15. Stocko, Z., Diveyev, B., Topilnyckyj, V. (2007). Diskrete-cotinuum methods application for rotating machine-absorber interaction analysis. *Journal of Achievements in Materials and Manufacturing Engineering*, *20*(1-2), 387–390.

16. Cherchyk, H., Diveyev, B., Martyn, V., Sava, R. (2014). Parameters identification of particle vibration absorber for rotating machines. *The International Congress on Sound and Vibration (ICSV)*, Proceeding of the Congress. Beijing, China.

17. Masanobu, I., Isao, Y., Koju, H. (2005). Design of Particle Granules Damper for Vertical Vibration with Approximate Analysis. *Journal of System Design and Dynamics*, *7*(4), 233–241.

18. Saeki, M. (2014). Analytical study of multi-particle damping. *Journal of Sound and Vibration*, *281*, 1133–1144.

19. Diveyev, B., Konyk, S., Malcolm, C. (2018). Dynamic properties and damping predictions for laminated plates: High order theories, Timoshenko beam. *Journal of Sound and Vibration*, *413*, 173–190.

MATHEMATICAL MODELING OF HIGH-FREQUENCY MAGAMP SWITCH B-H CHARACTERISTIC

Anna Yaskiv[1], Keyue Smedley[2], Alexander Abramovitz[3], Volodymyr Yaskiv[4], Natalia Kasatkina[5]

[1]West Ukrainian National University, 11 Lvivska str., Ternopil, Ukraine, 46009; annyaskiv@gmail.com
[2]University of California, Irvine, Irvine, CA 92697-2625, USA, smedley@uci.edu
[3]Holon Institute of Technology, 52 Golomb str., Holon 5810201, Israel; alabr@hotmail.com
[4]Ternopil Ivan Puluj National Technical University, 56 Ruska str., Ternopil, Ukraine, 46001; yaskiv@yahoo.com
[5]National University of Food Technology, 68 Volodymyrska str., Kyiv, Ukraine, 03001; nkasatkina@ukr.net

Abstract: The current paper features a problem of high-frequency MagAmp switch modeling for computer aided design programmes to enable MagAmp power converters design automation. A new mathematical model of MagAmp switch B-H characteristic is presented. An algorithm of its computer integration is described. Dependence of B-H characteristic on switching frequency is investigated for two configurations of MagAmp switches with cores of amorphous Co-based alloy with rectangular hysteresis loop. The simulation results are obtained, and maximum modeling error is calculated.

Keywords*: high-frequency MagAmp switch, B-H characteristic, magnetic hysteresis, mathematical model, computer simulation.*

1. Introduction

High-frequency MagAmp switches are used in pulse power converters when it is necessary to provide high reliability, efficiency, high level of dynamic characteristics [1,2]. They do not require complicated control circuits, PWM controllers, input rectifiers, leading to simpler power supplies' topologies, smaller number of components, mass and dimensions, and, consequently, reduced price of the device along with its increased reliability and efficiency. Such power converters are widely used in aviation, biomedical, space, lighting engineering, communications and IT, transport systems, etc. [3-6].

MagAmp switch consists of a core made of soft magnetic material with relatively square B-H characteristic, winding around it, and is supplemented with a diode to block applied voltage when necessary [7]. If MagAmp switch configuration turns out to be wrong for the required power supply specification, it has to be soldered out and formed again as a component with adjusted number of winds around the core, leading to increased power converter design time complexity. The automation of power supplies design is achieved with computer aided design (CAD) programmes for electric circuits. However, such computer simulation is based on the discrete parameters of electric circuits such as currents and voltages, and is not suitable for modeling of magnetic fields and nonlinear magnetic components. That is why there is a problem of creation of MagAmp switch model suitable for its integration into a library of components of CAD programmes for electric circuits.

Nowadays there are CAD programmes for modeling solely magnetic fields [8-10]. There are integrations of Jiles-Atherton [11] and John Chan [12] models of magnetic hysteresis into pSim and LTspice environments respectfully, but they are suitable only for modeling MagAmp linear operation mode [13]. Preisach model of magnetic hysteresis [14] and artificial neural networks [15,16] feature high computational complexity and require integration into CAD programmes for electric circuits. The integration of analytical hysteresis model by A. Nicolaide into LabWiev software [17,18] is developed only for magnetic fields investigation and cannot be used for electric circuits design automation. MagAmp switch equivalent circuits have been developed [19] however, their parameters need to be calculated for each specific topology.

2. Proposed mathematical model of MagAmp switch B-H characteristic

Since MagAmp switching properties are defined by its B-H characteristic, it's crucial to develop its mathematical model that will be possible to integrate into CAD programmes. The hysteresis loop was split into 4 parts corresponding to different stages of MagAmp switching cycle (fig.1). It was decided to represent the steep parts with fragments of a sinusoidal function, since each CAD programme for electric circuits has a model of digital generator of sine waveforms in their components library [20]. However, digital generators of sinusoidal waveforms are not capable of recursive signal generation. It means, that they cannot be used to model the downward branch of B-H characteristic.

A microcontroller model can be programmed in the required way, also having an advantage of already inbuilt analogue-to-digital and digital-to analogue converters [20].

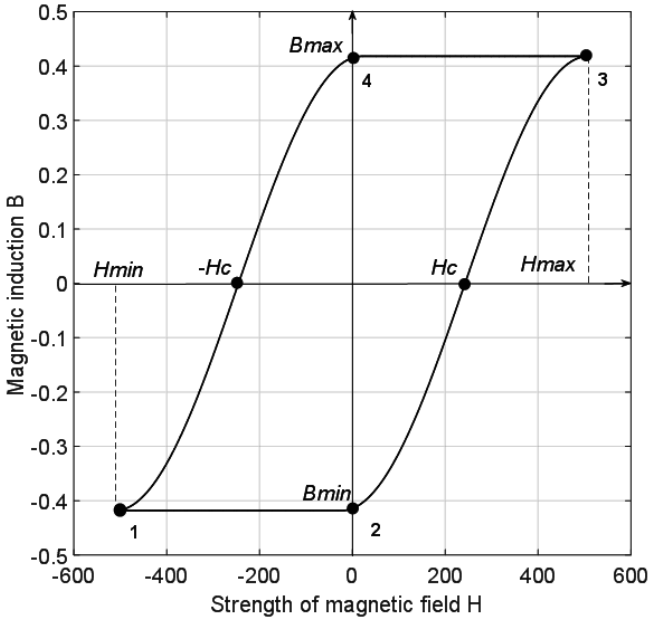

Fig. 1. Schematic diagram of MagAmp switch B-H characteristic, and the points that are crucial for its modeling

The curves that represent MagAmp core magnetization (parts 1-2, 2-3) and demagnetization (parts 3-4, 4-1) process can be mathematically described in the following way:

$$1-2:\begin{cases} g_n = g_{n-1}, \\ g_n = B_{\min}; \end{cases} \quad H_n = \overline{H_{\min}, H_{\min} + 2H_c}, B_n = B_{\min}, \tag{1}$$

$$2-3: g_n > g_{n-1}; \quad H_n = \overline{H_{\min} + 2H_c, H_{\max}}, B_n = k\sin(2\pi fnT_d + \varphi_1), \tag{2}$$

$$3-4:\begin{cases} g_n = g_{n-1}, \\ g_n = B_{\max}; \end{cases} \quad H_n = \overline{H_{\max}, H_{\max} - 2H_c}, B_n = B_{\max}, \tag{3}$$

$$4-1: g_n < g_{n-1}; \quad H_n = \overline{H_{\max} - 2H_c, H_{\min}}, B_n = k\sin(2\pi fnT_d + \varphi_2), \tag{4}$$

where g is a generated digital code that corresponds to a point on B-H characteristic. $n = \overline{1, N}$ — index of digital codes of electromagnetic variables, the other denotations are digital codes of corresponding constants. H_{min}, H_{max} are minimum and maximum values of strength of magnetic field respectfully. H_c is a coercive force. B_{min}, B_{max} are minimum and maximum values of magnetic induction respectfully. k is the amplitude of the waveform, for the full hysteresis loop $k=B_{max}$. For more simplicity, the current model suggests that saturation magnetic induction $B_s = B_{max}$, while in real physical systems B_{max} usually is magnetic induction value at $H=5H_c$ [20].

(1-4) constitute the mathematical model of MagAmp B-H characteristic. Saturation magnetic inductance B_s and coercive force H_c are its input parameters. They are the main magnetic characteristics of MagAmp cores and can be found in any MagAmp datasheet.

3. B-H characteristic mathematical model computer implementation algorithm

An algorithm of computer implementation of the proposed mathematical model is described below.

1. The codes corresponding to the values of constants and parameters necessary for the realization of computer model of MagAmp switch B-H characteristic are entered into the microcontroller's memory registers. They are π, own frequency of the digital generator of sinusoidal signals f; discretization frequency F (it equals to the discretization frequency of the signals within a particular electric circuits computer-aided design (CAD) programme); coefficient that determins the beginning phase *beg* of the waveform of sinusoidal signals digital generator. The user indicates the saturation induction B_s and coercive force H_c values.
2. The output model parameters are calculated with the following equations:
   The step of discretization

$$Teta = 2\pi \frac{f}{F} \quad ; \tag{5}$$

the beginning phase of the waveform

$$Tetab = beg \cdot Teta \; ; \tag{6}$$

coefficient of the digital generator of sinusoidal signals

$$b = 2 \cdot \cos(2\pi \frac{f}{F}) ; \tag{7}$$

the number of points within a half period of the sine waveform

$$k_{\max} = \frac{F}{2f} ; \tag{8}$$

the maximum value of coercive force

$$H_{\max} = H_c + H(k_{\max}) ; \tag{9}$$

the minimum value of coercive force

$$H_{\min} = H(k_1) - 2 \cdot H_c ; \tag{10}$$

3. Initial conditions for the digital generator of sinusoidal signals are set

$$\begin{aligned} G0 &= \sin Tetab \\ G1 &= \sin(Tetab + Teta) \end{aligned} \tag{11}$$

4. The two sequently generated code values (points on the sine waveform) g_{n-1} and g_n are compared
   a. If $g_n > g_{n-1}$ then, taking into account the initial conditions for the digital generator of sinusoidal signals (), a point on the upward part of the sine waveform is digitally generated. This point belongs to a model of a part of B-H characteristic that corresponds to the MagAmp switch transition to conductive state (MagAmp saturation):
   for k=1:n_{max}
   GF(k)=G0;
   GS(k)=G1;
   G=b*G0-G1;
   G1=G0;
   G0=G;
   H(k)=n;
   B(k)=G;
   b. If $g_n < g_{n-1}$ then a point is generated on downward part of the sine waveform which represents a part of B-H characteristic corresponding for MagAmp switch transition from on-state to off-state (from conductive to nonconductive state). Recursive computation is used here:
   for k=1:n_{max}
   GF(k)=G0;
   GS(k)=G1;
   M0=GF(n_{max+1}-n);
   M1=GS(n_{max+1}-n);
   M=b*M0-M1;
   H(k)=n;
   B(k)=M;
   c. When three subsequently generated codes of points on MagAmp switch B-H characteristic are equal $g_n = g_{n-1}$, $g_{n-1} = g_{n-2}$ then they are compared to the code of saturation inductance value B_s.
      i. If $g_n \leq -B_s$ then a code value is generated which corresponds to a point on lower horizontal part of MagAmp B-H characteristic, which represents MaAmp switch off-state (nonconductive state):
      $H_n = H_{min} \ldots H_{min} + 2H_c$
      $B_n = -B_s$;
      ii. If $g_n \geq B_s$ then a code value is generated which corresponds to a point on upper horizontal part of MagAmp B-H characteristic, which represents MaAmp switch on-state (conductive state):
      $H_n = H_{max} \ldots H_{max} - 2H_c$
      $B_n = B_s$.

The block-scheme of the algorithm of high-frequency MagAmp switch B-H characteristic computer model is shown in figure 2.

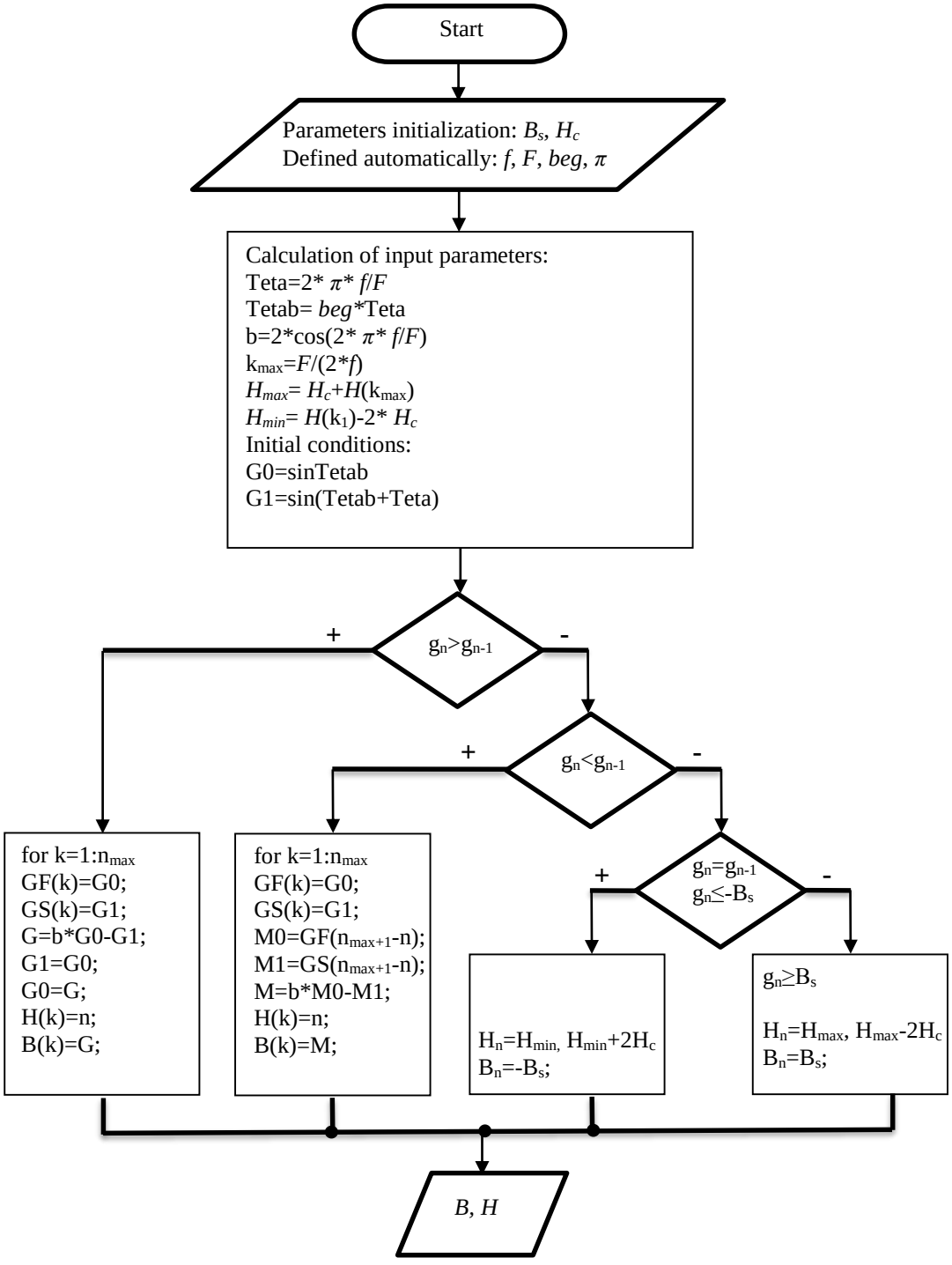

Fig. 2. Block-scheme of the algorithm of high-frequency MagAmp switch B-H characteristic computer model

4. Investigation of modeling capabilities of MagAmp switch B-H characteristic frequency dependence

The results of experimental investigation of MagAmp switch (with parameters: k_r=0,9997, d_{out}=16 мм, d_{in}=7 мм, h=5 мм, N=10) B-H characteristic dependence on the switching frequency are presented on fig.3. Tektronix TDS 1002 oscilloscope with discretization frequency of 60MHz was used.

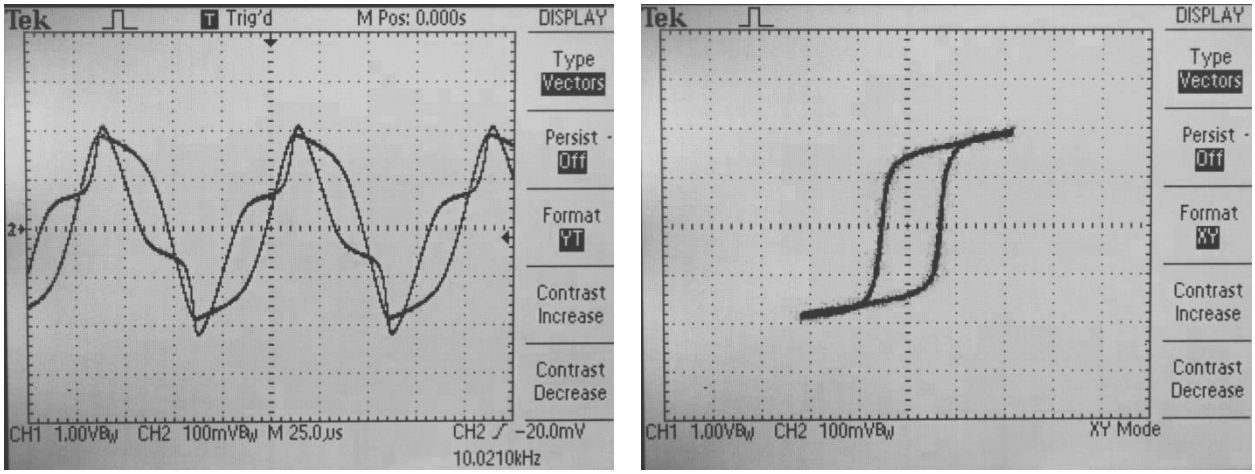

a) MagAmp switch waveforms and B-H characteristic at switching frequency *f*=10kHz

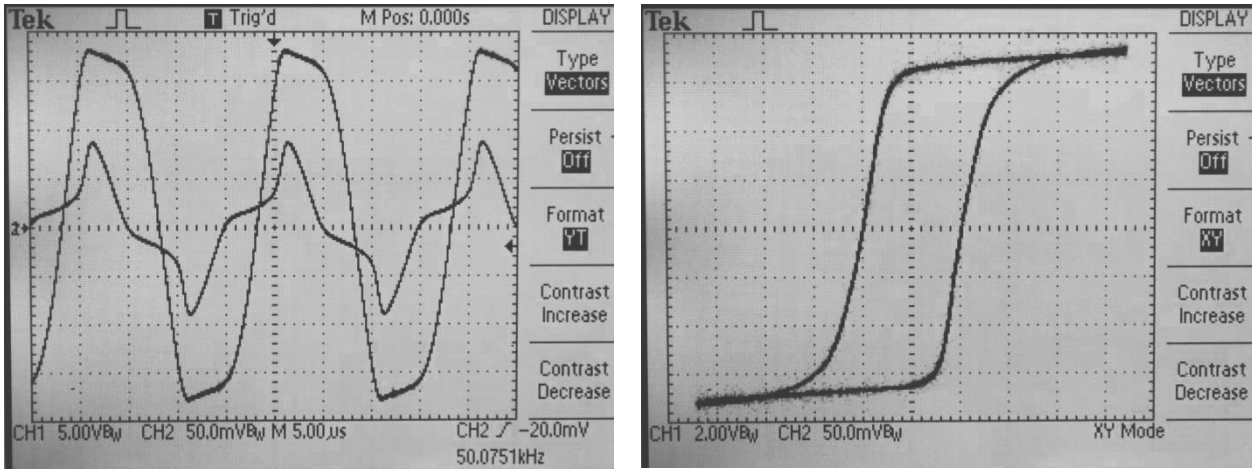

b) MagAmp switch waveforms and B-H characteristic at switching frequency *f*=50kHz

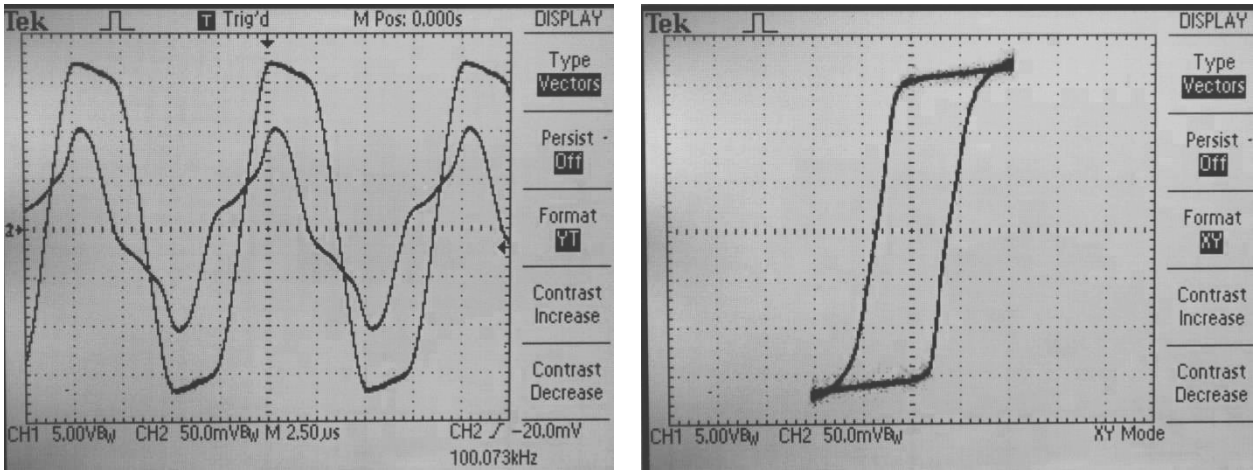

c) MagAmp switch waveforms and B-H characteristic at switching frequency *f*=100kHz

Fig. 3. Dependence of B-H characteristic on the frequency of MagAmp switch with the following parameters: k_r=0,9997, d_{out}=16 мм, d_{in}=7 мм, *h*=5 мм, *N*=10

The results of experimental investigation of MagAmp switch (with parameters: k_r=0,9997, d_{out}=27 мм, d_{in}=18 мм, *h*=12 мм, *N*=10) B-H characteristic dependence on the switching frequency are presented below.

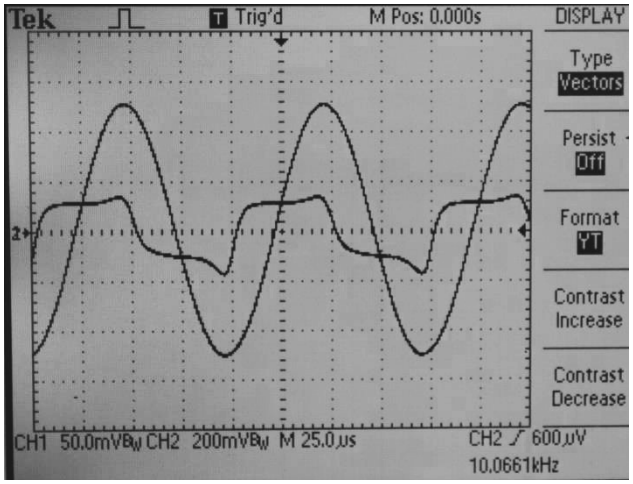

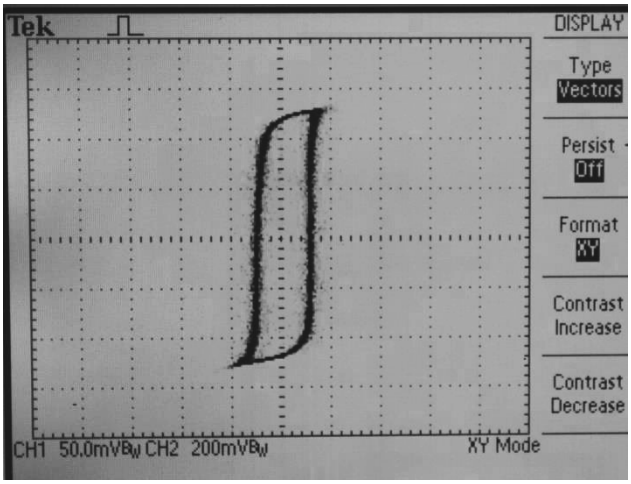

a) MagAmp switch waveforms and B-H characteristic at switching frequency *f*=10kHz

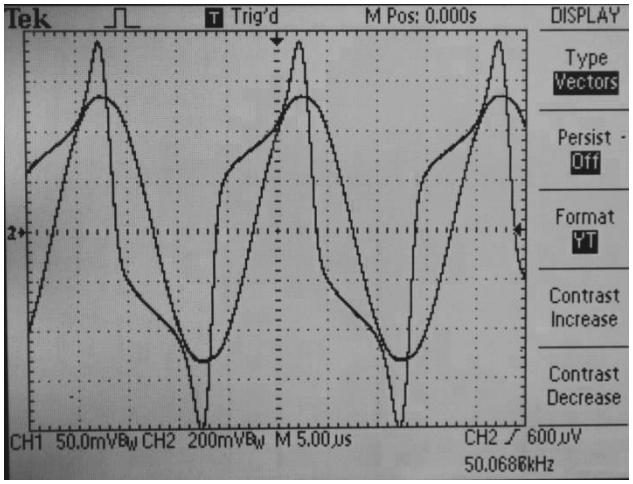

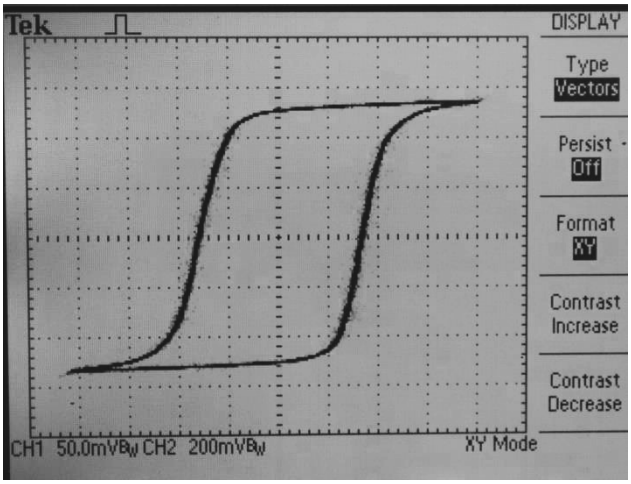

b) MagAmp switch waveforms and B-H characteristic at switching frequency *f*=50kHz

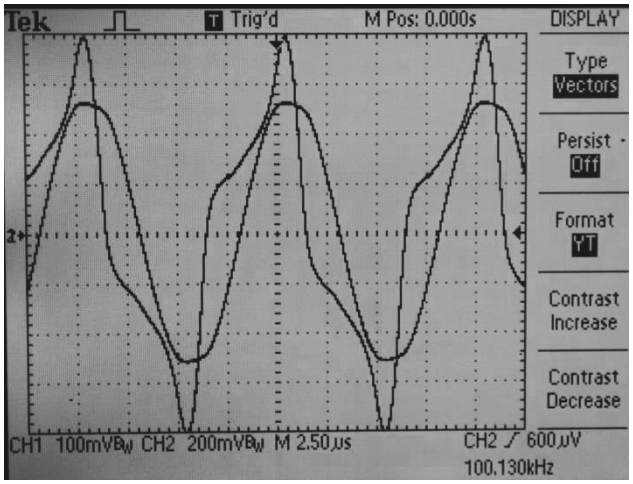

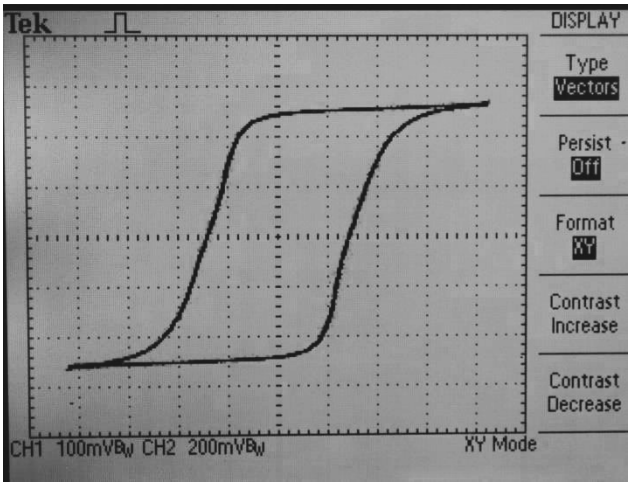

c) MagAmp switch waveforms and B-H characteristic at switching frequency *f*=100kHz

Fig. 4. Dependence of B-H characteristic on the frequency of MagAmp switch with the following parameters: k_r=0,9997, d_{out}=27 мм, d_{in}=18 мм, *h*=12 мм, *N*=10

The experimental results (fig. 3,4) prove that in both cases for the same MagAmp switch B-H characteristic changes depending on the switching frequency: the higher the frequency is, the wider is thehysteresis loop.

Change of the model's input parameters (coercive force, frequency of the generator, discretization frequency, beginning phase of the waveform, and the number of points needed to be generated) provides the regulation of steepness (fig. 5. a)) and width (fig. 5. b)) of the modelled hysteresis loop.

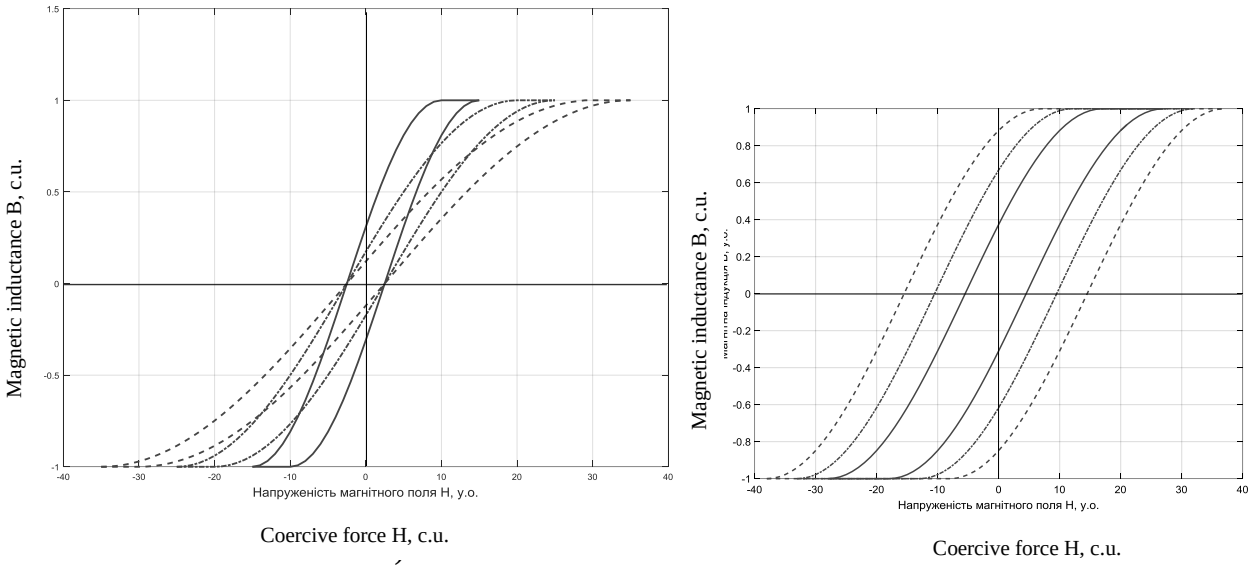

a) **b)**

Fig. 5. Computer realization of the mathematical model of B-H characteristic: a) dependence of the steepness of B-H characteristic model on the change of the ratio of discretization frequency *F* to the own frequency of the generator *f*; b) models of B-H characteristics with different values of coercive force H_c

The *H*, *B* axes values on Fig. 5 are given in conditional units (c. u.). Ratio of the oscilloscope and generator frequencies equals to the number of data points generated during one period (represented along H axes).

The calculated error of B-H characteristic modeling is ≤17,2%, which is smaller than the error of known magnetic hysteresis models, and can be further decreased by taking into account the slope of nearly horizontal parts of the loop (1-2 and 3-4, fig.1).

5.Conclusions

The use of basic digital components for the computer realization of proposed B-H characteristic mathematical model allows its integration in any CAD programme for electric circuits without any additional integrations.

The time complexity of the proposed model of MagAmp switch B-H characteristic is decreased, compared to A. Nicolaide's analytic model of magnetic hysteresis [17,18] which features a somewhat similar structure, however, the number of model's segments was decreased from 6 to 4. Moreover, A.Nicolaide's model is not suitable for power converters design automation, since its LabView integration [18] deals with magnetic fields only.

All input parameters of the proposed model are easy to find in any MagAmp datasheet, which eliminates an existing problem of parameters extraction for known models.

References

1. **Lee, J.; Chen, D. Y.; Jamerson, C.** Magamp postregulators – practical design considerations to allow operation under extreme loading conditions. Proceedings of IEEE APEC. **1988**. P. 368-376.
2. **Austrin, L.; Figueroa-Karlstrom, E.; Engdahl, G.** Evaluation of switching losses in magnetic amplifiers as an alternative to IGBT switching technologies. 4th IET International Conference on Power Electronics, Machines and Drives (PEMD 2008). **2008**. P. 250–254.
3. **Austrin L.** 2007. On Magnetic Amplifiers in Aircraft Applications. Royal Institute of Technology. Sweden. 98 p.
4. **NASA Technical Reports Server (NTRS) 19940009938:** Large space structures and systems in the space station era: A bibliography with indexes (supplement 05). 139 p. Available at: https://archive.org/details/NASA_NTRS_Archive_19940009938/page/n145/mode/2up.
5. **Toshiba**. Saturable cores for mag-amps. Available at: https://pdf.directindustry.com/pdf/toshiba-america-electronics-components/saturable-cores-mag-amps/33679-562725.html#search-en-saturable-cores-mag-amps.
6. **Chen, W.; Hui, S. Y.** A Dimmable Light-Emitting Diode (LED) Driver with Mag-Amp Postregulators for Multistring Applications. IEEE Transactions on Power Electronics. **2011**. Vol. 26, No 6. P. 1714–1722.
7. **Yaskiv, V.; Abramovitz, A.; Smedley, K.; Yaskiv, A.** 2015. MagAmp Regulated Isolated AC-DC Converter with High Power Factor. Special issue of journal COMMUNICATIONS - Scientific Letters of the University of Zilina, ISSN 1335-4205. No. 1A/2015. P. 28-34.
8. **Tatevosian, A. S.; Zaharova, N. V.; Shelkovnikov, S. V**. 2016. Eksperementalnoe issledovanie i raschet magnitnogo polia elektromagnita postoyannogo toka s rasshcheplennymi poliusami i poliusnymi nakonechnikami v

komplekse program ELCUT. Izvestiya Tomskogo politehnicheskogo universiteta. Inzhiniring georesursov, Vol.327, No 2, pp. 133-140. [In Russian]

9. **ANSYS Inc**. Balance of power. ANSYS Advantage, Vol. 8, No 2, 2014, pp. 33-35. Available at: https://www.ansys.com/-/media/ansys/corporate/resourcelibrary/article/balance-of-power-multiphysics-aa-v8-i2.pdf .
10. **Klatt, R.; Krawczyk, F.; Novender, W.-R.; Palm, C.; Weiland T**. MAFIA – A three-dimensional electromagnetic CAD system for magnets, RF structures, and transient wake-field calculations. Proceedings of the **1986** International Linac Conference, Stanford, California, USA. P. 276-278.
11. **Jiles, D. C.; Atherton, D. L**. Theory of Ferromagnetic Hysteresis. J. Magn. And Magn. Mater. **1986**. No 61. P. 48–60.
12. **Chan, J. H.; Vladimirescu, A.; Gao, A., X.; Liebmann, P.; Valainis, J**. Nonlinear Transformer Model for Circuit Simulation. IEEE Transactions on Computer-Aided Design, **1991**, Vol. 10, No 4, pp. 476 – 482.
13. **Yaskiv, A**. Matematychne modeliuvannia protsesiv peremagnichennia magnitomyakyh materialiv z vysokoyu krutyznoyu petli gisterezysu. Mizhnarodnyi naukovo-tehnichnyi zhurnal Vymiriuvalna ta Obchysliuvalna Tehnika v Tehnologichnyh Protsesah, **2015**, No 4 (53), pp. 112-118. [In Ukrainian]
14. **Preisach, F**. Uber die magnetische Nachwirkung. Zeitschrift fur Physik. **1935**. No 94. P. 861–890.
15. **Adly, A. A.; Abd-El-Hafiz, S. K.** Efficient modeling of vector hysteresis using a novel Hopfield neural network implementation of Stoner–Wohlfarth-like operators. Journal of Advanced Research. **2013**. No 4. P. 403–409.
16. **Konieczny, J., Dobrzañski, L. A., Tomiczek, B., Trzaska, J**. Application of the artificial neural networks for prediction of magnetic saturation of metallic amorphous alloys. Archives of Materials Science and Engineering. **2008.** Vol. 30, No 2. P. 105–108.
17. **Nicolaide, A**. An Approach to the Mathematical Modeling of the Hysteresis Curves of Magnetic Materials: the Minor Curves**. 2007**. P. 301-310.
18. **Motoasca, S.; Scutaru, G**. Hysteresis modeling of soft magnetic materials using LabView Programs. Advances in Electrical and Computer Engineering. **2010**. Vol 10, No 2. P.94-97.
19. **Edry, D., Ben-Yaakov, S**. A SPICE Compatible Model of Magamp Post. Regulators. *IEEE Applied Power Electronics Conf., APEC'92*. **1992**. P. 793 – 800.
20. **Yaskiv, A., Yavorskyy, B.** Integration of Magnetic Amplifier Switch Model into Computer Aided Design for Power Converters. Scientific journal of TNTU. **2019**. No 2 (94). P. 123-133.

THE PROCESS OF SHELL FORMATION AND OPTIMIZATION BY THE CRITERION OF ACCURACY OF THEIR GEOMETRIC SHAPE

Taras Dubynyak [1], Volodymyr Kruhlov [1], Roman Dzhydzhora[1], Manziy Oleksandra [2], Andreichuk Stanislav [2]

[1]*Ternopil National Ivan Puluj Technical University, Rus'ka str. 56, 46001, Ternopil, Ukraine; d_taras@ukr.net*
[2] *Lviv Polytechnic National University, Lviv, 12 Bandera street, Lviv, Ukraine, 79013; Ukraine, E-mail: lesly@ukr.net*

Abstract: The research is devoted to the process of deformation of a two-dimensional grid. The difficulty of describing the deformation process is that the situation behaves when deformed, which is different from the sheet solid material. This is due to it possible rotation relative to the perpendicular wires of the grid from one structure to another in the nodes. In addition, as shown in more detail below, the conditions that must satisfy the solution are different from the standard ones: the surface that should lie after deformation is given, while the solutions applied to the grid in nodes remain unknown in the formulation of the problem.

The deformation depends on the effort applied to the ends of the mesh element. The stiffness matrix of the element is located using the DIP-FEM package, for which a model of the element is created and at a given unit effort for each direction, the application of the displacement load is calculated.

Keywords: antenna, grid, wires, energy, deformation, clamp, punch, node

1. Introduction

The production of new generation antenna systems is based on new technological and design ideas, the implementation of which requires appropriate scientific and technical support, and is possible in close cooperation of production with scientific potential.

The main design and technological ideas that are implemented in antenna systems of the new generation are:

- preservation in the production of antennas of the basic principles of aviation technologies and with the exception of technological processes of the influence of subjective factors on product quality; optimization of structures according to the criteria - rigidity-accuracy-mass;
- use without stacking assembly and adjustment of antennas on objects;
- use of vector diffraction methods in optimizing the electro-dynamical characteristics of the antenna system at the design stage;
- antenna positioning control system, speed control of its movement, diagnostics of a condition at operation, self-testing, is carried out on the basis of digital information processing.

The study of the process of shell formation consists of predicting and verifying the deformation of a two-dimensional grid. The difficulty of describing the deformation process is that the grid behaves qualitatively differently when deforming than a sheet of solid material. This is due to its structure, in particular, the ability to rotate mutually perpendicular wires of the grid relative to each other at the nodes. In addition, the conditions that the solution must satisfy differ from the standard ones: the surface on which the grid should lie after deformation is given, while the forces applied to the grid at the nodes remain unknown when formulating the problem.

The process of deformation of the grid

This section is devoted to the development and verification of the deformation of a two-dimensional grid. The difficulty of describing the deformation process is that the grid behaves qualitatively differently than a sheet of solid material. This is due to its structure, in particular the ability to rotate mutual perpendicular wires of the grid relative to each other at the nodes. In addition, as discussed in more detail below, the conditions that must satisfy the solution are different from the standard: given the surface on which the grid should lie after deformation, while the forces applied to the grid at the nodes remain in the formulation of the problem unknown [1].

Therefore, the most general approach was used in solving the problem, namely the theorem on the minimum potential energy of the system in the equilibrium position. The friction in the system is, of course, neglected; it can be taken into account when improving the developed methodology. Minimization of potential energy is carried out numerically by iterative method [2]. Problem statement, solution methods and software implementation of the method are described below.

Therefore, the most general approach was used in solving the problem, namely the theorem on the minimum potential energy of the system in the equilibrium position. The friction in the system is, of course, neglected; it can be taken into account when improving the developed methodology. Minimization of potential energy is carried out numerically by iterative method. Problem statement, solution methods and software implementation of the method are described below.

Formulation of the problem

The surface of rotation is given, the equation of which is described by the following system:

$$\begin{cases} z=f(\rho), \\ \rho=\sqrt{x^2+y^2}; \end{cases} \quad (1)$$

The surface is given in a cylindrical coordinate system. At ρ_1, greater than some values of R_0, $f(\rho) = 0$. The grid, which in the undeformed state lay in the plane $z = 0$ and had a step s_1, is deformed so that it lies on a given surface. Forming is carried out by means of a rim which axis radius is equal to R_0 (Fig. 1).

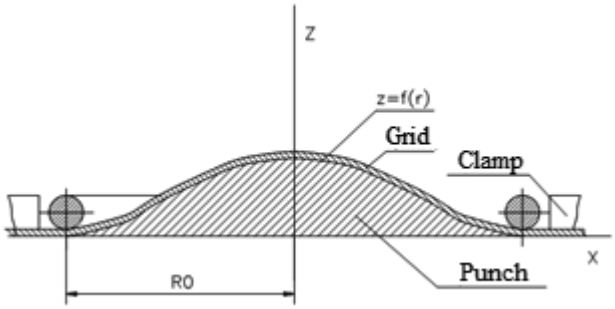

Fig. 1 Formation of a grid on a punch

Friction in the system is completely neglected. Task: to find the position of the grid elements after deformation [5].

Method of solution

Before developing a solution methodology, you should clarify exactly how set the position of the grid. The easiest way to do this is by attaching to the nodes of the grid (that is the points of intersection of mutually perpendicular wires of the grid). To do this, we assume that in the nodes are allowed only the rotation of the wires of the grid relative to each other, while shifts are not allowed. In fact, shifts (minor), of course, exist, but in the first approximate they can be neglected, so under the assumptions made, the position of the grid will be well known if the positions of its nodes are known. Therefore, the problem is to find the position of the nodes of the grid after deformation [3].

Description of the position of the grid

When solving the problem due to symmetry, it is advisable to consider only the part of the grid that is in the first quadrant. To find the position of the nodes of the grid as a whole, it is sufficient to consider that the grid has symmetry of C_4 relative to the z axis. The grid node will be numbered with two numbers-i and j (Fig. 2). The problem will be solved if the vectors of displacements of all nodes during deformation are found. Denote the displacement vector of the node (i, j) as u_{ij}. These vectors are finite numbers. Along with the vectors u_{ij}, we also introduce the vector-mapping function u (x, y). The meaning of this function is that each point (x, y) of the plane $z = 0$ corresponds to the vector u (x, y), and sets the mapping of the plane $z = 0$ on the surface, each point of which is a point (x, y) planes $z = 0$, shifted by the vector u (x, y). We consider the mapping to be mutually unique, and the function u (x, y) - itself to be continuously differentiated in the whole domain. We impose another condition on the function u (x, y): if x_j and y_i - coordinates of the node (i, j), then it should be: $u(x_j, y_i) = u_{ij}$. In other words, define the function u (x, y) so that it reflects the grid on the surface (1).

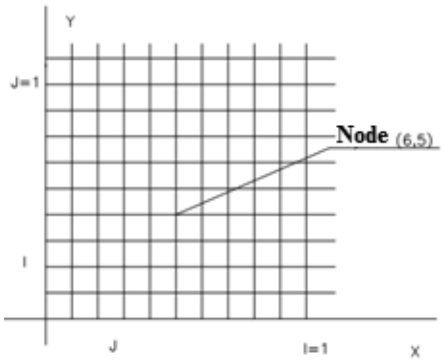

Fig. 2 Grid node numbering

Suppose that before the deformation of the grid, some of its wires were parallel to the x-axis, we, had the equation $y = y_0$. Whereas this follows directly from the definition of the function u (x, y), after deformation the wire will lie on a curve whose equation in vector form has the form:

$$\begin{cases} R(x) = R_x(x) \cdot i + R_y(x) \cdot j + R_z(x) \cdot k \\ R_x(x) = x + u_x(x, y_0), \\ R_y(x) = y + u_y(x, y_0), \\ R_z(x) = u_z(x, y_0); \end{cases} ; \quad (2)$$

where i, j, k- orts, respectively, the axes x, y, z of the global coordinate system.

Having R (x), you can also find tangent to the wire at any point.

Grid energy

When calculating the energy of the grid, we use the obvious fact: the energy of the whole grid is equal to the sum of the energies of its parts. The smallest element of the grid is the part of the wire the length of the period [4].

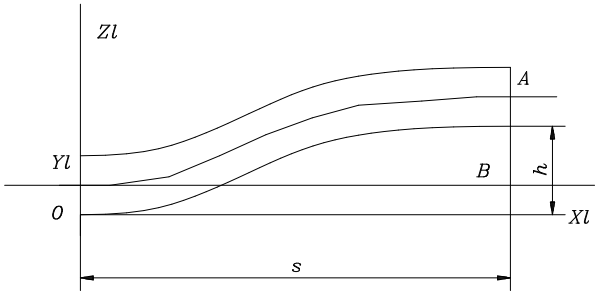

Fig. 3 Grid element

The energy of the whole grid can be found by calculating the energy of each element and adding the obtained values for all elements. Obviously, the energy of the element depends only on the deformation of the element itself. Deformation, in turn, depends on the effort applied to the ends of the element. Place the local coordinate system of the element as shown in Fig. 3. In this case, the point O (left end of the rod) will be considered rigidly fixed. Suppose that the force P and the moment M are applied at the end of the element. We combine these two force factors into one six-dimensional vector F_i, and $F_{1,2,3}= P_{x, y, z}$, and $F_{4,5,6} = M_{x, y, z}$. When applying these force factors, point A will move to some vector Δ and will return to some vector φ. The last two vectors are also combined into one vector D_i, and the correspondence $D_{1,2,3} = \Delta_{x, y, z}$, and $D_{4,5,6} = \varphi_{x, y, z}$. Within the application of Hooke's law, the relationship between the components F_i and D_i is linear. In the most general form, this connection is expressed by the formula:

$$F_i = \sum_{j=1}^{6} C_{i\ j} \cdot D_j \quad (3)$$

where C_{ij}-square matrix of the sixth order, which is called the matrix stiffness.
The inverse matrix is called the flexibility matrix: Suppose we have an equilibrium

$$B_{i\ j} = (C^{-1})_{i\ j} \quad (4)$$

state at some given forces F_i. Let's change these forces of dF_i. We will have an increase in displacements dD_i:

$$dD_i = \sum_{j=1}^{6} B_{i\ j} \cdot dF_j \quad (5)$$

When changing the displacements of the force applied to the element at point A perform some work. According to the law of conservation of energy, this work is equal to the change in the potential energy of the element. Therefore for the differential the potential energy of the element will have the following expression:

$$dU = \sum_{i=1}^{6} (\sum_{j=1}^{6} C_{i\ j} \cdot D_j) \cdot dD_i \quad (6)$$

It is easy to see that dU is really a complete differential. This is easily shown using the theorem on the change of the order of differentiation, which states that for the function U of the variables D_i and D_j the equality must hold:

$$\partial^2 U / \partial D_i \, \partial D_j = \partial^2 U / \partial D_j \, \partial D_i \tag{7}$$

It is easy to see, using (6), that condition (7) can be rewritten as $C_{ij} = C_{ji}$. This means that the stiffness matrix must be symmetrical. As practical calculations show, this is true. Therefore, dU is a complete differential. The function U itself can be found by simple integration and has the following form:

$$U = \frac{1}{2} \cdot \sum_{i=1}^{6} C_{ii} \cdot D_i^{\,2} + \sum_{j>i} C_{ij} \cdot D_i \cdot D_j . \tag{8}$$

According to the physical content of the function U as the potential deformation energy of the grid element, U must be positively defined. Specific numerical calculations confirmed this for one case. From physical considerations should be true and in general.

Finding the stiffness matrix of the element

The stiffness matrix of the element can be found using the DIP-FEM package. To do this, create a model of the element in the package according to Fig. 3. If the element is alternately applied in such a way that in each case in the vector F_i is different from 0 only one component (alternately from the first to the sixth), and this component is equal to 1. According to the relationship between displacements and forces for the element:

$$D_i = \sum_{j=1}^{6} B_{ij} \cdot F_j$$

B_{ij} is equal to D_i when applying a unit force in the "direction" j. C_{ij} is then located as a matrix inverted to B_{ij}. With a given unit effort for each direction of application, the displacement loads are calculated by the package. Illustrations showing the deformation of the element when applying loads are given in the graphic part of the work. Finding the inverse matrix is done by a program written in Borland Pascal. For a grid with a step of 7.5 mm from a steel wire with a diameter of 0.75 mm. the stiffness matrix is given below. As expected, it turned out to be symmetrical (accuracy to errors caused by rounding).

Table 1

The stiffness matrix of the grid element

i\j	1	2	3	4	5	6
1	2.582E+05	9.566E-10	1.405E+06	7.845E-13	-4.415E+02	2.163E-14
2	9.612E-10	8.962E+04	5.333E-11	3.361E+02	2.061E-13	-3.361E+01
3	1.405E+06	1.318E-11	1.181E+07	-2.354E-13	-8.395E+02	-2.311E-15
4	8.073E-13	3.361E+02	-3.356E-14	1.694E+00	-3.566E-16	-1.346E-01
5	-4.415E+02	2.092E-13	-8.395E+02	-3.414E-16	1.776E+00	-7.324E-17
6	1.891E-14	-3.361E+01	-2.328E-14	-1.346E-01	-7.048E-17	3.611E-01

Finding Di for an element

Consider an element that in the undeformed state is projected onto the plane z = 0 into a segment parallel to the x-axis. Let this element be bounded by nodes (j, i) and (j + 1, i). The coordinates of the nodes in the undeformed state have the following values:

$$\begin{cases} x_0 = (j-1) \cdot s, \\ y_0 = (i-1) \cdot s, \\ x_B = j \cdot s, \\ y_B = (i-1) \cdot s. \end{cases} \tag{9}$$

In the deformed state, the coordinates of the nodes are:

$$\begin{cases} x_o^i = x_o + u_x(x_o, y_o), \\ y_o^i = y_o + u_y(x_o, y_o), \\ z_o^i = u_z(x_o, y_o), \\ x_A^i = x_A + u_x(x_A, y_A), \\ y_A^j = y_A + u_y(x_A, y_A), \\ z_A^i = u_z(x_A, y_A). \end{cases} \tag{10}$$

The deformation vector Di of the element must be expressed in the local coordinate system of the element (Fig. 3). To do this, first of all, we find the orts of the local coordinate system (more precisely, their coordinates in the global coordinate system). As can be seen from Fig. 3, the orth of the x_l axis coincides with the tangent to the element at the point O. Therefore, according to (2), we have:

$$\begin{cases} i_l = \dfrac{l}{|l|}, \\ l_x = 1 + \dfrac{\partial \mathrm{u_x}}{\partial \mathrm{x}}, \\ l_y = \dfrac{\partial \mathrm{u_y}}{\partial \mathrm{x}}, \\ l_z = \dfrac{\partial \mathrm{u_z}}{\partial \mathrm{x}}; \end{cases} \tag{11}$$

where the derivatives are taken at the point (x_0, y_0).

Next, we assume that the orth of the z_l axis coincides with the normal to the surface (1) at the point O. Then:

$$\begin{cases} k_l = \dfrac{l}{|l|}, \\ l_x = -\dfrac{\partial \mathrm{z}}{\partial \mathrm{x}} = -\dfrac{x}{\rho}\dfrac{\partial \mathrm{z}}{\partial \rho}, \\ l_y = -\dfrac{\partial \mathrm{z}}{\partial \mathrm{y}} = -\dfrac{y}{\rho}\dfrac{\partial \mathrm{z}}{\partial \rho}, \\ l_z = 1; \end{cases} \tag{12}$$

Finally, the orth of the y_l axis is simply $j_l = [k_l, i_l]$ -as in any right coordinate system.
For an undeformed element, the coordinates of the end of A should be:

$$R_A^{\,0} = R_0 + i_l \cdot s + k_l \cdot h \tag{13}$$

where R_0 is the radius vector of the point O.
In fact, R_A has the form:

$$R_A = R_B + k_l \cdot h \tag{14}$$

where R_B is the radius vector of point B; k_l-normal to the surface (1) at point B.
From (13) and (14) the displacement vector is equal to:

$$\begin{cases} \Delta = R_A - R_A^O, \\ D_{1,2,3} = (\Delta \cdot (i_l, j_l, k_l)); \end{cases} \tag{15}$$

At small angles of rotation of the end (in radians) the following relations are also valid:

$$\begin{cases} D_4 = \varphi_x = -\left|k_l^i - k_l\right| \cdot sign\left[\ (k_l^i - k_l\ ) \cdot j_l\ \right], \\ D_5 = \varphi_y = -l_{Zl}, \\ D_6 = \varphi_z = l_{Yl}, \end{cases} \tag{16}$$

where l_{Zl}, l_{Yl}-components of the unit vector tangent to the element at point A in the local coordinate system. They can be found by (12), taking the derivatives at point B.

As follows, it was possible to express Di through u (x, y). When implementing the method, derivatives of u (x, y) should (of course, approximately) be expressed in u_{ij}. So, for example, for node (i, j) we will have:

$$\frac{\partial u_x}{\partial y} \approx \frac{u^x_{i+1,j} - u^x_{i-1,j}}{2s} \tag{17}$$

This D_i is expressed in u_{ij}, which is necessary.

Energy minimization

According to the method of solving the problem, the minimization of energy is planned to be carried out numerically as a minimization of the function of many variables. In this case, the energy depends on the changes u_{ij}. First we write the zero approximation [6]:

$$\begin{cases} u^x_{ij} = 0, \\ u^y_{ij} = 0, \\ u^z_{ij} = f(s\sqrt{(i-1)^2 + (j-1)^2}); \end{cases} \tag{18}$$

Then, as described above, we find the grid energy E (u_{ij}) i partial derived from energy by

$$a^m_{ij} = \frac{\partial E}{\partial u^m_{ij}}$$

To reduce the energy, we take the following approximations u_{ij} in the form:

$$(u^m_{ij})_{k+1} = (u^m_{ij})_k - \lambda \cdot (u^m_{ij})_k \tag{19}$$

where k is the approximation number;
λ-some constant became > 0;
The change in energy is expressed by the formula:

$$dE_k = \sum_{i,j,m} \frac{\partial E}{\partial u^m_{i,j}} du^m_{i,j} = -\lambda \sum_{i,j,m} (a^m_{i,j})^2_k \tag{20}$$

As can be seen from (20), $dE_k <= 0$, and $dE_k = 0$ only if all derivatives of E are equal to 0.

The value of λ should be chosen experimentally. By subtracting the derivatives at some point in the space u_{ij}, we can improve the solution for using (19) until E_k begins to grow. Then you should find the derivatives at a new point and continue the process. There is a way to find directly, but it requires numerical calculation of derivatives from E to u_{ij}. It is planned to implement it in the future.

References

1. Sulim, G.T. (2007). *Fundamentals of mathematical theory of thermoelastic equilibrium of deformable solids with thin inclusions*. Lviv: Research and Publishing Center NTSh.

2. Ovcharenko, V.A., Podlesny, S.V., Zinchenko, S.M. (2008). *Fundamentals of the finite element method and its application in engineering calculations. Tutorial*. Kramatorsk.

3. Morozov, E.M., Nikishkov, G.P. (1980). *Finite element method in fracture mechanics*. Moskva: Nauka.

4. Savelyev, I.V. (1966). *General physics course*. Moskva: Nauka.

5. Antsiferov, V.N., Bobrov, G.V., Druzhini, L.K.. (1987). *Powder metallurgy and spray coating: Textbook for universities*. Moskva: Metallurgy.

6. Duboviy, O.M., Yankovets, T.A. (2006). *Coating spraying technology. Tutorial*.

MODEL OF MOTION ROUTE OF UNMANNED AERIAL VEHICLES OPERATIONS WITH OBSTACLES AVOIDANCE

Leonid Romaniuk [1], Ihor Chykhira[1], Halyna Tulaidan [2], Andriy Mykytyshyn[1]

[1]Ternopil Ivan Puluj National Technical University, 56 Ruska str., 46001, Ternopil, Ukraine; romanyuk@tntu.edu.ua
[2]1Ternopil Volodymyr Hnatiuk National Pedagogical University, 2 Maxyma Kryvonosa str., 46027, Ternopil, Ukraine; tulaidan@tnpu.edu.ua

Abstract: The aerodynamic model of the group of unmanned aerial vehicles in space with obstacles is investigated in this paper, the model development is based on the methods of Dubins trajectory formation and Pythagorean spatial theorem concerning hodograph. It is determined that one of the classic trajectories used for unmanned aerial vehicle maneuver from one height to another is the intersection of circular spiral projected onto the X-Y plane in the form of a circle. The problem of obstacle avoidance is determined and Dubins diagram for two unmanned aerial vehicles routes in the environment with obstacles is given. On the basis of the specified scheme the algorithm of re-laying the UAV route with curvature adjustment by means of intermediate point which is taken out on the second scheme is described. Analysis of the known solutions in the field of increasing the route stability control for unmanned aerial vehicles and electronic suppression demonstrate the importance of the problem of forming the flight routes of unmanned aerial vehicles by passing opposing enemy areas, taking into account the peculiarities of air defense and electronic warfare application. The functional scheme of UAV recognition mechanism in the conditions of radio attacks is developed and the mechanism of formation of UAV safe movement in the conditions of radio attacks based on three basic techniques is defined.

Keywords: *unmanned aerial vehicle, obstacles, space, aerodynamic model, air traffic control, security, flight.*

Introduction.

In the context of route planning for the group of unmanned aerial vehicles (UAVs) that connect selected points, the restrictions which should be taken into account are obligatory. The main limiting factor is the curvature or turning radius. This, together with the shortest route planning, require the development of approaches taking into account limitation in calculating the overall route and safe trajectory of the UAV group.

Often it is advantageous to have short routes in order to minimize flight time, as well as reduce fuel consumption and associated with it energy and power. Scheduling techniques can be extended for obtaining a shorter route from longer routes in order to bypass obstacles or to synchronize the UAV arrival time. The algorithms for designing the shortest routes are used in various scientific fields, such as computational geometry, operations research and logistics. One of the well-studied problems in computational geometry is the algorithm for finding the shortest route, discovered in 1987. The task of the salesman and the Chinese postman are widely investigated in the field of operations research, but they are built in the form of a graph and have no solutions.

At present, while planning the flight trajectory, three types of trajectories are important: Dubins - a route with arcs of constant curvature; clothoid - routes similar to Dubins ones, but with arcs of variable curvature; Pythagoras – route hodograph (PH). Each of them has a number of advantages and disadvantages, but in UAV route modeling, their application is necessary.

The main threats to unmanned aerial vehicles in modern conditions are the possibility of their destruction by air defense systems (air defense), as well as disruption of radio communication and control system between the control center and UAV by means of electronic suppression (RES). Analysis of technological solutions shows that in most UAV survivals under the conditions of air defense systems application and UAV stability under the RES influence is considered without taking into account the possibilities of UAVs spatial maneuvering to bypass the air defense and RES. Existing automated UAV control systems (ACS) do not take into account the possibility of timely formation of "unmanned" zones, where the probability of destruction by air defense systems is higher than the safe value, as well as automated formation of UAV flight routes providing the required stable control level UAVs, including the case under radio attacks influence.

Analysis of available investigations and publications. In the current decade, there has been a steady increase in the investigations and developments concerning aerodynamic modeling in the direction of unmanned aerial vehicles.

A number of authors R.O. Bieliakov, H.D. Radzivilov, O.D. Fesenko, V.V. Vasylchenko, O.H. Tsaturian, A.V. Shishatskii, V.P. Romanenko [1] developed the method of building the intelligent automatic control system for unmanned aerial vehicle in order to minimize the error of the platformless inertial navigation system due to neural network application.

D.I. Bondariev, D.P. Kucherov, T.F. Shmeliova [2], investigated the main aspects of optimization of the light unmanned aerial vehicle control system by frequency criterion, mathematically substantiating the direction choice and obstacles avoidance.

Regarding the modeling of UAVs kinematics and flight dynamics the works by Y.H. Danyk, I.I. Balytskii, [3] and I.S. Katerynchuk, Y.H. Danyk and I.I. Balytsii [4] are worth noticing. The authors describe in detail the possibility of using automatic control of the UAV navigation system in the conditions of obstacles and the mechanisms of flight trajectory formation.

The principles of formation of safe UAV movement in the conditions of radio attacks is considered by many national [5-7] and foreign scientists.

A.O. Popov, V.V. Tverdokhlib [8], formulated the main aspects of the general electronic warfare problem. The authors consider the general trends and directions of development of domestic and foreign electronic warfare means, which shoul be taken into account while constructing aerodynamic models.

The possibilities of UAV sounding in the tasks of monitoring terrorist threats are revealed in paper [9]. A number of authors, Orlov V.V., Lysyi M.I., Sivak V.A., Kuprienko D.A., Kulchytsii V.M., Dobrovolskii A.B. proposed the sonar system for detecting moving objects, which is constructed using the network of sensors located in space. The main difference from the existing sound-location systems is the determination of time delay not by mutual correlation function, but by mutual function of signal uncertainty between the sensors.

The works by C. Mu, D. Wang [10], Z. Lin, D. Ma, J. Meng, L. Chen, Y. Vovk [11, 12] should be noted among the foreign scientists works.

Statement of the problem. In this paper it is necessary to develop the aerodynamic model for a group of unmanned aerial vehicles in space under the radio attacks conditions.

Statement of the basic research material. The use of two-dimensional route planning is frequently found in the literature [4]. This is be due to the small number of investigations concerning the route planning for ground robots, however, while working with aircrafts, the motion plane should be added to the height in the calculations of maneuvers in space. From the point of view of trajectory planning, the beginning of route planning remains similar to the initial one, i.e. the parameters are the same at the starting and final points. In fact, there are three spatial coordinates (x, y, d), and three angular orientations (rolling, pitching, yawing).

The investigation is carried out on the basis of two methods:

I) Dubins trajectories;

II) Pythagorean spatial theorem with respect to the hodograph (hereinafter - PH).

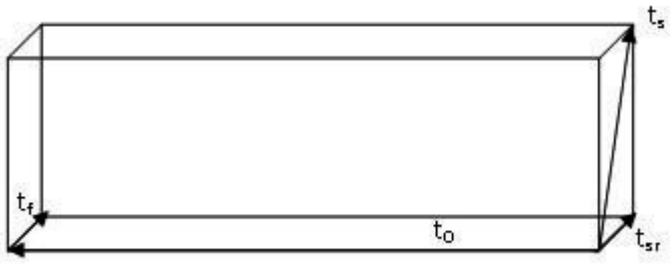

Figure 1 - Three-dimensional conditions of Dubins maneuver

One version of the "segment - arc" method is Dubins method. This smoothing method is to replace the adjacent to the polygonal line angle by the circle arc segments. It should be noted that, although the route according to Dubins method is smoothed, the curvature of this route is discontinuous, the gaps occur at the junction of segments and circles arcs.

Three-dimensional flight route $r(q)$ can be obtained by solving the following equation:

$$P_s(x_s, y_s, z_s, \theta_s, \psi_s) \xrightarrow{r(q)} P_f(x_f, y_f, z_f, \theta_f, \psi_f)$$
$$|k(t)| < k_{max}, |\tau(t)| < \tau_{max} \quad (1)$$

where $\tau(t)$ is curvature;

$k(t)$ is trajectory rotattion;

$r(q)$ is flight route;

$x_s, y_s, z_s, x_f, y_f, z_f$ are coordinates of the route beginning and end, respectively;

$\theta_s, \psi_s, \theta_f, \psi_f$ are rotation angles of the route beginning and end, respectively;

.

One of the classical trajectories used to maneuver the unmanned aerial vehicle from one altitude to another is the intersection of the circular spiral, which is projected onto X-Y plane in the form of a circle. The trajectory can be represented as a winding on the vertical cylinder surface. An important property of this curve is that both the curvature and torsion of the steel, which together gives the cylinder radius and the spiral turn. Compared to PH, the length of the spiral trajectory is longer than any other and is more accurate in the trajectory shape.

The generalization of two methods is the theorem.

Theorem 1. If two tangent vectors t_s and t_f are linked by the vector line t_0, as shown in Fig. 1, then the maneuver can be performed provided that all vectors lie in the same plane.

Figure 1 shows that two tangent vectors are in different planes, and the beginning of the tangent vector t_s does not lie in the plane defined by two vectors $t_f$and t_0.

In order to obtain the flight route, it is necessary to determine the initial maneuver of the arc touching the tangent vector t_s in the plane to obtain t_{sr} . This will ensure that this vector lies in the same plane as t_f i t_0. Dubins trajectory can be calculated using the expanded vector t_{sr} as a new tangent start vector. The normal vector n_{sr} can be defined as the norm to the tangent vector, as well as lying in the plane defined byt_f and t_0. The vector binormal b_{sr} is the right triple.

The initial trajectory consists of combined trajectory curvature relatively to the vector binormal, followed by rolling to build normal and binormal vectors, to form the final Dubins trajectory. Therefore, Dubins trajectory consists of one plane of the trajectory circle with the definition of curvature k_s,with the normal start of the circle trajectory with the definition of curvature k_s and rectilinear trajectory, and finally the end of the circle trajectory with the definition of curvaturek_f.

The application of Dubins method lies in the fact that in differential-geometric concepts the method of Pythagoras RN spatial trajectory is obtained using the first order of Hermitian interpolation. The resulting trajectory is further tuned to increase the UAV flight route by increasing the tangent vectors length.

The beginning of the maneuver can be determined taking into account the centerline between two positions. From the point of view of each position, positive or negative rotation from the tangent vector to the central vector is determined by the curvature sign for each maneuver. At the beginning of the maneuver and at its end, the UAV rotates according to the tangent vector t_s. Hence:

$$[t_{ms}, n_{ms}, b_{ms}] = [t_s, n_s, b_s]R_s \qquad (2)$$
$$[t_{mf}, n_{mf}, b_{mf}] = [t_f, n_f, b_f]R_f$$

where

$$R_s = \begin{pmatrix} 1 & 0 & 0 \\ 0 & cos(\phi_s) & -sin(\phi_s) \\ 0 & sin(\phi_s) & cos(\phi_s) \end{pmatrix}$$
$$R_f = \begin{pmatrix} 1 & 0 & 0 \\ 0 & cos(\phi_f) & -sin(\phi_f) \\ 0 & sin(\phi_f) & cos(\phi_f) \end{pmatrix} \qquad (3)$$

ϕ_s and ϕ_f are the rotation angles for the initial and final aircraft maneuvers.

Radius vectors can be defined as

$$r_s = [t_{ms}, n_{ms}, b_{ms}] \begin{pmatrix} 0 \\ \pm 1/k_s \\ 0 \end{pmatrix} \qquad (4)$$

and, similarly,

$$r_f = [t_{mf}, n_{mf}, b_{mf}] \begin{pmatrix} 0 \\ \pm 1/k_f \\ 0 \end{pmatrix} \qquad (5)$$

The base vectors are related

$$[t_f, n_f, b_f] = [t_s, n_s, b_s]R \qquad (6)$$

where *R* is the rotation matrix which should replace the axis from the start to the end.

Thus we have

$$R = (t_f, n_f, b_f) \cdot (t_s, n_s, b_s) \qquad (7)$$

Hence

$$R = \begin{pmatrix} t_f \cdot t_s & t_f \cdot n_s & t_f \cdot b_s \\ n_f \cdot t_s & n_f \cdot n_s & n_f \cdot b_s \\ b_f \cdot t_s & b_f \cdot n_s & b_f \cdot b_s \end{pmatrix} \qquad (8)$$

Connecting vectors form orthogonal set of vectors. Each vector lies in the corresponding plane of maneuver, which do not coincide. The internal connecting vector is common for both UAV maneuvers. Thus, you can write it in the following form:

$$a_s = a[t_{ms} \quad n_{ms} \quad b_{ms}]\alpha_s$$
$$a_f = a[t_{mf} \quad n_{mf} \quad b_{mf}]\alpha_f \qquad (9)$$

from

$$\alpha_s = \begin{pmatrix} \alpha_{ts} \\ \alpha_{ns} \\ \alpha_{bs} \end{pmatrix} \text{ та } \alpha_f = \begin{pmatrix} \alpha_{tf} \\ \alpha_{nf} \\ \alpha_{bf} \end{pmatrix} \qquad (10)$$

Frenet frame for two planes of maneuver is related to

$$[t_f \quad n_f \quad b_f] = [t_s \quad n_s \quad b_s]R,$$
$$[t_{mf} \quad n_{mf} \quad b_{mf}] = [t_f \quad n_f \quad b_f]R_f,$$
$$[t_{ms} \quad n_{ms} \quad b_{ms}] = [t_s \quad n_s \quad b_s]R_s. \tag{11}$$

By

$$[t_{ms} \quad n_{ms} \quad b_{ms}]R_s' = [t_s \quad n_s \quad b_s],$$
$$[t_{mf} \quad n_{mf} \quad b_{mf}]R_f' = [t_f \quad n_f \quad b_f] = [t_s \quad n_s \quad b_s]R = [t_{ms} \quad n_{ms} \quad b_{ms}]R_s'R \tag{12}$$

and

$$[t_{mf} \quad n_{mf} \quad b_{mf}]=[t_{ms} \quad n_{ms} \quad b_{ms}]R_s'RR_f \tag{13}$$

This means that

$$\alpha_s = R_s'RR_f\alpha_f$$
$$\alpha_f = R_f'RR_s\alpha_s \tag{14}$$

The radius vectors R_s and R_f can also be described in the axes of the maneuver beginning, as

$$r_s = [t_{ms}, n_{ms}, b_{ms}]\begin{pmatrix} 0 \\ \pm 1/k_s \\ 0 \end{pmatrix}$$
$$r_f = [t_{ms}, n_{ms}, b_{ms}]R_s'RR_f\begin{pmatrix} 0 \\ \pm 1/k_f \\ 0 \end{pmatrix} \tag{15}$$

Vectors can also be defined in the axes of the maneuver beginning , in the form

$$\alpha_s = {\pm 1}/{k_s}\,[t_{ms}, n_{ms}, b_{ms}]\beta_s,$$
$$\alpha_f = {\pm 1}/{k_f}\,[t_{mf}, n_{mf}, b_{mf}]\beta_f,$$
$$\alpha = {\pm 1}/{k_f}\,[t_{ms}, n_{ms}, b_{ms}]R_s'RR_f\beta_s \tag{16}$$

The length of Dubins route is the sum of lengths of these segments which is given as

$$h_{\text{Dubins route length}} = h_i + h_s + \alpha_t + h_f = {\alpha_i}/{k_s} + {\alpha_s}/{k_s} + \alpha\,{\alpha_f}/{k_f} \tag{17}$$

where h is the route length;
s, t and f are the initial route arc, the total route length, the final route arc;
i is the arc segment;
α is the arc angle;
k is rotation.

The PH route provides the curve displacement in closed polynomials form.

Equation (18) is polynomial designed to interpolate free vectors at the boundary. Free vectors have positions (x, y, z) and direction (θ, ψ) in space. The interpolation curve of such two vectors is called Hermit interpolation. The resulting curve will have tangent continuity, but not heredity of curvature. For UAV applications, it is important that the continuity of curvature is proportional to the lateral acceleration of the UAV. Thus, it is necessary to have controlled curvature at the boundaries of the interpolation curves, as well as to limit the maximum curvature.

$$Q(q) = \sum_{i=0}^{2} Q_i \binom{2}{i} q^i(1-q)^{2-i}, \qquad q \in [0,1] \tag{18}$$

This will ensure smooth UAV route. Now, PH curve is represented in the fifth order of the polynomial form as

$$r(q) = \sum_{k=0}^{5} b_k \binom{5}{k} q^k(1-q)^{5-k}, \qquad q \in [0,1] \tag{19}$$

where $b_k = (x_k, y_k, z_k)$ are control points, the vertices of which are determined by Bezier polygon control of with $k = 0, \ldots, 5$.

The initial and final configurations are $p_s\,(x_s, y_s, z_s, \theta_s, \psi_s)$ and $p_f\,(x_f, y_f, z_f, \theta_f, \psi_f)$, respectively. Four control points of Bézier polygons are calculated by first-order Hermitian interpolation in the following way:

$$b_0 = (x_s, y_s, z_s),$$
$$b_5 = (x_f, y_f, z_f),$$
$$d_0 = m_0[cos(\theta_s)cos(\psi_s), cos(\theta_s)sin(\psi_s), sin(\theta_s)],$$
$$d_5 = m_5[cos(\theta_f)cos(\psi_f), cos(\theta_f)sin(\psi_f), sin(\theta_f)],$$
$$b_1 = b_0 + {1}/{5}\,d_0,$$
$$b_4 = b_5 + {1}/{5}\,d_5, \tag{20}$$

Spherical coordinates are used for orientation. Constants m_0 і m_5 play an important role in compiling the interpolation curve.

The problem of bypassing obstacles is closely related to route planning, because the obstacles presence usually results in routes re-planning. Route planning with obstacles bypassing in 3D is more complicated, because in such planning there are infinite number of directions for maneuvers for both UAVs and obstacles.

In order to maneuver in the environment full of obstacles, the UAV should be able to calculate the trajectories that will float around these obstacles and should be able to reach the final point. Therefore, there is requirement to calculate Dubins composite trajectories that include evasion maneuvers. In case of single obstacle crossing rectilinear segment of the standard Dubins trajectory, two trajectory avoidance options should be calculated for each obstacle. The standard Dubins trajectory consists of five segments, with initial, intermediate and final arc maneuvers, along with two straight segments. In the initial and final arc, the maneuvers are modified in such a way that the segments are tangent to the obstacle circle.

If the UAV detects an obstacle by means of a sensor located on board, the airplane should re-plan the route either by changing the curvature between two points of the case or re-plan the route using the intermediate point. Obstacles are tested to determine if the radius of the obstacle crosses the trajectory or UAV "safety" . If the obstacle radius does not cross the UAV trajectory, then re-planning is not required. This can be done either by increasing the trajectory curvature, or by creating the intermediate point and simulating a new route which includes new track point.

Assuming that $O_{obstacle}$ is an obstacle in the UAV safety radius O_{safety}, the condition for collision avoiding is

$$O_{obstacle} \cap O_{safety} = \emptyset \tag{21}$$

The scheme for the environment full of obstacles is shown in fig. 2.

Obstacles are modeled in the form of polygons, the areas and coordinates of which are known. Route planning of a group of unmanned aerial vehicles can be written in the following form:

$$P_{s,i,j-1}\left(x_{s,i,j-1}, y_{s,i,j-1}, \theta_{s,i,j-1}\right) \xrightarrow{r_{i,j-1(q)}} P_{f,i,j}\left(x_{f,i,j}, y_{f,i,j}, \theta_{f,i,j}\right) \tag{22}$$

$$i = 1, \dots, n_{UAV}, \quad j = 2, \dots, n_p, \quad |k_i(q)| < k_{max}, \quad \coprod_{safety}, \coprod_{length}, \tag{23}$$

n_{UAV} is the number of unmanned aerial vehicles,

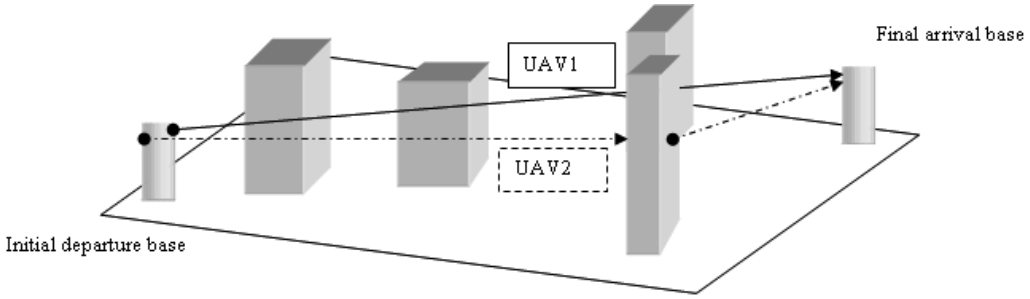

Figure 2 - Dubins routes for two unmanned aerial vehicles in the environment with obstacles.

In order to implement the algorithm, we take two UAVs. Both UAVs are homogeneous in their physical capabilities, and therefore they both move with the same speed and have curvature limitations.

The trajectories of two unmanned aerial vehicles in the environment with obstacles is shown in Fig. 2. The flight route of the second unmanned aerial vehicle UAV2 intersects the obstacle and the flight route of the first unmanned aerial vehicle UAV1. The curvature of Dubins route arc is varied to avoid the threat radius. The new safe route after increasing the curvature of UAV2 trajectory, to solve the same problem using the intermediate point is presented in Fig. 3.

Once the intersection obstacle is detected, the intermediate points are generated.

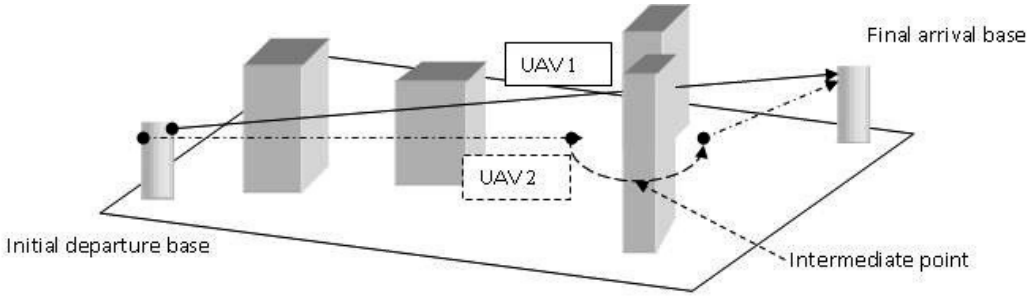

Figure 3 – Re-planning of UAV2 route with curvature adjustment using the intermediate point

The route intersection is determined interactively for the clothoids of arc segments, and the intersections of lines from ellipses can be detected using simple geometry.

The intermediate route is made for each intersection within the obstacle radius zone. After that, the routes are re-planed in order to pass through new UAV route modeling points.

The mechanism of UAV safe movement formation in the conditions of radio attacks is based on three basic techniques:

1) the method of clustering UAV flight zones according to the degree of control stability;

2) the method of UAV flight routes formation, taking into account the location of air defense and electronic warfare means;

3) methods for assessing the stability of providing information about the UAV route in terms of using air defense and REW means.

The technique of clustering flight zones for unmanned aerial vehicles according to the degree of control stability should automatically allow to form "non-flying" zones based on geotopological models of UAV flight zones and known location of air defense systems, in which drones and control zones can be damaged due to REP.

Elements of the novelty of this methodology, which distinguishes it from the results of the work known in the field of UAV flight route formation [9] and the work known in the field of cluster formation, are the consideration of two types of destabilizing effects as obstacles to UAV flight - air defense systems and electronic warfare effects as integral metrics of graph nodes of geotopological models of flight zones. At the same time, it is proposed to use the Lance-Williams mathematical hierarchical clustering algorithm and test the connectivity of the route network, using the strong connection method in order to create unmanned areas where UAVs can be damaged and areas with impaired control due to REP on UAVs from UAV graphic areas.

The method of forming UAV flight routes, taking into account the location of air defense and electronic warfare means, should automatically provide the formation of a series of UAV flight routes, ranked according to the degree of control stability, based on geotopological model of UAV flight zone and known unmanned areas where the UAV will be damaged, taking into account the potential loss of control in case of impact with UAV switchgear. At the same time, air defense zones should be completely excluded from consideration when forming UAV routes by cutting the scheme of geotopological model of the flight zone. REP zones are used to create routes [7]. However, it is necessary to choose the UAV flight route, where the total value of the suppression probability of the switchgear is minimal. This route corresponds to the trajectory with maximum stability control for unmanned aerial vehicles.

Conclusions. The method of construction the aerodynamic model of a group of unmanned aerial vehicles in space with obstacles is revealed in this paper. This model is an improved method of constructing the UAV flight route in the conditions of interference. The described aerodynamic model can be used as a stable model of the UAV group in the conditions of flight trajectory formation under the influence of radio attacks. The development of the mechanism of UAV safe movement formation in the conditions of radio attacks based on the methods for the increase of stability of providing information about the unmanned aircraft route the in the conditions of REP and air defense systems application is proposed. The improvement of the stability of providing information about the route will be achieved by grouping the unmanned aerial vehicles flight zones in the areas of air defense and electronic warfare influence, followed by the exclusion of air defense zones.

The algorithm for construction the aerodynamic model of a group of unmanned aerial vehicles in space with obstacles is resistant to external and internal influences.

References:

1. Belyakov, R.O., Radzivilov, G.D., Fesenko, O.D. (2019). Romanenko Methods of building an intelligent system for automatic control of unmanned aerial vehicles. *Radio electronics, informatics, management*, *1*, 218-229.
2. Bondarev, D.I., Kucherov, D.P., Shmelyova, T.F. (2015). Models of group flights of unmanned aerial vehicles using graph theory. *Science and Technology of the Air Force of the Armed Forces of Ukraine*, *3*(20), 68–75.
3. Danyk, Y.G., Balytsky, I.I. (2018). Methods for determining the safety of unmanned aerial vehicles. *Science-intensive technologies 4*(40), 526–534.
4. Danyk, Y.G., Katerynchuk, I.S., Balytsky, I.I. (2017). Methods of ensuring the safety of UAVs when performing special tasks in difficult conditions. *Modern information technologies in the field of security and defense*, *3*(30), 80–89.
5. Romaniuk, L., Chykhira, I. (2020). Aerodynamic model of a group of unmanned aerial vehicles in space with obstacles. *Computer-integrated technologies: education, science, production*, 38, 59-66.
6. Romaniuk, L., Chykhira, I. (2020). Automated air traffic control system for unmanned aerial vehicles. *Scientific notes of Tavriya National University named after V.I. Vernadsky. Series: Technical Sciences*, *31*(70), 131-135.
7. Romaniuk, L., Chykhira, I. (2020). The mechanism of formation of safe movement of UAVs in terms of radio attacks. *Municipal utilities. Series: Technical sciences and architecture, 4*(157), 178-183.
8. Popov, A.A., Tverdokhlibov, V.V. (2014). General trends in the development of electronic warfare. *Military-Technical Policy*, *4*, 4-11.
9. Orlov, V.V., Lysyi, M.I., Sivak, V.A. (2019).*Visnyk NTUU KPI. Seriia Radiotekhnika Radioaparatobuduvannia*, *79*, 24-32.
10. Mu, C., Wang, D. (2017). Neural-network-based adaptive guaranteed cost control of nonlinear dynamic systems with matched uncertainties. *Neurocomputing*, *245*, 46–54.
11. Lin, Z., Ma, D., Meng, J., Chen L. (2018). Relative ordering learning in spiking neural network for pattern recognition. *Neurocomputing*, *275*, 94–106.
12. Vovk, Y. (2016). Resource-efficient intelligent transportation systems as a basis for sustainable development. Overview of initiatives and strategies. *Journal of Sustainable Development of Transport and Logistics*, *1*(1), 6-10.

COMPUTER TOOL FOR GENERATING OF TEST RADIO SIGNALS FOR VERIFICATION OF THE RADIO COMPUTER SYSTEMS SOFTWARE

Liliya Khvostivska[1], Iryna Dediv[2], Mykola Khvostivskyy[3], Leonid Dediv[4]

[1] Ternopil National Ivan Puluj Technical University, Rus'ka str. 56, 46001, Ternopil, Ukraine; hvostivska@gmail.com
[2] Ternopil National Ivan Puluj Technical University, Rus'ka str. 56, 46001, Ternopil, Ukraine; iradediv@gmail.com
[3] Ternopil National Ivan Puluj Technical University, Rus'ka str. 56, 46001, Ternopil, Ukraine; hvostivskyy@tntu.edu.ua
[4] Ternopil National Ivan Puluj Technical University, Rus'ka str. 56, 46001, Ternopil, Ukraine; dediv@ukr.net

Abstract: A computer tool for generating test radio signals in the space of one repeat as an amplitude-modulated mix of composite waves of the radio signal transmitted in time space, and take into account repeat ability - as an amplitude-modulated mix of radio signals transmitted along the time axis of the k-th repeats.

The developed computer tool provides a verification procedure the correct operation of the software of radio computer systems by generating test radio signals according to the specified parameters with high correctness of their reproduction and taking into account the properties of repeat ability and stochasticity.

Keywords: *computer tool, test radio signals, simulation, generation, radio computer systems software, MATLAB*.

1. Introduction

As of mid-2021, there has been significant progress in the development of radio computer systems and their widespread use in various areas of human activity. The technology of designing radio computer systems includes an important stage of experimental set-up and testing through the procedure of verification of algorithms and software for radio signals processing [1]. Carrying out of field research (testing and set-up) of radio computer systems caused of the difficulty of interpreting the results (obtained in the process of radio signals processing) in an experimental research with variable conditions and requires large financial and time costs.

The development of a computer tool for generating test radio signals (RS) is an important problem in verification the correct work of the software of radio computer systems. The results of the verification allow detecting incorrectness in the software, which was developed based on algorithmic support that affect the correctness of all radio computer system.

Known computer tools by Leonov A.I., Leonov S.A., Nagulinko F.V., Galkin A.P., Lapin A.N., Samoilov A.G., Ghannam H., Klovsky D.D. Kontorovich V.Ya., Shirokov S.M., Glushkov A.N., Menshikh V.V., Khohlov N.S., Bokova O.I., Kalinin M.Y., Mordachev V. [1-7] and other do not allow generating RSs of random and periodic nature, which is an inherent property of real signals. Therefore, the development of a new computer tool for generating test radio signals is an important problem in the area of telecommunications for the development of algorithmic and software of radio computer systems.

2. The structure of test radio signals

As an example of a useful test signal, we used the data of the quantitative consumption of active power for five days. Fig. 1 shows the transmitting test radio signal $\xi(t)$, which structurally consists of a set of waves, which in total form a repeat of the radio signal, which primarily leads to a set of k-th repeat (days) of the radio signal with variable values of repeat (days) $T_1 = T_2 = \ldots = T_k$.

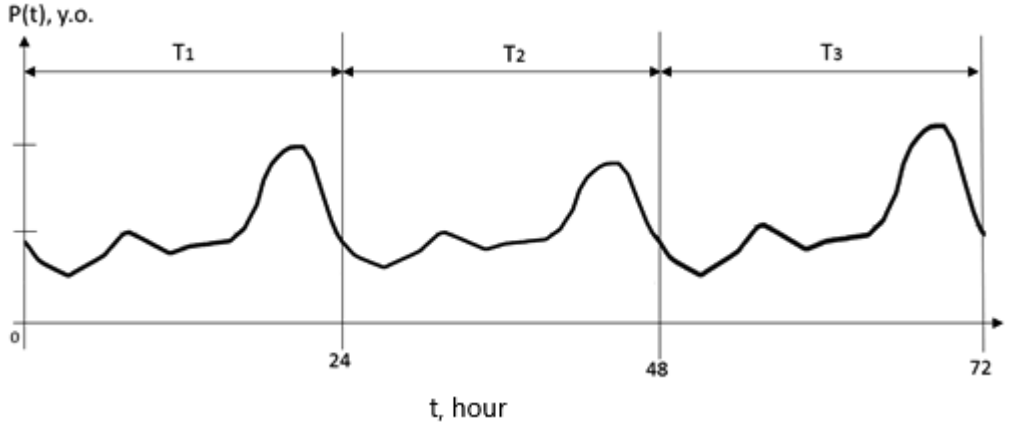

Fig. 1. Implementation of a useful signal of energy consumption (population 400,000 people.)

Taking into account the constructive structure of the radio signal (fig. 1), an algorithm of the generation a radio signal has been developed, which provides the process of generating random and repeated signals.

3. Mathematical and algorithmic support of generation test radio signals

According to the analysis of the structure of real signals, found that within one repeat the signal structurally consists of the n-th number of characteristic waves, which must be generated separately with their subsequent integration into a continuous implementation of the RS.

The algorithm for generating a test useful radio signal in the area of period is shown in fig. 2.

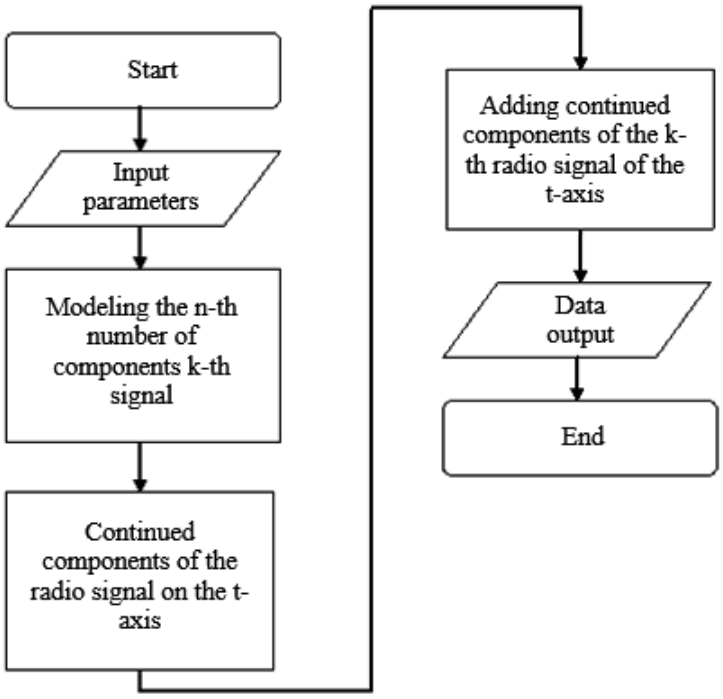

Fig. 2. Algorithm of generation a useful test radio signal in the area of one repeat

At the beginning stage, it is proposed to generate n-th signal waves within the k-th repeat, respectively, from 0 to T_{nk}, with their subsequent location on the time axis depending on their time zone, and the zones in which they are not localized are filled with zeros according to the expression:

$$\zeta_k(t) = \sum_{k \in Z} \tilde{\zeta}_{nk}(t),\ t \in [0, T_k), \tag{1}$$

where $\tilde{\zeta}_{nk}(t)$ - consistently localized wave signal in time $\zeta_{nk}(t),\ t \in [0, T_{nk})$ (1):

$$\tilde{\zeta}_{nk}(t) = \begin{cases} \zeta_{nk}(t), t \in [T_{(n-1)k}, T_{nk}) \\ 0, \quad t \notin [T_{(n-1)k}, T_{nk}) \end{cases}, \tag{2}$$

where T_{nk} – the time duration of the *n*-th signal wave on the *k*-th repeated, $T_{1k} \neq T_{2k} \neq \ldots T_{kn}$.

Fig. 3 is shown for a detailed understanding of the principle of forming a test radio signal, which illustrates the scheme of generating a test radio signal within the time of repeat.

The simulation model of the n-th wave generator of the test radio signal within the k-th repetition T_k is developed in the form of sinusoidal oscillations with exponential disappearance in a given time space, which takes into account the parameters of amplitudes of component waves, their time samples and their stochasticity:

$$\zeta_{nk}(t) = (A_{nk} + \psi_A)\sin(2 \cdot \pi \cdot (t + \psi_T) \cdot f_{nk}) \cdot e^{-t \cdot K_{nk}} \cdot L_{nk},\ t \in [0, T_{nk}) \tag{3}$$

where n – the current wavelength of the test radio signal at the specified time intervals, n=1,2,..., N ;

N - the number of waves of the test radio signal;

T_{nk} – the limit of time space of n-th wave on the k-th repeat;

A_{nk} - the amplitude of the n -th wave of the test radio signal;

f_{nk} - the frequency of fluctuation for half sinusoids test signal;

K_{nk} - coefficients of incline nk -th component of wave test radio signal;

L_{skj} - the values of the scaling factors of the nk-th wave of the test radio signal;

where $\psi_A(M\{A\}, D(A))$, $\psi_T(M\{T\}, D\{T\})$ - stochastic units of amplitude and time interval of the test radio signal (mathematical expectation $M\{A\}$ і $M\{T\}$ with the deviation $D\{A\}$ і $D\{T\}$);

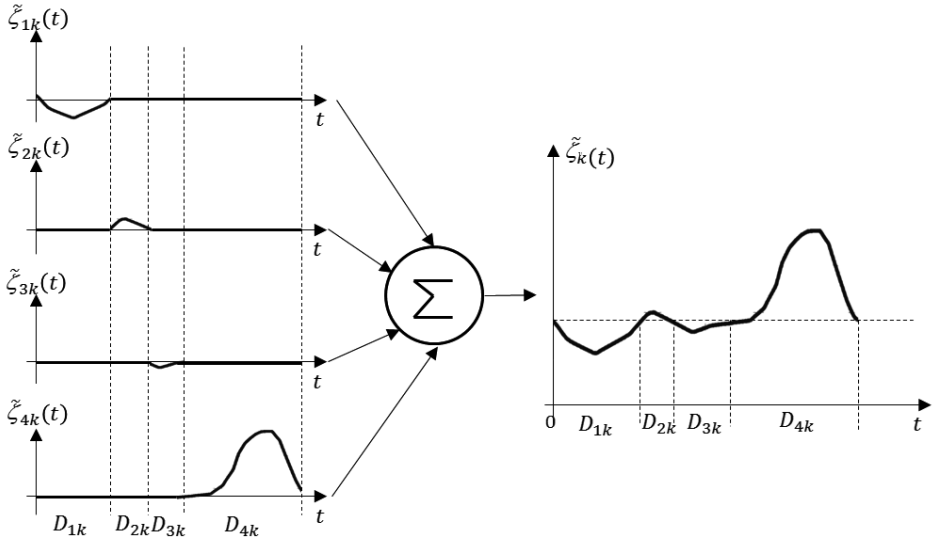

Fig.3. The scheme of formation of the k-th test radio signal within the repeat

Expressions (1) - (3) reflect the simulation model of the generator of test radio signals in the space of k-th repeats T_k, which combines stochastic of amplitudes and times.

Considering that the test radio signal must have repeat ability (almost periodic), so first of all it is necessary to generate a signal on the k-th repeats, the signal must be broadcast in time on the number of k-th repeats. The algorithm for generating a test radio signal stochastic and repeated is shown in fig. 4.

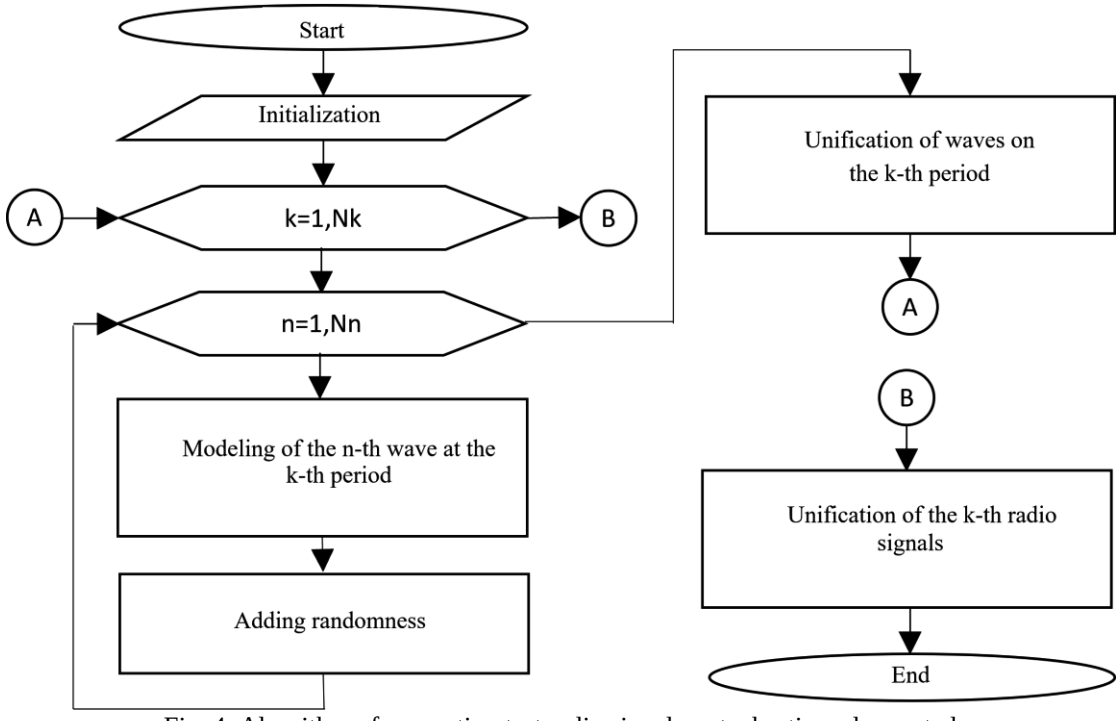

Fig. 4. Algorithm of generation test radio signal as stochastic and repeated

Considering algorithm (fig.4) for providing repeat ability of signal is carried out the procedure of modeling the k-th number of signals within the k-th repeat from 0 to T_k . Subsequently, the k-th number of signals are localized on the time axis depending on the zone of their time localization by arrangement according to the expression:

$$\xi(t)=\sum_{k\in Z}\tilde{\xi}_k(t), \quad t\in R \tag{4}$$

where $\tilde{\xi}_k(t)$ - periodically extended signal (repeated) on the time axis, $\tilde{\xi}_k(t), t\in R$:

$$\tilde{\xi}_k(t)=\begin{cases}\zeta_k(t), t\in[T_{k-1},T_k)\\ 0, \quad t\notin[T_{k-1},T_k)\end{cases}, \tag{5}$$

where $\zeta_k(t)$ - signal within the k-th repeat T_k , $\zeta_k(t), t\in[0,T_k)$ (1);

T_k – the time duration of the k-th signal repeat, $T_1\neq T_2\neq ..T_k$.

Fig. 5 illustrates a scheme of generating a test signal in the space of time repeat for a better understanding of the principle of the principle of modeling repeated signal with stochastic parameters.

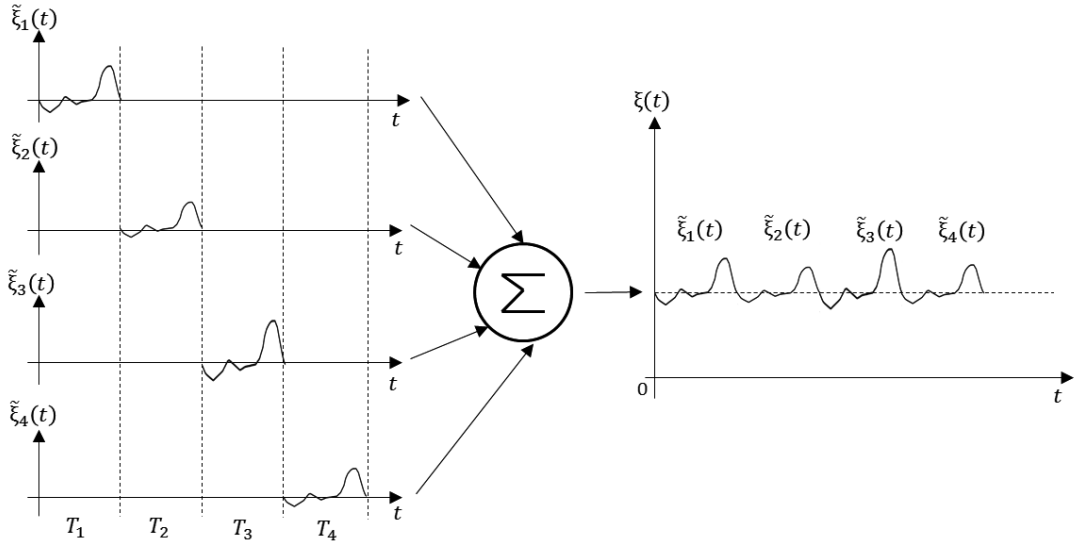

Fig.5. Scheme of generating a repeated radio signal with stochastic parameters

Taking into account the additive influence of inside and outside interference of the radio system, expression (3) will be:

$$\xi(t)=\sum_{k\in Z}\tilde{\xi}_k(t)+n(t), \qquad t\in R \tag{6}$$

where $n(t)$ - the white noise.

Substituting expression (2) in (1), (1) in (5) and (5) in (6) we get the expression to generate the signal of the k-th repeat:

$$\xi(t)=\sum_{k\in Z}\left(\left\{\sum_{k\in Z}\begin{cases}\zeta_{nk}(t), & t\in[T_{(n-1)k},T_{nk})\\ 0, & t\notin[T_{(n-1)k},T_{nk})\end{cases}, \quad \begin{matrix}t\in[T_{k-1},T_k)\\ t\notin[T_{k-1},T_k)\end{matrix}\right\}+n(t)\right). \tag{7}$$

where $\zeta_{nk}(t)$ - the n-th wave of the test radio signal within the k-th repeat.

To generate a radio signal modulated by the parameters of the amplitude, a modulation process was performed in accordance with existing algorithms, the implementation of which is represented by the expression:

$$\xi_{AM}(t)=\xi(t)\cdot\cos(2\cdot\pi\cdot f\cdot t+\varphi_0), \tag{8}$$

where $\xi(t)$ – non-modulated test signal (7);

f – the fluctuation of frequency of the carrier useful radio signal;

φ_0 – the begining phase of the carrier fluctuation of the test radio signal.

Expression (8) makes it possible to develop algorithmic and based on it software for computer generation of radio signals (including amplitude-modulated) for verification of software for radio systems.

4. The results of generating radio signals

Based on expression (8) and using the GUIDE utility of the MATLAB environment developed the software of the RS generator with a graphical interface, which is shown in fig.6-8.

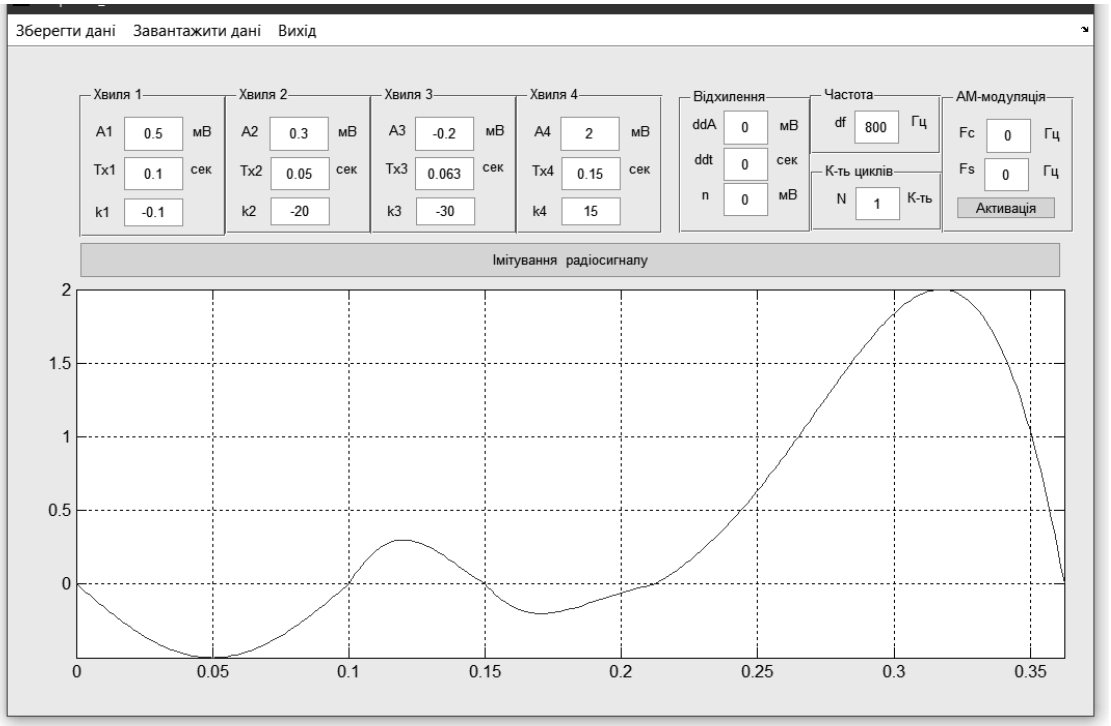

Fig. 6. The result of generating a test signal at N = 10 without interference

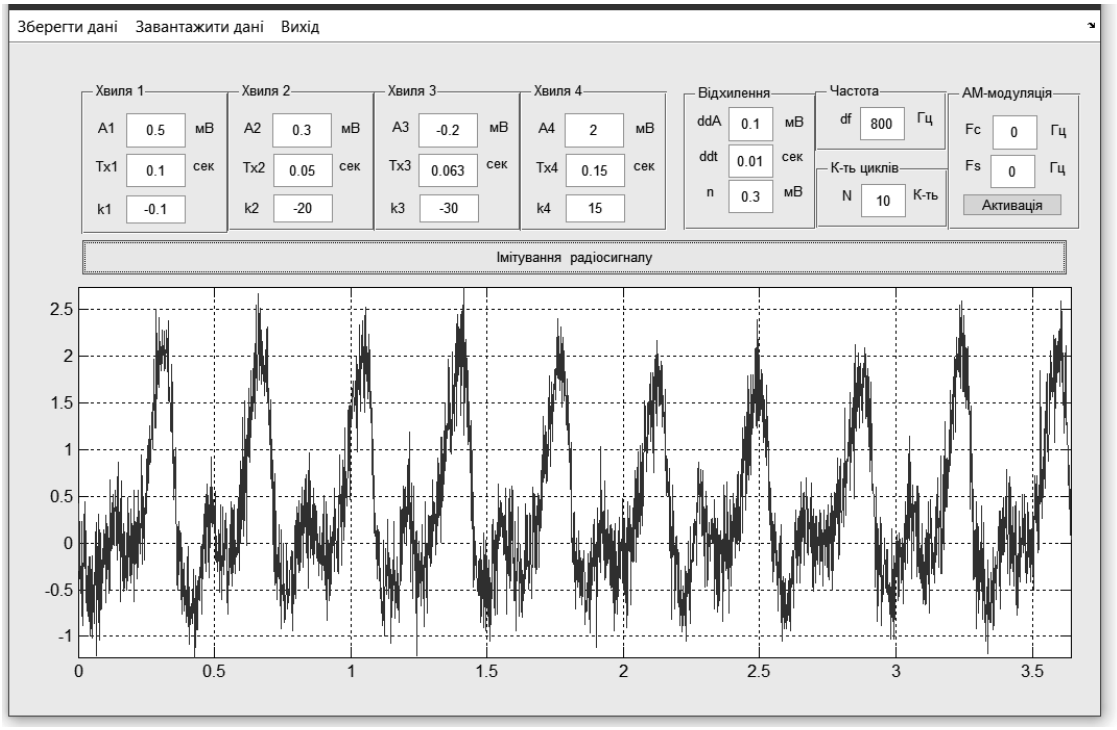

Fig. 7. The result of generating a test signal at N = 10 and interference of dispersion 0,3 mV^2

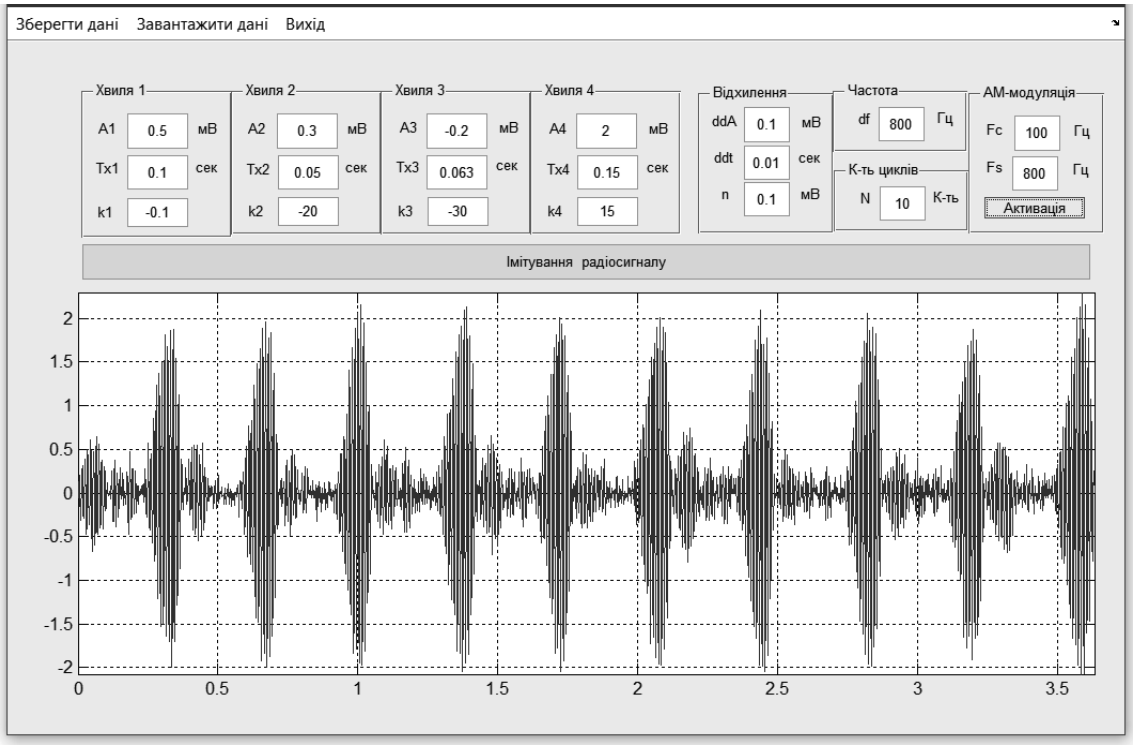

Fig.9. Computer tool interface of generating test signal

The developed software allows generating random and periodic RSs with different parameters of amplitudes, times and frequencies.

5. Conclusions

The developed model of generator of testing radio signal combines in its structure the parameters of stochasticity and repeat ability, which provided a probable reproduction of the form of test radio signals in relation to the experimental values of its parameters (parametric identification)

Developed software with a graphical shell allows you to generate testing radio signals for test the correct operation of the algorithms of radio computer systems.

It is determined that the obtained generated data of testing radio signals provide probable simulation of the constructive form of experimental radio signals of time and amplitude parameters, which indicates a high probability of generation and correctness of verification of algorithms and software of radio computer systems.

References

1. Leonov, A.I., Leonov, S.A., Nagulinko, F.V. (1990). *Testing of RS (evaluation of characteristics).* Moscow: Radio and communication.

2. Galkin, A.P., Lapin, A.N., Samoilov, A.G. (1979). *Modeling of communication systems channels.* Moscow: Communication.

3. Samoilov, A.G. (2003). Simulators of multibeam radio channels. Design and technology of electronic means, *4*, 32-36.

4. Ghannam, H. (2019). *Mathematical Modelling and Signal and System Design for Spectrally Efficient Future Wireless Communications*. (Doctoral thesis). Computer Science.

5. Klovsky, D.D., Kontorovich, V.Ya., Shirokov, S.M. (1984). *Models of continuous communication channels based on stochastic differential equations.* Moscow: Radio and communication.

6. Glushkov, A.N., Menshikh, V.V., Khohlov, N.S. (2017). Markov model based mathematical representation of radio signals. *Ural Conference on Measurements (UralCon)*, Proceedings of the 2nd International Conference. Chelyabinsk, Russia. doi: 10.1109/URALCON.2017.8120717.

7. Mordachev, V. (2000). Mathematical models for radio signals dynamic range prediction in space-scattered mobile radiocommunication networks. *Vehicular Technology Conference*, Proceedings of the Conference. doi:10.1109/VETECF.2000.887131.

METHOD OF DETECTING RADIO SIGNALS WITH PHASE MODULATION IN A MIXTURE WITH NOISE

Vasyl Dunets[1], Anatoly Martsenyuk[2], Kateryna Kamchatna-Stepanova[3], BohdanAndreichuk[4]

[1] Ternopil National Ivan Puluj Technical University, Rus'ka str. 56, 46001, Ternopil, Ukraine; vasyadunets@gmail.com
[2] Ternopil National Ivan Puluj Technical University, Rus'ka str. 56, 46001, Ternopil, Ukraine; oljynka23@gmail.com
[3]National Technical University "Kharkiv Politechnic Institute", 2 Kirpichova str., Kharkiv, Ukraine, 61002; katerina.ks@i.ua
[4]Ternopil Ivan Puluj National Technical University, 56 Ruska str., Ternopil, Ukraine, 46001

Abstract: Using Matlab software, a process of computer simulation of the phase modulation and demodulation process with different values of carrier frequency and phase deviation over the test signal in the form of an additive mixture of two deterministic sinusoidal signals under the influence of white Gaussian noise of various power. A justified method of detecting radio signals in a mixture with noise allows to expand the capabilities of radio systems, and the developed computer simulation model of radio signal is suitable for testing data processing algorithms to monitor and evaluate the signal-to-noise ratio in radio systems.

Keywords: radio signals, phase modulation, radio systems, matlab.

1. Introduction

Improving the efficiency of electronic devices and systems for various purposes, including information transmission and processing systems, still remains one of the main challenges facing modern radio systems. Today, a significant part of the frequency range suitable for radio systems is overlapped, and some parts of this range are heavily congested and poorly protected from the effects of various internal and external noise. Therefore, the task is to increase the efficiency of systems and their noise immunity, working in well-developed parts of the spectrum.

One of the options for solving this problem is the use of single-band signals for data transmission, which allow rational use of the frequency resource [1], but the disadvantage of this method is the low potential noise immunity. When using signals with continuous single-band phase modulation for information transmission, there is a problem of asymmetry of the spectrum of signals with continuous two-band phase modulation. In the works of Volkov A.A. [2] proposed a new method of signal generation with continuous single-band phase modulation and proposed different schemes for receiving such a signal and evaluated the noise immunity.

Despite the above work on the study of message transmission using single-band signals with phase modulation was not performed. Therefore, solving a scientific problem related to the reception and transmission of signals with single-band phase modulation, and their detection in a mixture with noise is an urgent scientific problem [3].

2. Algorithm for experimental research of test radio signals

When conducting an experimental study using computer simulation using Matlab software, the sequence of operations on which the experimental program will work was established [4]. Therefore, we will establish a sequential link, and present it in the form of a block diagram, which is shown in Figure 1.

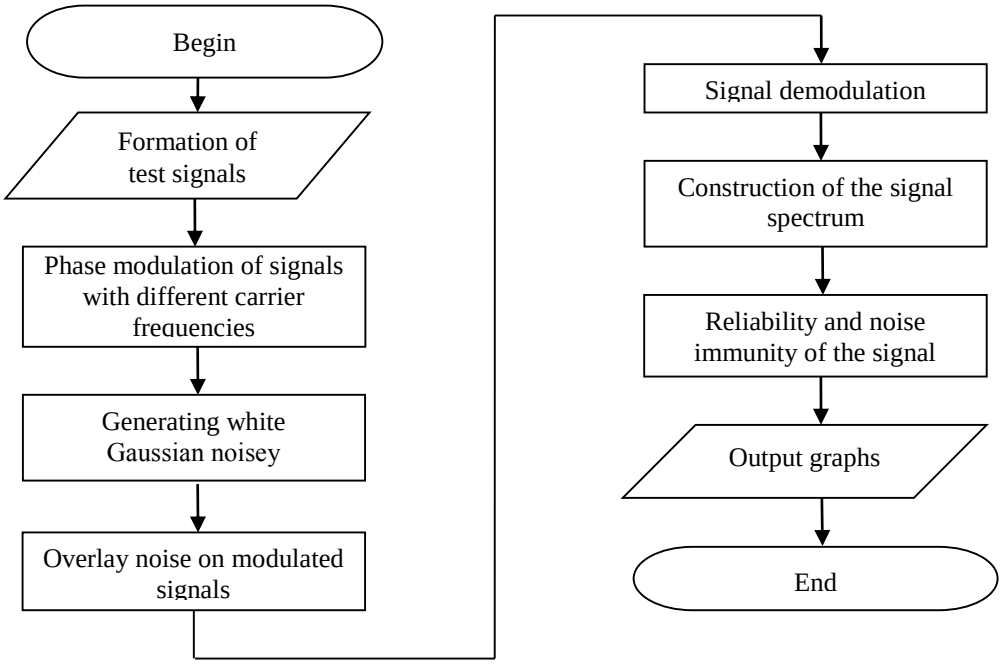

Fig. 1. Algorithm of the experiment

3. Generation of a test signal with phase modulation

We will conduct the experimental study according to the block diagram shown in Figure 1. Using the graphical interface Matlab we will display a test signal on the graph, the result of which is shown in Figure 2.

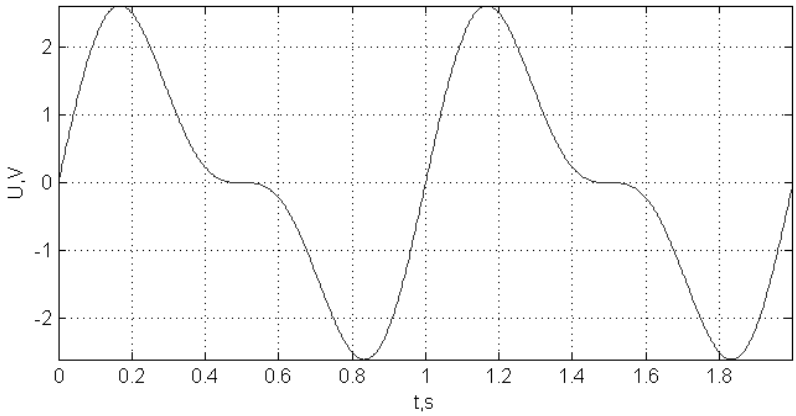

Fig. 2. Test signal with sampling rate parameters 400Hz

When transmitting a signal over a distance, it is necessary to convert the test signal (Figure 2) into one that would have a fixed frequency component by which it would be possible to distinguish the signal from others in the radio channel. Therefore, it is necessary to modulate the signal in the form of a simple oscillation, which is described by the following equation [5]:

$$\xi(i\Delta t) = s(i\Delta t) + n(i\Delta t), \quad (1)$$

where $s(i\Delta t)$ - discrete useful signal, $n(i\Delta t)$ - noise, Δt - sampling step ($\Delta t = \frac{1}{2f}$, f – signal frequency from the conditions of Kotelnikov theorem).

Accordingly, we set the values of the carrier frequencies *Fc* (5, 10, 15, 20, Hz) and determine the sampling frequency Fs in the input signal, and accordingly substitute into a given function. Figures 3.1 - 3.4 show graphs of the displayed simulated test signals using phase modulation.

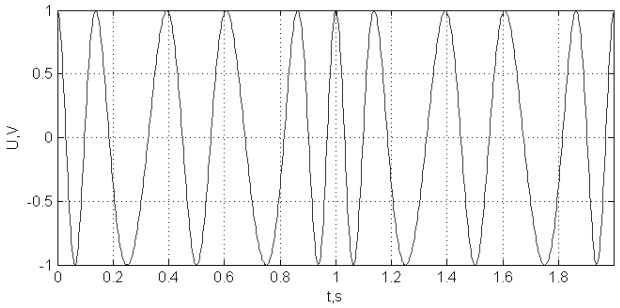

Fig. 3.1. Phase modulation with a carrier of 5 Hz, and the deviation of π/4 radians

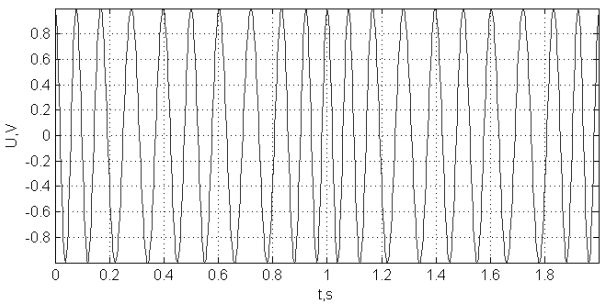

Fig. 3.2. Phase modulation with a carrier of 10 Hz, and the deviation of π/4 radians

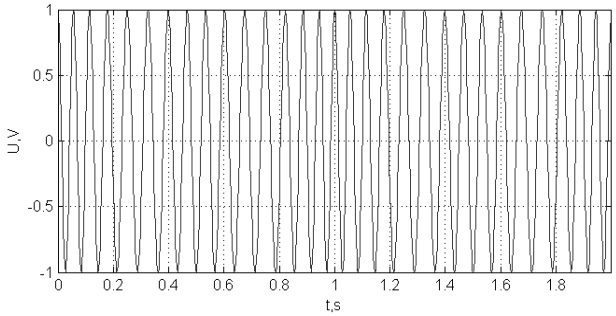

Fig. 3.3. Phase modulation with a carrier of 15 Hz, and the deviation of π/4 radians

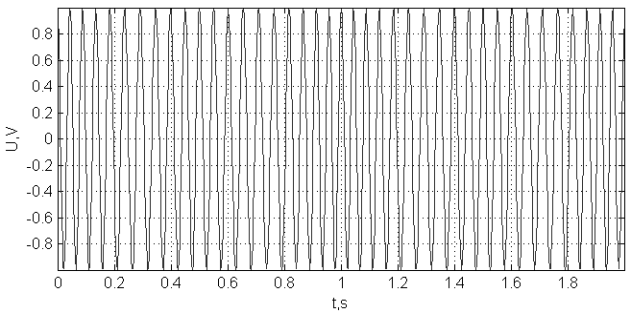

Fig. 3.4. Phase modulation with a carrier of 20 Hz, and the deviation of π/4 radians

In order to determine how noise-tolerant the phase-modulated communication channel is at different carrier frequencies, we simulate the simulated signal with white Gaussian noise with a standard deviation of 0.2 V., as shown in Figures 4.1-4.4.

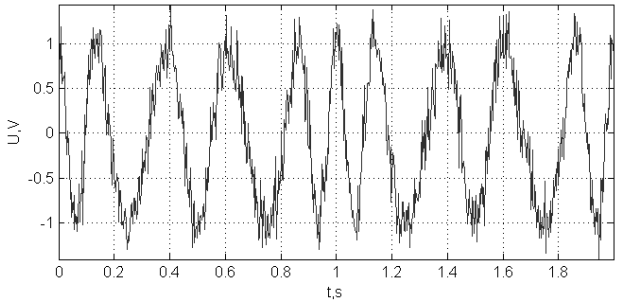

Fig. 4.1. A mixture of modulated signal (5 Hz) and noise

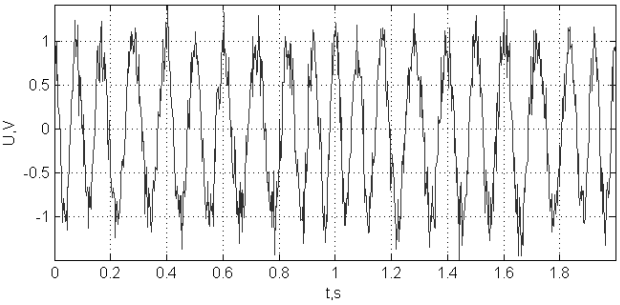

Fig. 4.2. A mixture of modulated signal (10 Hz) and noise

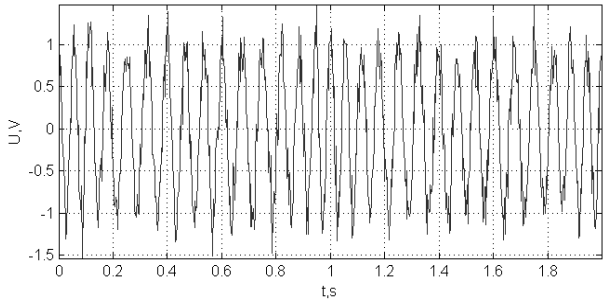

Fig. 4.3. A mixture of modulated signal (15 Hz) and noise

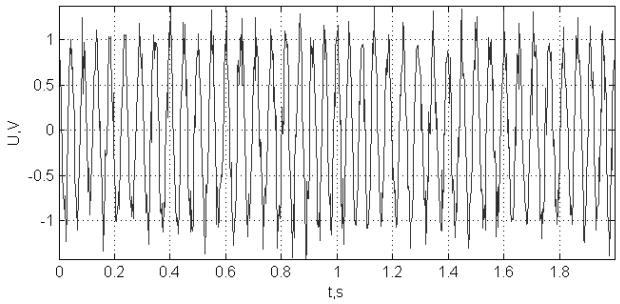

Fig. 4.4. A mixture of modulated signal (20 Hz) and noise

To determine how much this modulation is noise-tolerant for different carriers, we will carry out the demodulation process, the result of which is shown in Figures 5.1 - 5.4

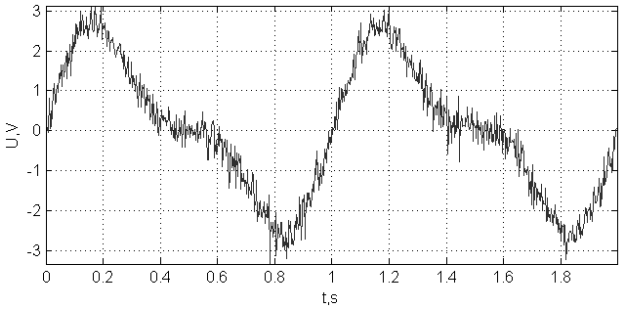

Fig. 5.1. Implementation of the demodulated signal (5 Hz)

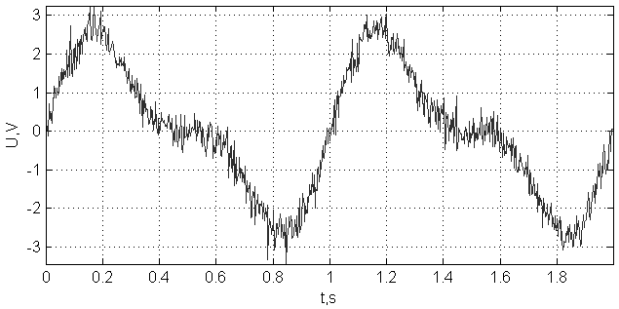

Fig. 4.2. Implementation of the demodulated signal (10 Hz)

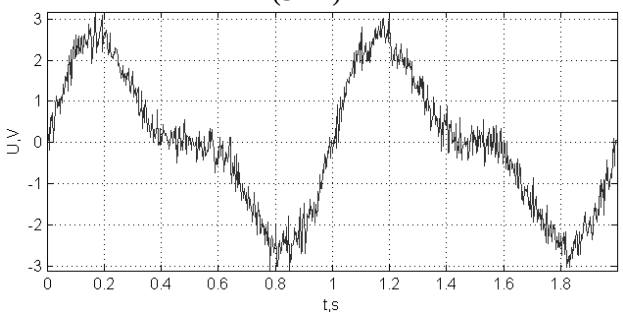

Fig. 4.3. Implementation of the demodulated signal (15 Hz)

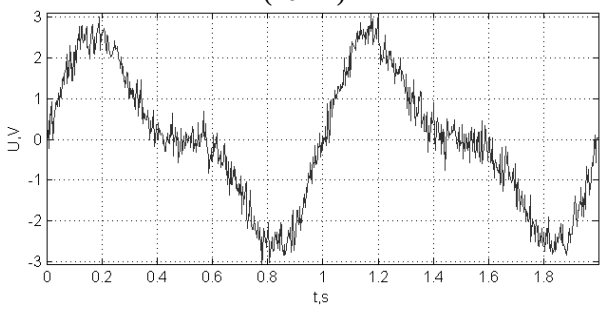

Fig. 4.4. Implementation of the demodulated signal (20 Hz)

Figures 4.1 - 4.4 show that the amplitude modulation procedure is not noise protected at different carrier oscillation frequencies, which is reflected in the presence of noise in the demodulated signals.

4. Evaluation of noise immunity and reliability of the communication channel with phase modulation

The main parameter of noise immunity during modulation is the signal-to-noise ratio [6].

The signal-to-noise ratio (SNR) is calculated as an expression $q = 10\log\left(\frac{E_{ÑÈÃÍÀËÓ}}{Å_{ÂÈÕ.ØÓÌÓ}}\right)$.

where $E_{ÑÈÃÍÀËÓ}$ - signal energy.

Accordingly, in order to determine the energy of the signal, it is necessary to find its frequency components (frequency response), and summing the sum of the squares of its harmonics we obtain the energy:

$$E = \left|A_n^2\right|, \quad (2)$$

where A_n - amplitude n - harmonics.

Using a discrete Fourier transform, we obtain a graph of the spectrum of the input signal shown in Figure 5.

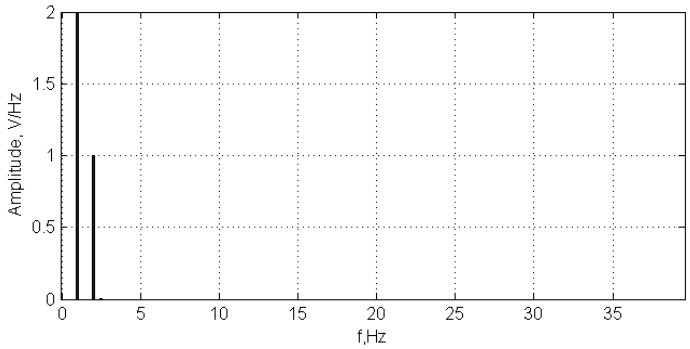

Fig. 5. The spectrum of the input test signal

Given that the test signal is the sum of two sinusoidal signals with frequencies of 1 Hz and 2 Hz, so in the constructed spectrum (Figure 5) such harmonic peaks are reflected at these frequencies.

Let's build graphs for simulated and de-simulated signals, Figures are shown in Figures 6.1-6.4, respectively simulated signals, in Figures 7.1-7.4 - demodulated signals.

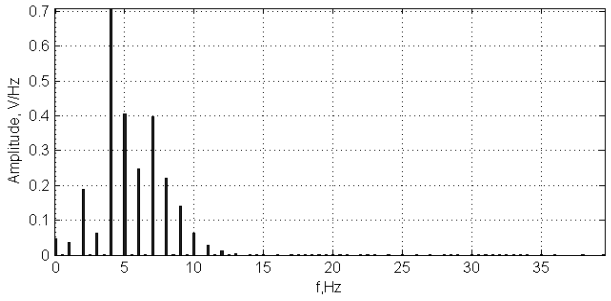

Fig. 6.1. Spectrum of phase-simulated signal (5 Hz)

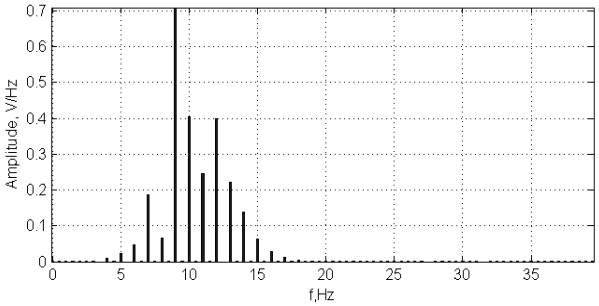

Fig. 6.2. Spectrum of phase-simulated signal (10 Hz)

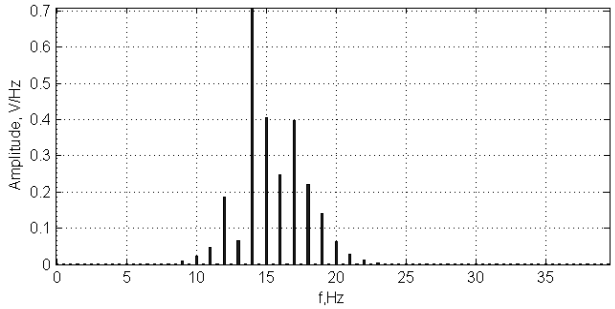

Fig. 6.3. Spectrum of phase-simulated signal (15 Hz)

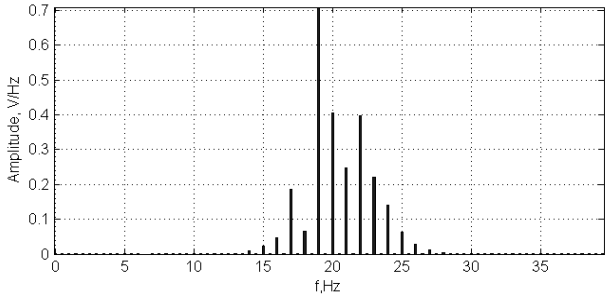

Fig. 6.4. Spectrum of phase-simulated signal (20 Hz)

In fig. 6.1 there is a selection of the main spectral components that correspond to the significant spectrum of the phase-simulated signal 5, 10, 15, and 20 Hz.

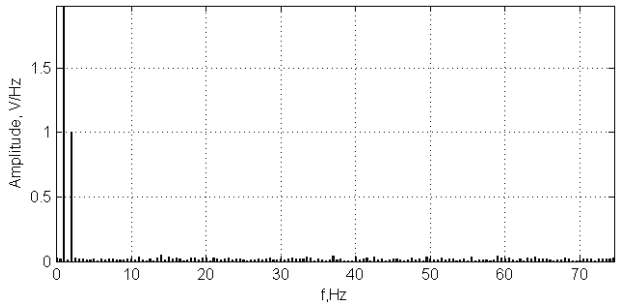

Fig.7.1. The spectrum of the demodulated signal (5 Hz)

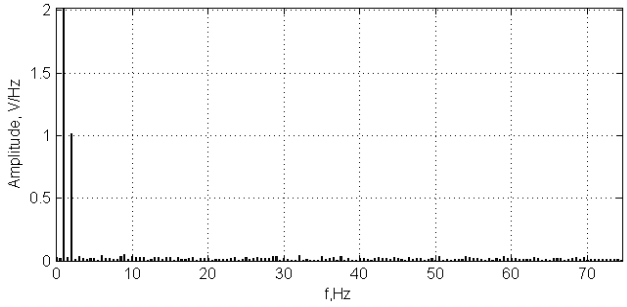

Fig. 7.2. The spectrum of the demodulated signal (10 Hz)

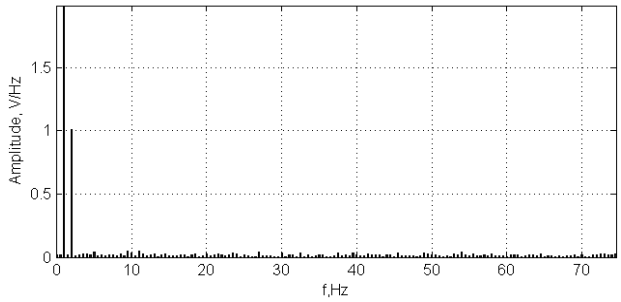

Fig. 7.3. The spectrum of the demodulated signal (15 Hz)

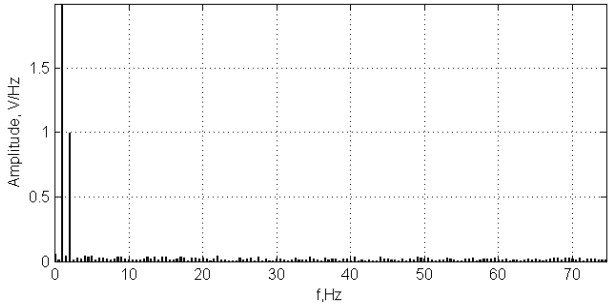

Fig. 7.4. The spectrum of the demodulated signal (20 Hz)

According to the results of the constructed spectra of demodulated signals (Fig. 7.1-7.4) we can say that the noise of the white noise type makes a significant contribution to the spectral structure of the output signal and is evenly distributed over the entire frequency domain.

Determine the signal energy according to formula 3:

Accordingly, in order to determine the energy of the signal, it is necessary to find its frequency components (frequency response), and summing the sum of the squares of its harmonics we obtain the energy:

$$E = \left| A_n^{\,2} \right|, \qquad (3)$$

where A_n - amplitude n - harmonica.

From the above graphs (Figures 7.1-7.4) it is seen that the spectral components are changed, ie there is a noise contribution to the total signal energy, which is equal to the energy difference of the input and demodelled, ie the modulus of the energy difference of the demodulated and input signal.

Let us plot the dependence of the signal-to-noise ratio on the carrier frequency which is shown in Figure 8.

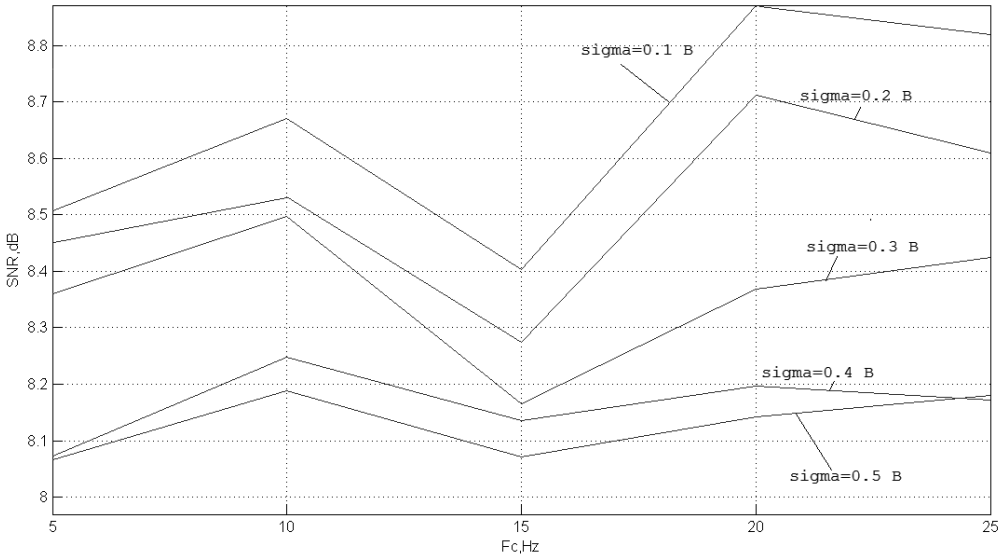

Fig. 8. The dependence of the signal-to-noise ratio on the carrier frequency at different standard deviations of BGS

Figure 8 shows that the value of the signal-to-noise ratio of the demodulated signal increases with increasing energy of the input noise and retains its structure at different carrier frequencies.

The indicator of radio communication data, in addition to the signal-to-noise ratio, is the deviation of the original from the original, so we build the dependence of the SNR on the standard deviation of different carriers.

The standard deviation is calculated by the following formula:

$$\sigma = \sqrt{\frac{\sum_{i=1}^{N}\left(x_i - M\{x\}\right)^2}{N-1}}, \qquad (4)$$

where N - number of samples; $M\{x\}$ - mathematical expectation of the difference between the output and the input signal.

Using formula 4, we construct the dependence of SNR on the standard deviation for different carriers, which is shown in Figure 9.

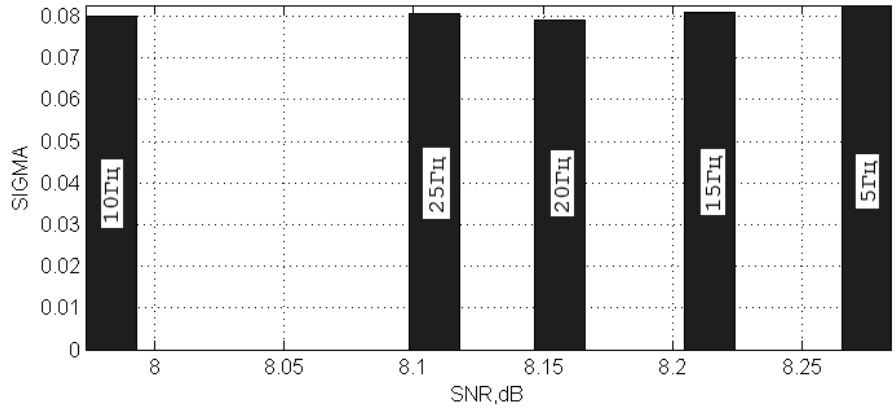

Fig. 9. SNR values at the standard deviation of the output signal from the input at carrier frequencies (5,10,15,20,25 Hz)

According to the values of Figure 9, it was found that at all frequencies used in the experiment, the standard deviation of the noise of the demodulated signal at different frequencies of the carrier oscillation remains almost the same. These results confirm the homogeneity of the noise immunity at different frequencies.

We construct graphs of dependence separately for each component (Fig. 10), by generating input noise of influence on the modulated signal of different power.

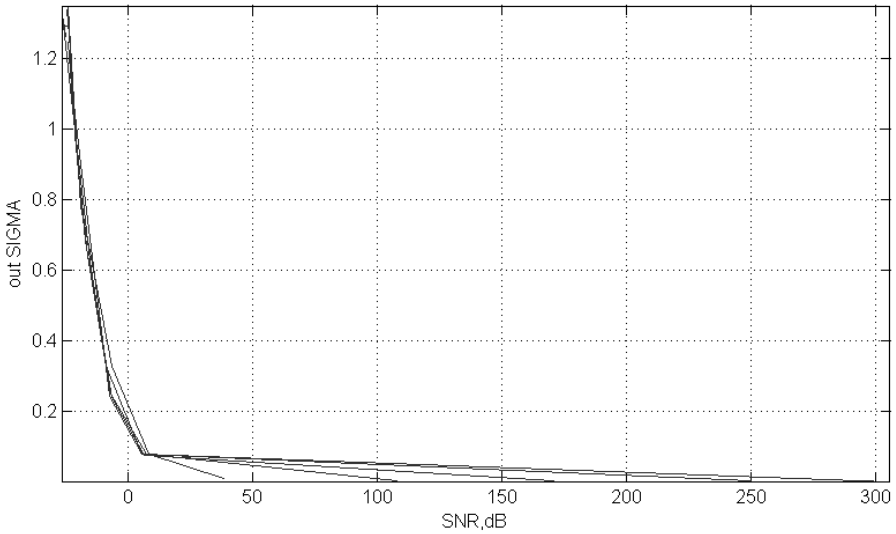

Fig. 10. Dependence of SNR at the standard deviation of the output signal from the input for carrier frequencies (5,10,15,20,25 Hz).

According to Figure 10, it is found that as the signal-to-noise ratio of the input signal increases, the standard deviation of the noise of the output signal at different frequencies attenuates exponentially. The detection curves of the phase-modulated test signal against the background of noise are shown in Figure 11.

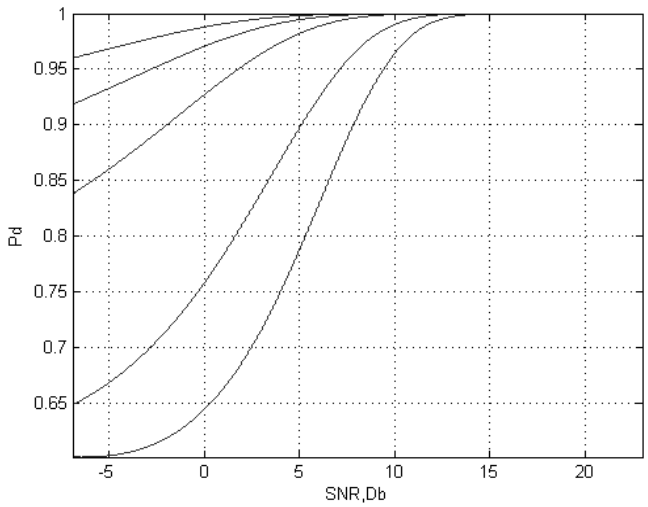

Fig. 11. Test signal detection curves

Considering the detection curves of the phase-modulated test signal against the background of noise (Figure 11), we see that the given probabilities do not depend on the waveform and is determined only by the peak signal-to-noise ratio.

5. Conclusions

From the study it is established that the proposed method of detecting a phase-modulated test signal in a mixture with noise at optimal reception with given probabilities and does not depend on the waveform and is determined only by the peak signal-to-noise ratio, ie signal-to-noise ratio. This method allows to expand the capabilities of radio systems, and the developed computer simulation model of the radio signal is suitable for testing data processing algorithms to monitor and evaluate the signal-to-noise ratio in radio systems.

References

1. Svanidze, V.G., Sokolov, M.A. (2004). Potential noise immunity of reception using a two-count signal scheme with discrete single-sideband angular modulation. *Problems of transport, 10*, 192-198.

2. Svanidze V. G. (2004) Noise immunity of information transmission systems with single-sideband phase shift keying: *Dis. Cand. tech. Sciences: 05.13.01: Saint Petersburg*, 139 c.

3. Kravchyk B., Dunets V. (2019). Detection of radio signals in interference with interference. IMST, 54.

4. Hvostivska L. V., Dunetc V. L., Serputko A. P. (2016). Simulation modeling of signals for testing algorithm of radiosystems. *Book of abstract the V International scientific and technical conference of young researchers and students "Current issues in modern technologies"*, 2, 123-124.

5. Khvostivsky M., Dediv L., Dunets V., Shadrina H. (2008). Electrocardiosignal simulation model based on the periodically correlated stochastic process. *Bulletin of TNTU* , 13, 201-205.

6. Dunetc V. L., Tsumbala T. I., Rakush R. V. (2016). Methods of optimal signal detection in the communication channel. *Book of abstract the V International scientific and technical conference of young researchers and students "Current issues in modern technologies"*, 2. 37-38.

APPROACH TO GAS CONSUMPTION PROCESS FORECASTING ON THE BASIS OF A MATHEMATICAL MODEL IN THE FORM OF A RANDOM CYCLIC PROCESS

Serhii Lupenko [1], Iaroslav Lytvynenko [2], Oleg Nazarevych [3], Grigorii Shymchuk [4], Volodymyr Hotovych [5]

[1]author's information: Department of Computer Science Ternopil Ivan Puluj National Technical University Ternopil, Ukraine, Ruska, 56 +380975818444, serhii.lupenko@gmail.com
[2]author's information: Department of Computer Science Ternopil Ivan Puluj National Technical University Ternopil, Ukraine, Ruska, 56 +380964511070, iaroslav.lytvynenko@gmail.com
[3]author's information: Department of Computer Science Ternopil Ivan Puluj National Technical University Ternopil, Ukraine, Ruska, 56 +380673827084, taltek.te@gmail.com
[4]author's information: Department of Computer Science Ternopil Ivan Puluj National Technical University Ternopil, Ukraine, Ruska, 56 +380979004016, gorych@gmail.com
[5]author's information: Department of Computer Science Ternopil Ivan Puluj National Technical University Ternopil, Ukraine, Ruska, 56 +380988028731, gotovych@gmail.com

Abstract: In the article, the approach to gas consumption process prediction on the basis of a mathematical model in the form of a cyclic random process is considered. The prediction is based on statistical information for previous years of gas consumption. An additive combination of three components was used as a mathematical model of gas consumption process: a cyclic random process, a trend component and a stochastic residue. The first component of the mathematical model in the form of a cyclic random process takes into account the scale factors, information about which is considered at the stage of prediction. Based on the caterpillar decomposition, ten components of the singular decomposition are obtained. The sum of nine components of singular decomposition forms a cyclic component – a cyclic random process. This component takes into account the scale factors of the amplitude of gas consumption process in each segment-cycle. The trend component of the mathematical model is the second component of the singular decomposition, and the stochastic residue is formed on the basis of the difference between the values of the studied gas consumption process and the sum of the cyclic and trend components. Computer simulation of realization of cyclic component of gas consumption process is carried out in the work, and also the annual forecast of gas consumption is made. The prediction results are compared with the real gas consumption process (information for last year's gas consumption was used). This paper does not take into account the effects of climatic conditions on the gas consumption process, but this is going to be done in further research, which will improve the accuracy of computer simulation and prediction.

Keywords: *cyclic process, gas consumption process, statistical processing, segmentation, cyclic random process*

Introduction (statement of the problem)

Gas consumption management is of particular urgency nowadays. The ability of analysis, simulation and prediction of gas consumption process are the vital problems set by the world leading gas companies. For their effective solution, modern software and hardware systems are needed that will provide the possibility to develop and control the gas consumption process. Development of new software complexes demands the improving of mathematical software, which involves the development of new mathematical models and methods of gas consumption processing. This will ultimately allow to form the forecast results based on the information obtained.

Objectives of the research

This research deals with creating a new mathematical model of gas consumption process using stochastic approach in the form of additive combination of three components, one of which is a cyclic random process that takes into account scale factors, other components are trend and stochastic residue.

Analysis of recent research

Consider the known approaches to forecasting gas consumption and analysis of their models. In [1, 2] the method of short-term forecast is described, which makes it possible to analyse and calculate the predicted values of gas consumption in the heating season, taking into account its cyclicity and ambient temperature. There are also approaches to forecasting natural gas consumption using a system of fuzzy conclusions based on the adaptive network (ANFIS) [3]. The combined method of forecasting natural gas consumption using the Bayesian model averaging (BMA) is given in [4]. The research [5] proposes an approach such as "grey forecast with a moving mechanism" (GPRM). In [6], a method for predicting natural gas consumption using neural networks and methods of multidimensional time series is described. In [7], a model for forecasting daily gas consumption is presented, designed for forecasting in a short range for 1-5 days

in advance. The forecast of natural gas demand based on the combinational forecasting model is given in [8]. The study [9] described a method for predicting the need for gas using artificial neural networks, design and training was performed using MLP (multilayer perceptron model). The variety of approaches to forecasting suggests that the tasks of forecasting need to be developed and improved, which applies to both short- and long-term forecasting.

The main part

Mathematical model of the random cyclic gas consumption process $\xi'(\omega,t)$ is presented as an additive model (1) which consists of three components.

$$\xi'(\omega,t)=\xi(\omega,t)+f_{tr}(t)+f_{rem}(\omega'',t), t\in\mathbf{W},\omega\in\mathbf{\Omega},\omega''\in\mathbf{\Omega''}, \quad (1)$$

where $\xi(\omega,t)$ is a cyclic component, $f_{tr}(t)$ is a trend function, $f_{rem}(\omega'',t)$ is a stochastic residue function.

In practice we are dealing with discrete data, we present mathematical model (1) is as follows

$$\xi'_{\omega}(l)=\xi_{\omega}(l)+f_{tr}(l)+f_{rem\omega''}(l), l\in\mathbf{W}=\mathbf{D}, \quad (2)$$

where $\xi_{\omega}(l)$ is implementation of cyclic component of gas consumption process, $f_{tr}(l)$ is a trend function, $f_{rem\omega''}(l)$ is a function of stochastic residue, l stands for discrete samples of gas consumption process, L is a number of samples of gas consumption process (registered implementations).

For obtaining the components of mathematical model (2) during processing of the real cyclic gas consumption process $\xi'_{\omega}(l), l=\overline{1,L}$ we apply the SSA-caterpillar method. This method is given in [10] and describes the transformation of a one-dimensional time series into a multidimensional one, which makes it possible to obtain components of a singular segmentation.

When applying the caterpillar method, we obtain k implementations of components $\left\{\bar{f}_k(l), k=\overline{0,K-1}, l=\overline{1,L}\right\}$, where $K=10$, l stands for parts of gas consumption process during 2006-2019, L is the number of discrete implementation samples.

The cyclic component is obtained by summing the components obtained on the basis of the caterpillar method, in particular, components: 0-1,3-9, component 2 is a component of the trend $\bar{f}_2(l)$

$$\xi_{\omega}(l)=\sum_{k=0}^{1}\bar{f}_k(l)+\sum_{k=3}^{9}\bar{f}_k(l), l=\overline{1,L}, \quad (3)$$

$$f_{tr}(l)=\bar{f}_2(l), l=\overline{1,L}. \quad (4)$$

The stochastic residue is obtained on the basis of the relation:

$$f_{rem\omega''}(l)=\xi'_{\omega}(l)-(\xi_{\omega}(l)+f_{tr}(l)), l=\overline{1,L}, \quad (5)$$

Consider $\xi_{\omega}(l)$, the cyclic component of the mathematical model (1), which carries information about the process of gas consumption in more detail, we present it as

$$\xi_{\omega}(l)=\sum_{i=1}^{C}f_i(l), l\in\mathbf{W}, \quad (6)$$

where C is the number of segments-cycles of the cyclic process of gas consumption, $\mathbf{W}$ is the domain of determining the cyclic process of gas consumption, and the domain of its values, for the case of the stochastic approach is the Hilbert space of random variables given on one probabilistic space $\left(\xi_{\omega}(l)\in\mathbf{\Psi}=\mathbf{L}_2(\mathbf{\Omega},\mathbf{P})\right)$. In the design (6), the segments-cycles $f_i(l)$ of the cyclic gas consumption process are determined by indicator functions, i.e.

$$f_i(l)=\xi_{\omega}(l)\cdot I_{\mathbf{W}_i}(l), i=\overline{1,C},\ l\in\mathbf{W}, \quad (7)$$

Herewith, the indicator functions, which allocate segments-cycles, were defined as:

$$I_{\mathbf{W}_i}(l)=\begin{cases}1, l\in\mathbf{W}_i,\\ 0, l\notin\mathbf{W}_i.\end{cases}, \; i=\overline{1,C}, \tag{8}$$

where $\mathbf{W}_i$ is the domain of determining the indicator function, which in the case of a discrete signal, i.e. $\mathbf{W}=\mathbf{D}$, is equal to a discrete set of samples

$$\mathbf{W}_i=\left\{l_{i,j}, j=\overline{1,J}\right\}, i=\overline{1,C}, \tag{9}$$

The segmental cyclic structure $\hat{\mathbf{D}}_c$ is taken into account by the set of time samples $\{l_i\}$ or $\left\{l_{i,j}\right\}, i=\overline{1,C}$, $j=\overline{1,J}$, where J - is the number of discrete samples in the cycle. This notation of the mathematical model (9) takes into account the rhythm of the cyclic gas consumption process due to the continuous function of the rhythm $T(l,n)$ namely

$$I_{\mathbf{W}_i}(l)=I_{\mathbf{W}_{i+n}}\left(l+T(l,n)\right), \; i=\overline{1,C}, n=1, l\in\mathbf{W}, \tag{10}$$

In order to estimate the rhythm function $T(l,n)$, the segment structure of gas consumption process (in this case the segment cyclic structure) was first determined as $\hat{\mathbf{D}}_c=\{l_i, i=\overline{1,C}\}$ which is a set of time moments that correspond to the boundaries of the segments-cycles of gas consumption process. In this case, the estimation of the segmental cyclic structure of gas consumption process can be performed using the segmentation method presented in [11]. It has been shown before that segmentation of gas consumption process is better not to carry out on the vertices, but on the depressions, which does not allow "blurring" of statistical estimates after processing the studied implementation.

The example of computer simulation of gas consumption process based on the mathematical model (1) is presented in Figure 8.

To adequately describe the real gas consumption process, it is also necessary to consider changes in the load amplitude on the segments-cycles, which are caused by various factors, such as climate (temperature, pressure, wind force etc.). In the design of mathematical model (1), the cyclic component (6) takes into account the segments-cycles of cyclic gas consumption process as multiplicative components considering the indicator functions and scale factors of gas consumption amplitude, i.e.

$$f_i(l)=\xi_\omega(l)\cdot\alpha_{\mathbf{W}_i}(l)\cdot I_{\mathbf{W}_i}(l), i=\overline{1,C}, \; l\in\mathbf{W}, \tag{11}$$

In formula (11), an additional component $\alpha_{\mathbf{W}_i}(l)$ that reflects the scale factors of gas consumption amplitude in each segment-cycle of the cyclic process, are introduced

$$\alpha_{\mathbf{W}_i}(l)=\begin{cases}\alpha_i, l\in\mathbf{W}_i,\\ 0, l\notin\mathbf{W}_i.\end{cases}, \; i=\overline{1,C}, \tag{12}$$

where α_i stands for the scale factors of gas consumption amplitude at every i-segment-cycle, are determined as follows:

$$\alpha_i=\frac{\alpha_{i\max}}{\alpha_{aver}}, \; i=\overline{1,C}, \tag{13}$$

where $\alpha_{i\max}$ is the maximum value of gas consumption range at i-segment-cycle (determined at the stage of segmentation of cyclic gas consumption process), α_{aver} is the average value of gas consumption range (the maximum

value of estimation range of mathematical expectation, is determined at the stage of statistical processing of cyclic gas consumption). The block diagram of the new approach to gas consumption process simulation will look as in Figure 1.

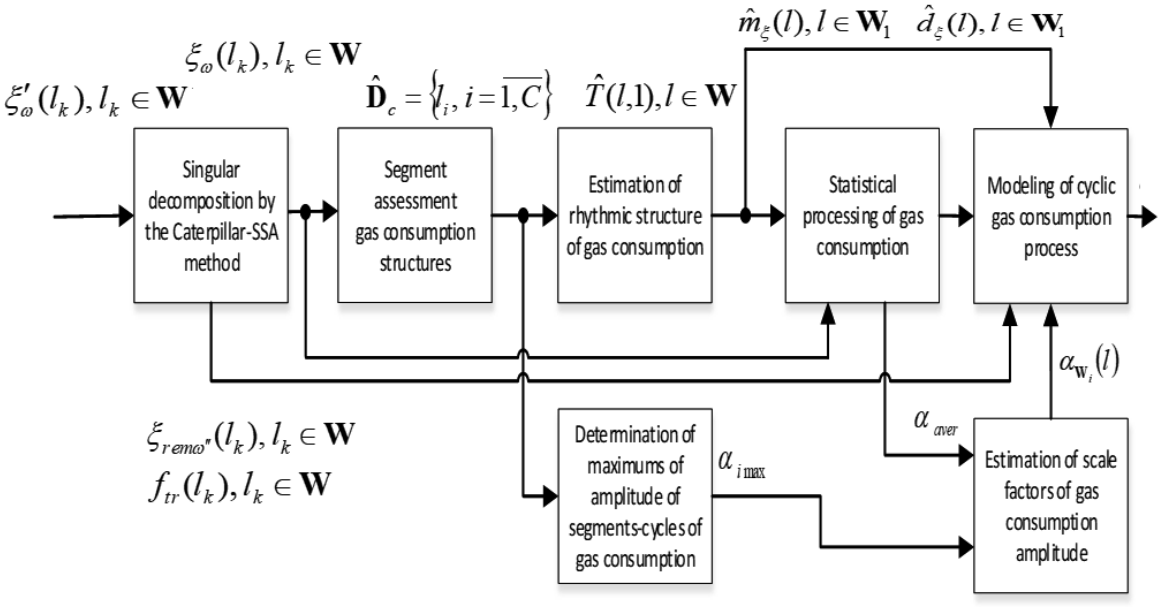

Figure 1. Block diagram of the method of computer simulation of gas consumption process

Consider and compare the results of computer simulation of gas consumption process, taking into account the scale factors of the component (11) and the component (7) of mathematical model.

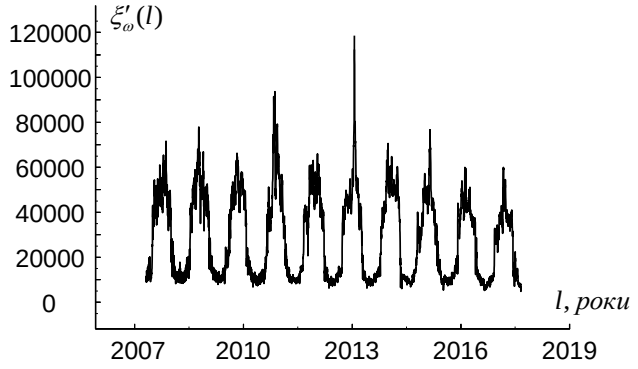

Fig. 2: Fragment of input implementation of cyclic gas consumption process

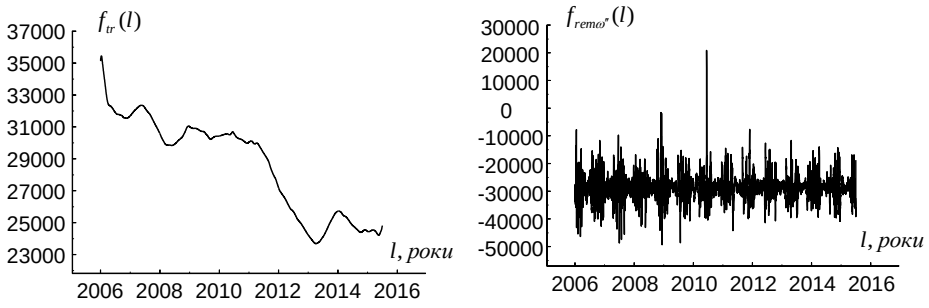

a) b)

Fig. 3: Estimated components of the mathematical model: a) trend component; b) stochastic residue

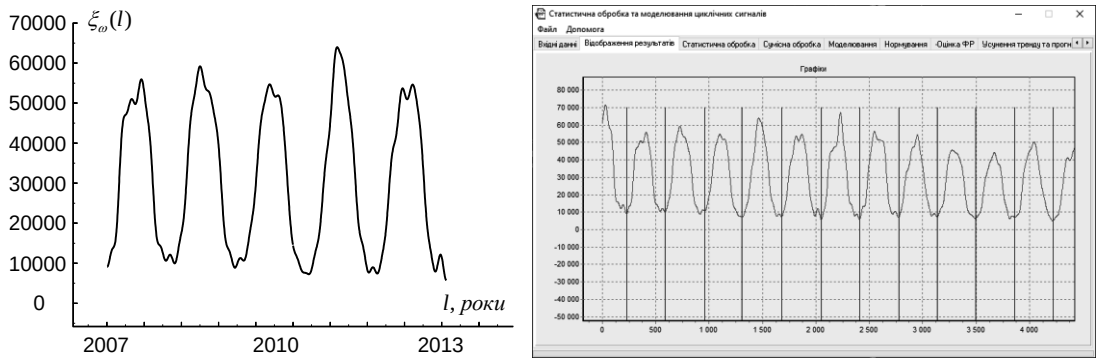

Fig. 4: Fragments of the studied implementation of gas consumption process for the case of segmentation by depressions: a) cyclic component; b) results of segmentation of the cyclic component into segments-cycles (on the abscissa axis the data are given in conventional units, the specified number of samples)

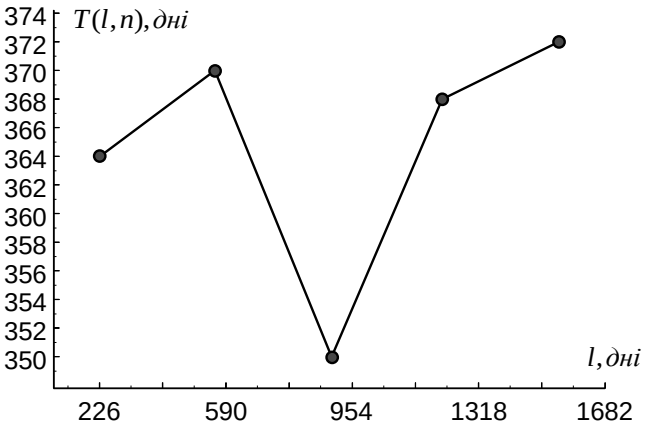

Fig. 5: Fragments of the result of estimated rhythm function (piecewise linear interpolation) of cyclic component of gas consumption process (based on segmentation into cycles by depressions)

Having obtained the segment structure $\hat{\mathbf{D}}_c$ and estimating the rhythmic structure (discrete rhythm function $T(l,n)$) by the methods proposed in [12, 13], the methods of statistical processing were applied taking into account the rhythm function [12, 13], while the estimation of mathematical expectation was determined:

$$\hat{m}_{\xi_{T(l,n)}}(l) = \frac{1}{M}\sum_{n=1}^{M}\xi_\omega\left(l+T(l,n)\right),\ l \in \mathbf{W}_1 = [l_1, l_2), \tag{14}$$

where $l_1 \neq 0$ in the general case, l_1, l_2 are discrete time samples which correspond to the beginning and end of the first segment-cycle, M is the number of cycles.

And the estimation of variance was determined as follows:

$$\hat{d}_{\xi_{T(l,n)}}(l) = \frac{1}{M}\cdot\sum_{n=1}^{M}\left[\xi_\omega\left(l+T(l,n)\right) - \hat{m}_{\xi_{T(l,n)}}\left(l+T(l,n)\right)\right]^2,\ l \in \mathbf{W}_1 = [l_1, l_2), \tag{15}$$

Applying the methods of statistical processing, we obtained statistical estimates of probabilistic characteristics (mathematical expectation $\hat{m}_{\xi_{T(l,n)}}(l), l \in \mathbf{W}_1$ and variance $\hat{d}_{\xi_{T(l,n)}}(l), l \in \mathbf{W}_1$ based on the rhythm function $T(l,n)$ of the cyclic component of gas consumption process. Examples of the obtained estimates are given in Figure 7.

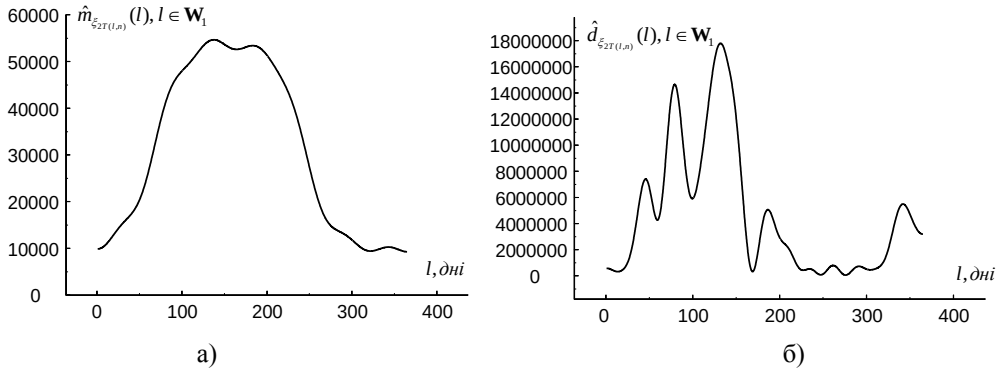

Fig. 7: Estimation of mathematical expectation and variance based on the estimated rhythm function of cyclic component of gas consumption process (segmentation into cycles by depressions): a) estimation of mathematical expectation; b) estimation of variance

Taking into account the obtained statistical estimates, carry out the computer simulation of cyclic components of gas consumption process implementations on the basis of two mathematical models (7) and (11).

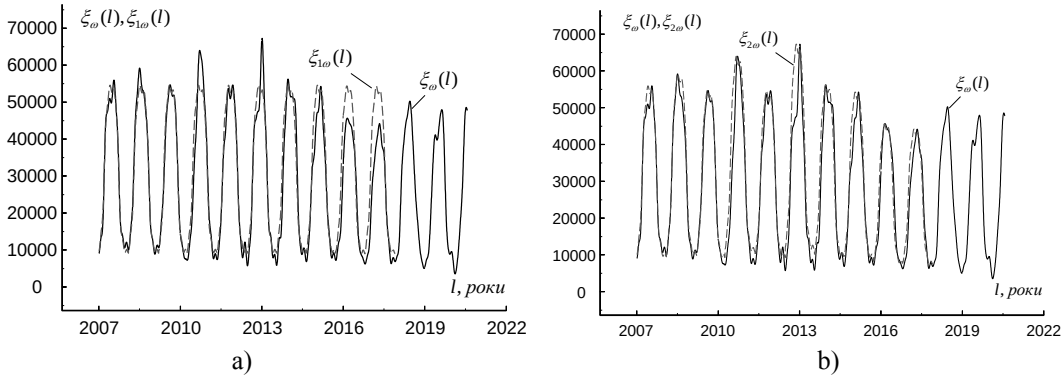

Fig. 8: Results of computer simulation of the cyclic component of gas consumption process based on two mathematical models: a) implementation of the cyclic component of gas consumption process of real data and simulated on the basis of a known model (7); b) implementation of the cyclic component of gas consumption process of real data and simulated on the basis of a new model (11)

In order to describe the approach to forecasting the gas consumption process, we determine the scale factor of gas consumption range for the forecast cycle (for example, in 2013) based on the average arithmetic value of gas consumption maximums range for 2007-2012. Note that this approach does not take into account information about climatic factors that affect the gas consumption process (temperature, pressure, humidity, etc.) for 2007-2012, as well as projected (expected) values of climatic indicators for 2013. However, the morphology of the gas consumption cycle segment $f_6(l)$ is taken into account on the basis of statistical information for previous years 2007-2012 in the form of an estimate of mathematical expectation (see Fig. 7, a).

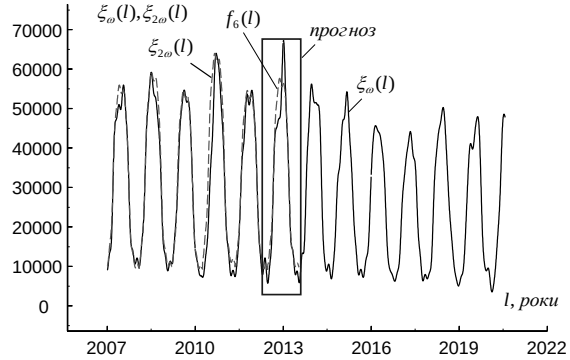

Fig. 9. Results of computer simulation of cyclic component of gas consumption process (2007-2012) and forecast of the gas consumption process for 2013

Figure 9 presents the forecast of annual gas consumption without taking into account climatic factors based on last year's gas consumption data. The dotted line shows the simulated values of gas consumption based on scale factors.

As climatic factors that significantly affect the consumption of natural gas by the population are not taken into account, the value of the maximum forecast amplitude is not defined precisely enough. In further scientific research there are going to be taken into account both climatic factors for previous years and forecasted (expected) climatic factors when drawing the annual gas consumption forecast.

Conclusions

In the research, an approach to forecasting the gas consumption process based on a mathematical model in the form of an additive mixture of three components: a cyclic random process taking into account scale factors, trend component and stochastic residue is developed. A new way to population gas consumption forecasting the is proposed, does not take into account climatic factors that significantly affect the process of gas consumption. The application of the proposed model considering the scale factors allowed to increase the accuracy of computer simulation (for 2007-2012), as evidenced by the obtained results.

In further research the values of scale factors obtained on the basis of aggregated data of climatic indicators in the developed mathematical model will be taken into account and comparative analysis of computer simulation of gas consumption based on a new mathematical model is going to be conducted.

References

1. Zagorodna, NV, Litvinenko, Ya. V., Frieze, ME (2010) Development of a method for short-term forecast of daily gas consumption during the heating period based on regression analysis. Journal of Ternopil National Technical University. Ternopil, No.4 P. 130–140.
2. Zagorodna, N., RKozak, R., Gancarczyk, T., Falat, P. (2016) Methods of monitoring, analysis and short-term prognosis of gas consumption taking into consideration its cyclic and non-stationary structure in heating season. 16th International Conference on Control, Automation and Systems (ICCAS). 16-19 Oct. 2016. P. 501-505. DOI:10.1109/ICCAS.2016.7832366
3. Mahdieh, O., Shahram, J., Reza, S-N. (2013) The Forecasting of Iran Natural Gas Consumption Based On Neural-Fuzzy System Until 2020 M. International Journal of Smart Electrical Engineering. Summer 2013, Vol. 2, No. 3; P. 181 - 184.
4. Wei, Z., and Jun Y.(2015) Forecasting natural gas consumption in China by Bayesian Model Averaging, Energy Reports, ISSN 2352-4847, Elsevier, Amsterdam, Vol. 1, pp. 216-220, DOI:10.1016/j.egyr.2015.11.001
5. Boran, F.E. (2014). Forecasting natural gas consumption in Turkey using Grey prediction. Energy Sources Part B 10, 208–213. https://doi.org/10.1080/15567249.2014.893040
6. Demirel, O.F., Zaim, S., Caliskan, A., Ozuyar, P. (2012). Forecasting natural gas consumption in Istanbul using neural networks and multivariate time series methods. Turkish J. Electr. Eng. Comput. Sci. 20 (5), 695–711. DOI:10.3906/elk-1101-1029
7. Gil, S., Deferrari, J. (2004). Generalized model of prediction of natural gas consumption. Trans. ASME 126 (2), 90–98. DOI:10.1115/1.1739239
8. Li, Y., Zhang, X., Li, T. (2014) China's Natural gas demand forecast based on the combination forecasting model. Henan Sci. 32 (10), 2138–2144. (in Chinese).
9. Szoplik, J. (2015) Forecasting of natural gas consumption with artificial neural networks. Energy 85, 208–220. DOI: 10.1016/j.energy.2015.03.084
10. Golyandina, N., Zhigljavsky, A. Singular (2020) Spectrum Analysis for Time Series / N. Golyandina, A. Zhigljavsky // SpringerBriefs in Statistics. Springer-Verlag Berlin Heidelberg. – 2020. P. 146.
11. Lytvynenko, I.V. (2017) The method of segmentation of stochastic cyclic signals for the problems of their processing and modeling. Journal of Hydrocarbon Power Engineering, Oil and Gas Measurement and Testing. 2017, Vol. 4, No. 2, pp. 93–103.
12. Lytvynenko, I.V. Lupenko, S.,Onyskiv, P. (2020). Method of Evaluation of Discrete Rhythm Structure of Cyclic Signals with the Help of Adaptive Interpolation. IEEE 15th International Scientific and Technical Conference on Computer Sciences and Information Technologies, CSIT 2020 - Proceedings, 2020, 1, pp. DOI: 10.1109/CSIT49958.2020.9321878
13. I. Lytvynenko, I., Horkunenko A., Kuchvara O., Palaniza Y. (2019). Methods of processing cyclic signals in automated cardiodiagnostic complexes. Proceedings of the 1st International. Workshop on Information-Communication Technologies & Embedded Systems, (ICT&ES-2019), Mykolaiv, November 13-14, 2019, Ukraine, 2019. P.116-127.

ALPHABETICAL INDEX

PROCEEDINGS of INTERNATIONAL CONFERENCE "ADVANCED APPLIED ENERGY and INFORMATION TECHNOLOGIES 2021"

December 15 – 17, 2021

ISBN: 978-617-8079-60-4

Editors: **Keyue SMEDLEY, Alexander ABRAMOVITZ, Frantisek DUCHON**
Technical Editor: YASKIV Volodymyr, FILIUK Yaroslav (Ternopil Ivan Puluj National Technical University, Ukraine)
All graphic material: Authors
Cover design: FILIUK Yaroslav (Ternopil Ivan Puluj National Technical University, Ukraine)
Design and Layout: FILIUK Yaroslav, NAKONECHYI Myroslav (Ternopil Ivan Puluj National Technical University, Ukraine)
Publisher: Zhytomyr, «Publishing house "Book-Druk"» LLC

Conference site: http://icaaeit.tntu.org.ua; **e-mail:** icaaeit@gmail.com;

Формат 60х84/8. Ум. друк. арк. 25,8.
Наклад 45 прим. Зам. № 0061.

Видавець
ТОВ «Видавничий дім “Бук-Друк”»
м. Житомир, вул. М. Бердичівська, 17А.
тел.: 063 101 22 33

Свідоцтво серія ДК № 7412 від 27.07.2021 р.

Друк та палітурні роботи ФОП О.О. Євенок
м. Житомир, вул. М. Бердичівська, 17А
тел.: 063 101 22 33, e-mail: bookovych@gmail.com

Свідоцтво серія ДК № 3544 від 05.08.2009 р.